Current Distribution and Hall Potential Landscape within the Quantum Hall Effect in Graphene and towards the Breakdown in a (Al,Ga)As Heterostructure

Von der Fakultät Mathematik und Physik der Universität Stuttgart
zur Erlangung der Würde eines
Doktors der Naturwissenschaften (Dr. rer. nat.)
genehmigte Abhandlung

Vorgelegt von

Konstantinos Panos

aus Reutlingen

Hauptberichter:	Prof. Dr. Klaus von Klitzing
Mitberichter:	Prof. Dr. Peter Michler
Tag der mündlichen Prüfung:	5.3.2014

Max-Planck-Institut für Festkörperforschung
Stuttgart, 2014

Contents

1. **Introduction** 1

I. **Principles of the quantum Hall effect** 3

2. **Structure and electrical properties of GaAs/Al$_x$Ga$_{1-x}$As-heterostructures** 7
   - 2.1. Landau level quantization . . . 8

3. **Structure and electrical properties of graphene** 11
   - 3.1. 2D crystal lattice of graphene and resulting band structure . . . 12
   - 3.2. Typical electrical transport measurements . . . 15
   - 3.3. Landau level formation in graphene . . . 16
     - 3.3.1. Experimental evidence for Landau level quantization in graphene 16
   - 3.4. Fabrication methods . . . 17
   - 3.5. Influence of the substrate . . . 18

4. **Quantum Hall effect: Present microscopic picture** 21
   - 4.1. Evolution of Hall potential profiles in GaAs/Al$_x$Ga$_{1-x}$As-heterostructures under QHE conditions . . . 22
   - 4.2. Depletion region of a 2DES: CSG-model for the electron concentration profile at 2DES edges . . . 25
   - 4.3. Self-consistent calculation . . . 27
   - 4.4. Current within incompressible stripes . . . 28
   - 4.5. Potential probes . . . 29
   - 4.6. Hot spots . . . 30
   - 4.7. Evolution of the QHE . . . 31

II. **Principles of the measurement technique** 33

5. **Scanning Force Microscopy** 35
   - 5.1. Relevant forces . . . 35
   - 5.2. Intrinsic potential difference and contact voltage . . . 38
   - 5.3. Mechanisms to detect the cantilever deflection . . . 38
   - 5.4. Dynamics of a cantilever . . . 40
     - 5.4.1. Dynamics of a cantilever under external forces . . . 41
   - 5.5. Scanning modes . . . 43
     - 5.5.1. Contact mode . . . 43

5.5.2. Intermittent mode 45
5.5.3. Non-contact mode 45
5.6. Operation principle of a scanning probe microscope 46
5.7. Summary 47

6. Measuring Hall potential profiles of a 2DES: Calibration technique 49
6.1. Detecting alterations: Switching between equilibrium and non-equilibrium 49
6.2. Considerations about form of switching 51
6.3. Effect of charge carrier density modulation 53
6.4. Voltage bias between tip and sample to avoid an electrostatic depletion 54
6.5. Summary 56

III. Microscopic picture of the QHE in graphene 57

7. Sample fabrication 61

8. Characterization of the flake 63

9. Scanning probe measurements 67
9.1. Interpretation in terms of compressible and incompressible stripes . . . 67
9.2. Presence of electron depletion and hole accumulation towards the edges 70
9.3. Back gate effect: not dominant 72
9.4. Fixed negative charges: matching our findings 74
9.5. Arrangement of fixed negative charges: simulation of various models . . 76
9.5.1. Homogeneous area charge arrangement 76
9.5.2. Effect of a fixed line charge distribution 79
9.5.3. Effect of surface charge distribution 81
9.5.4. Influence of doping 84
9.6. Possible origin of fixed charges 84
9.6.1. Edge chemistry of graphene 84
9.6.2. Edge effects 85
9.6.3. Surface effects 85
9.6.4. Silicon dioxide bulk effects 86
9.7. Consequences for the charge neutrality point 87
9.8. Summary 90

10. Influence of disorder in graphene on the QHE 95
10.1. Topographic bubbles 95
10.2. Domains with different charge carrier concentration 102
10.3. Summary 106

11. Summary 107

IV. Breakdown of the quantum Hall effect 109

12. Introduction to the breakdown of the QHE 113
- 12.1. Defining the breakdown . . . 113
- 12.2. Breakdown as limit for metrological accuracy . . . 114
- 12.3. Findings from previous experimental works . . . 115
  - 12.3.1. Sample geometry . . . 115
  - 12.3.2. Local probing . . . 116
  - 12.3.3. Other aspects . . . 117
- 12.4. Proposals for breakdown mechanisms . . . 117
- 12.5. Summary . . . 120

13. Towards the microscopic picture of the breakdown of the QHE 121
- 13.1. Sample characteristics and geometry . . . 122
- 13.2. Breakdown in transport . . . 122
- 13.3. Breakdown in line scans . . . 125
- 13.4. Edge-dominated breakdown . . . 128
  - 13.4.1. Simple model for the current distribution at the edge-dominated QHE . . . 130
  - 13.4.2. Consequences for the edge-dominated breakdown . . . 136
- 13.5. Bulk-dominated breakdown . . . 138
- 13.6. Transition region between edge- and bulk-dominated breakdown . . . 144

14. Conclusions and summary 147
- 14.1. Fitting of other experiments into our model . . . 148

V. Summary 151

15. Summary 153
- 15.1. Measurement technique . . . 154
- 15.2. QHE in graphene . . . 154
- 15.3. Breakdown of the QHE . . . 155
- 15.4. Outlook . . . 157

16. Zusammenfassung 159
- 16.1. Messtechnik . . . 160
- 16.2. QHE in Graphen . . . 160
- 16.3. Zusammenbruch des QHE . . . 162
- 16.4. Ausblick . . . 163

VI. Appendix 167

A. Sugestions for further experiments 169
- A.1. Graphene . . . 169
  - A.1.1. Finding the origin of fixed charges . . . 169

A.1.2. Consequences of the fixed charges 170
A.1.3. Breakdown of the QHE in graphene 172
A.2. Breakdown 172
A.3. SQUID measurements 174

B. Electrostatic simulations of graphene edges 177
B.1. Gauss-Seidel method to solve Poisson equation 179
B.2. Simple test on a line charge distribution 180
B.3. Charge transfer algorithm 184
B.4. Influence of the back gate on the edge 186
B.5. Summary 190

C. Models for fixed charge arrangements 193
C.1. Empirical function and parameter for a fixed line charge at the edge . . 193
C.2. Effect of line charge displacement 195
C.3. Including the doping 195
C.4. Empirical function and parameter for surface charges 197
C.5. Conclusion 201

D. Line charge model and GaAs/Al$_x$Ga$_{1-x}$As-heterostructures 203

E. Electric fields and Landau levels 207
E.1. Free electron ansatz 207
E.2. Bloch electron ansatz 208
E.3. Landau levels and electric fields in graphene 209
E.4. Conclusion 210

F. Electrostatic problems and elimination of dielectric constants 211

G. Artefacts and error sources 213
G.1. Theoretic considerations for artefacts in electrostatic force microscopy . 213
G.1.1. Sinusoidal modulation of tip-sample voltage 213
G.1.2. Rectangular modulation of tip-sample voltage 215
G.2. Setup related artefacts 216
G.2.1. Background noise 216
G.3. Sample related artefacts 217
G.3.1. Sample topography 217
G.3.2. Edges 218
G.4. Current induced artefacts 218
G.4.1. Parabola shift due to charge carrier density changes 218
G.4.2. Charging events 220
G.5. Comments on the GB8113 graphene samples 220
G.6. Summary 224

H. Sample parameter, geometry and processing 227
H.1. Graphene samples 227
H.1.1. Fabrication 227

H.1.2. Samples' characteristics 228
H.2. GaAs/Al$_x$Ga$_{(1-x)}$As-heterostructure samples 229
H.2.1. Fabrication 229
H.2.2. Samples' characteristics 232

I. Scanning tip properties and processing 239

J. Breakdown data 243
J.1. Sample 8379_20100120_B 243
J.2. Sample 8957_201112_B 246
J.2.1. Area scans for $B = 6.8\,\mathrm{T}$, $\nu \approx 1.94$ for current direction (i) . . . 250
J.2.2. Area scans for $B = 6.8\,\mathrm{T}$, $\nu \approx 1.94$ for current direction (j) . . . 258
J.2.3. High resolution area scans for $B = 6.8\,\mathrm{T}$, $\nu \approx 1.94$ 266
J.2.4. Area scans for $B = 6.1\,\mathrm{T}$, $\nu \approx 2.16$ for current direction (i) . . . 268
J.2.5. Area scans for $B = 6.1\,\mathrm{T}$, $\nu \approx 2.16$ for current direction (j) . . . 270
J.2.6. Area scans for $B = 6.55\,\mathrm{T}$, $\nu \approx 2.02$ 272
J.2.7. Area scans for $B = 6.5\,\mathrm{T}$, $\nu \approx 2.03$ 273

K. Bibliography 275

Symbols

Latin symbols

a	Shifting length between the two triangular sublattices in graphene
A	Apparent from context: Oscillation amplitude or curvature of the resonance shift parabola
$\vec{A}$	Vector potential
$\vec{a}_1$, $\vec{a}_2$	Basis vectors of a sublattice in graphene
A_0	Oscillation amplitude at resonance frequency
a_B^*	Effective Bohr radius
a_BGF	Back gate calibration factor
a_k	Width of the k-th incompressible stripe
b	Damping coefficient
B	Magnetic field
$\tilde{B}$	Reduced magnetic field
$\vec{b}_1$, $\vec{b}_2$	Basis vectors in reciprocal space
c	Distance from sample center where the charge carrier density becomes zero
C	Capacitance
c_l	Calibration constant for the line charge profile
c_s	Calibration constant for the surface charge profile
d	Apparent from context: thickness of silicon dioxide layer or distance
d_0	Depletion stripe width at the sample edge
D_it	Interface state density
$D(\varepsilon)$	Density of states
E	Apparent from context: electric field or energy
E_c	Critical electric field
f	Frequency
F	Force
f_0	Resonance frequency of an undamped oscillator
F_exc	Excitation force
F_pot	Potential force
$f(E)$	Fermi distribution function
H	Apparent from context: Hamilton operator or Hamakar constant
(i)	Specifier for one of two possible current directions. Current is oriented opposite to (j)
i, j	Indices of the numerical grid positions
I	Current

$I_{\mathrm{cr\_inter}}$	Critical current due to QUILLS
$I_{\mathrm{cr\_intra}}$	Critical current due to Cherenkov-like phonon emission
$I_{\mathrm{r}}, I_{\mathrm{l}}$	Current through the right and left incompressible stripe
(j)	Specifier for one of two possible current directions. Current is oriented opposite to (i)
k	Apparent from context: incompressible stripe index or spring constant
$\vec{k}$	Wave vector in reciprocal space
$k_{x,\mathrm{off}}$	x-axes offset of an ellipse in $\vec{k}$-space
l	Sample length
l_B	Magnetic length
m	Mass
m^*	Effective mass
n	Electron concentration
N	Apparent from context: Landau level index or number of charge carriers
$\mathcal{N}$	Number of charge carriers per unit length
n_{t}	Threshold charge carrier density where we stop filling the band
n_{L}	Landau level degeneracy for electrons
p	Apparent from context: pressure, power density, or hole concentration
P_{j}	Joule heating power
$\hat{p}$	Momentum operator
p_{L}	Landau level degeneracy for holes
p_x, p_y, p_z	x, y and z momentum operators
q	Charge
Q	Quality factor
q_{down}	Charges on the down side of a plate capacitor.
q_{m}	Mirror charge
q_{t}	Charge transfer parameter
q_{up}	Charges on the up side of a plate capacitor
R	Apparent from context: Resistance or radius
$\vec{R}$	Graphene atomic site position
R_{xx}	Longitudinal resistance
R_{xy}	Transversal or Hall resistance
S	Surface area
t	Distance from sample center where threshold charge carrier density n_t is reached
T	Apparent from context: oscillation/cycle period or temperature
T_e	Electron temperature
T_L	Lattice temperature
V	Apparent from context: bias voltage or volume
V_A	Modulation amplitude
V_{AC}	Voltage amplitude
V_B	Offset between parabola maximum and the working point
$V_{\mathrm{B-CNP}}$	Back gate voltage for charge neutrality in the bulk of a finite size sample
V_{BG}	Back gate voltage
$V_{\mathrm{BG-appl}}$	Applied back gate voltage in contrast to effective back gate voltage

	V_{BG}
V_{CNP}	Back gate voltage for charge neutrality in sample without edge effects
V_{com}	Voltage commonly applied on source and drain
v_{D}	Drift velocity
V_{D}	Drain voltage (relative to reference)
V_{DC}	DC voltage offset
v_{F}	Fermi velocity
V_{G}	Gate voltage (relative to reference)
V_{ID}	Current voltage converter output voltage proportional to drain current
V_{in}	Input signal for a lock-in amplifier
V_{IS}	Current voltage converter output voltage proportional to source current
$V_{\mathrm{IF-CNP}}$	Back gate voltage for charge neutrality in a infinite extended sample
V_{LI}	Output voltage of the lock-in amplifier feed with the tip resonance frequency shift
V_{LIA}	Output voltage of the lock-in amplifier while measuring the compensation voltage
$V_{\mathrm{LI}\alpha}$	Output voltage of the lock-in amplifier during current flow
$V_{\mathrm{LI}\beta}$	Output voltage of the lock-in amplifier during calibration run
$V_{\mathrm{LI-R}}$	Output voltage of the lock-in amplifier with rectangular excitation
$V_{\mathrm{r}}, V_{\mathrm{l}}$	Voltage across the right and left incompressible stripe
V_{Rmax}	Back gate voltage at the maximum of the resistance curve
V_{PM}	Tip to sample voltage to reach the maximum of the frequency shift parabola
V_{S}	Source voltage (relative to reference)
v_{s}	Sound velocity
V_{Tip}	Tip voltage (relative to reference)
x, y, z	Cartesian coordinates
w	Sample width
W_{c}	Capacitive energy
W_{vdW}	van der Waals potential energy
W_{i}	Interaction energy of ions
W_{m}	Energy due to mirror charges
$w_{\mathrm{r}}, w_{\mathrm{l}}$	Width of the right and left incompressible stripe
W_{short}	Short range potential energy
Y_E	Central coordinate
y_k	Distance to sample edge of the k-th incompressible stripe
Z	Mean electron activation energy due to temperature

Greek symbols

β	Drift velocity over Fermi velocity
γ	Berry phase
γ_0	Bonding energy of a π-bond

δ	Grid period
Δf	Resonance frequency shift
$\Delta\phi_{\text{int}}$	Internal or intrinsic part of electrostatic potential difference
ΔV_{FWHM}	Full width at half maximum of a graphene resistance over back gate voltage curve
ε	Single electron energy
$\varepsilon(k)$	Band structure, here explicitly of graphene
$\varepsilon_{\text{GaAs}}(k)$	Band structure of a GaAs/Al$_x$Ga$_{1-x}$As-heterostructure
$\varepsilon_{\text{GaAs}}(N)$	Landau level spectrum of a GaAs/Al$_x$Ga$_{1-x}$As-heterostructure
$\varepsilon_{\text{graphene}}(k)$	linear approximated band structure of graphene
$\varepsilon_{\text{graphene}}(N)$	Landau level spectrum of graphene
η	Total charge carrier concentration. Sign indicates carrier type
η_0	Back gate induced charge carrier concentration. Sign indicates carrier type. Edge effects not included
η_{d}	Charge carrier concentration induced by doping. Sign indicates carrier type
η_{D}	Dopants concentration. Sign indicates carrier type
η_{fl}	Line charge carrier density. Sign indicates carrier type
η_{fs}	Surface charge carrier density. Sign indicates carrier type
η_{l}	Line charge induced charge carrier concentration. Sign indicates carrier type
η_{m}	Charge carrier concentration induced by the back gate including edge effects
η_{Rmax}	Flake doping calculated from the resistance maximum
η_{s}	Surface charge induced charge carrier concentration. Sign indicates carrier type
θ_{H}	Hall angle
κ	Electrical compressibility
μ	Mobility
μ_{ch}	Chemical potential (energy)
μ_{elch}	Electrochemical potential (energy)
ν	Landau level filling factor
π	Binding band formed from p-orbitals
π^*	Antibinding band formed from p-orbitals
$\hat{\Pi}$	Momentum operator including magnetic field
ρ	Apparent from context: charge carrier density or resistivity
$\rho_{i,j}$	Charge carrier density at site (i,j)
σ	Conductivity
$\vec{\sigma}$	Matrix vector: $\vec{\sigma} = (\sigma_x, \sigma_y)$
σ^{ac}	Activation conductivity
σ_x	Pauli matrix: $\begin{pmatrix} 0 & 1 \\ 1 & 0 \end{pmatrix}$
σ_y	Pauli matrix: $\begin{pmatrix} 0 & -i \\ i & 0 \end{pmatrix}$
σ_z	Pauli matrix: $\begin{pmatrix} 1 & 0 \\ 0 & -1 \end{pmatrix}$

τ	Relaxation time
$\vec{\tau}$	Relative shift between the two triangular sublattices in graphene
ϕ	Apparent from context: electrostatic potential or wave function or phase
$\hat{\phi}$	Calibrated current-induced electrostatic potential changes
$\phi_{i,j}$	Potential at site (i, j)
ψ	Apparent from context: wave function or imaginary part of conjugate function
Ψ	Two-component wave function
ψ_A	Graphene wave function of sublattice A
ψ_B	Graphene wave function of sublattice B
ω_0	Resonance angular frequency of an undamped oscillator
ω_c	Cyclotron angular frequency
ω_m	Angular frequency of modulation
ω_r	Resonance angular frequency

Abreviations

2DES	Two-dimensional electronic system
2DHS	Two-dimensional hole system
CNP	Charge neutrality point
CSG	Chklovskii, Shklovskii and Glazman
CVD	Chemical vapor deposition
HOPG	Highly oriented pyrolytic graphite
IPA	Isopropanol
MIBK	Methyl isobutyl ketone
NEP	N-Ethylpyrrolidon
PLL	Phase locked loop
PMMA	Polymethyl methacrylate
QHE	Quantum Hall effect
QUILLS	Quasi-elastic inter-Landau-level scattering
SEM	Scanning electron microscopy
SFM	Scanning force microscopy
SPM	Scanning probe microscopy
STM	Scanning tunneling microscopy
STS	Scanning tunneling spectroscopy

Constants [1]

e	$1.602176487 \cdot 10^{-19}\,\mathrm{C}$	Elementary charge
ϵ_0	$8.854187817... \cdot 10^{-12}\,\mathrm{Fm}^{-1}$	Electric constant $1/\mu_0 c^2$

h	$6.62606896 \cdot 10^{-34}\,\mathrm{Js}$	Planck constant
$\hbar$	$1.054571628 \cdot 10^{-34}\,\mathrm{Js}$	Reduced Planck constant
k_B	$1.3806504 \cdot 10^{-23}\,\mathrm{JK}^{-1}$	Bolzmann constant
m_e	$9.10938215 \cdot 10^{-31}\,\mathrm{kg}$	Electron mass
$\phi_0 = \frac{h}{e}$	$4.135667334 \cdot 10^{-15}\,\mathrm{Wb}$	Magnetic flux quantum
$R_\mathrm{K} = \frac{h}{e^2}$	$25812.807557\,\Omega$	von Klitzing constant
R_K90	$25812.807\,\Omega$	Conventional value of von Klitzing constant

It should be mentioned that during the preparation of this work new CODATA recommended values for some used constants were published [2]. The changes have no significant impact within our accuracy and precision demands. Thus the recommended values of 2006 published in 2008 [1] are used throughout this thesis.

Material parameters

Silicon dioxide [3]

ϵ_r	3.9	Relative permittivity

Galiumarsenide [4]

ϵ_r	13.1	Relative permittivity
$\Delta\varepsilon_\mathrm{Gap}$	$1.43\,\mathrm{eV}$	Band gap
a	$0.564\,\mathrm{nm}$	Lattice constant
m^*	$0.067 \cdot m_e$	Effective mass of electron in the conduction band

Aluminumarsenide [4]

ϵ_r	10	Relative permittivity
$\Delta\varepsilon_{\mathrm{Gap}_\mathrm{i}}$	$2.15\,\mathrm{eV}$	Indirect band gap
$\Delta\varepsilon_{\mathrm{Gap}_\mathrm{d}}$	$3.14\,\mathrm{eV}$	Direct band gap
a	$0.566\,\mathrm{nm}$	Lattice constant

1. Introduction

One might think that the quantum Hall effect, 34 years after its discovery in 1980 by Klaus von Klitzing [5] (Nobel Prize 1985), has become unattractive for scientists today. In contrast, several new material systems and sub-classes of the effect bring vibrant interest into the semiconductor physics community. Recent topics are graphene with its linear bandstructure and "half-integer" QHE [6], HgTe quantum wells as a topological insulator with the quantum spin Hall effect (QSH) [7], and ferromagnetic (Bi, Sb)$_2$Te thin films with quantized Hall resistance plateaus without externally applied magnetic field called quantum anomalous Hall effect (QAH) [8], just to name the most important systems and effects.

Also metrology is preparing for a huge change - namely the conversion of the international system of units (SI) from man-made standards to natural constants [9]. The QHE is thereby important not only as a resistance standard [2] but also for the redefinition of the kilogram and the ampere [10, 11]. As a result the kilogram will be linked to the Planck constant h and the ampere to the elementary charge e by fixing the values of e and h. The current value for the resistance standard defined in 1990 as $R_{\mathrm{K-90}} = 25812.807\,\Omega$ has to be redefined. Therefore a solid understanding of the QHE is required.

Before beginning this work, there were already scanning probe measurements dealing with several aspects of the QHE [12–19]. The main result was today's microscopic picture of the QHE with current flow within so-called incompressible regions. An evolution of the current distribution with magnetic field was found that repeats itself on every quantum Hall plateau. The edge of the device, where the carrier density changes to zero on a length scale of a micrometer, has strong influence on the symmetry of the plateaus and the current distribution. At the low magnetic field side of a plateau the current flows within narrow stripes close to the edges. With increasing magnetic field the stripes become wider and shift towards the sample center, until they merge and the current then flows mainly in the sample bulk. In this regime, disorder stabilizes the QHE. These experiments contradict the often used Halperin-Landauer-Büttiker-picture, where current is assumed to flow in chiral edge states at the Fermi level.

Two main questions not addressed yet by the previous scanning probe experiments are addressed in this thesis. Namely, how graphene with its special bandstructure and the possibility to tune the system continuously from a n-type to a p-type material fits into today's microscopic picture, and what the microscopic evolution towards the breakdown of the QHE in GaAs/Al$_x$Ga$_{1-x}$As heterostructure samples is. The measurements were done on small devices with a width on the order of 10 µm. The confinement potential of the edges is reaching far into such devices and reduces the effect of the bulk.

This thesis is divided into six parts starting with two parts presenting essential background, before going on to the main experimental results. In part I we introduce the materials studied as well as today's microscopic picture of the QHE. In part II the measurement technique used to acquire the Hall potential profiles is recapped. Basic measurements on graphene will follow in part III where not only the microscopic picture of the QHE in graphene will be presented but more interestingly what we can learn about the graphene edges. The breakdown of the QHE will be studied in part IV and measurements of the Hall potential profiles evolution will be shown. The Hall potential profiles give the first clear and conclusive picture of the breakdown evolution and demonstrate that at least two breakdown scenarios exist. The summary of this thesis can be found in part V. Finally, in part VI we give supplementary information for the interested reader including suggestions for subsequent experiments and further details on the theoretical and experimental approaches.

Part I.

Principles of the quantum Hall effect

In this part of the thesis we want to lay the fundamentals for our later discussion and interpretation. We will first give some insights to the two material systems measured, namely in chapter 2 GaAs/Al$_x$Ga$_{1-x}$As-heterostructures and in chapter 3 graphene. Details on the high magnetic field behavior, in particular the Landau level formation, will be given.

Today's microscopic picture of the QHE will be built up in chapter 4 starting from the experiments of Peter Weitz and Erik Ahlswede in section 4.1. From the evolution with magnetic field seen in these measurements the depletion regions at the sample edges are important for the understanding. We will present in section 4.2 an analytic model that includes the self-screening of electrons and the depletion towards the edges. The model predicts the formation of two types of regions, where the electrochemical potential lies either within electronic states or within a gap region without electronic state. Self-consistent simulations described in section 4.3 overcome the problem of the analytic model, which is not self-consistent but give essentially the same result. The two types of regions are called compressible and incompressible regions because of their capability of changing the electron density. It may sound obvious how current flows with an applied bias, but in fact it is not. The experiments of Peter Weitz and Erik Ahlswede show that the current path coincides with the position of incompressible regions. That are the regions were the electrochemical potential lies in the gap without electronic states, as will be discussed in section 4.4. We will further take a look on potential probes, in section 4.5, and the formation of so called "hot-spots" at the source and drain contacts, in section 4.6. All together will be summarized on a final discussion about the evolution of QHE with magnetic field in section 4.7.

2. Structure and electrical properties of GaAs/$\mathrm{Al}_x\mathrm{Ga}_{1-x}$As-heterostructures

Gallium arsenide (GaAs) is a direct band gap semiconductor with a gap of 1.43 eV. Aluminum arsenide (AlAs) on the other hand is an indirect band gap semiconductor with a gap of 2.15 eV. The lattice constants of 0.564 nm for GaAs and 0.566 nm for AlAs do match nearly perfectly. Subsequent growth on each other is therefore possible with low defect density and interchange of gallium and aluminum in a continuous way is possible. The interchange is indicated with the x in $\mathrm{Al}_x\mathrm{Ga}_{1-x}$As and the interchangeability also allows for band gap engineering.

The GaAs/$\mathrm{Al}_x\mathrm{Ga}_{1-x}$As-heterostructures used in this thesis are modulation doped, a concept first applied by Dingle et al. [20], which reduces scattering of electrons on ionized donors. This allowed for high carrier mobilities and mean free paths and led to the discov-

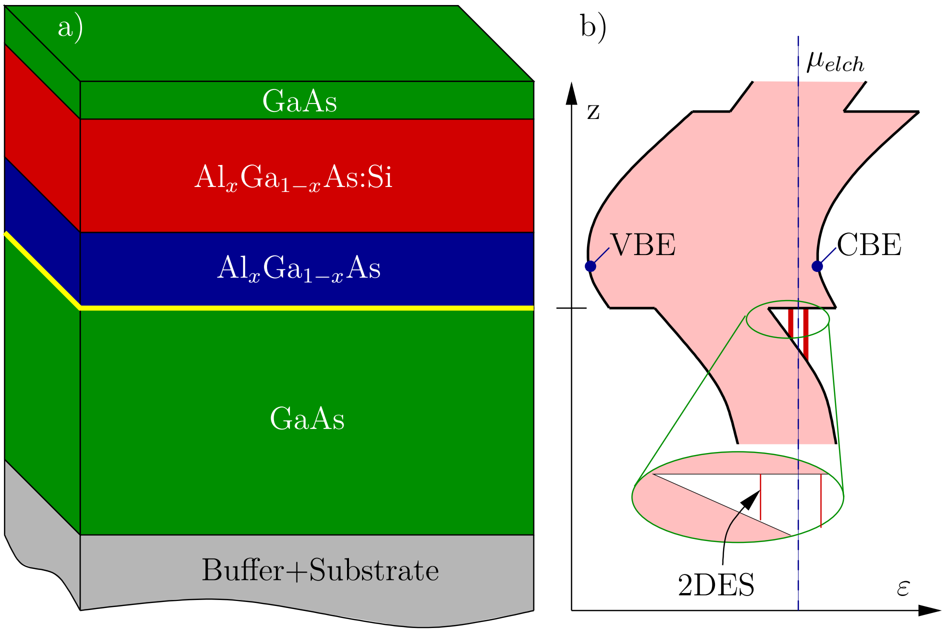
a)
GaAs
$\mathrm{Al}_x\mathrm{Ga}_{1-x}$As:Si
$\mathrm{Al}_x\mathrm{Ga}_{1-x}$As
GaAs
Buffer+Substrate
b)
μ_{elch}
z
VBE
CBE
2DES
ε

Figure 2.1.: Layer sequence of a GaAs/$\mathrm{Al}_x\mathrm{Ga}_{1-x}$As-heterostructures used in this work. In (a) the structure is shown and reads from top to bottom: Cap layer to protect against oxidation, doping layer with silicon as dopant, spacer to keep a distance between ionized dopants and 2DES, in yellow the interface where a triangular potential confines the 2DES, the gallium arsenide layer, lying on top of the buffer and substrate. In (b) the bending of the valence band edge (VBE) and conduction band edge (CBE) are shown.

ery of the fractional QHE [21, 22] and boosted the vast field of two- to zero-dimensional electron systems.

As shown in Fig. 2.1, the two-dimensional electron system (2DES) is positioned at the GaAs/$\mathrm{Al}_x\mathrm{Ga}_{1-x}$As interface with $x = 0.33$ for the heterostructures used in this work. The dopants are within the $\mathrm{Al}_x\mathrm{Ga}_{1-x}$As layer and are separated in addition by an $\mathrm{Al}_x\mathrm{Ga}_{1-x}$As spacer layer from the 2DES. This separation reduces scattering on ionized donors and increases the mobility of the electrons. This is the previous mentioned modulation-doping technique and is used also in high electron mobility transistors (HEMTs) [23]. The cap layer on top of the structure protects the covered $\mathrm{Al}_x\mathrm{Ga}_{1-x}$As layer from oxidation and pins at room temperature the electrochemical potential in the middle of the band gap of GaAs due to surface states. The buffer layer which consists of alternating layers of GaAs and AlAs is grown to smoothen the surface of the substrate.

Nowadays the typical electron mobility for such structures can reach easily $100\,\mathrm{T}^{-1}$ at a temperature of about 1 K. Values up to $360\,\mathrm{T}^{-1}$ have been reported [24]. High mobilities are equivalent to a low scattering center concentration allowing for long mean free paths. Thus the study of quantum interference and correlation effects like the fractional QHE becomes possible. Also very important is the behavior of a 2DES under high magnetic fields. The so-called Landau level quantization is observable and will be discussed in the next section.

2.1. Landau level quantization

Putting a 2DES into a perpendicular magnetic field enforces the electrons on cyclotron orbits and leads to a quantization of the allowed eigen-energies, called Landau levels. A very vivid way to understand the formation of Landau levels in a magnetic field is a semiclassical approximation: Due to the Bohr-Sommerfeld quantization rule, a Bloch electron on a closed orbit has to accumulate a phase of multiples of 2π plus a constant, which is, because of the lattice symmetry [25, 26],

$$\oint \vec{k} d\vec{r} = 2\pi(N + \frac{1}{2} - \frac{\gamma}{2\pi}). \tag{2.1}$$

γ is thereby the Berry phase [27,28] acquired after a closed loop within the crystal lattice. The Berry phase is zero for GaAs/$\mathrm{Al}_x\mathrm{Ga}_{1-x}$As-heterostructures. It was Onsager [26] who first used the Bohr-Sommerfeld quantization to find the allowed quantized cyclotron orbits of electrons in solids. Using the motion equation for a Bloch electron in a crystal lattice

$$\hbar\dot{\vec{k}} = -e\dot{\vec{r}} \times \vec{B}, \tag{2.2}$$

one finds the flux through the area enclosed by the orbit is quantized in units of the flux quantum $\phi_0 = h/e$

$$\frac{1}{2}\vec{B} \oint \vec{r} \times d\vec{r} = \phi_0(N + \frac{1}{2} - \frac{\gamma}{2\pi}). \tag{2.3}$$

In the k-space for a magnetic field in z direction one gets

$$\frac{1}{2}\vec{e}_z \oint \vec{k} \times d\vec{k} = \frac{B}{\phi_0}(N + \frac{1}{2} - \frac{\gamma}{2\pi}). \tag{2.4}$$

The area enclosed in k-space is calculated on the left side of equation (2.4) and is for circular orbits simply $S(\varepsilon) = \pi k^2(\varepsilon)$ leading to the expression

$$\pi k^2(\varepsilon) = \frac{B}{\phi_0}(N + \frac{1}{2} - \frac{\gamma}{2\pi}). \tag{2.5}$$

One can use now equation (2.5) to calculate the energy of the Landau levels using the bandstructure and the Berry phase of the given material. In GaAs/Al$_x$Ga$_{1-x}$As-heterostructures the band structure can be approximated near the Γ-point by

$$\varepsilon_{\mathrm{GaAs}}(k) = \frac{\hbar^2 k^2}{2m^*}, \tag{2.6}$$

resulting to a Landau level spectrum of

$$\varepsilon_{\mathrm{GaAs}}(N) = \hbar \frac{eB}{m^*}\left(N + \frac{1}{2}\right). \tag{2.7}$$

Each Landau level can be occupied by a certain number of electrons depending on the magnetic field. An often used parameter in quantum Hall physics is the filling of the Landau levels describing how many levels could be filled up by the present electron density. This parameter - called filling factor ν - is then given by the total electron density n divided by the Landau level degeneracy n_{L},

$$\nu = \frac{n}{n_{\mathrm{L}}}. \tag{2.8}$$

3. Structure and electrical properties of graphene

Graphene - an isolated carbon layer peeled off graphite - has become today a wonderful playground for two-dimensional physics due to its unique electronic bandstructure. It is also relatively easy and cheap to get, compared to two-dimensional electron systems from common semiconductor materials.

Described for the first time by Wallace [29] in 1947 as an approach to understand the properties of graphite, it was first fabricated in 1975 by Van Bommel et al. [30]. The isolation and electrical characterization of graphene was not achieved before 2004 [31]. Novoselov and Geim, who accomplished the isolation and attracted the interest of scientists on this material, were awarded with the Nobel Prize in 2010.

Recently much effort has been made to bring graphene into usage in industrial electronics. From the high mobilities of up to $100\,\mathrm{T}^{-1}$ [32] achieved, digital electronics would profit most but unfortunately the missing band gap does not allow for current on/off ratios comparable to the established silicon technology [33]. The existing methods to induce a band gap into graphene either reduce the mobility [34,35] or require impracticable high fields [36]. Materials like molybdenum disulfide, also a two-dimensional crystal, with suitable band gap are much more feasible in this respect and have already reached the level of state-of-the-art silicon technology [37]. Therefore graphene is mostly interesting in analog applications as long as novel approaches [38–40] do not overcome the basic problems originating from the missing band gap. Potential industrial usage has still been achieved as indium tin oxide replacement for transparent electrodes [41].

From a metrological point of view graphene is interesting because of very stable quantum Hall plateaus. The quantum Hall effect (QHE) in graphene can, for example, be sustainable up to room temperature [42], but can also be measured with a comparable precision to silicon or III-V-heterostructure devices [43, 44] in low temperatures. Superior to graphene are high breakdown currents [45, 46] that could allow the operation of secondary/industrial resistance standard in liquid nitrogen.

The literature and data available for graphene has grown dramatically since 2004 and a review is out of the scope of this work. Instead we want to refer to existing reviews [25, 33, 47–50] and shortly cover the topics affecting this work.

In this section we want to focus on structure, fabrication and electronic properties of graphene. First, we will discuss the electronic band structure of an idealized flake in section 3.1 before going over to typical transport measurements in section 3.2. The Landau level quantization is very special and will be discussed in section 3.3. The fabrication procedure with the main focus on micro-mechanical exfoliation follows in sections 3.4. Devices for transport measurements are usually made on different substrates: silicon dioxide, hexagonal boron-nitride, silicon carbide, and also by etching away the substrate getting free standing graphene. The respective properties are discussed in section 3.5.

3.1. 2D crystal lattice of graphene and resulting band structure

Graphene is - besides diamond, graphite, bucky balls and carbon nanotubes - one of carbons allotropes. It is characterized by sp^2-hybridization leading into a two-dimensional honeycomb lattice, see Fig. 3.1. The honeycomb lattice itself is composed of two triangular sublattices interpenetrating each other with a shift of $\vec{\tau}$ and base vectors $\vec{a_1}$ and $\vec{a_2}$. The remaining p-orbital of the carbon atom is responsible for the electrical conductivity and forms a binding π and antibinding π^* band. Using a nearest neighbor hopping formalism, Wallace calculated already 1947 the band structure [29].

The Hamiltonian for nearest neighbor hopping in graphene is (following [25])

$$H = -\gamma_0 \sum_{|\vec{R}\rangle} \left(|\vec{R}\rangle\langle\vec{R}+\vec{\tau}| + |\vec{R}\rangle\langle\vec{R}-\vec{a}_1+\vec{\tau}| + |\vec{R}\rangle\langle\vec{R}-\vec{a}_2+\vec{\tau}| \right) \tag{3.1}$$

where $|\vec{R}\rangle\langle\vec{R}+\vec{\tau}|$ describes the hopping of an electron from site $\vec{R}+\vec{\tau}$ to site $\vec{R}$. The contribution to the binding energy from the p orbitals is $\gamma_0 \approx 2.7\,\text{eV}$ [25] . Since the ansatz Bloch factors of electrons in sublattice A and B are

$$|\psi_\mathrm{A}\rangle = \frac{1}{\sqrt{N}} \sum_{|\vec{R}\rangle} e^{i\vec{k}\vec{R}} |\vec{R}\rangle, \tag{3.2}$$

$$|\psi_\mathrm{B}\rangle = \frac{1}{\sqrt{N}} \sum_{|\vec{R}\rangle} e^{i\vec{k}(\vec{R}+\vec{\tau})} |\vec{R}+\vec{\tau}\rangle, \tag{3.3}$$

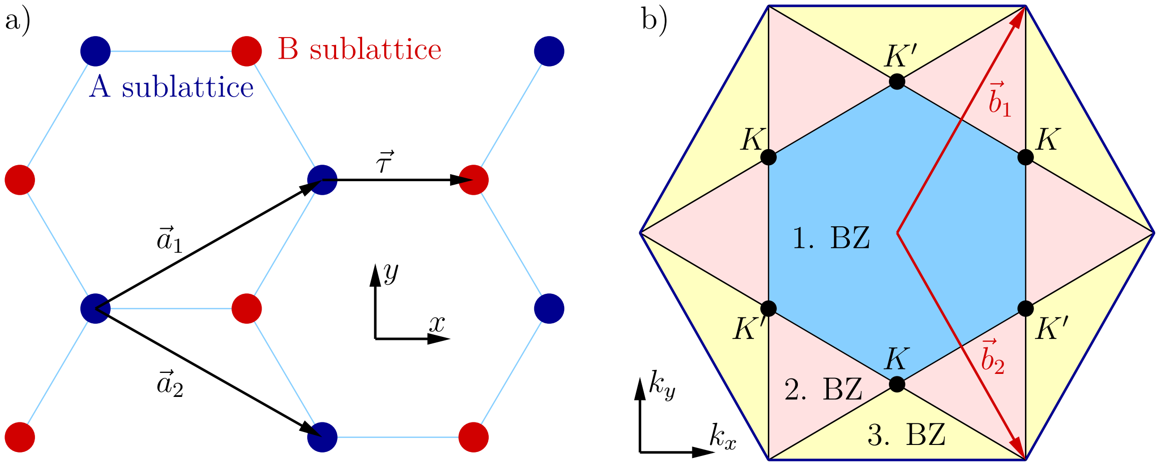

Figure 3.1.: (a) The crystal structure of graphene consisting of a honeycomb lattice that itself is composed of two triangular sublattices interpenetrating each other. The base vectors for one sublattice are $\vec{a}_1 = 0.5a(3, \sqrt{3})$ and $\vec{a}_2 = 0.5a(3, -\sqrt{3})$. The shift to the second sublattice is given by $\vec{\tau} = a(1, 0)$ and $a = 0.142\,\text{nm}$. (b) In the corresponding reciprocal $\vec{k}$ space the base vectors are $\vec{b}_1 = \frac{2\pi}{3a}(1, \sqrt{3})$ and $\vec{b}_2 = \frac{2\pi}{3a}(1, -\sqrt{3})$. The first three Brillouin zones of graphene are shown and regions colored equally belong to the same Brillouin zone. The corners or the first Brillouin zone are called K-points. Of the 6 only two are inequivalent: K and K'.

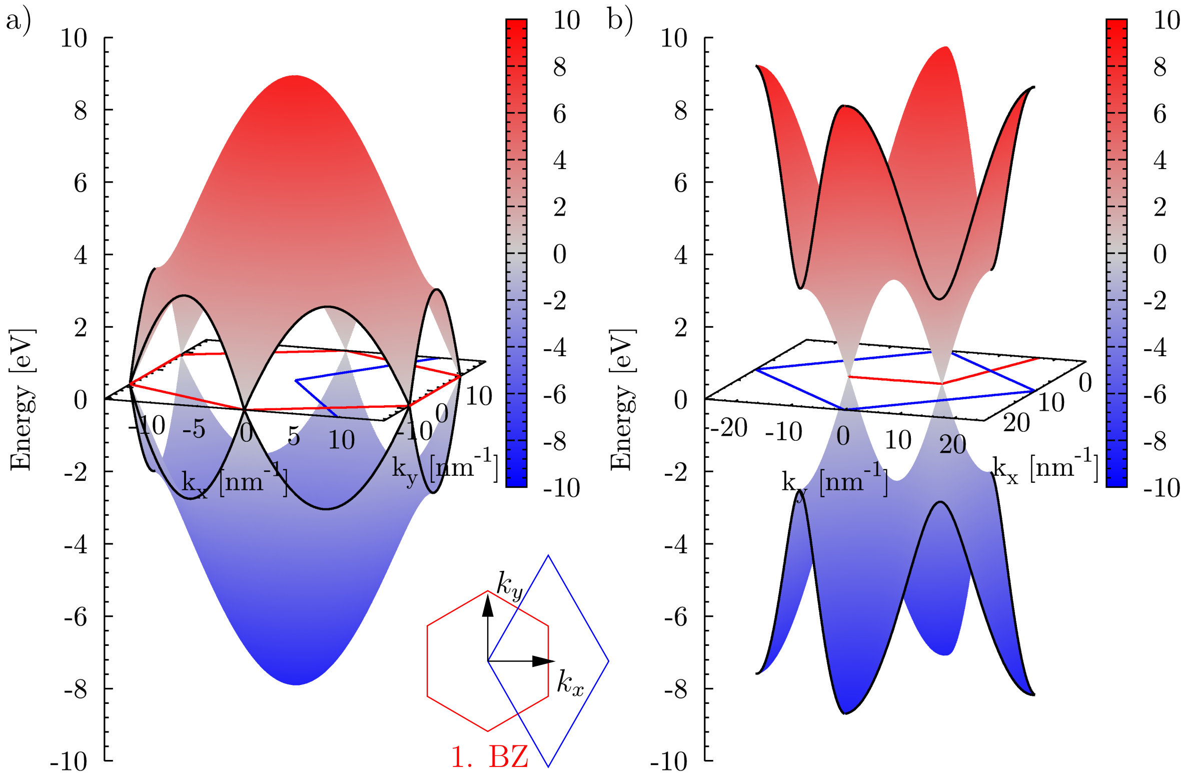

Figure 3.2.: Band structure of graphene from equation (3.6). In (a) only the first Brillouin zone is shown while in (b) parts of the first three Brillouin zones with total size of one zone are shown. The representation in (b) was chosen to emphasize the two inequivalent K-points.

and the Hamiltonian is transferring $|\psi_\mathrm{A}\rangle$ to $|\psi_\mathrm{B}\rangle$ and vice versa we can restate the problem in a matrix form:

$$H_\mathrm{K}\Psi = \begin{pmatrix} 0 & \langle\psi_\mathrm{A}|H|\psi_\mathrm{B}\rangle \\ \langle\psi_\mathrm{B}|H|\psi_\mathrm{A}\rangle & 0 \end{pmatrix} \begin{pmatrix} |\psi_\mathrm{A}\rangle \\ |\psi_\mathrm{B}\rangle \end{pmatrix} = \varepsilon(\vec{k}) \begin{pmatrix} |\psi_\mathrm{A}\rangle \\ |\psi_\mathrm{B}\rangle \end{pmatrix}. \tag{3.4}$$

The off-diagonal elements are due to the sublattice symmetry equal to each other:

$$E(\vec{k}) = \langle\psi_\mathrm{A}|H|\psi_\mathrm{B}\rangle = \langle\psi_\mathrm{B}|H|\psi_\mathrm{A}\rangle = -\gamma_0 e^{i\vec{k}\cdot\vec{\tau}} \left(1 + e^{-i\vec{k}\cdot\vec{a}_1} + e^{-i\vec{k}\cdot\vec{a}_2}\right). \tag{3.5}$$

Therefore the single quasi-particle energies $\varepsilon(\vec{k})$ are the eigenvalues of the matrix which are $\pm|E(\vec{k})|$. The band structure of graphene in the nearest neighbor hopping approximation becomes

$$\varepsilon(\vec{k}) = \pm\gamma_0 \sqrt{1 + 4\cos^2\left(\frac{\sqrt{3}k_y a}{2}\right) + 4\cos\left(\frac{3k_x a}{2}\right)\cos\left(\frac{\sqrt{3}k_y a}{2}\right)}. \tag{3.6}$$

Hereby the plus sign corresponds to the π^* band and the minus sign to the π band of graphene. The band structure is shown in Fig. 3.2. Thereby it was chosen only the first Brillouin zone in Fig. 3.2 (a). One can identify six points where the π^* band touches the

π band. These points are called K points and only two of the six are inequivalent: K and K' which are marked in Fig. 3.1. Figure 3.2 (b) shows a cutout in k space with an area of a single Brillouin zone emphasizing the linear dispersion close to the two inequivalent K points.

Close to the K points one can simplify equation (3.4) to

$$\hbar v_{\mathrm{F}} \vec{\sigma} \cdot \nabla \Psi = \varepsilon(\vec{k}) \Psi \tag{3.7}$$

where $\vec{\sigma} = (\sigma_x, \sigma_y)$ consists of the Pauli matrices applied onto the two sublattices. This shows that the dispersion relation close to the K points is linear. The velocity parameter introduced in (3.7) is

$$v_{\mathrm{F}} = \frac{\sqrt{3}\gamma_0 a}{2\hbar} \approx 10^6 \, \frac{\mathrm{m}}{\mathrm{s}}. \tag{3.8}$$

After including the dynamic part of the Schrödinger equation to eq. (3.7) we get

$$\hbar v_{\mathrm{F}} \vec{\sigma} \cdot \nabla \Psi = i\hbar \partial_t \Psi. \tag{3.9}$$

Equation (3.9) is equivalent to the two-dimensional Dirac-Weyl equation (Dirac equation for massless particles), that is why the cones at the K points are usually referred to as Dirac cones and the quasi-particles as massless Dirac fermions. The touching points of the Dirac cones - corresponding to the touching of the π and π^* bands - are referred to as Dirac points [47]. The velocity parameter v_{F} is the constant velocity of all quasi-particles and thus also the Fermi velocity.

The degeneracy caused by the two inequivalent Dirac cones in graphene is an additional degree of freedom for the quasi-particles called valley-isospin. The valley-isospin together with the quasi-particle spin degree-of-freedom causes the quantum Hall effect in graphene occurring at Landau level filling factor intervals of 4 [6].

Pristine graphene would have the Fermi level, the energy level up to which the bandstructure is filled up, going through the Dirac points. Graphene is considered to be charge neutral in this case. Shifting the Fermi level is possible by doping or electric gating and drives the system out of charge neutrality. One can induce free electrons by shifting the Fermi level upwards but also free holes when the Fermi level lies below the Dirac points. Thus we have to deal in graphene with positive and negative charges and we want to use in the following the charge carrier concentration including the charge sign by interchanging

$$\eta = -n \tag{3.10}$$

for an electrochemical potential above the Dirac point and

$$\eta = p \tag{3.11}$$

for an electrochemical potential below the Dirac point. This simplifies the treatment for a transition from positive charges (hole densities p) indicated by positive η to negative charges (electron densities n) indicated by negative η.

So far we described only the bandstructure of graphene. The practical implications for electrical transport measurements will be discussed in the following.

3.2. Typical electrical transport measurements

For the typical electrical characterization the graphene flakes are electrically contacted and their charge carrier density is tune by a gate. In the simplest approach one can use the Drude model [52, 53] to find the resistivity ρ

$$\rho = \frac{1}{q|\eta|\mu}. \tag{3.12}$$

The mobility μ is the average drift velocity v_{D} of a Drude particle with charge q over the electric field E causing this drift. It turned out that one can keep the mobility μ constant in a first approximation [54, 55], at least for high charge carrier densities. The sign of the charge q is canceled by the sign of the mobility, so that we have to take the absolute value of charge sign including charge carrier concentration η.

The gate used to tune the charge carrier concentration can be modeled with a simple capacitance model neglecting edge effects and density-of-states or correlation effects,

$$\Delta\eta = -\frac{\epsilon_0\epsilon_r\Delta V_{\mathrm{BG}}}{ed}. \tag{3.13}$$

A typical system to apply this is graphene on silicon dioxide with a highly doped silicon back gate. The thickness of the silicon dioxide dielectric ($\epsilon_r = 3.9$) is usually $d = 300\,\mathrm{nm}$ due to reasons discussed later on. The relation between charge carrier concentration η and back gate voltage V_{BG} is then $\Delta\eta \approx -7.18 \cdot 10^{14}\,\mathrm{V}^{-1}\mathrm{m}^{-2} \cdot \Delta V_{\mathrm{BG}}$.

A measurement of a graphene flake's resistivity over the back gate voltage is shown in Fig. 3.3 (a) at a temperature of 1 K. With the back gate voltage V_{BG}, one can tune the

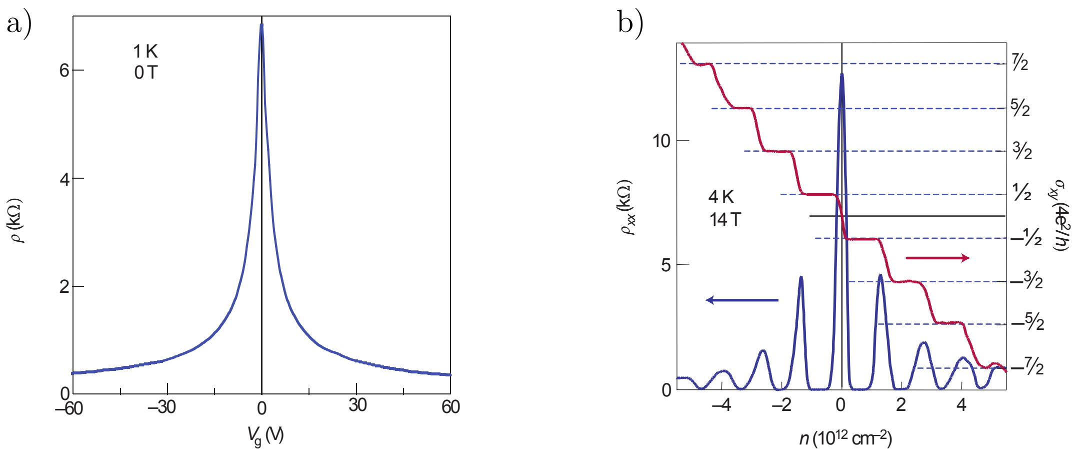

Figure 3.3.: Electrical characteristics of a graphene flake: (a) at zero magnetic field. Adapted by permission from Macmillan Publishers Ltd: Nature Materials [51], copyright (2014), (b) with magnetic field of 14 T. Reprinted by permission from Macmillan Publishers Ltd: Nature Materials [51], copyright (2014).

charge carrier concentration through zero due to graphene's bandstructure with the zero charge carrier density at the Dirac points. The resistivity versus back gate voltage curve shows therefore a peak at the back gate voltage ascribed to the flake's charge neutrality [55]. We want to stress here that this interpretation can only be an approximation for the experiments done in this thesis. An in-depth discussion will be given in section 9.7.

Furthermore after applying a magnetic field we can induce the QHE in graphene as shown in Fig 3.3 (b). As already mentioned, due to spin and valley isospin the conductivity steps between quantum Hall plateaus are $4e^2/h$. In addition the sequence does not start at $4e^2/h$ but rather on $2e^2/h$. This is a direct consequence of graphene's bandstructure. We already discussed that for parabolic band materials energetically equidistant Landau levels are formed. This is not the case for graphene and will be discussed in the following section.

3.3. Landau level formation in graphene

We can apply the Onsager formula [26] (2.4), as we did for GaAs/Al$_x$Ga$_{1-x}$As-heterostructures, also to graphene to get the Landau level spectrum. The bandstructure of graphene close to the K-points is given by

$$\varepsilon_{\mathrm{graphene}}(k) = \hbar v_{\mathrm{F}} k, \tag{3.14}$$

and the Berry phase is π [25]. The Landau level spectrum is thus square-root dependent on the magnetic field and the Landau level index N,

$$\varepsilon_{\mathrm{graphene}}(N) = \mathrm{sgn}(N) \cdot \sqrt{2e\hbar v_{\mathrm{F}}^2 B|N|}. \tag{3.15}$$

The sign of the Landau level index N is included here since for graphene positive and negative energies with respect to the Dirac points are allowed. They correspond to the two solutions solving the quadratic equation for the energy which results after inserting equation (3.14) into (2.4). This reflects the possible occurrence of electrons (positive N) and holes (negative N) in graphene.

3.3.1. Experimental evidence for Landau level quantization in graphene

So far we explained a semiclassical way to calculate a quantized Landau level spectrum. Here we want to discuss experiments able to measure the Landau level spectrum directly and in fact do confirm the theoretic findings.

The expected Landau level spectrum in graphene has a square root dependence on magnetic field B and Landau level index N, see equation (3.15) This has been verified to be true in scanning tunneling spectroscopy (STS) experiments on graphene samples weakly coupled on graphite [56, 57] and on silicon dioxide [58]. The measurements on graphite show very nice quantization, see Fig. 3.4, because of the reduced influence of the substrate. Unfortunately a variation of the charge carrier concentration is not possible due to a missing back gate. On the other hand the measurements on silicon dioxide are influenced strongly by strain, trapped and mobile charges. This results into broadening of

Landau levels. Actually first results where achieved after the substrates where chlorinated and annealed in forming gas to reduce the effect of trapped and mobile charges [58]. When following the found Landau levels as a function of the back gate voltage one finds them to be pinned at the Fermi level as long they are filled up. Once filled the Landau level spectrum is shifted fast until the next Landau level starts filling up [58]. This is shown in Fig. 3.5.

3.4. Fabrication methods

The fabrication method of choice for high quality graphene flakes up to now is the so-called micro-mechanical exfoliation or scotch-tape method [59]. Thereby one uses adhesive tape to strip off layers from a suitable graphite crystal. Further cleavage by subsequent division of the stripped-off material leads to graphite flakes on the tape with small number of layers. The final cleavage is done on a silicon/silicon dioxide substrate. Single layers can be easily identified via optical contrast for the right silicon dioxide thickness. This thickness is usually chosen to be 300 nm because of the maximum optical contrast under ambient light [60].

Since graphene is believed to have huge potential for electronic applications, big effort was put into finding fabrication methods for large area graphene. One of the most promising approaches is chemical vapor deposition (CVD) on substrates of transition metals [61–64]. Thereby carbon is absorbed into the transition metals during evaporation at elevated temperatures and forms closed graphene and multilayer graphene sheets while the solubility in the metal substrate is reduced during cool down. Single domain flakes produced this way can have up to millimeter size [65, 66]. Also fabrication in a rolling technique for transparent electrodes was already demonstrated [41]. Polymer foils with

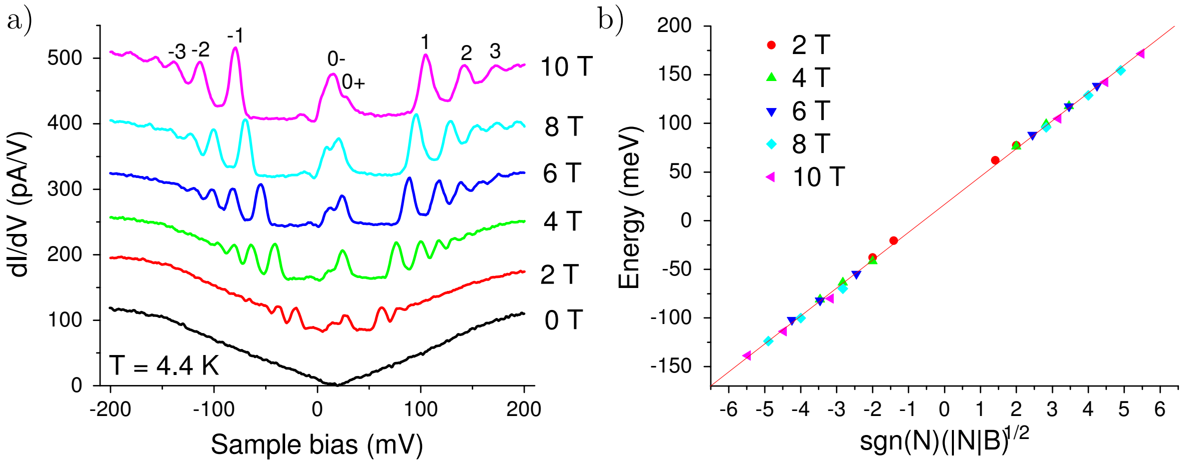

Figure 3.4.: Landau levels measured by scanning tunneling spectroscopy for a flake weakly coupled on a graphite substrate [56]. In (a) the Landau level spectra (as differential conductance versus bias voltage) for different magnetic field values are shown. Reprinted with permission from [56]. Copyright (2014) by the American Physical Society. In (b) the energy shift of the Landau levels is plotted over the square root of magnetic field B and Landau level index N. Adapted with permission from [56]. Copyrighted by the American Physical Society.

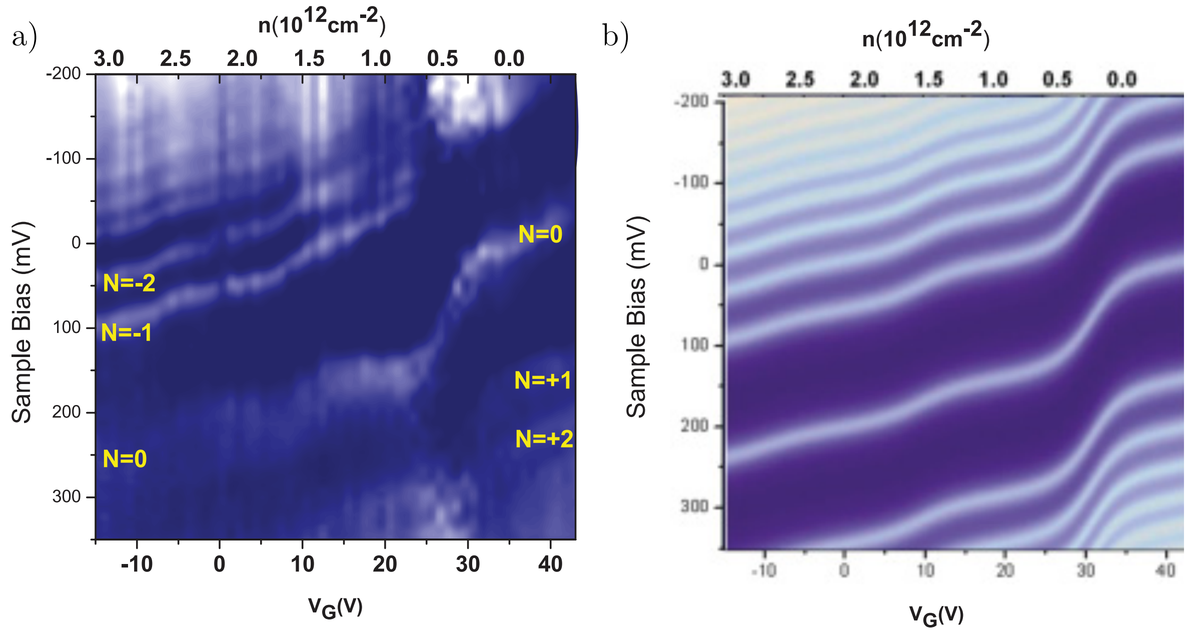

Figure 3.5.: Landau levels measured by scanning tunneling spectroscopy for a flake on chlorinated silicon dioxide [58]. The back gate was used to change the charge carrier concentration of the flake and making this way the filling up of the Landau levels visible. Measurements (a) and calculations (b). Reprinted with permission from [58]. Copyright (2014) by the American Physical Society.

a diagonal extend of up to 76 cm were thereby covered with multi-domain graphene.

Another often used method is the creation of epitaxial graphene on silicon carbide [30,67–71]. Heating up the silicon carbide substrate until silicon is removed from the first layers due to sublimation let the remaining carbon form graphene layers.

In chemical exfoliation a piece of graphite is ripped apart into single layers using the right solvents and sonication [72,73]. Oxidation followed by reduction can also be used to create single layer graphene [74,75]. Direct chemical synthesis is also possible but only for small sized flakes [76–78].

3.5. Influence of the substrate

The reason for the wide usage of silicon dioxide on silicon as substrate for graphene applications is - besides of its low price and availability - also the well established method for finding single-layer graphene via optical contrast [60]. The electrical characteristic is affected by charges in or on top of the silicon dioxide and by the surface roughness [79,80]. This inhomogeneities lead to puddles with varying charge carrier concentration [79,81], see Fig. 3.6. The size of the puddles in the example of Fig. 3.6 is about 0.3 µm. Typical charge carrier mobilities reached for graphene on silicon dioxide are in the order of $1\,\mathrm{T}^{-1}$ [82].

One way to improve electrical properties is to reduce the impact of silicon dioxide on graphene by bringing layers of materials between graphene and the silicon dioxide.

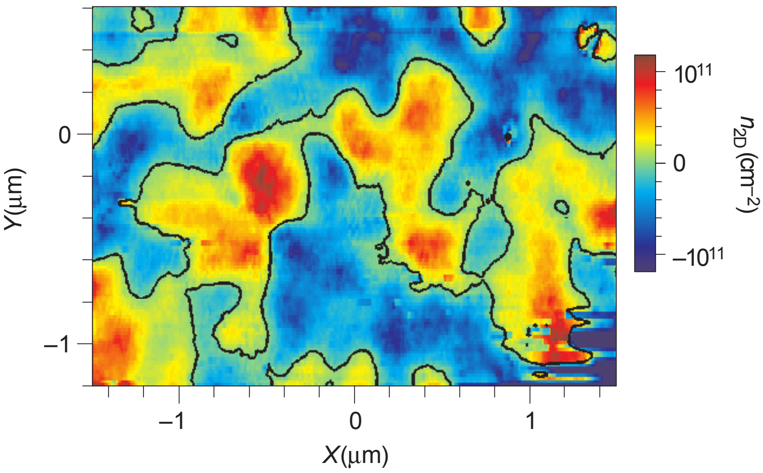

Figure 3.6.: Charge puddles measured with a scanning single-electron transistor by Martin et al. [79]. An area scan is shown to demonstrated the spatial extend of the puddles. Reprinted by permission from Macmillan Publishers Ltd: Nature Physics [79], copyright (2014).

These materials have to be flatter than thermally grown silicon dioxide and incorporate less defects. A popular material to do this is hexagonal boron-nitride. Reduced scattering is increasing mobility by about an order of magnitude reaching around $10\,\mathrm{T}^{-1}$ [83]. On the other hand, precise alignment of a graphene flake onto hexagonal boron-nitride can lead - depending on the relative orientation of both crystal layers - to a large period superlattice potential superposed to the graphene crystal potential. This can result in changes of the bandstructure, in particular the creation of secondary Dirac points [84] and the appearance of a fractal quantum Hall plateau structure known as Hofstadter butterfly [85].

Since today the best way to increase the charge carrier mobility is by suspending graphene and reduce thereby the interaction with the substrate dramatically. The highest mobilities reached are in the order of $100\,\mathrm{T}^{-1}$ [32], but a free standing membrane is unstable towards out-of-the-plane forces [86]. Ripples [32, 87–90] are therefore the dominating limiting factors for the charge carrier mobility.

4. Quantum Hall effect: Present microscopic picture

The quantum Hall effect (QHE) as shown in Fig. 4.1 is the development of plateau structures in the Hall measurements of a 2DES in high magnetic fields and low temperatures. Simultaneously the longitudinal resistance R_{xx} is approaching zero for temperatures going

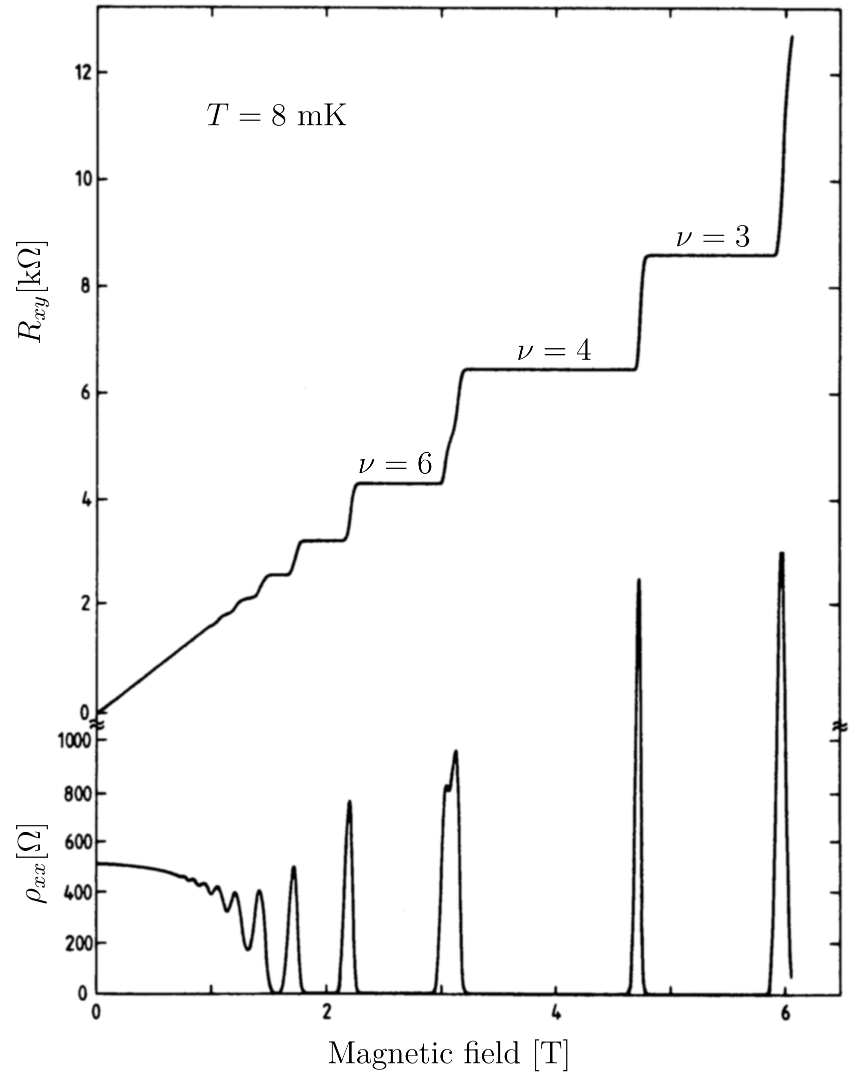

Figure 4.1.: Quantum Hall measurement consisting of the transverse resistance R_{xy} shown on the top and the longitudinal resistivity ρ_{xx} shown at the bottom. Adapted with permission from [91]. Copyrighted by the American Physical Society.

to zero.

In this chapter we want to build up the basics for the microscopic understanding of the quantum Hall effect. We will start with the experimentally measured Hall potential profiles under quantum Hall conditions by Ahlswede et al. [15]. A distinct evolution on the magnetic field observed is not explainable alone with the Landau level quantization. We will rather need to discuss the electrostatic depletion region along the 2DES edges before discussing other aspects of the QHE.

4.1. Evolution of Hall potential profiles in GaAs/Al$_x$Ga$_{1-x}$As-heterostructures under QHE conditions

In this section we want to recap the Hall potential profiles already measured by Ahlswede et al. [16]. His results across one plateau are shown in Fig. 4.2. The evolution is similar for all other quantum Hall plateaus and is shown color-coded in Fig. 4.3.

The evolution can be divided into 4 qualitatively different Hall potential profiles. Starting from the off-plateau region at filling factor $\nu = 1.67$, see Fig. 4.2, the Hall potential profile is essentially linear over the sample width. This is the classically expected behavior and is called the type I potential profile. The local current is proportional to the Hall potential gradient, see chapter E, indicating current flow over the entire sample width.

After increasing the filling factor the former linear profile starts becoming nonlinear with highest Hall potential drop in the bulk. Thus the current is flowing mainly at the sample bulk region. This is referred to as type II potential profile and is present at the higher magnetic field side of a quantum Hall plateau.

Further increase in the filling factor splits the nonlinear Hall potential drop in the bulk in two parts moving towards the edges leading into a flat bulk and two drops of the potential at the edges. Present at the lower magnetic field side of the plateau this profile is called type IIIa. The current is therefore concentrated at the two edges of the sample.

After leaving the quantum Hall plateau region at the lower magnetic field side the Hall potential profile is changing from type IIIa with a bulk potential without slope to a profile with tilted bulk potential. The currents at the edges are redistributed to the bulk region by lowering the magnetic field until a linear type I Hall potential profile is reached. Since this happens in a rather wide range of filling factors and magnetic fields we want to give this region the name type IIIb.

Figure 4.3 shows color-coded the Hall potential profile over a wide range of magnetic fields. One can clearly identify the repetition of the evolution with magnetic field described above for each quantum Hall plateau.

The remarkable feature of these measurements is the evolution of the Hall potential drop within the quantum Hall plateau. The drop is moving continuously from the bulk to the edges with decreasing magnetic field indicating the importance of edges. Therefore we want to discuss in the next section the effect of the 2DES depletion at the edges.

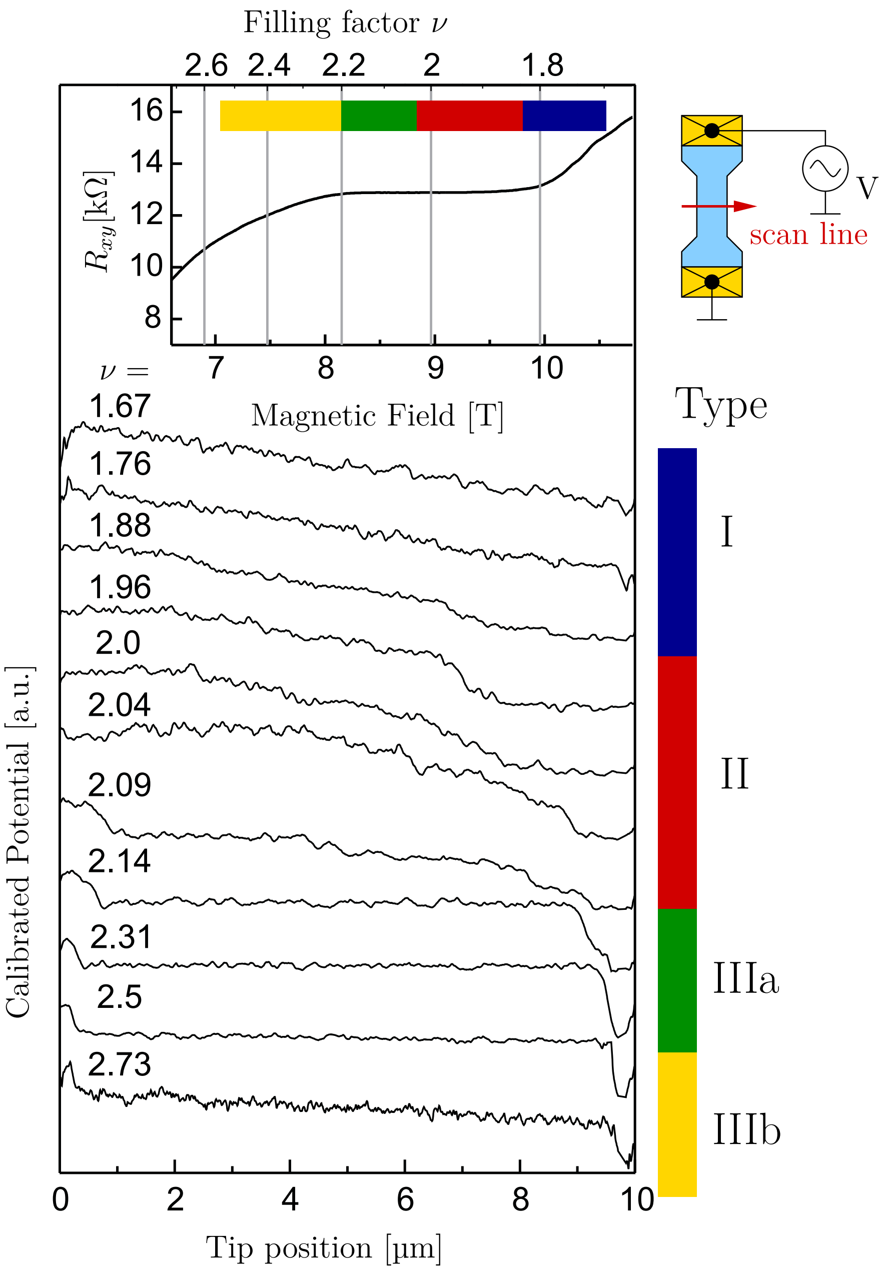

Figure 4.2.: Hall potential profiles, measured over the width of a two-terminal sample (see inset on right side), across a quantum Hall plateau. The inset shows the plateau in the Hall resistance curve around filling factor $\nu = 2$. Adapted with permission from [14]. Copyrighted by Elsevier.

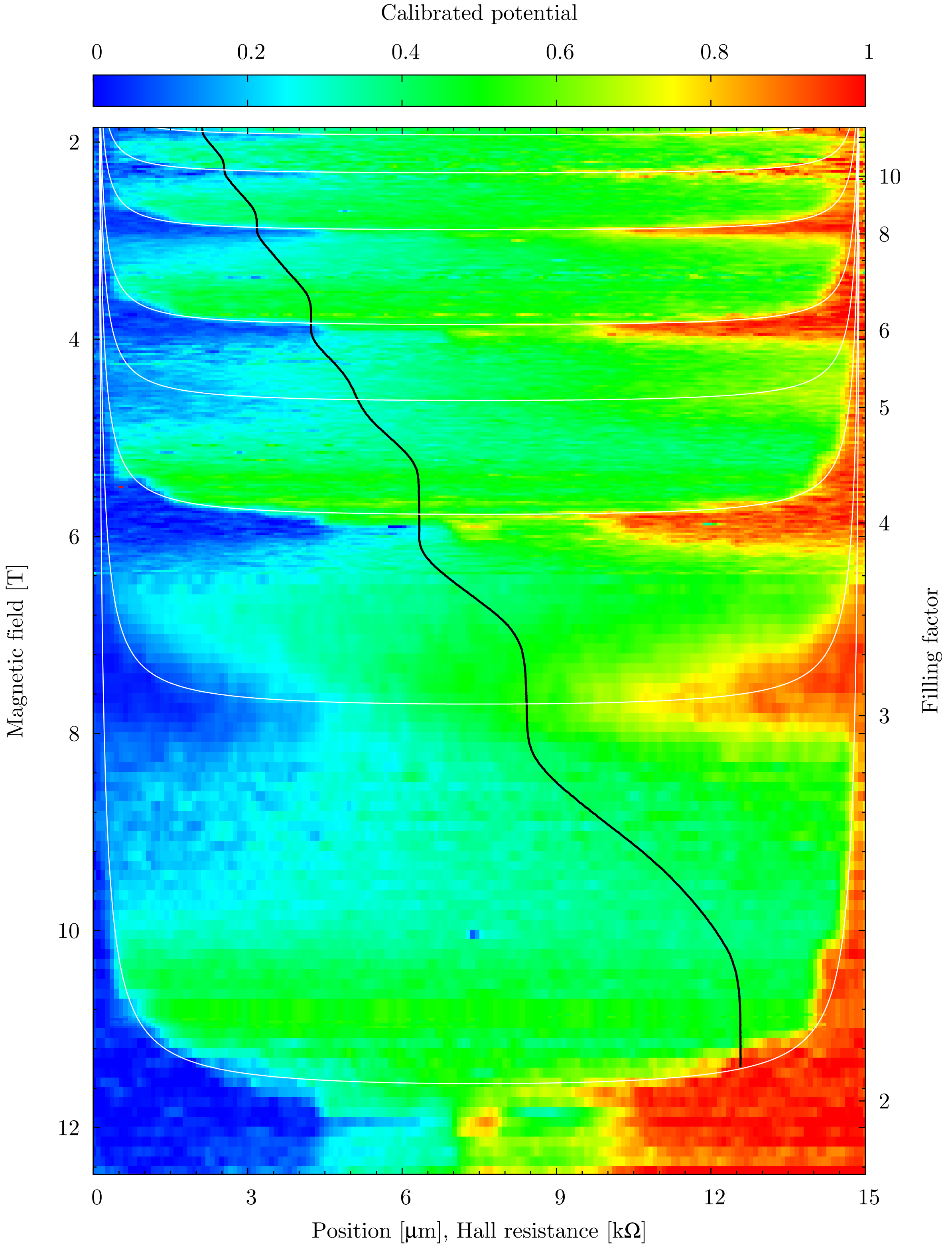

Figure 4.3.: Hall potential measurements of Ahlswede et al. [17] and position of incompressible stripes according to Chklovskii et al. [92]. No free parameter was available to match data and calculations. The Hall potential is shown in color-scale versus position over the Hall bar width and the applied magnetic field. We thank Erik Ahslwede for the access to his data to create this plot.

4.2. Depletion region of a 2DES: CSG-model for the electron concentration profile at 2DES edges

As electrons are free to move, they tend to arrange themselves minimizing electrostatic potential gradients leading to a reconstruction of the electrostatic potential landscape. This reconstruction or screening effect is especially important at edges where the electronic system is depleted and is often referred to as edge reconstruction. The origin of the depletion can be as simple as a gate, charging of surface states, edge chemistry and many more.

Before going into the actual redistribution of electrons we want to recap the importance of the electrochemical potentials μ_{elch} which consists of two parts: the chemical potential μ_{ch} and the electrostatic energy $q\phi$,

$$\mu_{\text{elch}} = \mu_{\text{ch}} + q\phi. \tag{4.1}$$

The chemical potential represents thereby the energy from the filling up of the band structure and includes that way the density of states. The electrostatic energy, as the name suggests, includes all electrostatic contributions to the energy of an electron. Since concentration gradients (i.e. gradients in the chemical potential) as well as electrostatics can redistribute electrons, the sum of both, thus the electrochemical potential, has to be equal all over the sample for thermodynamic equilibrium.

The presence of electrostatic fields will redistribute the charge carriers leading into a screening of the field. Especially interesting becomes this screening for 2DES in high magnetic fields where a pronounced Landau level structure is present. Chklovskii, Shklovskii and Glazman [92] solved for an in-plane gate geometry, shown in Fig. 4.4, the electrostatic problem for this situation. For simplicity a semi-infinite sample was calculated where the in-plane gate for the 2DES depletion lies within the same plane as the 2DES. A homogeneous background of positive charged dopants compensate for the negative electron charge in the 2DES bulk.

The common understanding of the edge reconstruction before Chklovskii et al. was to shift the chemical potential according to the electrostatic confinement potential and neglecting the screening effect by the electrons. This is depicted in Fig. 4.5 (a). The

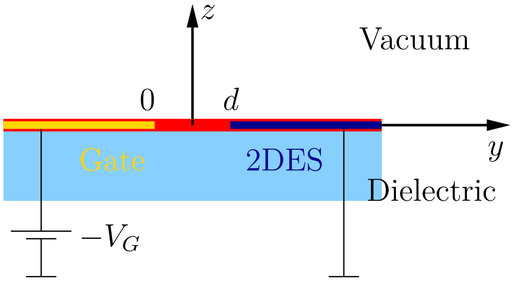

Figure 4.4.: Geometry used by Chklovskii, Shklovskii and Glazman [92] to calculate analytically the screening effects along a 2DES edge. Variables adapted to our needs. The 2DES as well as the gate are semi-infinite planes. Along the x-direction the system is translation invariant.

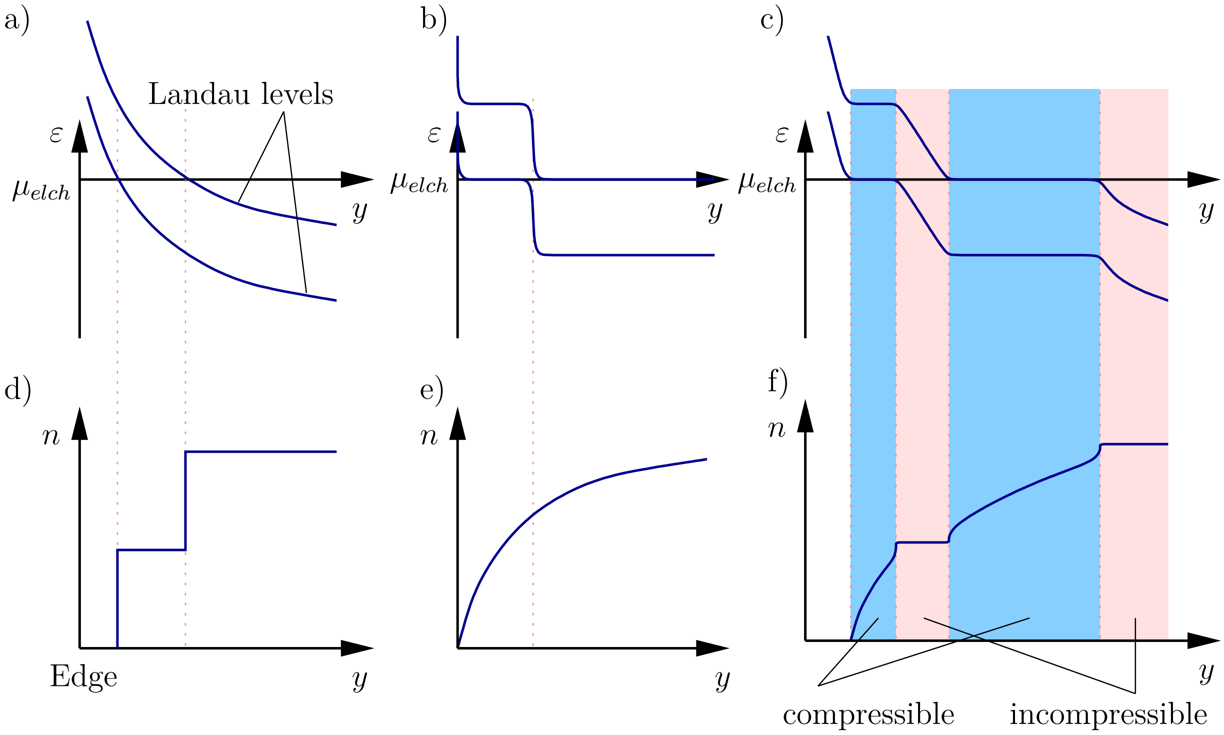

Figure 4.5.: Landau level structure and charge carrier concentration at a 2DES edge (a) ,(d) neglecting electrostatic energy, (b),(e) neglecting the chemical potential and (c),(f) taking electrostatic energy as well as chemical potential into account. Adapted in parts from [92].

charge carrier profile for this situation is shown in Fig. 4.5 (d) and has sharp jumps which induce high electric fields. Charge carriers will prefer a redistribution to reduce these electric fields.

Neglecting the chemical potential, electrons will redistribute to fully screen out electrostatic potential gradients. This situation is plotted in Fig. 4.5 (b) and (e). One can see that the Landau levels are bent extremely meaning also sharp jumps in the chemical potential. Therefore this will also not resemble the equilibrium situation.

What Chklovskii, Shklovskii and Glazman [92] found was an intermediate situation shown in 4.5 (c) and (f). From the edge to the bulk of a sample they found a distinct structure of stripes. First one finds the fully depleted region. The Landau levels here lie above the electrochemical potential. When the first Landau level comes close enough to the electrochemical potential it starts to get filled. Increasing the electron concentration from the edge to the bulk, the first Landau level is filled. The states are pinned to the electrochemical potential. After the first Landau level is completely filled it is bend energetically downwards. Here the second Landau level is shifted towards the electrochemical potential. During this shift the lower Landau level is completely filled while the upper one is completely empty. The structure of the electrochemical potential being positioned on top of a Landau level or between two is repeated until the bulk charge carrier concentration is reached.

In the regions of electrochemical potential on top of a Landau level, charge carriers can be easily redistributed since unoccupied states are easily accessible. Also charge can be added without a huge change of the chemical potential. This can be stated qualitative with the compressibility [93, 94]

$$\kappa = \frac{1}{n^2} \cdot \left(\frac{\partial n}{\partial \mu_{\mathrm{ch}}} \right). \tag{4.2}$$

Because of the high compressibility such a stripe is called compressible stripe.

For the stripes next to the compressible stripes a surplus of charge would go to the empty upper Landau levels. Therefore the chemical potential would change a lot when adding or removing charges leading into a low compressibility. These stripes are thus called incompressible.

One can estimate the position of an incompressible stripe when the charge carrier concentration without taking into account the chemical potential like in Fig. 4.5 (e) is known. Incompressible stripes will form where the charge carrier concentration is equal to an integer multiple of Landau level degeneracy. To calculate the needed charge carrier concentration profile one has to just solve for electrostatics. This is essentially what Chklovskii, Shklovskii and Glazman [92] did as the first step of their analysis. The analytic values they found for the position y_k and width a_k of the k-th incompressible stripes were checked by self-consistent simulations by Lier et al. [95] and were found to be a good approximation. Setting $y = 0$ for the edge of the gate electrode, the position of the incompressible stripe with local filling factor k is given by [95]

$$y_k = \frac{d_0}{1 - \left(\frac{k}{\nu}\right)^2}, \tag{4.3}$$

and the width of the stripes (neglecting spin)

$$a_k = \frac{4 y_k}{\nu} \sqrt{\frac{k a_{\mathrm{B}}^*}{\pi d_0}}. \tag{4.4}$$

Here $a_{\mathrm{B}}^* = 4\pi\epsilon_0\epsilon_r\hbar^2/e^2 m^*$ is the effective Bohr radius. The depletion length d_0 depends on the confinement, in other words on the gate voltage V_{G} and the electron concentration n,

$$d_0 = \frac{4\epsilon_0\epsilon_r V_{\mathrm{G}}}{\pi e n}. \tag{4.5}$$

In addition one has to choose the right value for the effective dielectric constant ϵ_r since the 2DES are covered only with a relatively thin semiconductor layer. The effective dielectric constant ϵ_r will lie therefore somewhere between the mean value of vacuum and semiconductor and the value of the semiconductor alone.

4.3. Self-consistent calculation

The calculations of Chklovskii et al. [92] from the previous section are an analytic approach that starts from an electron density profile at zero magnetic field neglecting the density of states [95].

A self-consistent approach was developed in the group of Gerhardts [95–102]. The main idea was to calculate from the electrostatic energy $-e\phi(y)$ and chemical potential $\mu_{\mathrm{ch}}(n(y))$ the electron density $n(y)$ and with the electron density the electrostatic energy and chemical potential. This defines a loop that after conversion results into the self-consistent profiles for the electron density, electrostatic energy and chemical potential. Adding a second superordinate loop, local Ohm's law can be included. This allows to calculate Hall potential profiles under current biasing [101].

One way to calculate from the chemical and electrostatic potential the electron density is to use the Thomas-Fermi-approximation

$$n(y) = \int D(\varepsilon) f(\varepsilon + e\phi(y) - \mu_{\mathrm{ch}}(y)) d\varepsilon. \tag{4.6}$$

The temperature enters via the Fermi function $f(E) = [\exp(E/k_{\mathrm{B}}T) + 1]^{-1}$ and the magnetic field B via the density of states $D(\varepsilon)$,

$$D(\varepsilon) = \frac{1}{\pi l_B^2} \sum_{n=0}^{\infty} \delta\left(\varepsilon - \hbar\omega_{\mathrm{c}}\left(n + \frac{1}{2}\right)\right). \tag{4.7}$$

The electrostatic potential is calculated with the Poisson equation from the electron density. The chemical potential arises from the filling of the density of states in equation (4.7).

The self-consistent calculations are superior to the Chklovskii et al. approach in the sense that the density of states is included self-consistently. Also by adding superordinate loops one can calculate nonequilibrium situations like current biasing. Nevertheless the self-consistent results for equilibrium are approximated sufficiently well equation (4.3), found by Chklovskii et al..

4.4. Current within incompressible stripes

Where within a device the externally applied current is flowing, that can be seen from the experiments of Ahlswede et al. [16]. Plotting the position of an incompressible stripe as calculated by Chklovskii et al. and given by equation (4.3) over the data of Ahlswede et al. results in a remarkable coincidence of stripe position and Hall potential drops, see Fig. 4.3. We want to stress that there is no free parameter to be adjusted for this plot. The current is proportional to the perpendicular electric field as discussed in more detail in chapter E. Within this interpretation current flows in Fig. 4.3 at the position of potential drops.

Therefore Ahlswede et al. concluded that the position of current flow coincides with the position of the innermost incompressible stripe. When entering a quantum Hall plateau from the lower magnetic field side the external current will flow at the sample edges. Increasing the magnetic field will widen and shift the two incompressible stripes towards the sample bulk. Since the Hall potential drops and the currents are positioned at the incompressible stripes, they will mimic this trend. Further increasing the magnetic field will bring the two innermost incompressible stripes close enough to each other so that they merge. The whole bulk becomes widely incompressible. Therefore current flow and

Hall potential drop happens in the bulk of the device.

For a microscopic picture we want to consider the situation where current is flowing within two incompressible stripes at the sample edges. Figure 4.6 (a) shows the equilibrium situation without external current. The Landau levels are plotted over the position and the filling of each Landau level is indicated by the filling of the circles over the Landau levels. Within the incompressible stripes the Landau levels are bend and thus all states have a drift velocity, see for details chapter E. Since the states of the right incompressible stripe have the opposite drift velocity compared to the states of the left incompressible stripe the total current is zero. It is worth mentioning that these currents are encircling the entire sample and are called persistent currents. They have to be distinguished from external currents because persistent currents do not carry any net current through the sample and are present already in equilibrium.

Is a current driven through the sample, the Landau level structure over the sample position has to change and will be similar to Fig. 4.6 (b). On the left side the Landau levels are bent less than the cyclotron gap while on the right side they are bent more than the gap. In comparison to the equilibrium situation the current density in the left stripe is reduced while the current density in the right stripe is increased. This means that the externally applied current flows within both incompressible stripes in addition to the persistent current.

The compressible and incompressible structure predicted by the CSG-model was so far measured by different scanning probe experiments [12, 14, 103–106]. It should be noted that depending on the type of scanning probe experiments only part of the compressible/incompressible Landscape becomes visible. Usually only features following the position of the innermost incompressible stripe are measured.

4.5. Potential probes

Potential probes are intended to measure the electrochemical potential of the 2DES locally and are usually wired to high impedance inputs of amplifiers to reduce the drained current as far as possible. The incompressible stripes which go all around the sample also pass by the potential probes as measured by scanning force microscopy, shown in Fig. 4.7. The

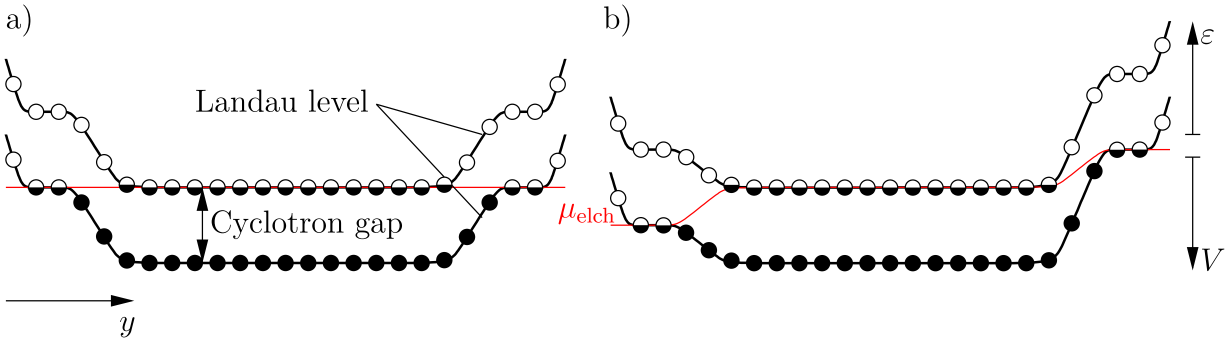

Figure 4.6.: Sketch of the Landau level bending from edge to edge of a 2DES The filling of the circles indicate the filling of the Landau levels. (a) Without and (b) with Hall voltage caused by the external biased current.

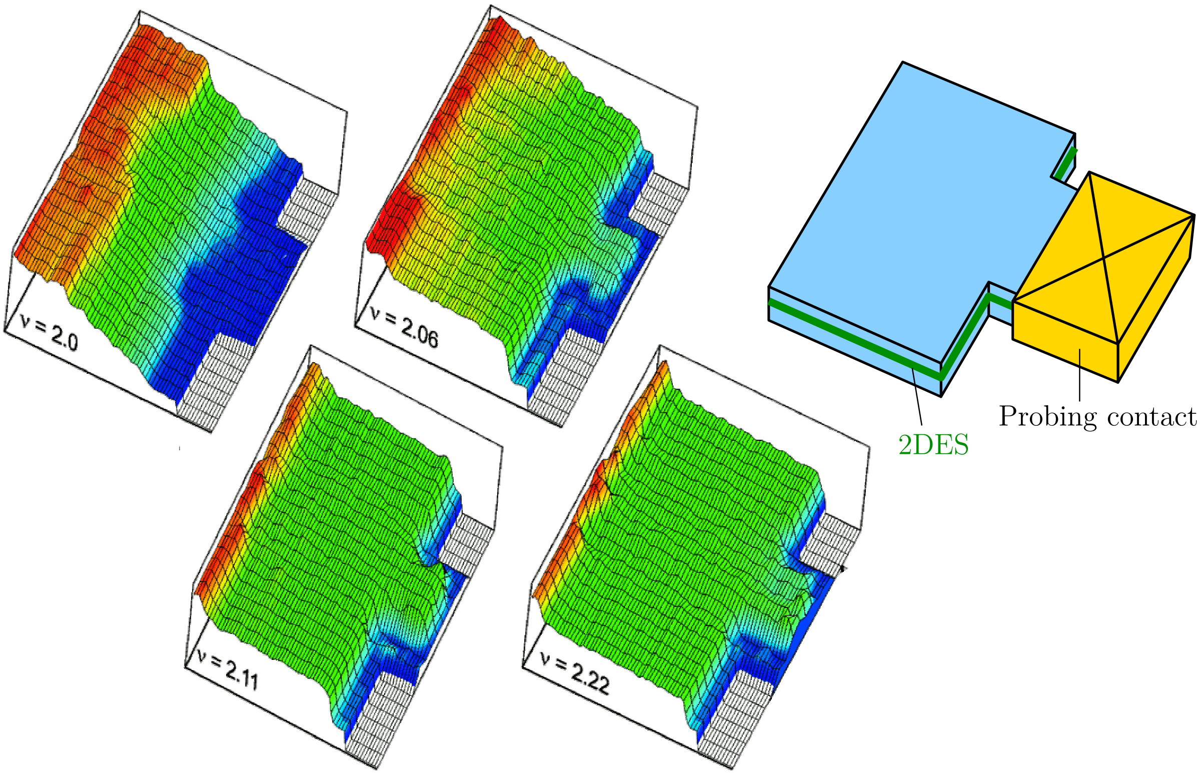

Figure 4.7.: Hall potential landscape of an area in front of a potential probing ohmic alloyed contact. Adapted from [17].

Hall potential landscape was measured in this figure over the area in front of the contact. The potential in front of the contact is flat indicating no current flow into the contact. This flat region is the outermost compressible stripe. and is found for all magnetic fields shown in Fig. 4.7. This indicates a depletion region in front of contacts. Indeed experiments studying the contact formation of alloyed gold/germanium/nickel contacts on GaAs/Al$_x$Ga$_{1-x}$As-heterostructures by Göktas et al. [107, 108] also indicate a reduced charge carrier concentration in front of contacts.

4.6. Hot spots

The term "hot spot" describes a hot area of a sample where strong dissipation is present. For the Hall effect it coincides with the current entry and exit points from the 2DES area to the ohmic contacts.

Whenever measuring the Hall effect at a junction between a material with high charge carrier density and Hall angle of nearly zero and a material with low charge carrier density and Hall angle nearly 90° there will be a hot spot somewhere at the interface. The reason is simply because the material with nearly zero Hall angle will have a very small Hall voltage drop along the interface compared to the Hall voltage drop of the material with nearly 90° Hall angle. Since the interface will follow the potential of the high charge carrier density material the interface will have a nearly constant electrostatic potential.

Therefore the material with nearly 90° Hall angle is unable to drive a current $j \propto EB^{-1}$ through the interface. Thus the current passes along the contact and focuses into a single spot: the hot spot.

Even though this was only a classical argumentation, experiments probing the hot spots in the QHE agree with this picture. Klaß et al. [109] used the Fontain effect to visualize the position of the hot spots. He found that the hot spot at the electron source contact (-) tends to become bigger than the one of the electron drain contact (+). Also he realized that for narrow contacts the hot spots seem to migrate away from the drain contact (+) but not from the source contact (-).

Later Ahlswede et al. [17] showed that the potential landscape under quantum Hall conditions directs the current to the classically expected position of the hot spot. Newer experiments by Komiyama et al. [110] were able to measure also a Tera-Hertz photon emission at the hot spots.

4.7. Evolution of the QHE

Figure 4.8 sums up what was said about the evolution of the QHE and gives an overview of the QHE evolution with magnetic field across one plateau.

Starting from the left in the off-plateau region, a fully compressible (light blue) sample is found. Incompressible regions may exist but they are too thin to be effective. Thus the Hall potential profile in the sample center is similar to the classical Hall profile, i. e., an almost linear profile denoted as type I in section 4.1.

Increasing the magnetic field the incompressible strips, plotted in white, become wide enough to become effective and are able to carry an externally applied current. They are positioned close to the edges of the 2DES (or 2DHS) and resemble a closed loop carrying also the persistent current. The Hall potential profiles in this regime have therefore a Hall potential drop at each of the two sample edges leading to the so-called type III potential profile. Since current is flowing close to the sample edges one could also call this regime the "edge-dominated" one.

Further increasing of the magnetic field let the incompressible stripes becoming wider and moving towards the 2DES bulk until they extend over the entire bulk. Hall potential profiles will show potential drops in the 2DES bulk giving the so-called type II potential profiles. The magnetic field region of bulk current could thus be called "bulk-dominated". Still due to disorder compressible islands could be found within the bulk incompressible region. Continuing to raise the magnetic field let the incompressible bulk region shrink in size until the sample becomes fully compressible again and classical behavior is obtained.

In terms of the technical current direction, the externally biased current enters the 2DES at the hot-spot of the source contact and leaves the 2DES over the hot-spot at the drain contact. Thereby the electrochemical potential of the drain (red) and source contact (blue) is carried via the outermost compressible stripe along the respective edge. There is no current entering the potential probes.

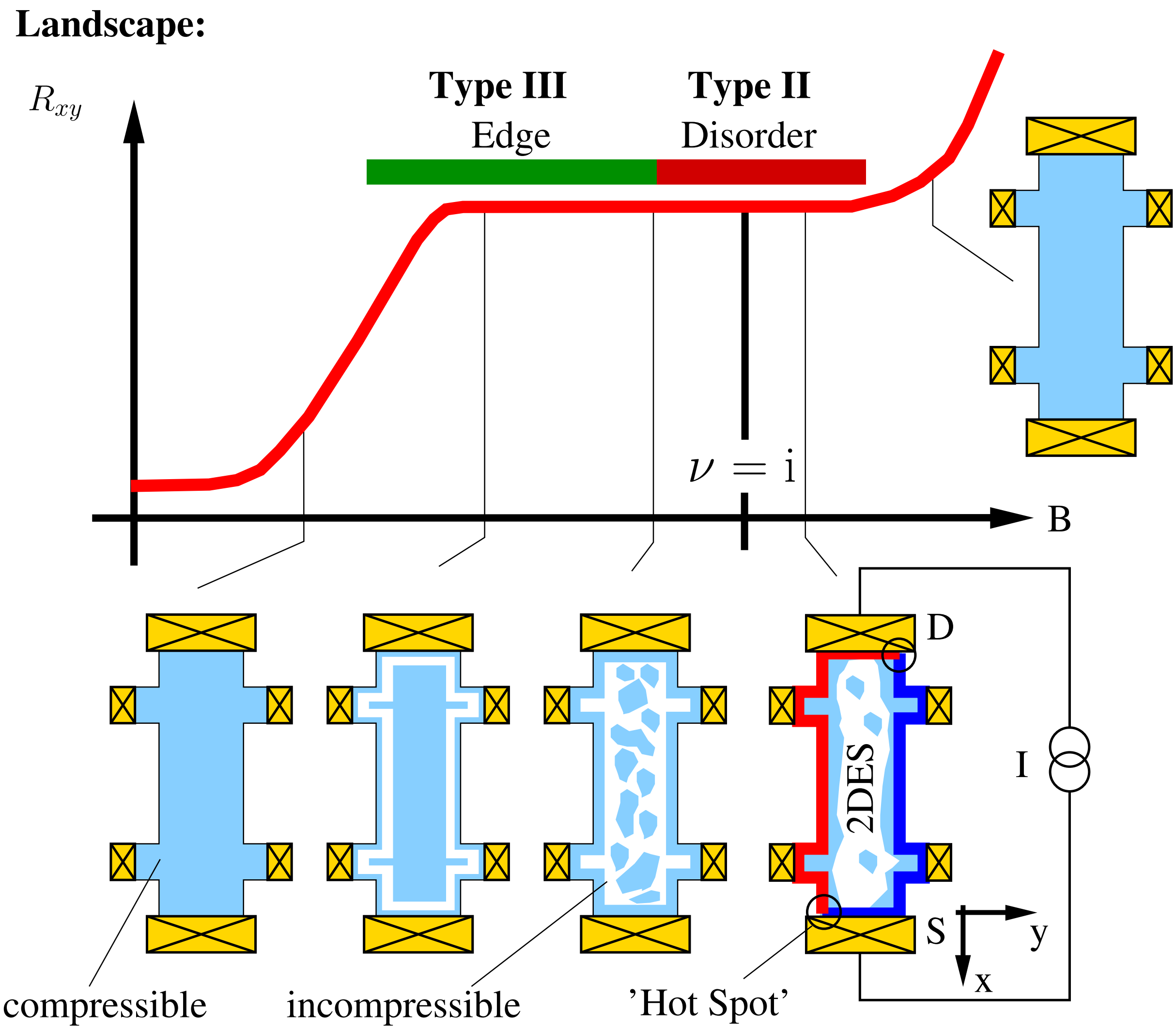
Landscape:
R_{xy}
Type III
Edge
Type II
Disorder
$\nu = \mathrm{i}$
B
D
S
I
2DES
y
x
compressible
incompressible
'Hot Spot'

Figure 4.8.: Evolution of the compressible/incompressible landscape inside the 2DES across a quantum Hall resistance plateau. Adapted with permission from [111]. Copyright © 2011, The Royal Society.

Part II.

Principles of the measurement technique

5. Scanning Force Microscopy

Scanning tunneling microscopy (STM) was developed by Binnig and Rohrer [116, 117] in 1982. A conducting sharp tip is brought into close proximity to a conductive sample and the tunnel current is used to control the height. By scanning the tip and simultaneously keeping the tunnel current constant, one can image the surface topology and the electronic structure of a surface with atomic resolution. This discovery had a huge impact on surface analysis and was awarded 1986 by the Nobel Prize.

The limitation of STM on conductive surfaces is a disadvantage which was overcome by measuring the force between tip and samples instead of the current. This was first achieved by Binnig, Quate and Gerber in 1986 [118]. Since then the scanning probe microscopy (SPM) was continuously improved and extended. It was 1995 when Giessibl [119], in parallel Kitamura and Iwatsuki [120], used non-contact mode to atomically resolve the 7x7 reconstruction of the silicon (111) surface. Non-contact mode means thereby that the tip does not touch the surface but oscillates above it. Since then, lots of different types of probes and techniques were developed.

In this thesis a cryogenic scanning probe microscope working in a low Helium atmosphere pressure ($p \approx 10^{-3}\,\mathrm{mbar}$) was used, operated at temperatures down to 1.4 K and in magnetic fields up to 15 T. The scanning range was 20 µm by 20 µm while the course alignment stage allowed for a movement of several millimeter in all three axis. Further details on the apparatus are given in [121].

In the following we want to discuss the principles of SPM with view on measurements of the Hall potential landscape. We will introduce the most important forces acting on the tip, and different operation modes with focus on non-contact mode. Thus we will look on how the dynamic reaction of the cantilever is upon external forces. Such an analysis was already given in detail by Peter Weitz [13]. We want here only to recap the most important concepts.

5.1. Relevant forces

The knowledge of the relevant forces is important to understand the measurement data. Subsequent we want to discuss shortly the most important forces acting between tip and sample: short range forces, van-der-Waals forces and electrostatic forces. Since we are interested in the electrostatic potential landscape of a 2DES we use a metallic tip and need to carefully consider the electrostatic forces.

Short range forces have their origin in overlapping of orbitals and the Coulomb repulsion of the nuclei. The distance where these forces become significant is limited to several 100 pm from the nuclei. They can be attractive (covalent bonding) or repulsive but are due to Paulis principle always repulsive for smaller becoming distance.

Fluctuations of the electron density in atoms lead to short time polarization of the atoms. The electric moments of that way polarized atoms can induce polarization in other atoms. These results in an attractive interaction. The interaction potential drops with distance r proportional to r^{-6}. In case the interaction partners are apart further than light can travel within the timescale of the fluctuation period, the interaction strength reduces. In that case the interaction is called retarded and its interaction potential drops with r^{-7}. The transition is expected by Meyer et al. [114] to happen at about 5 nm of distance between the interacting atoms.

Up to now we discussed only the interaction between two atoms. For an scanning force microscope with the tip hovering above the sample, far more than two atoms interact with each other. One has to transfer therefore the individual interatomic interaction into a solid body interaction to be able to deal with these forces. The Lifshitz-theory [122] using a continuum model is able to achieve this. For the calculation one assumes that the forces are additive and the bodies homogeneous [115]. For a model arrangement of a sphere with radius R at a distance d apart from a surface of a semi-infinite solid the van-der-Waals force would be, according to [115],

$$F_{\mathrm{vdW}} = \frac{2HR^3}{3d^2(d+2R)^2}. \tag{5.1}$$

Herein H is the material dependent Hamakar constant. It should be emphasized that the former r^{-7} dependence reduces for $R >> d$ to d^{-2} due to the integration over the interacting surface and tip volumes.

Electrostatic forces on the tip originate from static charges, intrinsic electrostatic potential differences and externally applied voltages. For the further treatment it is easier to consider the electrostatic energy stored in the tip/surface arrangement instead of the forces directly. The forces are then calculated by taking the gradient in tip/sample distance of the potential energy.

In an arrangement like in Fig. 5.1 we can find three electrostatic energy terms for the tip/surface arrangement. The first term comes from the interaction energy of the ions W_{i}. This is the energy one needs to bring all charges together including the image charges on the tip. Especially static charges from the ionized donors in the sample create a mirror

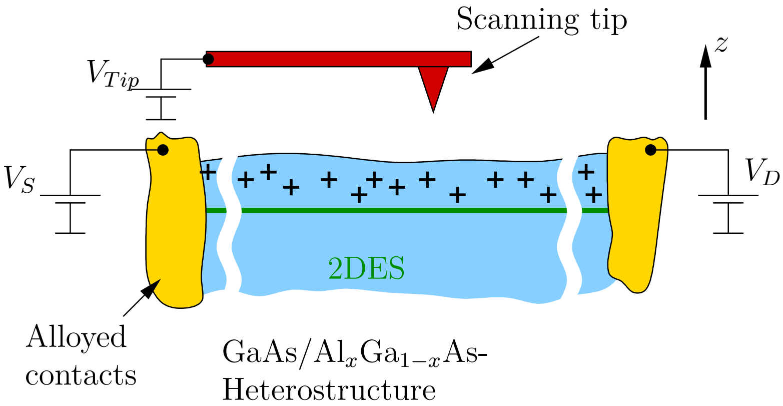

Figure 5.1.: Arrangement of tip and sample. The 2DES we want to probe is buried under a cap layer containing the donors.

charges q_m on the tip that has also to be included in W_i. Approaching the tip to the sample changes therefore this energy term leading to a contributing force.

The induce mirror charge q_m at the tip contributes on the other hand to the electrostatic energy as they feel the electrostatic potential of the tip. The tip-to-sample voltage consists thereby of two terms, an intrinsic $\Delta\phi_\mathrm{int}$ that we will discuss later on and the external applied voltage V. The energetic contribution of the mirror charges becomes thus

$$W_\mathrm{m} = q_\mathrm{m}(V + \Delta\phi_\mathrm{int}). \tag{5.2}$$

Finally the last force term originates from the capacitive energy between tip and 2DES W_c, built up by the geometric arrangement of tip and sample. Thus W_c reads

$$W_\mathrm{c} = \frac{1}{2}C(V + \Delta\phi_\mathrm{int})^2. \tag{5.3}$$

The resulting total interaction energy is the superposition of short range W_short, van der Waals W_vdW and electrostatic energy,

$$W = W_\mathrm{short} + W_\mathrm{vdW} + W_\mathrm{i} + W_\mathrm{m} + W_\mathrm{c}. \tag{5.4}$$

We let the coordinate system of the tip be the (x, y, z)-coordinate system and let the tip oscillate along the z direction. Then the force on the tip becomes simply the partial derivative of W along the z axes $\partial_z W$. Fig. 5.2 shows a sketch of the total potential of a tip with respect to the tip apex to sample distance.

But how to detect the forces acting on the tip? A first approach is to measure the deflection of the cantilever on which the tip is attached to. Read out mechanisms are discussed after the meaning of the intrinsic potential difference between tip and sample was clarified.

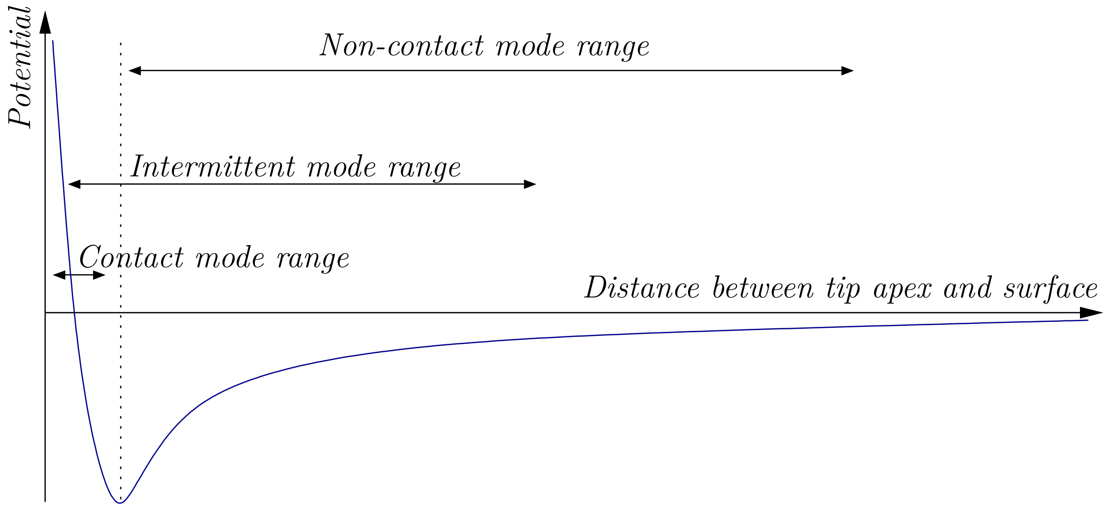

Figure 5.2.: Schematic representation of the interaction potential between tip and sample as a function of tip sample distance. Also shown the range of distance of the tip apex used in the different operation modes of the scanning force microscope.

5.2. Intrinsic potential difference and contact voltage

So far we have not specified the intrinsic potential difference $\Delta\phi_{\text{int}}$ any further. Therefore Fig. 5.3 sketches what happens to two different metals when contacted. For the uncontacted case one finds different work functions for the Fig. 5.3 (a). After contacting, Fig. 5.3 (b), a charge transfer from the metal with the lower work function to the one with the higher occurs until the mobile charge carrier of the two metals have the same energy, the electrochemical potential μ_{elch}. An electrostatic field is built up which causes an intrinsic electrostatic potential difference $\Delta\phi_{\text{int}}$. Applying a DC voltage between the two metals, $V_{\text{DC}} = -\Delta\phi_{\text{int}}$ can eliminate the electric field and recovers the situation without electrical contact between the metals, Fig. 5.3 (c). Thus the intrinsic electrostatic potential difference is equal to the work function difference of the metals which is also the chemical potential difference $\Delta\mu_{\text{ch}}$

$$q\Delta\phi_{\text{int}} = W_2 - W_1 = \Delta\mu_{\text{ch}}. \tag{5.5}$$

In the following we want to replace $\Delta\phi_{\text{int}}$ by $\Delta\mu_{\text{ch}}/e$. We will discuss the effect on our measurement data by chemical potential changes induced by our measurement set up in section 6.3.

5.3. Mechanisms to detect the cantilever deflection

There are plenty of methods to detect the deflection of a cantilever holding a scanning tip. A selection of them picked from [114] is shown in Fig. 5.4 and discussed in the following:

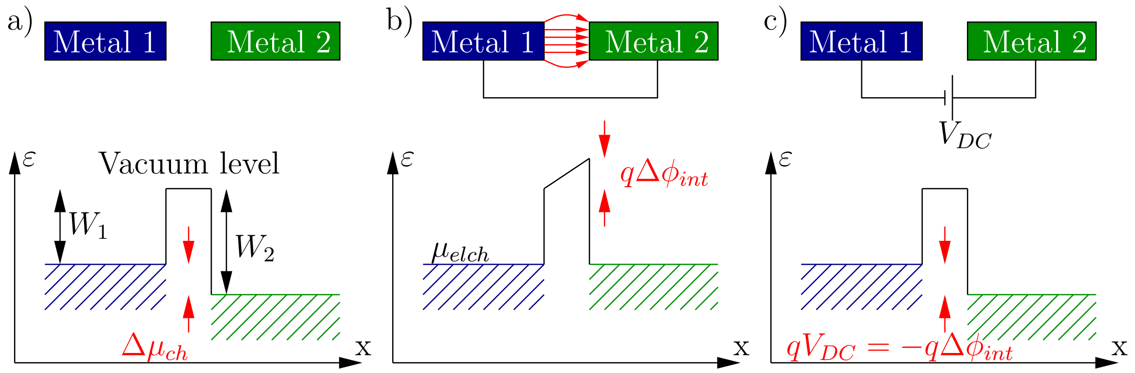

Figure 5.3.: Effect of chemical potential difference. (a) Without electrical contact the vacuum level is the reference to compare the two metals. The work function is the energy difference between vacuum level and electrochemical potential. (b) After electrically contacting the metals to each other, electrons will flow from the metal with lower work function to the one with higher. This will continue until an electrostatic field builds up between the two metals counteracting the diffusion current and restores equilibrium. The two metals are now at the same electrochemical potential μ_{elch}. The chemical potential difference $\Delta\mu_{\text{ch}}$ was compensated by an electrostatic potential energy difference $q\Delta\phi_{\text{int}}$. (c) After applying a voltage the electric field between the metals can be removed.

(a) The method used preferably is the measurement of a laser beam deflection from the back side of the cantilever. A 4-quadrant photodiode is used to detect the deflection of the beam. Therefore not only the bending but also the torsion of the cantilever can be detected. The alignment precision necessary for the beam source, cantilever and photodiode demands these elements to be adjustable. It is easier therefore to move the sample instead of the tip. Also the whole setup of the detection system needs relatively huge amount of space.

(b) Using interferometry to determine the deflection of a cantilever takes less space than with beam deflection. This approach does not allow to measure the cantilever's torsion.

(c) A capacitive arrangement between the back side of the cantilever and a metal electrode allows for detecting the bending as well as exciting the cantilever to oscillate. Forces on the cantilever due to this detection mechanism can also be a disadvantage and have to be considered during the measurement.

(d) An interesting method to detect very small distance changes is by an STM positioned on the back side of the cantilever. The first SPM by Binning et al. [118] was actually built that way. The drawback of this technique is that the STM tip has to be positioned and approached to the SPM cantilever with similar precision and difficulties as the SPM tip to the sample.

(e) A very elegant method is the usage of a piezoelectric cantilever. The cantilever becomes itself the sensor and excitation element [123]. Such tips can easily be home made by glueing etched tips onto standard clock quartzes [124, 125]. The stiffness of the quartz material allows especially for combined STM/SPM systems.

(f) Piezoresistive tips change their resistance depending on the deflection. They can be produced from Silicon [126], usually by ion implantation on one side of the cantilever. The piezoresistive effect is due to a change in the band structure of silicon upon mechanical strain [127]. Piezoresistive tips have a low sensitivity compared to other detection methods. Still atomic resolution is reachable [119].

From these detection mechanisms one had to be choose for our experiments. This was done with the following argumentation by other members of our group before this thesis was started. All optical detection methods can be excluded for our purpose since the samples we want to study are optically sensitive and the unavoidable stray light will affect them. Also the space in a sample holder is limited and simple solutions are preferable because the cool down itself brings lots of challenges, and reliability is key for an effective usage of such a tool. Essentially piezoresistive and piezoelectric tips fulfill this requirement. The setup was designed for the use of piezoresistive cantilevers mainly because the existing knowledge and experience in the group. Piezoelectric cantilevers are superior to piezoresistive cantilevers in terms of signal quality. But also operation mistakes are more severe with piezoelectric tips than with piezoresistive ones because of the higher stiffness. The reliability is therefore higher with piezoresistive cantilevers that is why they where uses throughout this thesis.

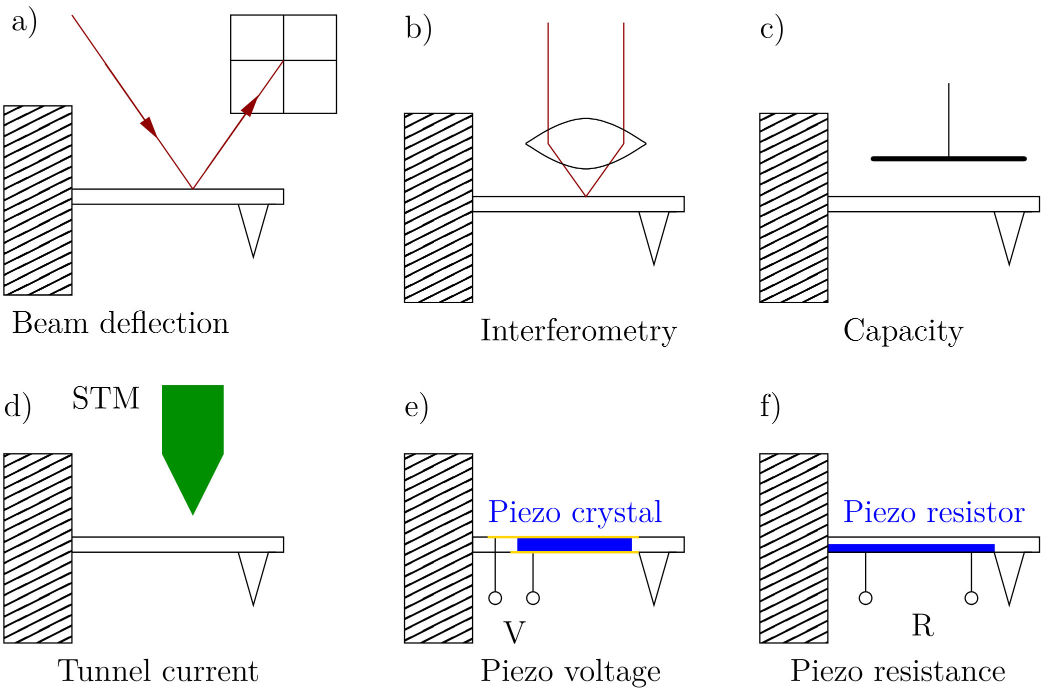
a)
Beam deflection
b)
Interferometry
c)
Capacity
d)
STM
Tunnel current
e)
Piezo crystal
V
Piezo voltage
f)
Piezo resistor
R
Piezo resistance

Figure 5.4.: Sketch of some detection mechanisms adapted from [114].

5.4. Dynamics of a cantilever

The static deflection is not the only way to read out forces acting on a cantilever and thus we want to look next on the dynamic properties of an oscillating cantilever with forces acting on it.

A cantilever can be modeled by an excited, damped harmonic oscillator [128] with an effective mass m, damping coefficient b and spring constant k,

$$m\ddot{z} + b\dot{z} + kz = F_{\text{exc}}(t). \tag{5.6}$$

The excitation $F_{\text{exc}}(t)$ is used is usually monochromatic with the frequency f. Sweeping f, a resonance for the cantilever oscillation is found at [13]

$$f_{\text{r}} = \frac{1}{2\pi}\sqrt{\frac{k}{m} - \frac{b^2}{4m^2}} = f_0\sqrt{1 - \frac{1}{4Q^2}}, \tag{5.7}$$

where Q is the quality factor of the oscillator and f_0 the resonance frequency of the undamped oscillator

$$f_0 = \frac{1}{2\pi}\sqrt{\frac{k}{m}}, \tag{5.8}$$

$$Q = \frac{m\omega_0}{b}. \tag{5.9}$$

Our measurements were done in a helium atmosphere with pressure of around 10^{-3} mbar

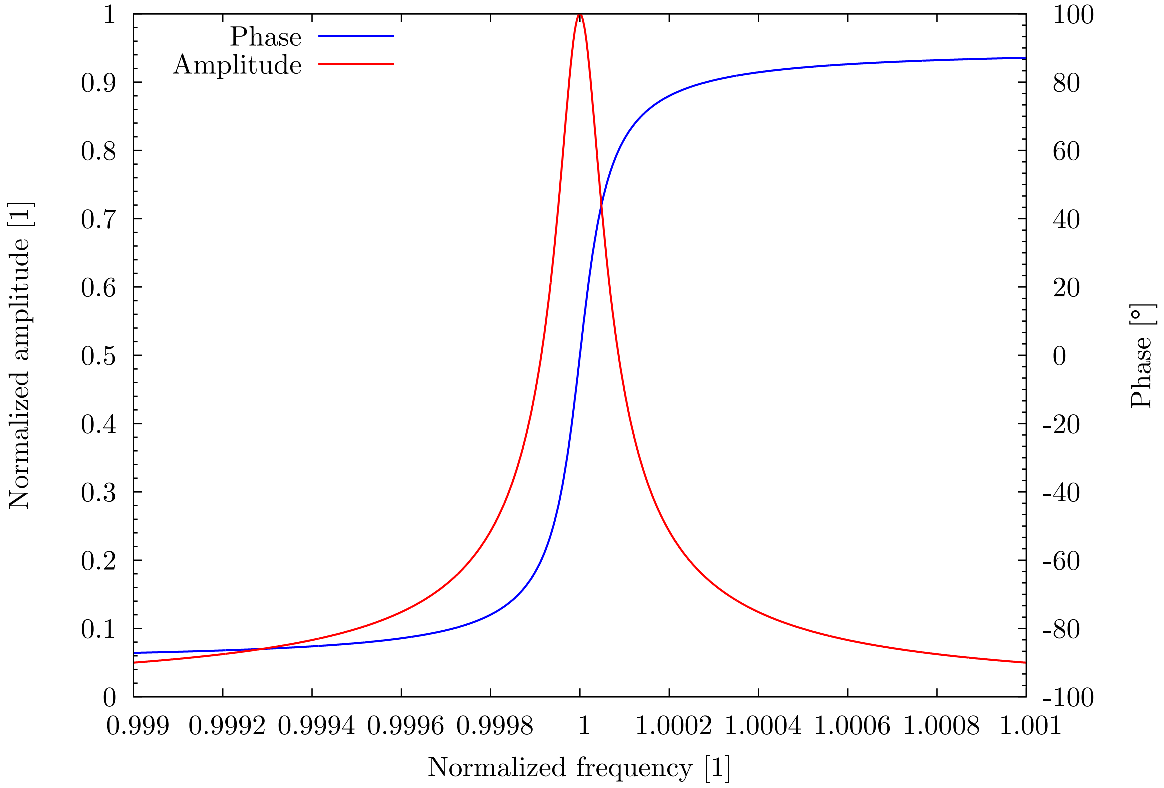

Figure 5.5.: Resonance profile for an SPM cantilever with quality factor of $Q = 10000$.

and at temperatures in the range of 1.5 K. Typical values for the quality factor of the used tips measured under this conditions throughout this thesis lay between 10000 and 30000.

Further calculations [112] lead to the cantilever's oscillation amplitude and phase shift relatively to the excitation at frequency f

$$A(f) = \frac{A_0 f_0^2}{\sqrt{Q^2(f^2 - f_0^2)^2 + f_0^2 f^2}}, \tag{5.10}$$

$$\phi(f) = \arctan\left(\frac{f^2 - f_0^2}{f_0 f} Q\right). \tag{5.11}$$

Here A_0 is the amplitude at resonance frequency f_0. Figure 5.5 shows such a resonance profile $A(f)/A_0$ versus f/f_0.

5.4.1. Dynamics of a cantilever under external forces

In the following we want to discuss the dynamic motion of a cantilever under an additional static external force. We are especially interested at the information one can retrieve when measuring dynamic properties, like resonance frequency.

We start again with equation (5.6) but add the external forces F_{pot} which are considered to originate from a nearby surface

$$m\ddot{z} + b\dot{z} + kz = F_{\text{pot}}(z_0 + z) + F_{\text{exc}}(t). \tag{5.12}$$

The coordinate z describes thereby the distance of the tip apex to its resting position z_0 above the surface and $F_{\text{pot}}(z_0 + z)$ is the force due to the sample at the actual position $(x, y, z + z_0)$.

Equation (5.12) can be simplified for the case of keeping the cantilever oscillating with constant amplitude which means that the damping term $b\dot{z}$ is compensated by the excitation F_{exc} leading to

$$m\ddot{z} + kz = F_{\text{pot}}(z_0 + z). \tag{5.13}$$

When confining ourselves to forces slowly varying within the tip oscillation range we can write the Taylor series of the forces and stop it after the second term,

$$F_{\text{pot}}(z_0 + z) \approx F_{\text{pot}}(z_0) + \partial_z F_{\text{pot}}(z)|_{z=z_0} \cdot z. \tag{5.14}$$

The constant term only shifts the resting point of the tip by $\Delta z_0 \approx F_{\text{pot}}(z_0) \cdot k^{-1}$ and can be neglected as long as the force gradient does not change relevantly. Inserting equation (5.14) into equation (5.13) and neglecting the constant term one can combine the force gradient and the restoring force,

$$m\ddot{z} + (k - \partial_z F_{\text{pot}}(z)|_{z=z_0}) \cdot z = 0. \tag{5.15}$$

This combination is the crucial point since we transformed the original equation (5.12) by this into a free harmonic oscillator with effective spring constant of $k - \partial_z F_{\text{pot}}(z)|_{z=z_0}$. This will shift the resonance frequency f_{r} which we can find with the ansatz

$$z(t) = Ae^{i2\pi f_{\text{r}} t} + A^* e^{-i2\pi f_{\text{r}} t}. \tag{5.16}$$

The resonance frequency f_{r} is thus

$$f_{\text{r}} = \frac{1}{2\pi}\sqrt{\frac{k - \partial_z F_{\text{pot}}(z)|_{z=z_0}}{m}}. \tag{5.17}$$

Retrospectively we have to set the excitation on this frequency f_{r} to keep the argumentation valid. A further simplification can be achieved when equation (5.17) is approached with a Taylor series up to the second term around the undisturbed resonance frequency $f_0 = 0.5\pi^{-1}\sqrt{k \cdot m^{-1}}$. This can be done when the force gradient is much smaller than the spring constant $k >> \partial_z F_{\text{Pot}}(z)|_{z=z_0}$ which basically was also assumed for equation (5.14). The resonance angular frequency reads then

$$f_{\text{r}} \approx f_0 \cdot \left(1 - \frac{\partial_z F_{\text{pot}}(z)|_{z=z_0}}{2k}\right). \tag{5.18}$$

Therefore the resonance frequency shift

$$\Delta f \approx -f_0 \cdot \frac{\partial_z F_{\mathrm{pot}}(z)|_{z=z_0}}{2k}. \tag{5.19}$$

allows to measure the force gradient at the tip position. A positive $\partial_z F_{\mathrm{pot}}(z)|_{z=z_0}$ usually expected for an attractive force will yield a negative resonance frequency shift.

The so far described derivation for small force gradients is sufficient for the need of our experiments. This is because, compared to other SPM techniques, we have large distances between tip and sample due to the buried 2DES. We still want to mention that a more precise solution of this problem is possible by transferring equation (5.13) into an integral equation [129, 130]. The resonance frequency shift of electrostatic and van-der-Waals forces can thereby be calculate including the tip geometry.

5.5. Scanning modes

The analysis done so far allows for two different scanning modes. A static and a dynamic mode. In the static mode the cantilever usually touches the surface and the mode is called therefore contact mode. The oscillating mode does not touch the surface giving it the name non-contact mode. These two modes are the two extreme cases shown in Fig. 5.6 where the amplitude and mean tip apex position are sketched depending on the tip-apex-to-sample distance. One can identify a region where the amplitude is reduced due to tapping on the surface. This gives a third scanning mode called tapping or intermittent mode.

Piezoresistive as well as other types of cantilevers are available with different spring constant. For the right choice one needs to understand the needs of the used detection mode and the interaction strength between tip and sample. As orientation for the order of magnitude of this force one can take the strength of a covalent bond. We can get an estimate of the strength via the stretching oscillation of diatomic molecules [114]. The spring constant found that way lies around 5 Nm^{-1}. Cantilevers with spring constants higher than 5 Nm^{-1} can be considered as hard and the ones with lower spring constant as soft cantilevers. A more detailed discussion about the scanning modes and the required spring constants is given in the following.

5.5.1. Contact mode

The technically easiest way to acquire a topographic scan is with the contact mode because only the static deflection of the tip is used and no additional dynamic excitation and complicated readout is needed.

The image generated is usually interpreted as topography but this should not be taken guaranteed. Even though the acting forces are in the nano Newton range the resulting pressure due to the small contact area are in the Mega Pascal range [13]. Thus there is a deformation of the sample surface at the position of the tip which can also become permanent. In addition friction can be a relevant factor. To surmount this problem one has to separately measure friction using a suitable detection method.

The interaction between tip and surface has relevant terms from many atoms and an

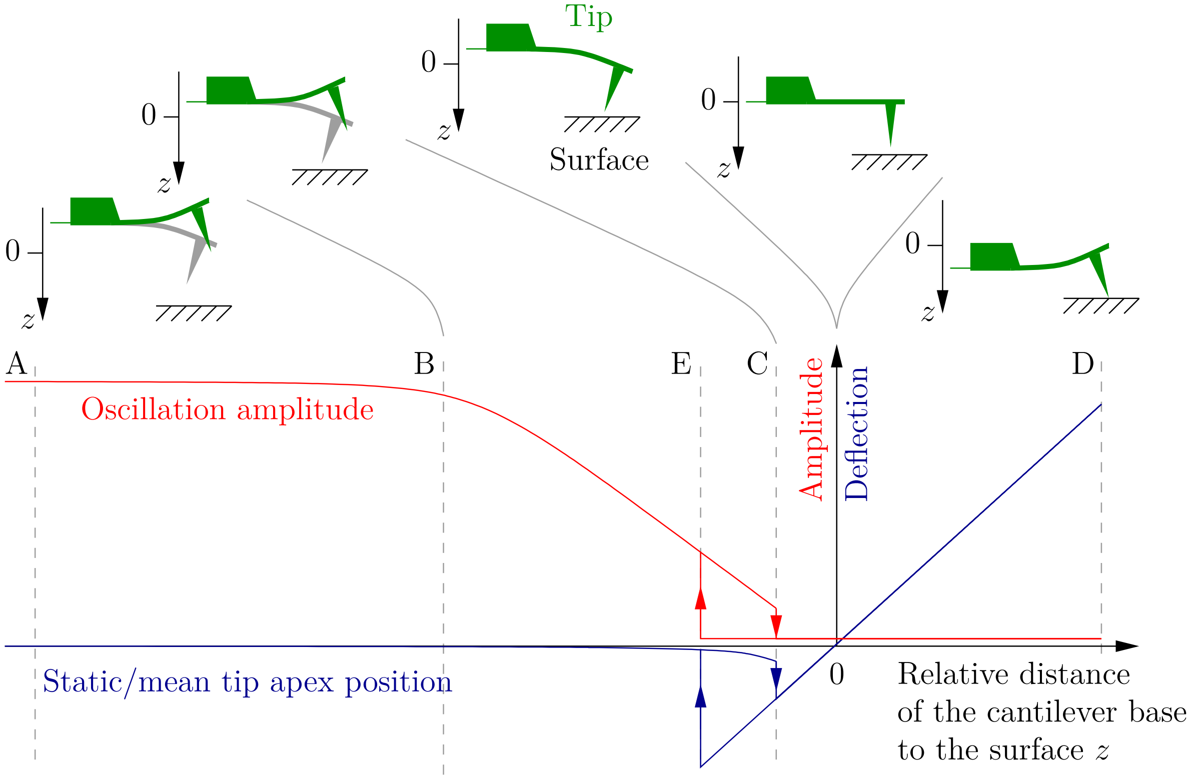
Tip
Surface
0
z
A
B
E
C
D
Oscillation amplitude
Amplitude
Deflection
Static/mean tip apex position
0
Relative distance
of the cantilever base
to the surface z

Figure 5.6.: Sketch of the tip behavior approaching the sample surface. In blue the mean deflection is drawn and in red the amplitude of an oscillating tip like used in intermittent and non-contact mode. During the approach in the range A to B the tip oscillates freely. Further approach lets the tip tap the surface so that the amplitude is reduced in the region between B and C. At the moment when the attractive force to the tip becomes bigger than the retraction force the tip snaps to contact. The amplitude becomes zero at this point indicated as C and the tip is bend towards the surface. The mean deflection is now also the static deflection and equals the distance to the surface. Further approach is reflected linearly in the deflection in the regions C to D and the point with zero deflection can be used to calibrate the absolute distance to the surface. Retracting the tip follows again the linear trend passes the point C and the release of the tip is found at the point E. The mean deflection of the tip after passing E becomes nearly zero again and the oscillation recovers.

atomic resolution is therefore not possible in this mode. This is because the expected diameter of the contact area is according to Meyer et al. [114] 1 nm to 4 nm within ultra high vacuum.

The direct contact to the surface demands for small forces. The cantilever spring constant should be chosen to be soft when measuring in this mode. In Fig. 5.6 the deflection of the cantilever during the approach is shown in blue. When the attractive force between tip and surface becomes stronger than the Force due to the tip spring constant the tip snaps onto the surface. This is marked in Fig. 5.6 as C and is referred to as "snap-to-contact", "snap-in" or "jump-to-contact". Before a measurement can be started the tip has to approach the surface and has to snap-to-contact. Any feedback loop keeping the tip to sample distance constant has to be adjusted so that the reverse process, the "jump-off" see Fig. 5.6 E, does not happen during the scan. Thus to make the working area shown in Fig. 5.6 C to E larger as well as for reducing forces, soft cantilevers are preferred for this mode.

5.5.2. Intermittent mode

In the intermittent mode the tip oscillates and is close enough to the surface so that it taps the surface once in each period of the cantilever oscillation. The term "tapping mode" is hence also used. For the height regulations the amplitude is used. In Fig. 5.6 the range B to C is where tapping mode can be done.

The advantage for the intermittent mode over the contact mode is the reduction of the contact with the surface. Correctly used, this mode reduces both the amount of plastic deformations at the sample surface and the lateral forces like friction.

To avoid a "snap-in", harder cantilevers have to be used and the excitation has to be high enough so that the tip can escape from the surface. Pablo et al. [131] could show that with to small excitation an intermittent mode is not possible. Instead the measurement mode switches from non-contact to contact mode directly.

According to Pablo et al. [131] the amplitude in the region between B and C shown in Fig. 5.6 is approximately proportional to the distance from the surface. With known tip-sample distance this can be used to determine the peak-to-peak oscillation amplitude in the region A to B of Fig 5.6. One should take care to stay at the resonance frequency with the excitation when utilizing this method to determine the amplitude because the resonance frequency shift becomes important in between B and C and leads to nonlinear deviations when the tip is not excited resonantly.

5.5.3. Non-contact mode

A contact-free method can be realized when the dynamic properties of a cantilever under external forces are utilized. Thereby the cantilever is excited at its resonance frequency and the shift of the resonance frequency due to external forces is used as the feedback signal for the tip height regulation.

In terms of cantilever stiffness similar statements can be made as for the intermittent mode. A snap-in should be avoided by using stiffer cantilevers and using high enough excitation amplitudes.

In this thesis all topography scans where done in the non-contact mode. The potential measurements described in the next chapters are also based on the non-contact mode. Even though stiff non-contact mode tips are preferable we used soft tips intended for contact mode. This was done mainly because of reliability reasons. The change of tip in a cryogenic vacuum system is very time consuming. The contact mode tips we used, see for more details chapter I, with spring constant of 5 Nm^{-1} usually survive crashes of the tip into the sample surface, and thus do not need to be changed immediately after an accident.

5.6. Operation principle of a scanning probe microscope

The basic principle for an SPM is always the same even for STMs. One scans the surface with the tip and uses some feedback signal either for generating the image or for compensating the height which becomes then the image. For topographic scans the tip is attempted to be kept at the same height using the feedback signal. Figure 5.7 shows the minimum setup for this task. At least one closed loop and one open loop controller is needed. The open loop controller is used for the x-y positioning while the closed loop controller adjusts the z-position. The feedback is required to generate the height signal and to avoid crashes of the tip into the surface.

It should be emphasized here that this basic principle suffers from all sorts of artefacts, depending on the type of sample. These artefacts are out of the scope of this work and the reader is adverted to the literature [112–115]. The few artefacts relevant for us will be discussed in the appendix G.

The basic setup of a non-contact SPM is shown in Fig. 5.8. The measurement of the resonance frequency is done with a second feedback loop. The phase of the oscillation is thereby used as feedback signal to stay at the resonance. The device doing this is thus called "Phase Locked Loop" (PLL) and basically consists of three elements: A controllable frequency generator for the excitation of the tip. A lock-in amplifier locked to the frequency generator to detect the tip oscillations amplitude and phase, and a control

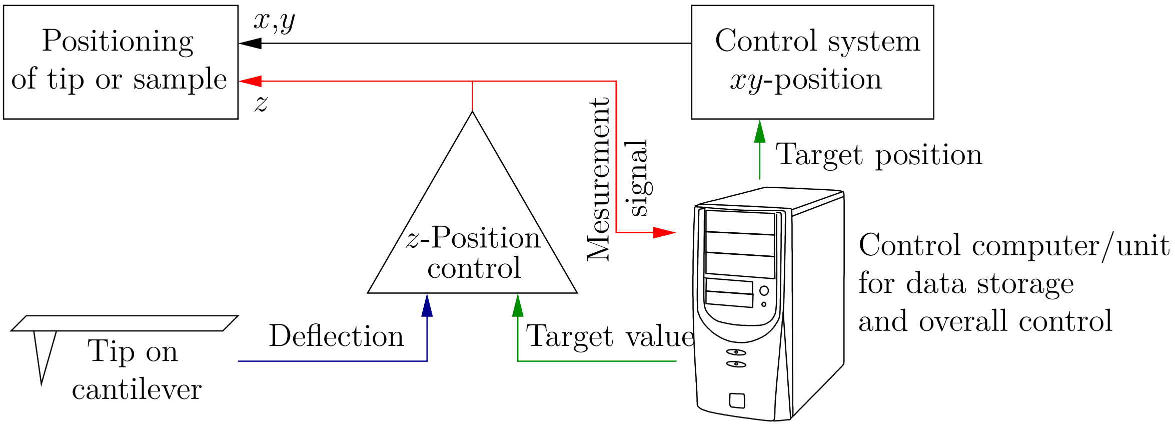
Positioning of tip or sample
x,y
z
Control system xy-position
Mesurement signal
Target position
z-Position control
Control computer/unit for data storage and overall control
Deflection
Target value
Tip on cantilever

Figure 5.7.: Operation principle of a Scanning Probe or Scanning Tunneling Microscope for measuring topography.

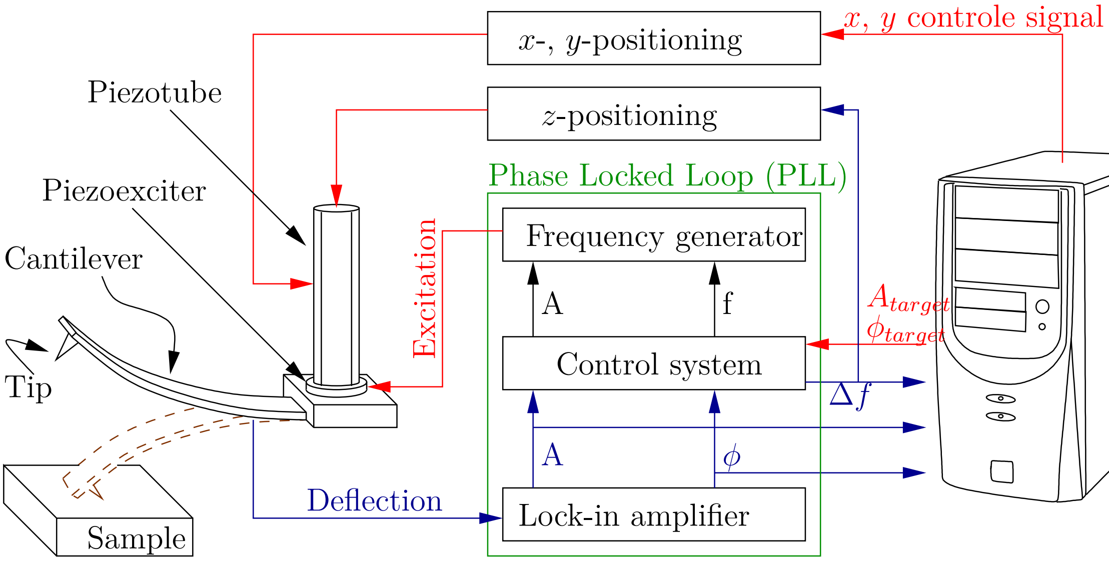
x-, y-positioning
x, y controle signal
z-positioning
Piezotube
Piezoexciter
Cantilever
Tip
Sample
Phase Locked Loop (PLL)
Excitation
Frequency generator
A
f
A_{target}
ϕ_{target}
Control system
Δf
A
ϕ
Deflection
Lock-in amplifier

Figure 5.8.: Sketch of a non-contact SPM setup.

circuit to keep the phase constant.

In addition to the control of the phase the PLL can also include a control to keep the amplitude constant. This is nice when scanning in an environment with unpredictable strong forces reducing thereby artefacts due to amplitude effects. Also it reduces the recovery time of the tip amplitude after a crash. On the other hand a crash is more severe if undetected since due to the feedback the tip excitation will ramp up to keep the amplitude constant. The amplitude control of the PLL was thus not used in this thesis because of the increased risk of tip losses.

5.7. Summary

In this chapter the principles of scanning probe microscopy were described. We started with relevant forces acting on a scanning tip and discussed the possibilities to measure the cantilever deflection. Dynamic properties of the scanning cantilevers were recapped to be able to understand the most common operation modes: contact, intermittent and non-contact mode. We argued that due to size constrictions in the cryostat, sample needs and reliability, piezoresistive tips are the best choice in our case. We found that the non-contact mode suits our scanning needs best. One can use it to measure force gradients and it will be shown in the next chapter how it can be used to measure local potential variations. Finally we put everything together to describe the basic principle of operation of our SPM system.

6. Measuring Hall potential profiles of a 2DES: Calibration technique

In this chapter we want to discuss how to extract the Hall potential landscape through scanning force microscopy (SFM). As was already explained in the previous chapter the resonance frequency shift of the tip in non-contact mode is proportional to the gradient of the total force acting on the tip. Though a modulation of the sample potential compared to the potential of the tip one can alter the electrostatic contribution of the tip signal. By filtering with a lock-in amplifier the electrostatic contribution can be extracted. Unfortunately this signal is not simply the current induced electrostatic potential change but is affected by the tip-sample arrangement, the static charge distribution and intrinsic electrostatic potentials between tip and sample. A calibration measurement is therefore needed to eliminate these factors.

We will also discuss how to calibrate for the contact potential between tip and sample. This has to be done since the built-in potential difference would deplete or accumulate charges under the tip.

The measurement technique described here can lead to artefacts if not applied correctly. To identify such artefacts we prepared a chapter in the appendix G dealing exclusively with this topic.

6.1. Detecting alterations: Switching between equilibrium and non-equilibrium

In the following we want to sketch the derivation of the measurement technique used in this thesis. A more detailed derivation can be found in the thesis of Peter Weitz [13].

From the previous chapter we know that the tip signal is proportional to the force gradient on the tip. Since the main degree of freedom for the tip lies along the z-axis and our tip signal resembles mainly this movement direction we want to focus on it and neglect other movement directions. The force becomes then

$$\begin{aligned} F = &- \partial_z W_{\mathrm{short}} - \partial_z W_{\mathrm{vdW}} - \partial_z W_{\mathrm{i}} \\ &- \partial_z q_{\mathrm{m}} (V + \Delta\mu_{\mathrm{ch}}/e) - \frac{1}{2}\partial_z C (V + \Delta\mu_{\mathrm{ch}}/e)^2. \end{aligned} \tag{6.1}$$

A second derivation gives us the force gradient

$$\begin{aligned} \partial_z F = &- \partial_z^2 W_{\mathrm{short}} - \partial_z^2 W_{\mathrm{vdW}} - \partial_z^2 W_{\mathrm{i}} \\ &- \partial_z^2 q_{\mathrm{m}} (V + \Delta\mu_{\mathrm{ch}}/e) - \frac{1}{2}\partial_z^2 C (V + \Delta\mu_{\mathrm{ch}}/e)^2. \end{aligned} \tag{6.2}$$

which is in a first approach proportional to the resonance frequency shift, see (5.19).

Modulating the bias voltage of the sample modulates also the local tip-to-sample voltage. We use

$$V = V_{\mathrm{DC}} + V_{\mathrm{AC}} \cdot \sin \omega_{\mathrm{m}} t, \tag{6.3}$$

as modulation with a DC component V_{DC} and a sine wave AC component with amplitude V_{AC} and angular frequency $\omega_{\mathrm{m}} = 2\pi f_{\mathrm{m}}$ which was chosen to be about four orders of magnitude smaller than the resonance angular frequency ω_{r} of the tip. This gives in a first glance a quite confusing force gradient

$$\begin{aligned}
\partial_z F = &- \partial_z^2 W_{\mathrm{short}} - \partial_z^2 W_{\mathrm{vdW}} - \partial_z^2 W_{\mathrm{i}} \\
&- \partial_z^2 q_{\mathrm{m}} (V_{\mathrm{DC}} + V_{\mathrm{AC}} \cdot \sin \omega_m t + \Delta\mu_{\mathrm{ch}}/e) \\
&- \frac{1}{2} \partial_z^2 C (V_{\mathrm{DC}} + V_{\mathrm{AC}} \cdot \sin \omega_m t + \Delta\mu_{\mathrm{ch}}/e)^2 \qquad (6.4) \\
= &- \partial_z^2 W_{\mathrm{short}} - \partial_z^2 W_{\mathrm{vdW}} - \partial_z^2 W_{\mathrm{i}} \\
&- \partial_z^2 q_{\mathrm{m}} \cdot V_{\mathrm{AC}} \cdot \sin \omega_m t - \partial_z^2 q_{\mathrm{m}} (V_{\mathrm{DC}} + \Delta\mu_{\mathrm{ch}}/e) - \partial_z^2 C (V_{\mathrm{DC}} + \Delta\mu_{\mathrm{ch}}/e) \cdot V_{\mathrm{AC}} \cdot \sin \omega_m t \\
&- \frac{1}{2} \partial_z^2 C (V_{\mathrm{DC}} + \Delta\mu_{\mathrm{ch}}/e)^2 - \frac{1}{2} \partial_z^2 C V_{\mathrm{AC}}^2 \cdot \sin^2 \omega_{\mathrm{m}} t. \qquad (6.5)
\end{aligned}$$

We can now clearly identify several terms not depending at all on $\sin \omega_{\mathrm{m}} t$, two being proportional to $\sin \omega_{\mathrm{m}} t$ and one being even proportional to $\sin^2 \omega_{\mathrm{m}} t$. Using a lock-in amplifier one can now filter out terms depending on ω_{m}. Since $\sin^2 \omega_{\mathrm{m}} t = 0.5 + 0.5 \sin 2\omega_{\mathrm{m}} t$, by locking on ω_{m} we just get as an amplifier output signal V_{LI}

$$V_{\mathrm{LI}} \propto \partial_z^2 q_{\mathrm{m}} \cdot V_{\mathrm{AC}} + \partial_z^2 C (V_{\mathrm{DC}} + \Delta\mu_{\mathrm{ch}}/e) \cdot V_{\mathrm{AC}}. \tag{6.6}$$

The data got from the lock-in amplifier at equation (6.6) shows a proportionality to the applied AC voltage amplitude V_{AC}. In case we do not apply the AC voltage commonly to all contacts but rather keep some at a fixed potential, currents and potential gradients will be present inside the sample. The local modulation of the electrostatic potential will be proportional to the local AC voltage $V_{\mathrm{AC}}(x, y)$. The measured signal from the lock-in amplifier will include this locality but also q_{m}, C and $\Delta\mu_{\mathrm{ch}}/e$ depend on position. (We want to neglect the z-position in the following since the tip is moved only within the $x - y$-plane). Equation (6.6) become in total

$$V_{\mathrm{LI}\alpha}(x, y) \propto \{\partial_z^2 q_{\mathrm{m}}(x, y) + \partial_z^2 C(x, y)[V_{\mathrm{DC}} + \Delta\mu_{\mathrm{ch}}/e(x, y)]/e\} \cdot V_{\mathrm{AC}}(x, y). \tag{6.7}$$

The position dependent prefactor can be eliminated when measured separately. In case we do not allow for current flow, V_{AC} becomes independent of position and we do indeed measure only the prefactor:

$$V_{\mathrm{LI}\beta}(x, y) \propto \{\partial_z^2 q_{\mathrm{m}}(x, y) + \partial_z^2 C(x, y)[V_{\mathrm{DC}} + \Delta\mu_{\mathrm{ch}}/e(x, y)]/e\} \cdot V_{\mathrm{AC}}. \tag{6.8}$$

The prefactor can then be eliminated by dividing equation (6.7) by (6.8) which results into the calibrated current-induced electrostatic potential change

$$\hat{\phi}(x,y) = \frac{V_{\mathrm{LI}\alpha}}{V_{\mathrm{LI}\beta}} = \frac{V_{\mathrm{AC}}(x,y)}{V_{\mathrm{AC}}}. \tag{6.9}$$

In practice this means one scans once for a trace of $V_{\mathrm{LI}\alpha}$ and once more along the same trace to acquire $V_{\mathrm{LI}\beta}$. The actual setup doing this is shown in Fig. 6.1 and an example measurement demonstrating the calibration in Fig. 6.2. We want to emphasize here that the maximum of the calibrated potential profile neither has to be one nor has the minimum to be zero. This depends on the actual scan position and also on the amount of dissipation in the sample.

From this result one can nicely see that the data resulting from the measurement technique resembles the changes within the sample away from the thermal equilibrium situation.

6.2. Considerations about form of switching

In the previous section we discussed the basic calibration technique using a sine waveform as modulation. In this section we want to discuss the effect of the waveform on the result. Therefore we need to go into details of lock-in amplifier functionality.

In a lock-in amplifier the key elements are a multiplier where the input signal $V_{\mathrm{in}}(t)$ is multiplied with the reference signal $\sin\left(\frac{2\pi}{T}\cdot t + \Delta\phi\right)$ with phase shift $\Delta\phi$ and a low pass filter through which the multiplied signal is passed. The low pass filter can mathematically be written as an integration over time divided by the time integrated. Since this is

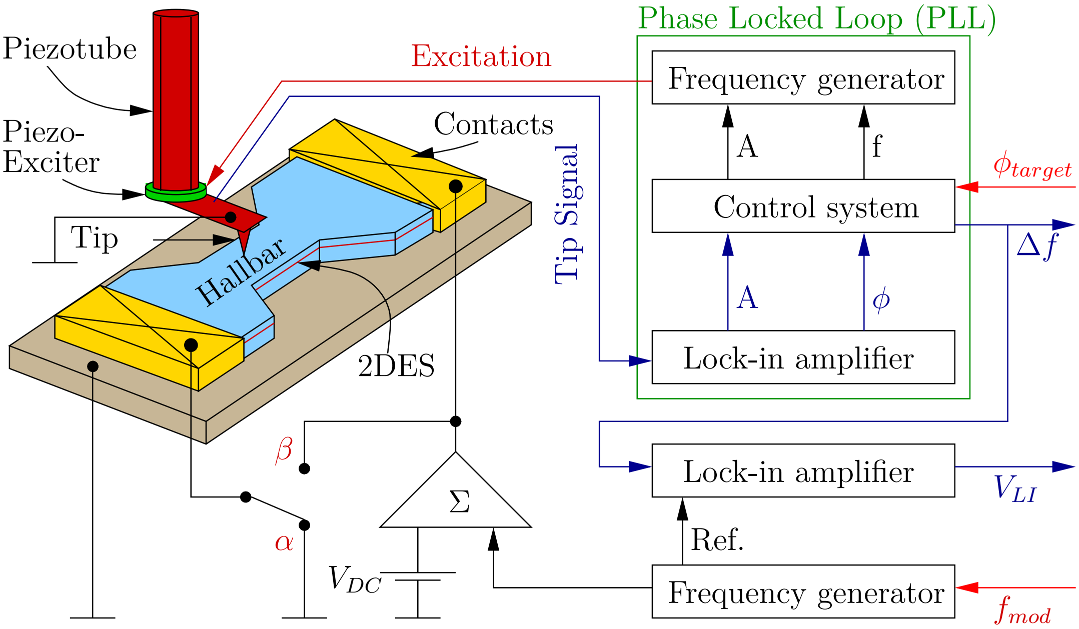
Piezotube
Piezo-
Exciter
Tip
Hallbar
Contacts
2DES
Excitation
Tip Signal
Phase Locked Loop (PLL)
Frequency generator
A
f
Control system
A
ϕ
Lock-in amplifier
ϕ_{target}
Δf
β
α
Σ
V_{DC}
Lock-in amplifier
V_{LI}
Ref.
Frequency generator
f_{mod}

Figure 6.1.: Calibration technique to measure the current induced potential changes. The switch with positions α and β handles the two successive measurements of $V_{\mathrm{LI}\alpha}$ and $V_{\mathrm{LI}\beta}$.

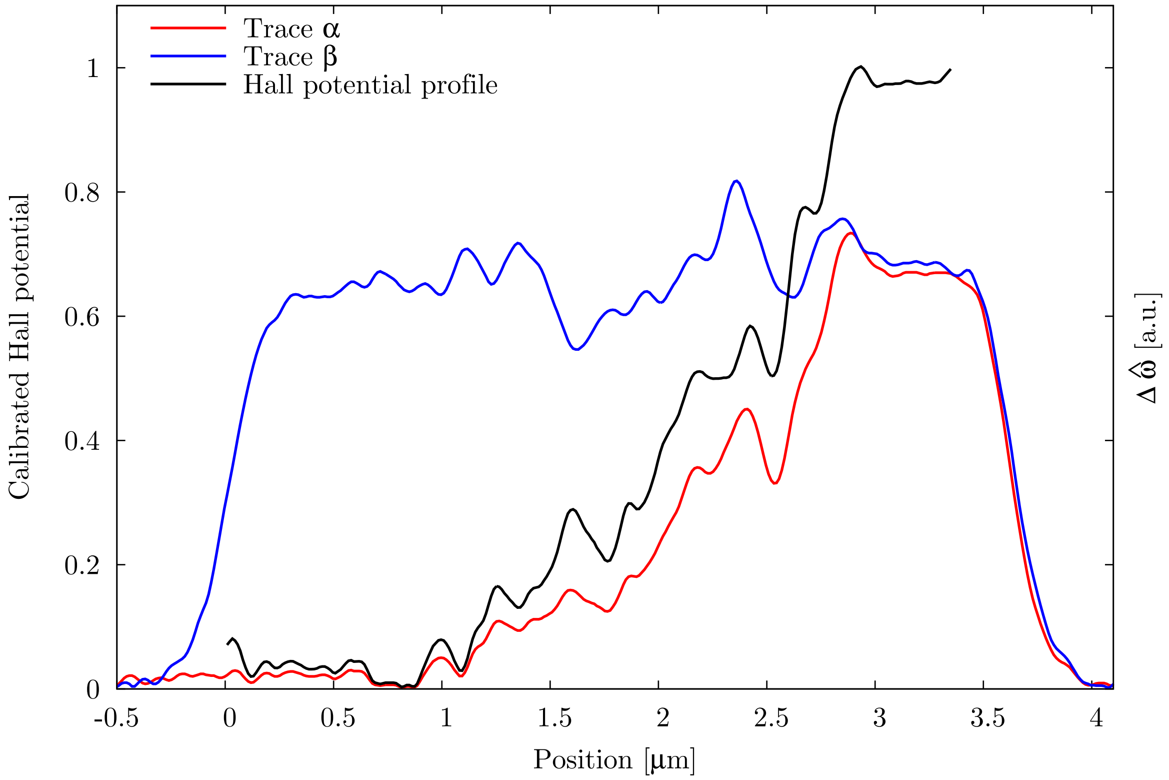

Figure 6.2.: Example data showing trace α and β in arbitrary units and the resulting Hall potential profile.

a periodic problem in time it is suficient to integrate over one full period T. The overall output V_{LI} is then

$$V_{\mathrm{LI}} = \frac{1}{T} \int\limits_0^T \sin\left(\frac{2\pi}{T} \cdot t + \Delta\phi\right) \cdot V_{\mathrm{in}}(t) dt \tag{6.10}$$

which is nothing else than the Fourier component of $V_{\mathrm{in}}(t)$ at frequency $1/T$. By adding a second channel with the reference signal shifted by 90 degree one can get also the phase information which we do not consider in the following.

This equation gives us beside the amplitude also a weighting. Values for $V_{\mathrm{in}}(t)$ near the maximum and minimum of $\sin\left(\frac{2\pi}{T} \cdot t + \Delta\phi\right)$ contribute most to the result. Also $V_{\mathrm{in}}(t)$ represents the states the sample is modulated through. When intermediate states are passed through they will contribute to the final result according to their weight given by eq. (6.10). This washes out nonlinear features which are expected for breakdown phenomena. Therefore it is important to get around this averaging.

One ansatz to deal with the averaging is the use of a rectangular shaped waveform for modulation instead of a sine. Thereby the voltage is set to the bias voltage V for the first half of the period and is zero for the second half of the period. Evaluating eq. (6.10) with $\Delta\phi$ assumed to be zero (adjusting right the phase of the lock-in amplifier) results in

$$V_{\mathrm{LI}} = \frac{1}{\pi}\left[V_{\mathrm{in}}(V) - V_{\mathrm{in}}(0)\right]. \tag{6.11}$$

Equation (6.11) looks very intuitive since only the difference between the biased and unbiased states is measured. However using a rectangular shaped waveform throws us back in equation (6.5) since the square of a rectangular signal with amplitude A is still a rectangular signal just with amplitude A^2

$$[Ar(\omega_{\mathrm{m}}t)]^2 = A^2 r(\omega_{\mathrm{m}}t). \tag{6.12}$$

Skipping all modulation independent terms, equation (6.5) becomes for a rectangular modulation:

$$\begin{aligned}\partial_z F =& -\partial_z^2 q_{\mathrm{m}}(V_{\mathrm{DC}} + V_{\mathrm{AC}} \cdot r(\omega_{\mathrm{m}}t) + \Delta\mu_{\mathrm{ch}}/e) - \frac{1}{2}\partial_z^2 C(V_{\mathrm{DC}} + V_{\mathrm{AC}} \cdot r(\omega_{\mathrm{m}}t) + \Delta\mu_{\mathrm{ch}}/e)^2 \\ =& -\partial_z^2 q_{\mathrm{m}} \cdot V_{\mathrm{AC}} \cdot r(\omega_{\mathrm{m}}t) - \partial_z^2 q_{\mathrm{m}}(V_{\mathrm{DC}} + \Delta\mu_{\mathrm{ch}}/e) - \partial_z^2 C(V_{\mathrm{DC}} + \Delta\mu_{\mathrm{ch}}/e) \cdot V_{\mathrm{AC}} \cdot r(\omega_{\mathrm{m}}t) \\ & - \frac{1}{2}\partial_z^2 C(V_{\mathrm{DC}} + \Delta\mu_{\mathrm{ch}}/e)^2 - \frac{1}{2}\partial_z^2 C V_{\mathrm{AC}}^2 \cdot r^2(\omega_{\mathrm{m}}t). \end{aligned} \tag{6.13}$$

This leads to a lock-in amplifier output signal of

$$V_{\mathrm{LI-R}} \propto \left[\partial_z^2 q_{\mathrm{m}} + \partial_z^2 C(V_{\mathrm{DC}} + \Delta\mu_{\mathrm{ch}}/e)\right] \cdot V_{\mathrm{AC}} + \frac{1}{2}\partial_z^2 C V_{\mathrm{AC}}^2. \tag{6.14}$$

In conclusion, one acquires an additional quadratic dependence on V_{AC} while measuring and one has to take care to remain in the linear regime. Peter Weitz realized this [13] and suggest to keep $V_{\mathrm{DC}} > 2 \cdot V_{\mathrm{AC}}$ to be below 20 % error. Another way to check for the quadratic term is to measure $V_{\mathrm{LI-R}}$ over V_{AC} and map that way directly the nonlinearities. This was the preferred way for the later described breakdown measurements since $V_{\mathrm{LI-R}}$ was anyhow measured on different V_{AC}.

6.3. Effect of charge carrier density modulation

In case the applied bias changes the electron concentration the chemical potential does change too. This happens for example in samples with close-by gates, where the applied source to drain voltage at the sample already can change locally the electron density significantly. Thus we want to have a glance on equation (6.5) in the case of a varying chemical potential difference $\Delta\mu_{\mathrm{ch}}(\omega_{\mathrm{m}}t)$. For a smooth varying chemical potential over electron density and therefore applied AC-bias, one can write $\Delta\mu_{\mathrm{ch}}(\omega_{\mathrm{m}}t)$ approximately as the sum of an offset and the first Fourier component

$$\Delta\mu_{\mathrm{ch}}(\omega_{\mathrm{m}}t) \approx \Delta\mu_{\mathrm{ch0}} + \Delta\mu_{\mathrm{ch1}} \cdot \sin(\omega_{\mathrm{m}}t). \tag{6.15}$$

Since the successive lock-in amplifier measurement is only sensitive to the first Fourier component the following calculation is even true for a non-smooth varying chemical potential.

Equation (6.5) becomes after skipping all frequency independent terms to

$$\begin{aligned}\partial_z F = &- \partial_z^2 q_\mathrm{m} \cdot [V_\mathrm{AC} \cdot \sin\omega_\mathrm{m} t + V_\mathrm{DC} + \Delta\mu_\mathrm{ch0}/e + \Delta\mu_\mathrm{ch1}/e \cdot \sin(\omega_\mathrm{m} t)] \\ &- \frac{1}{2}\partial_z^2 C\, [\, V_\mathrm{DC}^2 + (\Delta\mu_\mathrm{ch0}/e)^2 + 2V_\mathrm{DC} \cdot \Delta\mu_\mathrm{ch0}/e \\ &+ 2V_\mathrm{DC}V_\mathrm{AC}\sin(\omega_\mathrm{m} t) + 2V_\mathrm{DC}\Delta\mu_\mathrm{ch1}/e \cdot \sin(\omega_\mathrm{m} t) \\ &+ 2\Delta\mu_\mathrm{ch0}/e \cdot V_\mathrm{AC}\sin(\omega_\mathrm{m} t) + 2\Delta\mu_\mathrm{ch0}/e \cdot \Delta\mu_\mathrm{ch1}/e \cdot \sin(\omega_\mathrm{m} t) \\ &+ V_\mathrm{AC}^2 \sin^2(\omega_\mathrm{m} t) + \Delta\mu_\mathrm{ch1}^2/e^2 \cdot \sin^2(\omega_\mathrm{m} t) + 2\Delta\mu_\mathrm{ch1}/e \cdot V_\mathrm{AC}\sin^2(\omega_\mathrm{m} t)\,]\,. \end{aligned} \tag{6.16}$$

The lock-in amplifier output will therefore show

$$V_\mathrm{LI} \propto \left\{ -\partial_z^2 q_\mathrm{m} - \partial_z^2 C\,[V_\mathrm{DC} + \Delta\mu_\mathrm{ch0}/e] \right\} \cdot [V_\mathrm{AC} + \Delta\mu_\mathrm{ch1}/e] \tag{6.17}$$

The prefactor in equation (6.17) is the same as in equation (6.6). Thus the calibration has to be done in the same way as before but the result will be proportional to $[V_\mathrm{AC} + \Delta\mu_\mathrm{ch1}/e]$ instead of V_AC. We want to emphasize here that with this modulation V_AC is the local electrostatic potentials change and thus $[V_\mathrm{AC} + \Delta\mu_\mathrm{ch1}/e]$ the local electrochemical potential change.

In conclusion, for a smooth $\mu_\mathrm{ch}(n)$, that can be approximated by a constant plus the first Fourier coefficient, the introduced measurement technique returns the calibrated electrochemical potential changes.

6.4. Voltage bias between tip and sample to avoid an electrostatic depletion

The intrinsic electrostatic difference between tip and sample - present at zero voltage bias between tip and sample (see Fig. 5.6) - might cause electrostatic depletion in the sample's 2DES. Therefore, one needs to compensate this effect by an appropriate DC-voltage at the tip. Using a simple capacitor model like in equation (3.13) we can estimate the change in charge carrier concentration caused by the intrinsic electrostatic potential difference. With $\epsilon_r \approx 13$, $d = 100\,\mathrm{nm}$ and $n = 2 \cdot 10^{15}\,\mathrm{m}^{-2}$ we would be able to deplete the electronic system with an electrostatic potential difference of $\Delta\phi = 300\,\mathrm{meV}$.

Such small electrostatic potential differences can occur easily by the work-function difference, that is why the compensation of the chemical potential difference of the tip and sample is a must. In addition one should not forget the mirror charges q_m sitting on the tip. They interact with the 2DES in the sample and alter by this the electrostatic potential difference to be compensated. Therefore the DC-voltage to be applied at the tip is not exactly the chemical potential difference $\Delta\mu_\mathrm{ch}$. It is rather the DC-voltage with least force between tip and sample. We use the measurement scheme shown in Fig. 6.3 to determine this voltage. When exciting the tip using the tip-to-sample voltage, the amplitude of the oscillation will be proportional to the acting force between the electronic system and the tip. This force microscopy mode is referred to as Kelvin probe microscopy [132–135].

The force acting on the tip was already derived and lead to equation (6.1). When one uses again a lock-in amplifier to measure the amplitude, like we did for the measurement scheme of equation (6.7), one gets

$$V_{\mathrm{LIA}} \propto \left|\partial_z q_{\mathrm{m}} + \partial_z C \left(V_{\mathrm{ts}} + \Delta\mu_{\mathrm{ch}}/e\right)\right| \cdot V_{\mathrm{AC}}. \tag{6.18}$$

Measurement V_{LIA} over the tip-to-sample voltage V_{ts} resembles a V-shape profile where both flanks are linear. It should be emphasized here that the resonance frequency changes with the tip-to-sample voltage V_{ts}. We have therefore to follow the resonance frequency shift to observe the dependence of equation (6.18). The compensation voltage V_{DC} is equal to the tip-to-sample voltage for reaching the minimum of $V_{\mathrm{LIA}}(V_{\mathrm{ts}})$

$$V_{\mathrm{DC}} = -\frac{\partial_z q_{\mathrm{m}}}{\partial_z C} - \Delta\mu_{\mathrm{ch}}/e. \tag{6.19}$$

We want to stress here the fact, that the tip-to-sample voltage for the maximum of the resonance frequency shift parabola as shown in Fig. 6.4

$$V_{\mathrm{PM}} = -\frac{\partial_z^2 q_{\mathrm{m}}}{\partial_z^2 C} - \Delta\mu_{\mathrm{ch}}/e \tag{6.20}$$

is not equal to the compensation voltage V_{DC}. This is due to the mirror charges on the tip and is important for the measurement techniques. It allows us to apply the compensation voltage V_{DC} between the tip and the sample to not disturb the 2DES and still have a finite measurement signal which is vanishing for a tip-to-sample voltage of V_{PM}.

Figure 6.4 shows an example of a measurement to determine the compensation voltage V_{DC}. The minimal force acting on the tip is found for $V_{\mathrm{DC}} = 717\,\mathrm{mV}$ while the maximum of the resonance shift parabola is found at $V_{\mathrm{PM}} = 863\,\mathrm{mV}$. Since we are using the slope of the resonance shift parabola to generate our measurement signal from equation (6.7) and (6.8), the offset between V_{DC} and V_{PM} is important.

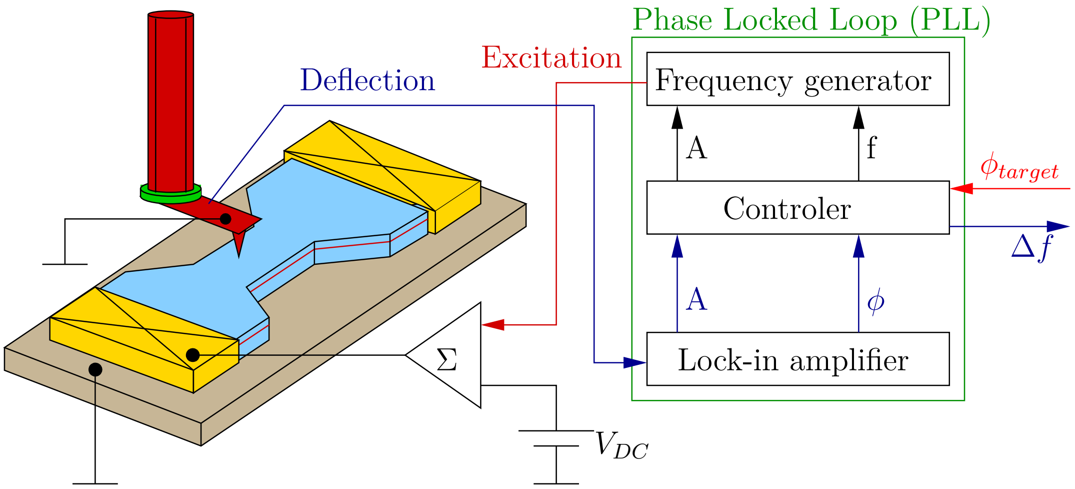

Figure 6.3.: Kelvin-probe measurement scheme used to determine the compensation voltage V_{DC}.

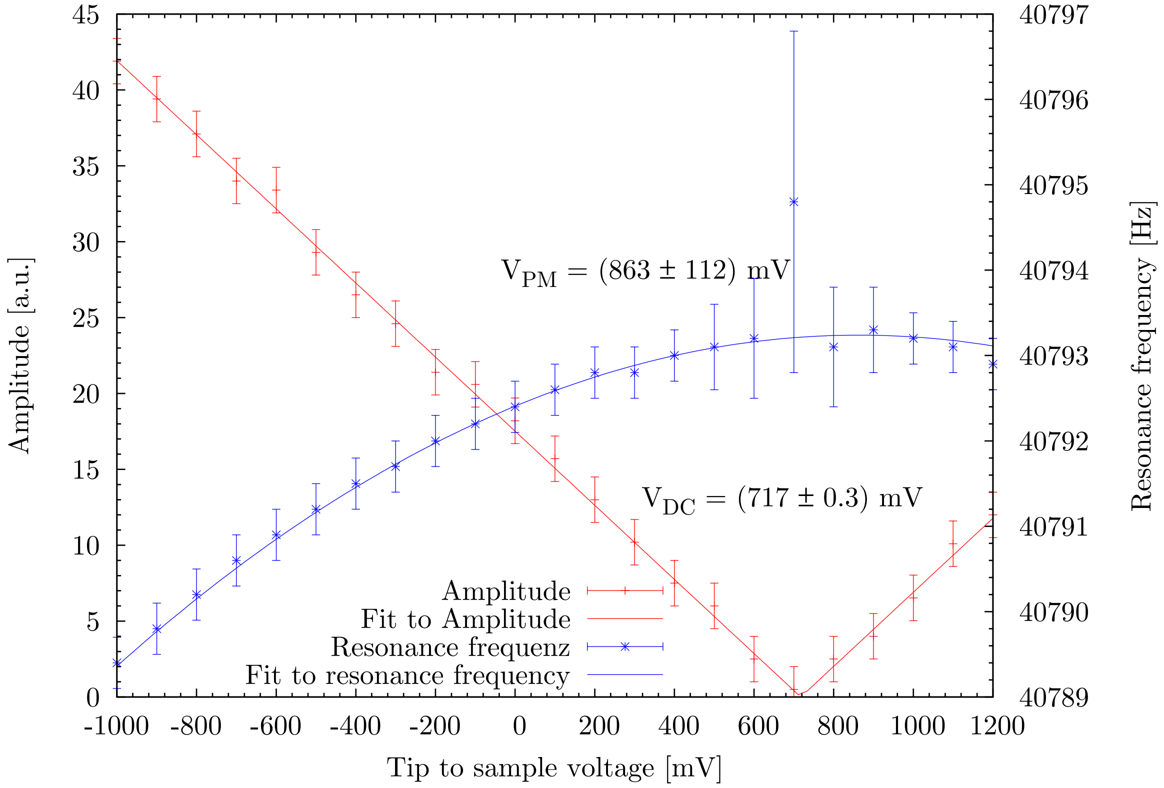

Figure 6.4.: Determination of the compensation voltage between a gold covered tip and a 2DES within a GaAs/Al$_x$Ga$_{1-x}$AS-heterostructure.

6.5. Summary

We have shown how one can use an SFM with metalized and contacted tip to measure current induced electrochemical potential changes within samples. Thus only the changes compared to the equilibrium situation of the sample, in other words without applied bias, are made visible. The strength of the presented method is that it can be used for buried carrier systems as long the electrostatics is not shielded. Also the contact potential can be corrected so that the tip influence can be minimized.

Hall potential measurements are expected to show nonlinear changes when the bias is increased to high values. A sinussoidal modulation would average over such nonlinear changes. We discussed therefore a way to avoid averaging by changing the form of switching. A rectangular modulation waveform does not average but suffers from a non-linear response of the measurement signal on local electrochemical potential changes. Usually this non-linear term is strongly suppressed and one has to take care not to stay away from the non-linear regime. We preferred such a rectangular modulation for all our breakdown measurements but a sinussoidal for the graphene measurements.

Part III.

Microscopic picture of the QHE in graphene

To approach the microscopic picture of the Quantum Hall effect in graphene the Hall potential profiles had to be measured. This was done with the technique described in section II for three different graphene flakes. For the interpretation of the measured Hall potential profiles we went a similar route as for GaAs/Al$_x$Ga$_{1-x}$As heterostructures. The characteristic change of the Hall potential drop position and the existence of Landau levels in graphene let us conclude that an incompressible/compressible landscape like in GaAs/Al$_x$Ga$_{1-x}$As heterostructure samples is formed. Furthermore the position of the Hall potential drops can be fitted with the position of incompressible stripes. The formation of the quantum Hall effect in graphene is therefore also based on current flow in incompressible stripes, see section 9.1.

The interpretation in terms of compressible and incompressible stripes suggests a change of charge carrier concentration towards the edges. We found that for the n-type graphene the electron concentration is reduced towards the edges but in p-type graphene the hole concentration is increased. Otherwise we would not understand the evolution of the measured Hall potential profile across a quantum Hall plateau on the p-type graphene. A possible origin for the behavior towards the edges are fixed negative charges near the edges of the flake. A more in-depth discussion is given in section 9.5 and 9.6.

In the following, first we want to discuss sample fabrication in section 7. Afterwards the characterization of the sample will be presented in section 8 before we come to the Hall potential profile measurements in section 9 and their interpretation. The given interpretation was applicable for all three measured graphene flakes. However due to disorder and built-in inhomogeneities on two of the flakes the key features are more complicated and we will postpone their discussion to the end of this part at section 10.

7. Sample fabrication

The samples used in this work were fabricated by Benjamin Krauss from our institute. He used the so-called scotch-tape method [59]. Thereby one uses scotch-tape to mechanically cleave graphite peaches from a suitable graphite substrate. We used highly oriented pyrolytic graphite (HOPG). The scotch-tape is then pressed on a silicon-oxide-on-silicon wafer with predefined marker system for the flake localization. The thermally grown silicon oxide on arsenic doped silicon had a thickness of 300 nm and there was no passivation of mobile ions (see discussion in section 9.6.4 for further details on mobile ions).

After optical localization of a single layer flake, gold contacts were patterned with e-beam lithography (for a detailed procedure see section H.1).

Finally, after glueing the sample with silver paste into the chip carrier and bonding the sample was ready for mounting into the sample holder as shown in Fig. 7.1.

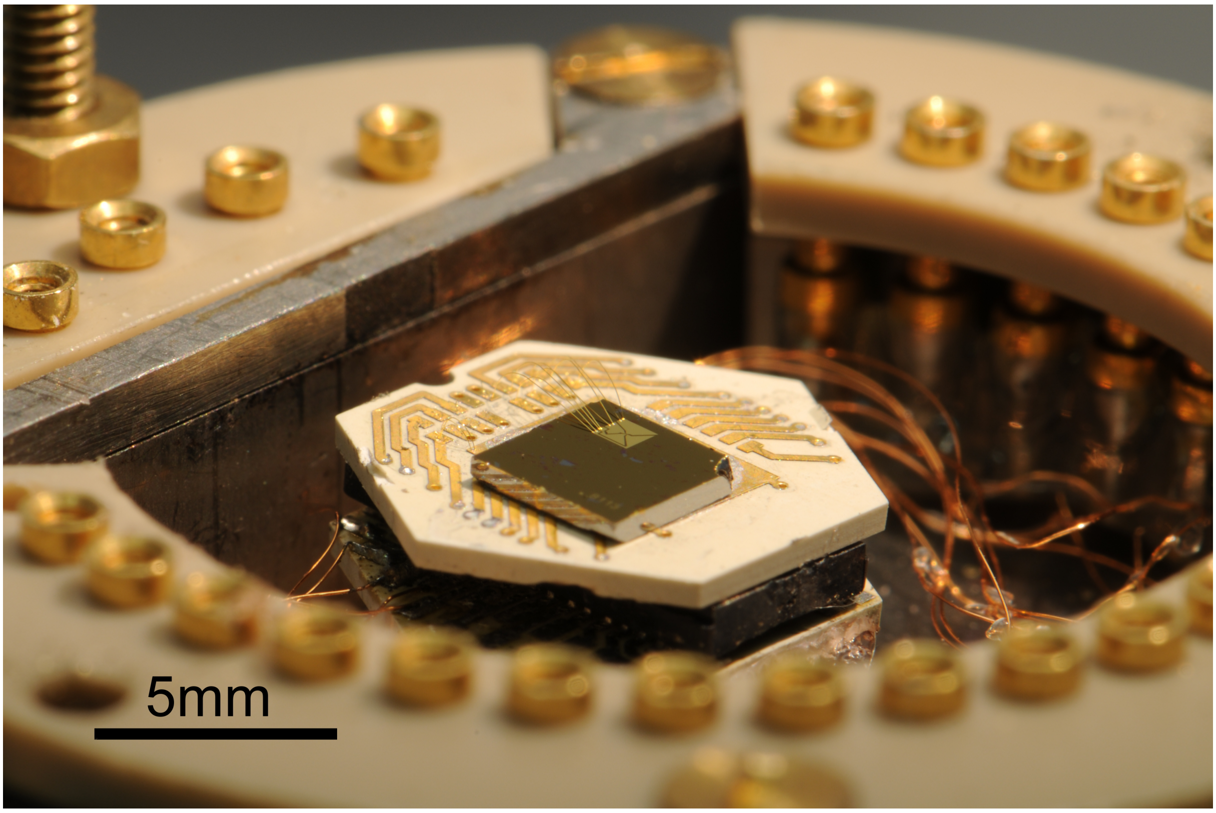

Figure 7.1.: Fully processed sample (GB8113) glued on a chip carrier and mounted on the coarse positioning stage.

8. Characterization of the flake

Before the characterization the sample was pumped inside the sample holder over night and was after that slowly cooled down (down to 4 K in about 10 hours) to a temperature of 1.4 K. The contact to the back gate degraded during the cooling down process. An additional leakage led into an effective division of the supplied voltage to the back gate by a factor of 14. This is already corrected in the shown graphs and further described in the appendix G.5.

The two-terminal resistance was measured as shown in Fig. 8.1 (a) by keeping the applied bias voltage V fixed while recording the current I using a current-to-voltage converter integrated in our home-made electronics.

Since the size of the flake with length $l = 8.8\,\mu\text{m}$ and width $w = 3.5\,\mu\text{m}$ is known from scanning electron microscope (SEM) picture taken after the SPM-measurements, see Fig.8.2, one can determine a lower limit of the mobility μ from the conductivity σ at zero magnetic field from equation (3.12). The charge carrier concentration can be calculated from a capacitance model where d is the distance between back gate and flake:

$$\eta = \frac{\epsilon_0 \epsilon_r (V_{\text{BG}} - V_{\text{CNP}})}{e \cdot d}. \tag{8.1}$$

The correction V_{CNP} is necessary to account for doping and work function differences between flake and the doped substrate and represents the charge neutrality point, here set equal to the maximum of the resistance V_{Rmax}. We will show later, that V_{CNP} is not equal to the maximum of the resistance curve as often used in the literature [25, 47]. But since we need the mobility only for classification the error by setting them equal is

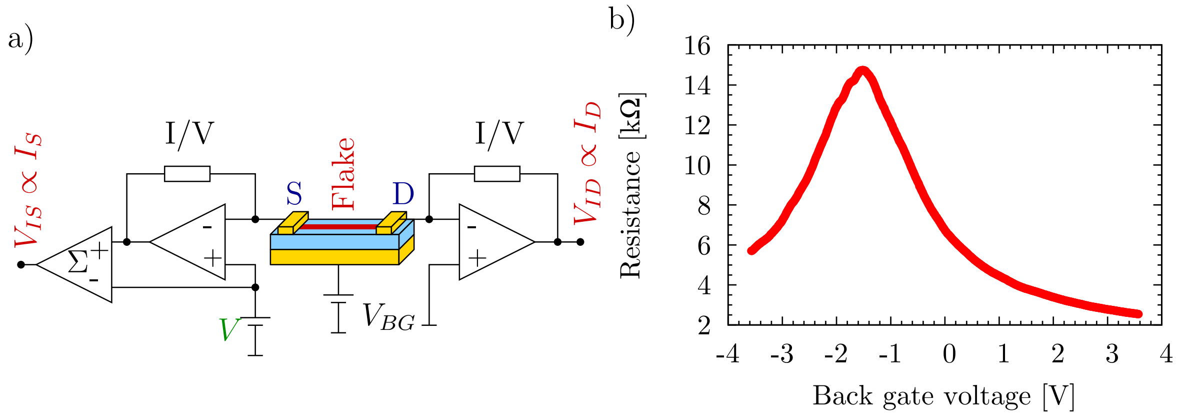

Figure 8.1.: (a) Schematics of the transport measurement setup and (b) the resulting resistance over back gate voltage. The applied bias voltage V was chosen at 10 mV to match the scanning bias situation.

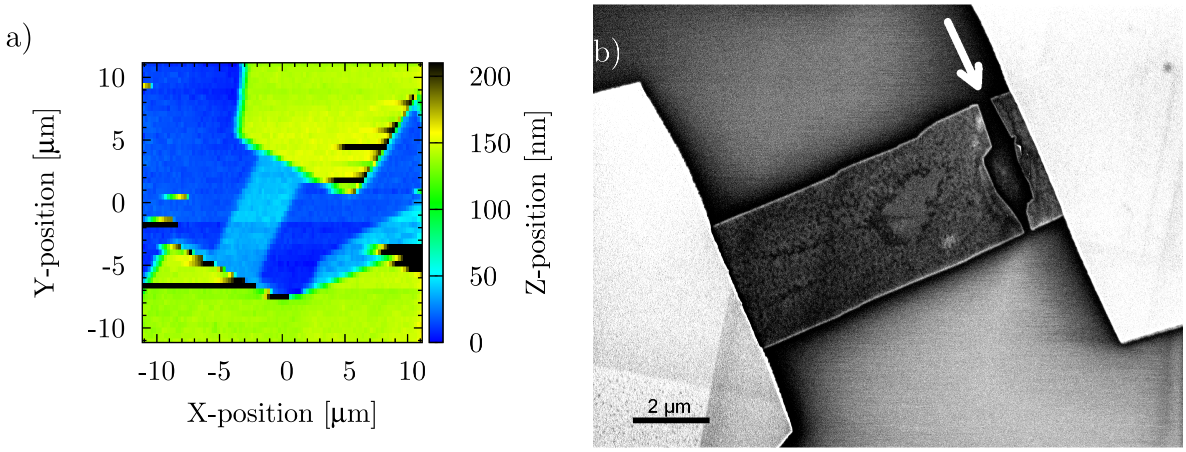

Figure 8.2.: A non contact topography scan of the graphene flake is shown in (a). The scale in the Z-axes has to be interpreted as arbitrary units since the chemical potential differences enhance the visibility of the flake by altering the measured height. The X,Y,Z coordinate system is the SPM coordinate system and is rotated round the Z axis with respect to the x, y, z coordinate system of the sample. In (b) a scanning electron microscopy (SEM) image taken after the measurements was done. The flake was destroyed close to the right contact (see arrow) in the attempt to current anneal it.

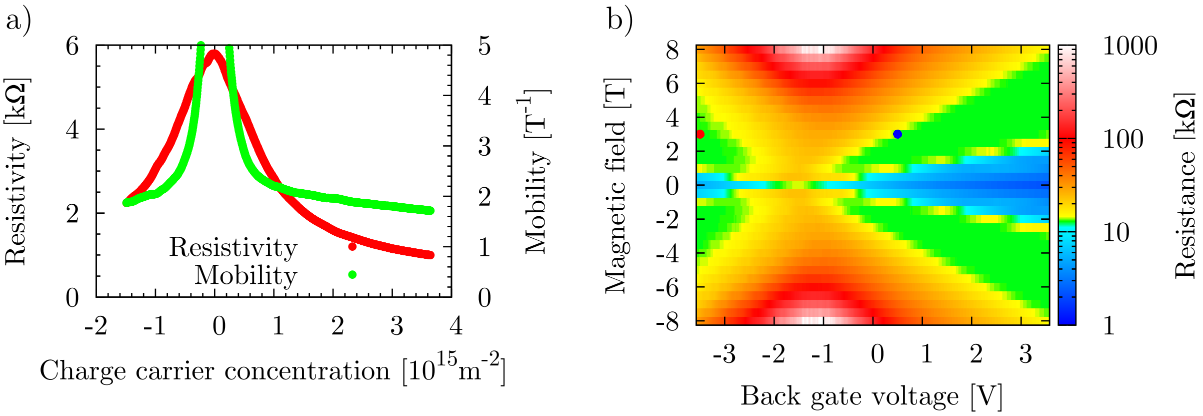

Figure 8.3.: (a) Mobility versus charge carrier concentration. (b) Color coded resistance versus back gate voltage and magnetic field. (Applied source-drain bias voltage $V = 10\,\mathrm{mV}$). Also drawn are a blue and a red point at a magnetic field of 3 T that have equal charge carrier density. The step-like features along the magnetic field axes in (b) are due to the fact, that traces were taken along the back gate voltage axis for different magnetic field values in rough steps of 0.5 T.

acceptable. Finally we find

$$\mu = \frac{l \cdot d}{R(V_{\mathrm{BG}}) \cdot w \cdot \epsilon_0 \epsilon_r \cdot (V_{\mathrm{BG}} - V_{\mathrm{CNP}})}. \tag{8.2}$$

Since the measured resistance is found in the denominator, the error because of the contact resistance included in our measurements decreases the mobility and this formula gives therefore a lower limit for the mobility. Figure 8.3 (a) shows beside the resistivity $\rho(V_{\mathrm{BG}})$ also the mobility $\mu(V_{\mathrm{BG}})$. For comparison with other experiments we chose the values further off the resistance maximum at a charge carrier density of $2.0 \cdot 10^{15}\,\mathrm{m}^{-2}$ which results in about $\mu \approx 2\,\mathrm{T}^{-1}$.

Other values used for comparison are the position of the resistance maximum at $V_{\mathrm{BG}} = -1.5\,\mathrm{V}$ and the full width at half maximum in the resistance over back gate voltage curve of $\Delta V_{\mathrm{FWHM}} = 2.8\,\mathrm{V}$ and respectively a charge carrier density change of $\Delta n = \epsilon_0 \epsilon_r \Delta V_{\mathrm{BG}} d^{-1} \approx 2.0 \cdot 10^{15}\,\mathrm{m}^{-2}$. All these values are quite good for exfoliated graphene on the used $\mathrm{Si/SiO_2}$ substrate [31].

Scanning probe microscopy (SPM) scans have been performed in non-contact mode aiming for topography of the graphene flake. The result is shown in Fig. 8.2 (a). The graphene flake appears therein light blue in contrast to the dark blue of the substrate. Since we use a metallic tip, the chemical potential difference between tip and flake can cause strong forces. This is not the case on the silicon dioxide surface and the effect has a different strength on the gold surface. The scans include that way material specific information and do not resemble the real topography.

The next step was applying a magnetic field B. Figure 8.3 (b) shows resistance traces for different magnetic field values. Following in this figure the position of the filling factors $\nu = 2$ and $\nu = -2$ plateaus (in green) one finds the positions to resemble straight lines meeting at the resistance maximum for zero magnetic field. It also seems that the slope for the hole side, plateau below $V_{\mathrm{BG}} = -2\,\mathrm{V}$, is bigger than for the electron side for positive back gate voltages. This indicates an electron-hole asymmetry in this flake. As we will see later directly in the Hall potential measurements this has to do with the charge carrier density profile in the flake. To further explain this we want to consider the plateau edge towards the resistance maximum of the filling factors $\nu = 2$ and $\nu = -2$ quantum Hall plateaus. Two points with equivalent total charge carrier density are drawn in Fig. 8.3 (b). The blue point for n-type graphene is found at the quantum Hall plateau edge. The red point in the $\nu = -2$ plateau is still well within the plateau region. Starting from these two points and going towards the resistance maximum by reducing the charge carrier concentration we leave the $\nu = 2$ plateau but still stay on the $\nu = -2$ plateau. From measurements on $\mathrm{GaAs/Al}_x\mathrm{Ga}_{1-x}\mathrm{As}$ heterostructures we know that plateaus are extended towards the side where we find the edge-dominated QHE. We can assume therefore already from this measurement that the edge-dominated quantum Hall regime is found for the p-type graphene at the lower hole density side of the plateaus. Current flow is found where the charge carrier density is a multiple of the Landau level degeneracy. To find current flow at the edges for smaller total carrier density, the carrier density has therefore to be higher at the edges.

9. Scanning probe measurements

The scanning probe measurements were done in the geometries depicted in Fig. 9.1 (a) and (b). The measurements have been made at a magnetic field of $B = 3\,\mathrm{T}$. It should be stressed here that resistance and Hall potential profiles where measured in parallel. Due to a substrate related effect, further described in section G.5, the maximum of the resistance curve was shifted to $V_{\mathrm{BG}} = 3.15\,\mathrm{V}$. The simultaneous measurement of transport and Hall potential profiles still allows for interpretation.

In the color coded data of Fig. 9.1 (c) and (d) one finds superposed as reference in black the resistance curve. Across the maximum of the resistance at $V_{\mathrm{BG}} = 3.15\,\mathrm{V}$ the polarity of the Hall voltage is switched. Above $V_{\mathrm{BG}} = 3.15\,\mathrm{V}$, electrons should be present in the flake and below this back gate voltage value holes should dominate electrical transport. The switching of the polarity is therefore expected.

Three striking features can be found in the data: (1) Within the quantum Hall plateaus we find the Hall potential drops to evolve from one single drop at the center for the lower voltage side of a plateau to two distinct drops moving apart while approaching the higher voltage side of a plateau. The position of the drops sketch a u-shape. We will call this in the following the *asymmetry within a plateau* since obviously the center of a quantum Hall resistance plateau versus filling factor does not give a symmetry point. (2) Across the resistance maximum at $V_{\mathrm{BG}} = 3.15\,\mathrm{V}$ the u-shape does not flip upside down and creates therefore an additional asymmetry. We want to call this the *asymmetry across the charge neutrality point.* (3) Looking at the maximum of the resistance peak one finds a finite slope in the potential profiles, see Fig. 9.1 (e) for $V_{\mathrm{BG}} = 3.15\,\mathrm{V}$. The back gate voltage where the bulk slope is closest to zero is found at $V_{\mathrm{BG}} = 2.26\,\mathrm{V}$ well below the maximum of the resistance. Since the position of the resistance maximum is referred in the literature as the charge neutrality point (CNP) and one would expect no bulk slope at the CNP, we want to name this the *CNP offset.*

It should be mentioned here that some artifacts from the measurement technique can be found in the graphs of Fig. 9.1 which are well understood and further described in the appendix chapter G. We shortly want to mention the ones present here: The black areas below $V_{\mathrm{BG}} = -1.5\,\mathrm{V}$ as well the orange and yellow between $V_{\mathrm{BG}} = 1.5\,\mathrm{V}$ and $V_{\mathrm{BG}} = -1.5\,\mathrm{V}$ are expected to appear in red. The noisy lines below $V_{\mathrm{BG}} = -1.5\,\mathrm{V}$ at both edges are due to the impact of the back gate stray fields on the scanning tip.

9.1. Interpretation in terms of compressible and incompressible stripes

In this section we want to interpret our data similar to the known result of GaAs/Al$_x$-Ga$_{1-x}$As heterostructure samples, using compressible and incompressible stripes. For the development of a compressible and incompressible landscape, as needed for our in-

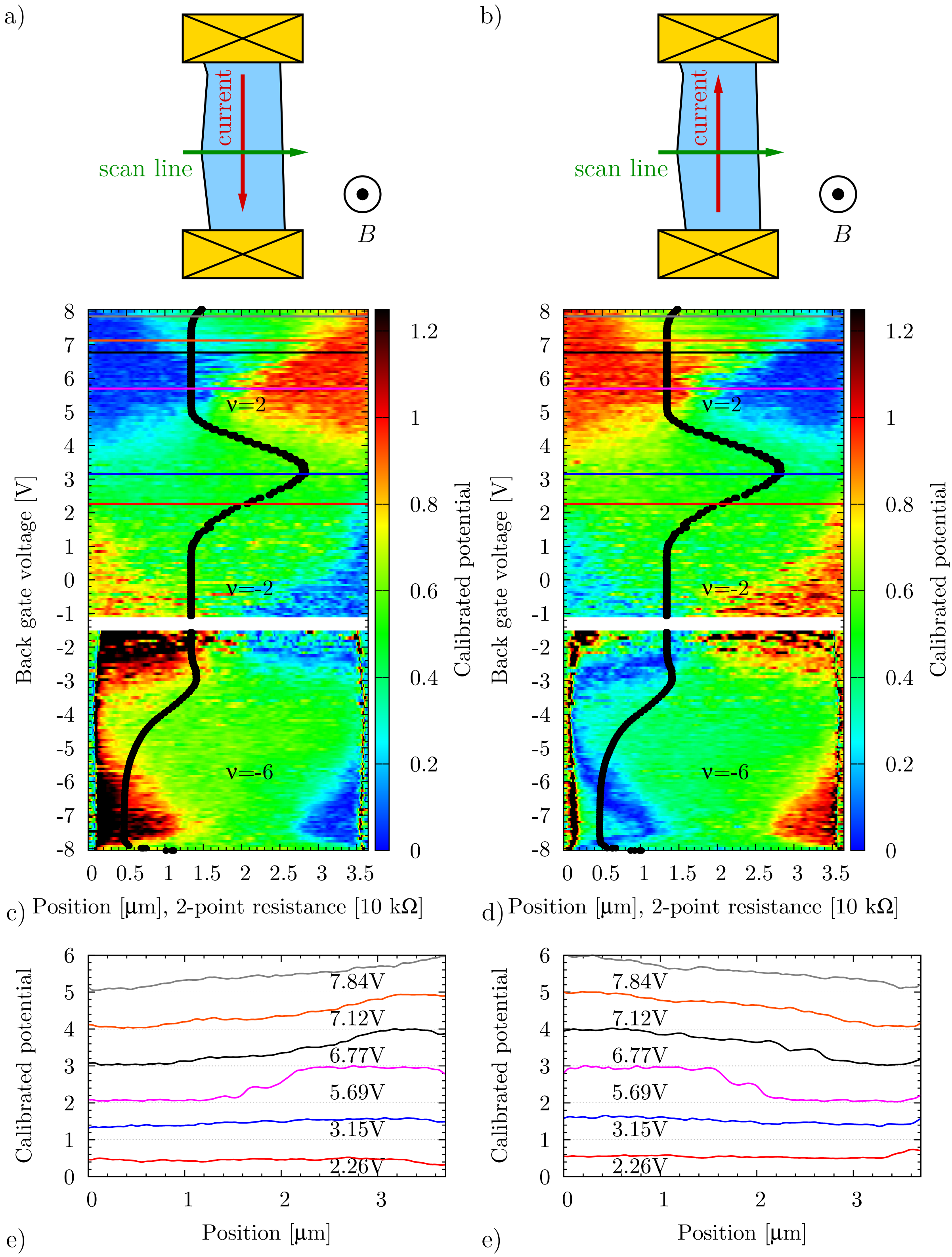

Figure 9.1.: Hall potential profiles for a bias situation as depicted in (a) across the middle of the flake (c). Hall potential profiles as line plots (averaged with the four nearest neighbor profiles) are show again in (e). Similar for (d), (f) but for reversed current direction (see (b)).

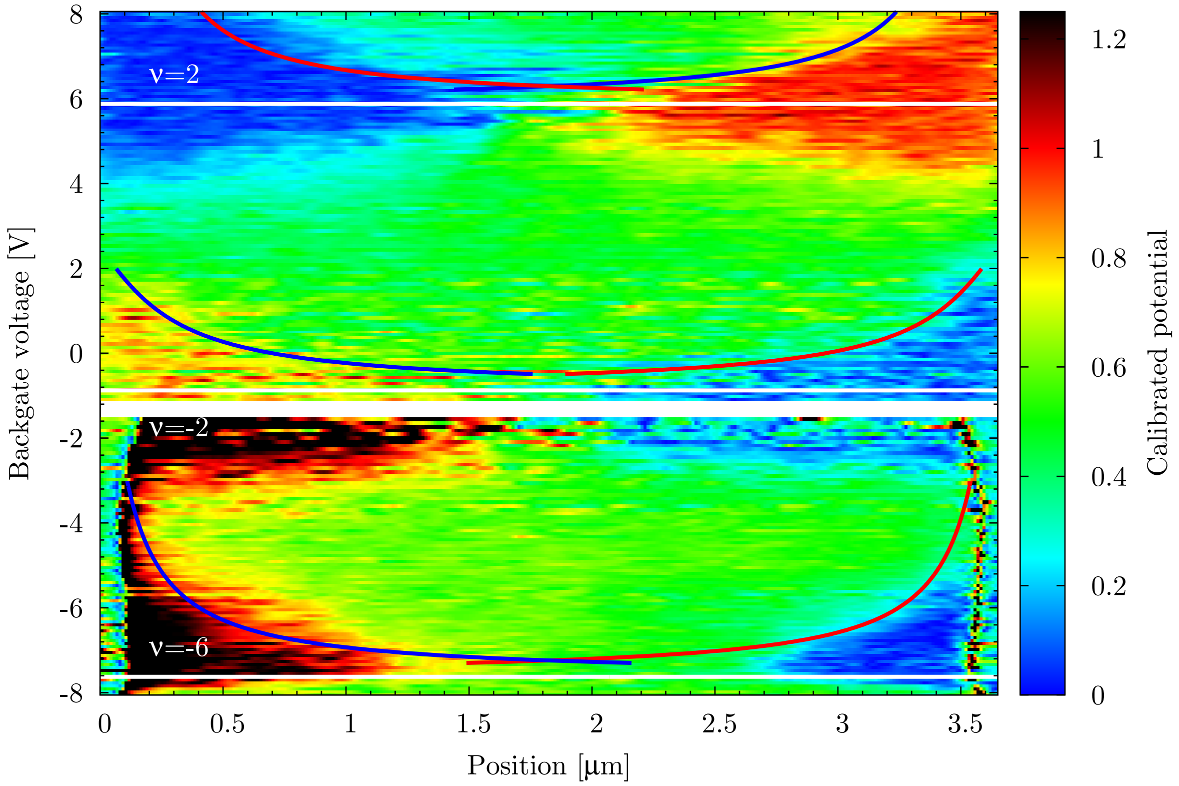

Figure 9.2.: Fitting of the Hall potential drops with the CSG-formula (4.3). The data fits nicely but the CSG-formula assumes side gate electrodes which are not present at this sample. Still we can conclude, the charge carrier concentration is changing towards the edges. A side gate voltage of $V_{\mathrm{SG}} = 6.0\,\mathrm{V}$, a charge neutrality at the back gate voltage $V_{\mathrm{CNP}} = 2.5\,\mathrm{V}$ and a back gate voltage to filling factor conversion factor of $16/27\,\mathrm{V}^{-1}$ where chosen through fitting of the CSG-formula to our data.

terpretation, two requirements have to be fulfilled: (1) Discrete energy levels which are present over the flake area, e.g. Landau levels in a 2DES. (2) A smooth confinement potential [92, 136] along the edges which does not vary significantly within one magnetic length [92]. These two requirements ensure that a compressible and incompressible landscape can evolve within a flake. A more in depth discussion on the formation of the compressible and incompressible landscape was given in section 4.2.

As it was shown in section 3.3.1, Landau levels develop at high magnetic fields and low temperatures in graphene. Several details differ from the Landau level structure of a parabolic band structure material, namely Landau levels are not equidistant in energy but follow a square root behavior on the Landau level index N. This means we have to be careful, when drawing the Landau level bending for several adjacent incompressible stripes but still the first requirement is fulfilled.

The second requirement is more difficult since there is no experiment which has been probing the compressibility across a graphene flake. Scanning probe experiments on graphene usually probe only a single point or only a small portion of the bulk [56,57,137]. Scans at the edges have been performed for graphene on graphite -i.e. anther substrate -

and show a nearly atomically sharp confinement potential and essentially no reconstruction [138]. The way to approach the problem in our case comes from former measurements on GaAs/Al$_x$Ga$_{1-x}$As-heterostructures. There an edge depletion due to charges at the etched interfaces causes a characteristic evolution of the compressible/incompressible landscape. It could be proven that incompressible stripes carry the dissipation-less current. As for the GaAs/Al$_x$Ga$_{1-x}$As-heterostructures in graphene we found a distinct evolution of the Hall potential drops. We called this evolution in section 9 the u-shaped structure or the asymmetry within a quantum Hall plateau. Thereby the Hall potential drops, positioned at both edges at the higher back gate voltage side of the plateaus, move closer together for decreasing back gate voltage and merge. In a first approach we tried to fit this structure with the CSG-formula (4.3), see section 4.2. The result is shown in Fig. 9.2. The fit seems to be reasonable proving the position of the Hall potential drops to be where incompressible strips are expected. It should be emphasized here, that without the formation of a compressible and incompressible structure the Hall potential profiles in the center of a long flake would be spread over the whole bulk region linearly. In conclusion, the electron and hole density towards the flake edges is changing. The Landau levels have to bend due to this and create thereby incompressible regions which carry the current. The density variation extends into the flake bulk in the order of 1 µm.

The drawback of the CSG-formula is that it assumes gates to deplete the 2DES. There are no side gates for depletion in our structure and the origin of the density changes has to be fixed charges. Therefore the parameter used for the fit do not give us any further insight. In the next section we try to overcome this problem by finding a suitable replacement for the CSG-formula.

9.2. Presence of electron depletion and hole accumulation towards the edges

In the previous section we have shown that a change of the charge carrier concentration can be found towards the edges. Here we want to discuss the origin of this spatial variation. There might be two reasons: (1) the back gate which causes stray fields at the flake edges, and (2) suitable arrangements of fixed charges close to the edges.

Before discussing these possibilities we want to investigate the measured profiles towards the edges in more detail. A simple way to find the position of incompressible stripes was described by Chklovskii, Shklovskii, and Glazman [92]: finding the crossing point of Landau level degeneracy and charge carrier concentration. This is the position where a Landau level is completely filled and the next higher one in energy has to be filled but it has first to be bend downwards in energy leading to an incompressible stripe. We want to do this qualitatively for the filling factor $\nu = 2$ plateau in n-type graphene. In Fig. 9.3 (a) our measurement data are shown together with the marked positions of the Hall potential drops for three back gate voltage values. As explained before, the position of the Hall potential drops within a quantum Hall plateau are also the positions of the incompressible stripes. Figure 9.3 (b) shows the Landau level degeneracy and the electron density for different back gate voltages. The blue areas are compressible while the pink ones are incompressible. As we go from top to bottom (from red to blue to black) we come closer to the charge neutrality point and therefore reduce the electron

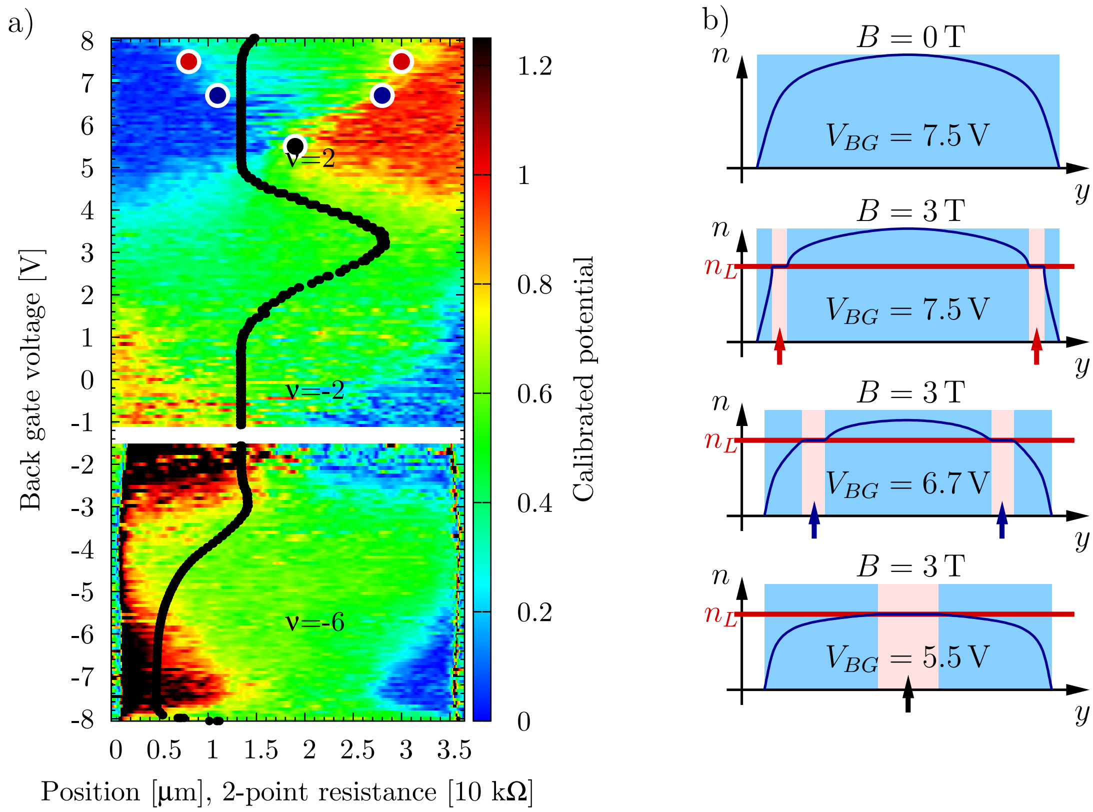

Figure 9.3.: Change of incompressible stripe position for n-type graphene. (a) Color coded Hall potential profiles with three chosen positions of incompressible stripes. (b) Scheme of charge carrier density profiles for the back gate voltage given in (a). The upmost electron concentration profile corresponds to the situation without magnetic field. Reducing the back gate voltage from top to bottom decreases the electron concentration. It also moves the incompressible stripes towards the center. The profile for the electron concentration has to decrease therefore towards the edges.

concentration. The Landau level degeneracy remains unchanged since we do not change the magnetic field. To keep this qualitative analysis simple we neglect deformation of the charge carrier profile and just scale the profile by a factor to mimic the electron density change. To follow the position of the incompressible stripes in the measurements by the intersections between electron concentration and Landau level degeneracy the electron concentrations has to reduce towards the edges as shown in Fig. 9.3 (b).

The same analysis can be done to determine the position of the incompressible stripes versus the total filling factor or respective back gate voltage for p-type graphene. The respective diagrams are shown in Fig. 9.4. This time when we follow the colored dots from the top to the bottom (from red to blue to black) we go away from the charge neutrality point and increase the hole density. To get the found positions for the incompressible stripes the hole density has therefore to increase, see Fig. 9.4 (b). The occurrence of hole accumulation towards the graphene edges for flakes on silicon oxide was also measured by Lee et al. with scanning photocurrent microscopy [139].

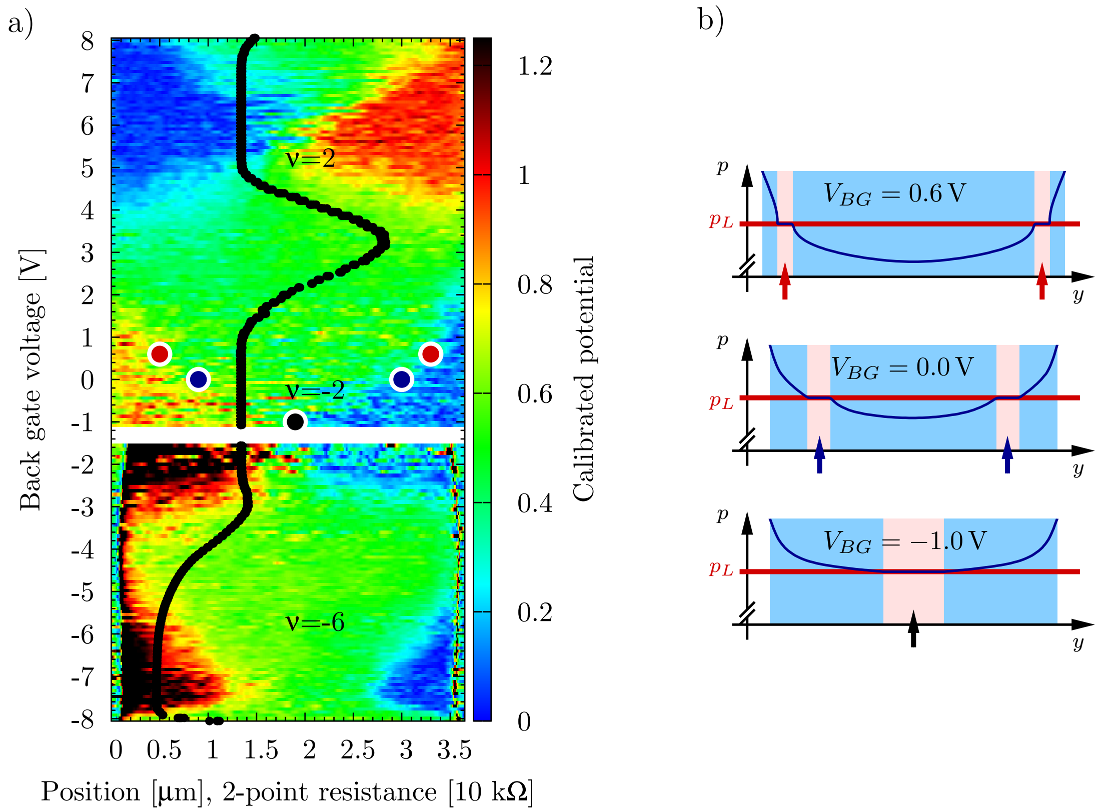

Figure 9.4.: Change of incompressible stripe position for p-type graphene. (a) Color coded Hall potential profiles with three chosen positions of incompressible stripes. (b) Scheme of charge carrier density profiles for the back gate voltage given in (a). Reducing the back gate voltage from top to bottom increases the hole concentration. It also moves the incompressible stripes towards the center. The profile for the hole concentration has to increase therefore towards the edges.

9.3. Back gate effect: not dominant

Usually the electric stray fields from the back gate, shown in Fig. 9.5 for a simplified arrangement, even though changing the charge carrier concentration towards the edges of the graphene flakes are neglected [31, 141]. Here we want to discuss the significance of the back gate with respect to our experiments. As a first approach we want to simplify the arrangement by enlarging the graphene flake to a semi-infinite plane and handle the back gate as infinite plane. Thus we will find the effect of one edge only. We also want to neglect quantum capacitance by handling graphene like a perfect metal. An analytic solution for this problem was already given by Maxwell [140] and the equipotential lines as well as the force lines are shown in Fig. 9.5. The charge carrier density profile η_m towards the edge calculated by Maxwell and adapded to our needs reads

$$\eta_\mathrm{m} = -\frac{\epsilon_0 V_\mathrm{BG}}{e\frac{d}{\epsilon_r}} - \frac{\epsilon_0 V_\mathrm{BG}}{e\frac{d}{\epsilon_r}} \frac{1}{1 + \frac{\epsilon_r \pi}{d} y + \ln\left(1 + \frac{\epsilon_r \pi}{d} y\right)} \left[1 + \frac{1}{1 + \frac{\epsilon_r \pi}{d} y}\right]. \tag{9.1}$$

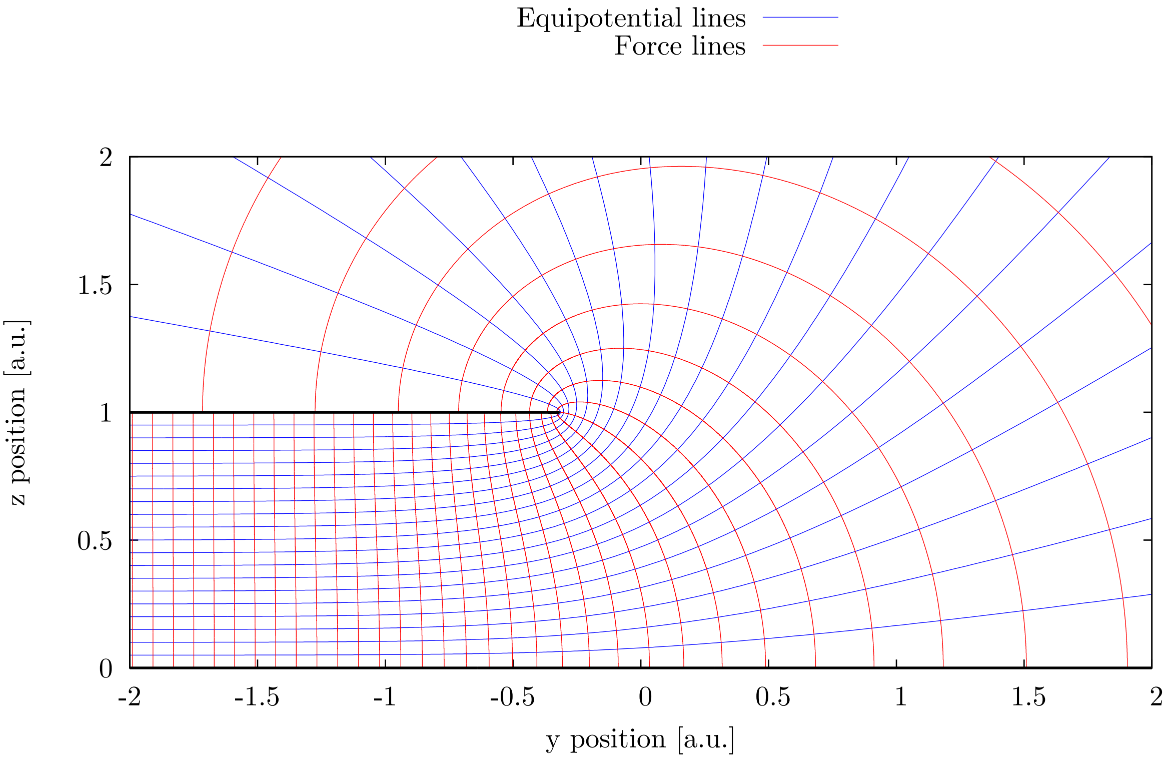

Figure 9.5.: Equipotential and force lines for a semi-infinite plane parallel to a infinite plane as calculated by Maxwell [140]. The infinite plane lies in the x-axes and extend perpendicular to the graph and the semi-infinite plane is the black line at $y = 1 = d$. More details can be found in the Appendix in section B.4.

The thickness of the silicon dioxide is d and ϵ_r its dielectric constant. Analytic solutions for the back gate effect on small graphene ribbons with 300 nm silicon-dioxid dielectric including quantum capacitance do also exist [142]. Unfortunately they are limited to flake widths of the order of the dielectric thickness letting us stick to Maxwell's formula.

To include quantum capacitance and also for simulations to be explained later on we prepared a simulation able to handle problems, translation invariant along the x-axes. The simulation consists of a self-consistent loop where we solve Poisson equation and adjust the charge carrier density according to the solution. The rearrangement of the charges gives now new boundary conditions for the Poisson equation to be solved. Running the loop until no significant changes occur any more, we obtain a self-consistent charge carrier distribution. For the charge carrier rearrangement we use the gradient of the electrochemical potential. The quantum capacitance enters via the dependence of the chemical potential on the charge carrier density. In the simulation we calculate an infinitely long flake with 5 µm width. Due to technical reasons we actually do not calculate a single flake but grating of flakes with period of 20 µm and thus 15 µm distance between to adjacent flakes. 10 µm away from the back gate a ground plane was positioned to define the boundary conditions of our 10 µm × 10 µm large area in the y-z-crosssection we solved. A discusion of the simulation in detail can be found in the appendix under

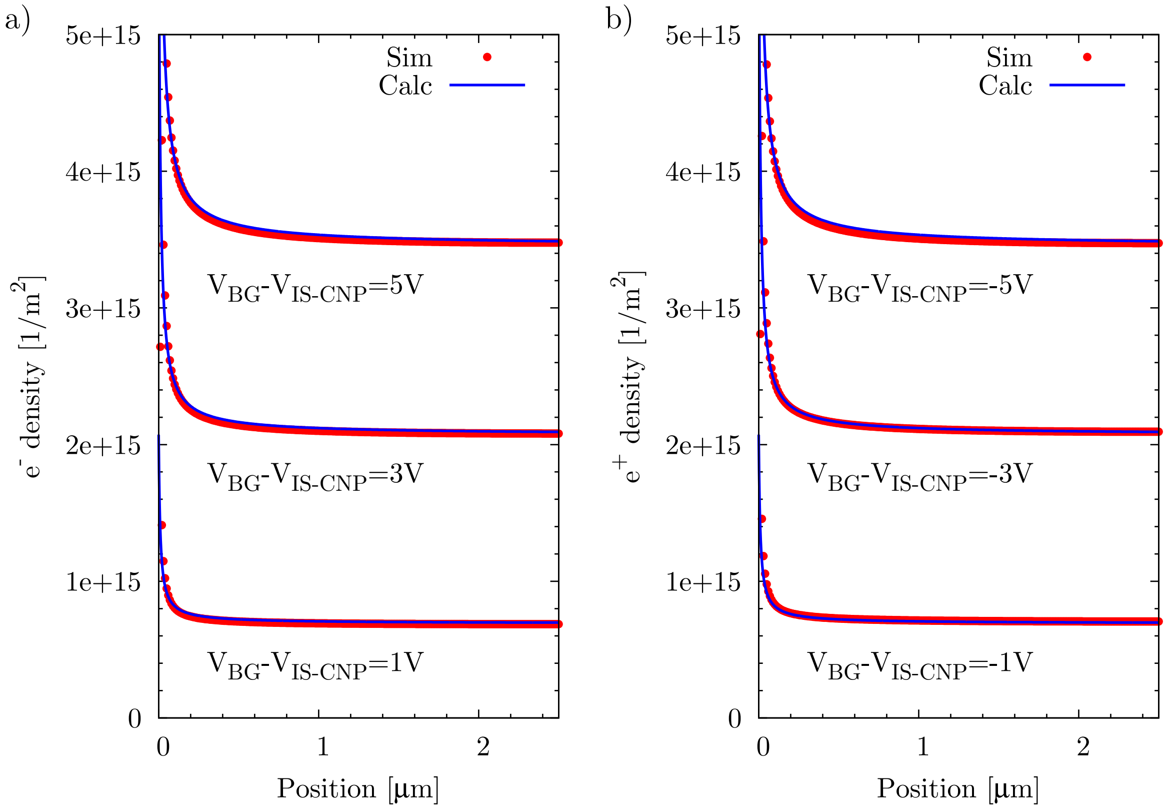

Figure 9.6.: Effect of the back gate simulated and compared to Maxwell's calculation [140]. (a) Electron, (b) hole concentration profile versus position away from the edge. The back gate effect results into a hole accumulation at the flake edges for p-type graphene as concluded from our measurements. In n-type graphene an accumulation of electrons towards the flake edges is found by the simulation. In contrast, our conclusion from the measurements was a depletion of electrons towards the edges.

chapter B.

Figure 9.6 and 9.7 shows the result of simulation for the stray field problem and, for comparison, Maxwell's formula for different back gate voltage values. Unfortunately the result does not fit with the decrease of the electron density towards the edges found in Fig. 9.3 for n-graphene. Even though p-graphene is described qualitatively correct we need another explanation for the data.

9.4. Fixed negative charges: matching our findings

Assuming fixed charges at the edges of the graphene flakes leads also to a variation of the charge carrier concentration towards the edges already for $V_G = 0\,\mathrm{V}$. If we further assume negative fixed charges we arrive at a local dependence of the charge carrier concentration as shown in Fig. 9.8. The electron density for n-graphene reduces towards the edges and the hole density for p-graphene increases. This was also deduced as a necessary requirement from Fig. 9.3 and 9.4 to explain the data.

With fixed negative charges at the edges we can explain the asymmetry within the

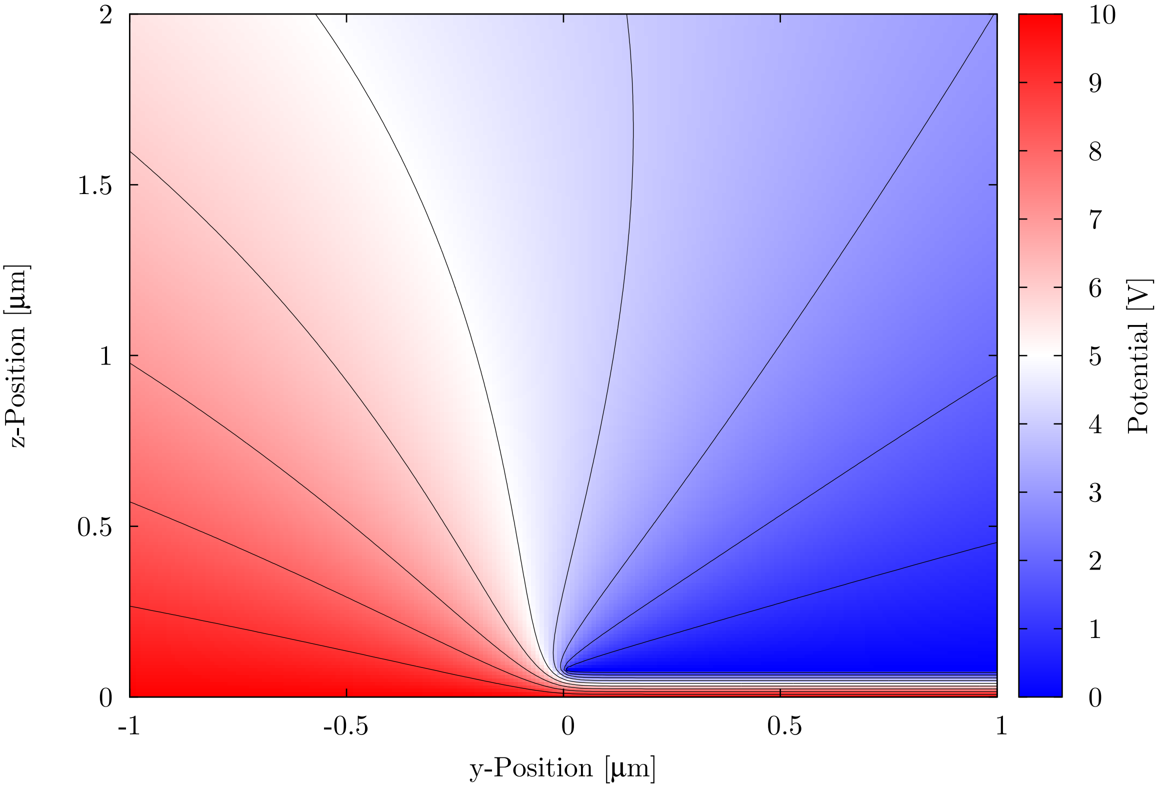

Figure 9.7.: Color coded potential and equipotential lines from the performed simulation on the effect of the back gate, see section B.4. The flake extends from zero to 5 µm and is positioned 80 nm over the back gate with vacuum as dielectric. Thus the situation is equivalent with silicon dioxide as dielectric and 312 nm distance to the back gate.

quantum Hall plateaus and across the charge neutrality point. Furthermore one can identify in Fig. 9.8 (a) a negative electron concentration. The origin of the negative concentration is a result of the simulation allowing for charge redistribution independent of charge carrier type. The sign change is therefore equivalent to a charge carrier type change. This implies for n-type graphene a region at the edges consisting of holes instead of electrons. The overall charge carrier profile seems not to be deformed but rather shifts by changing the back gate voltage. This is of course only true for small back gate voltages. For sufficiently high back gate voltage the back gate will dominate the charge carrier profile and the u-shaped structure for n-graphene can be flipped upside down. Whether this happens at a reachable back gate voltage depends on the geometry and amount of fixed charges. In the specific case we can conclude from the measurements that the back gate effect is negligible within our parameter space.

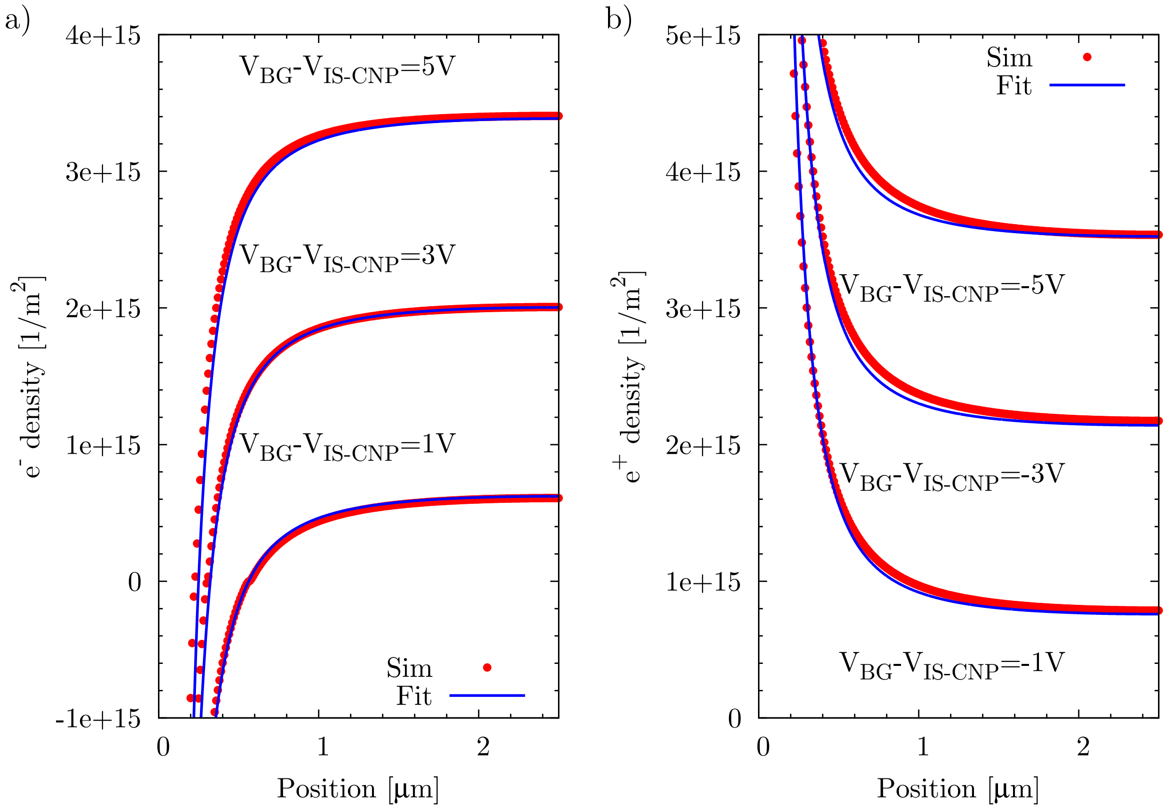

Figure 9.8.: Effect of negative fixed charges at the edges of the graphene flake. (a) Electron, (b) hole concentration profile versus position away from the edge. The change of the charge carrier concentrations towards the edges fit to the requirements deduced from the Figures 9.3 and 9.4.

9.5. Arrangement of fixed negative charges: simulation of various models

In the previous section we found that fixed negative charges close to the flake edges can explain qualitatively the evolution of Hall potential profiles with changing the back gate voltage. In this section we want to try a more quantitative analysis of the charge and arrangement.

Figure 9.10 shows some possible geometries for the fixed charge arrangement. We want to neglect the effect of dopants on or beneath the graphene flake at the moment and discuss the impact of such doping at the end of this section.

9.5.1. Homogeneous area charge arrangement

The situation in Fig. 9.10 (a) assumes a homogeneous arrangement of fixed charges at the silicon dioxide surface beneath the flake. This would resemble a situation, where the surface of the silicon dioxide acquired the charges before the flake transfer. The effect of this charge distribution can be made clear at the back gate voltage exactly counteracting the homogeneous charge arrangement. Imagine a parallel plate capacitor like in Fig. 9.9

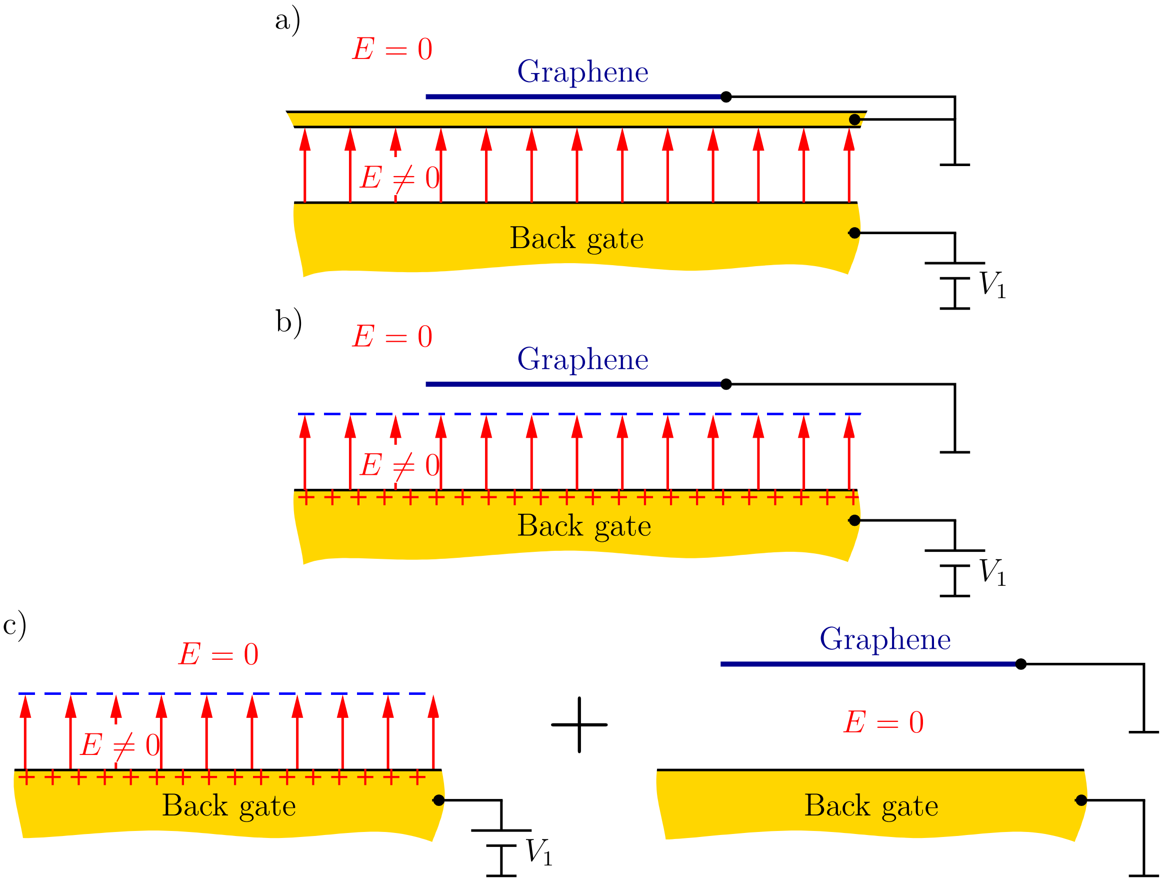

Figure 9.9.: Model for a homogeneous area charge arrangement. The actual situation of homogeneous charges on the silicon dioxide surface can be replaced by a capacitor on which the graphene flake is lying (a) in case the voltage applied to the back gate V_1 counteracts the effect of the homogeneous charges (b). In that case the problem can be replaced by the sum of two solutions $\phi = \phi_1 + \phi_2$ (c) where one includes the homogeneous charge and the other the graphene flake.

(a). After a voltage V_1 is applied at the back gate, charges will be positioned at the plate surfaces. Removing the top plate but keeping the charges on this plate in position as well as keeping the back gate voltage to V_1 does not change the electrostatic situation. Figure 9.9 (b) shows this arrangement were the electric field from the back gate is exactly compensated by the homogeneous area charge distribution resulting into no effect of the back gate on the graphene flake. For this specific back gate voltage value, the charge density of the back gate surface will be equal to that of the charged layer.

This situation of Fig. 9.9 (b) can be partitioned in two separate problems that can be solved individually. The reason is the superposition principle in electrostatics. If we have two solutions ϕ_1 and ϕ_2 of the Poisson equation for two different charge arrangements ρ_1

and ρ_2:

$$\Delta\phi_1 = \frac{\rho_1}{\epsilon_0\epsilon_r}, \tag{9.2}$$

$$\Delta\phi_2 = \frac{\rho_2}{\epsilon_0\epsilon_r}, \tag{9.3}$$

then also the sum of the two solutions is the solution of the Poisson equation for the sum of the two charge densities:

$$\Delta(\phi_1 + \phi_2) = \Delta\phi_1 + \Delta\phi_2 = \frac{\rho_1 + \rho_2}{\epsilon_0\epsilon_r}. \tag{9.4}$$

Boundary conditions have to be treated in addition. The potentials and the electric fields at the boundaries add up when going from ϕ_1 and ϕ_2 to $\phi_1 + \phi_2$.

In this case the partition of the problem would be done like shown in Fig. 9.9 (c). We include all the fixed charges into ϕ_1 and the graphene flake into ϕ_2. ϕ_1 just resembles the capacitive arrangement of Fig. 9.9 (a). As boundary conditions it delivers zero for the plane close to the flake and V_1 for the back gate. The ϕ_2 resulting for the particular situation is zero everywhere. Interesting becomes the situation if we deviate in the biasing for ϕ_2 from the given one in Fig. 9.9 (c). The superposition still holds so that we can wrap the problem back. The solution for ϕ_2 was given in section 9.3 for arbitrary back gate voltage. Adding up ϕ_1 to ϕ_2 will give the solution of the full problem. Interesting is that the graphene flake is affected by the solution ϕ_2 only. The applied bias on the back gate on the other hand is the sum of the boundary conditions of ϕ_1 and ϕ_2 at the back gate. Hence if we apply the voltage $V_1 + V_2$ on the back gate and V_1 is the boundary condition for ϕ_1 then the flake behaves as if there are no fixed charges and only the V_2 is applied to the back gate.

In other words, around the back gate voltage of V_1 the charge density profile towards the graphene edges has to flip upside down. Only the charge neutrality point in applied back gate voltage is therefore shifted by the fixed negative charges. The back gate effect dominates charge arrangement at the edges but with an offset equal to the charge neutrality point. This contradicts our observation where no flip of the charge density profile was found at the charge neutrality point. Hence there has to be a different fixed charge carrier density below the graphene and besides it. For a comparison one can calculate the doping of the flake using the position of the resistance maximum V_{Rmax} which is

$$\eta_{\mathrm{Rmax}} = \frac{\epsilon_0\epsilon_r V_{\mathrm{Rmax}}}{ed} = 2.26 \cdot 10^{15}\,\frac{1}{\mathrm{m}^2}. \tag{9.5}$$

For the whole back gate voltage range swept no flip of the charge carrier profile was observed so that the charge at the surface has to be at least $\eta_{\mathrm{fs}} = -5.8 \cdot 10^{15}\,\mathrm{m}^{-2}$. The span between η_{Rmax} and η_{fs} given by $\eta_{\mathrm{Rmax}} - \eta_{\mathrm{fs}}$ is therefore at least 3.5 times higher than η_{Rmax} the charge density at the charge neutrality point.

Instead of a homogeneous fixed charge distribution, a variation is required. The possible remaining arrangements are sketched in Fig. 9.10 (b) to (d). The two extreme cases are a homogeneous charge density everywhere except under the flake Fig. 9.10 (b) and a line

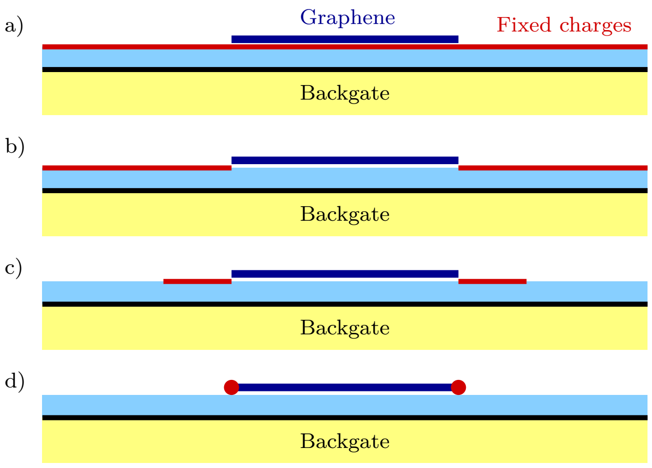

Figure 9.10.: Possible arrangements/positions for fixed charges.

charge distribution just at the graphene edges, Fig. 9.10 (d). Of course every intermediate constellations like in Fig. 9.10 (c) is also possible. We want to discuss in the following only the two extreme cases starting with the charged edges first.

9.5.2. Effect of a fixed line charge distribution

The edges of the graphene flakes in a clean environment would have one dangling bond per two edge atoms. Since in the process of creating real samples the flakes interact with air, water and different solvents it can be expected to find adsorbents and chemically bond species at the edges. The most probable species are oxygen and water due to the high electron affinity [143, 144] and their presence during processing. The high electron affinity in the order of 1 eV on the other hand leads to accumulation of charges at the edge. Beside this there are other mechanisms like edge bound states [145–147] which could cause charge accumulation. This geometry is therefore quite reasonable.

To handle different geometries a simulation was prepared which is described in section B. A typical situation for a fixed negative line charge at the edges is shown in Fig. 9.11. The equipotential lines around the line charge are without graphene circles with center the position of the line charge. The graphene flake acts similar to a perfect metal by deforming the circular equipotential lines. But the charge carrier concentration of graphene is compared to metals low and thus the screening will not be perfect. The result is nicely seen in the equipotential lines squeezed together close to the line charge at the side the flake is positioned. Between back gate and flake the electric field decays very fast in contrast to the top side of the flake where the fields can extend freely.

It can be found by further analysis of the simulation, that the charge density created by a line charge at such geometry is described satisfactory by

$$\eta_{\text{l}} = \frac{c_{\text{l}} \eta_{\text{fl}}}{y^2}. \tag{9.6}$$

Here y is the distance from the flake edge where the line charge η_{fl} is positioned. c_{l} is a calibration constant depending on the fixed charge arrangement and determined by

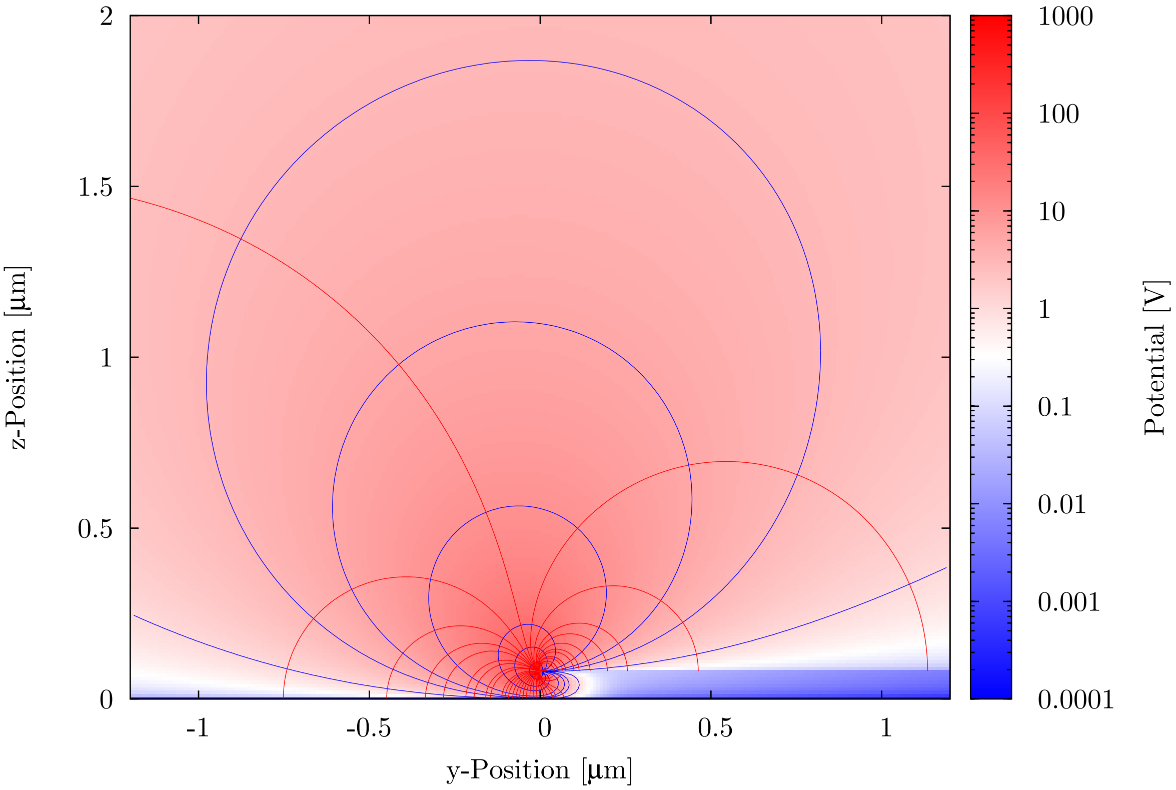

Figure 9.11.: Color coded potential and equipotential lines from the performed simulation with line charges at the flake edges, see section C.1. In the particular situation the back gate as well as the flake was grounded and a line charge of $-5 \cdot 10^{10}\,e\mathrm{m}^{-1}$ was chosen. The flake extends from zero to 5 µm and is positioned 80 nm over the back gate with vacuum as dielectric. Thus the situation is equivalent with silicon dioxide as dielectric and 312 nm distance to the back gate.

fitting to the simulations. Its values was found to be

$$c_{\mathrm{l}} = -4.3 \cdot 10^{-9}\,\mathrm{m}. \tag{9.7}$$

Since we do not measure the charge carrier density in our measurements directly we use the position of the incompressible stripes to determine η_{fl}. To do this we need to calculate the position of the k-th incompressible stripes y_k from the charge carrier concentration η_{fl}. The first approach, already used by Chklovskii, Shklovskii and Glassman [92], is to set the degeneracy kn_{L} of the k-th Landau level equal to the charge carrier concentration:

$$kn_{\mathrm{L}} = \frac{c_{\mathrm{l}}\eta_{\mathrm{fl}}}{y_k^2} + \eta_0, \tag{9.8}$$

and resolve for y_k with $\eta_0 = \nu n_{\mathrm{L}}$:

$$y_k = \sqrt{\frac{c_{\mathrm{l}}\,\eta_{\mathrm{fl}}\,\nu}{\eta_0(k-\nu)}} \tag{9.9}$$

The fit to the date can be seen in Fig. 9.12. The line charge density found to fit best was $-3.4 \cdot 10^{10}\,\mathrm{m}^{-1}$ which gives only a rough estimation due to the uncertainty of the charge neutrality point and the filling factor ν. A more descriptive number is the number of electrons per zigzag edge atom needed. We would need about four electrons per edge atom for the found line charge. This is not a satisfactory result since a surplus of one electron per dangling bond would result in only half an electron per edge atom. We can conclude therefore that either an agglomeration of adsorbents is found at the edges or, the more realistic option, line charges do not deliver the dominant arrangement for fixed negative charges.

9.5.3. Effect of surface charge distribution

The approach taken for the surface charge distribution (Fig. 9.10 (b)) is the same as for the line charge distribution. A simulations was used to find a suitable function of the surface charge effect and this was then used to fit our data. The found charge carrier

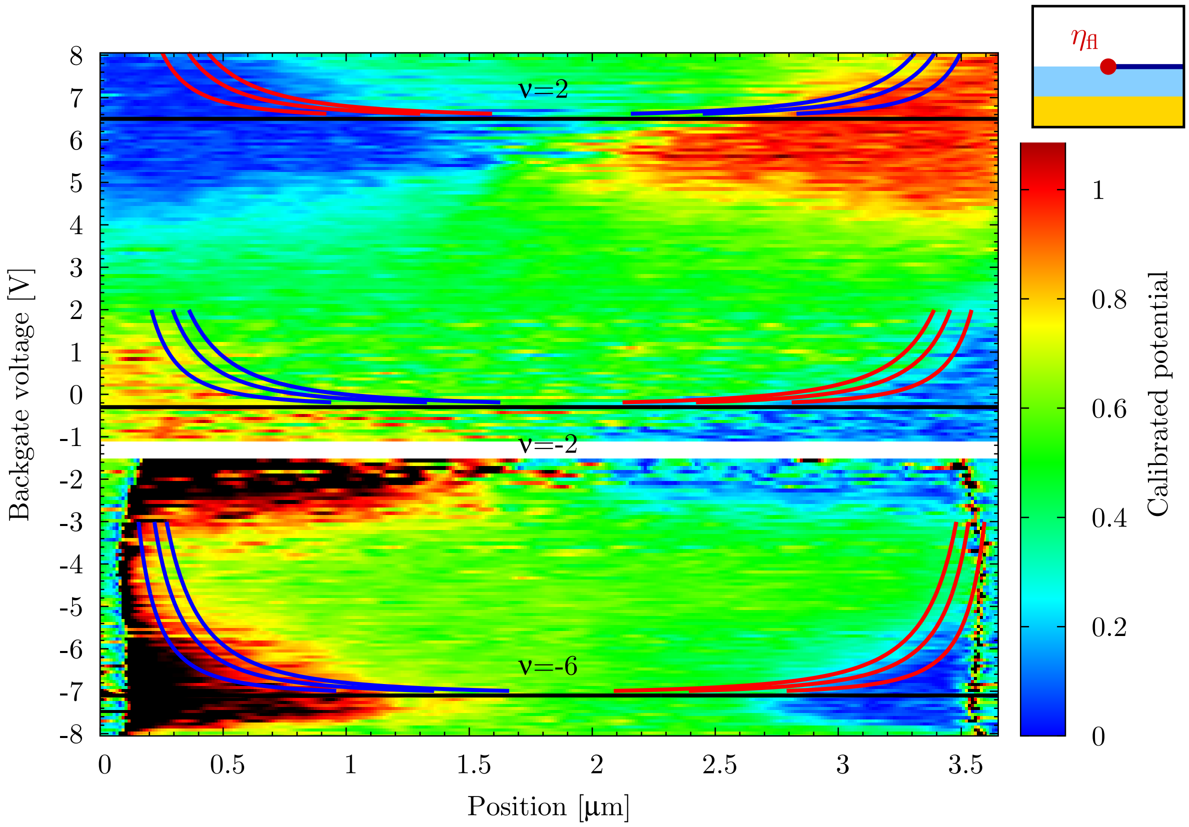

Figure 9.12.: Fit of the incompressible stripe position to our data with a line charge approach. The charge neutrality point was set to 3.1 V and the conversion factor back gate voltage to filling factor ν was set to 4/6.8 (ν over $(V_{\mathrm{BG}} - V_{\mathrm{CNP}})$). The shown lines have from the innermost to the outermost a line charge density of $-5.1 \cdot 10^{10}\,em^{-1}$, $-3.4 \cdot 10^{10}\,em^{-1}$ and $-1.7 \cdot 10^{10}\,em^{-1}$.

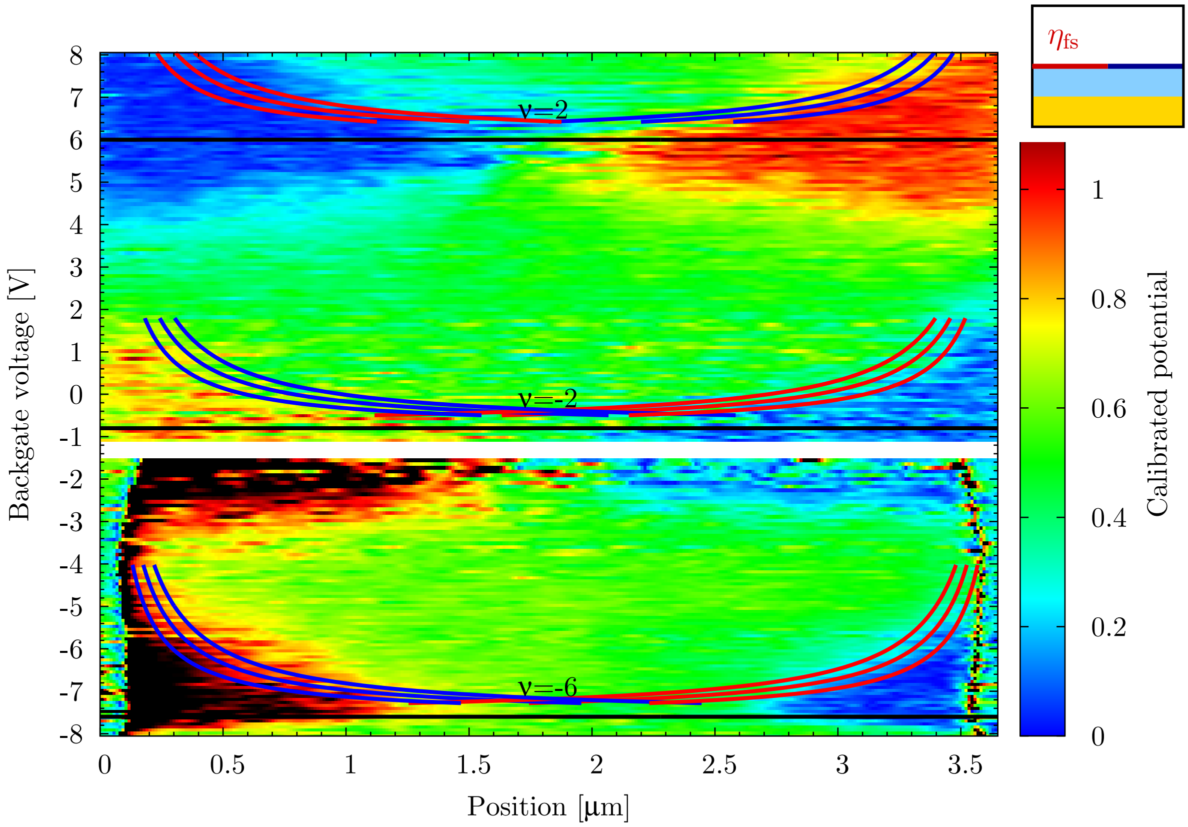

Figure 9.13.: Fit of the incompressible stripe position to our data with a surface charge approach. The charge neutrality point was set to 2.6 V and the conversion factor back gate voltage to filling factor ν was set to $4/6.8\,\mathrm{V}^{-1}$ (ν over $(V_{\mathrm{BG}} - V_{\mathrm{CNP}})$). V_{CNP} found here is of course not equal to V_{CNP} found for line charges since the charge density profile differs. The shown lines have from the innermost to the outermost a line charge density of $-3.3 \cdot 10^{16}\, e\mathrm{m}^{-2}$, $-2.6 \cdot 10^{16}\, e\mathrm{m}^{-2}$ and $-2.0 \cdot 10^{16}\, e\mathrm{m}^{-2}$.

concentration profile η_{s} was

$$\eta_{\mathrm{s}} = \frac{c_{\mathrm{s}} \eta_{\mathrm{fs}}}{y}, \tag{9.10}$$

with a calibration constant of

$$c_{\mathrm{s}} = -1.8 \cdot 10^{-8}\,\mathrm{m}. \tag{9.11}$$

Again we use the Chklovskii, Shklovskii and Glazman [92] approach to find the position y_k of the k-th incompressible stripe:

$$k n_{\mathrm{L}} = \frac{c_{\mathrm{s}} \eta_{\mathrm{fs}}}{y_k} + \eta_0, \tag{9.12}$$

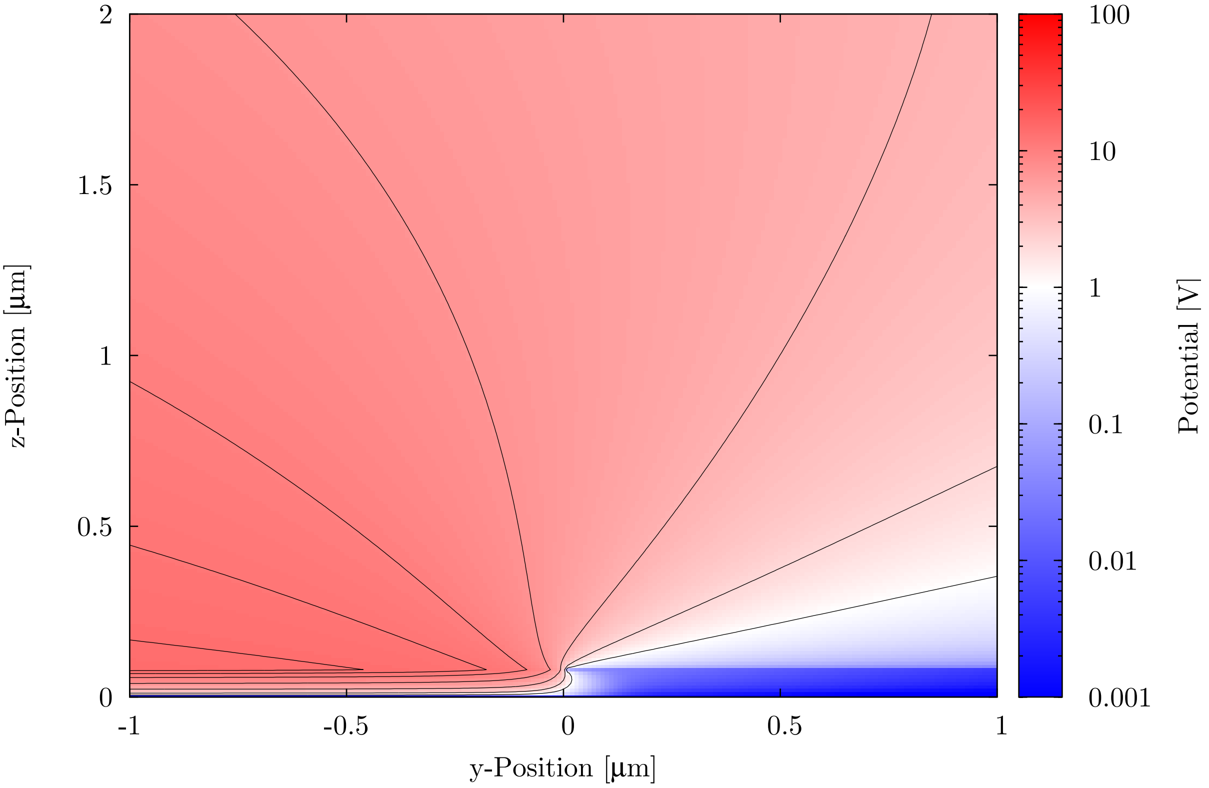

Figure 9.14.: Color coded potential and equipotential lines from the performed simulation with surface charges at the flake edges, see section C.4. In the particular situation, the back gate as well as the flake was grounded and a surface charge of $-1 \cdot 10^{16}\,e\mathrm{m}^{-2}$ was chosen. The flake extends from zero to 5 µm and is positioned 80 nm over the back gate with vacuum as dielectric. Thus the situation is equivalent with silicon dioxide as dielectric and 312 nm distance to the back gate.

and find it to be

$$y_k = \frac{c_\mathrm{s}\eta_\mathrm{fs}\nu}{\eta_0(k-\nu)}. \tag{9.13}$$

Figure 9.13 shows the corresponding fit to the data, while Fig. 9.14 shows the electrostatic potential in a cross-section close to the flake edge. The found $2.6 \cdot 10^{16}$ electrons per square meter is equivalent to a square lattice of electrons with nearest neighbor distance of about 6 nm. This is one order of magnitude higher than the doping of the flake calculated before ($2.26 \cdot 10^{15}\,\mathrm{m}^{-2}$). As already mentioned this is necessary to maintain the charge carrier density profile over the scanned back gate voltage range nearly unchanged.

We would like to point out that the charge neutrality point found via the fits for fixed line charge distribution (section 9.5.2) is naturally different from the charge neutrality point found here. This is because the charge carrier density profiles have different curvature from the edge towards the flake's bulk.

9.5.4. Influence of doping

So far we neglected doping. Here we want to discuss its influence and show why we can perform the previous discussion without including it. As we saw in section 9.3 we can use the superposition principle to partition the electrostatic problem into two separate parts with solutions ϕ_1 and ϕ_2.

Let us assume ϕ_1 corresponds to the solutions already given above for the systems of interest without doping and ϕ_2 is the solution we get from the dopants and the uncharged graphene flake alone. This way we removed the complication arising from different biasing and defined the required boundary conditions of ϕ_2. ϕ_2 has to be zero on the flake and on the back gate. Thereby we simplified the flake to become a perfect metal. With another simplification by assuming the back gate to lie far away compared to the flake-dopant distance we find an arrangement where the dopants are just mirrored by the flake. As further described in the appendix section C.3 we find just an offset of the charge carrier concentration η_d of the graphene flake which is opposite in sign to the dopant density η_D

$$\eta_\mathrm{d} = -\eta_\mathrm{D}. \tag{9.14}$$

The superposition principles allows thus to add the doping to the previous considerations if necessary and simplifies the interpretation.

9.6. Possible origin of fixed charges

Looking into the literature one finds a vast number of possible impurities and fixed charges for the thermally grown silicon dioxide and graphene on silicon dioxide systems. In the following we want to discuss some of them and try to order them by their respective arrangement. The edge chemistry of graphene is discussed in section 9.6.1. While physical edge effects can be found in section 9.6.2. Section 9.6.3 deals with surface effects, mainly of silicon dioxide and section 9.6.4 is about silicon dioxide bulk effects.

9.6.1. Edge chemistry of graphene

Pure graphene edges posses a high number of dangling bonds which make them chemically active. Hence the edges can bind to molecules coming from the atmosphere, e.g. ambient air especially water and oxygen [148].

Density functional theory calculations have shown that armchair edges are stabilized in ambient conditions by oxygen and zigzag edges by water [148]. All these types of bonds or accumulations at the edges do bind mobile electrons at the edge leading into an edge line charge and a remnant smooth mobile charge carrier distribution that reduces towards edges. The maximal line charge achievable is 4 electrons on 3 zigzag edges atoms (which had before dangling bonds) if one assumes an accumulation of one electron per oxygen bond. (For the actual constellation see configuration $z_{\mathrm{o}4}$ in [148].) This corresponds to a line charge density of about $-5.4 \cdot 10^9\,\mathrm{m}^{-1}$, which is a factor of 6 smaller than the line charge extracted from the experiment. Chemistry alone is therefore not sufficient to explain our experiments.

9.6.2. Edge effects

A remarkable effect found on graphite was the agglomeration of water on terrace-steps by Luna in 1999 [149]. The amount of agglomeration depends on the humidity and could be completely removed after seven days in dry air. In contrast only pumping, as done in our experiment, does not guarantee that the agglomeration is removed completely. It is shown for silica that bringing the sample into vacuum is not sufficient to remove all adsorbed water [150, 151]. Water molecules could therefore enhance the amount of fixed charge at the edges of graphene. Unfortunately no studies on the behavior of nanodroplets at graphene on silicon dioxide where done up to now, so that this possibility remains pure speculation.

Another effect found on graphene edges are localized states at the edges. This "edge states" are due to the presence of an discontinuity of the graphene lattice and have nothing in common with "edge states" in the Büttiker picture. Theoretical [145] and experimental work [147] show that these localized edge states exist but only if zigzag edges or mixed edges are present. It was also shown that the edge states do not participate in magneto-transport at typical fields of several Tesla [146]. In that case a charge of up to 0.1 elementary charge per sequential zigzag site can be localize at the edges [145, 146]. This is about two orders of magnitude too small for our experimental findings. But it tells us that even for a flake not influenced by the environment the charge density towards the edges is not constant.

9.6.3. Surface effects

In the following section we want to cover effects due to the surface of silicon dioxide and graphene. Since the topic is quite complex we focus in the bare facts while giving the references for further details.

It is well known that graphene under ambient conditions tends to be p-doped [152,153]. Charge impurities on and beneath the flake are responsible for the doping and especially oxygen and water can induce charge densities in the order of $10^{17}\,e\mathrm{m}^{-2}$ [153]. Charge density fluctuations in the flake have been found to be about $4.0 \cdot 10^{15}\,e\mathrm{m}^{-2}$ [154]. Also hysteresis of the resistance curves at room temperature are contributed to dipolar charge impurities [150,155]. It was also shown that after vacuum annealing at 200°C of flakes on a p-silicon/silicon dioxide substrate the flakes become n-type [156]. The doping level was about $4.0 \cdot 10^{16}\,e\mathrm{m}^{-2}$ leading the authors to the conclusion of positive remnant doping charges coming from the silicon dioxide. Fits to theoretical models incorporating impurity scattering required the charge impurities on the substrate to be around $3.0 \cdot 10^{15}\,e\mathrm{m}^{-1}$ [54, 141, 157].

It is also known that the usage of photoresist (especially polymethyl methacrylate (PMMA)) for patterning leaves residues on the sample and dopes the flakes [80, 158]. Shadow masks can be used as workaround [159,160] or annealing at elevated temperatures [158].

Using Kelvin probe measurements Moser et al. was able to show that the application of sticky tape on silicon dioxide leaves residues that have a dipole moment changing the contact potential of silicon dioxide by about $-0.5\,\mathrm{V}$ to $-2\,\mathrm{V}$ [161].

Also the exposure to water changed the contact potential difference between tip and graphene by about 1.3 V [161]. For the silicon dioxide, water is expected to bind on silicanol groups and cannot be removed fully in vacuum [150, 151]. The density of water molecules on a silicon dioxide surface can be expected to be about $10^{17}\,\mathrm{m}^{-2}$ [150]. Since it acts as slow charge trap [162–164] it is well capable to induce the surface charge densities we found in our experiment.

Water is not the only adsorbent material on a silicon dioxide surface. Takahagi et al. could show that organic materials from atmosphere (solvents and plasticizers) as well as material from the plastic transport vessels and materials used in processing could be found on the surface [165].

In conclusion, the surface of silicon dioxide as well as that of graphene is usually contaminated by oxygen water and organic materials and annealing is a must to remove them. Since we did not anneal our samples a high amount of remnant adsorbents can be expected well capable of inducing a surface charge density as found in our experiments. Since the silicon oxide substrate was heated during the mechanical exfoliation of the graphene flakes it is likely that a relative small amount of water was encapsulated between flakes and substrate. The top side of the flakes and the open area of the silicon oxide remains unprotected to all following processing steps while the area covered by graphene is not directly affected. Any residuals with different sticking probability on graphene and the silicon oxide could cause an inhomogeneous area charge distribution. For example the exposure to ambient air will cover the silicon oxide surface with water while graphene is hydrophobic [166].

9.6.4. Silicon dioxide bulk effects

Thermally grown silicon dioxide on silicon is a material rich of charge centers. Beside mobile charged ions like sodium and potassium there are oxide trapped charges, fixed charges and interface trapped charges at the silicon/silicon dioxide interface [23, 167], see Fig. 9.15 .

Mobile alkali ions can be either demobilized in phosphosilicate glass, that is fabricated by letting phosphorus diffuse into the silicon dioxide, or by chlorine neutralization, where

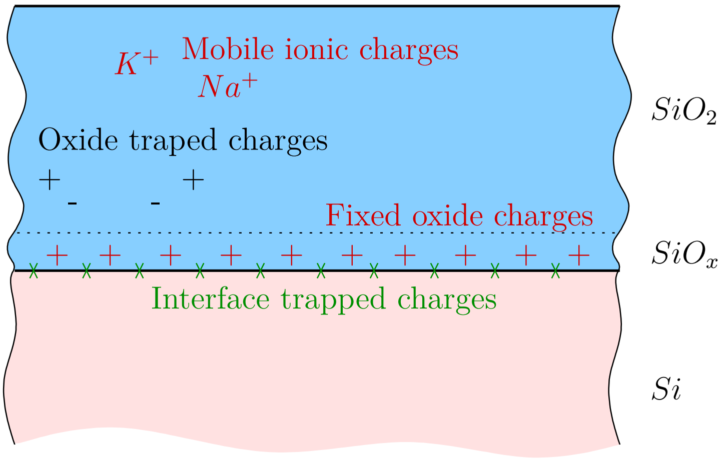

Figure 9.15.: Charges in thermally grown silicon dioxide on silicon, adapted from [167].

the alkali atoms bind to the chlorine which itself localizes at the Si-SiO$_2$ interface. Mobile alkali ions are charged positively which requires them not to be the dominant source of fixed charges in our experiment. On the other hand the alkali atoms in our wafer were neither demobilized nor neutralized so that with sufficiently high fields they can be displaced. We explain a shift of the resistance maximum which occurred after we applying a high negative voltage to the back gate this way, see section G.5 for further details. Shifting of the charge neutrality point in Raman experiments within the Smet group was explained this way [168]. Arsenic is the dopant material used in our n-silicon wafers and has a high diffusion constant for high temperatures in silicon dioxide [169]. In its ionized form it is also positive and can therefore not be the dominant contribution to the found charges.

Fixed oxide charges can be found in a layer of about 2.5 nm thickness above the silicon/silicon dioxide surface [23, 167]. They are positively charged since they consists of ionized silicon and cannot cause our experimentally determined charges that are found to be negative.

Oxide trapped charges in contrast to fixed oxide charges can be positive or negative [23, 167] and are causes by effects like ionizing radiation. Since this was not done intentionally in our case, the amount of oxide trapped charges can be expected to be low relative to the other defect types.

Interface trapped charges unlike to the previously mentioned defect types are connected to the electronic system of the doped silicon, since they are positioned at the interface between silicon and silicon dioxide [23,167]. They can be charged therefore over the silicon and can be positive and negatively charged. Hydrogen annealing at 450 °C can remove most of the interface trapped charges but was not done to our knowledge for our wafer. A typical interface state density is then about $D_{\mathrm{it}} \approx 10^{16}\,\mathrm{m}^{-2}\mathrm{e}^{-1}\mathrm{V}^{-1}$. With the band gap of silicon of 1.12 eV this gives the right magnitude of states needed in our experiments. The fact that they are coupled to the silicon bulk removes them from the list of possible fixed charge sources creating the charge carrier density profile in the graphene flake.

In conclusion, all silicon dioxide bulk charges are not able to explain our measurements.

9.7. Consequences for the charge neutrality point

When speaking about the charge neutrality point in graphene people think of a homogeneous graphene flake where the Fermi level crosses the Dirac points. The total free charge carrier density should be minimized and the remnant hole and electron concentration due to thermal activation should be equal and thus neutral. The tuning parameter to reach charge neutrality is often the back gate voltage.

Even though the definition of the charge neutrality point is rather simple it is not straight forward to find it for a real flake. In literature [55] the position V_{Rmax} of the resistance maximum in a two-terminal configuration is often used to determine the charge neutrality point. Here we want to discuss how our previous findings affect the charge neutrality point. In particular we will discuss how a non-flat charge carrier profile within graphene given by a fixed area charge beside the graphene flake will make the common understanding of "charge neutrality" unreliable. We will calculate for this the resisitivity for such a situation, assuming zero magnetic field and a fixed mobility of the charge carriers independent of the density.

For an infinitely wide flake the edge effects do not affect the transport and the resistance maximum coincides with the charge neutrality of the flake. We want to call this the infinite flake charge neutrality point which is located at the back gate voltage $V_{\mathrm{IF-CNP}}$. Without doping $V_{\mathrm{IF-CNP}}$ is equal to zero.

In a finite flake the edge effects induce a characteristic charge carrier profile shifting the point where the bulk of the flake is charge neutral. We want to call the voltage where the center of the flake is charge neutral the bulk charge neutrality point $V_{\mathrm{B-CNP}}$.

As here charge-neutrality exists in the bulk but not at the edges, the resistance maximum might not necessarily appear at $V_{\mathrm{B-CNP}}$, but at a different value V_{Rmax}.

In the following we want to give a more quantitative analysis by calculating $V_{\mathrm{IF-CNP}}$, $V_{\mathrm{B-CNP}}$ and V_{Rmax}. From our data we concluded that the best fitting charge carrier profile has the form

$$\eta(y, V_{\mathrm{BG}}) = \eta_0(V_{\mathrm{BG}}) + \frac{c_{\mathrm{s}}\eta_{\mathrm{fs}}}{y + \frac{w}{2}} - \frac{c_{\mathrm{s}}\eta_{\mathrm{fs}}}{y - \frac{w}{2}} \tag{9.15}$$

Thereby the charge carrier concentration η_0 induced by the back gate excluding edge

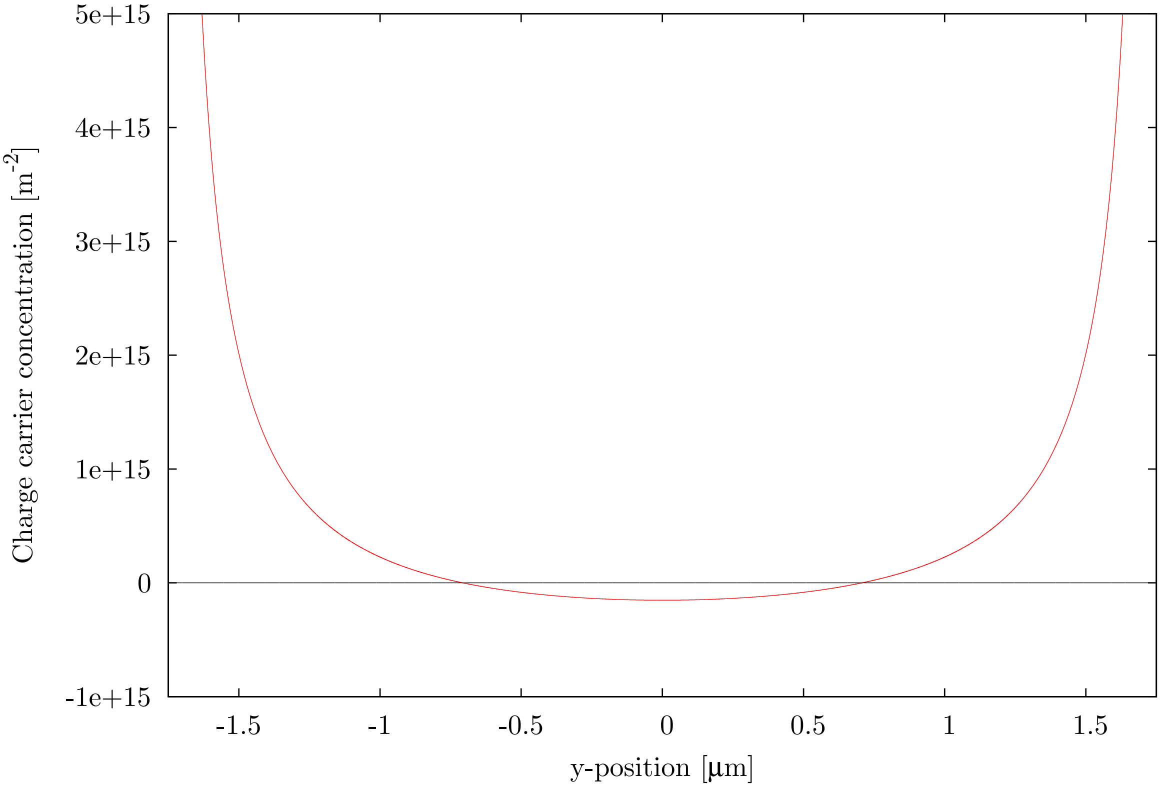

Figure 9.16.: Profile of the charge carrier distribution across a graphene flake as derived from the fits on the data.

effects is

$$\eta_0(V_{\mathrm{BG}}) = -\frac{\epsilon_0\epsilon_r V_{\mathrm{BG}}}{ed}. \tag{9.16}$$

This profile is shown in Fig. 9.16. Formula (9.15) has the disadvantage that η diverges at the edges $y = \pm w/2$ and is therefore not to be integrable over the flake width. Since for real samples the surface charge is finite due to finite size of the flake the real charge carrier density profile has to be integrable. In other words the charge carrier density will not shoot up to infinity towards the edges but rather will reach a threshold in the order of the nearby surface charge density. We therefore set an integration threshold n_t and do not allow the charge carrier concentration to rise above this threshold. We choose n_t to be equal to the surface charge density η_{fs} for the final evaluation but keep it unrelated for the calculation. The positions $\pm t$ where we reach the threshold can be found by setting equation (9.15) equal to n_t which results in

$$t \equiv |y(\eta = n_t)| = \pm\sqrt{\frac{w^2}{4} + \frac{c_{\mathrm{s}}\eta_{\mathrm{fs}}w}{\eta_0 - n_t}}. \tag{9.17}$$

In the same way we can find the positions $\pm c$ where η is equal to zero:

$$c \equiv |y(\eta = 0)| = \sqrt{\frac{w^2}{4} + \frac{c_{\mathrm{s}}\eta_{\mathrm{fs}}w}{\eta_0}}. \tag{9.18}$$

These are the points in the flake's cross section where the charge carrier type changes. At the voltage where c itself is equal to zero, the bulk of the flake is charge neutral. By setting $c = 0$ we can easily determine $V_{\mathrm{B-CNP}}$:

$$V_{\mathrm{B-CNP}} = \frac{4c_{\mathrm{s}}\eta_{\mathrm{fs}}ed}{\epsilon_0\epsilon_r w}. \tag{9.19}$$

The back gate voltage where the flake bulk changes its charge carrier type is exactly $V_{\mathrm{B-CNP}}$ within our simple model

To find the resistance maximum V_{Rmax} we want in first place assume a translation invariant sample along x-direction and follow the argumentation of [170] (local Ohm's law, $\nabla\vec{j} = 0$ and $\nabla \times \vec{E} = 0$) but only within the Drude model. The resulting set of formulas for our problem is then

$$j_x(y) = \frac{I}{\rho_{xx}(y) \int\limits_{-w/2}^{w/2} \frac{1}{\rho_{xx}(y)}dy}, \tag{9.20}$$

$$E_x(y) = \rho_{xx}(y)j_x(y), \tag{9.21}$$

$$\rho_{xx}(y) = \frac{1}{\sigma_0(y)} = \frac{1}{q|\eta(y)|\mu}. \tag{9.22}$$

Here we assume that the mobility μ is independent of charge carrier density and type. Considering the previous mentioned threshold and that from equation (9.20) and (9.21) we get $V_x = \int_0^l E_x dx = E_x l$, the integral form of Ohm's law becomes:

$$V_x = \frac{lI}{q\mu\mathcal{N}}, \tag{9.23}$$

$$\mathcal{N} = 2\int_c^t \eta(y)dy - 2\int_0^c \eta(y)dy + 2(w-t)n_t \tag{9.24}$$

$$= 2(t-2c)\eta_0 + 2c_\mathrm{s}\eta_\mathrm{fs} \ln \frac{w+2t}{w-2t}\frac{(w-2c)^2}{(w+2c)^2} + 2(w-t)n_t. \tag{9.25}$$

where $\mathcal{N}$ is the integration of the absolute charge carrier density profile $|\eta(y)|$ of the cross section. The integration from zero to c gives the contribution of the n-type region. When there is no n-type region, c becomes arithmetically complex (see equation (9.18)), one has to set $c = 0$ to let equation (9.24) stay valid. Figure 9.17 shows $\mathcal{N}$ and V_x/I for a flake width $w = 3.5\,\mu\mathrm{m}$. The blue and green curves show the two integrals of $\mathcal{N}$ - as formulated in equation (9.24) - separately. The blue curve corresponds to the hole concentration and the green to the electron concentration. The total charge carrier concentration is shown in red and after the electron concentration becomes zero the total concentration is equal to the hole concentration. The maximum in the resistance or the minimum in the conductance can be found by setting the first derivative of equation (9.25) equal to zero. This was solved numerically and is plotted in Fig. 9.18. For a flake width of $3.5\,\mu\mathrm{m}$ we find $V_\mathrm{Rmax} = 1.44\,\mathrm{V}$, $V_\mathrm{B-CNP} = 1.09\,\mathrm{V}$ and $V_\mathrm{Rmax} - V_\mathrm{B-CNP} = 0.35\,\mathrm{V}$. In the width range of one micrometer and above, V_Rmax remains linear in the double logarithmic plot. V_Rmax can be fitted in this range by $V_\mathrm{Rmax} = \alpha V_\mathrm{B-CNP}$ where α is just constant factor. Doing this fit we get as an approximation

$$V_\mathrm{Rmax} \approx \frac{4}{3} \cdot V_\mathrm{B-CNP} = \frac{16 c_\mathrm{s}\eta_\mathrm{fs} e d}{3\epsilon_0\epsilon_r w}. \tag{9.26}$$

To get a feeling how the threshold n_t - introduced to avoid the divergence of equation (9.15) at the edges - influences our results we calculated several traces with different n_t and compared them. Figure 9.19 shows the results in blue for choosing n_t to be $3.8 \cdot 10^{15}\,\mathrm{m}^{-2}$. This is ten times smaller than for the actual used threshold density of $3.8 \cdot 10^{16}\,\mathrm{m}^{-2}$ which is plotted in black. The red curve was calculated with $n_t = 1.91 \cdot 10^{19}\,\mathrm{m}^{-2}$ which is half the carbon atom density of graphene. It should be emphasized that the chosen range of n_t was about four orders of magnitude and even though the effect seems big for small width it is very small especially for the flake size in the range of $4\,\mu\mathrm{m}$ we are dealing with.

9.8. Summary

In summary, we have presented Hall potential profiles measured on a exfoliated graphene sample under a fixed magnetic field of $B = 3\,\mathrm{T}$ and a temperature of $T = 1.5\,\mathrm{K}$. By varying the back gate voltage we changed the charge carrier density, going from hole

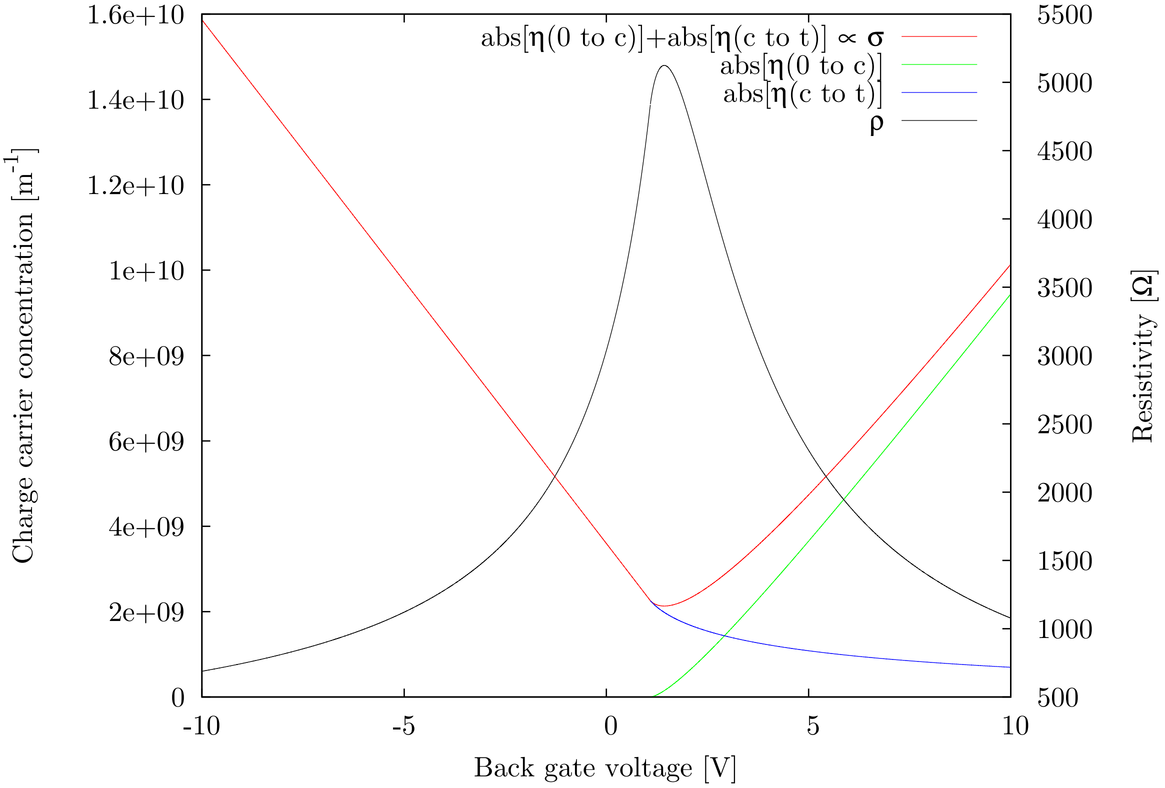

Figure 9.17.: Charge carrier concentration and resistivity found with our model.

dominated flake to an electron dominated flake. The Hall potential profiles measured for the different charge carrier densities show a characteristic evolution with the back gate voltage. This evolution is equivalent to the Hall potential profile evolution found in GaAs/Al$_x$Ga$_{1-x}$As-heterostructure samples under quantum Hall conditions [12–14]. Together with the knowledge of Landau level formation in graphene known from other measurements [56–58] we conclude that a compressible and incompressible landscape is formed also in graphene. As was interpreted for the GaAs/Al$_x$Ga$_{1-x}$As-heterostructure samples we expect the current to flow within the incompressible regions of the sample.

The position dependence of the found Hall potential drops in n-type graphene was similar to that of GaAs/Al$_x$Ga$_{1-x}$As-heterostructures. Going over a quantum Hall plateau by increasing the charge carrier concentration via the back gate voltage one finds fist two Hall potential drops at the edges. The width of these drops is increasing and their position is moving towards the flake bulk with increasing charge carrier density. At a certain point the two Hall potential drops merge to form a single drop over the sample bulk.

We concluded as for GaAs/Al$_x$Ga$_{1-x}$As-heterostructures there exists a depletion of electrons for n-type graphene extending from the edges about 1 µm into the flake bulk. On the other hand for p-type graphene the hole concentration has to increase towards the edges.

To explain both observations we introduced fixed charges around the edges of the flake. Two different models where discussed in detail: (1) Charges only at the graphene edges,

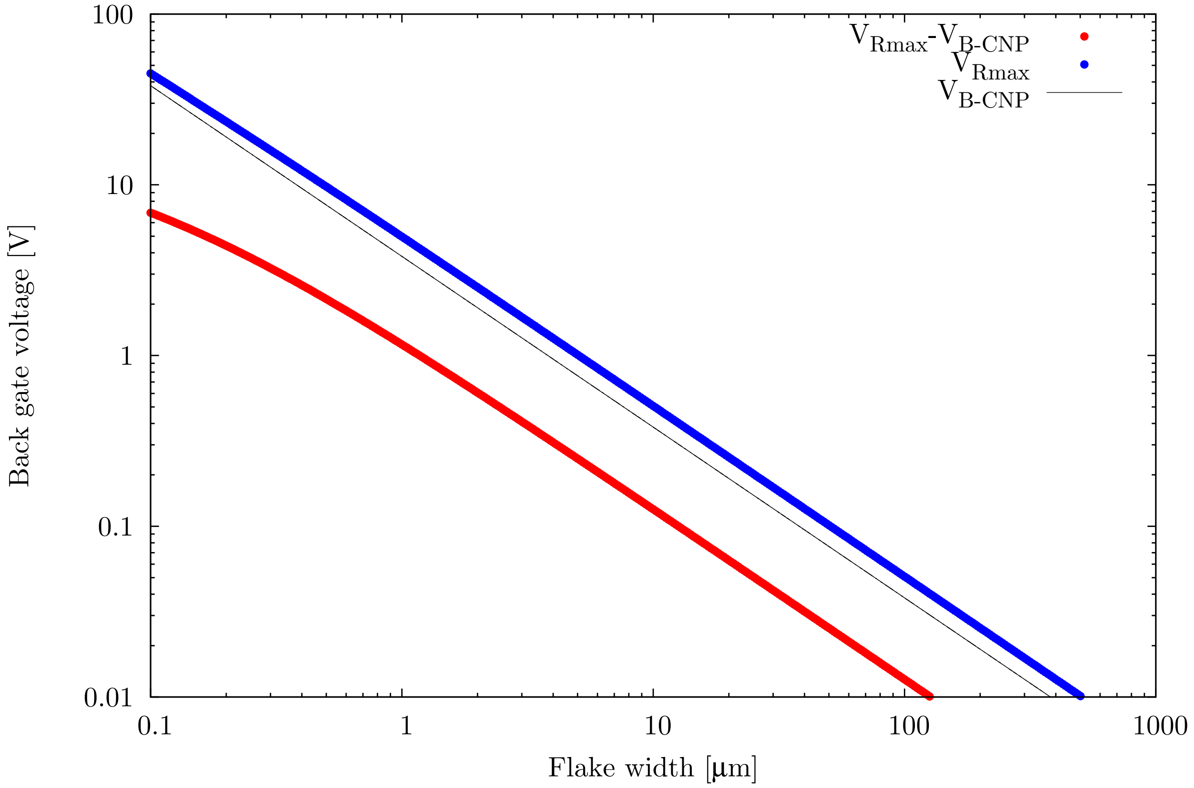

Figure 9.18.: Back gate voltage value for the bulk charge neutrality point $V_{\mathrm{B-CNP}}$ (equation (9.19)) and the resistance maximum V_{Rmax} (minimum of equation (9.25)), both versus the flake width. Also the distance between V_{Rmax} and $V_{\mathrm{B-CNP}}$ is visible. The charge neutrality point of an infinite flake $V_{\mathrm{IF-CNP}}$ was chosen to be zero. The fixed surface charge density $\eta_{\mathrm{fs}} = -3.8 \cdot 10^{16}$ was chosen to be similar to the one extracted from our measurements.

referred to as line charge distribution, leading to a charge carrier density profile which follows a y^{-2} dependence. (2) Charged surfaces beside the graphene flake, referred to as surface charge distribution, leading to a charge carrier density profile following a y^{-1} dependence. We were able to determine values for the fixed negative charge density from our measurements for both models. Thereby the surface charge model delivers more realistic numbers. While for the line charge model we would need more than one electron sitting on graphene edge atom we require only a square lattice of electrons with a lattice constant of 6 nm for the surface charge model. A possible source for this fixed surface charge would be water that adsorbes on the silicon dioxide surface and acts as charge traps [162–164].

The local variation of the charge carrier density found had two important consequences: First, one expects to find a pn-junction near the edges sufficiently close to the charge neutrality point for n-type graphene. Second, a good definition of charge neutrality in a flake strongly affected by edges is not possible. Most important, the maximum of the resistance curve will generally not mark the position of the charge neutrality point in the flake bulk.

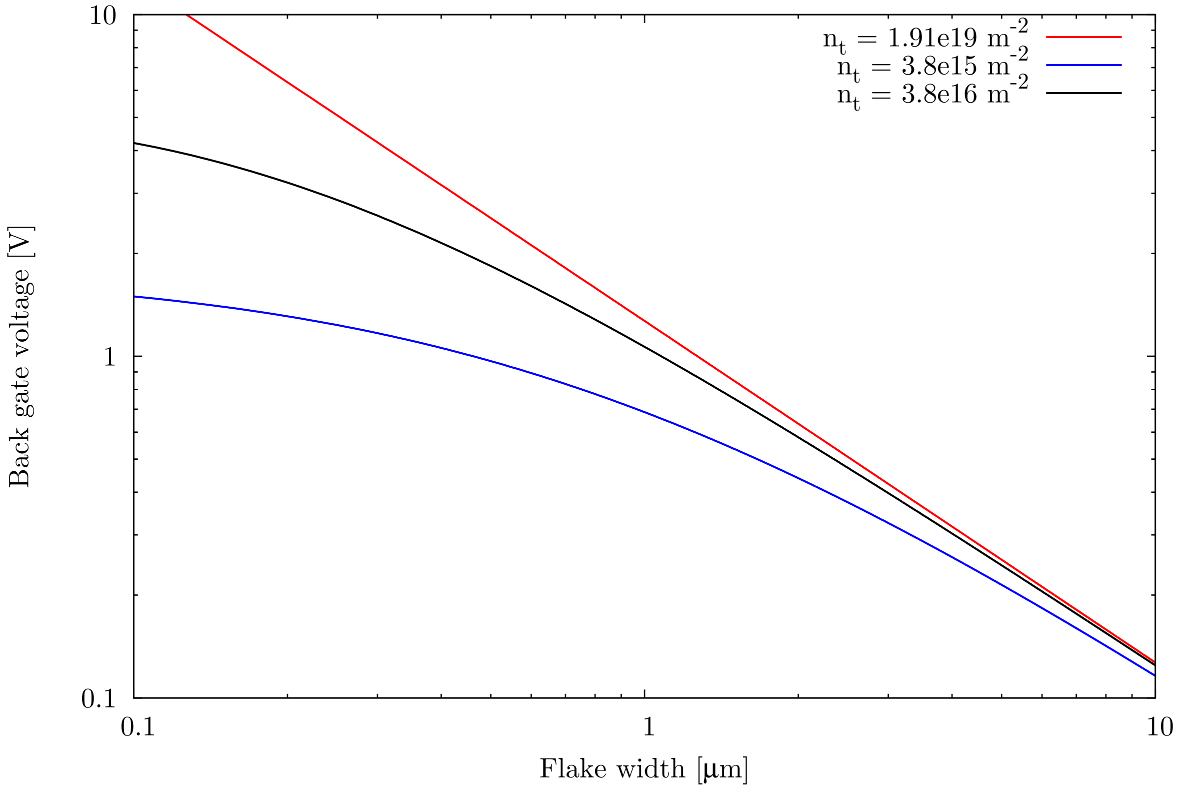

Figure 9.19.: Effect of the threshold density n_t on $V_{\mathrm{Rmax}} - V_{\mathrm{B-CNP}}$. While changing the threshold density n_t by 4 orders of magnitude $V_{\mathrm{Rmax}} - V_{\mathrm{B-CNP}}$ is not changing much for flakes wider than one micron.

10. Influence of disorder in graphene on the QHE

In contrast to two-dimensional systems in GaAs/Al$_x$Ga$_{1-x}$As-heterostructures, graphene on silicon dioxide is a highly disordered system. Scanning probe measurements with an Single-Electron-Transistor (SET) by Martin et al. [79] show puddles of locally varying charge carrier concentration.

Beside strong random potential variation, originating from silicon dioxide surface corrugations and adsorbents leading to these puddles, rolling up [88, 171], folding [172, 173] and strain induces artificial gauge fields [174, 175] are possible.

In the following we want to show scanning probe results on flakes with different sort of disorder and want to discuss how the previous model for the microscopic picture of the QHE in graphene fits in. First we want to show the effects of topographic bubbles in the graphene flake, before showing the effect of carrier concentration differing locally within the flake.

10.1. Topographic bubbles

The flake discussed in the following (ID: GB9438a, see section H.1) was found from topographic scans to have topographic bumps or bubbles, see Fig. 10.1 (a). This was also confirmed by SEM images taken after the measurements and shown in Fig. 10.1 (b) and contrast enhanced by software in Fig. 10.2 (a). The structure of the bubbles was hardly visible in the topographic scans due to the topographic resolution of the here used SPM. [1] In our reference scan trace β, (see measurement scheme in Fig. 6.2), the bumps are also observable. Figure 10.3 shows beside trace β in (a) also the resonance frequency shift during the scan over the flake in (b). Also here the bumps can be identified easier than in the topographic scans.

From the electrical characterization the flake GB9438a appeared to be an average sample. The mobility extracted from the resistance-over-back-gate curve was about $1\,\mathrm{T}^{-1}$ at a density of $3 \cdot 10^{15}\,\mathrm{m}^{-2}$ and the full-width-at-half-maximum of the resistance curve was $7.7\,\mathrm{V}$ ($\Delta n = 5.5 \cdot 10^{15}\,\mathrm{m}^{-2}$). In comparison the flake (GB8113) used in the previous chapter had a mobility of about $2\,\mathrm{T}^{-1}$ and a full-width-at-half-maximum in the resistance-over-back-gate-voltage trace of $2.8\,\mathrm{V}$.

First we want to discuss the Hall potential profiles across the center of the flake. In Fig. 10.4 the scans for a magnetic field of $5\,\mathrm{T}$ are shown. When looking at the Hall potential profiles, at the edges one can clearly identify a flip of the edge potentials from

---

[1] The used SPM was intended for a relatively large scan range of $20\,\mu\mathrm{m} \times 20\,\mu\mathrm{m}$. Therefore the scanning tube has a length of $75\,\mathrm{mm}$ which reduces the possible resolution due to vibration noise. Also construction-conditioned, the mechanical path from tip to sample is not as rigid as it could be.

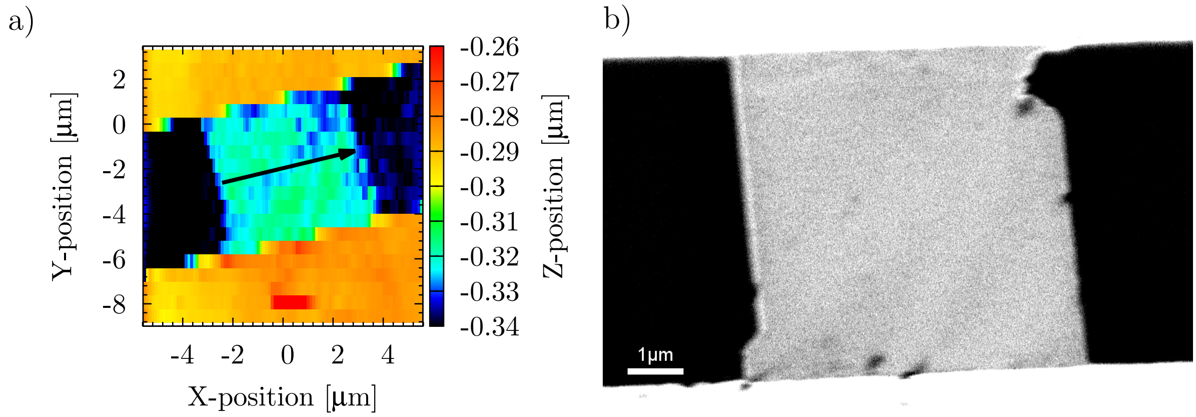

Figure 10.1.: (a) Topographic scan and (b) SEM image of the flake GB9438a. The SEM picture was taken after the measurements. The X,Y,Z coordinate system is the one of the scanning tube and is rotated around the Z axis to form the x, y, z-coordinate system of the flake.

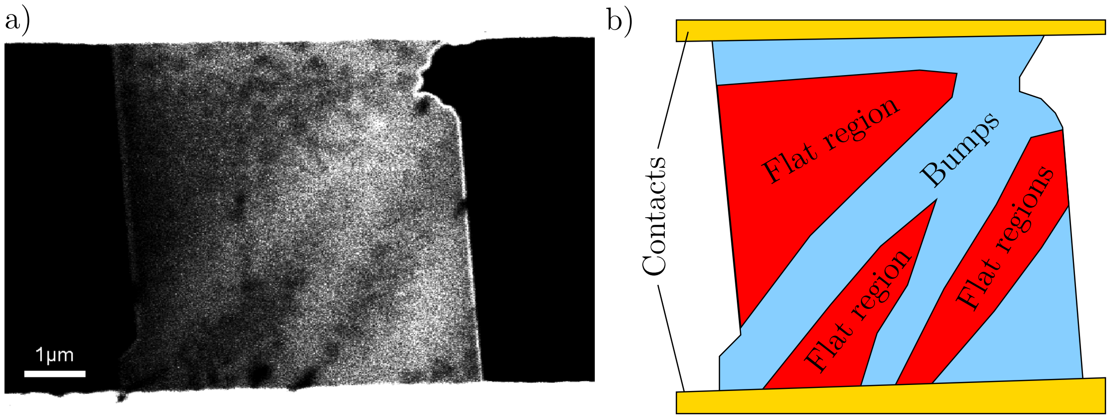

Figure 10.2.: (a) SEM pictures taken at an angle of 45 °on the flake GB9438a to identify bumps and further processed by software to enhance the visibility. (b) Scheme of the flat flake regions. These flat regions will turn out to represent individual domains.

positive to negative across the resistance maximum V_{Rmax} at about 2.6 V.

Changing the current direction (Fig. 10.4 (a) and (b)) should in a first approximation not change the inner structure of the flake. Compressible and incompressible regions remain the same and the positions of the current entry and exit points - the so-called hot spots, see section 4.6 - do not change. Therefore the change of the current direction results into an inversion of the potential profiles as seen in comparison of Fig. 10.4 (a) and (b).

However in contrast to the clean graphene flake presented before, here the Hall potential drop is positioned mainly close to one sample edge. The regime where this behavior is found correspond to the edge dominated quantum Hall plateau regions. where we would expect to find the Hall potential drop at two stripes, one at each flake edge. Instead the currents prefers to flow at only one edge and not being equally distributed at both edges as shown in the previous chapter 9. Here the Hall potential drop moves from one edge to the bulk while lowering the back gate voltage.

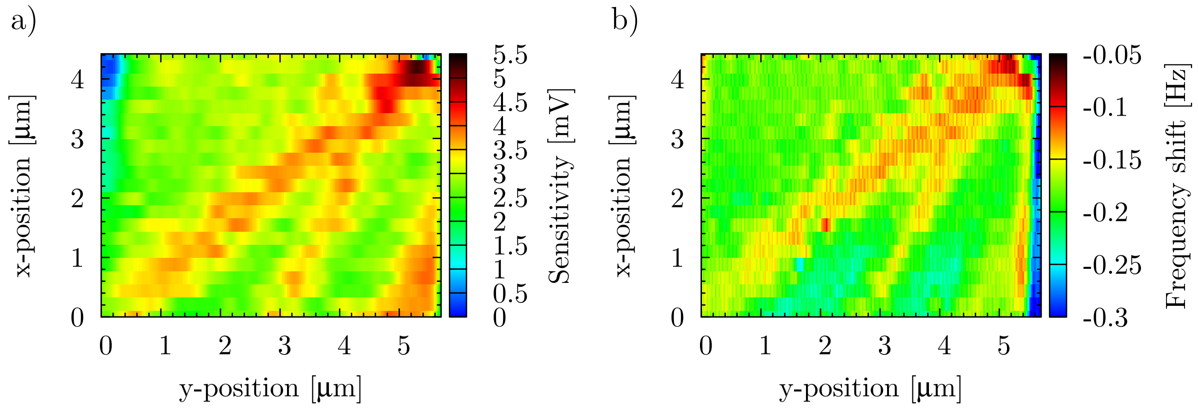

Figure 10.3.: Scans of (a) measurement sensitivity and (b) resonance frequency shift over the area of flake GB9438a. The Sensitivity was measured at a back gate voltage of 2 V and the resonance frequency shift at −1.5 V. The particular voltages were chosen because the bubble structure was visible on them best.

Also across the resistance maximum V_{Rmax}, the edge which the current prefers is swapped. The current path seems to depends on the position of the current entry and exit points (hot spots) which are changing when going from electrons to holes as charge carriers. Sketches of the qualitative current path through the flake for n-type graphene ($V_{\mathrm{BG}} = 7\,\mathrm{V}$) and p-type graphene ($V_{\mathrm{BG}} = 7\,\mathrm{V}$) are shown in Fig. 10.4 (c) and (f). Reversing current direction from Fig. 10.4 (c) to (e) does not change the position of the hot spots and does not change the current path but changing the carrier type from Fig. 10.4 (c) to (d) does change the position of the hot spots and thus also the current path. Figure 10.4 (g) to (j) are area scans of the Hall potential under similar conditions as the sketches above them which reveal the real current path through the flake and agree qualitatively with the sketches. Another way to change the position of the hot spots and thus the current path, is by flipping the magnetic field. The comparison with the non-flipped magnetic field measurements is shown in Fig. 10.5 and one can identify a mirroring of the data over the back gate axes. The imperfections of the mirroring are attributed to the error in determining the same scan position. The influence of the magnetic field on the SPM coarse positioning table leads to this error. Nevertheless the scan with flipped magnetic field appears qualitatively as it should according to the expected hot spot positions. In a direct comparison we find a similar current path for n-type graphene with positive magnetic field Fig. 10.5 (g) and for p-type graphene and negative magnetic field (j). The same is true for p-type graphene and positive magnetic field (h) and n-type graphene and negative magnetic field (i). This can be understood assuming an inhomogeneous flake that consists of several weakly coupled domains and where the current entry and exit point affects strongly the current path.

After understanding this complication we can ask how these measurements fit to the electrostatic model described in chapter 9. To answer this question we fitted the data of Fig. 10.4 (a) with our surface charge model. The result is plotted in Fig. 10.6 giving a acceptable fit at a surface charge density of $3 \cdot 10^{16}\,\mathrm{em}^{-1}$. We therefore conclude that the electrostatic model is well applicable also to this flake and that the charge carrier density

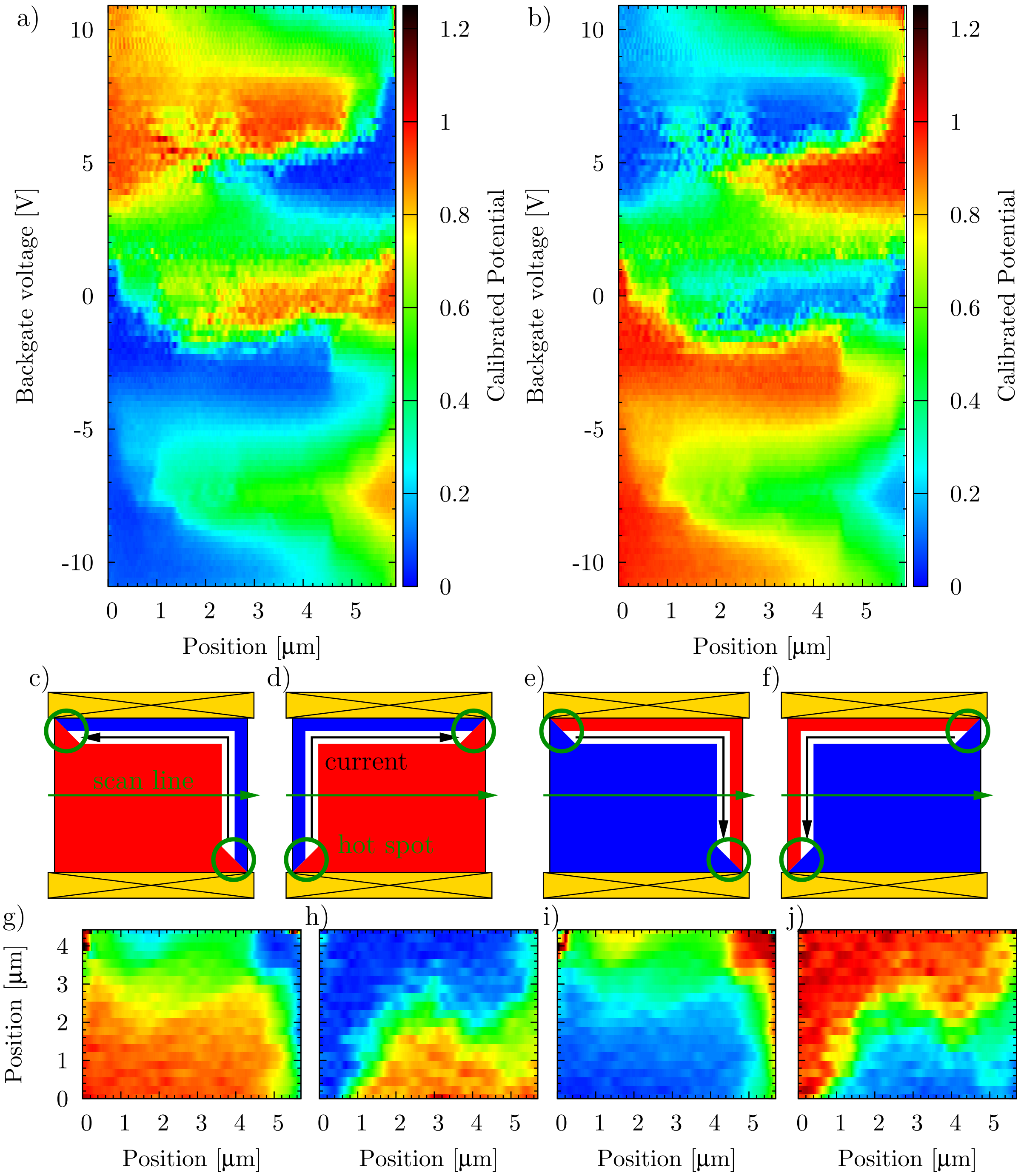

Figure 10.4.: Hall potential profiles for the flake GB9438a. (a) and (b) were measured with opposite current directions. A schematic drawing of the Hall potential over the entire flake area is shown in (c), (d), (e) and (f). The green arrow shows the scan line over the flake while the black arrows show the current flow. With green circles the position of the hot spots is marked. (c) and (d) are two situation from the measurement in (a) namely for (c) a back gate voltage of about 7 V and for (d) about 0 V. Similarly (e) is at a back gate voltage of about 7 V and (f) for about 0 V for the measurement in (b). It should be emphasized that on one hand the position of the hot spots does not change while changing the current direction. On the other hand the position does change when the charge carrier type is changed when going over the charge neutrality with the back gate. (g), (h), (i), and (j) are real area scans at this flake for (g), (i) 7 V and (h), (j) −1.5 V. (g) and (h) have the current direction of (a), while (i) and (j) have the current direction of (b).

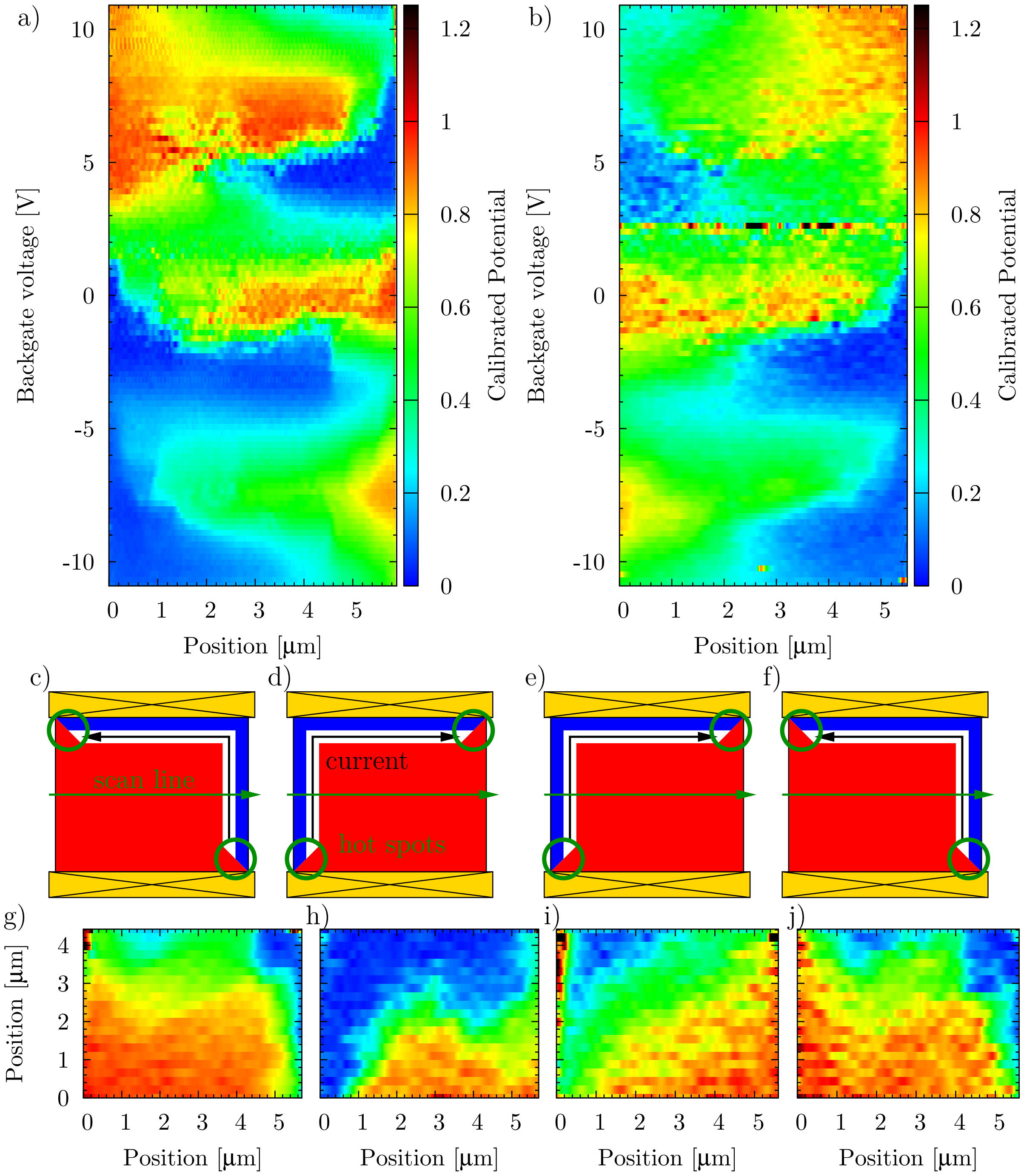

Figure 10.5.: Comparison of Hall potential profiles for flake GB9438a for magnetic field of (a) 5 T and (b) -5 T. The current direction was equal in both cases. A schematic drawing of the Hall potential over the full area of the flake is shown in (c) and (e) for 7 V and in (d) and (f) for 0 V. The green arrow shows the scan line on the flake while the black arrows show the current flow. With green circles the position of the hot spots is marked. (c) and (d) are two situation from the measurement in (a). Similarly (e) and (f) represent the flake area for -5 T in (b). It should be emphasized that the position of the hot spots does change as depicted when the direction of the magnetic field is reversed or the charge carrier type is changed. The real area scans in (g), (h), (i) and (j) done on the flake confirm the schematic drawings. (g) and (h) were measured at 5 T and (i) and (j) at -5 T. The back gate voltage for (g) and (i) was 7 V for (h) -1.5 V and for (j) 0 V.

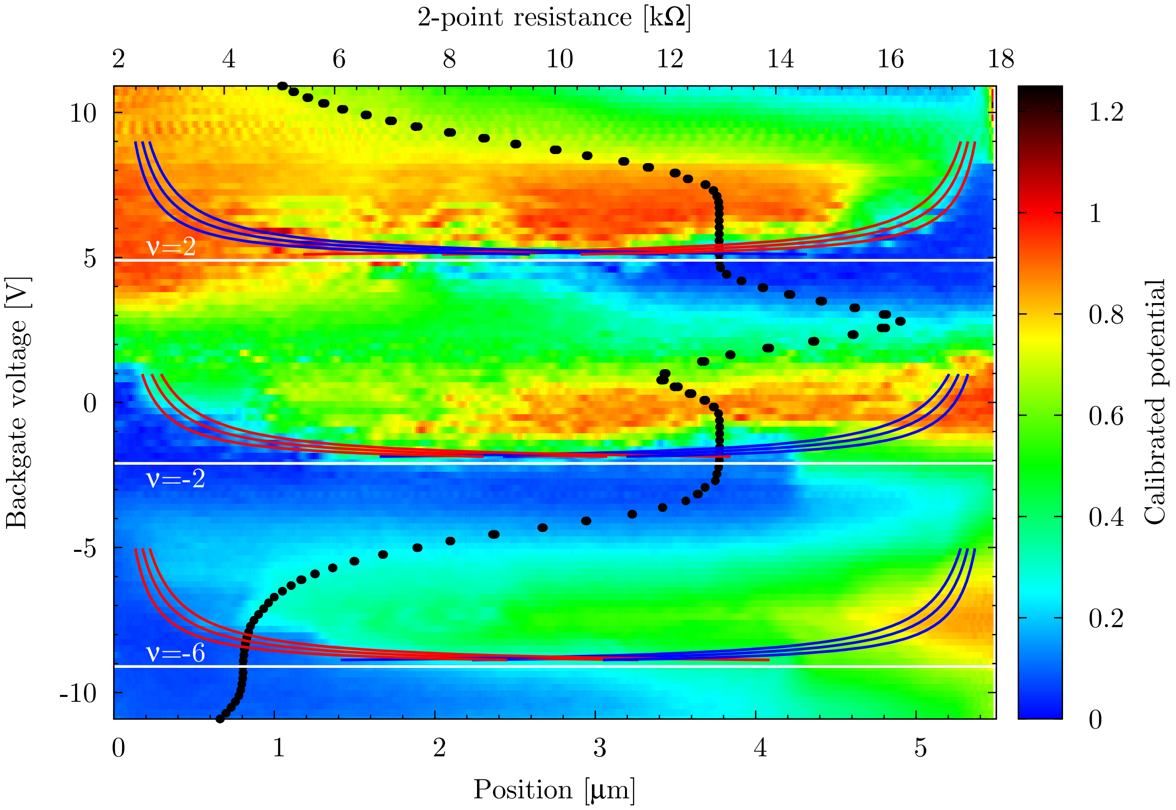

Figure 10.6.: Incompressible stripe position when a surface charge density of $3 \cdot 10^{16}\,\mathrm{em}^{-1}$ is assumed. Data from Fig.. 10.4 (a).

profile caused by surface charges is responsible for the Hall potential profile evolution.

Having a flake fragmented in several domains we can ask if it is possible to measure the outline of such a domain. We need for that to make the potential profile scans over the entire flake area. This was done and is shown in Fig. 10.7 for the filling factor $\nu = 2$ plateau. The current enters the flake at the upper left corner and flows towards the second hot spot at the lower right corner. The outline of a domain can be seen when incompressible stripes are close to the domain boundaries but still carry the full current. This is the case for Fig. 10.7 (c) where the uppermost and lowermost contour line follow roughly the domain walls. At $y = 4\,\mu\mathrm{m}$ and $x = 3\,\mu\mathrm{m}$ the current leaves the domain.

That way one can identify at least one big domain at the upper left corner coinciding with one of the topographically found bubbles. The structure already shown in Fig. 10.2 (b) indicates the found domains as nodes, or flat regions within the flake. The bubbles act as domain boundaries. A possible reason for this could be artificial gauge fields due to the strain within the curved flakes [174, 175].

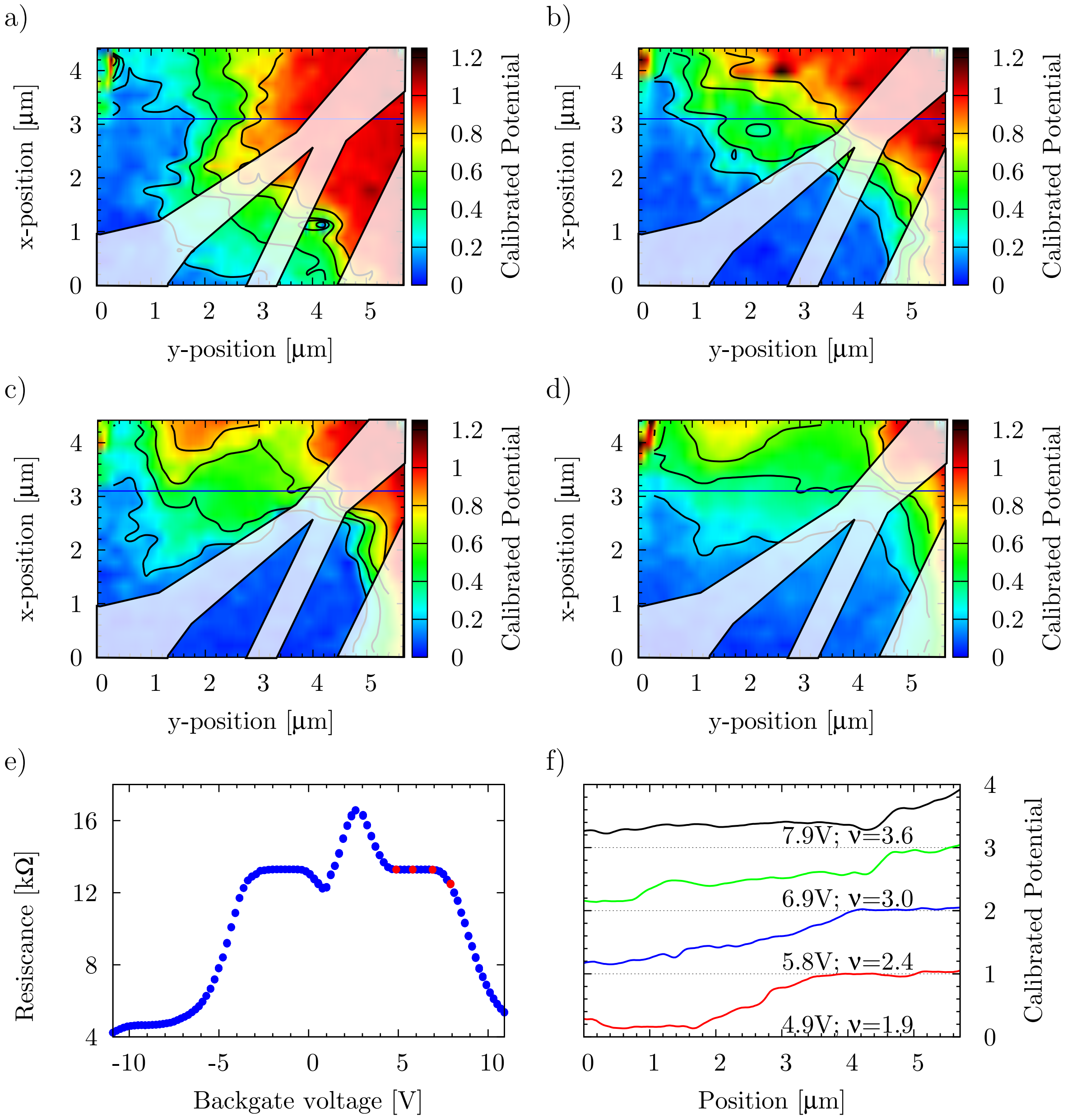

Figure 10.7.: Area scans (a-d) on flake GB9438a. Plotted is almost the entire flake area with the source contact at the bottom edge and the drain contact at the top edge of the scan. The brightened areas are expected to be domain walls. The resistance over back gate voltage curve is shown in (e). The red dot mark the position the area scans were taken. From (a) to (d) the back gate voltages were 4.9 V, 5.8 V, 6.9 V and 7.9 V. (f) shows a line-cut through the area scans. The position is marked with the blue line in (a-d). The u-shaped structure found in section 9 can be identified in (f).

10.2. Domains with different charge carrier concentration

In the previous section we discussed the effect of domain formation, where the domain boundaries dominated the current path. In this section we want to discuss domains where the boundaries are not defined by topological effects but rather built-in local variations of the charge carrier concentration are the key for the understanding.

The flake showing these features (GB9438b see section H.1) was again from electrical characterization measurement an average flake with mobility of about $0.7\,\mathrm{T}^{-1}$ at a density of $3 \cdot 10^{15}\,\mathrm{m}^{-2}$. The full width at half maximum in the resistance over back gate curve was $\Delta V_{\mathrm{FWHM}} = 10.6\,\mathrm{V}$ corresponding to a density span of $\Delta n = 7.6 \cdot 10^{15}\,\mathrm{m}^{-2}$. A SEM micrograph of the flake taken after the measurements is shown in Fig. 10.8

Again we want to look at the Hall potential drops. Figure 10.9 (b) shows the measured Hall potential profiles of flake GB9438b. Going over a quantum Hall plateau from lower to higher back gate voltage, the drops occur first at the edges and move towards the bulk for increasing voltage. The right edge is not visible in the scan because the stage movement limit was reached. Scanning across the entire flake was therefore not possible.

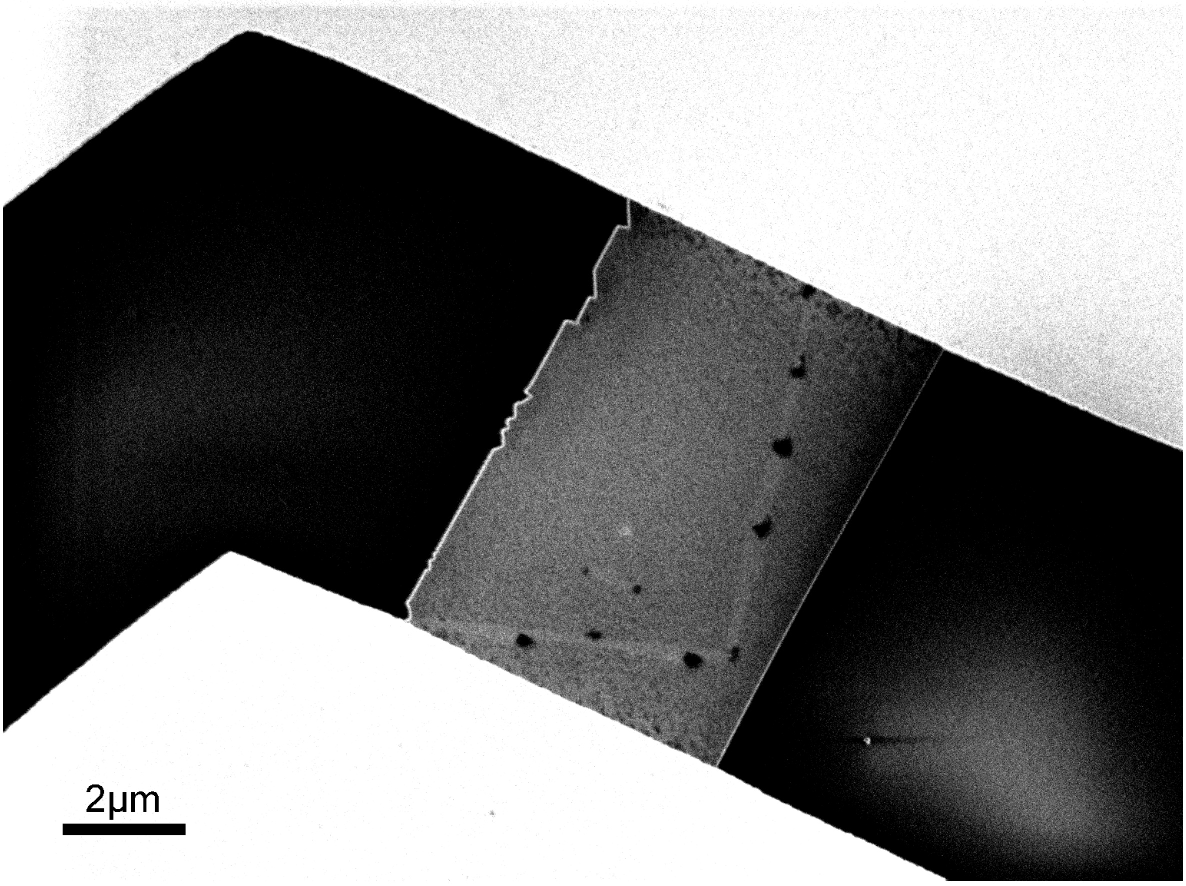

Figure 10.8.: SEM picture of the flake GB9438b. The picture was taken after the measurements. The scanned edge was the one on the left.

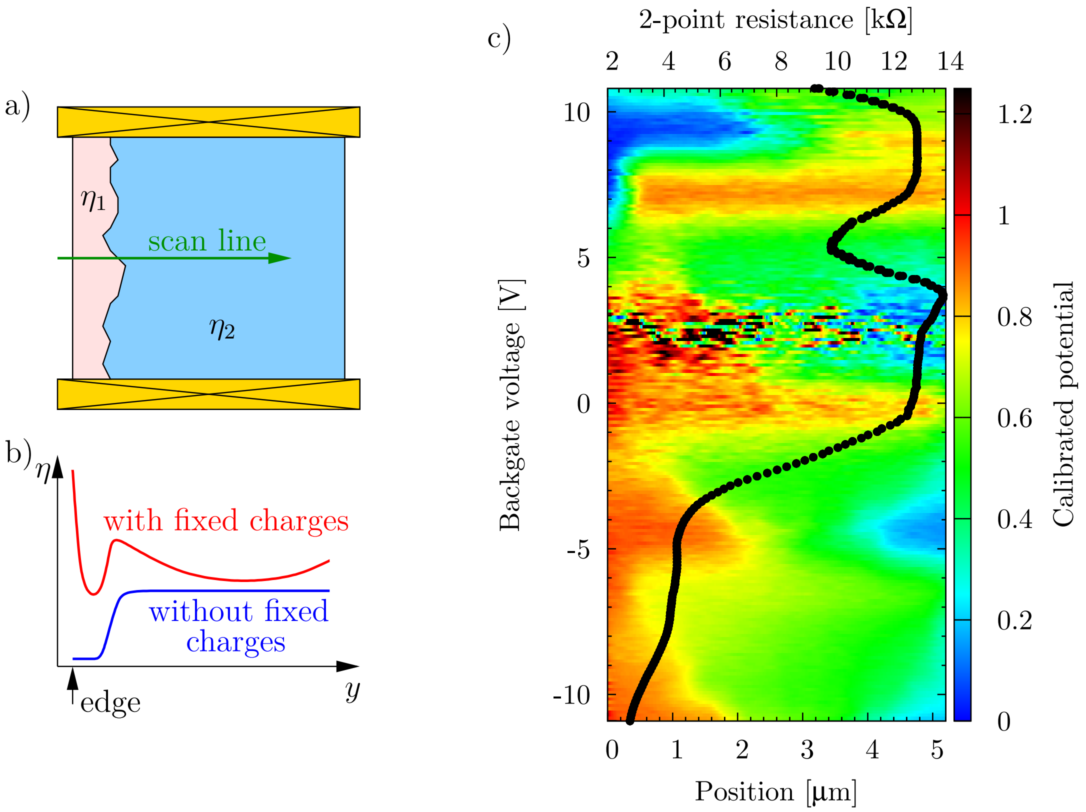

Figure 10.9.: (a) Scheme of the flake and the two charge carrier density domains. The green arrow shows the scan line which does not go across the entire flake due to positioning constrains. (b) Scheme of the charge carrier density profile of the flake. In blue we drew the expected charge carrier density without fixed negative charges and in red with the fixed charges beside the flake. (c) Bare Hall potential profiles for flake GB9438b. The Hall potential drops seem to be at the edge for the lower back gate voltage side of a plateau. At the higher back gate voltage side of a plateau the Hall potential seems to drop over the bulk. This is opposite to what was found in section 9 and is due to domain formation shown in (a).

Nevertheless the Hall potential drops over the back gate voltage evolution resemble an upside down flipped u-shaped feature.

This seems to contradict what was found in the sections 9, where the u-shaped structure was not flipped upside down. We therefore want to have a look on the Hall potential profiles in a line representation rather than color-coded. Figure 10.10 shows the Hall potential profiles around filling factor $\nu = 2$. One can identify a region at the left edge and one in the center of the flake showing a Hall potential drop. There is no additional drop at the right edge side because we were not able to scan across the entire flake due to technical range constraints. At $V_{\mathrm{BG}} = 7.5\,\mathrm{V}$ the whole potential drop is located at the edge. While increasing the back gate voltage the potential drop at the edge decreases its amplitude while the one at the center increases it. In other words the current is split up in two regions and is redistributed continuously between the two while the back gate voltage is swept. In addition we find for this back gate voltage range a nicely quantized Hall plateau. This means that two regions with equal filling factor exist in the flake

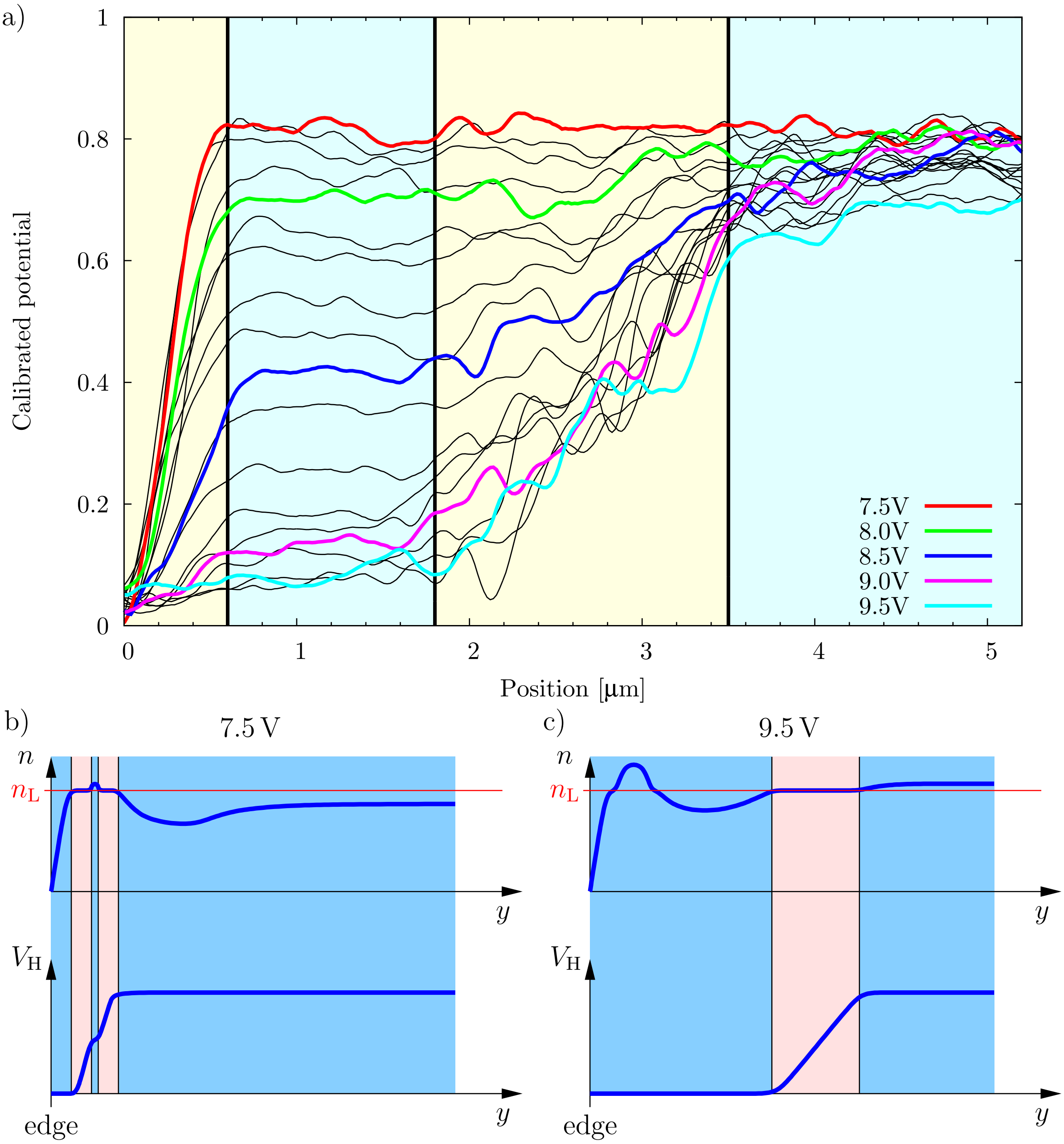

Figure 10.10.: (a) Lines of the Hall potential profiles around $\nu = 2$ for flake GB9438b. One can identify two incompressible stripes in the light yellow marked regions that are displaced in back gate voltage. The light turquoise regions remain within the shown back gate voltage range compressible and no Hall potential falls across them. Changing the back gate voltage changes the distribution of Hall potential drop among the two incompressible stripes. In particular for a back gate voltage of 9.5 V the right or bulk stripe is carrying the full current as sketched in (c) while at 7.5 V the left stripe carries the current and is sketched in (b). During the current redistribution with back gate voltage the stripes do not change their position significantly leading to the interpretation of two distinct domains.

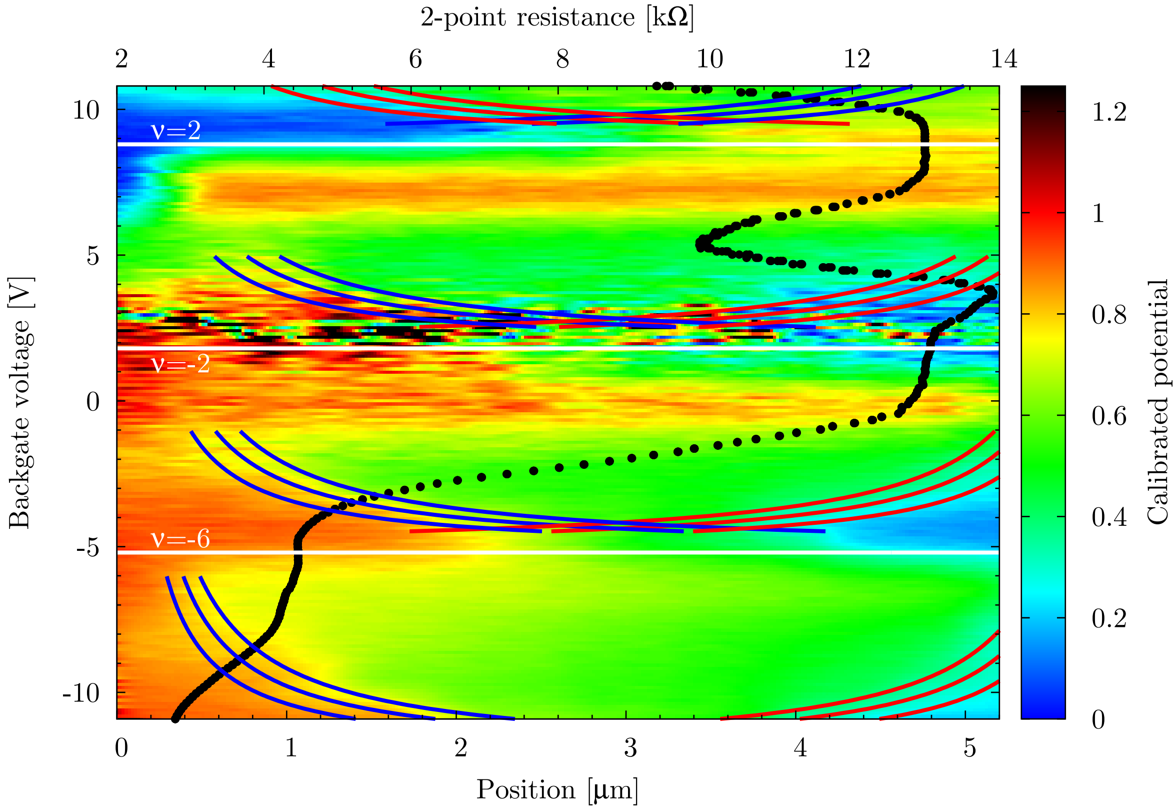

Figure 10.11.: Hall potential profiles for flake GB9438b and the position of incompressible stripes assuming a surface charge density of $1 \cdot 10^{17}\,\mathrm{em}^{-2}$.

that have Hall potential drops with similar evolution but shifted in the back gate voltage values. To be more explicit: the domain at the left edge shown in Fig. 10.10 reaches filling factor $\nu = 2$ at a lower back gate voltage than the bulk domain. Since the two regions do not move and merge together each of them is specially constrained through their individual evolution of compressible/incompressible landscape. The only way such a feature can appear is by a locally different doping of the flake as shown in Fig. 10.9 (a).

In particular when the left domain reaches $\nu = 2$ in its bulk while increasing the back gate voltage the central domain is compressible. The current flows at the left edge. Further increasing of the back gate voltage induces a $\nu = 2$ region in the central domain capable of carrying a Hall current. While the incompressible region in the left domain tend to decrease their size the central domain tends to increase its incompressible regions. Therefore the current is redistributed from the edge to the bulk.

After having identified these features we want to show that one can still see the features discussed in the previous sections by fitting the Hall potential drops - identified as the position of an incompressible stripe - of the bulk region. This is shown in Fig. 10.11 with a surface charge density of $1 \cdot 10^{17}\,em^{-2}$, which is about three times higher than what was found in the previous fits.

10.3. Summary

In summary, disorder affects strongly the position and back gate dependence of potential drops. The transport properties do not show significant features allowing to identify that the flake is "defect". It is because incompressible regions still carry the current while on a quantum Hall plateau. The effect of the edges can be altered due to the presence of long range disorder but seems to be overall preserved in its nature.

11. Summary

From our measurements of the Hall potential profiles on graphene flakes under quantum Hall conditions together with the experimental observation of Landau level formation in graphene in the group of Andrei [56–58] we conclude that also in graphene a compressible/incompressible landscape is formed. Further we could show, that while positioned on a quantum Hall plateau, current flow coincides with the position of incompressible stripes. The evolution of the QHE in graphene is therefore governed by the same principles as in GaAs/Al$_x$Ga$_{1-x}$As-heterostructures studied earlier [12–16, 19].

More interesting though is that the pattern found for the incompressible stripe positions requires a smooth confinement not reported up to now for graphene. Since the confinement of the pure graphene edges is expected to be sharp, additional charges, dipoles or gates have to be present that create the smooth confinement. From our Hall potential profile evolution with back gate voltage we found for n-type graphene a depletion of the electron density towards the edges like in the earlier studies of GaAs/Al$_x$Ga$_{1-x}$As-heterostructures. But to explain the evolution for p-type graphene a hole accumulation has to be present towards the edges. both observation can only be explained by fixed negative charges that are positioned on the area not covered by graphene.

To determine the exact origin of these charges further investigation is needed. Possible explanations could be glue/resist residues or water molecules close to the edges of the flakes. We believe water, which is easily adsorbed on the silicon dioxide surface and acts as a charge trap [162–164], to be the dominant source of fixed negative charges. Explicit suggestions for further experiments tackling this question can be found in section A.

Finally disorder can affect graphene flakes strongly. However whenever incompressible stripes pass through the sample, they can carry a dissipationless Hall current leading to a quantum Hall plateau. Also once the QHE is observable also the characteristic features connected to incompressible stripes are found in the Hall potential profiles but distorted by the disorder.

Part IV.

Breakdown of the quantum Hall effect

Increasing the current or voltage bias of a quantum Hall sample while on a quantum Hall plateau will lead beyond a certain bias level to a deviation of the plateau's quantized resistance value. This deviation is crucial for metrology since it limits the precision with which one can measure the resistance h/e^2. The reason for that is simple: the QHE was shown to be precise within 10 digits [176–178] by comparing different samples and host materials. Also when positioned on a plateau, any noise on magnetic field or biasing will be strongly suppressed due to the flat nature of the plateau. The main source of noise is the measurement setup itself [179, 180] and to improve in signal-to-noise one has to increase the current bias in quantum Hall experiments. This again is limited due to the breakdown.

Interestingly the first magneto-resistance measurements on a 2DES at large bias were performed before the discovery of the QHE. Kawaji and Wakabayashi investigated already 1976 Shubnikov-de-Haas oscillations on a silicon MOSFET inversion layer [181] and found a strong effect on the source-drain bias. Shortly after the discovery of the QHE several studies were investigating its limits [182–184]. It turned out that the most important parameters for the accuracy of the effect are temperature and current biasing. Thereby a continuous increase of the longitudinal resistance is found when increasing the temperature while an abrupt increase of the longitudinal resistance is observed when increasing the current over a critical value [183].

In this part we want to discuss our measurements of the Hall potential profiles while entering the breakdown of the QHE. We want to start in chapter 12 with an introduction into the breakdown and the existing experimental and theoretic work. Afterwards the actual discussion of our data will be given in chapter 13. The focus will be to adapt the existing microscopic picture of the QHE to the breakdown of the QHE. We will end this part with a summary and conclusion in chapter 14, where we also want to discuss how other experiments fit into our model.

12. Introduction to the breakdown of the QHE

In this chapter we want to give a short summary of the key experimental and theoretical investigations of the breakdown of the QHE so far. We start with defining the breakdown and introducing the common parameter "critical current" in section 12.1. We will point out that the discussion should not be limited to this single parameter but the evolution of the QHE evolving from low to high bias and for different filling factor values within a quantum Hall plateau. Then we want to discuss in section 12.2 why the breakdown is the limit for accuracy in determining the quantized resistance before giving the summary of experimental and theoretical work - found in literature - in section 12.3 and section 12.4, respectively. For further reading we suggest the review of Nachtwei [186].

12.1. Defining the breakdown

The usual way to define the electrical breakdown of the QHE is by an abrupt increase of the longitudinal resistance of several orders of magnitude while the bias current is increased [111, 183, 186]. The bias current at this sudden increase is called breakdown current. Often the highest breakdown current within one plateau was considered ([187–191]). For comparability this breakdown current is normalized by the width of the Hall bar yielding typical values around $1\,\mathrm{Am}^{-1}$ for filling factor $\nu = 2$.

From today's point of view, this focus on the highest breakdown current is quite unsatisfactory because of nowadays microscopic picture where a certain evolution within a plateau is described, see section 4. Therefore rather than studying the breakdown from an electrical transport point of view we want to look at it from the microscopic picture. The analysis over a whole quantum Hall plateau is therefore necessary.

We also want to study the evolution over the sample bias voltage. Thus we start at small bias voltages considered to be well quantized and continuously increase the bias until well beyond the breakdown. The transition is not always abrupt, as pointed out by Ebert et al. [183]. Hence we want to define the whole evolution observable on a quantum Hall device with increasing bias as the electrical breakdown of the QHE.

The typical way of biasing [111, 183, 186] for breakdown measurements is current biasing. A schematic is shown in Fig. 12.1 (a). In case of an increased 2-terminal sample resistance the voltage applied to the sample will change to drive the required current due to the current biasing scheme. To minimize the overall resistance, the built-up voltage could induce uncontrolled changes in the Hall potential landscape of the sample. Such changes within the Hall potential landscape indicate a history dependence that could cause effects like hysteresis. Hence we prefer a voltage biasing scheme showed in Fig. 12.1 (b) where under quantum Hall conditions the externally applied voltage is about the Hall voltage and that does not suffer this problem. This detail is of course only relevant when nonlinear effects like the breakdown of the QHE are present, and thus important for the later interpretation.

12.2. Breakdown as limit for metrological accuracy

When following the technical guidelines for reliable dc quantum Hall measurements, accuracy is limited by thermal voltages, noise rectification and 1/f noise [180]. All these effects are a matter of the used setup and cannot be completely avoided. On the other hand they do not change with sample bias. Thus a bias as high as possible is aspired.

The target accuracy for metrology lies in ten parts per billion [180]. This is for a resistance of $R_{\mathrm{K90}} = 25812.807\,\Omega$ about $0.3\,\mathrm{m}\Omega$ and can be reached for low enough temperature and high enough magnetic field [91,179,182]. An estimation about the deviations from the quantized value can be done with the so called resistivity rule [192, 193]

$$\beta\rho_{xx} = B\frac{d\rho_{xy}}{dB}, \tag{12.1}$$

where β is a constant. Equation (12.1) relates the slope $d\rho_{xy}/dB$ to the longitudinal resistivity. In a simple approximation one can assume a linear slope over a quantum Hall plateau leading to

$$\beta\rho_{xx} \approx B\frac{\Delta\rho_{xy}}{\Delta B}, \tag{12.2}$$

$$\Delta\rho_{xy} \approx \frac{\beta\Delta B}{B}\rho_{xx} = \alpha\rho_{xx}. \tag{12.3}$$

The uncertainty in the Hall resistivity $\Delta\rho_{xy}$ becomes then proportional to the magnetic field uncertainty and the longitudinal resistivity ρ_{xx}. The overall proportionality factor between $\Delta\rho_{xy}$ and ρ_{xx} is constant and usually assumed to be of the order of 1 [194, 195]

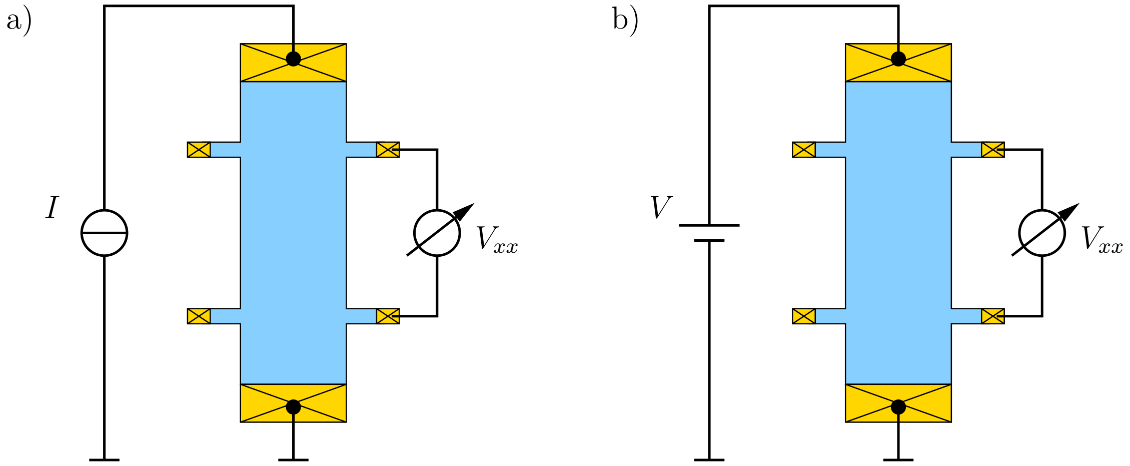

Figure 12.1.: Two biasing schemes for characterizing the breakdown of the QHE. (a) current biasing and (b) voltage biasing.

allowing us to estimate the error by measuring only ρ_{xx}. [1]

We can estimate therefore the amplitude of the error introduced by the breakdown of the QHE by taking the classical Hall longitudinal resistivity as order of magnitude. The relative error is

$$\frac{\Delta\rho_{xy}}{\rho_{xy}} \approx \alpha\frac{\rho_{xx}}{\rho_{xy}} = \alpha\cot\theta_{\mathrm{H}} \approx \frac{\alpha}{\mu B}. \tag{12.4}$$

which links the Hall angle θ_{H} to the error. A typical deviation due to breakdown can lie in parts per thousand while the target accuracy for metrology as mentioned before lies in ten parts per billion.

Thus one needs to stay below the critical current of a sample to not let dissipation become the dominant source of error. Since the critical current was found to depend on the width of the sample [187–190, 196, 197] it is also recommended - apart from lowest possible temperature and highest possible magnetic field - to use an as wide samples as possible [180].

12.3. Findings from previous experimental works

The importance to understand the breakdown of the QHE was realized shortly after the discovery of the QHE. It was 1983 when Ebert et al. [183] made the first in-depth study on the breakdown. He found an abrupt onset of longitudinal voltage upon increasing bias current but only a smooth one upon increasing temperature. He also pointed out that the breakdown is not always nicely defined by an abrupt onset of the longitudinal voltage but a pre-breakdown can be observed where a smooth onset of the longitudinal voltage happens.

In the following we want to sum up the most important experiments, reported in literature, dealing with QHE breakdown. At first we want to discuss experiments mainly aiming on geometry effects followed by local probing experiment. Other important experiments will be discussed at the end.

12.3.1. Sample geometry

Striking features of the breakdown are its width and length dependence. It was found that for low and medium mobility sample (μ in the order of $10\,\mathrm{T}^{-1}$) the critical current depends linear on the width [187, 189, 190, 196]. For medium to high mobility samples (μ in the order of $100\,\mathrm{T}^{-1}$) the critical current follows a sub-linear trend over the sample width [188, 197].

The length dependence is more complicated. It was found that the breakdown occurs after a certain traveling length of the electrons [198–200]. This was attributed to a heating effect which accumulates along the sample. Kaya et al. demonstrate that after constricting the sample width so that the current in the constricted area becomes overcritical, the breakdown is observable as a longitudinal voltage drop only after a certain traveling length of the electrons [201]. In addition he also showed the reverse process where hot electrons where injected into an undercritical sample area [202, 203]. Here the electrons cooled down after a certain traveling length and the QHE was recovered.

---

[1] As explained in the technical guidelines for reliable dc measurements of the quantized Hall resistance by Delahaye et al. [180] there are more measurements to be done to estimate for a maximum error!

On the other extreme narrow constrictions of 1 µm and length of 10 µm where found by Bliek et al. [204] to have a very high critical current density which is about 10 times higher than for wide samples.

For Silicon MOSFETs it was found by van Son et al. [205, 206] that the starting point of dissipation and thus longitudinal voltage drop lies at current injecting contact. This is different from the behavior in GaAs/Al$_x$Ga$_{1-x}$As-heterostructures described in the previous paragraphs.

Another striking feature depending on the Hall bar geometry is the abruptness of breakdown. Kawaguchi et al. [199] showed that the longer a sample is the sharper is also the onset of longitudinal voltage with increasing current bias.

12.3.2. Local probing

The first attempt for local probing the Hall potential profile was by measuring the electric potential of alloyed contacts distributed over the 2DES cross section. This method of course does only work in case of some longitudinal conductivity in the 2DES bulk, meaning within the breakdown of the QHE. Ebert et al. [207] did this experiment and found that the Hall voltage drop at the off-plateau region is linear. This behavior changes by varying the filling factor within the plateau region. For certain filling factor ranges they observed that the Hall voltage drops dominantly at only a fraction of the cross section width. For the lower magnetic field side of the plateau, the inner voltage probes show values close to the high Hall potential side. For the higher magnetic field side of the plateau, values close to the low Hall potential side are measured while at the center of the plateau the voltage drop is positioned around the center of the sample. Dorozhkin et al. did a similar experiment [208] but yielding the mirrored features with respect to the Hall potential.

An elegant method to image distribution within the 2DES is probing the local temperature by the Fontain-pressure effect of superfluid helium ^{4}He. This way Klaß et al. [109] could demonstrate the formation of hot spots at one corner of the electron injecting and absorbing contacts. Also the hot spot at the current injecting contact was bigger than the one at the absorbing contact. Even more striking, after the current was applied through small narrow 2DES contact areas, the hot spot moved from the metal/2DES contact interface to the end of the constriction.

Cyclotron emission was measured locally by a Japanese group [110, 209–213] by using a second quantum Hall sample. This second sample was positioned in a certain distance from the first and tuned by a separate magnetic field to be sensitive to the far infrared photons emitted at inter Landau level transitions from the first sample. The hot spots measured by the Fontain-pressure effect could be confirmed with this method. Also the spectrum could be analyzed indicating the contribution of higher Landau levels within the hot spots. The scans also show different behavior depending on filling factor. For filling factors above integer values, cyclotron emission sets in at the positive Hall voltage side of the sample. For filling factors below integer values, two types were observed. In the first the emission starts from the hot spot at the negative contact extending along its boundary to the 2DES and follows the negative Hall voltage side of the sample. In the second type, cyclotron emission is measured across a path through the bulk of the sample. We will discuss these findings again in section 14.1.

Scanning probe measurements on the breakdown of the QHE were initiated already by Weitz [13] and later continued by Ahlswede [17] here in the group. They found different behavior for all three types of Hall potential profiles ("types" described in the introduction, see section 4.1). For type I the linear Hall potential drop is changing abruptly. The current is mainly confined at a narrow stripe. This abrupt change is found where the longitudinal differential resistance over bias has a negative slope. For type II no changes were found before the breakdown but unfortunately the breakdown was not entered in this region. In type III an asymmetric current distribution between the two incompressible stripes at the edges was found and in addition a finite slope of the Hall potential profile in the bulk. Unfortunately Ahlswede stopped his analysis at that stage.

Recent scanning capacitance measurements by Suddards et al. [106] were able to make the compressible landscape surrounding the innermost incompressible stripe visible. They found an abrupt change of the capacitive landscape upon increasing the bias above its critical value. The picture observed after the breakdown suggests compressible conductivity over the whole sample.

12.3.3. Other aspects

One can use the breakdown of the QHE for nuclear spin resonance. Landau level transitions include also spin flips and due to angular momentum conservation the nuclear spins of the crystal lattice have to be involved. Kawamura et al. [214] showed that one can use the breakdown to disturb the aligned nuclear spins and they were able to measure the evolution of the breakdown along a long sample by nuclear magnetic resonance.

In big samples the breakdown can occur not only in a single onset jump but can also jump over several steps [184, 197, 215–217]. Also a hysteresis was observed for abrupt on-setting dissipation [183, 216].

12.4. Proposals for breakdown mechanisms

Most theoretical models about the breakdown of the QHE try to explain the sudden onset of the breakdown. Therefore most mechanisms proposed can set in very abruptly. In the following we want to discuss the most widely used breakdown mechanisms namely inter and intra Landau level scattering and electron heating.

At inter Landau level transitions or Zener tunneling [218–221] electrons are expected to tunnel from the highest occupied to the lowest unoccupied Landau level, see Fig. 12.2. This tunneling should be enhanced dramatically by the Landau level bending due to the external electric field bias leading to the breakdown of the QHE. The problem of this model is that it yields breakdown current densities that are two orders of magnitude higher than measured in wide samples under the assumption of a linear Hall voltage drop over the full sample width [186, 189]. Most used is thereby the model by Eaves and Sheard [220] known under the acronym QUILLS: quasielastic inter Landau level scattering. The transition is assumed to be isoenergetic while the Landau levels are bend across the sample width. Also scattering centers or phonons have to assist because of

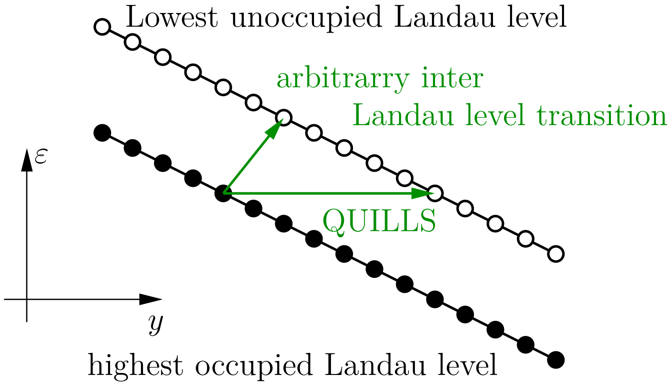

Figure 12.2.: Landau level bending under high electric field along y-direction: Shown are the highest occupied and lowest unoccupied Landau level and possible inter Landau level transitions.

momentum conservation. The resulting critical current

$$I_{\text{cr\_inter}} = \frac{e^2}{h} i \frac{\hbar\omega_{\text{c}}}{e l_B \left[(2n+1)^{1/2} + (2n+3)^{3/2}\right]} \tag{12.5}$$

$$= \frac{e^2}{h} i \frac{\sqrt{\hbar e} B^{3/2}}{m^* \left[(2n+1)^{1/2} + (2n+3)^{3/2}\right]} \tag{12.6}$$

succeeds to find the magnetic field dependence of $B^{3/2}$ measured in experiments [191,222].

Středa et al. [223] suggested a model where electrons moving with a drift velocity higher than the speed of sound in GaAs exhibit a Cherenkov-like phonon emission effect. Due to energy and momentum conservation the phonon emission takes place via collective intra Landau level transitions. The critical current derived from this model

$$I_{\text{cr\_intra}} = \frac{e^2}{h} i v_s B d_{\text{eff}} \tag{12.7}$$

is about the same order of magnitude as found in experiments. The sound velocity of GaAs is thereby $v_{\text{s}} = 2470\,\text{ms}^{-1}$ [224] and d_{eff} is the effective current carrying width. But this model gives the magnetic field dependence to be only proportional to B.

Electron heating models [183,222,225,226] have the advantage of not requiring a precise knowledge about the actual heating mechanism. The basic idea is the balance of Joule heating and the energy loss rate of electrons during steady state. Joule heating is thereby proportional to the local power density given by the scalar product of current density and electric field

$$\vec{j}\vec{E} = (\tilde{\sigma}\vec{E})\vec{E} = \sigma_{xx}(E_x^2 + E_y^2) \approx \sigma_{xx}E_y^2. \tag{12.8}$$

The approximation in the final step can be done in a geometry with current-flow along the x-direction within high magnetic fields due to the Hall angle being nearly 90 ° which means $E_x << E_y$. The local electron temperature $T_e(\vec{r})$ at position $\vec{r}$ is introduced to account for the local heating of the electron system which is higher than the lattice temperature T_{L}. The energy loss rate is in general a function of the local electric field and the local electron and lattice temperature but often estimated as the energy difference of electrons at temperature T_e and T_L over a relaxation time τ [222],

$$\frac{Z[T_e(\vec{r})] - Z[T_\mathrm{L}]}{\tau}. \tag{12.9}$$

The energy Z is thereby calculated via the energetic distribution of electrons within the bands

$$Z(T) = \int\limits_{\mu_\mathrm{elch}}^{\infty} (\varepsilon - \mu_\mathrm{elch}) D(\varepsilon) f(\varepsilon) d\varepsilon \tag{12.10}$$

with $D(\varepsilon)$ being the density of states and $f(\varepsilon) = \{\exp[(\varepsilon - \mu_\mathrm{elch})/k_\mathrm{B}T] + 1\}^{-1}$ the Fermi-Dirac distribution. In addition the conductivity $\sigma_{xx}(\vec{r})$ is assumed to be position dependent. To be more specific it depends on the local electron temperature and the local electric field $E_y(\vec{r})$

$$\sigma_{xx}(\vec{r}) = \sigma_{xx}[T_e(\vec{r}), E_y(\vec{r})]. \tag{12.11}$$

The starting point for any heating model is therefore a differential equation like the following one:

$$\frac{Z[T_e(\vec{r})] - Z[T_\mathrm{L}]}{\tau} = \sigma_{xx}[T_e(\vec{r}), E_y(\vec{r})] E_y^2(\vec{r}). \tag{12.12}$$

For a stationary state fluctuations should not run the system out of equilibrium. This means that a surplus dissipation due to a small increase in electron temperature has to be balanced or overcompensated by the surplus energy loss rate. The consequence of not satisfying this condition is a sudden increase in electron temperature and conductivity. Komiyama et al. [222] used this model setting $T_\mathrm{L} = 0\,\mathrm{K}$ together with Landau levels with infinitesimally small broadening and a thermally activated conductivity

$$\sigma^{ac}(T) = \frac{e^2}{h} \exp\left(-\frac{\hbar\omega_\mathrm{c}}{2k_\mathrm{B}T}\right) \tag{12.13}$$

to calculate a critical electric field E_c where an abrupt jump of the electron temperature happens. The critical field

$$E_\mathrm{c} = B\sqrt{\frac{2\hbar}{m^*\tau}} \tag{12.14}$$

includes the relaxation time τ and Komiyama argued that $1/\tau$ has to be proportional to the density of states of a Landau level resulting into

$$\frac{1}{\tau} \approx \frac{B}{1\,\mathrm{T}} \times \frac{1}{1\,\mathrm{ns}}. \tag{12.15}$$

Thus his model is able to reproduce the experimentally measured magnetic field dependence of the critical current. Güven et al. [227] derived with this ansatz a model fitting nicely to the spatial onset of dissipation measured by Kaya et al. [201].

12.5. Summary

In summary we have given a definition of the breakdown as a general on-setting of longitudinal voltage drop during QHE conditions and thus including also non-abrupt changes into our discussions. We stated that the electric breakdown of the QHE is the limiting factor for the resistance standard as realized today and gave a review of relevant experiments. Thereby we recapped the importance of sample geometry with the following general findings for samples based on GaAs/$\mathrm{Al}_x\mathrm{Ga}_{1-x}$As-heterostructures:

- The critical current scales with the width of the sample. Two types of scaling are observable: First, linear scaling for low mobility samples and, second, sub-linear scaling for high mobility samples.
- Hot spots are found where expected from a Drude-like picture of the Hall effect and they extend with increasing bias.
- In narrow and short constrictions, breakdown currents can be up to 10 times higher than expected from critical current densities derived from wide samples.
- The sharpness of the longitudinal voltage onset depends on the sample geometry.
- Injecting a slightly overcritical current into a long constriction and measuring the longitudinal voltage drop for different positions along the constriction suggests an evolution of the breakdown along the sample length.

We also described some local probing experiments starting with inner contacts and the Fontain-pressure effect of liquid ^{4}He. Measurements of cyclotron emission, scanning probe microscopy and scanning capacitance measurements on the breakdown were recapped.

From a theory point of view we introduced the three most popular breakdown mechanism: electron heating, intra and inter Landau level scattering. Still today no conclusive picture exists. Also all these models have no handle on the inhomegeneities of a sample. Bulk disorder as well as the depletion towards the edges are not included. But also how these inhomogeneities will affect the current flow within a sample during breakdown is not obvious. We will attack this problem experimentally in the following chapter.

13. Towards the microscopic picture of the breakdown of the QHE

In this section we want to show and interpret the features of the breakdown in Hall potential scans to get a deeper understanding of its evolution. We will show that the microscopic picture of the QHE based on compressible and incompressible regions is widely usable to describe the breakdown.

In the following we want to discuss in section 13.1 the sample characteristics and the used geometry before going into the details of transport measurements in section 13.2 which allows to link Hall potential profile features with the QHE breakdown. The Hall potential line scans introduced in section 13.3 show on the lower and upper Hall plateau side two distinct types of evolution which we call the edge-dominated breakdown, see section 13.4, and the bulk-dominated breakdown, see section 13.5. After discussing the two types of evolution observed at the two sides of the quantum Hall plateau, we finally want to go over the transition regime in section 13.6.

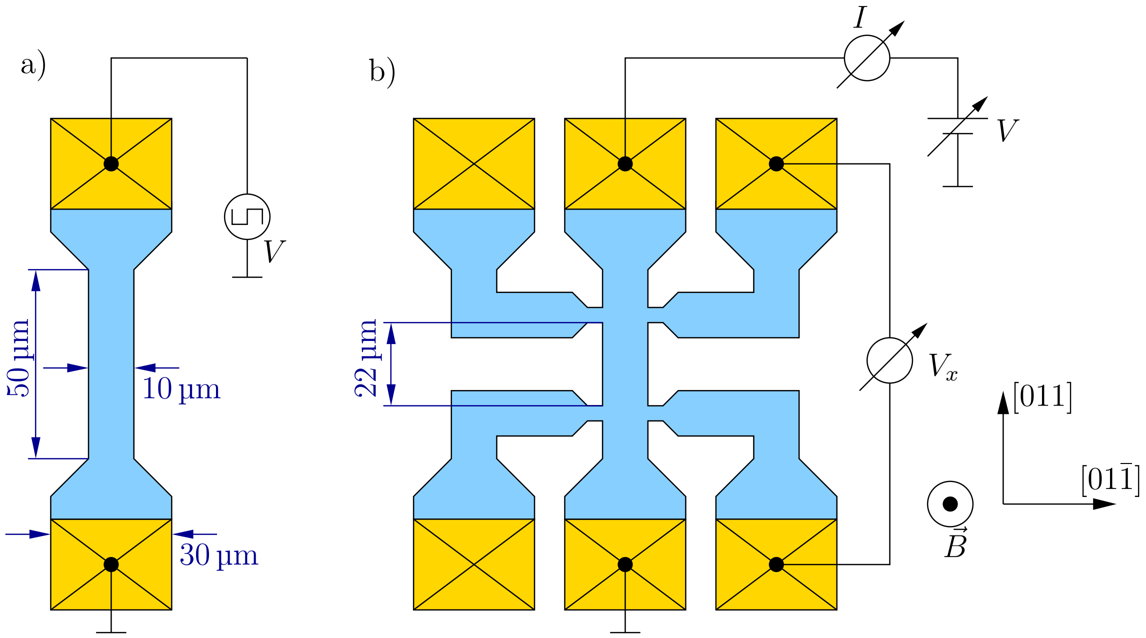

Figure 13.1.: Sketch of the Hall bar geometries used for the sample characterization. All have straight contact interfaces perpendicular to the [011] crystal direction. (a) Two-terminal Hall bar, (b) Hall bar extended by potential probes.

13.1. Sample characteristics and geometry

A schematic of the sample geometry is shown in Fig. 13.1. Two different Hall bar geometries were realized on each sample with different focus for each. It is important to note here that ohmic contacts to a 2DES in GaAs/Al$_x$Ga$_{1-x}$As-heterostructures are strongly anisotropic [107, 108]. Contacts usually have meander shaped interface to overcome this obstacle. Since we wanted straight contacts to be able to scan in front of them, we took care to orient spatial our current carrying contacts in the right direction. Therefore all our contacts interfaces are oriented perpendicularly to the [011] crystal direction and are straight.

The first geometry, Fig. 13.1 (a), has a constriction in the center. The main focus of this design was to reduce the influence of current carrying contacts by increasing their width. Most of the data that will be presented in the following were measured on this geometry.

The second geometry, Fig. 13.1 (b), is the extension of (a) by potential probes. The advantage of this geometry is the simultaneous four terminal measurement of electrical transport and Hall profiles. The disadvantage is the possible influence of the probes. The determination of the charge carrier concentration of the samples was done by fitting on the Hall resistance for low magnetic fields on a Hall bar with the geometry shown in Fig. 13.1 (b). For the mobility we measured the zero field conductivity with transmission line measurements (TLM). Further details about the samples and their characterization can be found in section H.2.

We used two samples from different heterostructures for the measurements shown. The first sample (8379_20100120_B) from wafer #8379 [1] had a charge carrier density of $n = 2.8 \cdot 10^{15}\,\mathrm{m}^{-2}$ and a mobility of $\mu = 38\,\mathrm{T}^{-1}$. Most line scans were measured on this sample. The second sample (8957_201112_B) was from wafer #8957 [1] and had a charge carrier density of $n = 3.2 \cdot 10^{15}\,\mathrm{m}^{-2}$ and a mobility of $\mu = 51\,\mathrm{T}^{-1}$. All area scans where performed on this sample. For further details on the samples we refer to the appendix chapter H.

13.2. Breakdown in transport

As already described in section 12.1 the key feature of the breakdown of the QHE is an increase of the longitudinal resistance of several orders of magnitude. Figure 13.1 (b) shows the measurement scheme used to measure this increase. The longitudinal voltage drop is thereby measured while sweeping the sample bias voltage. Some resulting curves are shown in Fig. 13.2. The actual shape of the curves depends on the magnetic field or equivalently on the filling factor ν. The longitudinal voltage drop V_x has therefore to be measured over a two-dimensional parameter space spanned by sample bias voltage V and magnetic field B or corresponding filling factor ν. The result is plotted color-coded in Fig. 13.3. The selection in Fig. 13.2 is showing only the curves for the fields where Hall potential profiles were measured.

There are two asymmetries visible in Fig. 13.3: First, the characteristic shape of the

---

[1] All our GaAs/Al$_x$Ga$_{1-x}$As-heterostructures where grown in Werner Dietsche's group from our institute.

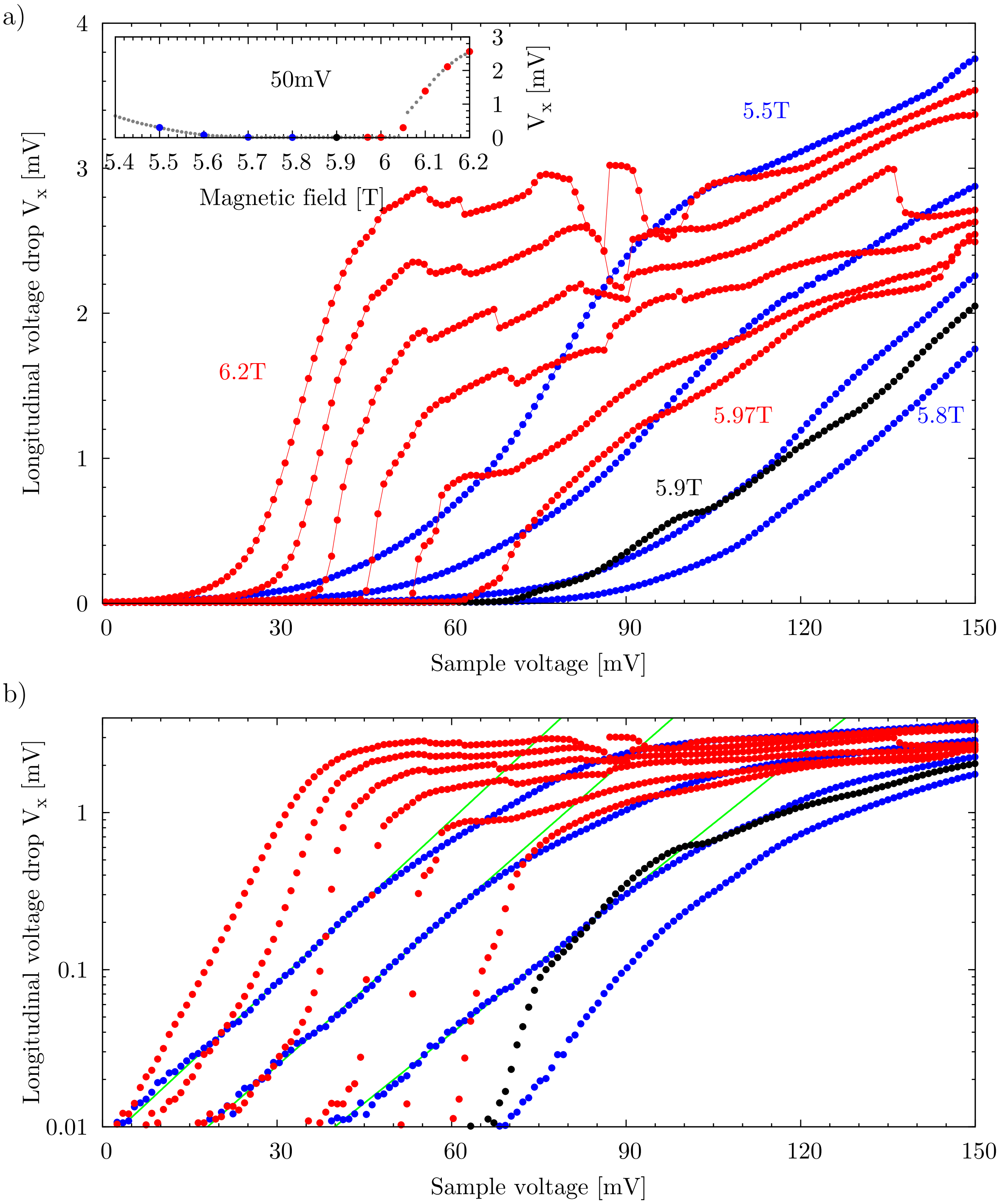

Figure 13.2.: Longitudinal voltage drop over sample voltage for all potential scans on sample 8379_201001_B in (a) with linear scale and in (b) in logarithmic scale. The measurement points are drawn as dots while the lines serve as guide to the eye. In red are drawn the rather abrupt on-setting curves which are from the left to the right for the magnetic fields of 6.2 T, 6.15 T, 6.1 T, 6.05 T, 6.0 T, and 5.97 T. They correspond to the filling factors 1.89, 1.90, 1.92, 1.93, 1.95, and 1.96 respectively. The jumps after the first onset of longitudinal voltage with increasing bias are not measurement artefacts and are similar to features described by Cage et al. [216]. In blue and black are plotted the smoothly on-setting curves. The black curve was measured with a magnetic field of 5.9 T corresponding to $\nu = 1.98$ and the blue curves from the left to the right for 5.5 T, 5.6 T, 5.7 T, and 5.8 T. They correspond to the filling factors 2.13, 2.09, 2.05, and 2.02 respectively. The inset in (a) should illustrate the positions of the traces in magnetic field. The gray lines in (b) are exponential fits.

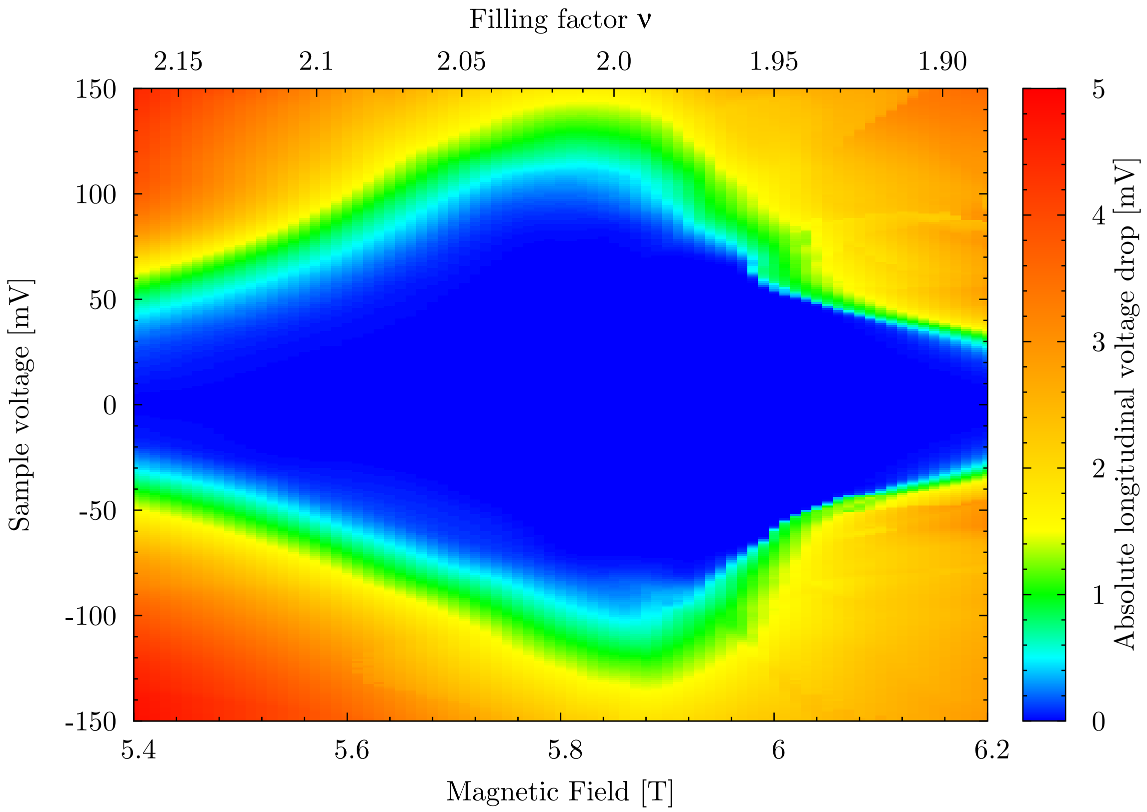

Figure 13.3.: Color-coded absolute longitudinal voltage drop over magnetic field and bias voltage. Beside the up-down asymmetry there is an asymmetry around a magnetic field of 5.9 T: While below 5.9 T the onset of the longitudinal voltage drop is rather smooth it becomes rather abrupt above 5.9 T.

longitudinal voltage onset is different for magnetic fields below 5.9 T and above 5.9 T. This can be seen quantitatively in Fig. 13.2. Below 5.9 T the onset is rather smooth while above 5.9 T it is found to be rather abrupt. Second, there is no exact up-down mirror symmetry across zero sample bias.

The fit lines of Fig. 13.2 (b) are exponential functions in the form

$$f(V) = Ae^{\frac{V}{V_{\mathrm{T}}}} \tag{13.1}$$

where A and V_{T} are fitting parameters. The values for V_{T} are for the three fits from left to right 12.6 mV, 13.4 mV and 14.6 mV. They are altogether quite close to the cyclotron gap of about 10 mV.

The found continuous and abrupt onset of the longitudinal voltage drop can be linked to the compressible and incompressible landscape inside the samples which is described in the following section.

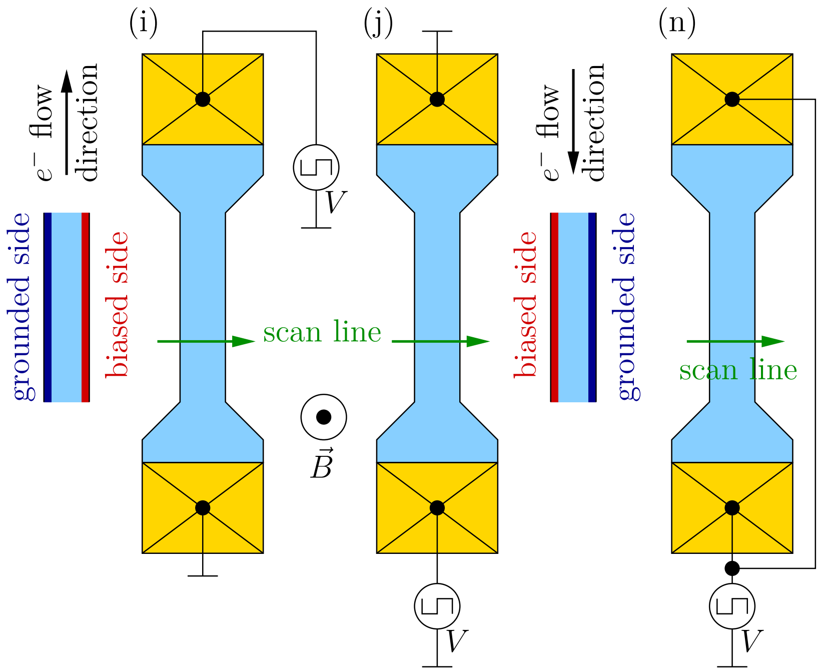

Figure 13.4.: Biasing scheme for the two current directions (i) and (j) and the calibration measurement (n). The applied voltage is rectangular shaped with 50% duty cycle and going from ground to the bias V. Also shown are the expected edge potentials in the colors used for the color codes Hall profile diagrams.

13.3. Breakdown in line scans

To identify the features of the breakdown of the QHE in the line scans, we increased the bias voltage V stepwise for fixed magnetic field B and measured the Hall potential profiles. We consider source to be the electron injecting contact and drain the electron absorbing contact. Source was in our case always kept on electric reference ground while drain was connected to the positive pole of the voltage source. We want to emphasize here the difference between potential ϕ and electrostatic energy $q\phi$. The electrostatic energy $q\phi$ has - due to the negative sign of q for electrons - the opposite sign of the potential ϕ.

In Fig. 13.4 the biasing scheme is recapped at the two-terminal Hall bar. While (i) and (j) represent the biasing scheme for the two current directions, (n) represents the calibration measurement. The bias is a 50% duty cycle rectangular signal going from zero to the positive bias V. Also depicted to the left of (i) and to the right of (j) are the corresponding edge potentials, in blue meaning "ground" and red meaning "V". These two colors correspond to the ones chosen for the color-coded plots. Representative results for this type of measurement can be found in Fig. 13.7 and 13.14.

First We want to concentrate on the Hall potential measurements for sample 8379_2010-01_B. An overview of the data for the current direction (i) is given in Fig. 13.5 and 13.6. Each color-coded plot was measured at a different magnetic field and the corresponding longitudinal voltage traces are shown in Fig. 13.2, colored as described in the figure caption of the Hall potential scans. There are two clear trends distinguishable within the set

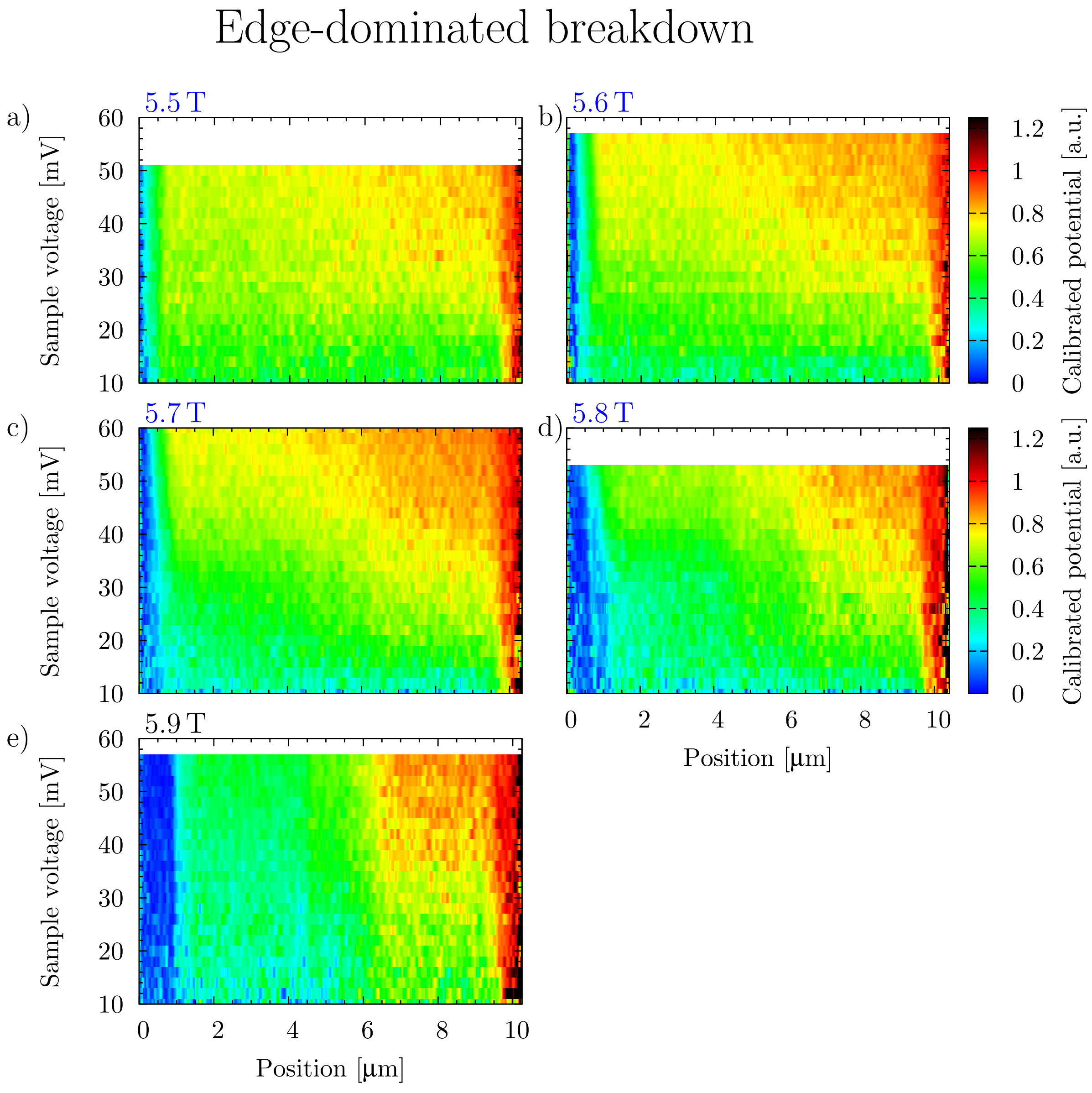

Figure 13.5.: Color-coded Hall potential profiles over bias voltage and position for 5.5 T (a) to 5.9 T (e) in steps of 0.1 T. The plots correspond to the blue and black electrical transport curves of Fig. 13.2. The bias voltage span was chosen to be equal for all plots for better comparison.

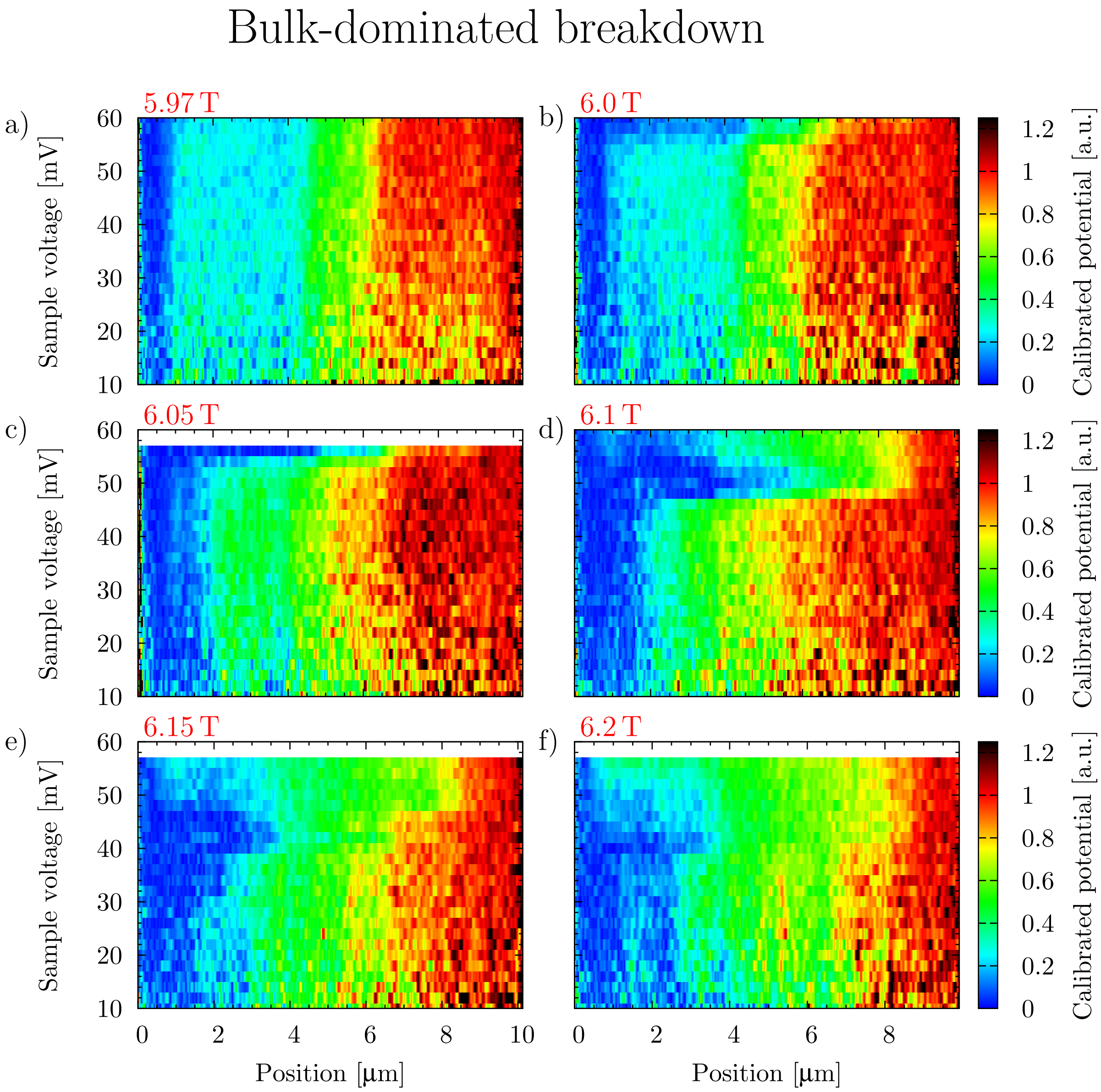

Figure 13.6.: Color-coded Hall potential profiles over bias voltage and position for 5.97 T (a) and for 6.0 T (b) to 6.2 T (f) in steps of 0.05 T. The plots correspond to the red electrical transport curves of Fig. 13.2. The bias voltage span was chosen to be equal for all plots for better comparison.

of data acquired: First, for low bias and magnetic fields up to 5.9 T, the Hall potential drops occur at both edges of the sample. Increasing the bias voltage induces a smooth transition from a symmetric to an asymmetric distribution of Hall voltage drop between the edges, see Fig. 13.5. Further increasing the bias also induces a tilt of the former flat potential profile in the bulk. The second behavior, found for low bias above magnetic fields of 5.9 T, starts with a voltage drop in the bulk. Its Hall potential profile does not change for increasing bias until it undergoes a rather abrupt change, see Fig. 13.6.

There are some complications in the transition regime between these two distinct evolutions that will be discussed later on. Independent of these complications the main message is that we found in the Hall potential profiles breakdown transitions fitting in their qualitative behavior to those of the transport measurements. The transition from the smooth to the abrupt breakdown in transport as well as in the Hall potential profiles occurs at the same magnetic field of 5.9 T.

We want to call the smooth breakdown the *edge-dominated breakdown*, since the Hall potential drops occur at the edges. In contrast the abrupt breakdown is called *bulk-dominated* by us because the Hall potential drop occurs in this case at the bulk.

In the following we will discuss the edge- and bulk-dominated breakdown in more details.

13.4. Edge-dominated breakdown

In the edge-dominated breakdown of the QHE the Hall potential profiles show potential drops at the edges. This situation is preserved beyond the breakdown justifying the name "edge-dominated". This can be seen in Fig. 13.7 showing the scans for a magnetic field of 5.6 T for both current directions, where (a) and (c) represent current direction (i) and (b) and (d) current direction (j). Also beside the color-coded plots (c) and (d), selected lines are plotted in (a) and (b) to clarify our descriptions.

While increasing the sample bias, first one observes a shift of the bulk potential to a higher potential, nicely visible in Fig. 13.7 (a) and (b). This means an asymmetric distribution of current evolves since the potential drops on the edges become unequal. More remarkable is that the current or potential drop at the lower Hall potential side becomes always higher. In other words we find the larger current fraction on the side where external current and the persistent current are flowing in the same direction. Beside this asymmetry the originally flat potential landscape of the bulk becomes tilted. This tilt is clearly observable only after the longitudinal voltage drop V_x has increased significantly.

As discussed before, the Hall potential landscape changes smoothly for increasing bias and the position of Hall potential drops remain the same except of the emerging drop over the bulk. We interpret this behavior as the overall preservation of the incompressible landscape while undergoing the breakdown transition. Thus we also expect to find the measured Hall potential profile equally or quasi "translation invariant" along the sample. To demonstrate the translation invariance area scans on sample 8957_201112_B were performed. A sketch of the measurement arrangements and the electrical transport curves are shown in Fig. 13.8 and the actual area scans can be found in Fig. 13.9. One can clearly see the bulk potential shifting from green to red while the profile is mostly identical along

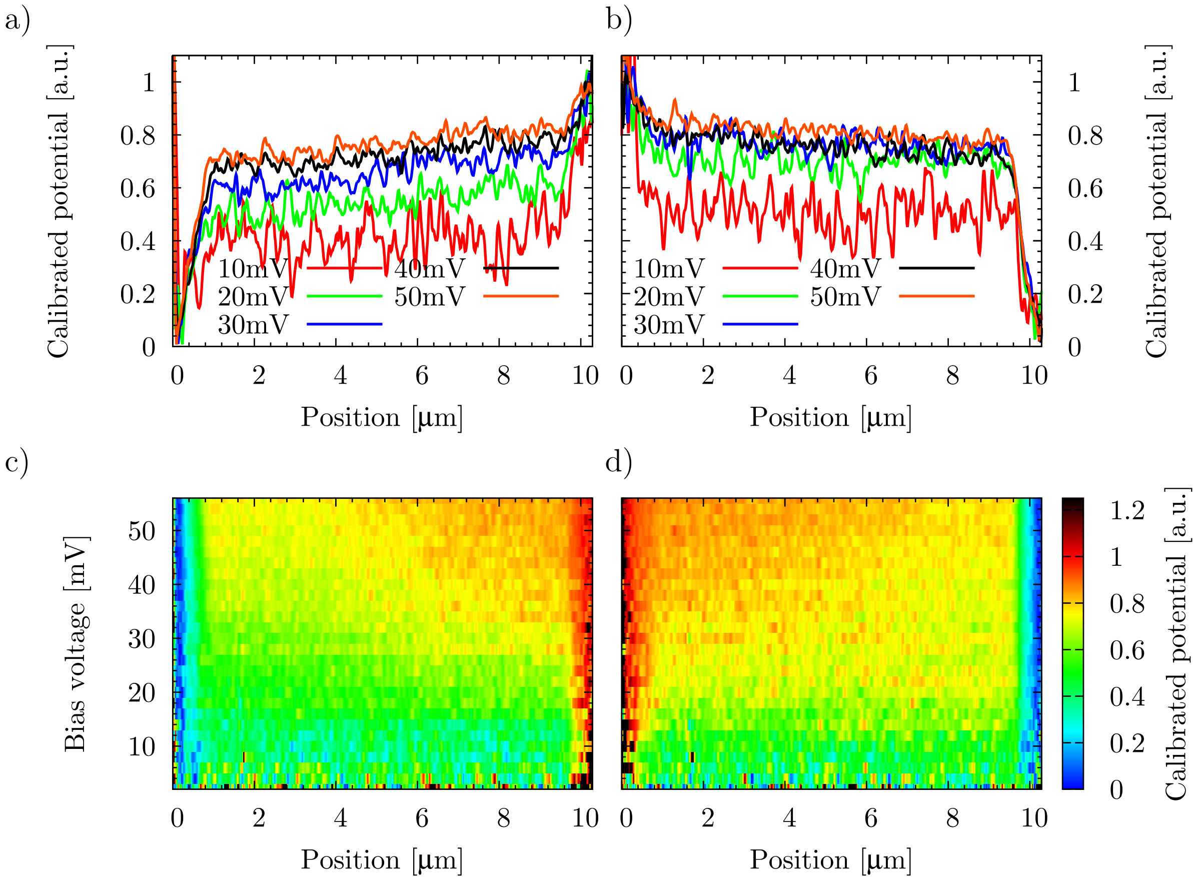

Figure 13.7.: Hall potential profiles for a magnetic field of 5.6 T and filling factor $\nu = 2.09$. The bias voltage was increased to run into the breakdown. (a) and (b) show chosen line scans while (c) and (d) show the full data set in color coded plots. (a) and (c) were measured in the bias scheme shown in Fig. 13.4 as (i) while (b) and (d) in the scheme denoted as (j).

the sample. The deviation from the translation invariance is found at the corner where the electrons are traveling to. This could be an indication of heating along the traveling path of the electrons usually observed for long samples [97,198–200,202,222]. However we want to neglect this feature and argue that the incompressible landscape remains nearly unchanged.

Self-consistent simulations from Gerhardts [102] showed that the observed asymmetry is a result of just the biasing without the need of any breakdown mechanism. The simulations, shown in Fig. 13.10, predict a changing width for the incompressible stripes at the edges. Also the two incompressible stripes are affected differently by the applied bias. While for the lower Hall potential side the external bias leads into an increasing stripe width the stripe at the biased side decreases its width. The result is a higher voltage drop and higher current on the lower Hall potential side than for the higher Hall potential side.

In the following, we want to discuss in more details a simple model explaining the origin of the asymmetry before we discuss the consequences for the edge-dominated breakdown in section 13.4.2.

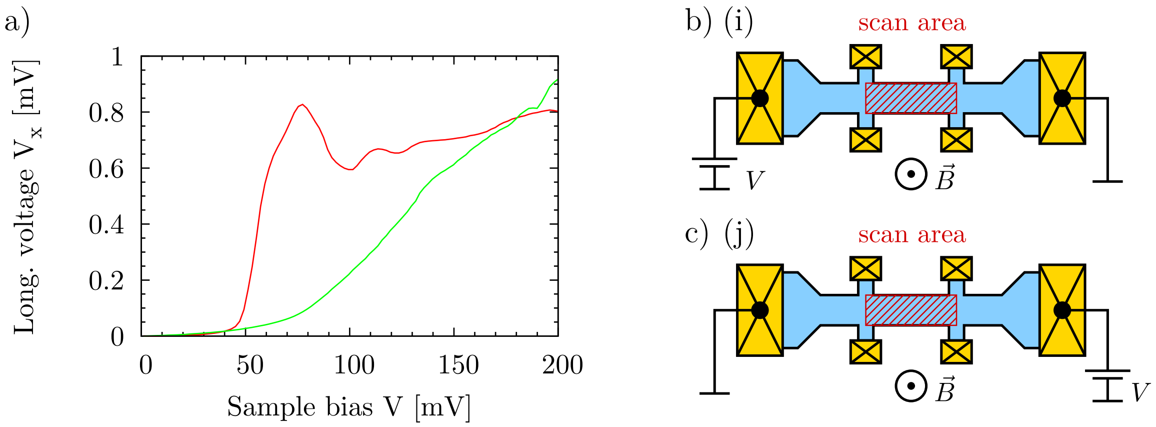

Figure 13.8.: (a) Longitudinal voltage drop as a function of sample bias for sample 8957_201112_B. The green trace corresponds to the edge dominated breakdown at a magnetic field of 6.1 T and filling factor $\nu = 2.17$ while the red trance corresponds to the bulk dominated breakdown at a magnetic field of 6.8 T and filling factor $\nu = 1.94$. (b) shows the area scanned and biasing scheme for the plots of the left hand side of Fig. 13.9 and 13.15 (meaning (a), (c), (e), (g), (i) and (k)). And (c) the area scanned and biasing scheme for the right hand plots of Fig. 13.9 and 13.15.

13.4.1. Simple model for the current distribution at the edge-dominated QHE

From our Hall potential measurements we know that an asymmetry in the current distribution in the edge dominated QHE is built up which was predicted by self-consistent calculations. Unfortunately the self-consistent calculation do not give an easy and comprehensible reason for this asymmetry. Thus we want to introduce in the following a simple and comprehensive model that reproduces the measured asymmetry. It is based on five simplifications:

- A translation invariant 2DES to reduce the problem on one dimension.
- Negligence of currents within compressible regions.
- The integral of the inverse resistivity ρ_{xx} over an incompressible stripe to be proportional to the stripe width. One way to accomplish this is by assuming a constant ρ_{xx} over an incompressible stripe.
- The confinement is equal for the left and right edge.
- The incompressible stripe width is changing according to the theoretical prediction of Chklovskii et al. [92].

Translation invariance is a good assumption for long samples as used in our experiments and reduces the complexity of the problem. Since we force the current to flow in the x

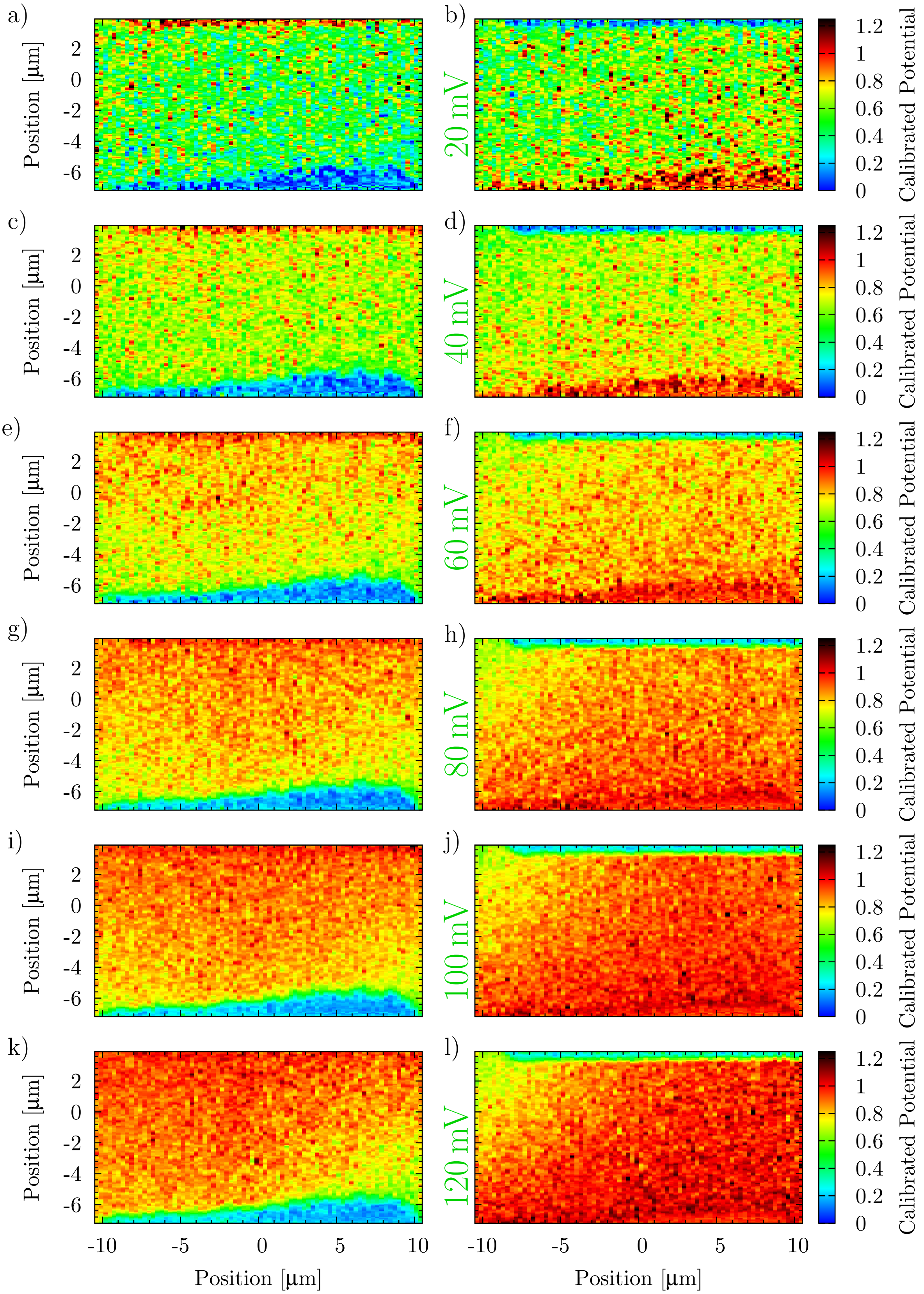

Figure 13.9.: Area scans on sample 8957_201112_B at a magnetic field of 6.1 T and filling factor $\nu = 2.17$. From top to bottom the bias voltage was increased from 20 mV to 120 mV in steps of 20 mV. The scans of the left side have the opposite current flow direction than of the right side. The actual scanning scheme is shown for the scans on the left hand side in Fig. 13.8 (b) and for the scans on the right hand side in Fig. 13.8 (c).

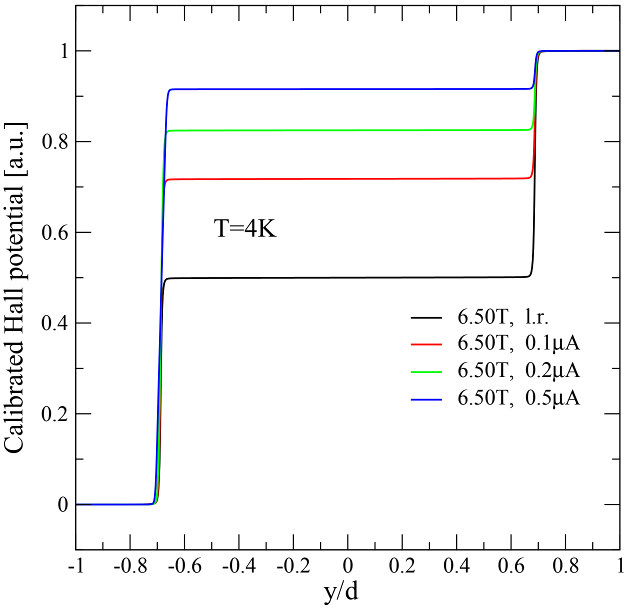

Figure 13.10.: Simulations by Gerhardts (similar data published in [102]) showing Hall potential profiles for increasing bias. "l.r." stands for linear response and resembles the Hall potential profile without current. The simulations for the edge dominated regime at 6.5 T show the bulk potential shift also without any breakdown mechanism.

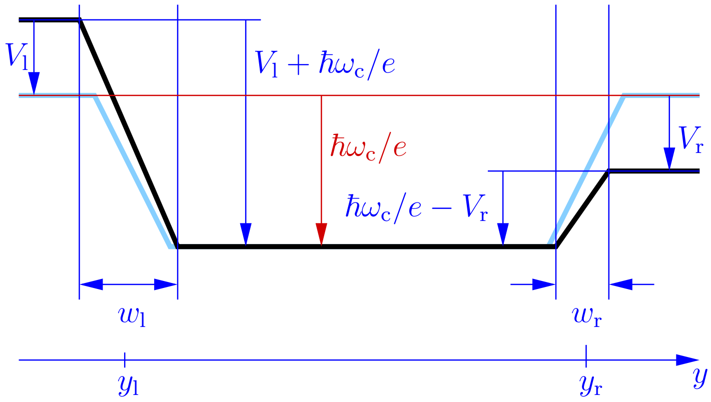

Figure 13.11.: Bending of a Landau level during edge-dominated QHE: for zero bias in "light blue" and for finite bias in "black". Relevant voltages and widths are sketched.

direction: $\vec{j} = j_x \cdot \vec{e}_x$, only two Ohm's equations remain:

$$E_x = \rho_{xx} j_x \tag{13.2}$$

$$E_y = \rho_{xy} j_x . \tag{13.3}$$

During the QHE the current flows mainly within incompressible stripes allowing us to neglect the compressible regions without significant error. Doing so reduces the problem to the properties of the two incompressible stripes with the position y_l and y_r and width w_l and w_r, see Fig. 13.11. Integrating equation (13.3) over the full cross section results in

$$\int E_y dy = \int\limits_{y_\mathrm{l}-w_\mathrm{l}/2}^{y_\mathrm{l}+w_\mathrm{l}/2} E_y dy + \int\limits_{y_\mathrm{r}-w_\mathrm{r}/2}^{y_\mathrm{r}+w_\mathrm{r}/2} E_y dy, \tag{13.4}$$

$$\tag{13.5}$$

leading to

$$V = V_\mathrm{l} + V_\mathrm{r}, \tag{13.6}$$

meaning that the applied bias voltage V is split between the two incompressible stripes with voltage V_l and V_r.

We further assume the integral of the inverse resistivity ρ_{xx} over an incompressible stripe to be proportional to the stripe width w with the proportionality constant a

$$\int\limits_{y_\mathrm{l}-w_\mathrm{l}/2}^{y_\mathrm{l}+w_\mathrm{l}/2} \frac{1}{\rho_{xx}} dy = a w_\mathrm{l}. \tag{13.7}$$

This can be achieved by assuming a constant ρ_{xx} over the incompressible stripe or an arbitrary $\rho_{xx}(y)$ common to all incompressible stripes that is scaled along the y-axes with changing incompressible stripe width. Calculating the current I_l through the left stripe with the equations (13.2) and (13.3) we get

$$I_\mathrm{l} = \int\limits_{y_\mathrm{l}-w_\mathrm{l}/2}^{y_\mathrm{l}+w_\mathrm{l}/2} \frac{E_y}{\rho_{xy}} dy = \int\limits_{y_\mathrm{l}-w_\mathrm{l}/2}^{y_\mathrm{l}+w_\mathrm{l}/2} \frac{E_x}{\rho_{xx}} dy \tag{13.8}$$

$$= \frac{V_\mathrm{l}}{\rho_{xy}} = a E_x w_\mathrm{l}. \tag{13.9}$$

Equivalently we get for the current I_r in the right stripe

$$I_\mathrm{r} = \frac{V_\mathrm{r}}{\rho_{xy}} = a E_x w_\mathrm{r}. \tag{13.10}$$

For a translation invariant solution E_x has to be constant over the entire 2DES area to have zero curl: $\nabla \times \vec{E} = 0$. Thus $a \rho_{xy} E_x$ is constant leading together with the equations

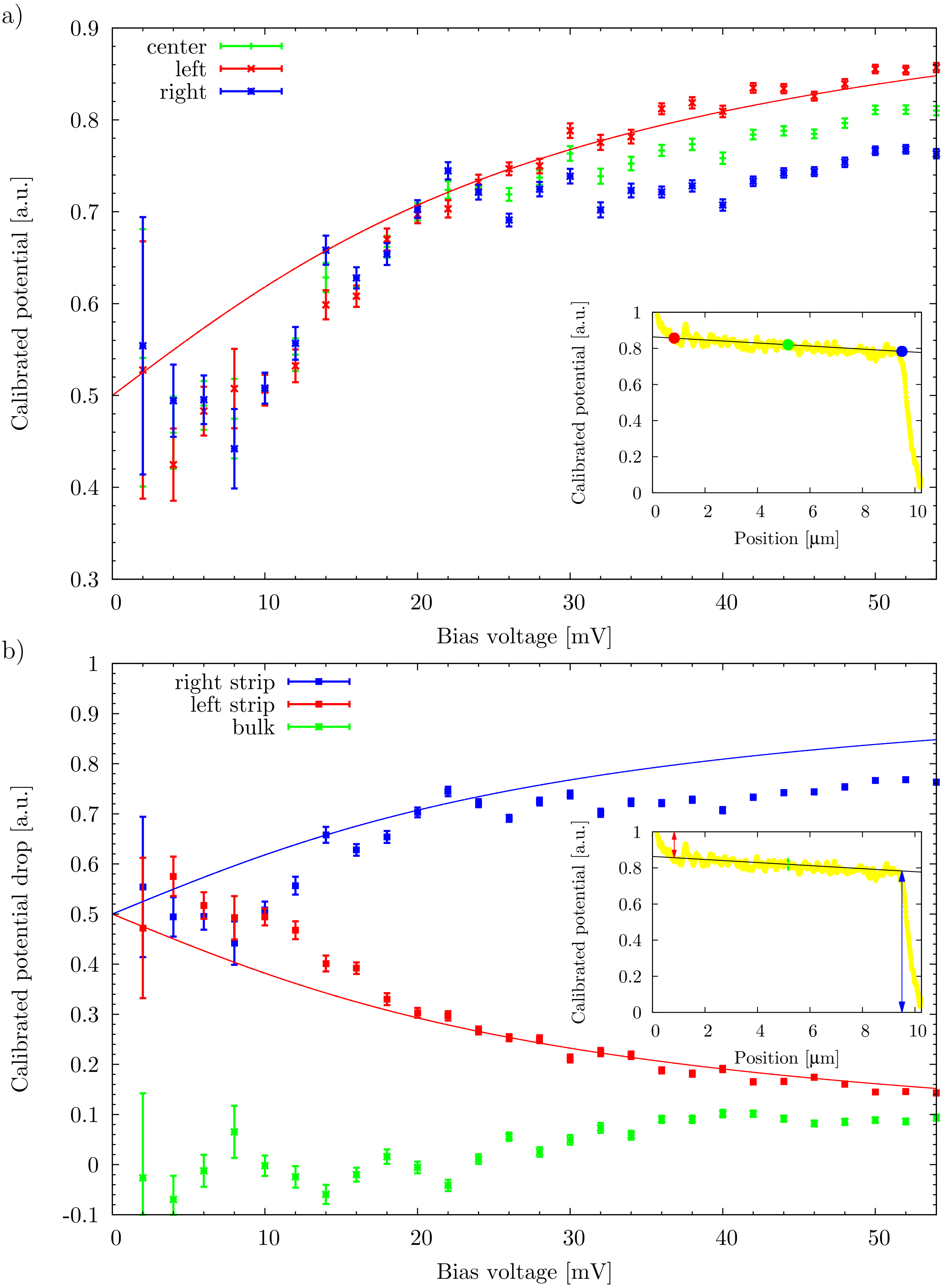

Figure 13.12.: (a) Hall potentials and (b) potential drops extracted from the Hall potential profiles for a magnetic field of 5.6 T and filling factor $\nu = 2.09$. The bias voltage was increase to run into the breakdown. Each point represents a fitting result from the data shown in Fig. 13.7. The insets show what data was plotted on the example of the Hall potential profiles for 50 mV of bias. The two lines are the result (13.16), (13.17) of our model and the color is matched to the color of the corresponding data points. It should be emphasized that the asymptotic limits of (13.16) and (13.17) are one and zero.

(13.9) and (13.10) to the relation

$$\frac{V_\mathrm{l}}{w_\mathrm{l}} = \frac{V_\mathrm{r}}{w_\mathrm{r}}. \tag{13.11}$$

which is equivalent of having the same Hall electric field in both incompressible stripes.

It should be emphasized that the assumption of homogeneous incompressible stripes is very harsh. In particular an incompressible stripe is expected to have an inner structure which can be found in simulations [102]. The structure appears because the finite thermal activation of electrons is more effective at the edges of the incompressible stripes causing the resistivity ρ_{xx} to be higher at the edges than in the center. The self-consistent calculations also show that for the dominant stripe the bending of the electrochemical potential happens in a smaller width than the actual width of the incompressible stripes. This transforms the originally Gaussian like profile of the inverse resistivity $1/\rho_{xx}(y)$ within the incompressible stripe to a smeared rectangular-like profile. The electric field follows the trend of the conductivity and is highest in the center of an incompressible stripe. Still the qualitative behavior assuming homogeneous incompressible stripes is represented in view of simulations by Gerhardts et al. [102] correctly and the results are sufficient for the qualitative analysis we want to make.

Further we use the dependence of the stripe width w_l or w_r on the Landau level potential shift $\hbar\omega_\mathrm{c}/e + V_\mathrm{l}$ or $\hbar\omega_\mathrm{c}/e - V_\mathrm{r}$ known from Chklovskii et al. [92],

$$\alpha^2 w_\mathrm{l}^2 = \hbar\omega_\mathrm{c}/e + V_\mathrm{l}\,, \tag{13.12}$$

$$\alpha^2 w_\mathrm{r}^2 = \hbar\omega_\mathrm{c}/e - V_\mathrm{r}\,, \tag{13.13}$$

$$w_\mathrm{l} = \frac{1}{\alpha}\sqrt{\hbar\omega_\mathrm{c}/e + V_\mathrm{l}}\,, \tag{13.14}$$

$$w_\mathrm{r} = \frac{1}{\alpha}\sqrt{\hbar\omega_\mathrm{c}/e - V_\mathrm{r}}\,. \tag{13.15}$$

Here α is a proportionality factor. It depends on the details of the confining potential.

In summary we have found with our assumptions the following relations:

- External bias voltage is split between the two incompressible stripes, see equation (13.6).
- The Hall electric field is equal in both incompressible stripes, see equation (13.11).
- The dependence of the stripe width on the voltage across the incompressible stripe is given by equations (13.14) and (13.15).

These relations result into the following voltage drops over the left and right incompressible stripe, correspondingly,

$$V_\mathrm{l} = \frac{V}{2} - \frac{\hbar\omega_\mathrm{c}}{e} + \sqrt{\frac{V^2}{4} + \left(\frac{\hbar\omega_\mathrm{c}}{e}\right)^2}\,, \tag{13.16}$$

$$V_\mathrm{r} = \frac{V}{2} + \frac{\hbar\omega_\mathrm{c}}{e} - \sqrt{\frac{V^2}{4} + \left(\frac{\hbar\omega_\mathrm{c}}{e}\right)^2}\,. \tag{13.17}$$

Thus the current will partition such that the Hall electric field will be equal in both incompressible stripes. Due to the boundary conditions namely the asymmetric width change of the incompressible stripes upon the external bias, the resulting partitioning will also be asymmetric.

The results (13.16) and (13.17) are drawn in Fig. 13.12 together with actual data which are a further analysis of the data shown in Fig. 13.7. How to obtain those values from the data is shown in the insets of Fig. 13.12: We fit the inner flat compressible region of the Hall potential profiles with a linear function and read out either the calibrated potential or the potential drops at the boundaries and at the center of the inner compressible region (see colored dots in Fig. 13.12). Also the insets show just one fit for the case of 50 mV bias. Doing the fit for all Hall potential profiles of Fig. 13.7 (d) and plotting the results over the bias voltage results in the traces of Fig. 13.12. Thus Fig. 13.12 (a) gives the calibrated Hall potential as a function of bias for the inner side of the left (red) and right (blue) incompressible stripe as well as for the sample center (green). In Fig. 13.12 (b) the calibrated Hall potential drop across the left (red) and across the right (blue) incompressible stripe and across the bulk compressible region is plotted over the bias voltage. It should be emphasized that the Hall potential drops in Fig. 13.12 (b) at the two incompressible stripes do not add up to one for high bias. This is because the on-setting bulk potential drop (green points) becomes a significant portion of the total Hall potential drop. The sum of bulk and edge currents is in our theoretical analyses by definition equal to one.

We also want to emphasize here that the result of the model is independent of the actual proportionality factors and thus independent of local details of the sample as long as it has the same boundary conditions at both edges. The only relevant quantities for the actual shape are the applied bias V and the cyclotron gap $\hbar\omega_c/e$.

A similar approach can be taken in a Corbino geometry. Assuming an infinite radius for the inner contact the problem can be treated translation invariant again. But this time it is obvious that the external voltage is the sum of the voltages over the incompressible stripes (neglecting again compressible regions). They can be treated similar to two series resistors. Relation (13.11) is then found easily via the finite radial current that has to passes through both incompressible stripes. Together with the width relations from Chklovskii et al. we get exactly the same asymmetry in the partitioning of the circulating current as for the biased current in a Hall geometry.

13.4.2. Consequences for the edge-dominated breakdown

From the model in the previous section and the self-consistent simulation we can clearly conclude that the asymmetry is not an indication of the breakdown. It is rather the result of an asymmetric bias-dependent width of the incompressible stripes. Another feature observed in our measurements, namely the tilt of the bulk potential, together with an unchanged compressible and incompressible landscape is a better indication for the breakdown. It means that part of the current flows within compressible regions with longitudinal resistivity much higher than associated to incompressible stripes and thus leads to a relevant longitudinal voltage drop.

The key question is how these currents in the compressible regions are formed. Figure 13.13 shows the Landau level structure along a scan and was created in scale with our

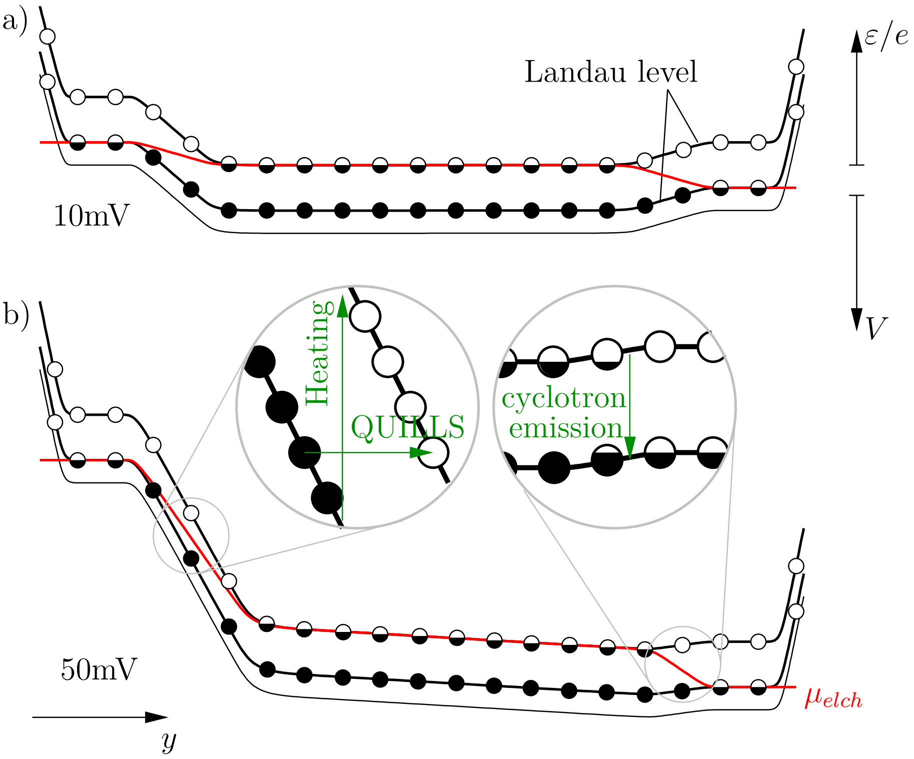

Figure 13.13.: Landau level structure along the scan direction for the edge-dominated QHE region. The two diagrams are shown in scale to our experiments within the energy axes and the compressible stripes have been widened for better clarity. 10 mV are applied in (a) and 50 mV in (b). Possible transitions for the situation in (b) are drawn with green arrows.

experiments along the energy axes. One can identify that at the dominant incompresssible stripe carrying most of the current, here on the left, the Landau levels come very close to each other. Overlapping of electron wavefunctions from different Landau levels could become possible allowing for isoenergetic inter Landau level transitions, the so-called QUILLS effect. The QUILLS transition is drawn in Fig. 13.13 as a horizontal transition. From an energetic point of view Joule heating

$$P_{\mathrm{j}} = \int jEdA \approx l \cdot w \cdot \sigma_{xx} j_x^2 \tag{13.18}$$

is also located mainly within the dominant incompressible stripe due to its remaining longitudinal conductivity (by thermal excitation). Thus further excitations of electrons across the gap due to heating could become possible within the dominant stripe. The heating of the electron system is drawn in Fig. 13.13 as vertical transition. Any mixture of the two transitions could be possible.

Two important features of the edge dominated breakdown have been discussed up to now: First, the transition is continuous, and second, the Hall potential profile along the sample remains almost translation invariant. Usual theoretical approaches aim to explain abrupt change of longitudinal resistance or at least consider a strong onset after critical current values. To still be able to explain continuous behavior with either the mechanism are not intrinsically abrupt or a feedback has to be present under the given circumstances. The very same feedback mechanism can be assumed here to allow QUILLS as well as Joule heating to create continuous transitions. QUILLS as well as Joule heating excite locally electrons that can enter compressible regions and lead to current within compressible regions. This will limit the voltage drop across the dominant incompressible stripe giving a feedback mechanism.

Up to now only the dominant stripe which carries most of the current, positioned at the left side in Fig. 13.13, was discussed. The second incompressible stripe is also affected by the increasing bias since it decreases its width with bias. At high enough bias the stripe will shrink that much in width that it cannot effectively shield the electric field across it. Cyclotron emission will become possible, as depicted for the right stripe in Fig. 13.13. There electron from the partially filled upper Landau level could transit to the lower Landau level which is emptied towards the edge. Via the cyclotron emission the electrons would loose energy leading to dissipation and finite longitudinal voltage. Such a process was suggested in a similar way by Ikushima et al. [212]. Cyclotron emission as described here is independent from the processes happening at the dominant stripe. Thus for the two incompressible stripes in the sample we suggest two independent processes leading to a longitudinal voltage drop. But to find a longitudinal voltage drop at both sides or edges of a Hall bar, as measured and shown Fig. 13.3 [2], one needs both processes to be active. We expect thus to have cyclotron emission at the high Hall potential edge of our sample after a significant longitudinal voltage is present.

13.5. Bulk-dominated breakdown

In the bulk-dominated breakdown, current flow and potential drop are found in the bulk of the sample, see Fig. 13.14. Increasing the bias leads to no significant changes in the Hall potential landscape before the longitudinal voltage becomes relevant. At the onset of longitudinal voltage drop also the Hall potential landscape changes strongly.

The bulk-dominated regime is not as handy as the edge-dominated regime because of the strong influence of local disorder. The position within the sample and the surroundings disorder dominated compressible and incompressible landscape become important parameters making the interpretation difficult. For example, one can identify the abrupt change within the Hall potential landscape of Fig. 13.14 (d) to be about 10 mV higher in bias than for Fig. 13.14 (c). Also the term "stripe" indicating a thin and long entity as used in the edge-dominated regime is not accurate for the bulk-dominated regime. We want to replace it here by "segment" indicating one part of a cross-section that has the appropriate properties.

Since the electric fields present in the bulk-dominated regime are much smaller than for the edge-dominated regime, and there only smooth transitions were observed, we do not expect here a sudden redistribution of electrons that completely changed the compressible and incompressible landscape. Changes are expected only at the transition regions between compressible and incompressible segments. We will therefore assume - like for the edge-dominated breakdown - that the incompressible landscape remains

---

[2] We rather reverse the bias and measure at the same edge, which is equivalent because the edge where the dominant stripe is found swaps by reversing the bias.

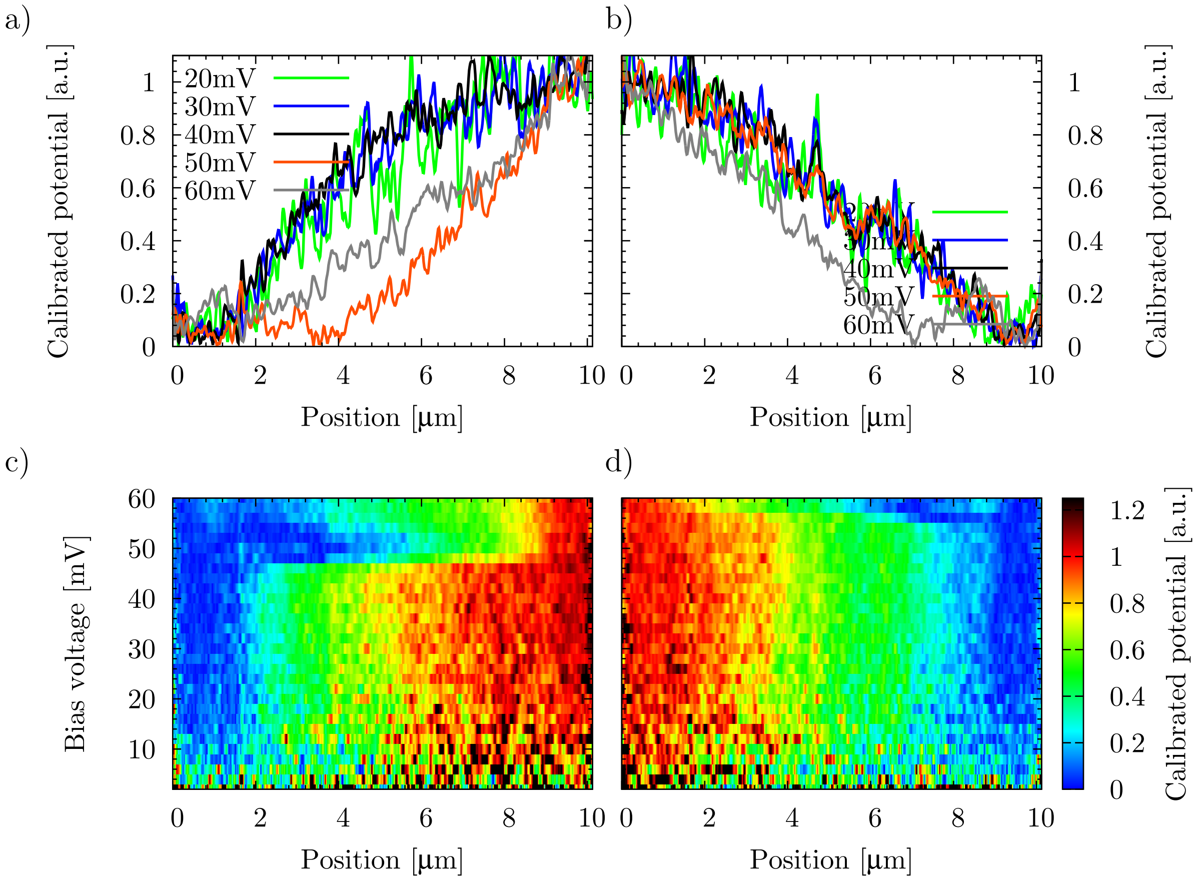

Figure 13.14.: Hall potential profiles for a magnetic field of 6.1 T and filling factor $\nu = 1.92$. The bias voltage was increase to run into the breakdown. (a) and (b) show chosen line scans while (c) and (d) show the full data set in color coded plots. (a) and (c) were measured in the bias scheme shown in Fig. 13.4 as (i) while (b) and (d) in the scheme denoted as (j).

mainly the same and only changes in the incompressible segment width happen. Further understanding of this region can only happen with area scans discussed in the following.

The area scans measured on sample 8957_201112_B for the bulk-dominated breakdown are shown in Fig. 13.15. One can identify clearly the different evolution for the two current directions (i) and (j). The simple situation for low bias becomes complex for high bias beyond the onset of the longitudinal voltage, resulting into complicated current paths through the sample.

Throughout these complications a trend is still observable. The current carrying region becomes narrower and has the tendency to be found at the lower Hall potential side of the sample.

A way to get a handle on the bulk dominated breakdown is to simulate a small slice of the sample as shown in Fig 13.16. In a first approximation one can treat the Hall potential profile within this slice as translation invariant and use well known self-consistent techniques for calculations. Gerhardts prepared such a self-consistent calculation, which are shown in Fig. 13.17, by adding to the confinement an oscillating density of donors. Due to the oscillations many incompressible segments of same integer filling factor can

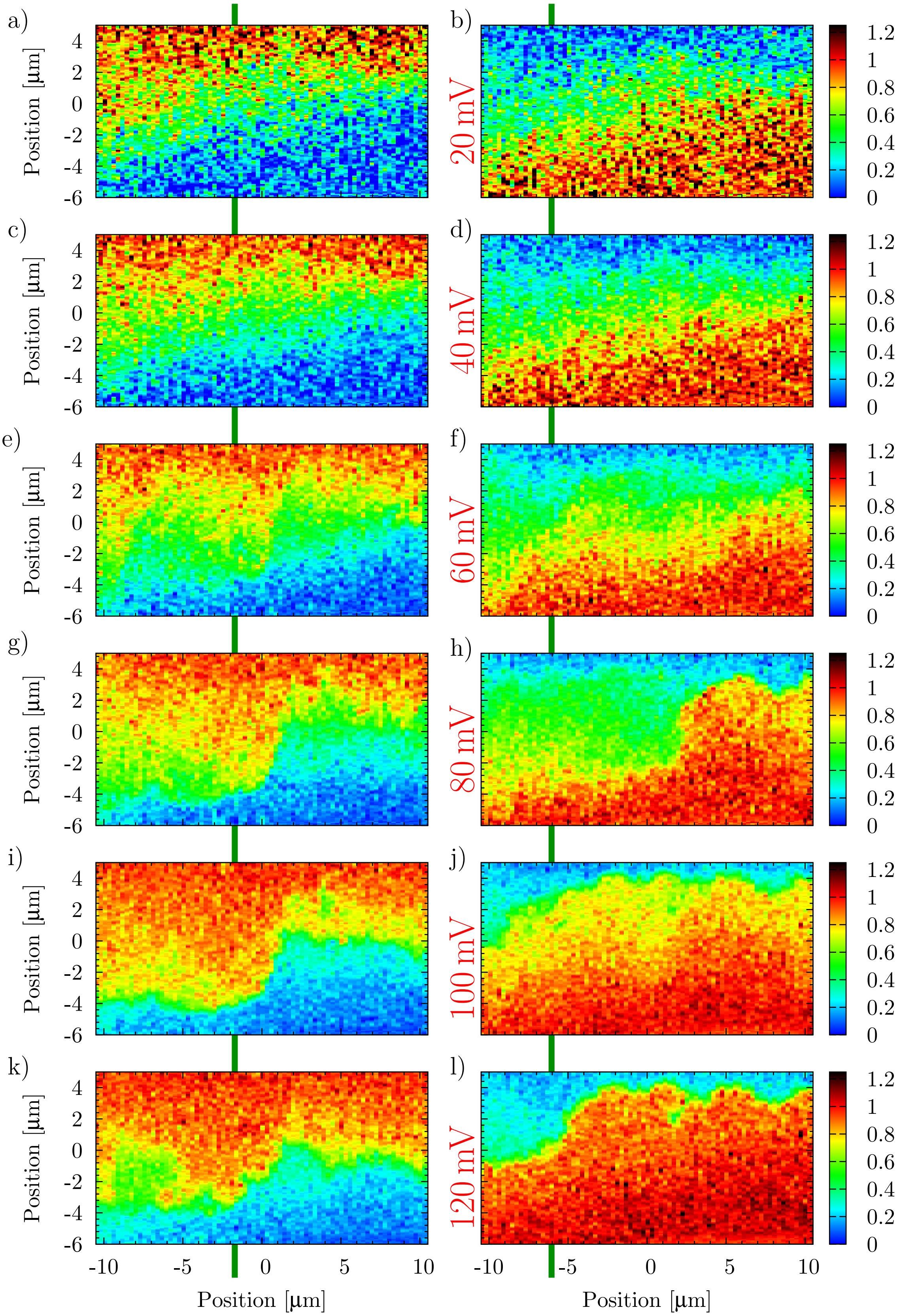

Figure 13.15.: Area scans on sample 8957_201112_B at a magnetic field of 6.8 T and filling factor $\nu = 1.94$. From top to bottom the bias voltage was increased from 20 mV to 120 mV in steps of 20 mV. The scans of the left side have the opposite current flow direction than of the right side. The actual scan ranges and applied bias schemes are indicated for the scans on the left hand side in Fig. 13.8 (b) and for the scans on the right hand side in Fig. 13.8 (c). The green lines mark the position of slices that will be analyzed lateron.

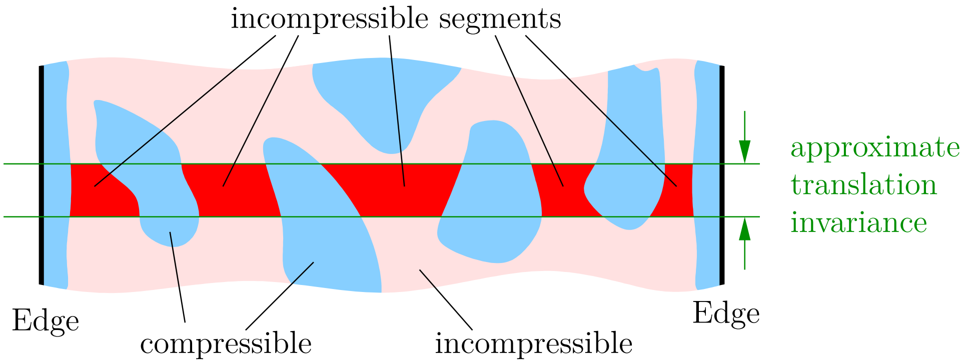
incompressible segments
approximate
translation
invariance
Edge
compressible
incompressible
Edge

Figure 13.16.: Taking a small slice of a disorder dominated Hall potential landscape. In a first approximation the profile within this slice can be treated translation invariant.

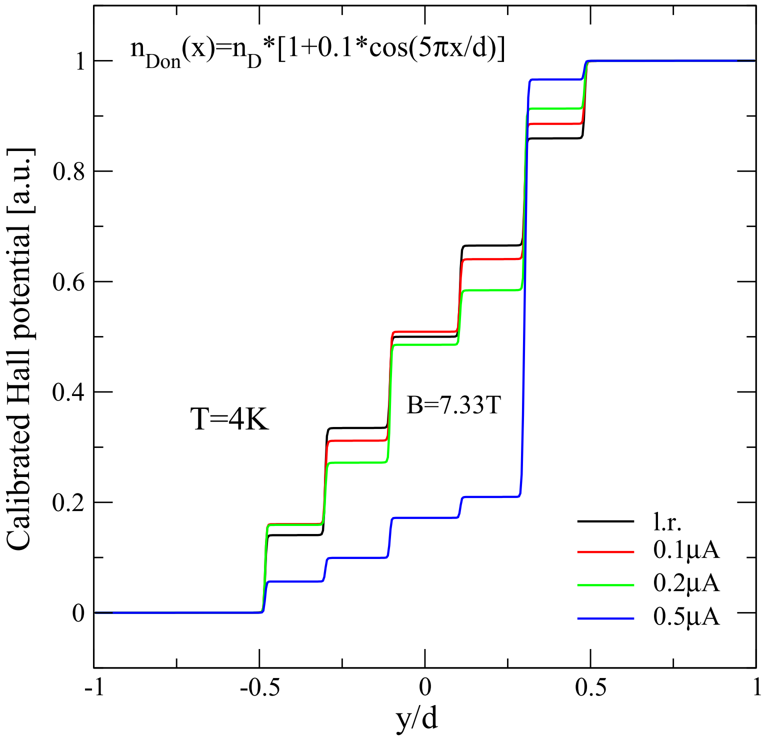

Figure 13.17.: Self-consistent calculated Hall potential profiles at a translation invariant sample with oscillating donor density, calculations by Gerhardts [228]. "l.r." stands for linear response and resembles the Hall potential profile without current. Several incompressible stripes evolve at the here shown bulk-dominated regime at 7.33 T. One stripe dominates electronic transport for high bias.

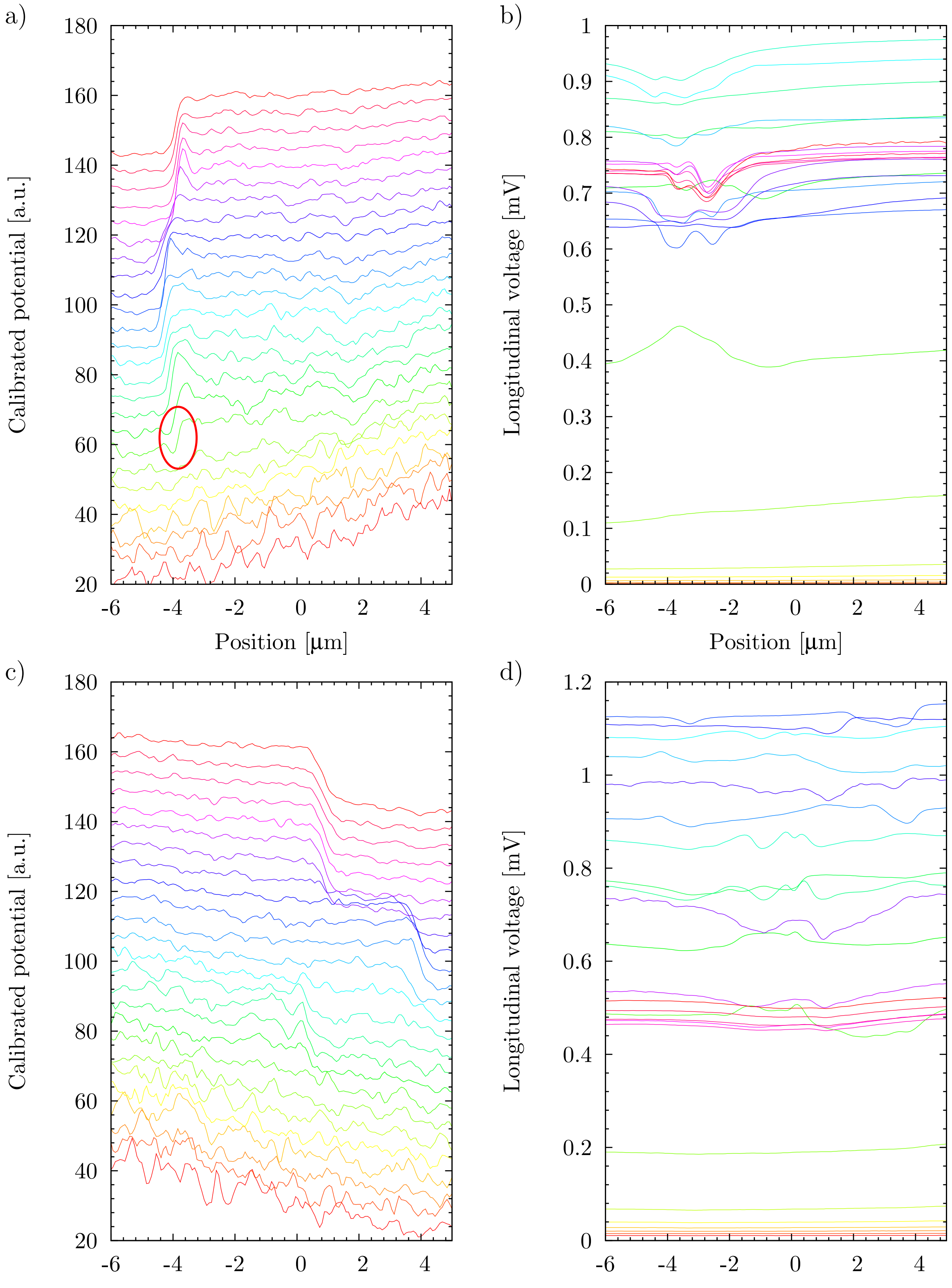

Figure 13.18.: Hall potential profiles (a) and (c) and longitudinal voltage (b) and (d) as a function of y-position for a x-position in (a) and (b) of $-1.6\,\mu\text{m}$ and in (b) and (d) $-6.0\,\mu\text{m}$. (a) and (c) are measured in the configuration (i) of Fig. 13.8 while (b) and (d) in the configuration (j). The scan-lines are also marked in Fig. 13.14. For (a) and (c) the line were scaled by factor of 20 and offset by the applied bias voltage in mV. The colors of the lines in (b) and (d) correspond to those of the matching scans in (a) and (c).

be found and each of them carrying a fraction of the current at low bias. Increasing the current, it will depend a lot on the actual details where the current through the sample is flowing. Figure 13.17 shows for 7.33 T a change of the Hall potential profile which is equivalent to the one measured in Fig. 13.14. In the simulation this change of the Hall potential profile depends strongly on the magnetic field and thus on the details of the incompressible landscape. Of course this translation invariant calculations are only a first step and in view of the strong local dependence of the Hall potential profile translation invariance should be abandoned to describe the incompressible landscape during the bulk-dominated breakdown more accurate.

We learn from this simulation that the actual details are very important and that dominant regions can evolve that carry most of the current. These regions would then be subject to QUILLS or heating.

To confirm this theoretical approach we repeated the area-scans of Fig. 13.15 with higher bias voltage resolution in intervals of 5 mV and lower spatial resolution. Specifically we had a look on each scan line of the area scan over the sample bias and searched for a weak spot. Figure 13.18 (a) and (c) show the line scans for the x-position of $-1.6\,\mu\mathrm{m}$ in the (i) current direction and x-position of $-6.0\,\mu\mathrm{m}$ in the (j) current direction. The positions are also indicated with green lines in Fig. 13.15. In (b) and (d) the corresponding longitudinal voltage is plotted as a function of tip position with the color matching to those of the Hall potential profiles. Thus (b) and (d) resemble a scanning gate experiment. Even though we tried to reduce the scanning gate effect by applying a DC-bias to the tip to not affect the 2DES, the high bias voltage applied to the sample will cause unavoidably a disturbance. One can see from Fig. 13.18 (b) and (d) that the tip has no effect on the longitudinal voltage for small bias and that the scanning gate effect begins to be effective only after the breakdown is well developed. The scanning gate signal is for Fig. 13.18 (b) nicely correlated with the structure in (a). Here the weak spot of the sample is easily identified and marked with the red circle. Already 1 µm away in x-direction this sharp feature is not present or is starting to smear out.

For the reverse current direction there was no such clear candidate as weak spot. The chosen line at x-position of $-6.0\,\mu\mathrm{m}$ represents still a sharp transition with a dominant current carrying channel. On the other hand the scanning gate effect seems not to be as clearly correlated as for Fig. 13.18 (a) and (b). The longitudinal voltage shows features during the onset of the breakdown over the whole cross-section instead of having features only close to the dominant segment. We contribute this to the fact that the scanned position is not the only choice for a weak spot within the sample and in particular neighboring slides to the scan-line can have similar effects on the scanning gate signal at different positions. Astonishingly one finds in Fig. 13.18 (c) several regions that become dominant one after another.

The discussed measurements show that disorder dominates the characteristic of the bulk-dominated breakdown. Each sample can have a distinct evolution due to its unique inhomogeneities. For a microscopic picture, self-consistency is crucial since the current is not found to be distributed in a simple manner and changes in bias change the Hall potential profile non-linearly. The important point for the bulk dominated breakdown is that the self-consistency together with the disorder can create locally within the sample a dominant incompressible segment carrying most of the current with high electric fields present. This region becomes then a weak spot subject to QUILLS or heating leading to an abrupt breakdown transition.

13.6. Transition region between edge- and bulk-dominated breakdown

In the transition region around 5.9 T the situation is not defined that strict as can be seen in Fig. 13.19. There we can see that a finite Hall potential drop is found in the bulk well before the breakdown of the QHE. Thus we can conclude that the sample center becomes incompressible before its surroundings so that there is no transition from edge transport to bulk transport but rather bulk transport sets in while edge transport is still present. The possible compressible and incompressible landscape in this situation is shown schematically in Fig. 13.21 (a). There - if true - we also see that the charge carrier concentration has to be lower in the sample center than at the edges.

One way to explain this feature would be the inhomogeneities of this particular sample. Another more interesting possibility is that this feature is general for etched Hall bars. In

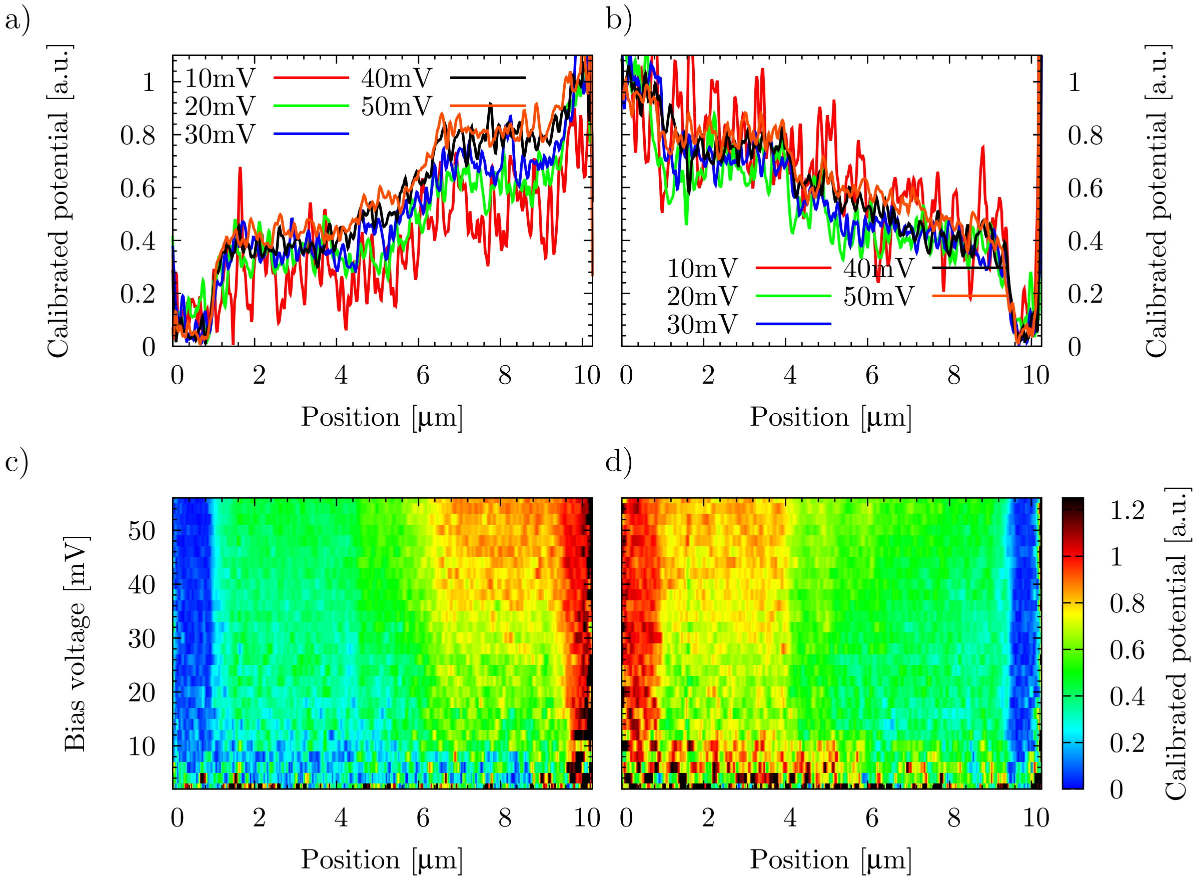

Figure 13.19.: Hall potential profiles for a magnetic field of 5.9 T and filling factor $\nu = 1.98$. The bias voltage was increase to run into the breakdown. (a) and (b) show chosen line scans while (c) and (d) show the full data set in color coded plots. (a) and (c) were measured in the bias scheme shown in Fig. 13.4 as (i) while (b) and (d) in the scheme denoted as (j).

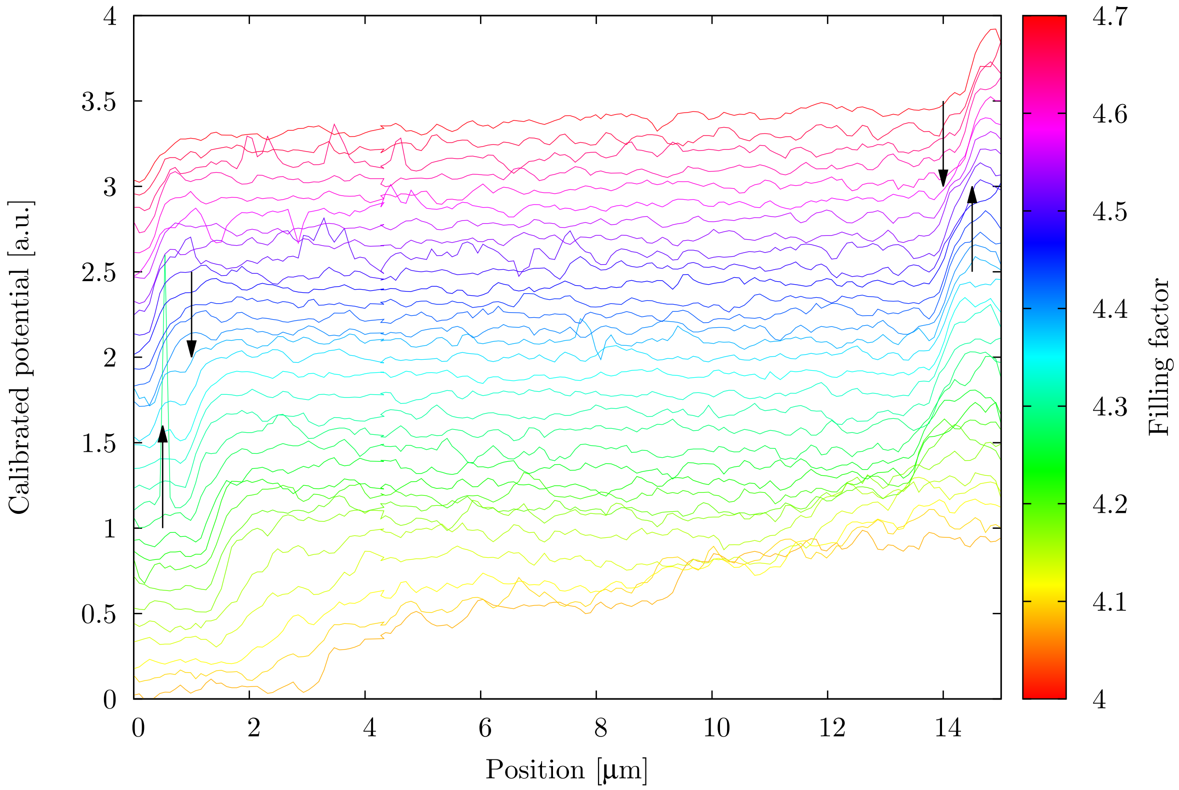

Figure 13.20.: Data of calibrated Hall potential profiles by Ahlswede et al. [17] close to filling factor $\nu = 4$. The data was offset for better visibility. The coexistence of two distinct incompressible stripes can be observed for filling factor $\nu = 4.36$ or equivalently magnetic field $B = 5.375\,\mathrm{T}$ on the left side and for $\nu = 4.56$ or $B = 5.15\,\mathrm{T}$ on the right side. The position of the corresponding incompressible stripes are marked with black arrows. We thank Erik Ahslwede for the access to his data to create this plot.

that case we should be able to find such features also in other measurements. Explicitly we had a detailed look on the data of Ahlswede et al. [16] which are plotted in Fig. 13.20 near filling factor $\nu = 4$. Two times in these scans there coexist two incompressible stripes at a single edge. The position where these incompressible stripes emerge or disappear are marked with black arrows. Hence at the edges the electron density has to have local maxima as shown in Fig. 13.21 (b) for one of the coexistence cases. The order of magnitude of the described effect is different for the two measurements on the different heterostructures as can be seen by comparing Fig. 13.21 (a) with (b). Still we find in both cases charge carrier density maxima at the edges. A sketch explaining why this behavior should be general is given in Fig. 13.21 (c). Due to the higher amount of surface states close to the edges it is more likely for such donor to be ionized. Thus except of the surface charges depleting the 2DES towards the edges we also have to consider ionized donors accumulating charges towards the edges. This can lead to local or global charge carrier density maxima depending on the actual arrangement.

The coexistence of bulk and edges incompressible regions carrying current makes the interpretation of the transition region a bit more complicated especially since the tran-

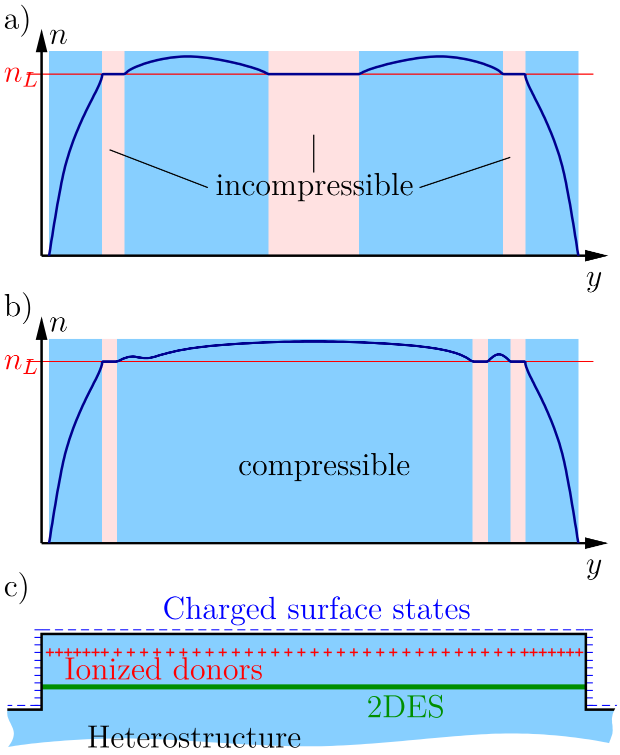

Figure 13.21.: (a) Charge carrier concentration as a function of position for the measurements of Fig. 13.19. (b) Charge carrier concentration as a function of position for the data of Ahlswede et al. [16] at $\nu = 4.56$ which are shown in Fig. 13.20. (c) Scheme for the possible origin of the charge density fluctuation towards the edges. Due to charging of surface states, Donors at the edges are more likely to be ionized enabling a local maximum of the charge carrier concentration near the edges.

sition is position and sample dependent. Still some general remarks can be made for this particular situation. We already defined incompressible segments as the distinct incompressible part for a single cross section. Taking such a cross section we can count and characterize the incompressible segments. For a low count of segments it is likely that a dominant segment will evolve while increasing bias and will lead to a continuous breakdown transition. We can increasing the number of segments by increasing the magnetic fiend. Then it becomes more likely that such a dominant stripe cannot evolve since many equivalent stripes can carry the current. Increasing the bias and thus changing incompressible segment widths leads then to rather abrupt changes of the current path. This happens also after a significant longitudinal voltage is present and has as signature fluctuations on the longitudinal voltage over bias trace. The black trace in Fig. 13.2 shows faint indications of such fluctuations while in the red traces jumps are occurring.

In conclusion, the transition region depends a lot on the details of the sample and is mainly affected by how the bulk disorder joins and takes over current transport with increasing magnetic field.

14. Conclusions and summary

From measurements of Hall potential profiles we could identify two distinct types of breakdown transitions, which were distinguishable both with longitudinal voltage measurements and with measurement of the Hall potential profile:

- A **continuous** transition present in the magnetic field regime, where incompressible regions are present at the sample edges.
- A **rather abrupt** transition present for magnetic fields where the bulk of a sample is mainly incompressible and disorder leads to compressible droplets inside the incompressible landscape.

We were able to explain these behaviors using the present microscopic picture of the QHE as basis.

We further concluded from the smooth changes in the edge-dominated regime that the incompressible stripe positions are almost unchanged and from previous theoretical studies by Chklovskii et al. [92] and the group of Gerhardts [102, 170] that:

- The position of incompressible and compressible stripes does not change significantly with applied bias.
- Incompressible stripes change their width with applied bias.

Considering the area scans at the bulk-dominated breakdown transition we could found in addition:

- One of the present incompressible stripes or regions will emerge as the dominant and will carry most of the current.

For the edge-dominated breakdown the dominant stripe will be the one at the lower potential edge, while for the bulk-dominated breakdown it depends strongly on the sample details, where a dominant segment will emerge. Also the dominant segment in the bulk-dominated breakdown can emerge abruptly and be replaced by another segment at higher bias. In the dominant stripe or segment the electric fields are high and could induce inter-Landau-level transitions.

Mechanisms for the edge-dominated breakdown can be all-electric-field induced inter-Landau-level transitions. Therefore QUILLS and Joule heating are two possible choices. The dominant mechanism of these two will be determined by the sample geometry, since heating effects need a certain length to fully evolve, while QUILLS a certain electric field. In the literature [198, 199, 204, 222] one can find that for samples shorter than 100 µm the onset of dissipation is not abrupt anymore. This indicates a transition region between the two mechanisms. Since our Hall bars have a total length of 80 µm, one could expect QUILLS to be dominant. We want to emphasize that at the edge-dominated quantum

Hall regime the current flows along the Hall bar edge leading to much longer current paths taking into account the way to the potential probes and back.

Another aspect is the smooth onset of longitudinal voltage for the edge-dominated breakdown. QUILLS depends strongly on the applied electric field, which is limited by tunneling events. In contrast the created heat is proportional to the longitudinal resistivity, which is increased while the system heats up. Again this can only be considered as hint to the dominant mechanism, also because the initial sample temperature affects strongly heating effects but less the QUILLS effect.

As shown in the experiments on the bulk-dominated breakdown, weak spots emerge in a sample that have comparable electric fields to the dominant stripes in the edge-dominated breakdown. First theoretical approaches on a translation invariant model are in agreement with this observation. Thus the mechanism for the bulk-dominated breakdown - even though sounding strange - can be the very same as for the edge dominated one. From the evolution, where these high electric fields seem to be just at one spot within the sample, it seems more likely that QUILLS is the dominant mechanism.

14.1. Fitting of other experiments into our model

We discussed for the edge-dominated breakdown that photon emission should occur at the higher Hall potential side of the sample, see Fig. 13.13. This can be checked by measurements of cyclotron emission. Measurements by Japanese groups [110, 209–213] on 3 mm long and 0.5 mm wide samples show different scenarios for a filling factor smaller than integer value but always the same features for a filling factor above integer value. We chose to show here some of these scans in Fig. 14.1. The ones at the right side

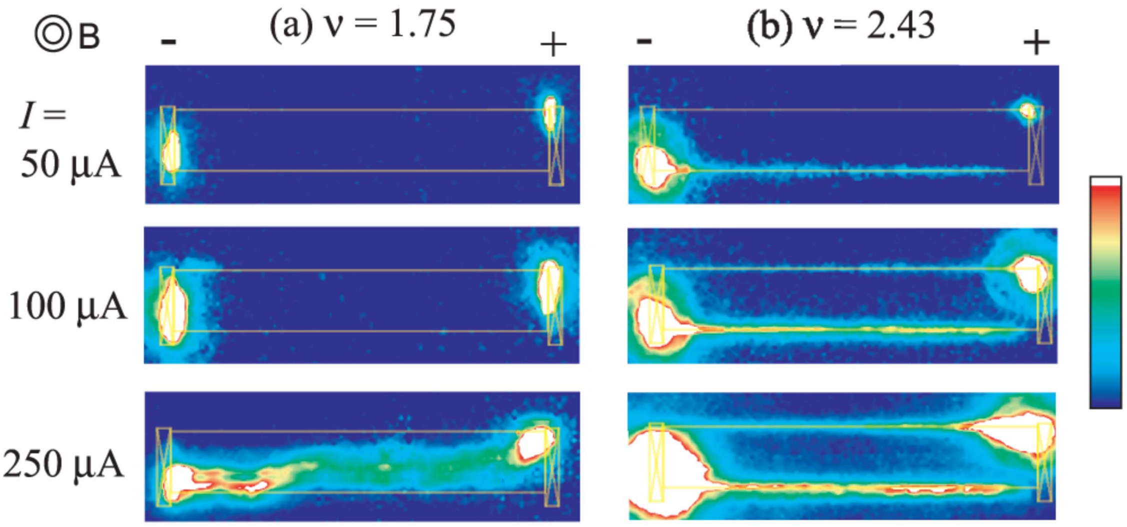

Figure 14.1.: Cyclotron emission of two samples at different filling factor by Ikushima et al. [213]. The samples were 3 mm in length and 0.5 mm in width. The magnetic field was in both cases 6.14 T. Reprinted with permission from [213]. Copyright (2014) by the American Physical Society.

are interesting for the edge dominated breakdown regime. The lower edge is the higher Hall potential edge and for 50 µm bias cyclotron emission is observable at this edge in agreement with our expectation.

A further increase of the bias will scatter that many electrons to the lowest unoccupied Landau level that the scattered electrons will find holes in the highest occupied Landau level of the incompressible stripe to recombine and emit light. As seen from Fig. 14.1 (b) this is the case already for a bias of 100 mV.

Cyclotron emission studies for the filling factor range of integer value and below, meaning bulk dominated breakdown, are not very conclusive. Two distinct scenarios have been identified. The first one shows the cyclotron emission starting from the hot spot at the negative biased contact and evolving along this contact before continuing following onward the Hall bar edge. For this case it was shown that the longitudinal voltage is linked to the emitting area. The second scenario shows no cyclotron emission when breakdown is entered. Only well above the onset of dissipation cyclotron emission sets on along the full length of the Hall bar. This scenario is shown in Fig. 14.1 (a).

Another experiment that agrees with our results is the measurement of the breakdown of the QHE with asymmetric edges. This can be achieved easily in gate define Hall bars. Siddiki et al. [229] did such experiments with high mobility samples, which should pronounce the edge-dominated breakdown, and found different quantum Hall plateau widths by reversing the current direction. Their results are shown in Fig. 14.2 and they argued that the incompressible stripe width is responsible for the stability against breakdown. They assumed also that the edge dominated quantum Hall plateau region mainly contributed in this experiment. By widening the correct stripe, the one which we called the dominant stripe, using a smooth confinement potential the quantum Hall plateaus become wider. This are the black traces of Fig. 14.2.

For our treatment of the edge-dominated breakdown we assumed a translation invariant

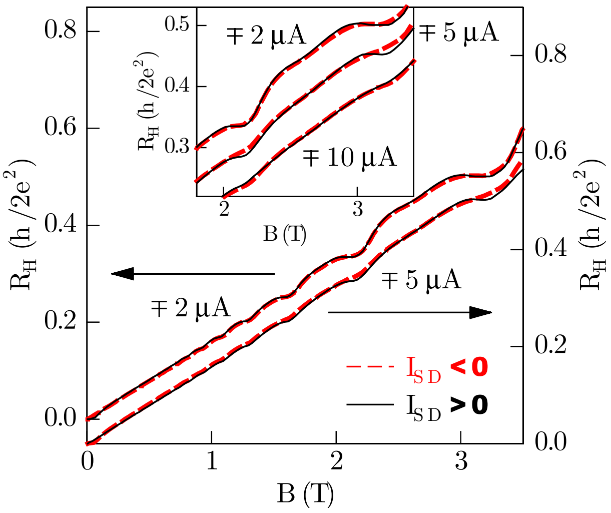

Figure 14.2.: Hall resistance over magnetic field for a gate-defined Hall bar with asymmetric edges taken from [229] and publisched under the creative commons BY-NC-SA licence. The inset shows in more detail the quantum Hall plateaus with filling factor $\nu = 6$ and $\nu = 4$, taken with different bias currents: 2 µA, 5 µA, 10 µA.

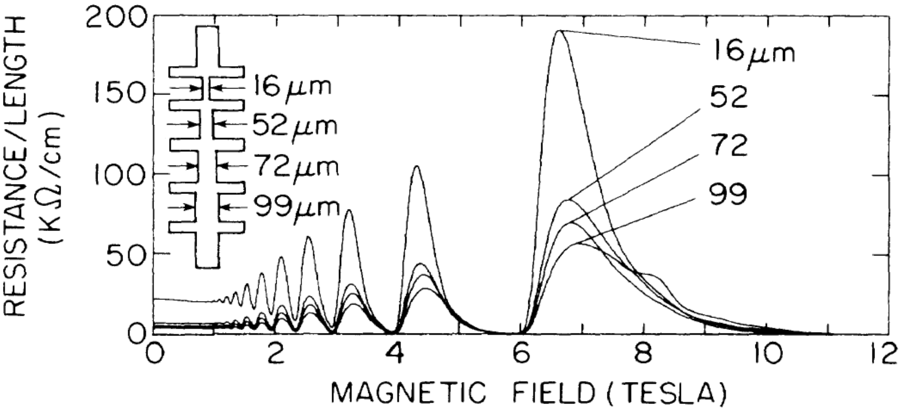

Figure 14.3.: Data adapted from Kane et at. [230] demonstrating a collapse of the longitudinal resistance over length traces for the edge-dominated magnetic field regime independent of the sample width. Measurements were done at small currents before the breakdown. The inset shows the sample geometry. Adapted with permission from [213]. Copyrighted by the American Physical Society.

model as long as the longitudinal voltage drop remains relatively small and dissipation is not significant. An experiment that fits nicely to such model was done by Kate et al. [230]. They measured the longitudinal resistance R_{xx} depending on the Hall bar width. It turned out that after normalizing R_{xx} with the length over which it was acquired the traces from the edge-dominated regime collapse to a single trace.

Part V.

Summary

15. Summary

Since its discovery in 1980 the quantum Hall effect (QHE) is becoming more and more important, currently because of the topological insulators and the aspired new definition of the kilogram by fixing the value of the Planck constant. The relation between the Planck constant and the kilogram is made within the Watt balance experiment via the QHE, the actual resistance standard, and the Josephson effect, the actual voltage standard. The reachable measurement precision of the QHE is therefore of significant importance, since the precision of derived quantities is co-determined by the precision of the QHE. It turns out that the largest error comes from the electrical breakdown of the QHE, which occurs for high currents. Interestingly this effect is not fully understood yet. However, to be able to give answers to fundamental questions, like how well the quantum Hall resistance resembles h/e^2, an accurate microscopic picture has to be present. In the literature one finds predominantly the edge state picture as microscopic explanation which was developed by Halperin and Büttiker. However for the past 15 years scanning force microscopy measurements have uncover another picture. Thereby the formation of a so-called compressible and incompressible landscape within the quantum Hall sample is the key element. Still the edge state picture is very popular today for explaining experiments and for theoretical predictions, even though it assumes obviously the wrong current distribution. Topological insulators are literally set equal to the QHE due to the edge state picture. Interference experiments are described nearly exclusively within this picture. In particular the edge state picture is used in experiments looking for non-abelian statistics for some fractional QHE state, to derive for example conclusions for the character of the wave function of the 5/2 state, a candidate for quantum information processing.

Because the microscopic picture is crucial for reliable conclusions and statements, we investigated in this thesis the limits of the compressible/incompressible landscape picture. We studied the breakdown of the QHE, which is challenging because of many influencing factors like sample geometry, mobility, and temperature, and deliver for the first time a conclusive microscopic picture. In addition, we could explain the QHE in graphene, a monolayer graphite with relativistic quasi particles, within the compressible/incompressible landscape picture.

The actual form of the compressible/incompressible landscape has its origin in the variations of the charge carrier density. Incompressible regions, carrying the current under quantum Hall conditions, are formed where Landau levels are fully occupied. The charge carrier concentration changes most strongly at the edges of the two dimensional electron (2DES) or hole system (2DHS). This leads to a characteristic evolution at the edges. Only after the Landau levels in the bulk are completely filled, which happens for the right magnetic field or charge carrier concentration, the disorder in the sample bulk affects the formation of the compressible/incompressible landscape.

15.1. Measurement technique

To measure the Hall potential profiles we used a scanning force microscope under quantum Hall conditions at a temperature of 1, 5 K and magnetic fields up to 10 T. In general, two difficulties accompany such a local electrostatic measurement on a 2DES or 2DHS. Typically the 2DES or 2DHS is buried under a material layer. Graphene is one of few exceptions. The second difficulty is that local donor or acceptor ions complicate the electrostatic measurement. To overcome this problems, Peter Weitz [13] developed a calibration technique, which allows to measure the change of the electrostatic potential after biasing relative to equilibrium. Additionally this technique reduces the influence of the scanning tip onto the 2DES or 2DHS, which under the right measurement conditions becomes negligible. We discuss possible artifacts within this measurement technique in the appendix G.

15.2. QHE in graphene

Graphene is an interesting material because of its linear band structure (see section 3), the resulting relativistic quasi particles and the possibility to tune a device continuously from n-type to p-type. The graphene samples studied here are the usual "graphene on silicondioxide" samples and were fabricated by Benjamin Krauss. We measured on this sample Hall potential profiles during QHE for different back gate voltages, which correspond to different filling factors. The most important measurement result is presented in Fig. 9.1. The observed Hall potential profiles in n-type graphene is equivalent to the one in GaAs/Al$_x$Ga$_{1-x}$As-heterostructure samples, recapped in chapter 4. Thus there is a depletion of electrons at the flake edges that extend about 1 µm into the flake bulk. This is schematically shown in Fig. 9.3. The position of the Hall potential drops and therefore also the position of the current path follows the position of incompressible stripes and is shown in Fig. 9.2. It is also theoretically supported in chapter E.

The more interesting situation is for p-type graphene. To explain the observed Hall potential profile evolution, see Fig. 9.4, holes have to accumulate at the flakes edges.

The found "electron-hole asymmetry", in which electrons deplete while holes accumulate towards the edges, cannot be explained by the geometric arrangement alone. The back gate electrode influences the edges stronger than the flake bulk due to stray fields, but always accumulates charges toward the edges. The simplest additional assumption to create a suitable model is that negative charges are fixed at or close to the graphene flake edge. To solve this electrostatic problem, a suitable self-consistent simulation was developed, described in detail in the appendix B. The simulation shows that with fixed negative charges at the graphene edges, we can explain the accumulation of holes as well as the depletion of electrons. Furthermore, we determined approximate analytic function by fitting the simulation data for two extremal cases, a line charge distribution along the flake edges and a homogeneous surface charge distribution besides the graphene flake. This approach is described in detail in the appendix C. From the found approximations we could calculate the position of the incompressible regions depending on the amount of fixed charge. Fitting the measured positions determined from the Hall potential profiles we were able to propose values for the amount of fixed charge. We concluded from the obtained values that fixed surface charge is more reasonable than a fixed line charge. The deduced fixed surface charge carrier density is $-3 \cdot 10^{-16}\,\mathrm{m}^{-2}$ and is equivalent to a square arrangement of electrons with a period of 6 nm. The appropriate fit can be found in Fig. 9.13. The cause of the fixed surface charge is likely water, which easily adsorbes on the silicon dioxide surface and acts as a charge trap [162–164]. Further possible causes for fixed charges can be found in section 9.6.

The assumed fixed negative charge leads to two interesting consequences that are confirmed by experimental data. First, there are pn-junctions parallel to the edges for n-type graphene. Second, the definition of a charge neutrality point becomes difficult as described in section 9.7. For these inhomogeneous charge density profiles we analyzed the dependence of the back gate voltage to reach the resistance maximum over the sample width. We compared these back gate voltages with the back gate voltage necessary to reach charge neutrality only in the center of the flake. As shown in Fig. 9.18, these two voltages are systematically offseted from each other and depend strongly on the flake width. This offset is found in our Hall potential measurements in Fig. 9.1 also. There one can identify an offset between the back gate voltage value for the Hall potential profile without slope and the voltage value for the resistance maximum. This result is especially relevant, because normally the charge neutrality point is set equal to the position of the resistance maximum.

Because of the two dimensionality of graphene, the substrate and adsorbates can influence a flake strongly. Also topographic defects like folds are possible. This was the case in some of our measurements. One of the flakes showed bubbles in the topographic structure. The bubbles or bumps could be identified as a kind of domain boarders. Current prefers flowing in the flat regions of the flake and shows within the flat regions the expected evolution with back gate voltage. This could be demonstrated with area scans as shown in Fig. 10.7. Another flake showed additional adsorbate-doping at the edges compared to the bulk. Looking at the Hall potential profiles measured on this flake in Fig. 10.10, one can identify two distinct incompressible regions exhibiting displaced evolution with respect to the back gate voltage. Even with the measurements showing complex structures for this flake the QHE can be explained within the compressible/incompressible landscape picture.

15.3. Breakdown of the QHE

The measurements on the breakdown of the QHE were done on GaAs/$\mathrm{Al}_x\mathrm{Ga}_{1-x}$As-heterostructure samples (see chapter 2 for details on the base material). We could identify from the breakdown in the electrical measurements as well as in the Hall potential profile evolution with increasing bias voltage two distinct breakdown types.

At the lower magnetic field side of the quantum Hall plateaus the longitudinal voltage drop increases continuously with increasing voltage bias. This can be seen in the blue traces of Fig. 13.2. In addition, one finds a continuous evolution with voltage bias in the respective Hall potential profiles shown in Fig. 13.5. There the flat portion of the profile in the bulk is shifting continuously upwards. Currents flow for this breakdown type, even after the breakdown, mainly at the 2DES edges. We call this type of breakdown the edge-dominated breakdown. In contrast, for the high magnetic field side of a quantum Hall plateau one finds abrupt transitions. Abrupt changes can be found in the longitudinal voltage drop, red traces in Fig. 13.2, as well as in the Hall potential profiles, Fig. 13.6, after increasing the bias voltage over a critical value. Since for this type of breakdown current flows predominantly in the bulk of the sample, we call this transition the bulk-dominated breakdown.

With a closer look on the edge-dominated breakdown, one can recognize that with increasing bias, an increasing asymmetric distribution of the current between the two current carrying incompressible stripes evolves. As seen in Fig. 13.7, first there is no current in the bulk region, but then a bulk current appears and increases continuously with increasing bias. With a self-consistent simulation done by Prof. Gerhardts, it could be shown that the asymmetric current distribution is a natural nonlinear response of the 2DES and is independent from the breakdown. In a simple model, a width change of the incompressible stripes due to voltage bias is responsible for the asymmetric voltage distribution. While one of the stripes is widened because of the additional Hall potential drop across the stripe, the other stripe gets smaller. The current through a stripe is in our model proportional to its width and results in the measured asymmetry. Figure 13.12 shows a comparison of our model to measured data. In the context of the strong simplifications done in our model, it fits remarkably well to the measured data.

Even though the asymmetry is not caused by the breakdown, it can boost the breakdown. Due to the asymmetry, high electric fields are present in one of the incompressible stripes. The mechanism of the breakdown could have its origin in the high electric fields present. The continuous nature of the transition let us conclude that the mechanism is either intrinsically not abrupt or self-limiting. A possible mechanism could be the so-called quasi-elastic inter-Landau-level scattering (QUILLS). QUILLS increases the longitudinal resistance of the stripe carrying most of the current, or dominant stripe. As already mentioned, the second stripe reduces its width with increasing Hall voltage. After the stripe gets small enough electrons can fall from the partially filled upper Landau level to the empty states of the lower Landau level across the incompressible stripe. This leads to an increase of the longitudinal resistivity of this stripe.

In the bulk-dominated breakdown, the simple Hall potential profile does not help the understanding since the problem is not translation invariant anymore. One has to scan a larger area of the sample instead. This was done as shown in Fig. 13.15 and we could identify a concentration of the current for high voltage bias. In Fig. 13.16 the Hall potential profile of the cross section with this Hall potential jump (current concentration) is plotted as a dense sequence with bias voltage as parameter. One can identify after exceeding a critical bias voltage a sudden change of the Hall potential profile and thus a redistribution of the current. A relevant portion of the total current flows then through the mentioned constriction. Here the self-consistent simulations of Prof. Gerhardts helped to explain this effect. In a first approach Prof. Gerhardts simulated a translation invariant sample with a confinement potential including oscillations. As result he found the coexistence of several incompressible segments where the current distribution depends strongly on the details, especially the biased current. Such as in the edge-dominated breakdown for increasing bias a dominant segment evolves carrying most of the current. After most of the current flows through the dominant stripe high electric fields are also built up. They can lead to the breakdown and are strongly localized, as demonstrated in our measurements shown in Fig. 13.16 and 13.15. Therefore we assume

QUILLS to be the logical explanation for the breakdown mechanism in this situation.

There is also a transition region between the edge- and bulk-dominated breakdown. To explain our findings, we needed an inhomogeneously ionized donor layer, which could be a finding general to etched $Al_xGa_{1-x}As$-heterostructure mesas. As result additional incompressible stripes with equal filling factor can appear within the sample. We searched for indications of such an inhomogeneity in measurements of Ahlswede et al. and found them as shown in Fig. 13.20. This observation seems to be plausible as due to the etching of the mesa, additional surface states close to the 2DES edges are created which are partially occupied by the donors' electrons. Thus the density of ionized donors is higher at the mesa edges than in the bulk. In spite of a homogeneous doping one can expect in such a scenario an increase of the electron concentration towards the edges, before it finally drops to zero.

15.4. Outlook

The measurements presented in this thesis do not complete the studied subject. Instead new interesting questions arise that will be touched in the following by suggestions on further experiments. The interested reader is referred to the appendix A where we discuss exclusively possible experiments.

In graphene the fixed negative charges are of special interest. Still not conclusively determined is the origin of the fixed charge. Hall potential profiles before and after trying to reduce the amount fixed charge could help the understanding of origin. The reduction of fixed charge can be achieved in different ways. For example, the treatment of the flake with ammonia or vitamin C. Ammonia turns out to be simplest to handle, since we can bring it in to the sample area in-situ during the experiment. If water on the open silicon dioxide surface is responsible for the fixed charge, then the fixed charge can be fully removed by annealing in vacuum. The change or removal of the substrate could also bring valuable information. A hint that this removes the fixed charge can be seen from electrical transport measurements, by Young et al. [231]. They measured high resistance maxima for graphene on boron nitride on graphite devices. Side gate electrodes parallel to the flake edges could screen a substantial portion of surface charge and additionally can be used to tune the edge character. The influence of etching is also of interest. In this work we disclaimed the usage of an etching process, but it is not uncommon to etch flakes for quantum Hall measurements.

A reduction of fixed charge would also be visible in electrical transport experiments. The width of a quantum Hall plateau should for example depend on the charge density profile. The smallest plateau width should be reached for most flat charge density profile. After the reduction of fixed negative charge the back gate electrode would dominate the charge density profile of the flake. Measuring the width of different quantum Hall plateaus over magnetic field and back gate voltage a kink or local minimum should be observable for a single back gate voltage value.

Furthermore, we can develop electrical transport experiments from our measurements and models that allow for a fast test for fixed charges. We predicted, for example, a systematic shift of the back gate voltage value for the resistance maximum with the sample width when fixed charge is present. One method to show this width dependence is to prepare a device from one flake that allows for measurements on different widths. The position of the resistance maximum should then shift with decreasing width to higher back gate voltages.

The breakdown of the QHE in graphene occurs at much higher critical currents than in GaAs/Al$_x$Ga$_{1-x}$As-heterostructures. Hall potential measurements should help to study the origin of the higher critical currents. The disorder and the huge Landau level splitting in graphene should play a crucial role.

We explained our results on the breakdown of the QHE in GaAs/Al$_x$Ga$_{1-x}$As-heterostructures with a width change of incompressible stripes or segments. This fundamental requirement is yet to be confirmed directly. The difficulty to do this is of technical nature since the width of such stripe is close to the resolutions limit of the measurement technique.

In our model for the edge-dominated breakdown we had two incompressibe stripes at the 2DES edge, those widths depend on the bias. In one of the stripes the width is increasing while in the other the width is decreasing. From our theoretical model the width of the (under bias) smaller stripe approaches asymptotically zero. We used as basis for this result the incompressible stripe width as calculated from the CSG-model, which is not self-consistent. For the case of zero approaching stripe width the question arises how justified is the prediction. Since the stripe width is linked to the total current through the stripe the previous questions is equivalent of asking if a reversal of the total current through an incompressible stripe is possible. A way to tackle this question is the precise measurement of the hall potential drop over the smaller stripe by the used measurement technique or for example using Single-Electron-Transistors. A more elegant possibility is the measurement of the absolute current through an incompressible stripe. This is only possible with a current sensitive sensor, for example a SQUID. Again a non-trivial calibration is required, that is described in appendix A.

A feature that we saw in our measurements - but could not be studied - was the collapse on a single trace of the longitudinal voltage drop for different magnetic fields. This feature was observed only for small bias voltage ranges in the bulk-dominated breakdown. For this type of breakdown, we also found abrupt changes in the current path through the sample. One could therefore conclude that these two features are correlated and by changing the bias voltage, one "jumps" from one current path to another.

The critical current in the edge-dominated breakdown is explicitly determined from the self-consistent asymmetry in the current distribution. This leads to the question, if there is a way to change the critical current for this breakdown type using side gate electrodes. As was already described beforehand, we expect two distinct mechanisms to increase the longitudinal resistivity of the two incompressible stripes. It is not clear, if the two mechanisms occur synchronously within the device. Using asymmetric confinement potentials one could try to shift the onset of the two mechanisms relative to each other and answer this question. Siddiki et al. had already shown, that asymmetric boundary conditions lead to a current direction dependent critical current. But under which conditions a maximal critical current is reached, this was not studied. If the critical current can be increased using side gate electrodes, this is therefore the most interesting question resulting from this thesis.

16. Zusammenfassung

Seit seiner Entdeckung 1980 nimmt der Quanten-Hall-Effekt (QHE) immer mehr an Bedeutung zu, aktuell wegen sogenannten topologischen Isolatoren und der angestrebten Neudefinition des Kilogramms durch die Fixierung des Planckschen Wirkungsquantums. Dabei wird die Relation zwischen Planckschem Wirkungsquantum und dem Kilogramm (im Wattwaagen-Experiment) durch den QHE - dem Widerstandsstandard - und den Josephson-Effekt - dem Spannungsstandard - gegeben. Die erreichbare Messgenauigkeit des QHEs ist hierbei von besonderer Bedeutung, da sie auch die prinzipielle Genauigkeit aller abgeleiteten Größen mitbestimmt. Es stellt sich heraus, dass die Genauigkeit im Wesentlichen durch den elektrischen Zusammenbruch des QHEs für hohe Ströme gegeben ist, welcher noch nicht vollständig verstanden wurde. Um aber fundamentale Aussagen über den QHE, wie z.B. darüber, wie genau der Hallwiderstand mit h/e^2 übereinstimmt, treffen zu können, muss ein akkurates mikroskopisches Bild als Grundlage genommen werden. In der Literatur findet man vorwiegend das Randkanalmodel zur mikroskopischen Beschreibung des QHE, welches von Halperin und Büttiker geprägt wurde. Jedoch zeigen Rastermikroskop-Messungen von mehr als 10 Jahren, die zum Großteil in unserer Gruppe durchgeführt wurden, ein anderes Bild. Die Bildung einer kompressiblen und inkompressiblen Landschaft in den Quanten-Hall-Proben ist dabei ein integraler Bestandteil dieses Bildes. Trotzdem wird auch heutzutage noch das Randkanalbild, welchem offensichtlich die falsche Stromverteilung zugrunde liegt, zur Beschreibung von Experimenten und für theoretische Vorhersagen verwendet. So setzt man zum Beispiel gerne topologischen Isolatoren bildlich dem QHE gleich. Interferenzexperimente verwenden beinahe ausschließlich diese Randkanäle zur Beschreibung. Explizit werden beim fraktionalen QHE, das Vielteichen-Pendant zum QHE, mit den Randkanalbild z.B. Rückschlüsse über den Charakter der Wellenfunktion des 5/2-Zustands gezogen, eines Zustandes der eine mögliche Basis für Quanteninformationsverarbeitung bildet.

Aber gerade weil das mikroskopische Bild entscheidend für belastbare Aussagen ist, haben wir uns in dieser Arbeit explizit an die Grenzen des kompressiblen/inkompressiblem Landschaftsbildes begeben. Dabei wurde der Zusammenbruch des QHEs untersucht, der aufgrund der vielen Einflussfaktoren, wie Probengeometrie, Mobilität, Temperatur, eine Herausforderung darstellt und bis vor dieser Arbeit mikroskopisch nicht verstanden war. Außerdem wurde gezeigt, dass der QHE in Graphen, also in einer Monolage Graphit mit relativistischen Ladungsträgern, sich ebenfalls im kompressiblen/inkompressiblen Landschaftsbild erklären lässt.

Der genaue Verlauf der kompressiblen/inkompressiblen Landschaft bildet sich dabei aufgrund Variationen in der Ladungsträgerdichte. Inkompressible Bereiche, die den Strom unter Quanten-Hall-Bedingungen tragen, bilden sich dort, wo Landau Niveaus gerade voll besetzt sind. Die Ladungsträgerdichte ändert sich am stärksten an den Ränder der zweidimensionalen Elektronen- (2DES) oder Lochsysteme (2DLS) und führt zu einer charakteristischen Evolution am Rand. Erst wenn Landau-Niveaus durch die richtige

Wahl des Magnetfeldes oder der Ladungsträgerdichte im Probeninneren voll besetzt sind, beeinflusst die Unordnung des Probeninneren die kompressiblen/inkompressiblen Landschaft.

16.1. Messtechnik

Zur Bestimmung der Hallpotentialprofile haben wir ein Rasterkraftmikroskop unter Quanten-Hall-Bedingungen, das heißt explizit Temperaturen von $1,5\,\mathrm{K}$ und Magnetfeldern von bis zu $10\,\mathrm{T}$, verwendet. Eine solche lokale elektrostatische Messung an einem 2DES oder 2DLS ist aber im allgemeinen von zwei Schwierigkeiten begleitet. Das 2DES oder 2DLS befindet sich in der Regel vergraben unter einer Materialschicht. Graphen bildet dabei eine von wenigen Ausnahmen, leidet aber unter der zweiten Schwierigkeit. Lokale Donator- oder Akzeptorionen erschweren elektrostatische Messungen. Um diese Probleme zu umgehen, entwickelte Peter Weitz [13] eine Kalibrierungsmessung, welche die Messung von Änderungen des elektrostatischen Potentials relativ zum Gleichgewicht ermöglicht. Gleichzeitig erlaubt diese Kalibrierungstechnik eine Messung mit geringer Beeinflussung der Probe. Einflüsse auf die Probe sowie Messartefakte könne jedoch nicht ganz ausgeschlossen werden, sind jedoch bei richtiger Anwendung der Messtechnik vernachlässigbar. Wir haben trotzdem in Anhang G möglichen Artefakte diskutiert.

16.2. QHE in Graphen

Graphen ist aufgrund seiner linearen Bandstruktur (siehe Abschnitt 3) und die damit verbundenen relativistischen Quasiteilchen als Materialsystem interessant. Die hier untersuchten Graphen-Proben entsprechen den gängigen "Graphen auf Siliziumdioxid" Proben und wurden von Benjamin Krauss aus der Gruppe von Jurgen Smet für uns hergestellt. Wir haben an solchen Proben Hallpotentialprofile im Quanten-Hall-Bereich aufgenommen, während wir mithilfe der Rückelektrode die Ladungsträgerdichte und damit den Füllfaktor verändert haben. Das wichtigste Messergebnis ist wiedergegeben in Abb. 9.1. Die gefundene Evolution des Hallpotentialprofiles in n-Typ-Graphen ist dabei äquivalent zu der, die in GaAs/Al$_x$Ga$_{1-x}$As Heterostrukturproben gemessen wurde, und im Kapitel 4 nochmal dargestellt ist. Es findet sich also eine Verarmung von Elektronen an den Rändern der Graphenfloke, die etwa $1\,\mu\mathrm{m}$ in die Flocke hineinreicht, und schematisch in Abb. 9.3 gezeigt wird. Die Position der Hallpotentialabfälle und damit auch die Position des Stromes folgt der Position von inkompressiblen Bereichen in der Flocke, wie in Abb. 9.2 dargestellt und in Kapitel E theoretisch begründet wird.

Interessanter ist jedoch der Bereich, in dem das Graphen p-dotiert ist. Um die vorgefundene Evolution der Hallpotentialabfälle zu erklären, müssen sich Löcher an den Rändern der Flocken anhäufen, siehe Abb. 9.4.

Die hier gefundene "Elektron-Loch-Asymmetrie", bei der Elektronen zum Rand hin verarmen und Löcher sich zum Rand hin anhäufen, galt es zu erklären. Dabei reicht die geometrische Anordnung alleine nicht aus. Die Rückelektrode beeinflusst zwar aufgrund von Streufeldern die Ränder stärker als das Flockeninnere, sorgt aber immer für eine Anhäufung von freien Ladungsträgern am Rand. Das nächsteinfache Model zur Beschreibung nimmt fixe negative Ladungen neben der Flocke an. Um dieses elektrostatische Problem jedoch zu lösen, mussten wir eine auf unser Problem angepasste selbstkonsistente Simulation entwickeln. Diese wird im Anhang B näher beschrieben. Die Simulation zeigte, dass die Annahme von fixen negativen Ladungen neben der Flocke die Anhäufung von Löchern und die gleichzeitige Verarmung der Elektronen erklärt. Weiterhin wurden aus der Simulation für zwei Extremfälle, nämlich Linienladungen entlang der Flockenränder und homogene Flächenladungen neben der Flocke, näherungsweise analytische Verläufe der Ladungsträgerdichte bestimmt. Das Vorgehen dabei wird im Anhang C beschrieben. Aus diesen Ladungsträgerdichteprofilen konnten wir die Position der inkompressiblen Bereiche in Abhängigkeit der fixen negativen Ladungen bestimmen. Über eine Anpassung an unseren Messdaten konnten wir somit Aussagen über die fixen Ladungen treffen. Dabei scheint uns eine fixe Flächenladung vernünftiger als eine Linienladung. Die gefundene Flächenladung liegt bei etwa $-3 \cdot 10^{-16}\,e\mathrm{m}^{-2}$ und entspricht einer Quadratgitteranordung von Elektronen mit einem Abstand von 6 nm. Die entsprechende Anpassung an die Daten findet sich in Abb. 9.13. Die Ursache für eine solche fixe Flächenladung ist wahrscheinlich Wasser, das sich gerne auf der Siliziumoxidoberfläche anlagert und als Ladungsfalle fungiert [162–164]. Weitere Überlegungen zu den möglichen Ursachen für fixe Ladungen finden sich im Abschnitt 9.6.

Durch die Annahmen von fixen Ladungsträger ergeben sich zwei interessante Konsequenzen, die sich mit den experimentellen Daten decken. Zum einen erhält man unweigerlich pn-Übergänge parallel zu den Rändern, sobald man die Flocke zum n-Typ dotiert. Zum anderen wird die Definition eines Ladungsneutralitätspunktes schwierig, wie in Abschnitt 9.7 gezeigt wird. Denn aufgrund des Ladungsträgerdichterprofils ist die Flocke an keiner Rückelektrodenspannung frei von beweglichen Landungsträgern. Für diese inhomogenen Profile haben wir uns an einer Modellflocke theoretisch angeschaut, wie sich der Wert der Rückelektrodenspannung, um das Widerstandsmaximum zu finden, sich mit der Breite der Flocke entwickelt. Diese haben wir mit dem Wert der Rückelektrodenspannung für Ladungsneutralität nur im Zentrum der Flocke verglichen. Wie in Abb. 9.18 gezeigt, liegen diese beiden systematisch versetzt zueinander und hängen stark von der Flockenbreite ab. Dieser Versatz findet sich auch in unseren Hallpotentialmessungen von Abb. 9.1 wieder. Er ist erkennbar an den unterschiedlichen Werten für die Rückelektrodenspannung, für die man das Hallpotentialprofil mit geringster Steigung und das Widerstandsmaximum findet. Dieses Ergebnis ist besonders relevant in Anbetracht dessen, dass Ladungsneutralität einer Flocke üblicherweise mit dem Widerstandsmaximum gleichgesetzt wird.

Durch die zweidimensionale Struktur von Graphen können das Substrat und Adsorbate die Flocken stark beeinflussen. Aber auch topographische Defekte wie Falten sind möglich. So auch in einigen unser Messungen an Graphen. Eine der Flocken wies Erhöhungen auf, sozusagen Blasen in der topographischen Struktur. Wir konnten diese Blasen als eine Art Domänenrand identifizieren. Strom fließt vorzugsweise in flachen Bereichen der Flocke, und zeigt dort auch die erwartete Evolution mit der Rückelektrodenspannung, wie in Abb. 10.7 mit Hilfe von Flächenabrasterungen gezeigt wurde. Eine zweite untersuchte Flocke wies unterschiedliche Dotierung an den Rändern als im Flockeninneren auf. Schaut man sich die Hallpotenitalprofile in Abb. 10.10 nahe Füllfaktor $\nu = 2$ an, so stellt man fest, dass zwei inkompressible Bereiche mit versetzter Evolution relativ zur Rückelektrodenspannung in dieser Flocke existieren. Trotz der komplexeren Verhältnisse ließen sich auch solche Graphen-Flocken im Rahmen des heutigen mikroskopischen Bildes des QHEs beschreiben.

16.3. Zusammenbruch des QHE

Die Messungen am Zusammenbruch des QHEs wurden an Proben aus GaAs/Al$_x$Ga$_{1-x}$As Heterostrukturen (siehe Kapitel 2) durchgeführt. Bei der Untersuchung des Übergangs in den Zusammenbruch konnten wir sowohl im elektrischen Transport als auch bei den Hallpotentialprofilen zwei Quantum-Hall-Plateaubereiche identifizieren, die sich grundsätzlich voneinander unterscheiden.

An der Quanten-Hall-Plateauseite hin zu niedrigeren Magnetfeldern wurde ein Übergang gefunden, dessen longitudinale Spannungsabfall kontinuierlich mit zunehmender Betriebspannung ansteigt. Das spiegelt sich in Abb. 13.2 in den blauen Kurven wider. Außerdem findet man in den Hallpotentialprofilen von Abb. 13.5 ebenfalls eine kontinuierliche Änderung. Dabei schiebt sich der flache Abschnitt in der Mitte der Profile kontinuierlich nach oben. Ströme fließen in diesem Bereich sogar nach dem Zusammenbruch vorwiegend an den 2DES-Rändern. Daher haben wir diesen Übergang den randdominierten Zusammenbruch genannt. Im Gegensatz dazu findet man auf der hohen Magnetfeldseite eines Quanten-Hall-Plateaus abrupte Übergänge. Sowohl die longitudinalen Spannung, roten Kurven in Abb. 13.2, als auch die Hallpotentialprofile in Abb. 13.6 weisen sprunghafte Änderungen bei Erhöhen der Betriebspannung über einen kritischen Wert hinaus auf. Da in diesem Magnetfeldbereich der Stromfluss bis zum Zusammenbruch über breite Bereiche im Probeninneren stattfindet, nennen wir diesen Übergang den vom Probeninneren dominierten Zusammenbruch.

Bei genauerer Betrachtung des randdominierten Zusammenbruchs, stellt man fest, dass eine asymmetrische Verteilung des Stromes zwischen den zwei stromführenden inkompressiblen Streifen mit zunehmender Betriebsspannung entsteht. Wie auch in Abb. 13.7 zu erkennen, fließt zunächst durch das Probeninnere kein Strom, setzt aber mit zunehmender Betriebspannung kontinuierlich ein. Mithilfe einer selbstkonsistenten Simulation, die Prof. Gerhardts durchführte, konnte die asymmetrische Stromverteilung als eine natürliche, nichtlineare Antwort des 2DES auf eine Erhöhung der Hallspannung identifiziert werden, die zunächst nichts mit dem Zusammenbruch zu tun hat. In einem einfachen Modell ist im Wesentlichen eine Breitenänderung der inkompressiblen Streifen für diese Asymmetrie verantwortlich. Während einer der Streifen durch den Hallspannungsabfall breiter wird, wird der andere schmaler. Der Strom durch den jeweiligen Streifen ist in unserem einfachen Model proportional zur Breite des Streifens, wodurch wir die gemessene Asymmetrie erhalten. Abbildung 13.12 zeigt einen Vergleich zwischen dem Modell und gemessenen Daten, die im Rahmen der starken Vereinfachung hervorragend übereinstimmen.

Auch wenn die Asymmetrie nicht vom Zusammenbruch verursacht wurde, kann sie umgekehrt den Zusammenbruch fördern. So findet man hohe elektrische Felder in einem der beiden inkompressiblen Streifen. Der Mechanismus des Zusammenbruchs könnte demnach in den hohen elektrischen Felder seinen Ursprung haben. Die kontinuierliche Natur des Übergangs lässt den Schluss zu, dass der Mechanismus nicht intrinsisch abrupt oder selbstregulierend ist. Mit solch einem Mechanismus, z.B. QUILLS, erhöht sich der Längswiderstand des dominanten inkompressiblen Streifens. Wie bereits erwähnt reduziert der zweite inkompressiblen Streifen mit zunehmender Hallspannung seine Breite. Ab einer gewissen Breite können Elektronen aus den teilweise besetzten oberen Landau Niveau quer über den inkompresiblen Streifen in unbesetzte Zustände des unteren Landau Niveaus fallen. Das führt zu einer Erhöhung des Längswiderstandes auch des zweiten Streifens.

Beim durch das Probeninnere dominierten Zusammenbruch kommt man mit simplen Hallpotentialprofilen bei der Untersuchung nicht weiter. Man muss stattdessen über eine größere Fläche der Probe rastern. Das wurde in Abb. 13.15 gemacht und wir konnten eine Engstelle für den Strom identifizieren. Diese haben wir als dichte Abfolge von Hallpotentialprofilen als Funktion der Betriebspannung in Abb. 13.16 dargestellt, die zeigt, wie plötzlich mit steigender Hallspannung der Zusammenbruch passiert. Man erkennt an dieser Eng- oder Schwachstelle eine abrupte Änderung des Hallpotentialprofils, so dass nach der Änderung ein beträchtlicher Teil des Stromes durch diese Engstelle fließt. Auch hier trugen die selbstkonsistenten Simulationen von Prof. Gerhardts zum Verständnis bei. In einem ersten Anlauf simulierte er eine translationsinvariante Probe mit oszillierendem Einschlusspotential. Er fand die Koexistenz von vielen inkompressiblen Segmenten, wobei die Stromverteilung stark von den Details, insbesondere aber der Größe des aufgeprägten Stromes abhängt. Wie auch beim randdominiertem Zusammenbruch bildete sich in der Simulation ein dominantes Segment heraus, das fast den ganzen Strom trug. Im dominanten Segment finden sich, nachdem der Hauptteil des Stromes dort fließt, hohe elektrische Felder. Diese können zum Zusammenbruch führen und sind, wie in unseren Messungen von Abb. 13.16 und 13.15 gezeigt, stark lokalisiert. Damit scheint uns QUILLS hier als vernünftigste Wahl für den Mechanismus des Zusammenbruchs.

Wir fanden auch eine Art Übergangsbereich zwischen Rand- und vom Probeninneren dominiertem Zusammenbruch. Besonders hervorzuheben ist hierbei, dass wir eventuell eine inhomogene ionisierte Donorschicht in der $\mathrm{Al}_x\mathrm{Ga}_{1-x}\mathrm{As}$ Schicht gefunden haben, die zusätzliche inkompressible Randstreifen generiert. Wir haben Indikatoren für eine solche Inhomogenität auch bei den Messungen von Ahlswede et al. gesucht und, wie in Abb. 13.20 gezeigt, auch gefunden. Diese inhomogene Ionisierung von Donatoren hat ihre Ursache in der Herstellung unserer Mesastrukturen durch Ätzen. Durch das Ätzen erzeugt man zusätzliche Oberflächenzustände in der Nähe der Ränder des 2DES, die natürlich von den Donatorelektronen teilweise besetzt werden. Dadurch würde man eine höhere Konzentration ionisierte Donatoren an den Rändern der Mesa erhalten. Trotz homogener Dotierung kann mal also erwarten, dass zu den Rändern hin die Elektronendichte zunächst ansteigt, bevor sie auf Null sinkt.

16.4. Ausblick

Die hier vorgestellten Messung schließen keineswegs die jeweilige Thematik ab, sondern führen zu weiteren interessanten Fragestellungen, die im Weiteren kurz angerissen werden. Der interessierte Leser wird auf Anhang A hingewiesen, der sich ausschließlich mit Details der weiterführenden Experimenten befasst.

Bei Graphen sind die fixen negativen Ladungen von besonderem Interessen. Dabei gilt es herauszufinden, was die genaue Ursache dieser Ladungen ist. Hallpotentialmessungen nach dem Versuch, die fixen Ladungen zu reduzieren, könnten dabei helfen. Die Reduktion der fixen Ladungen könnte dabei auf unterschiedlichste Art und Weise passieren. Zum Beispiel die Behandlung der Flocke mit Ammoniak oder Vitamin C. Dabei ist Ammoniak besonders einfach, da es sich in den Probenbereich während des Experimentes in-situ einleiten lässt. Ist die Anlagerung von Wasser an der offenen Siliziumdioxid-Oberfläche für die fixen Ladungen verantwortlich, so lässt sich dies rückstandslos unter Aufheizung in Vakuum entfernen. Desweiteren könnte das Ändern oder Entfernen des Substrats eine Eingrenzung zulassen. Einen Hinweis darauf, dass wir die fixen Ladungen entfernen können, geben elektrische Transportexperimente von Young et al. [231], bei denen ein besonders hohes Widerstandsmaximum in Graphen auf Bornitrid auf Graphit gemessen wird. Es könnten auch Seitenelektroden parallel zu den Graphen Rändern verwendet werden, die einen großen Teil der Flächenladung abschirmen würden und eine Abstimmung zur Reduktion des nicht geschirmten Anteils zuließen. Auch der Einfluss eines Ätzprozesses wäre von Interesse. In dieser Arbeit wurde zwar auf einen solchen Prozessschritt verzichtet, jedoch ist es nicht unüblich, Flocken vor Quanten-Hall-Messungen zu ätzen.

Eine Reduktion der fixen Ladungen würde sich aber auch auf elektrische Transportmessungen auswirken. So sollte die Quanten-Hall-Plateaubreite von dem Ladungsträgerdichteprofil in der Probe abhängen. Die kleinste Plateaubreite ist bei dem flachsten Profil zu erwarten. Die Reduktion der fixen Ladungen würde dafür sorgen, dass die Rückelektrode den dominanten Einfluss auf das Dichteprofil hat. Es ergebe sich eine bestimmte Rückelektrodenspannung bei der die Quanten-Hall-Plateaubreite ein lokales Minimum erreicht.

Desweiteren können aus unseren Messungen und Modellen auch elektrische Transportexperimente entwickelt werden, die eine schnelle Suche nach fixen Ladungen zulassen. Wir haben zum Beispiel wegen den fixen Ladungen neben den Flocken und dem damit verknüpften Ladungsträgerdichteprofil eine systematische Verschiebung des Widerstandsmaximums vorhergesagt. Eine Methode, das zu zeigen, wäre eine Probe aus einer einzigen Flocke zu erzeugen, die Messungen an unterschiedlichen Breite der Flocke zulässt. Die Position des Widerstandsmaximums sollte dann mit kleiner werdender Breite zu höheren Rückelektrodenspannungen hin wandern.

Der Zusammenbruch in Graphen wird bei höheren kritischen Strömen gefunden als bei GaAs/Al$_x$Ga$_{1-x}$As Heterostrukuren. Hier sollte mithilfe von Hallpotentialprofilmessungen die Ursache näher untersucht werden. Die Unordnung und die Laundau-Niveauaufspaltung sollte dabei eine große Rolle spielen.

Beim Zusammenbruch in GaAs/Al$_x$Ga$_{1-x}$As Heterostrukutren haben wir unsere Ergebnisse über die Breitenänderung von inkompressiblen Streifen erklärt. Diese fundamentale Voraussetzung sollte daher überprüft werde. Die Schwierigkeiten sind hierbei hauptsächlich technischer Natur, da die Breite solch eines Streifens nahe an der Auflösungsgrenze unserer Messtechnik liegt. Eine qualitative Aussage ist jedoch bei sorgfältiger und direkter Messung möglich.

In unserem Model für den randdominierten Zusammenbruch hatten wir zwei inkompressible Streifen, dessen Breiten sich mit dem Strom ändern. In einem der Streifen nimmt die Breite zu, während in dem anderem die Breite abnimmt. Es stellt sich die Frage, ob wir den dünner werdenden Streifen auf eine Breite von Null bringen können und was eine weitere Erhöhung des Hallspannungsabfalls über den "Streifen" verursachen würde. Um diese Frage beantworten zu können, müssen wir den absoluten Strom durch einen inkompressiblen Streifen messen können. Das ist aber mit der hier verwendeten Messtechnik nicht möglich. Wir benötigen dafür einen stromsensitiven Sensor, z.B. ein SQUID. Aber selbst dann ist eine nicht triviale Kalibrierung erforderlich, die im Detail im Anhang A beschrieben ist.

Ein Merkmal, was wir in unseren Messung gefunden, jedoch nicht untersuchen konnten, ist der Kollaps der longitudinalen Spannungsabfälle über der Betriebspannung auf eine einzige Kurve. Die geschieht für kleinere Betriebsspannungsbereiche, wenn Messungen der longitudinalen Spannungsabfälle bei verschiedenen aber nahe beieinanderliegenden Magnetfeldern aufgenommen werden. Dieses Merkmal wurde nur im vom Probeninneren dominierten Zusammenbruch gefunden. Das war auch der Bereich, in dem sich der Strom abrupten Änderungen in seinem Pfad durch die Probe unterzieht. Man könnte also vermuten, das der Strompfad beim Verändern der Betriebspannung in eine anderen "springt", wir also eine Art bistabile Zustände vorfinden.

Explizit beim randdominiertem Zusammenbruch wurde der kritische Strom durch die selbstkonsistente Asymmetrie der Stromverteilung bestimmt. Es stellt sich sofort die Frage, inwiefern mittels Seitenelektroden der kritische Strom beeinflusst werden kann. Wie oben bereits beschrieben, erwarten wir zwei unterschiedliche Mechanismen zur Erhöhung des Längswiderstandes der zwei inkompressiblen Streifen. Es ist nicht klar, inwiefern diese zwei Mechanismen zeitgleich in den Proben aktiv sein müssen oder es überhaupt sind. Mithilfe von asymmetrischen Randbedingungen könnte man den Einsatz dieser Mechanismen in Abhängigkeit von der Betriebsspannung zueinander versetzen und diese Frage damit beleuchten. Außerdem haben Siddiki et al. bereits gezeigt, dass asymmetrische Einschlusspotentiale zu einen stromrichtungsabhängigen kritischen Strom führen. Unter welchen Bedingungen jedoch ein maximaler kritische Strom erreicht wird, wurde noch nicht untersucht. Ob der kritische Strom durch Seitenelektroden erhöht werden kann, bleibt damit eine der interessantesten aufgeworfenen Fragen dieser Arbeit.

Part VI.

Appendix

A. Sugestions for further experiments

The experiments presented in this thesis answer basic questions about the QHE in graphene and the breakdown of the QHE. The answers pose also new questions. In the following we want to pose some of these questions and give suggestions how to tackle them.

A.1. Graphene

In our graphene experiments we found an unexpected charge carrier density distribution and proposed a model of fixed negative charges as explanation. Still we were not able to determine with certainty the origin of these fixed charges. Thus we want to present different approaches to further limit the possible sources of fixed charges. There are also interesting consequences due to the fixed charges for transport measurement that will be discussed afterwards. Finally we want to point out that the electrical breakdown in graphene is found for much higher critical currents than in GaAs/Al$_x$Ga$_{1-x}$As heterostructure samples. This will be discussed with some suggestions in the end of this section.

A.1.1. Finding the origin of fixed charges

We assume that the fixed negative charges, needed to explain our observations, are positioned on the substrate surface beside the graphene flake. In our experiment we do not had a direct way to measure these charges. But we can try to change their amount and repeat the experiment to verify the effect.

The easiest way to do such change is by exposing the sample to different chemicals. Ammonia and Vitamin C [232] are candidates to eliminate negative charges. In our case the sample can easily be exposed to ammonia, since the sample holder consists of a vacuum chamber where small amount of ammonia can be ingested. The result of a reduced fixed negative charge would be a distinct and different evolution of the Hall potential profiles over the back gate voltage. It is also easier to reach a back gate voltage which dominates the charge carrier profile within graphene. In this case the evolution of the Hall potential profiles over the back gate voltage, where the potential drop marked a u-shaped structure, will flip upside down.

We also believe that water molecules on the silicon oxide are responsible for the fixed negative charges. Water sticks very good on silicanol groups present on the surface of siliconoxide. Putting the sample in vacuum is not sufficient to remove the water. But heating is. Thus measuring the Hall potential evolution before and after backing within the sample holder under vacuum would be a test for water.

Another possibility to handle with water would be to remove or cover the silicanol groups. Thus free standing graphene as well as graphene on hexagonal boron nitride should not suffer that much from fixed negative charges. But Hall potential measurements on these systems would not only remove or reduce the effect of surface charges. Also charges in the substrate bulk, if relevant, will be reduced. The only contribution that does not change significantly by changing or removing the substrate is the edge chemistry of graphene. This gives a possibility to exclude line charges as possible fixed charge arrangement.

Beside reducing the effect of fixed negative charges by reducing the amount of charges also screening the charges is possible. Using side gates like shown in Fig. A.1 (a) would thus reduce dramatically the fixed charge effects. We further could bias the side gates such that they compensate for the not covered surface between side gates and graphene flake. This could be checked by Hall potential measurements. Also the influence of the side gate voltage on the QHE plateau widths and the Hall potential profile evolution would be an interesting measurement itself. It would return the relative importance concerning plateau width between bulk dominated and edge dominated QHE. The side gates are also beneficial for the scanning measurements itself because the tip is not affected by the back gate as strongly as without side gates.

A way to completely overcome the disadvantage of the side gates leaving an open unshielded area is to extend the contacts along the edges like in Fig. A.1 (b). One removes the effect of fixed charges completely by the expense of the chemical potential difference between the graphene flake and the contacts. The overall advantage is that the chemical potential difference can be tuned by the used material and the back gate voltage to become from its effect significantly smaller than the fixed charges. Also after applying a high magnetic field the edges will have - due to the Hall angle - a potential close to that of the contact, like shown in Fig. A.1 (c). Only in this respect and condition the shielding segment of the contact is negligible.

Another aspect is processing! The flakes we measured so far had the minimum amount of processing steps. Especially no etching of the flake edges was performed. Of course for samples used today etching is an important processing step. How this step alters the charge environment is thus of strong interest and should be studied in a Hall potential measuring experiment.

A.1.2. Consequences of the fixed charges

The fixed negative charges we found beside our graphene flaked have consequences also for electrical transport measurements. The most peculiar is the width dependence of the resistance maximum. This was calculated for an idealized flake without disorder and with fixed charges as derived from our measurement. The effect was shown in Fig. 9.18 and is for small flake widths significant. A quick way to check thus for fixed charges is by measuring this width dependence. The difficulty to do so is the individual doping of graphene flakes. Especially inhomogenieties make this measurement difficult. We have therefore to prepare a sample out of a single flake to at least have the same doping. A possible design is shown in Fig. A.2 and would contain for a simpler analysis two terminal devices with equal aspect ratio. Except of inhomogenieties also an applied etching process

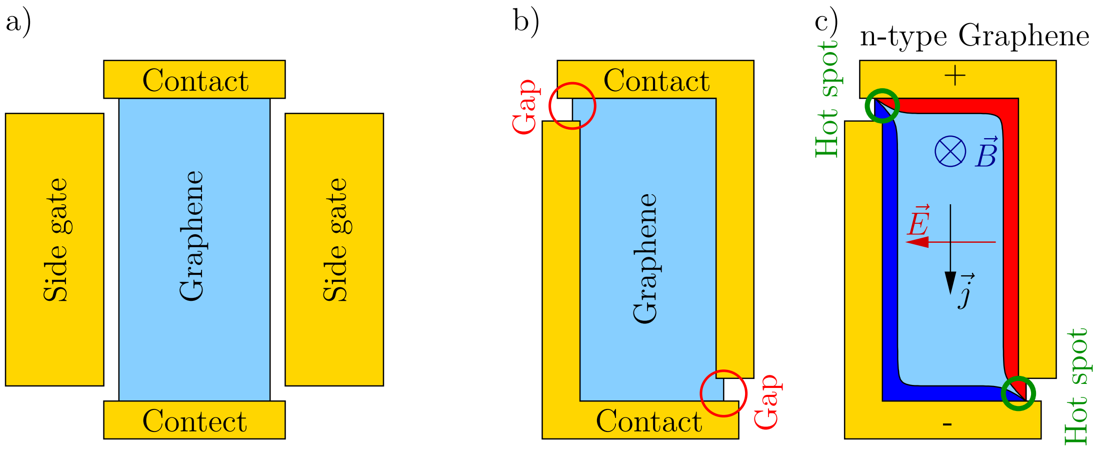

Figure A.1.: Sample geometries for experiments to shield edge effects. (a) Geometry with side gates to affect electrostatically the confinement potential. (b) Shielding with the current contacts. With zero magnetic field the gaps marked in red will dominate. Turning on the magnetic field will force the current to flow across the sample. As depicted in (c) two hot spots, encircled in green, will form where the current will enter and leave the sample.

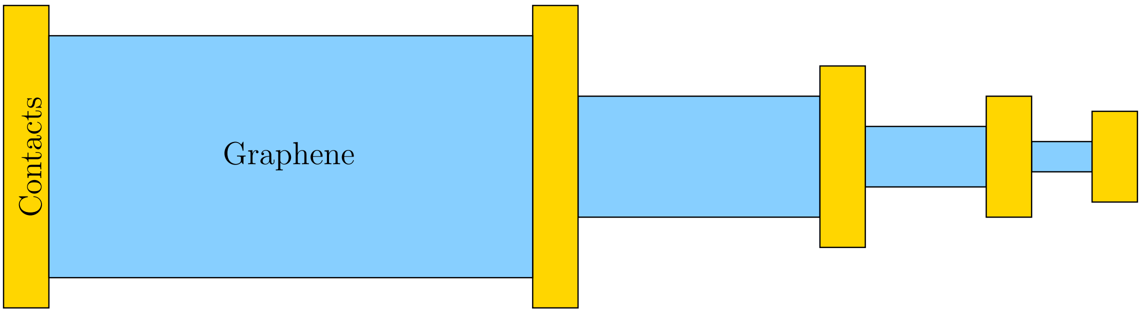

Figure A.2.: Sample design to check for width dependence of the resistance maximum.

is a critical point that could make this measurement difficult to interpret.

Except of the fixed charges also the back gate is affecting the charge carrier density profile inside the flakes. For sufficiently large back gate voltage, or sufficiently low fixed charges, the back gate effect can become dominant. This is interesting because the back gate allows to change the type of charge carriers that is accumulated at the flake edges. And during this change there will be a point in the back gate voltage where the charge carrier density profile in the flake is flattest. A flat carrier density profile means essentially that the quantum Hall plateau side where two distinct incompressible stripes at the edges carry the current, is strongly suppressed. The plateau width is expected to be smallest around this back gate voltage range. Of course this requires a quantum Hall plateau at the back gate voltage value with flattest charge carrier density profile. This can easily be achieved by using the magnetic field to tune the filling factor independently of the back gate voltage. Measuring the plateau width over back gate voltage and magnetic field should thus deliver kinks at one specific back gate voltage value.

A.1.3. Breakdown of the QHE in graphene

The breakdown of the QHE in graphene was measured by Baker et al. to be at current densities one orders of magnitude higher than in GaAs/$\mathrm{Al}_x\mathrm{Ga}_{1-x}$As-heterostructures [46]. Since we have also studied the breakdown on GaAs/$\mathrm{Al}_x\mathrm{Ga}_{1-x}$As-heterostructures we are also interested on the reasons for the much higher breakdown currents in graphene. On one hand the Landau level spacing can easily become bigger in graphene than in other materials explaining the QHE measurable in room temperature [42]. On the other hand graphene is assumed to be strongly disordered.

Hall potential measurements on the breakdown of the QHE in graphene could thus reveal the importance of disorder for the breakdown in graphene. From the measurement we have done so far we cannot conclusively give an answer. It is also important to include the breakdown transition and compare the bulk-dominated breakdown with the edge-dominated. In case disorder is important for the breakdown the critical currents should show strong deviations in critical current between bulk- and edge-dominated breakdown.

A.2. Breakdown

The measurements of the breakdown of the QHE delivered a microscopic picture on how the evolution with increasing voltage bias is driven. We relied in our model on the theoretical prediction of a incompressible stripe or segment width depending on bias. Therefore the change in width of incompressible stripes should be measured. We can use the measurement technique used in this thesis but one should be aware of two complications. First the measurement signal is the convolution of the tip sensitivity profile and the feature to be measured, here the course of a Hall potential drop. Since the feature to be observed is similar in size than the tip sensitivity profile a quantitative analysis becomes unreliable but a qualitative observation of the width change should be possible. Still noise is a problem since we are looking for small relative changes. One has thus to suppress noise by increasing the integration or average time. Second the measurement technique uses lock-in amplifiers that average the signal over time. By moving the tip for a scan, this results into a correlation of points measured within a certain time span. Measuring two neighboring points we have to make sure they are not correlated via the lock-in. The time span to wait is given by the integration time set at for the lock-in amplifier and one should wait at least five times this value before a new independent result can be assumed. Overall this gives a long measurement that has to be conducted with care. It should be also mentioned here that the incompressible stripe width could be bigger than what we measure here. This is because, as shown by Gerhardts et al., the incompressible stripe are not homogeneous and current tends to flow dominantly in the center of the stripes, therefore the largest Hall potential drop is found there.

Related to this question is also the limit of the width change. We want to consider here the situation with two distinct incompressible stripes at the edges, as in the edge-dominated breakdown. For increasing bias the external current flow in one of the stripes is in the same direction of the persistent current and increases the width of this stripe. But for the other stripe the external current flows against the persistent current reducing the stripe width. The question arising is what happens to the stripe with decreasing width if we continue to increase the current through it? We are especially interested

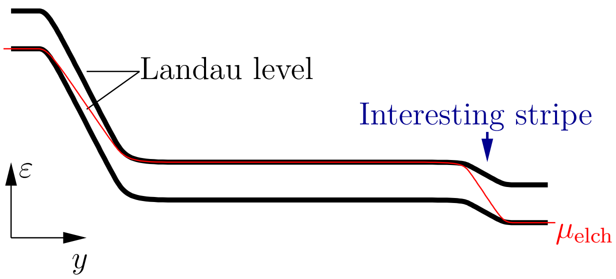

Figure A.3.: Landau level scheme for external currents within the incompressible stripe bigger than the persistent current.

if we can drive more external current than the original persistent current through this stripe which would lead into an Landau level scheme shown in Fig. A.3. Of course we can give an answers to these questions already with the measurements presented in this thesis, but we are not able to measure the exact gap between the Landau levels by our technique. The value of $\hbar\omega_c/e$ that was used throughout the thesis is effectively reduced with unknown amplitude by the spin splitting (there are known several effective g-factors of GaAs and it is not clear which to take). Thus we suggest the direct measurement of current using a SQUID (superconducting quantum interference device). Details on such a measurement are given in the following section.

With our breakdown model we can also try to understand more complicated sample structures. For example asymmetric confinement potentials at the edges. Siddiki et al. [229] did such measurements and compared the stability of quantum Hall plateaus with switching the current direction. He indeed could find an asymmetric breakdown with current direction. But a systematic study on how the breakdown transition is affected by an asymmetric confinement is still missing. Especially the dependence of the critical current on the asymmetry is of interest. In our model for the edge-dominated breakdown we also assume the breakdown mechanism to be effective only at the dominant edge. For the other edge we assumed cyclotron transitions of the electrons. This of course can only happen for small enough stripes. With asymmetric boundary conditions we could try to suppress the cyclotron emission while still have the breakdown mechanism only at the dominant stripe. The signature of such a situation would be a longitudinal voltage drop at the dominant edge and simultaneously a much smaller longitudinal voltage drop at the other edge. This might be possible as real samples are not translation invariant. This experiment delivers therefore information about what happens within the stripe which is not dominant.

In our measurements we also see some features that we did not investigate yet. Locking on the longitudinal voltage drop over bias voltage, for example in Fig. 13.2, one can identify for the bulk-dominated breakdown jumps after the onset of significant longitudinal voltage drops. These jumps become even more peculiar when traces are compared that are very close in magnetic field to each other. In this case it can happen, that the two traces compared collapse for small bias range on top of each other. This could be interpreted into an identical current paths through the sample. Since we also measured abrupt changes in the current path in our Hall potential profile measurements, the explanation sounds reasonable. Still measurements linking these jumps in longitudinal voltage with changing current path are missing. If true this could explain measurements done by Cage et al. [216]. He found in wide and high quality samples that the longitudinal voltage is jumping over well defined steps when sweeping magnetic field.

A.3. SQUID measurements

We want to discuss here an experiment with a static SQUID that should be able to answer the question if we can completely reverse the direction of the total current, meaning persistent plus external current, in the edge-dominated regime. We have to measure thus directly the total current within an incompressible stripe including the persistent current. This is not possible with the measurement technique used in this thesis since we can only measure the changes compared to thermal equilibrium. Therefore the persistent current flowing already during equilibrium is not measured and we need another technique like the one with a SQUID described next.

The arrangement of the sample and SQUID is shown in Fig. A.4 (a) while the sample itself is shown in Fig. A.4 (b). The main idea is to use a current carrying wire close to the SQUID to cancel the effects of the current through the sample with a feedback loop. The current through the wire is then proportional to the current through the incompressible stripe.

Even though this sounds like a piece of cake there are some calibration issues to be solved first. The easy task is to calibrate for the proportionality constant between feedback loop and real current through the samples. Only the arrangement is important for this calibration. We thus have to know the distance between SQUID and currents in the sample and the distance between SQUID and current carrying wire. The distance of the SQUID to the wires can be measured by a relative measurement of two neighboring

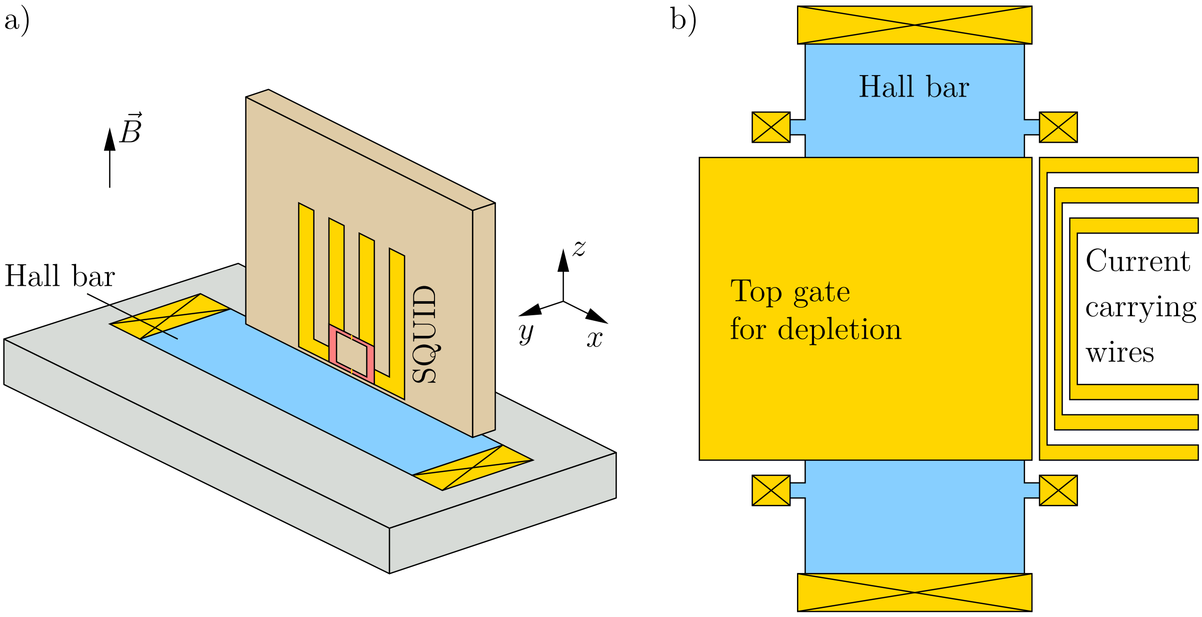

Figure A.4.: (a) arrangement of the static SQUID measurement and (b) actual sample design.

wires. The distance to the current in the sample is more tricky because we do not want to actively confine the current position. We need to make a relative measurement again, but this time a side gate has to shift the sample current until a maximum value is measured in the SQUID. During this situation the current is closest possible to the SQUID with a distance that has to be measured directly before the cool down. Releasing the current to its original path will give a correction to the signal that depends only on the lateral shift. Together with the distances to the current wires this gives the total calibration value.

The external magnetic field will give us an additional arbitrary offset since we will not be aligned perfectly perpendicular to the external field. This means that we also have to determine the zero current level. We could simply take the situation without biasing as the zero and assume to know the Landau level splitting. Since there are some complications affecting the Landau level gap like spin splitting we consider this not to be the best solution. We prefer to fully deplete the sample with a top gate zeroing this way any current and determining the zero point for our SQUID and feedback loop. After this calibration we can simply ramp up the current and measure directly the amount of current passing through the incompressible stripes.

B. Electrostatic simulations of graphene edges

For the understanding of the measured Hall potential profiles a certain electrostatic situation has to be assumed at the edges of graphene flakes on silicon oxide substrates. In particular we assume fixed negative charges either at the edges or on the open silicon oxide surface which alter the charge carrier concentration within the graphene flake towards the edges. To encourage this assumption as well as to deepen our understanding of the edge electrostatics we prepared a self-consistent electrostatic simulation of the charge carrier profile towards the edges.

Charge transport j within the flake is therein proportional to the gradient of the electrochemical potential μ_{elch}

$$j \propto \Delta\mu_{\mathrm{elch}}. \tag{B.1}$$

The electrochemical potential itself is the sum of the chemical potential μ_{ch} and the electrostatic energy $q\phi$

$$\mu_{\mathrm{elch}} = \mu_{\mathrm{ch}} + q\phi. \tag{B.2}$$

We choose to stay in a framework of positive carrier charge which simplifies the analysis of the results. Positive values in the charge carrier concentration η correspond throughout this chapter to holes and negative η to electrons. The chemical potential μ_{ch} of graphene (can be found, for example, in [233]) is proportional to the square root of the charge

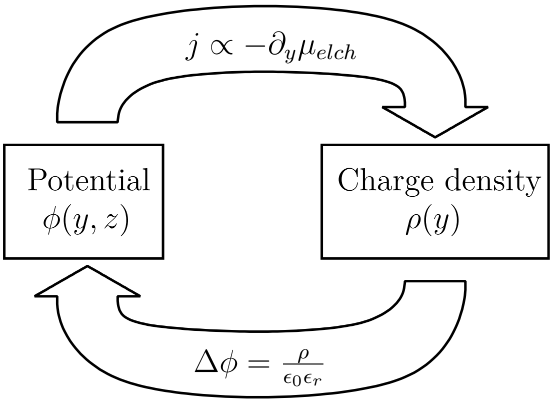
$j \propto -\partial_y \mu_{elch}$
Potential
$\phi(y,z)$
Charge density
$\rho(y)$
$\Delta\phi = \frac{\rho}{\epsilon_0 \epsilon_r}$

Figure B.1.: Sketch of the self-consistent loop.

carrier density η

$$\mu_{\mathrm{ch}}(\eta) = \mathrm{sgn}(\eta)\sqrt{|\eta|\pi v_{\mathrm{F}}^2\hbar^2} \tag{B.3}$$

It changes significantly by varying the charge carrier density in contrast to metals where μ_{ch} is nearly independent of the charge carrier concentration and can be neglected. This is why simply solving Poisson equation is here not sufficient and why we have to use a self-consistent simulation including the chemical potential variation on η.

In detail the self-consistent loop is drawn schematically in Fig. B.1. Starting from a given charge density distribution $\rho(y) = e\delta(y)$ we can find the electrostatic potential ϕ with the Poisson equation. With equation (B.3) and the found electrostatic potential we can now calculate current flow and thus a new charge carrier distribution. By this we have closed a loop. This loop is repeated until equilibrium is reached, i.e., all gradients in the electrochemical potential have disappeared.

For the geometrical considerations we want to assume a long rectangular graphene flake. In Fig. B.2 the geometry is shown schematically. The coordinate system was chosen according to a real sample, where x is the current flow direction, y shows across the sample and z perpendicular to it. Looking on a cross-section of this flake at the (y, z)-plane far away from contacts, the electrostatics would not change much when varying the x-position. Therefore we want to simplify the problem into a translation invariant one along the x-axes. In addition there is a mirror symmetry over the center of the flake through the (x, z)-plane. We will exploit that by only solving half of the geometry/flake taking into account this symmetry. Details on how the Poisson equation is discretized and solved can be found in section B.1 followed by a test to analytically solvable problems in section B.2.

The determination of the charge carrier distribution inside the graphene reduces into a one-dimensional problem and is further discussed in section B.3, followed by an analytic test.

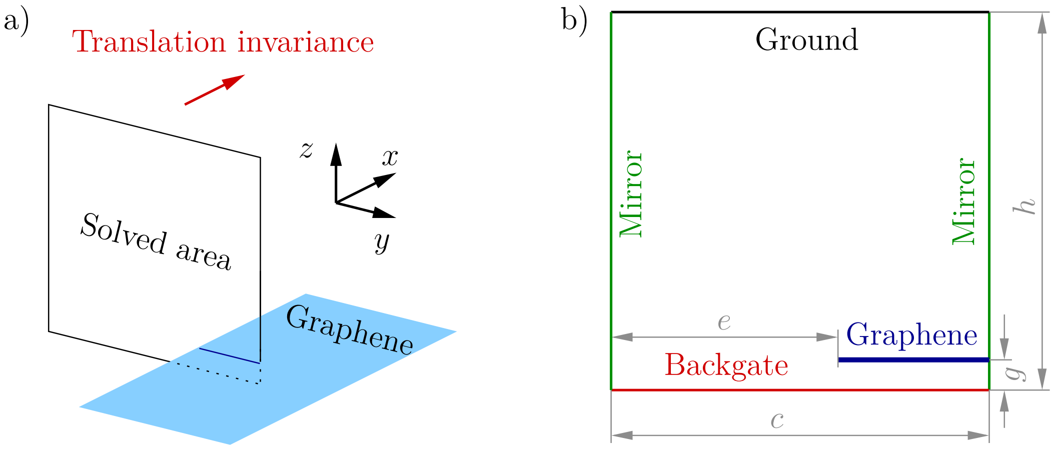

Figure B.2.: Schematic geometry of the calculated area.

B.1. Gauss-Seidel method to solve Poisson equation

The solution of the Poisson equation is the first step to determine the charge distribution. For the numerical solution of the two-dimensional Poisson equation

$$\partial_y^2\phi(y,z) + \partial_z^2\phi(y,z) = -\frac{\rho(y,z)}{\epsilon_0\epsilon_r}, \tag{B.4}$$

we need to discretize (finite differences method [234]). We will follow the derivation of Pang [235]. First one calculate the Taylor series of $\phi(y,z)$ in a distance of δ and $-\delta$ from y (and z):

$$\phi(y+\delta,z) = \phi(y,z) + \delta\partial_y\phi(y,z) + \frac{1}{2}\delta^2\partial_y^2\phi(y,z) + \frac{1}{6}\delta^3\partial_y^3\phi(y,z) + O(\delta^4), \tag{B.5}$$

$$\phi(y-\delta,z) = \phi(y,z) - \delta\partial_y\phi(y,z) + \frac{1}{2}\delta^2\partial_y^2\phi(y,z) - \frac{1}{6}\delta^3\partial_y^3\phi(y,z) + O(\delta^4). \tag{B.6}$$

In equation (B.5) as well as (B.6) we find the second derivative $\partial_y^2\phi(y,z)$ we are interested in to be replaced in equation (B.4). The error made by this approximation is proportional to δ^4 ($O(\delta^4)$). The sum of equation (B.5) and (B.6) leads after some transformations to

$$\partial_y^2\phi(y,z) = \frac{1}{\delta^2}[\phi(y+\delta,z) + \phi(y-\delta,z) - 2\phi(y,z)] + O(\delta^2). \tag{B.7}$$

In the same way we can find

$$\partial_z^2\phi(y,z) = \frac{1}{\delta^2}[\phi(y,z+\delta) + \phi(y,z-\delta) - 2\phi(y,z)] + O(\delta^2). \tag{B.8}$$

Putting equation (B.7) and (B.8) into the Poisson equation (B.4) we find the discretized Poisson equation

$$\phi(y,z) = \frac{1}{4}\left[\phi(y+\delta,z) + \phi(y-\delta,z) + \phi(y,z+\delta) + \phi(y,z-\delta) + \frac{\delta^2\rho(y,z)}{\epsilon_0\epsilon_r}\right] \tag{B.9}$$

In the chosen representation of the Poisson equation, the value of the potential ϕ in the position (y,z) is the average of the nearest neighboring points plus one fourth of the charge at (y,z) divided by the dielectric constant.

The transition to a discretized equation can be made more obvious by changing from actual coordinates to indexes as shown in Fig. B.3

The according representation of the Poisson equation is therefore

$$\phi_{i,j} = \frac{1}{4}\left[\phi_{i+1,j} + \phi_{i-1,j} + \phi_{i,j+1} + \phi_{i,j-1} + \frac{h^2\rho_{i,j}}{\epsilon_0\epsilon_r}\right]. \tag{B.10}$$

Equation (B.10) can be understood as a system of linear equations that can be solved, for example, by the Gauss-Seidel-method. The Gauss-Seidel-method is an iterative method. Thereby a new $\phi_{i,j}$ is calculated according to equation (B.10) for each step. Doing so the $\phi_{i,j}$ converge to the final result. A twist special to the Gauss-Seidel-method is that one does not distinguish between new and old $\phi_{i,j}$ within an iteration step. This

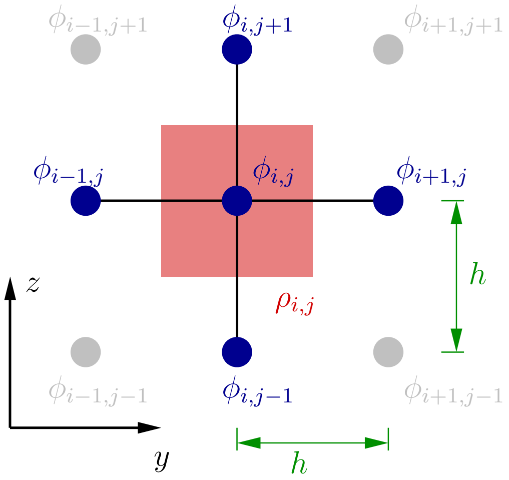

Figure B.3.: Labeling of grid positions and physical quantities for the Poisson solver. The (y, z) plane is covered by a equidistant grid with node positions labeled by (i, j). Physical quantities, e.g. ρ ϕ, at position (i, j) are referred by $\rho_{i,j}$ $\phi_{i,j}$.

means that after the calculation of a new $\phi_{i,j}$ it replaces the old value in memory. Thus in the calculation of for example the new $\phi_{i+1,j}$, also the new $\phi_{i,j}$ is used.

Finally we want to have a look on boundary conditions. In the simplest case the boundaries have all fixed potentials and do not need to be touched. But in case a boundary should acts as mirror we have to adjust equation (B.10). In this case one or two points of equation (B.10) are outside of the calculated area but we know their value because of the mirroring. They are replaced by the points across the mirror line inside the calculated area. This will be explicitly the case at the right boarder of the area calculated. We give the points on this boarder the index (c, j) and equation (B.10) transforms for such a point to

$$\phi_{c,j} = \frac{1}{4}\left[2\phi_{c-1,j} + \phi_{c,j+1} + \phi_{c,j-1} + \frac{h^2\rho_{c,j}}{\epsilon_0\epsilon_r}\right]. \tag{B.11}$$

Before using our implementation of this method to solve Poisson equation in the self-consistent loop we want to run a test. This is done in the following section.

B.2. Simple test on a line charge distribution

A simple test of the code solving Poisson equation in the above described way is the simulation of a single straight infinitely long line charge along the x direction. The simulated results can be compared with analytic solutions of the problem.

The geometry of the simulation is shown in Fig. B.4 (a). Here the line charge is positioned in the center of the simulated area and the edges of this area have been set to ground.

To find the analytic solution first the radial electric field $E(r)$ of an infinitely long straight line charge has to be calculated. r is here the distance to the line charge within

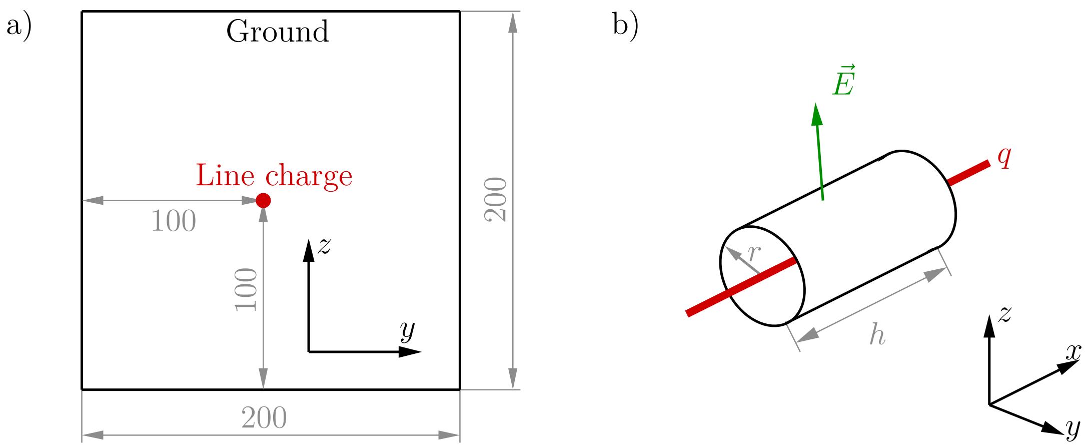

Figure B.4.: (a) Charge arrangement and simulated area. (b) Geometry for the calculations of the electric field $\vec{E}(r)$ of a line charge q.

the (y, z)-plane. Because of the symmetry of the problem, cylindrical coordinates have been used where the line-charge is positioned on the z-axes. The electric field vector is thereby directed parallel to the radial direction $\vec{e}_r$. Gauss's law in the integral formulation

$$\int\limits_S DdS = \int\limits_V \rho dV \tag{B.12}$$

has been used in the geometry shown Fig. B.4 (b) to calculate the electric field. The flux of electric displacement field $D = \epsilon_0 \epsilon_r E$ perpendicular to the surface S of the volume V is the same as the charge within the volume V. Due to the symmetry only the lateral surface of the cylinder has to be taken into account leading for an arbitrary cylinder length l, see Fig. B.4 (b), to

$$\epsilon_0 \epsilon_r E(r) 2\pi r l = ql. \tag{B.13}$$

Therefore the electric field radially to the line charge decays with r^{-1}:

$$E(r) = q \cdot \frac{1}{\epsilon_0 \epsilon_r 2\pi r}. \tag{B.14}$$

The potential can be found by integrating the electric field $E(r)$ in equation (B.14):

$$\begin{aligned} \phi(r) &= -\int\limits_0^r E(r)dr + \phi_1, \\ &= -q \cdot \frac{ln(r)}{\epsilon_0 \epsilon_r 2\pi} + \phi_{\text{offset}}. \end{aligned} \tag{B.15}$$

ϕ_{offset} and ϕ_1, respectively, are offsets or, in other words, a gauge degree-of-freedom. They have to be set according to the boundary conditions of the simulation, meaning $\phi(r)$ to be zero at the boundaries. The comparison between simulation and calculation can be found in Fig. B.5. A good agreement can be found which proofs the Poisson solver of the simulation to run correctly.

To exclude also scaling errors and an accidental fit of the simulation at the chosen model dimensions, we changed the size of the simulated area by changing the size of the node spacing δ. Three simulations are shown in Fig. B.5. It appears like only the scale in the position axes has changed while the graph remained the same. This comes from the actual charge density and the Poisson equation as we will show in the following. Our line-charge lies on top of the z-axes in a cylindrical coordinate system and is not affected by a stretch of the coordinate system in the radial direction. Therefore the stretch can be accounted by just scaling the argument of ϕ in the two-dimensional Poisson equation in cylindrical coordinates by a scalar a:

$$\frac{1}{r}\frac{\partial}{\partial r}[r\frac{\partial}{\partial r}\phi(a\cdot r)] = -\frac{\rho(r)}{\epsilon_0\epsilon_r}. \tag{B.16}$$

To come back to the non-scaled Poisson equation we need to transform the coordinate from r to u:

$$u = a\cdot r, \qquad i.e. \qquad \frac{\partial u}{\partial r} = a. \tag{B.17}$$

Doing so we find the scalar a^2 as factor on the left side of the equation:

$$\frac{a}{u}\frac{\partial u}{\partial r}\frac{\partial}{\partial u}\left[\frac{u}{a}\frac{\partial u}{\partial r}\frac{\partial}{\partial u}\phi(u)\right] = -\frac{\rho\left(\frac{u}{a}\right)}{\epsilon_0\epsilon_r}, \tag{B.18}$$

$$\frac{a^2}{u}\frac{\partial}{\partial u}\left[u\frac{\partial}{\partial u}\phi(u)\right] = -\frac{\rho\left(\frac{u}{a}\right)}{\epsilon_0\epsilon_r} \tag{B.19}$$

To further resolve the right side of equation (B.19) we have to specify the charge distribution:

$$\rho(r) = q\frac{\delta(r)}{2\pi r}. \tag{B.20}$$

Here the δ-function in cylindrical coordinates has been used, causing the one over r dependence, and the 2π being a result of skipping the angular delta function. Knowing that a factor inside a delta function can be replaced by its inverse in front of the delta function we further find

$$\rho\left(\frac{u}{a}\right) = q\frac{a\cdot\delta\left(\frac{u}{a}\right)}{2\pi u} = q\frac{a^2\cdot\delta(u)}{2\pi u} = a^2\cdot\rho(u). \tag{B.21}$$

With this we can reduce equation (B.19) to the non-scaled Poisson equation

$$\frac{1}{u}\frac{\partial}{\partial u}\left[u\frac{\partial}{\partial u}\phi(u)\right] = -\frac{\rho(u)}{\epsilon_0\epsilon_r}, \tag{B.22}$$

which proves that scaling the radial axis does not change the potential landscape for this particular problem. The direct consequence is that in Fig. B.5 the graphs have to be

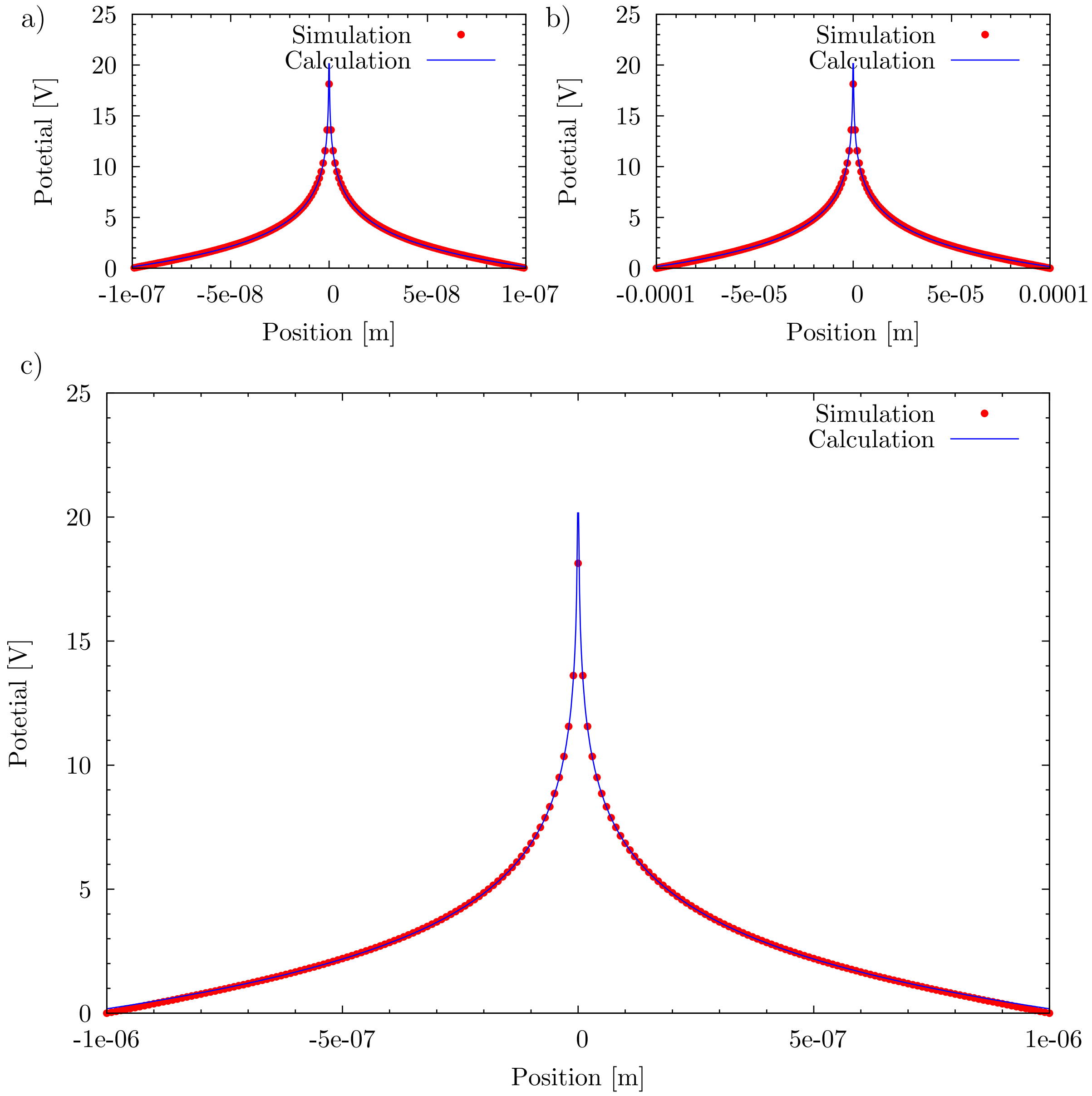

Figure B.5.: Comparison between simulation and analytic solution. The three diagrams show the solution for a line charge as described in Fig. B.4 for different lattice spacing δ. The only fit parameter available was ϕ_{offset} which had to be set so that $\phi(r)$ at the boundaries becomes zero. The potential axis scaling remains identical independent of the chosen δ.

identical after taking care of the boundary conditions:

$$\phi^{(a)}(r) = \phi^{(b)}(a \cdot r) + const. \tag{B.23}$$

B.3. Charge transfer algorithm

As already mentioned before we need for our self-consistent loop, shown in Fig. B.6, to transfer charges from and to the flake. The reason behind this necessity is the dependence of the local chemical potential μ_{ch} on the local charge carrier density ρ, see equation (B.3). The amount of charge locally transferred is proportional to the negative gradient of the electrochemical potential μ_{elch} since this represents the net driving force. We are only interested in the static equilibrium situation. Therefore we can neglect the details affecting the dynamics and it is sufficient to introduce a (positive) transfer parameter q_{t}

$$d\rho(y) = -q_{\mathrm{t}} \cdot \partial_y \mu_{\mathrm{elch}}(y) \tag{B.24}$$

to achieve convergence into equilibrium. $d\rho(y)$ is thereby the charge density added to the position y. Since we choose the coordinate system such that we cut across the graphene flake, see Fig. B.2, the problem became one dimensional. This is why the electrochemical potential and the charge density depends only on y. The value o the parameter q_{t} was chosen so that the simulation does not diverge but also converges in an appropriate number of iteration steps. We can use this simple approach because we have here an open system allowing for free charge redistribution.

Before deriving the final discrete iterative formula we have to include two difficulties originating from the chosen and given geometry. As shown in Fig. B.2 a simple way to reduce calculation power is to assume a mirror-symmetric flake. Doing so we need to calculate only one half of the flake. What we also have to do is to keep the flake on a given electrochemical potential which is given by the external contacts. Since we did

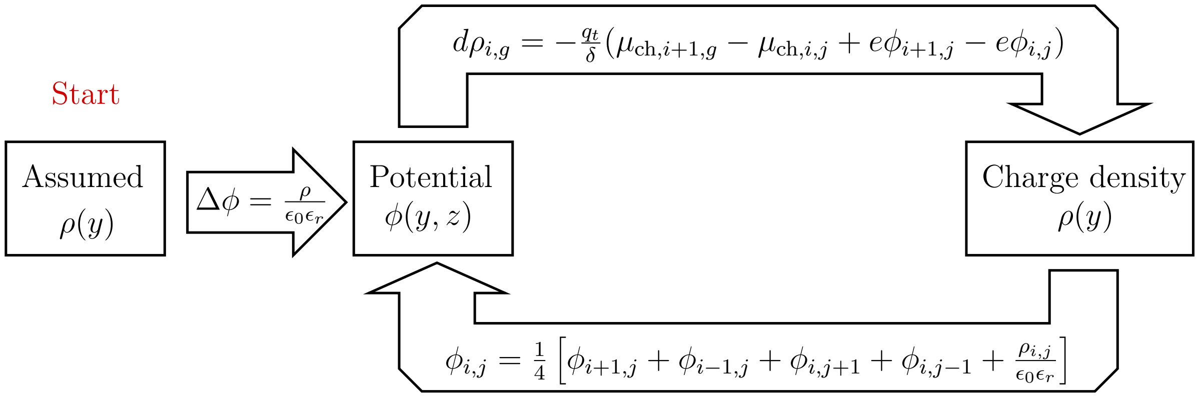
$d\rho_{i,g} = -\frac{q_t}{\delta}(\mu_{\mathrm{ch},i+1,g} - \mu_{\mathrm{ch},i,j} + e\phi_{i+1,j} - e\phi_{i,j})$
Start
Assumed $\rho(y)$
$\Delta\phi = \frac{\rho}{\epsilon_0\epsilon_r}$
Potential $\phi(y,z)$
Charge density $\rho(y)$
$\phi_{i,j} = \frac{1}{4}\left[\phi_{i+1,j} + \phi_{i-1,j} + \phi_{i,j+1} + \phi_{i,j-1} + \frac{\rho_{i,j}}{\epsilon_0\epsilon_r}\right]$

Figure B.6.: Calculation scheme for finding the charge carrier concentration. Starting from an guessed $\rho(y)$ we calculate with the Poisson solver the electrostatic potential ϕ. From there we calculate the change of charge carrier density with equation (B.28) once leading to a new ρ. Then we calculate once the potential change with equation (B.10) to find a new ϕ. This loop is repeated until no significant changes occur.

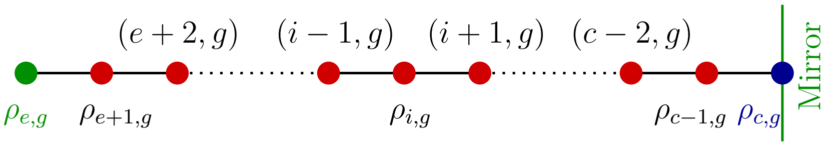

Figure B.7.: Labeling of points on the graphene flake.

not include any contacts in this simulation we have to do this artificially. But instead of keeping the electrochemical potential constant we preferred to keep the electrostatic potential constant. This is technically much easier and introduces only a negligible error.

The point on the grid, where both problems - fixing the electrostatic potential and handling the mirroring - have to be taken into account, is (c, g) (see Fig. B.7), which is the center of the flake. Fixing the electrostatic potential means simply setting

$$\phi_{c,g} = const, \tag{B.25}$$

where the constant was chosen usually to be zero. The mirroring of the potential at the boundaries is taken care by replacing the points beside the boundary lying outside the calculated area by their mirror points inside the calculated area. This was discussed in section B.1 and explicitly given in equation (B.11). Thereby we get a local minimum or maximum in the electrochemical potential and therefore no change of $\rho_{c,g}$ can be calculated by equation (B.24). The charge density $\rho_{c,g}$ has also to be a local minimum or maximum for symmetry reasons and has to be adjusted to its neighbors to guarantee conversion of the algorithm. We achieve this by simply setting

$$\rho_{c,g} = \rho_{c-1,g}. \tag{B.26}$$

In addition we have to consider the situation at the site (e, g) (see Fig. B.7), which is the flake edge. Here we want later to fix the charge to simulate a charged graphene edge. In equilibrium the $\rho_{e,g}$ and $\rho_{e+1,g}$ will have opposite polarity. This is simply because the fixed density $\rho_{e,g}$ attracts charges with opposite polarity. The gradient of the electrochemical potential $\partial_y \mu_{\text{elch}}$ between these two sites becomes very large and is not allowed to be resolved by charge transfer since we want to keep the edge charge fixed. Therefore to calculate $d\rho_{e+1,g}$ we are only allowed to use the numerical gradient between site $(e+1, g)$ and $(e + 2, g)$. Otherwise the simulation will diverge. To treat all points similar this means in general

$$d\rho_{i,g} = \frac{q_{\text{t}}}{\delta} \cdot (\mu_{\text{elch},i+1,g} - \mu_{\text{elch},i,g}). \tag{B.27}$$

Important to note is the change of the sign of $d\rho_{i,g}$ compared to equation (B.24). This is because without the sign change we calculate the change of charge at site $(i + 1, g)$ which is the inverse of site (i, g). Actually after resolving the electrochemical potential with equation (B.2) the final discretizes formulation for charge transfer becomes

$$d\rho_{i,g} = \frac{q_{\text{t}}}{\delta} \cdot (\mu_{\text{ch},i+1,g} - \mu_{\text{ch},i,g} + e\phi_{i+1,g} - e\phi_{i,g}). \tag{B.28}$$

The chemical potential can be found in equation (B.3). Minor changes, to include the parameters used in the simulation like charge density ρ and lattice spacing δ, deliver the applicable formulation for chemical potential as used in the simulation:

$$\mu_{\mathrm{ch}}(\rho) = \mathrm{sgn}(\rho)\sqrt{\frac{|\rho|\delta\pi v_{\mathrm{F}}^2\hbar^2}{e}}. \tag{B.29}$$

The scheme of a full simulation is given in Fig. B.6. We start with a charge carrier density ρ that we guessed, and use equation (B.10) iteratively until the solution for this charge density is found. From thereon we calculate in a loop once with equation (B.28) a new charge carrier density and then once with equation equation (B.10) a new electrostatic potential. This is repeated until no significant changes happen any more.

B.4. Influence of the back gate on the edge

So far we explained the two parts of our self-consistent loop within the electrostatic simulation. We showed already that we can calculate the electrostatics in case no charge transfer is allowed. In this section we want to test our simulation in case charge transfer is allowed. We will look on the influence of the back gate on the edges of a graphene

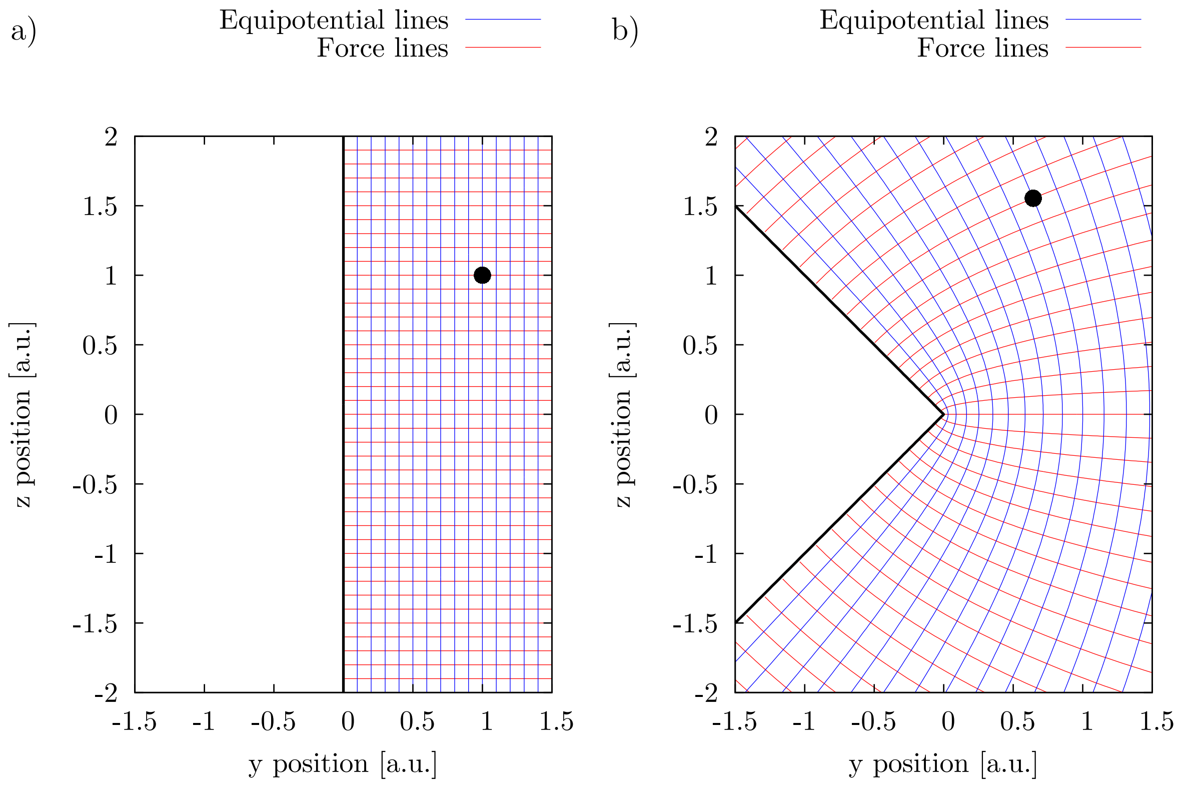

Figure B.8.: Conformal mapping of the half-plane with positive real part in (a) by $f(x+iy) = (x+iy)^{1.5}$ resulting in (b). The equipotential and force lines keep their meaning after the transformation.

flakes for this. Since already C.K. Maxwell calculated the charge distribution of the geometry we use [140], this becomes a good test for the charging algorithm developed last section. Before going into the result we want to briefly describe Maxwell's way to solve the problem of a finite plate capacitor using conjugate functions.

Two function ϕ and ψ are conjugate functions if they can be formulated as a function f of $y + iz$ in the following form:

$$\phi + i\psi = f(y + iz). \tag{B.30}$$

Figure B.8 shows an example of conformal mapping, meaning the transformation of $y+iz$ to $f(y+iz)$. Explicitly the function $y+iz$, plotted in Fig. B.8 (a), was mapped to Fig. B.8 (b) by the function $f(y + iz) = (y + iz)^{1.5}$. As can be seen, conformal mapping conserves the right angles between the blue and red line in Fig. B.8. One can also show that ϕ and ψ fulfill the two-dimensional Laplace equation (translation invariance in one dimension). Using conjugate functions one can shift the problem of solving Laplace equation into finding the conjugate functions. In addition, lines of equal height in ϕ are always perpendicular to lines of equal height in ψ. Interpreting lines of equal height in ϕ as equipotential lines, lines of equal height in ψ become force lines. Without changing the electrostatic landscape, metal surfaces can be placed along equipotential lines that divide the area into two segments.

For the arrangement of interest, a semi-infinite plane over an infinite plane, see Fig. B.9, Helmholtz found suitable conjugate functions [140]

$$y = A\psi + Ae^{\psi}\cos\phi \tag{B.31}$$
$$z = A\phi + Ae^{\psi}\sin\phi. \tag{B.32}$$

For $\phi = 0$ we find the infinite plane at $z = 0$ and for $\phi = \pi$ a semi-infinite plane at $z = A\pi = d$ extending from $y = -A$ to $y = -\infty$. The potential difference between the two planes is thus π and we have to scale ϕ and ψ by $k = V/\pi$ to achieve the desired situation with electrostatic potential difference of V. The equipotential and force lines

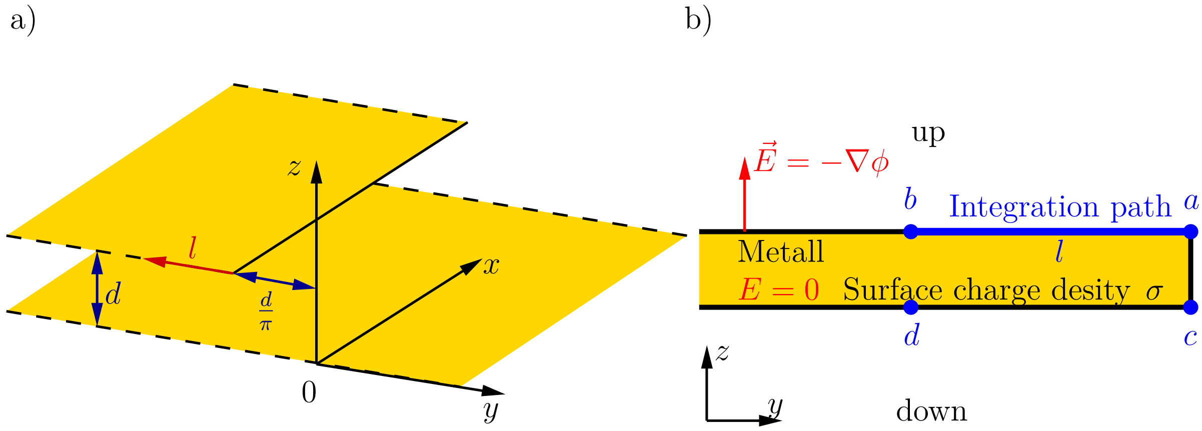

Figure B.9.: (a) Geometry to be solved with a semi-infinite and an infinite plane. (b) Definition of the integration path and upper and lower side.

are plotted in Fig. B.10.

We are interested here in finding the charge density positioned on the semi-infinite plane. First we have to find the charges on the plane between two points a and b. We know the electric field discontinuity $\Delta E = -k\vec{e_z}\nabla\phi = \sigma/(\epsilon_0\epsilon_r)$ at the metal planes (zero field inside the plane, $-k\nabla\phi$ outside), where σ is the surface charge. Therefore we can find the charge per unit length q by integrating over $-\epsilon_0\epsilon_r k\nabla\phi$ along the surface of the plane (y-direction), as shown in Fig. B.9 (b) for the upper side of the semi-infinite plane

$$q = -\epsilon_0\epsilon_r \int_a^b k\,\partial_z\phi\,dy. \tag{B.33}$$

Since the integral runs along an equipotential line parallel to the y-axes, we can simplify the gradient by the derivative along the z-direction. One can easily show with $\partial_z\phi = \vec{e_z}\nabla\phi$ and the properties of conjugate functions that

$$\partial_z\phi = -\partial_y\psi \tag{B.34}$$

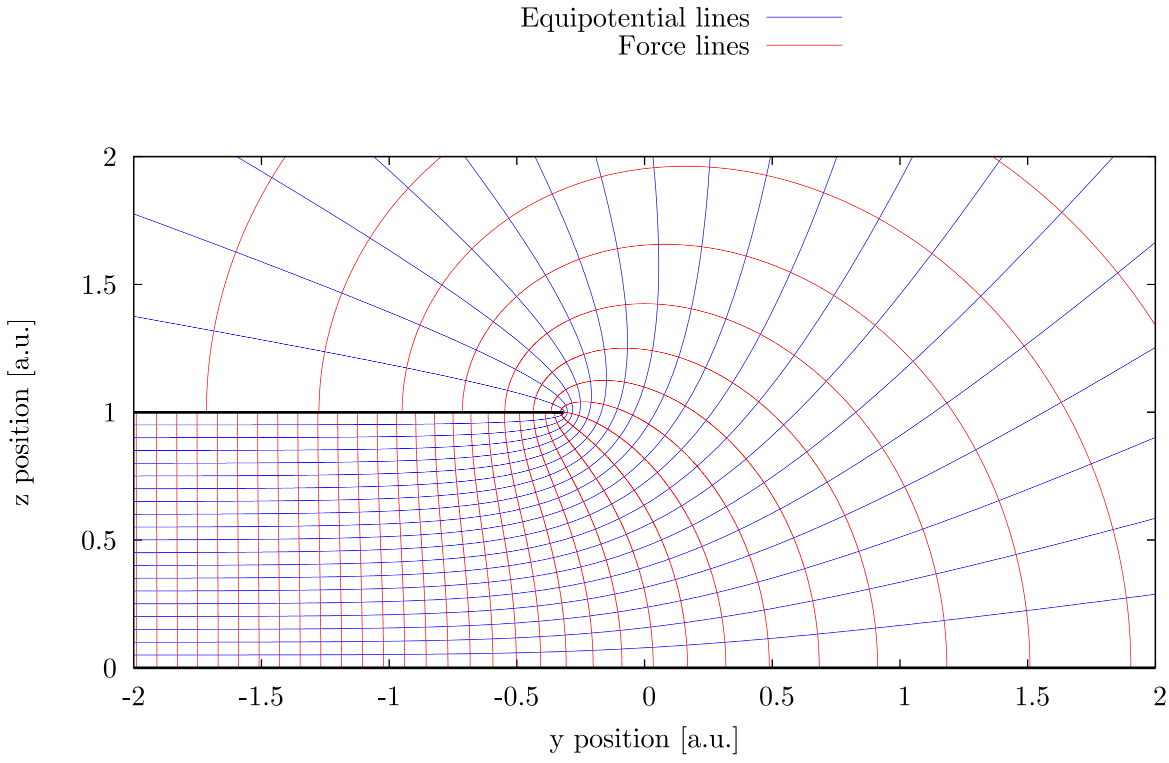

Figure B.10.: Geometry described by equation (B.31) and (B.32). Equipotential and force lines are drawn for a semi-infinite plane parallel to a infinite plane. The infinite plane lies in the x-axes and extend perpendicular to the graph and the semi-infinite plane is the black line at $y = 1 = d$.

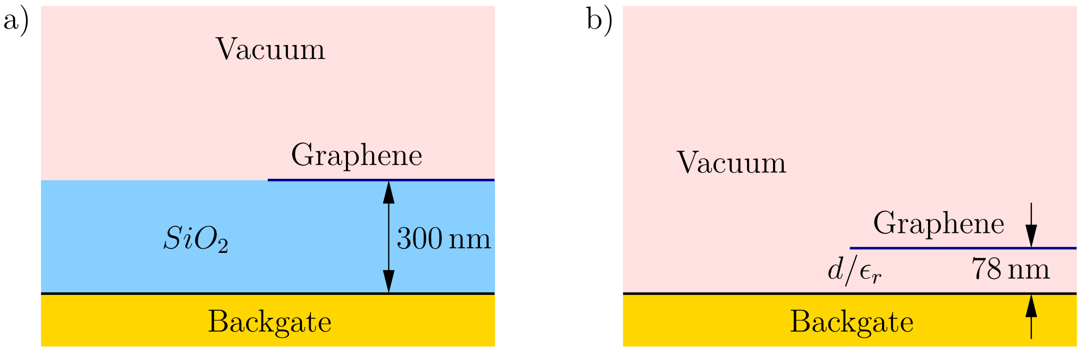

Figure B.11.: (a) Real geometry with dielectric and (b) equivalent geometry without dielectric but scaled distance d/ϵ_r.

is always valid and that equation (B.33) simplifies to

$$q = \epsilon_0 \epsilon_r k[\psi(b) - \psi(a)]. \tag{B.35}$$

This means we can calculate quite simple from ψ the amount of charge on a metal plane.

As it is shown in Fig. B.9 (b) to find the charge density on the semi-infinite plane we have to distinguish between the upper and lower side of the plane. We want to follow the notation of Fig. B.9 (b) giving the two charges per unit length q_{up} and q_{down}, where q_{up} results from the integration from a to b and q_{down} from the integration from c to d. Further we want to consider the accumulated charge per unit length from the edge up to a distance l with in the semi-infinite plane. This results in

$$q_{\mathrm{down}}(l) = \frac{\epsilon_0 \epsilon_r V}{d}\left(l + \frac{d}{\pi}\right), \tag{B.36}$$

$$q_{\mathrm{up}}(l) = \frac{\epsilon_0 \epsilon_r V}{\pi} \ln\left[1 + \frac{\pi}{d} l \ln\left(1 + \frac{\pi}{d} l\right)\right]. \tag{B.37}$$

The charge carrier density η at each position on the semi-infinite plane can be found with

$$\eta = \frac{\partial_l q}{e}. \tag{B.38}$$

Since graphene is two-dimensional there is no sense in distinguishing between q_{down} and q_{up}. We consider instead the sum $q_{\mathrm{down}} + q_{\mathrm{up}}$. The total charge carrier density η_{m} at position l becomes with equations (B.36), (B.37) and (B.38)

$$\eta_{\mathrm{m}}(V, l) = \frac{\epsilon_0 \epsilon_r V}{ed} + \frac{\epsilon_0 \epsilon_r V}{ed} \frac{1}{1 + \frac{\pi}{d} l + \ln\left(1 + \frac{\pi}{d} l\right)}\left[1 + \frac{1}{1 + \frac{\pi}{d} l}\right]. \tag{B.39}$$

In a real experiment we apply the voltage on the back gate instead of on the flake. This

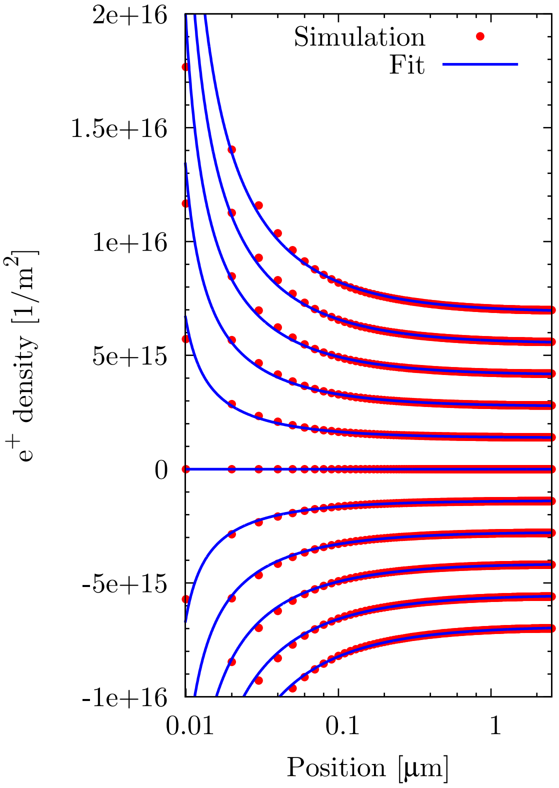

Figure B.12.: Comparison between Maxwell's charge carrier density from equation (B.40) and the simulation results. The back gate was swept from $-10\,\mathrm{V}$ (uppermost line) to $10\,\mathrm{V}$ (lowermost line) in steps of $2\,\mathrm{V}$.

leads to a sign change because of $V_{\mathrm{BG}} = -V$ and results in

$$\eta_{\mathrm{m}}(V_{\mathrm{BG}}, l) = -\frac{\epsilon_0 V_{\mathrm{BG}}}{e\frac{d}{\epsilon_r}} - \frac{\epsilon_0 V_{\mathrm{BG}}}{e\frac{d}{\epsilon_r}} \frac{1}{1 + \frac{\epsilon_r \pi}{d} l + \ln\left(1 + \frac{\epsilon_r \pi}{d} l\right)} \left[1 + \frac{1}{1 + \frac{\epsilon_r \pi}{d} l}\right]. \tag{B.40}$$

Also the dielectric was included in here. Since the silicon oxide lies between the two planes, as can be seen in Fig. B.11, we can account for it by removing it and changing the distance between the planes. This is done by scaling d with the relative dielectric constant ϵ_r to d/ϵ_r.

As seen in Fig. B.12 there is an excellent agreement between simulation and calculation meaning the charge creation algorithm is working correctly.

B.5. Summary

In this chapter we explained how we find the charge carrier concentration in graphene near the edges. We use a self-consistent loop consisting of two elements. First a Poisson solver and second a charge transfer algorithm including electrostatic and charge carrier density. The charge carrier density determines the local chemical potential and is the reason why a self-consistent loop is necessary. Using the Poisson solver the electrostatic part for the charge transfer algorithm is calculated. Using the local electrostatic and charge carrier density gradients the local amount of charge is changed. The new charge distribution goes then into the Poisson solver. The self-consistent simulation was also tested on the analytic solvable semi-infinite parallel plate capacitor.

C. Models for fixed charge arrangements

To extract valuable information from the simulation described in chapter B, different geometries of fixed charges were tested. Analytic functions were then fitted onto the simulated data to be used for further analysis on the Hall potential profiles.

C.1. Empirical function and parameter for a fixed line charge at the edge

The analytic determination of the charge density profile across an edge is difficult. Therefore we decide to find a suitable function by fitting proper analytic functions to our simulation. We added a line charge in our geometry as shown in Fig. C.1 and did several runs with different amount of line charge. The back gate was kept thereby at zero. Finally we tried to fit all the data by just one function. The fit was intended to be best between 100 nm to 1 µm. The charge carrier density present in the samples for filling factor $\nu = 2$ was in the order of $10^{15}\,\mathrm{m}^{-2}$ ($B = 3\,\mathrm{T}$, $V_{\mathrm{BG}} - V_{\mathrm{CNP}} = 2\,\mathrm{V}$, $n = 1.39 \cdot 10^{15}\,\mathrm{m}^{-2}$). Therefore the fit was also pushed to be optimal in the density range of $10^{15}\,\mathrm{m}^{-2}$ to $10^{16}\,\mathrm{m}^{-2}$.

The simulated area was 10 µm ×10 µm in size and the flake of 5 µm cross-section was centered at the right edge of the area 80 nm above the lower fixed potential plane representing the back gate. The line charge was positioned at both edges because of the symmetric calculation (calculating only half the flake and mirroring for the other half).

We assumed for on infinitely large graphene flake a charge carrier density profile $\eta_{\mathrm{l}}(y)$ that goes with y^{-2}. In particular the profile should be proportional to the line charge η_{fl} with the proportionality constant c_{l} leading to the profile

$$\eta_{\mathrm{l}}(y) = \frac{c_{\mathrm{l}}\eta_{\mathrm{fl}}}{y^2}. \tag{C.1}$$

Since we simulate a finite size flake with width w we have to consider the effect of the second edge too, leading to the used fit function

$$\eta_{\mathrm{l}}(y) = \frac{c_{\mathrm{l}}\eta_{\mathrm{fl}}}{y^2} + \frac{c_{\mathrm{l}}\eta_{\mathrm{fl}}}{(w-y)^2}. \tag{C.2}$$

Using this function we achieved a good agreement with the simulation as can be seen in Fig. C.1. Thereby $y = 0$ is at the simulated edge of the flake. Here c_{l} is the constant we have to determine by the fit, and the value extracted was

$$c_{\mathrm{l}} = -4.3 \cdot 10^{-9}\,\frac{1}{\mathrm{m}}. \tag{C.3}$$

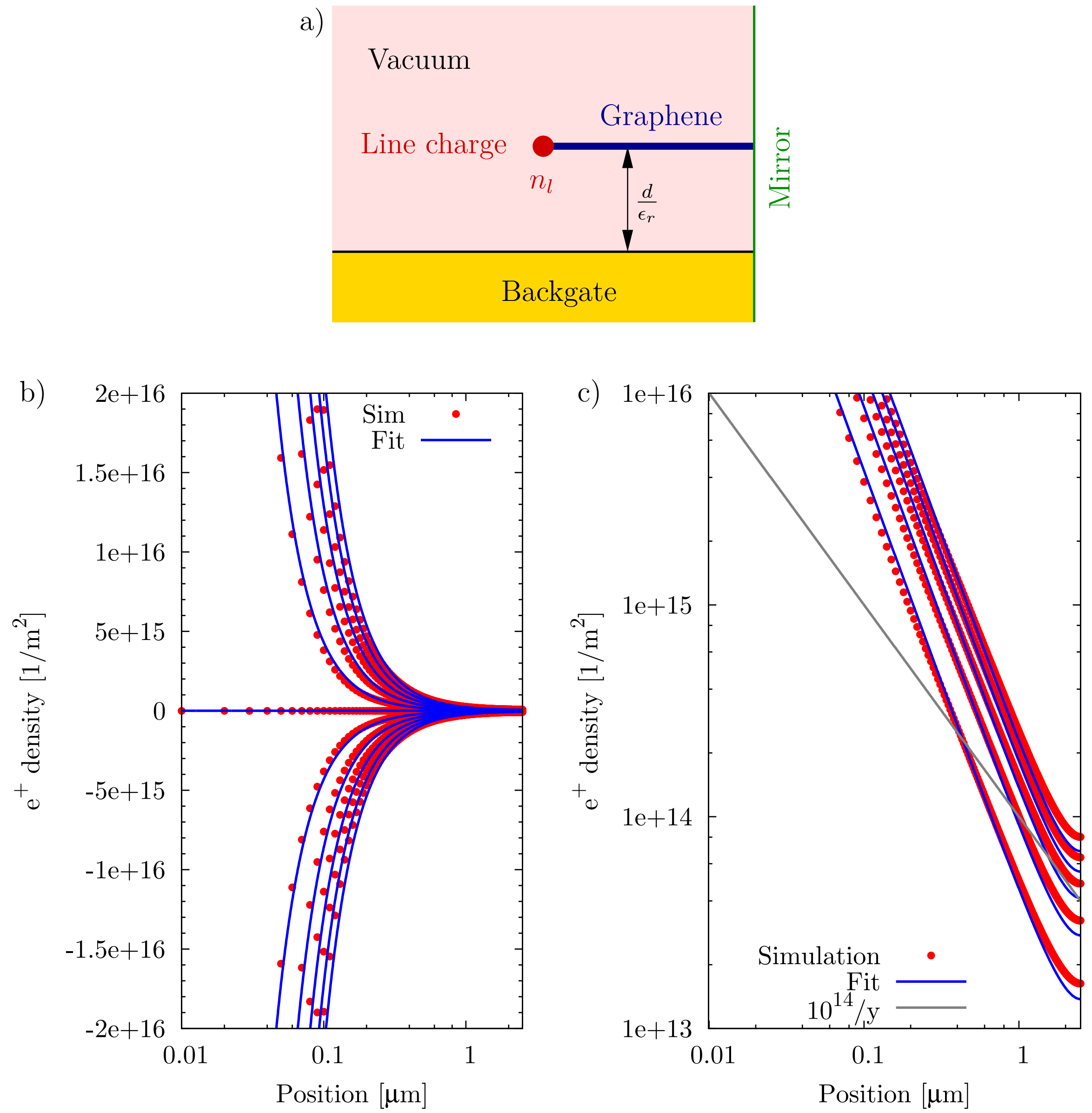

Figure C.1.: Simulation of fixed line charge with the arrangement shown in (a) and fitted with a y^{-2} function (see equation (C.2)) (a) presented in linear scale and (b) in double logarithmic scale. Also shown in (c) is a y^{-1} function for comparison. The line charge was changed from zero (undermost line) to $-5 \cdot 10^{10}\,e/\mathrm{m}$ (uppermost line) in steps of $1 \cdot 10^{10}\,e/\mathrm{m}$. The parameters for the simulation shown in Fig. B.7 (b) are: $c = h = 1001$; $e = 750$; $g = 8$. g represents d/ϵ_r and is set to be equivalent to 80 nm meaning a d of 312 nm. The simulated flake has a cross-section of 5 µm and is 15 µm from its mirrors away. The line charge η_{fl} is positioned at (e, g). The distance to the upper grounded plane is 9.92 µm.

Even though the model of Chklovskii et al. [92] was intended for a different arrangement not involving fixed charges, we wanted to see how well it fits. Chklovskii et al. calculated a charge carrier density profile that goes with y^{-1} far away from the edges. This function (C.2) is plotted in addition in Fig. C.1 (b) and (c). As can be seen easily in case of line charges the model of Chklovskii et al. fails to describe the charge carrier density profile. It has to be emphasized here that this is not true for surface charges discussed in section C.4.

C.2. Effect of line charge displacement

A question on our model is how the distance between graphene flake and the line charge affects the results. To answer this question we run a simulation where we displaced the line charge by a distance s, see Fig. C.2 (a). The result is plotted in Fig. C.2 (b) half logarithmic and in (c) double logarithmic.

Two features are observable. First, the total induced charge in the flake reduces with the displacement of the line charge. And second, the profile of the charge carrier density changes from a y^{-1} profile to a y^{-2} profile at zero displacement. Thus our model is applicable only in case the line charge is sitting at the graphene edge.

C.3. Including the doping

Doping in graphene can be done in several ways, for example, by adsorbates on the flake or charged defects on or inside the supporting substrate. In our simulation we included doping as a charged layer between the graphene and the back gate. To account correctly for its effect we start with Gauss's law in the integral form

$$\int_{\partial V} D dA = \int_{V} \rho dV \tag{C.4}$$

to extract the relation between charge density and electric field discontinuity in the geometry shown in Fig. C.3 (a):

$$E_1 + E_2 = \frac{e\eta_\mathrm{D}}{\epsilon_0 \epsilon_r}. \tag{C.5}$$

Since the graphene and the back gate were chosen to be grounded, see Fig. C.3 (b), the voltage difference between back gate and doping layer ($E_1 d_1$) has to be equal to the difference between graphene and doping layer ($E_2 d_2$):

$$E_1 d_1 = E_2 d_2. \tag{C.6}$$

Using relation (C.5) and (C.6) one can find the doping induced charge carrier concentration η_d:

$$\eta_\mathrm{d} = -\frac{\epsilon_0 \epsilon_r E_1}{q} = -\eta_\mathrm{D} \frac{d_2}{d_1 + d_2}. \tag{C.7}$$

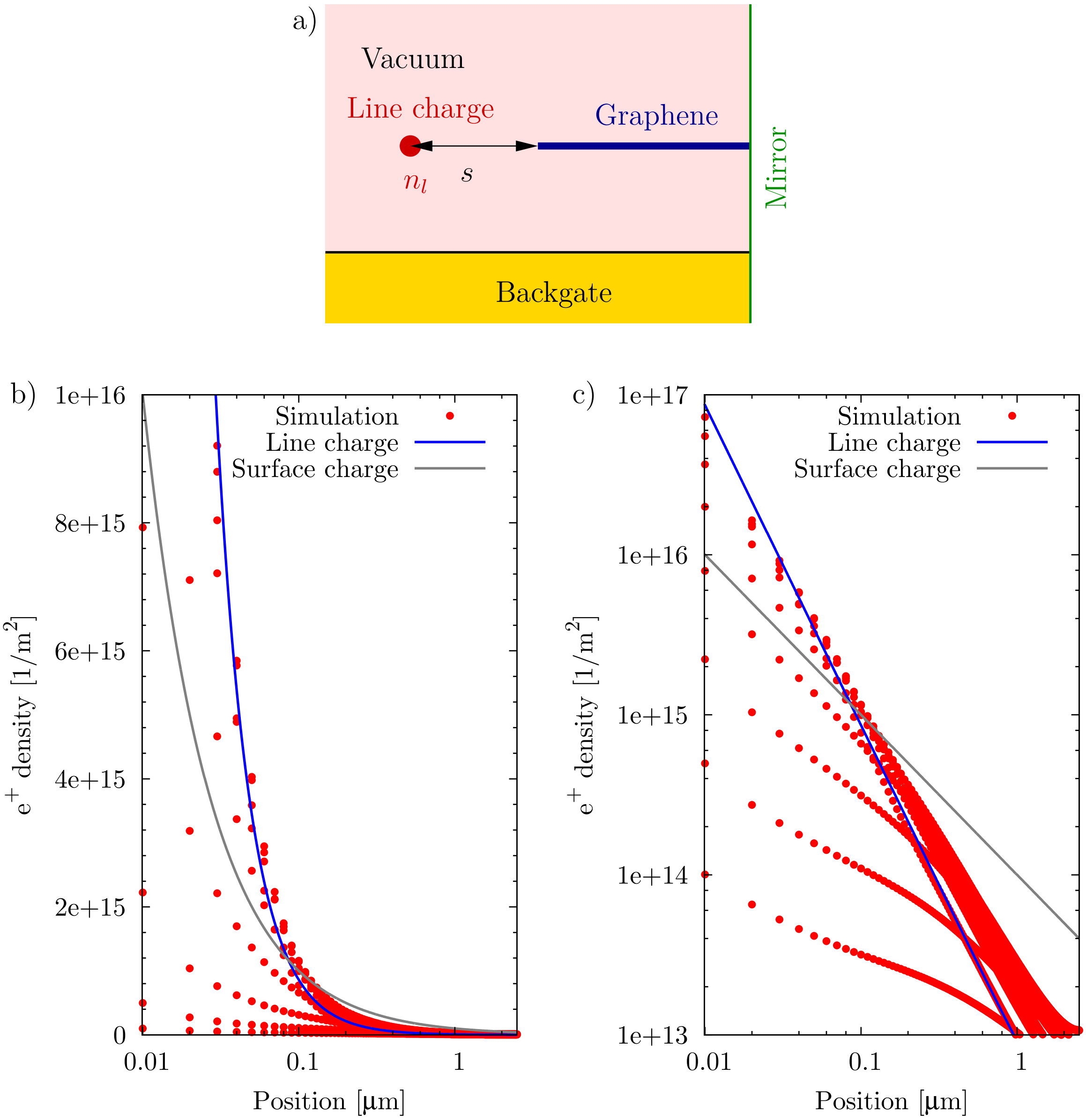

Figure C.2.: Effect of line charge displacement from the graphene flake edge with the arrangement shown in (a). The data was plotted in (b) with linear charge density axes and in (c) double-logarithmic. Traces were displacement compared to the previous calculations from top to bottom oriented at leftmost data point by 0, 1, 2, 4, 8, 16, 32, 64 and 128 lattice spaces. The data with zero displacement fits nicely to our line charge model with the used line charge of $-2 \cdot 10^9\, e/\mathrm{m}$. Increasing the displacements, the gray y^{-1} trace from the surface charge model becomes the much better fit.

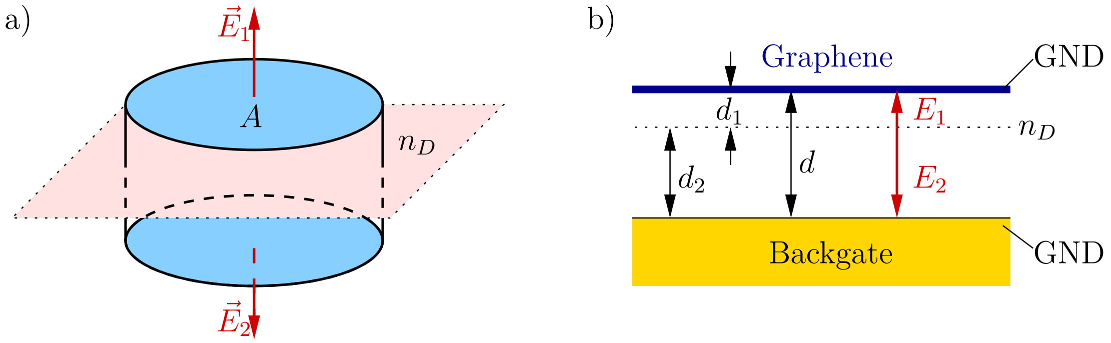

Figure C.3.: Definition of the Gauss volume (a) and position of the doping layer as well the directions of electric fields. Geometry used in the simulation (b).

For our simulation we have to deviate from this idealized model because of the finite size of the flake. Thus at the edges we expect to deviate from this simple relation. Fortunately the simulations, as plotted in Fig. C.4 for the arrangement in (a), show no significant deviation. While in graph (b) no line charges at the edges were present and the back gate was changed, in (c) the back gate was kept to zero and the amount of line charge was varied. No parameter was free for fitting here. The parameter c_l from equation (C.1) was already fixed by the fit in Fig. C.1.

In conclusion, the effect of doping at the edge seems to be negligible as long as the dopands are close and only under the graphene flake. The simple equation (C.7) describes the effect of doping well enough and we do not see any significant deviation in the simulations.

C.4. Empirical function and parameter for surface charges

Running the simulation with fixed surface charge distribution besides the graphene flake, as shown in Fig. C.5, one finds another dependency of the charge density distribution towards the edges. A suitable function for an infinitely wide flake is a y^{-1} function

$$\eta_\mathrm{s}(y) = \frac{c_\mathrm{s}\eta_\mathrm{fs}}{y}. \tag{C.8}$$

c_s is thereby the proportionality constant and η_fs the surface charge density. This is in contrast to the case of fixed line charge distribution where we had found a y^{-2} function. Of course since we are simulating a finite size flake with width w we have to consider the effect of the second edge. The fit function is thus modified to

$$\eta_\mathrm{s}(y) = \frac{c_\mathrm{s}\eta_\mathrm{fs}}{y} + \frac{c_\mathrm{s}\eta_\mathrm{fs}}{w-y}. \tag{C.9}$$

It is important to note that the fit was tried to be best for densities between $10^{15}\,\mathrm{m}^{-2}$ to $10^{16}\,\mathrm{m}^{-2}$ because this is also the order of magnitude to fit best to the depletion expected

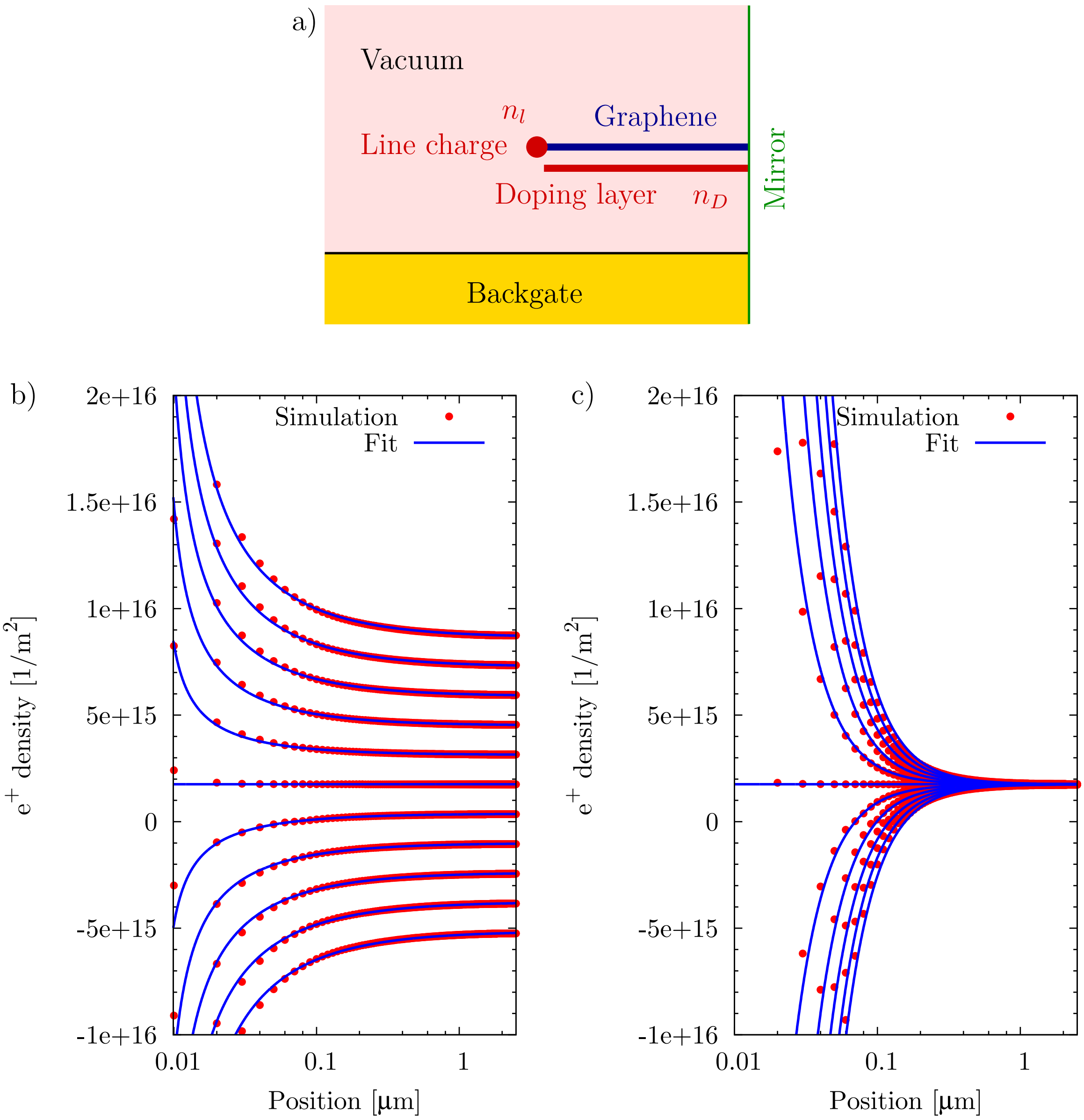

Figure C.4.: Influence of doping on the graphene flake in an arrangement shown in (a). (b) for different back gate voltages without line charge at the edges and (c) for different amount of line charge at the edge with fixed back gate. The capacitive edge effect, line charge induced charging and bulk charging simply adds up. For (b) $\eta = \eta_\mathrm{m} + \eta_\mathrm{d}$ (equations (B.40), (C.7)) and for (c) $\eta = \eta_\mathrm{l} + \eta_\mathrm{d}$ (equations (C.1), (C.7)). The back gate was changed in (b) from $-10\,\mathrm{V}$ (uppermost line) to $10\,\mathrm{V}$ (lowermost line) in steps of $2\,\mathrm{V}$ and the line charge was changed in (c) from $-1 \cdot 10^{10}\, e/\mathrm{m}$ (uppermost line) to $1 \cdot 10^{10}\, e/\mathrm{m}$ (undermost line) in steps of $0.2 \cdot 10^{10}\, e/\mathrm{m}$. The doping layer was offset from the graphene flake by one grid size corresponding to a distance of 10 nm. The parameters for the simulation shown in Fig. B.7 (b) are: $c = h = 1001$; $e = 750$; $g = 8$.

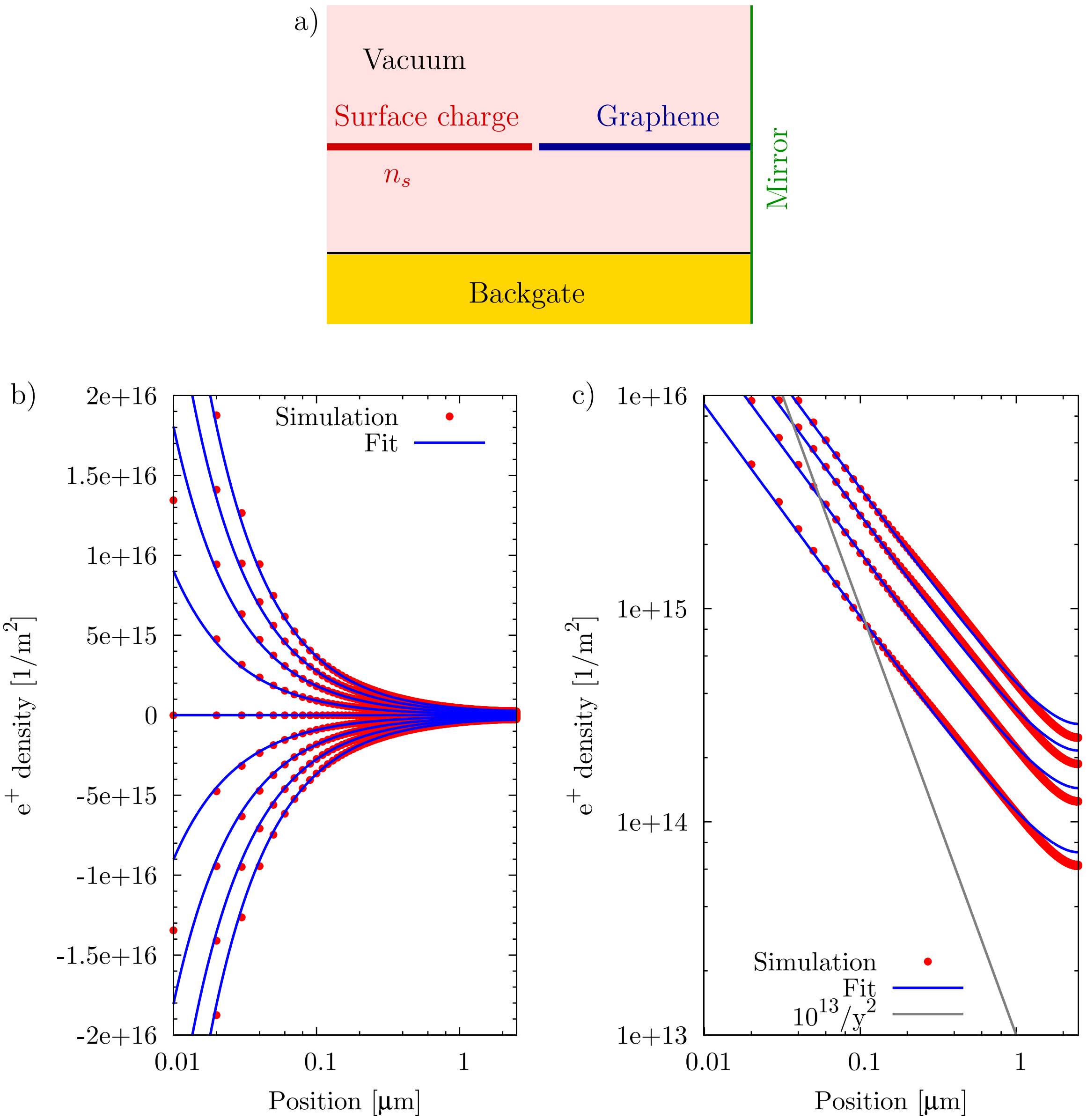

Figure C.5.: Simulation with fixed surface charges in an arrangement shown in (a) fitted with a y^{-1} function (see equation (C.9)) (b) presented in linear scale and (c) in double logarithmic scale. The surface charge was changed from $-2 \cdot 10^{16}\, e/\mathrm{m}^2$ (uppermost line) to $2 \cdot 10^{16}\, e/\mathrm{m}^2$ (undermost line) in steps of $0.5 \cdot 10^{16}\, e/\mathrm{m}^2$. In (c) only the negative surface charge densities are plotted. Also shown in (c) is a y^{-2} function for comparison. The parameters for the simulation shown in Fig. B.7 (b) are: $c = h = 1001$; $e = 750$; $g = 8$.

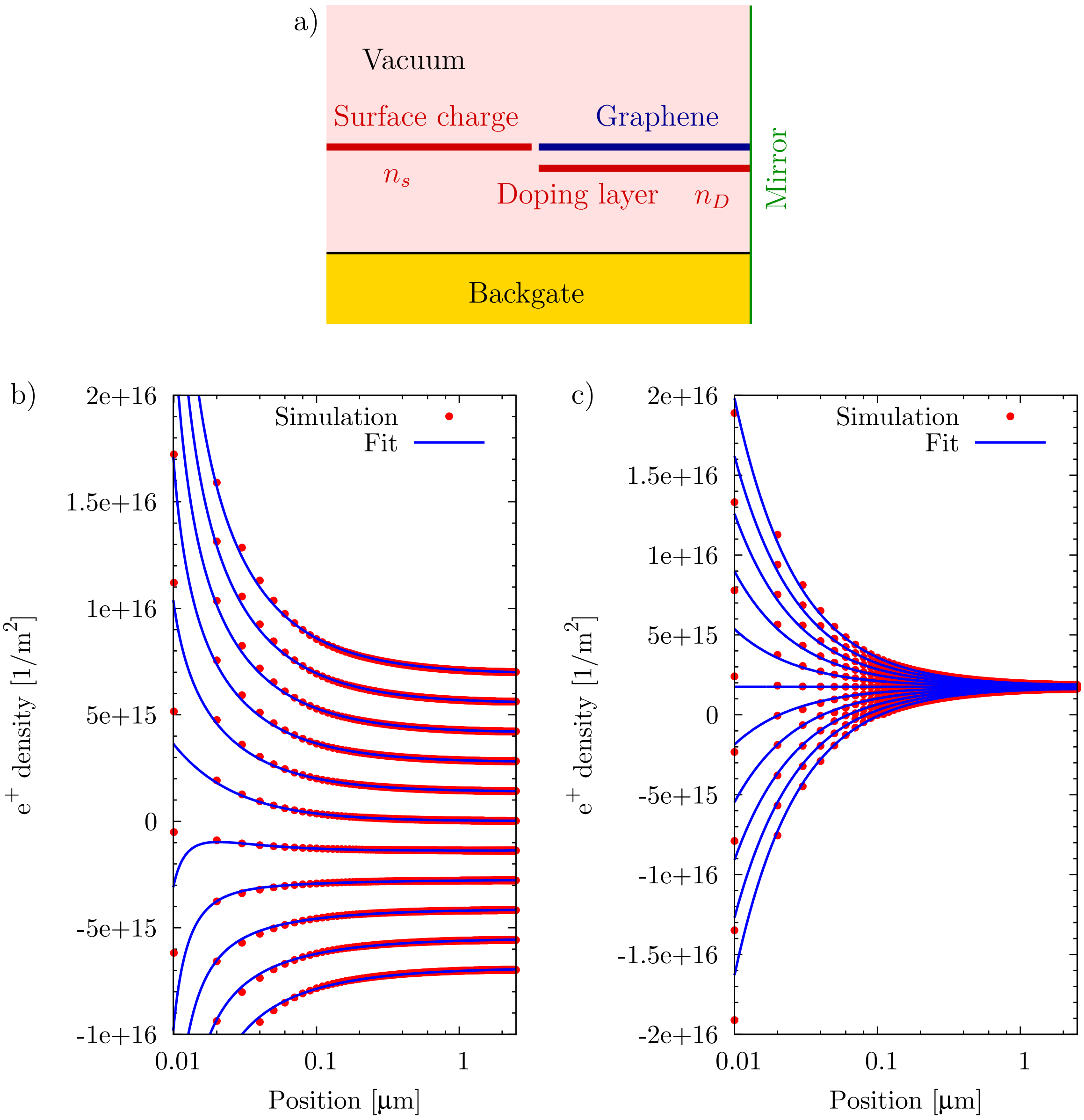

Figure C.6.: (a) Schematics of the surface charge arrangement simulated. (b) Different back gate voltages to check for influence of the back gate. The capacitive effect adds up as expected to the surface charge effect: $\eta = \eta_\mathrm{m} + \eta_\mathrm{s}$ (from equation (B.40) and (C.8)). The back gate was swept in (b) from $-10\,\mathrm{V}$ (uppermost line) to $10\,\mathrm{V}$ (lowermost line) in steps of $2\,\mathrm{V}$. (c) Sweep of fixed surface charge amount while a constant doping level was applied. The total charge carrier density is the sum of the doping effect and the surface charge effect: $\eta = \eta_\mathrm{d} + \eta_\mathrm{s}$ (from equation (C.7) and (C.8)). The surface charge was swept from $-1 \cdot 10^{16}\,e/\mathrm{m}^2$ (uppermost line) to $1 \cdot 10^{16}\,e/\mathrm{m}^2$ (lowermost line) in steps of $0.2 \cdot 10^{16}\,e/\mathrm{m}^2$. The doping layer was offset from the graphene flake by one grid size corresponding to a distance of $10\,\mathrm{nm}$. The parameters for the simulation shown in Fig. B.7 (b) are: $c = h = 1001$; $e = 750$; $g = 8$.

from Hall potential profiles. The parameter c_s was fixed by the simulation in Fig. C.5 to

$$c_\mathrm{s} = -1.8 \cdot 10^{-8}\,\frac{1}{\mathrm{m}} \tag{C.10}$$

Furthermore we checked the back gate effect to the surface charge effect in Fig. C.6 (b). Also the effect of doping is shown in Fig. C.6 (c), which obviously also simply adds up to the surface charge effect.

C.5. Conclusion

In conclusion, we have found in this chapter analytic functions for the charge carrier density profile for two distinct fixed charge arrangements. The profiles could be fitted with a single parameter for each fixed charge geometry. Also the effect of doping was discussed. Table C.1 sums up the results.

Cause	Parameter	Section described
Doping $\eta_\mathrm{d}(y) = -\eta_\mathrm{D}\dfrac{d_2}{d_1+d_2}$		C.3
Back gate $\eta_\mathrm{m}(y, V_\mathrm{BG}) = -\dfrac{\epsilon_0 V_\mathrm{BG}}{e\frac{d}{\epsilon_r}} - \dfrac{\epsilon_0 V_\mathrm{BG}}{e\frac{d}{\epsilon_r}} \cdot \dfrac{1}{1+\frac{\epsilon_r\pi}{d}y + \ln\left(1+\frac{\epsilon_r\pi}{d}y\right)}\left[1+\dfrac{1}{1+\frac{\epsilon_r\pi}{d}y}\right]$		B.4
Line charge $\eta_\mathrm{l}(y) = \dfrac{c_\mathrm{l}\eta_\mathrm{fl}}{y^2}$	$c_\mathrm{l} = -4.3 \cdot 10^{-9}\,\frac{1}{\mathrm{m}}$	C.1
Surface charge $\eta_\mathrm{s}(y) = \dfrac{c_\mathrm{s}\eta_\mathrm{fs}}{y}$	$c_\mathrm{s} = -1.8 \cdot 10^{-8}\,\frac{1}{\mathrm{m}}$	C.5

Table C.1.: Summary of fit functions for the free charge carrier profile η at the edge of the graphene flake caused by doping, applied back gate voltage, the presence of a line charge distribution at the edge or surface charges beside the graphene flake.

D. Line charge model and GaAs/Al$_x$Ga$_{1-x}$As-heterostructures

The development of the line charge model was mainly driven by the idea that the chemistry at graphene edges leads to charging at the edges. In etched GaAs/Al$_x$Ga$_{1-x}$As-heterostructures the confinement of the 2DES happens via surface charges. The GaAs surface is charged so that the electrochemical potential μ_{elch} is pinned midgap. Within the Chklovskii et al. (CSG) model [92] the midgap pinning at edges of GaAs semiconductors is used to find a suitable side gate voltage replacing the surface charges. Strictly speaking, by doing this the CSG model assumes a wrong charge distribution for etched GaAs/Al$_x$Ga$_{1-x}$As-heterostructure samples. We want to show here that this error is not that important by fitting our line charge mode to the data of Erik Ahlswedel. We want to emphasize that a model considering only a line charge in etched GaAs/Al$_x$Ga$_{1-x}$As-heterostructure sample edges is far of reality too. On every surface of the heterostructure filled surfaces states can be found. Nevertheless this fit will show that not only for graphene it is difficult to decide which fixed charge arrangement is present. We will encounter the same problem for the GaAs/Al$_x$Ga$_{1-x}$As-heterostructure samples.

Figure D.1 revises the results of Erik Ahlswede [16] and shows the positions of incompressible stripes deduced from the CSG model:

$$B_{\text{CSG}}(y,k) = \frac{B|_{\nu=1}}{k}\sqrt{1-\frac{d_0}{y-y_{\text{l}}}}\cdot\sqrt{1-\frac{d_0}{y_{\text{r}}-y}}, \tag{D.1}$$

$$d_0 = \frac{4\epsilon_0\epsilon_r V}{\pi e n_0}, \tag{D.2}$$

and from our line charge model

$$B_{\text{lc}}(y,k) = \frac{B|_{\nu=1}}{k} - \frac{c_{\text{l}}\eta_{\text{fl}}R_{\text{K}}e}{k}\left(\frac{1}{(y_{\text{l}}-y)^2}+\frac{1}{(y_{\text{r}}-y)^2}\right). \tag{D.3}$$

It should be stressed that the depletion region present in GaAs/Al$_x$Ga$_{1-x}$As-heterostructure samples effectively displaces the line charge from the 2DES. As discussed in section C.2 the y^{-2} dependence is modified by the displacement to a y^{-1} dependence. We want to intentionally neglect this fact to demonstrate the difficulty to distinguish different charge arrangements by a simple fit. The lines shown in Fig. D.1 are the result of slightly different filling factor $\nu = 1$ position $B|_{\nu=1}$. Namely $B|_{\nu=1} = 23.46\,\text{T}$ for the CSG model and $B|_{\nu=1} = 23.2\,\text{T}$ for the line charge model. Also the sample edges had to be chosen differently. While $y_{\text{l}} = 0\,\mu\text{m}$ and $y_{\text{r}} = 15\,\mu\text{m}$ was chosen for the CSG model, $y_{\text{l}} = -0.3\,\mu\text{m}$

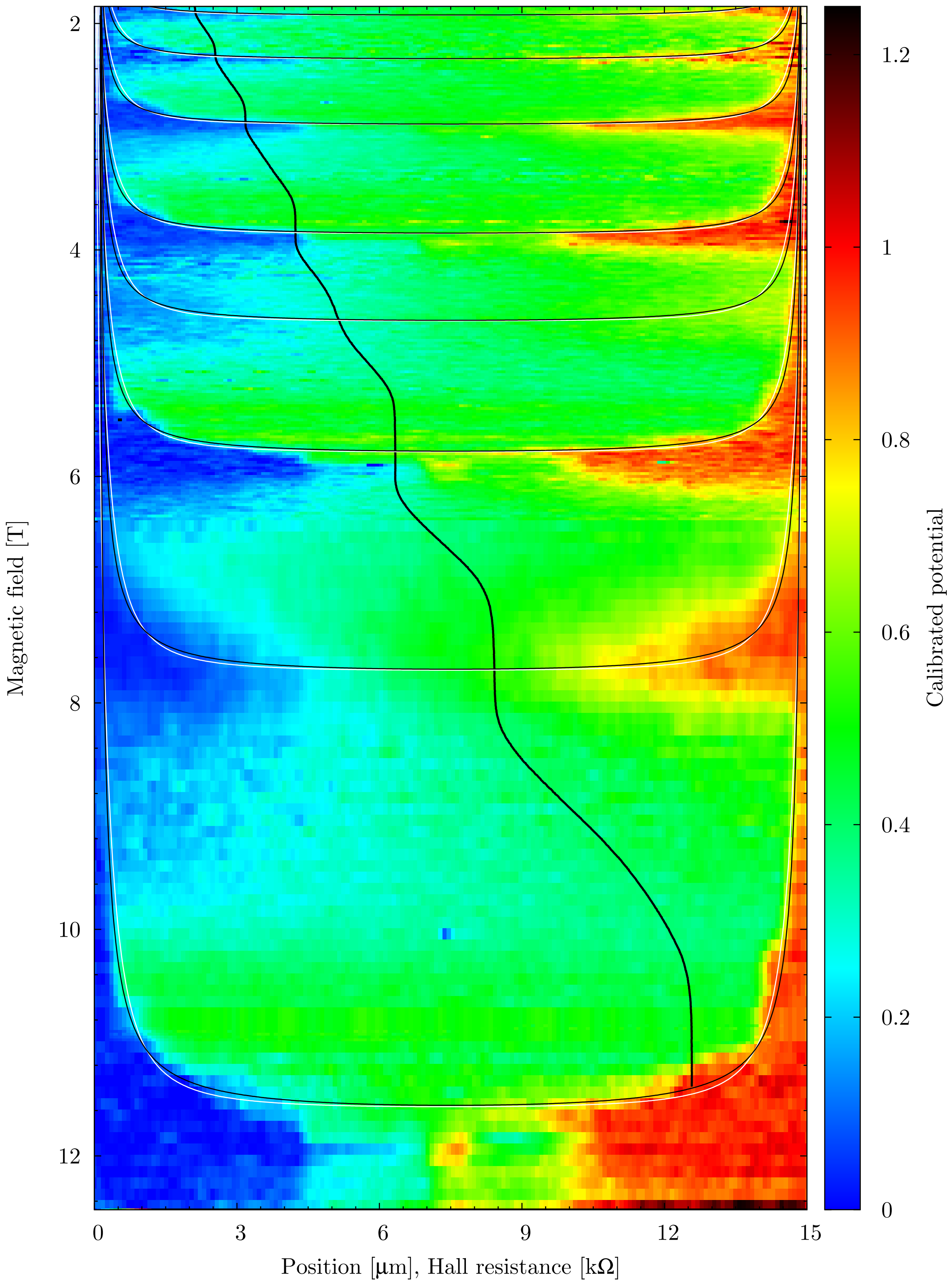

Figure D.1.: Data from Erik Ahlswerde [17] compared with the Chklovskii, Shklovskii and Glazman (CSG) model [92], black lines and no free parameters, and fitted with the line charge model, white lines. We thank Erik Ahslwede for the access to his data to create this plot.

and $y_\mathrm{r} = 15.3\,\mu\mathrm{m}$ produced a suitable result for the line charge model. We chose for no reason $c_\mathrm{l} = 4.3 \cdot 10^{-9} \cdot \epsilon_r$ and found a η_fl of about $9 \cdot 10^9\,\mathrm{m}^{-1}$.

From the data shown in fig. D.1 no clear statement can be derived onto which model is better suited but it should be emphasized that the CSG model has no free parameter in contrast to the line charge model. This comparison shows that the model details cannot be tested with this type of measurement.

E. Electric fields and Landau levels

For the interpretation of Hall potential profiles under quantum Hall conditions the effect of electric fields on Landau levels is crucial. In the following we want to discuss several approaches to handle this problem. For quasi-particles with mass, one can calculate from the momentum expectation value the current density. Also solving the equation of motion for Bloch electrons under magnetic and electric fields leads to a solution for particles with mass. The same ansatz is not easy solvable for massless particle. Instead we will show how one can eliminate the electric field by applying a Lorentz boost transformation which results in an additional drift velocity.

E.1. Free electron ansatz

We want to calculate in the following the expectation value of the current density $j_x = qnv_{\mathrm{D}}$. This requires to calculate the expectation value of the momentum operator to find the drift velocity v_{D} which is for massive particles the quasi-particle momentum divided by the quasi-particle mass. As first step we want to include the magnetic field B in z-direction to our problem. To do this we add the vector potential $\vec{A} = -yB \cdot \vec{e}_x$ into the momentum operator ([4] page 256)

$$\hat{\vec{\Pi}} = -i\hbar\nabla + q\vec{A}. \tag{E.1}$$

The current can now be calculated via the expectation value of the momentum $\langle\hat{\Pi}_x\rangle$ for the quantum mechanical solutions of the problem ([236] page 18)

$$j_x = \frac{qn}{m^*}\langle\hat{\Pi}_x\rangle = \frac{qn}{m^*}\langle\psi| - i\hbar\partial_x + qB_z y|\psi\rangle. \tag{E.2}$$

Equation (E.2) is not applicable for quasi-particles without mass like in graphene but works fine for massive quasi-particles like electrons in GaAs/Al$_x$Ga$_{1-x}$As-heterostructures.

To solve equation (E.2) we have first to find the solutions of the Schrödinger equation (we follow here the approach described in [17]). The electric field E in y-direction is added as the potential term $V(y) = yE$ of the Hamilton operator. Schrödinger's equation reads then

$$\left[-\frac{(-i\hbar\partial_x - eBy)^2}{2m^*} - \frac{\hbar^2\partial_y^2}{2m^*} - eEy\right]\psi(x, y) = \varepsilon\psi(x, y) \tag{E.3}$$

and we can simplify it by taking the ansatz $\psi = e^{ik_x x}\phi(y)$ to

$$\left[-\frac{\hbar^2\partial_y^2}{2m^*} + \frac{e^2B^2}{2m^*}\left(y - \frac{\hbar k_x}{eB} - \frac{Em^*}{eB^2}\right)^2 - \frac{m^*E^2}{2B^2} - \frac{\hbar k_x E}{B}\right]\phi(y) = \varepsilon\phi(y). \tag{E.4}$$

We can further simplify equation (E.4) by introducing the magnetic length l_B, the central coordinate Y_E and the cyclotron frequency ω_c

$$l_B = \sqrt{\frac{\hbar}{eB}} \tag{E.5}$$

$$\omega_\mathrm{c} = \frac{eB}{m^*} \tag{E.6}$$

$$Y_E = l_B^2 k_x + \frac{eE}{m^*\omega_\mathrm{c}^2}. \tag{E.7}$$

The Schrödinger equation for the shifted wavefunction $\phi(y + Y_E)$ becomes then the one of an energetically shifted harmonic oscillator

$$\left[-\frac{\hbar^2\partial_y^2}{2m^*} + \frac{\omega_\mathrm{c}^2}{2m^*}y^2\right]\phi(y+Y_E) + \left[-\frac{m^*E^2}{2B^2} - \frac{\hbar k_x E}{B}\right]\phi(y+Y_E) = \varepsilon\phi(y+Y_E). \tag{E.8}$$

The Landau level spectrum will therefore be

$$\varepsilon = \hbar\omega_\mathrm{c}\left(n + \frac{1}{2}\right) - \frac{m^*E^2}{2B^2} - \frac{\hbar k_x E}{B}. \tag{E.9}$$

With this result we can calculate the expectation of the current density given in equation (E.2). The operator $\hat{\Pi}_x$ consists of two operators $-i\partial_x$ and y and some constants. Thus we need the expectation value for $-i\partial_x$ which is due to the ansatz for ψ equal to k_x We also need the expectation value for y. Due to the symmetry of the harmonic oscillator solutions the central coordinate will be the expectation for y. We get therefore for the current

$$j_x = -\frac{en}{m^*}\left(\hbar k_x - eBl_B^2 k_x - \frac{e^2EB}{m^*\omega_\mathrm{c}^2}\right) = \frac{enE}{B}. \tag{E.10}$$

E.2. Bloch electron ansatz

A more handy solution of this problem can be achieved when looking on Bloch electrons in semiclassical orbits. Bloch electrons will travel along closed orbits as a response to a magnetic field. An additional electric field tilts and shifts these orbits. The actual path is given by the equation of motion of crystal electrons ([237] page 60)

$$\hbar\dot{\vec{k}} = q\left(\vec{E} + \dot{\vec{r}} \times \vec{B}\right). \tag{E.11}$$

The bandstructure enters via the velocity ([237] page 57)

$$\dot{\vec{r}} = \frac{1}{\hbar}\nabla_k \varepsilon \tag{E.12}$$

For 2DES with parabolic band structure one gets

$$\hbar \begin{pmatrix} \dot{k}_x \\ \dot{k}_y \end{pmatrix} = q \left[\begin{pmatrix} 0 \\ E \end{pmatrix} + \frac{\hbar}{m^*} \begin{pmatrix} k_y B \\ -k_x B \end{pmatrix} \right] \tag{E.13}$$

which is solved easily by an ellipse $\vec{k}(t)$. Also the ellipse is offseted in k_x-direction by

$$k_{x,\mathrm{off}} = \frac{m^* E}{\hbar B}. \tag{E.14}$$

Since the ellipse itself has an average k-value of zero the average of the offseted ellipse will be $k_{x,\mathrm{off}}$ and the current becomes with equation (E.2) and $p_x = \hbar k_{x,\mathrm{off}}$

$$j_x = \frac{qnE}{B}. \tag{E.15}$$

The solution shown in this section can be solved that simple only for a parabolic band structure. Within a linear band dispersion the path in k-space as well as in real space is no longer an ellipse. An analytic solution become difficult so that we have to go another way to solve this problem for linear band dispersion and thus for graphene.

E.3. Landau levels and electric fields in graphene

In case of graphene we want to describe the quantum mechanical approach as done by Lukose et al. [238]. Magnetic and electric fields included to the Dirac-Weyls equation the same way as described before with the small difference that we deal here with a vector equation. This gives the Dirac-Weyls equation for the quasi-particle in graphene close to the K-points

$$v_\mathrm{F} \begin{pmatrix} qEy/v_\mathrm{F} & p_x - ip_y + qBy \\ p_x + ip_y + qBy & qEy/v_\mathrm{F} \end{pmatrix} \cdot \psi(x,y,t) = i\hbar\partial_t \psi(x,y,t). \tag{E.16}$$

The usual ansatz for the wavefunction is a plane wave along the x-direction,

$$\psi(x,y,t) = e^{ik_x x}\phi(y,t), \tag{E.17}$$

and simplifies equation (E.16) to

$$v_\mathrm{F} \begin{pmatrix} -eEy/v_\mathrm{F} & \hbar k_x - ip_y - eBy \\ \hbar k_x + ip_y - eBy & -eEy/v_\mathrm{F} \end{pmatrix} \cdot \phi(y,t) = i\hbar\partial_t \phi(y,t). \tag{E.18}$$

This equation can be transformed with a Lorentz boost to effectively eliminate the electric field. The result is the Dirac-Weyls equation of an electron in a reduced magnetic field

$$\tilde{B} = B\sqrt{1-\beta^2}. \tag{E.19}$$

where β defines the drift velocity v_D of the new coordinate system with

$$\beta = \frac{v_\mathrm{D}}{v_\mathrm{F}} = \frac{E}{v_\mathrm{F}B}. \tag{E.20}$$

The solution within this drifting system with velocity $v_\mathrm{D} = E/B$ has to be back transformed into the original coordinate system and reads after that

$$\varepsilon = \hbar\frac{v_\mathrm{F}}{l_B}(1-\beta^2)^{3/4} \cdot \mathrm{sgn}(n)\sqrt{2|n|} - \hbar v_\mathrm{F}\beta k_x. \tag{E.21}$$

Other ways to solve this problem are by using appropriate matrix transformations to simplify the eigenvalue determination as done by [239]. Also straight forwardly decoupling the vector equation and bringing it into the differential equation for the Hermite polynomials resulting into a complicated term for the energy is possible.

In contrast to the parabolic band materials where the cyclotron gap stays unchanged after an electric field is applied, in linear band materials the cyclotron gap shrinks. At $E/B = v_\mathrm{F}$ the Landau level structure quenches and is not present for higher electric fields.

In conclusion, we found that independent of the band structure electrons acquire a drift velocity $v_\mathrm{D} = E/B$ for perpendicular magnetic and electric fields.

E.4. Conclusion

All three paths to calculate the current density shown in this chapter result in the same result. Namely that charge carriers in Landau levels subjects to electric fields acquire a drift velocity $v_\mathrm{D} = E/B$ that is proportional to the applied electric field. This is in particularly also true for graphene. The current in such a situation becomes then

$$j_x = \frac{qnE}{B}. \tag{E.22}$$

F. Electrostatic problems and elimination of dielectric constants

An often found problem in electrostatics is a geometry with several dielectric materials. To solve such a problem one has to solve the following extended Poisson equation:

$$\epsilon_r(\vec{r})\Delta\phi(\vec{r}) + \nabla\phi(\vec{r})\nabla\epsilon_r(\vec{r}) = \frac{\rho(\vec{r})}{\epsilon_0}, \tag{F.1}$$

which results from $\nabla D = \rho(\vec{r})$ and $D = \epsilon_0\epsilon_r(\vec{r})\nabla\phi(\vec{r})$. This problem can be simplified in cases of a simple geometry and discrete dielectric constants by a coordinate transformation. The transformation has to be done such that the amount of charge q

$$q = \iint\limits_{\partial V} \vec{D} \cdot d\vec{A} = \iint\limits_{\partial V} \epsilon_0\epsilon_r(\vec{r})\vec{E}(\vec{r}) \cdot d\vec{A} \tag{F.2}$$

and potential differences V

$$V = \int\limits_{\vec{a}}^{\vec{b}} \vec{E}(\vec{r}) \cdot d\vec{s} \tag{F.3}$$

remain the same. As a consequence also the capacitance remains after this transformation the same.

From equation (F.2) we can eliminate the dielectric by scaling the electric field in parallel to the area element

$$\epsilon_r(\vec{r})\vec{E} \cdot d\vec{A} = \vec{E}_\mathrm{t} \cdot d\vec{A} \tag{F.4}$$

$$q = \iint\limits_{\partial V} \epsilon_0\vec{E}_\mathrm{t}(\vec{r}) \cdot d\vec{A}. \tag{F.5}$$

Doing so the dielectric constant for the scaled problem becomes one. Furthermore the electric field at the boundaries of different dielectrics becomes continuous. Only the electric field in parallel to the area element has to be scaled and not the whole field vector. This is in particular important for the boundaries between different dielectrics.

To also fullfil equation (F.3) a scaling of the integration path is necessary:

$$\vec{E}(\vec{r}) \cdot d\vec{s} = \frac{\vec{E}_\mathrm{t}}{\epsilon_r(\vec{r})} \cdot \epsilon_r(\vec{r})d\vec{s}_\mathrm{t} \tag{F.6}$$

$$d\vec{s} = \epsilon_r(\vec{r})d\vec{s}_\mathrm{t}. \tag{F.7}$$

The path between a and b is thereby streched according to the dielectric constant $\epsilon_r(\vec{r})$. We have now to find a suitable transformation $\vec{s}_{\mathrm{t}}(\vec{s})$ to bring the path stretch onto the integration limits. In the simplest case of $\vec{s}_{\mathrm{t}}(\vec{s}) = \epsilon_r^{-1}(\vec{r})\vec{s}$ this results into

$$V = \int\limits_{\frac{\vec{a}}{\epsilon_r(\vec{a})}}^{\frac{\vec{b}}{\epsilon_r(\vec{b})}} \vec{E}_{\mathrm{t}}(\vec{r}) \cdot d\vec{s}. \tag{F.8}$$

It should be stressed here, that for the given transformation $\vec{s}_{\mathrm{t}}(\vec{s})$ the vector $\vec{s}$ as well as $\vec{s}_{\mathrm{t}}$ have to follow the symmetry of $\epsilon_r(\vec{r})$.

In the simple case of an infinite sized layer of dielectric material with thickness d and dielectric constant ϵ_r we have to reduce the thickness of the dielectric to $d_{\mathrm{t}} = d{\cdot}\epsilon_r^{-1}$ and use a dielectric constant of one while solving Poisson equation. The solution found gives the same capacitance, charge distribution on conductors and potential between conductors. The backward transformation is therefore in most cases not necessary. Except of the reset of dielectric thickness and the dielectric constant also the electric field perpendicular to the boundary has to be scaled inside the dielectric with $E = E_{\mathrm{t}} \cdot \epsilon_r^{-1}$ for the back transformation. Electrodes or charge arrangements in any configuration not penetrating the dielectric does not affect the validity of this scaling. This is because the scaled volume is free of electrodes and charges.

G. Artefacts and error sources

In chapter 6 we have discussed the measurement technique used in this thesis. But we have skipped the possible artefacts and error sources. In the following we want to close that gap by first deepen our understanding of the measurement results in the theoretical section G.1. Second we want to use the theoretical considerations to discuss artefacts due to the setup in section G.2 and due to the sample in section G.3. Finally we will explicitly mention the difficulties for sample GB8113 in section G.5 before we sum up this chapter.

G.1. Theoretic considerations for artefacts in electrostatic force microscopy

G.1.1. Sinusoidal modulation of tip-sample voltage

We have already shown in chapter 6 that the resonance frequency shift felt by the SFM-tip we use for our measurements is proportional to the force gradient. Since the actual frequency shift is important for the further analysis we want to rephrase equation (6.2) in the following way

$$\Delta f \propto \partial_z F = -\frac{1}{2}\partial_z^2 C \left(V + \Delta\mu_{\mathrm{ch}}/e\right)^2 - \partial_z^2 q_{\mathrm{m}} \left(V + \Delta\mu_{\mathrm{ch}}/e\right) - \partial_z^2 W_{\mathrm{o}}. \tag{G.1}$$

The first term in equation (G.1) originates from the capacitiv energy stored between the SFM-tip and the 2DES and is proportional to the square of the electrostatic potential difference between SFM-tip and 2DES. The electrostatic potential difference consists of the chemical potential difference $\Delta\mu_{\mathrm{ch}}/e$ giving the built-in electrostatic potential difference and the applied voltage V (=electrochemical potential difference). The second term originates from the image charges on the tip feeling the electrostatic potential difference to the 2DES. In the third term we included all contributions that are usually independent of the electrochemical potential difference between tip and 2DES. As a result $\Delta f(V)$ is a parabola with maximum at (see equation (6.20) from section 6.4)

$$V_{\mathrm{PM}} = -\frac{\partial_z^2 q_{\mathrm{m}}}{\partial_z^2 C} - \frac{\Delta\mu_{\mathrm{ch}}}{e}. \tag{G.2}$$

Replacing V by $\hat{V} + V_{\mathrm{PM}}$ we can shift the parabola maximum to zero. This simplifies equation (G.1) to

$$\Delta f(\hat{V}) \propto A \left(\hat{V}\right)^2 + const. \tag{G.3}$$

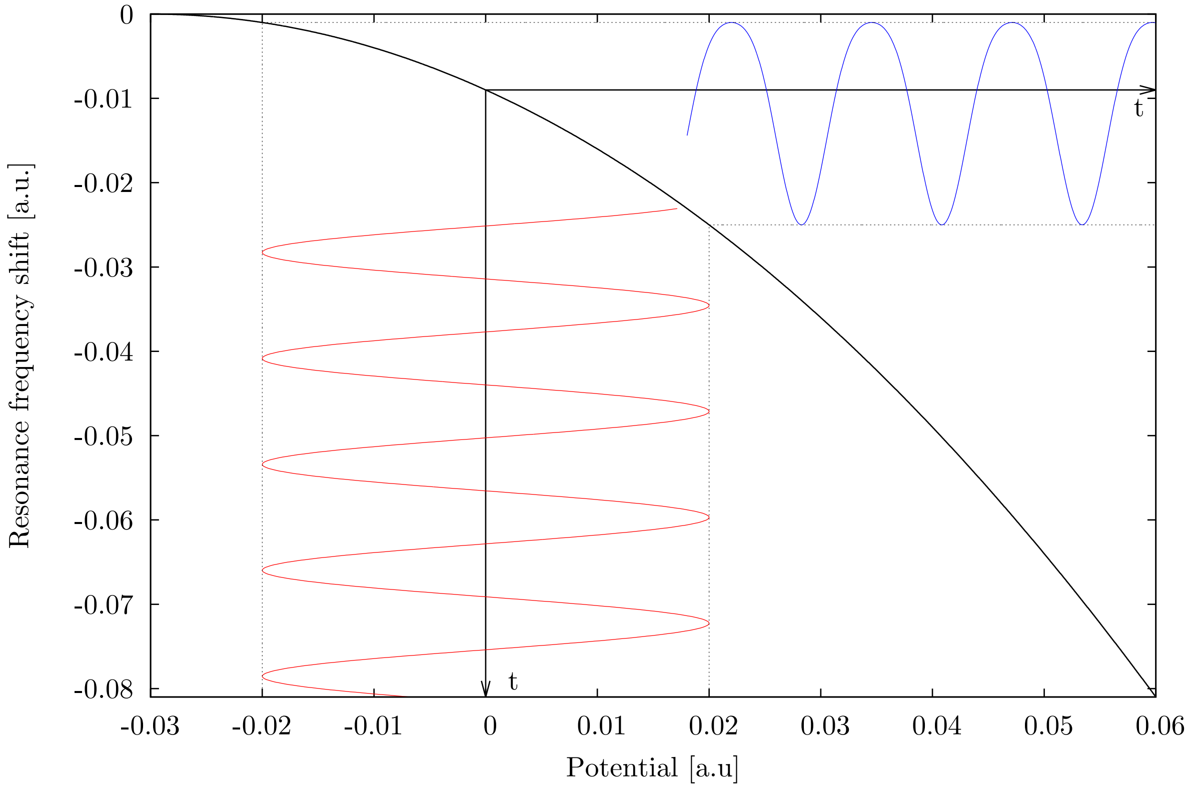

Figure G.1.: Transformation of a sine excitation shown in red via the resonance shift parabola shown in black. The result is plotted in blue. The position of transformation was chosen close to the parabola maximum to emphasize the non-linear terms of the transformation.

A sinusoidal modulation

$$\hat{V} = V_\mathrm{A} \sin(\omega_\mathrm{m} t) + V_\mathrm{B} \tag{G.4}$$

at the 2DES results then in

$$\begin{aligned} \Delta f(t) &= A\left[V_\mathrm{A}\sin(\omega_\mathrm{m}t) + V_\mathrm{B}\right]^2 + const \qquad &(G.5)\\ &= AV_\mathrm{A}^2\sin^2(\omega_\mathrm{m}t) + 2AV_\mathrm{A}V_\mathrm{B}\sin(\omega_\mathrm{m}t) + AV_\mathrm{B}^2 + const \qquad &(G.6)\\ &= +\frac{1}{2}AV_\mathrm{A}^2 - \frac{1}{2}AV_\mathrm{A}^2\cos(2\omega_\mathrm{m}t) + 2AV_\mathrm{A}V_\mathrm{B}\sin(\omega_\mathrm{m}t) + AV_\mathrm{B}^2 + const. \qquad &(G.7)\end{aligned}$$

The result is illustrated in an example plotted in Fig. G.1. We get a resonance frequency shift that is modulated at two frequencies: ω_m and $2\omega_\mathrm{m}$.

The curvature A of the parabola can be found from (G.1) and with $\Delta f \approx -f_0 \frac{\partial F}{2k}$ (see [13]) to be:

$$A \approx -2\pi f_0 \frac{\partial_z^2 C}{4k}. \tag{G.8}$$

Here k is the spring constant of the cantilever.

We use a lock-in amplifier for read out which is in our case sensitive to the signals with angular frequency ω_m. The resulting amplitude measured by the lock-in amplifier b_1 is

$$b_1 \propto A V_\mathrm{A} V_\mathrm{B}. \tag{G.9}$$

This means that the measurement data is not only proportional to the AC-component of an excitation but also proportional to the distance to the parabola maximum. And of course, the bigger the curvature A of the parabola the higher the output signal.

G.1.2. Rectangular modulation of tip-sample voltage

Since we prefer to use a rectangular modulation over a sinusoidal one, we want also to calculate the lock-in amplifier response to a rectangular excitation $V_\mathrm{r}(t)$

$$V_\mathrm{r}(t) = \begin{cases} V_\mathrm{A} + V_\mathrm{B} & 0 < \omega_\mathrm{m} t \mod 2\pi \leq \pi, \\ V_\mathrm{B} & \pi < \omega_\mathrm{m} t \mod 2\pi < 2\pi \end{cases} \tag{G.10}$$

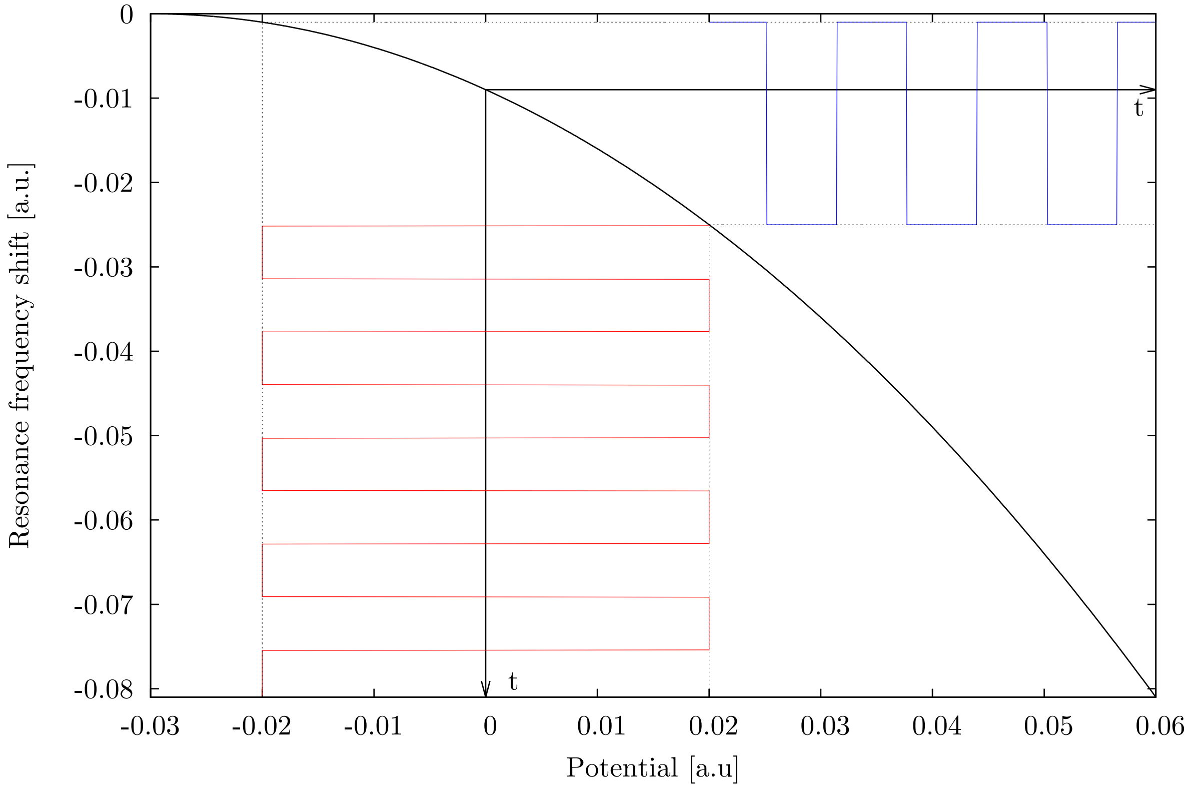

Figure G.2.: Transformation of a rectangular excitation shown in red via the resonance shift parabola in black. The result is plotted in blue.

Inserting $V_\mathrm{r}(t)$ in equation (G.3) as $\hat{V}$ one finds the resonance frequency shift

$$\Delta f_\mathrm{r}(t) = \begin{cases} A\left[V_\mathrm{A}+V_\mathrm{B}\right]^2 + const & 0 < \omega_\mathrm{m} t \mod 2\pi \leq \pi, \\ A\left[V_\mathrm{B}\right]^2 + const & \pi < \omega_\mathrm{m} t \mod 2\pi < 2\pi \end{cases} \tag{G.11}$$

This is shown in Fig. G.2. Since we are interested in the frequency decomposition of $\Delta f_\mathrm{r}(t)$ we looked at the Fourier coefficients that can be found for example in [240]. $\Delta f_\mathrm{r}(t)$ can be written as $\sum_{j=1}^{\infty} a_j \sin(j\omega_\mathrm{m} t) + const$ with

$$a_j = \begin{cases} \frac{2AV_\mathrm{A}^2+4AV_\mathrm{A}V_\mathrm{B}}{j\pi} & j \,\text{odd}, \\ 0 & j \,\text{even} \end{cases} \tag{G.12}$$

The usual lock-in amplifier reading would be a_1 with

$$a_1 \propto AV_\mathrm{A}^2 + 2AV_\mathrm{A}V_\mathrm{B}. \tag{G.13}$$

Compare to the case of sinusoidal modulation an additional parabolic term is found. In our experiments we want the quadratic term to be as small as possible compared to the linear term.

G.2. Setup related artefacts

G.2.1. Background noise

Noise is usually not considered as artefact since it alters the results randomly and can be reduced by averaging. In our case averaging is done by a finite integration time with an lock-in amplifier. In this case noise prevents us from reaching zero signal. For a large signal to noise ratio the noise bloom is not a problem and will average out.

Background noise will be reduce except at the measurement frequency since we use lock-in amplifiers. In addition we used the lock-in amplifiers to measure positive amplitudes to avoid the search for the correct phase. Plotted in the complex plain, see Fig. G.3 (a), the effect of the noise is an additional random vector with length corresponding to the amplitude of the noise away from the data vector without noise .

Problematic is a vanishing measurement signal (x, y) because one gets only positive contribution from noise $(x_\mathrm{n}, y_\mathrm{n})$ that do not average out when considering only the amplitude

$$V_\mathrm{LI} = \sqrt{(x+x_\mathrm{n})^2 + (y+y_\mathrm{n})^2}. \tag{G.14}$$

Thus one gets due to noise an offset for data points close to zero. As shown in Fig. G.3 (b) a high (x, y) signal results in a amplitude and phases fluctuating around the signal values. Turning of the signal (x, y) results in measuring the noise amplitude an the locked frequency with random phase.

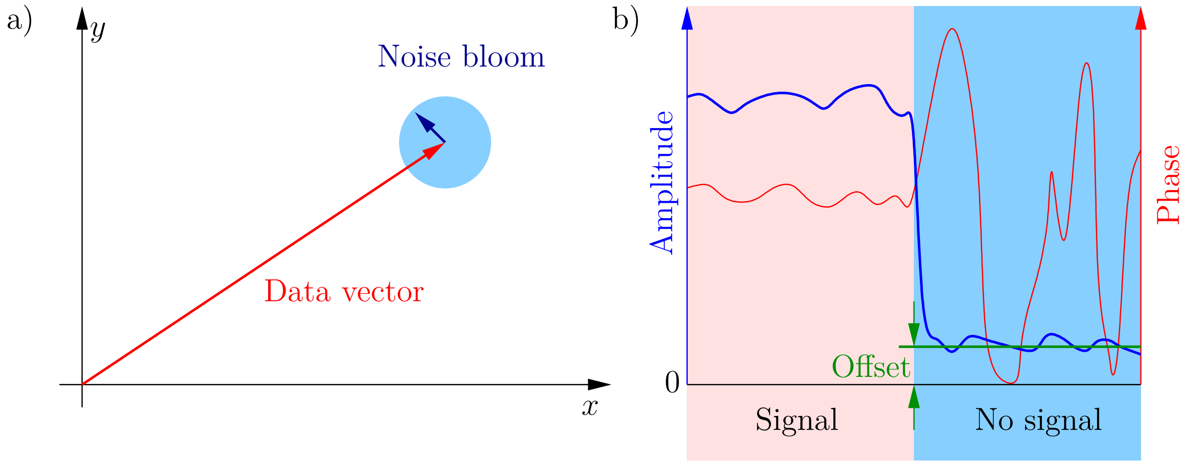

Figure G.3.: Effect on noise on measurements with a lock-in amplifier. (a) Noise bloom within the measurement space. (b) Amplitude and phase measured by the lock-in amplifier for the case with and without signal. Noise creates a finite signal of offset in the case of no signal with random phase.

G.3. Sample related artefacts

G.3.1. Sample topography

The sample topography should ideally not affect the scan results for the Hall potential profile, since the calibration method of chapter 6 will remove its influence. In reality there are occasions where this is not the case. A crash, an uncontrolled and unwanted touch of the SFM-tip on the sample, is one of them. After a crash the signal from the PLL feed to the lock-in amplifier (see Fig. 6.2) will include a step. The Fourier decomposition of the signal will give a broad spectrum that will cause the lock-in amplifier to deliver a measurement signal that is huge compared to the usual level in comparable sites. The result can look like shown in Fig. G.4. In (a) the tip was touching the sample at the

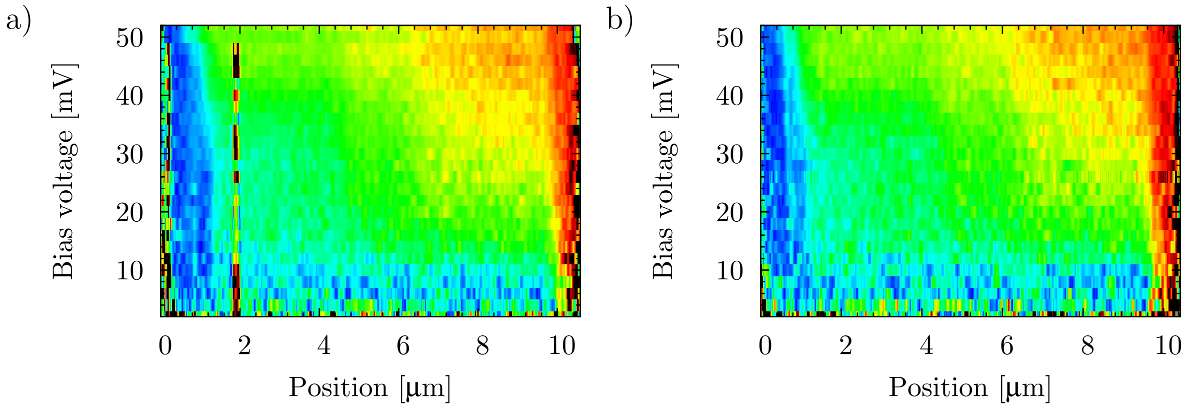

Figure G.4.: (a) Topography related artefact measured on sample 8379_20100120_B. (b) Resolution of the artefact by changing the scan height.

position of about 2 µm. As a result there is an irregular, sometimes black line with increasing bias visible at this position. Repeating the scan with bigger tip to sample distance removes the artefact. This is shown in Fig. G.4 (b). Compare to other artefacts there is no dependence on bias, letting the identification become quite simple.

G.3.2. Edges

At the edge of a sample we find a transition of conductive 2DES to non conductive substrate. It is thus not surprising to find effects related to this transition especially as the workfunction difference changes. In particular we want to discuss here an overshoot of the sensitivity beside the sample edges where no 2DES is present. The sensitivity can be defined as the measured amplitude for a given modulation amplitude. This is the prefactor of equation (6.8) and is proportional to the frequency shift parabola curvature A and the offset V_{B} to the parabola maximum as found in equation (G.9). The overshoot can be seen in the upper part of Fig. G.5 in the red dots. The 2DES area extends from the position -6 to 5. But the sensitivity is higher in the regions beside the 2DES. This overshoot is not present in all measurements and usually does not affect our results but it is still interesting why the sensitivity does not go monotonic to zero at the edges.

For the analysis we measured the resonance frequency shift parabola of the cantilever depending on position. We fitted each parabola to extract the curvature and the tip to sample voltage at the parabola maximum. The results are plotted in the lower part of Fig. G.5. As expected the curvature A which depends on the capacitive coupling between tip and 2DES reduces after the tip is not positioned over the Hall bar. On the other hand the position of the parabola maximum is shifted drastically. The position of the parabola maximum depends on the mirror charges on the tip, the capacitive coupling of tip and sample and the chemical potential difference between tip and sample, see equation (6.20). The chemical potential of the Hall bar should be only in the order of a volt different from the chemical potential of the bulk material. Therefore we expect the main shift of the parabola maximum to be due to the capacitive and mirror charge term. In total we find a reduction of the parabola curvature by a factor of five. On the other hand the measurement offset from the parabola maximum V_{B} increases by a factor of 20. As we can see from equation (G.9) keeping the excitation amplitude V_{A} constant, the sensitivity is proportional to the product of curvature A and offset V_{B}. The blue dots in the upper part of Fig. G.5 show the product AV_{B} which is proportional to the sensitivity. It fits qualitatively to the directly measured sensitivity.

G.4. Current induced artefacts

G.4.1. Parabola shift due to charge carrier density changes

We have discussed in chapter 6 the effect of charge carrier density change onto our measurement results in case only the chemical potential is changed. We thus want to remind of equation (G.9) where we found that the measurement signal we get from our lock-in amplifier is proportional to the voltage offset between operation point and the parabola maximum V_{B}. Here we want to discuss what can happen if the position of the resonance frequency shift parabola is changed. In case V_{B} is large compare to the

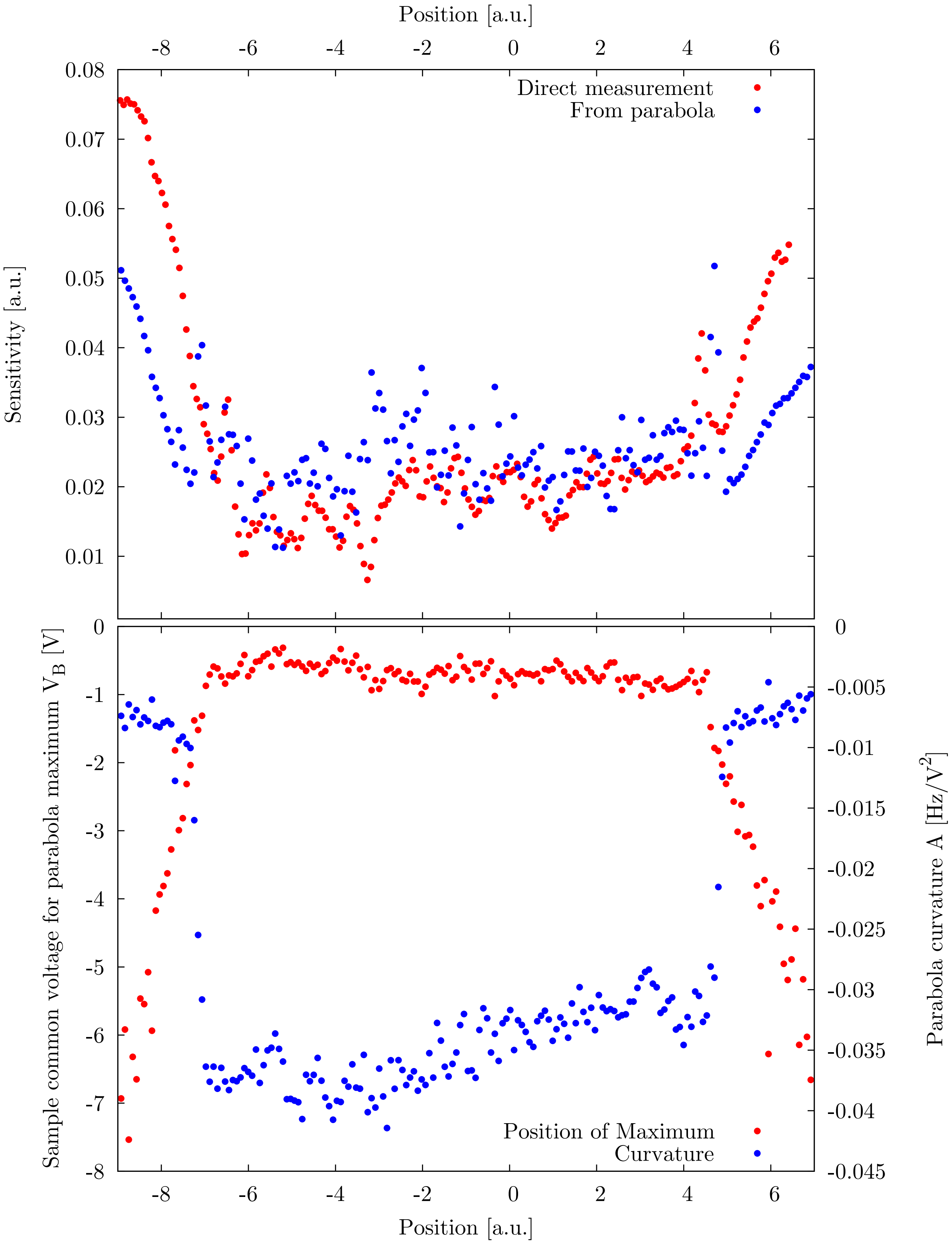

Figure G.5.: Sensitivity, curvature and position of maximum for the resonance frequency parabola. Also plotted is the reconstruction of the sensitivity by multiplying the curvature with the position of the parabola maximum.

parabola position change we can neglect the shift since the error is small. But if we measure close to the parabola maximum and V_B is small, errors due to parabola shifts can become large.

On the other hand the shift of the parabola has to be nonlinear to the modulation to cause a measurable effect because linear terms just cancel out.

G.4.2. Charging events

A measurement on GaAs/Al$_x$Ga$_{1-x}$As-heterostructure samples, where we measured the Hall potential profiles for different bias voltages, is presented in Fig. G.6 (a). Black regions can be seen which have a calibrated Hall potential higher than one. This corresponds to a local Hall voltage higher that the applied bias voltage which cannot be the case.

The output of the lock-in amplifier for rectangular modulation, taken on a fixed scan position while ramping up the sample bias is plotted in Fig. G.6 (b) and represents the resonance frequency shift over the bias V, see Fig. G.6 (e). A jump of the signal is clearly observable at a bias of 40 mV. After the single jump the curve just continues with an offset. Thus the error entering our measurements by current induced charging events becomes smaller the higher the bias. This can be seen in Fig. G.6 (a), where for increasing bias the black region is smoothly changing to red then yellow and green.

Of course this jump can be measured also in DC. That was done and plotted in Fig. G.6 (c) and (d). The resonance frequency shift was plotted color-coded over the sample bias and a common voltage V_com added to source and drain. The graph (c) is a control experiment where the sample bias was applied on source and drain. This makes the bias to become a common offset but more important there is no current flowing through the sample. In contrast there is current flowing in Fig. G.6 (d) and one finds no jump in the control experiment. Furthermore the jump position does not depend on the common voltage. This means that changing the sample potential relative to the surroundings does not affect this feature and excludes the electrostatic influence of the tip as reason.

The curve in Fig. G.6 (b) is described theoretically by equation (G.1). One possibility of finding a jump in this curve is a local charging event changing $\partial_z^2 q_\mathrm{m}$ and $\partial_z^2 W_\mathrm{o}$. We therefore believe to load a charge trap that is formed only after applying a current through the sample. Such a trap could look like the sketch of Fig. G.6 (f).

The jumps in Fig. G.6 (b) and (d) have the same sign of slope as the parabola at that point. An excitation transferred over the curve of Fig. G.6 (b) in the way shown in Fig. G.1 or G.2 will acquire an increased amplitude. Divided by the amplitude without this jump, calibrated values bigger than one can occur. In case the jumps would have a slope opposite to the parabola the calibrated potential becomes smaller and can become zero. This can be seen in Fig. G.7 where all the blue areas except of the one at the let side are due to this artefact.

G.5. Comments on the GB8113 graphene samples

We already mentioned in section 8 that the measurements on flake GB8113 were accompanied with technical difficulties. Even though measurements on other flakes did not have these difficulties, see section 10, flake GB8113 had the lowest disorder and shows

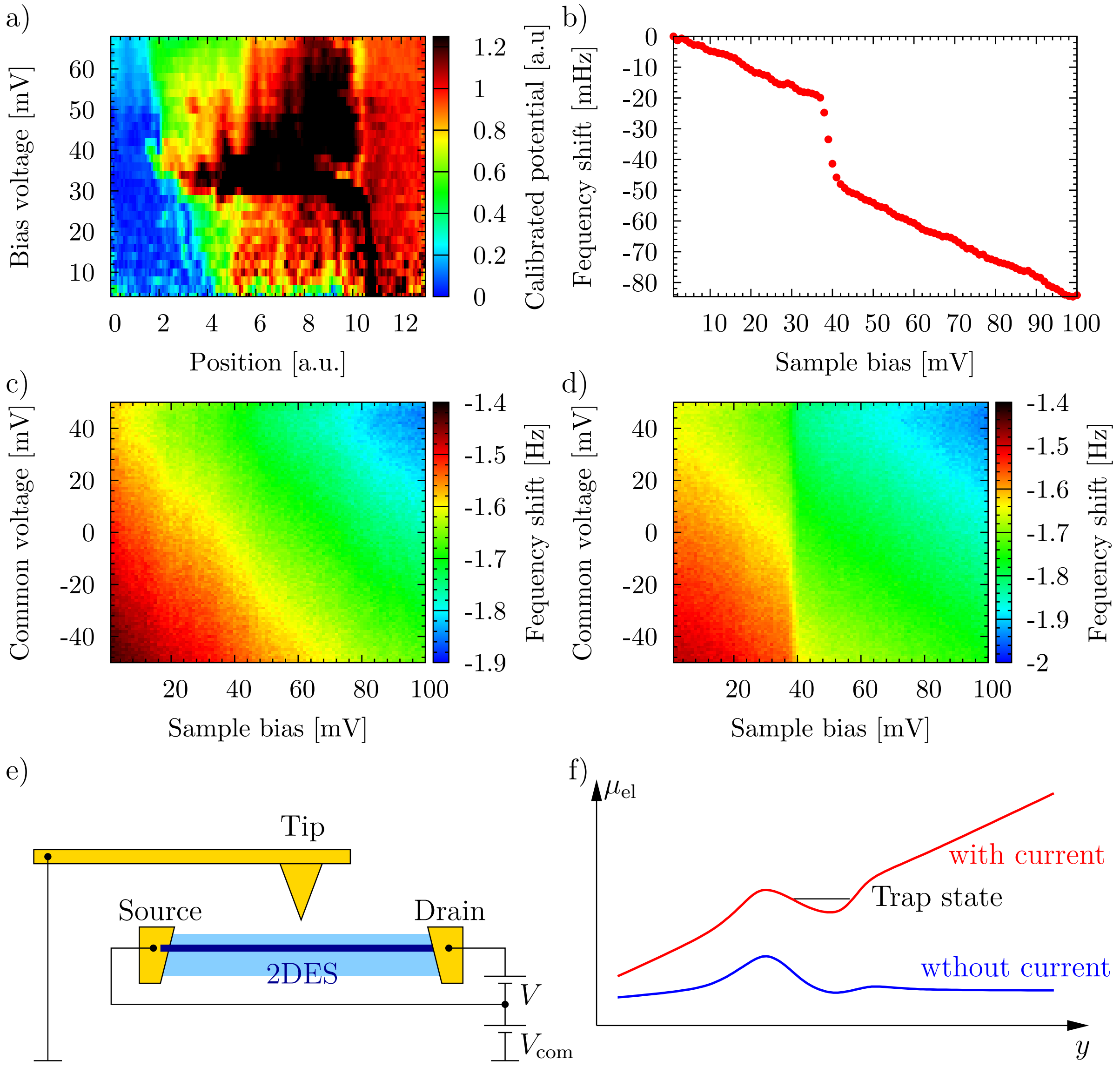

Figure G.6.: (a) Example of current induced artefact. Measuring the relative resonance frequency shift with rectangular excitation for one position graph (b) is observed. Thereby the excitation has to be applied as bias V on the sample as depicted in (e). The resonance frequency shift was measured in (c) and (d) as function of a common voltage V_{com} and a DC bias. One can turn on and off the jump in the frequency shift by switching on and off the current. (c) was measured without current and (d) with current. (e) Biasing scheme and (f) sketch of a possible current induced charge trap.

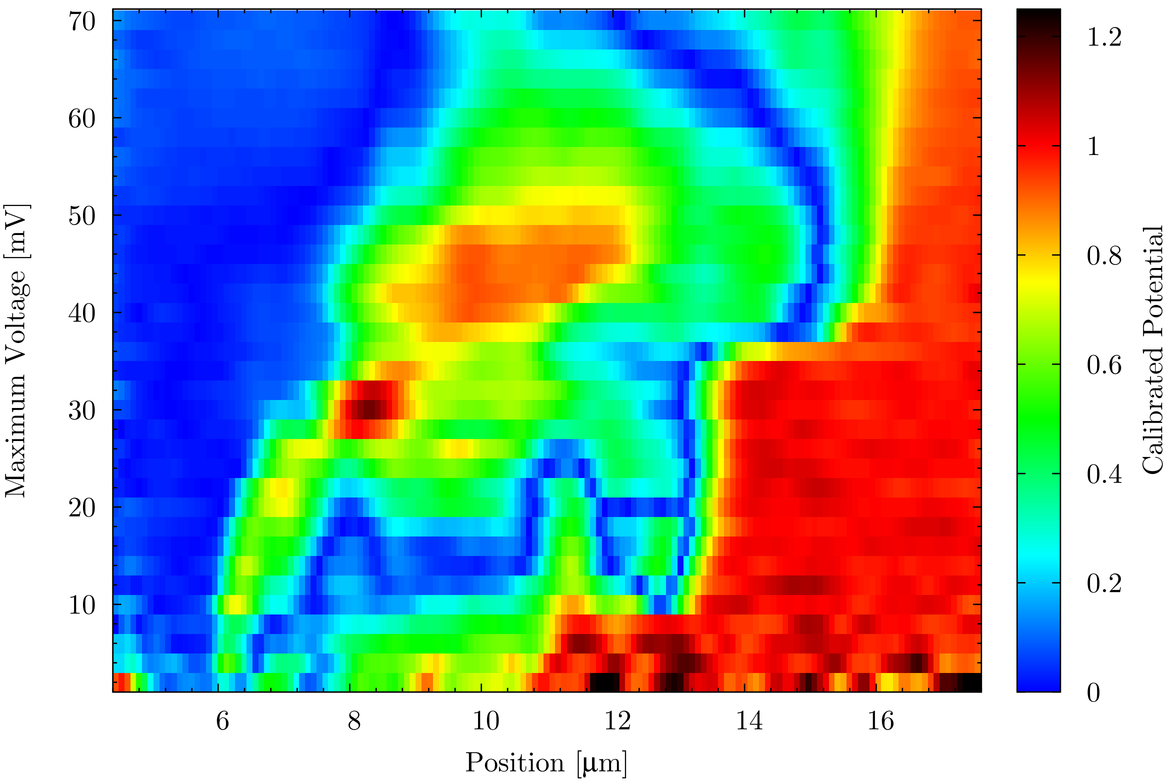

Figure G.7.: Measurement of Hall potential profiles on a GaAs/Al$_x$Ga$_{1-x}$As-heterostructure sample as function of position and source-drain bias with several types of artefacts.

the interesting features best. We will therefore verify in the following that the technical difficulties do not affect our findings.

One of the technical difficulties on sample GB8113 was a problem with the back gate. It turned out that during the cool down process the silver paste making the connection from the holder to the sample back gate degraded. The contact resistance to the back gate became very large and an additional leakage current from the back gate to ground created a voltage divider with effective division of 14. The linear dependence of the charge carrier concentration on the back gate voltage was proven and the effective voltage determined via transport sweeps. Thereby a voltage - denoted as common voltage V_{com} - was applied to the graphene flake relatively to the same reference as the back gate voltage $V_{\mathrm{BG-appl}}$ allowing to increase or decrease the voltage difference between back gate and flake. Thus the common voltage V_{com} applied to the flake adds up to the applied back gate voltage $V_{\mathrm{BG-appl}}$ and scales the coordinate axes of the resistance curve:

$$V_{\mathrm{BG}} = a_{\mathrm{BGF}} \cdot V_{\mathrm{BG-appl}} + V_{\mathrm{com}}(V_{\mathrm{BG-appl}}) \qquad \text{(G.15)}$$

V_{BG} is the back gate voltage effective for the graphene flake and a_{BGF} is the correction factor coming from the leakage. Measuring several resistance traces with different $V_{\mathrm{com}}(V_{\mathrm{BG-appl}})$ one gets stretched resistance curves. They collapse onto a single curve only after a_{BGF} was chosen correctly which is shown in Fig. G.8 for a_{BGF} being 1/14.

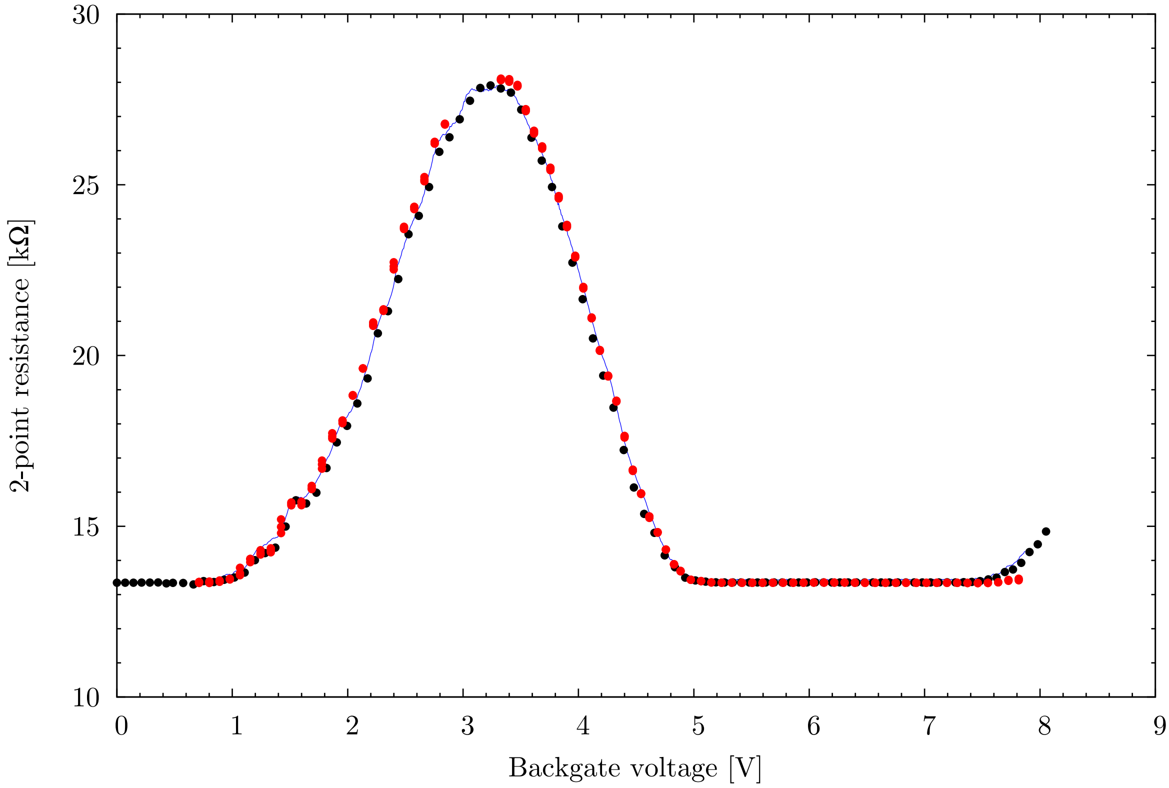

Figure G.8.: Determination of scaling factor and proof of linearity by adjusting three transport curves.

From such an analysis we can also estimate the error of the scaling (a_{BGF}) to be within ±13 %.

A second problem was that after we set the back gate voltage to a high negative value we found a shift of the resistance maximum. This can be explained by the shift of in room temperature mobile charges within the silicon dioxide. Charging of the silicon dioxide is known from optical measurements to happen in the used Si/SiO$_2$ substrates [168]. It should be emphasized here that this charging is uniform and does not produce an inhomogeneous doping of the flake. It rather shifts the charge neutrality point as happened here. We can see that easily from the scan before the charge shifting event, see Fig. G.9. All features discussed on the scan after the shift can be found also in Fig. G.9 before the shift. The u-shaped structure of the p-side is not completely visible but the upper ends can be clearly seen confirming the asymmetry across the resistance maximum.

The artefacts found in the data are due to low measurement sensitivity, see equation (G.9), as shown in a map in Fig. G.10. The dark blue regions in this map are areas with nearly no sensitivity of the measurement technique. Noise is amplified strongly resulting into the noisy stripes at the edges for a back gate voltage below −1.5 V and over the whole cross section between −1.5 V and −2.5 V. The reason for this particular pattern of the measurement-sensitivity comes from the position of the resonance frequency shift parabola. Due to the common voltage we apply to reduce the effect of the tip we cross the resonance frequency shift parabola maximum at about −1.5 V. At the dark blue

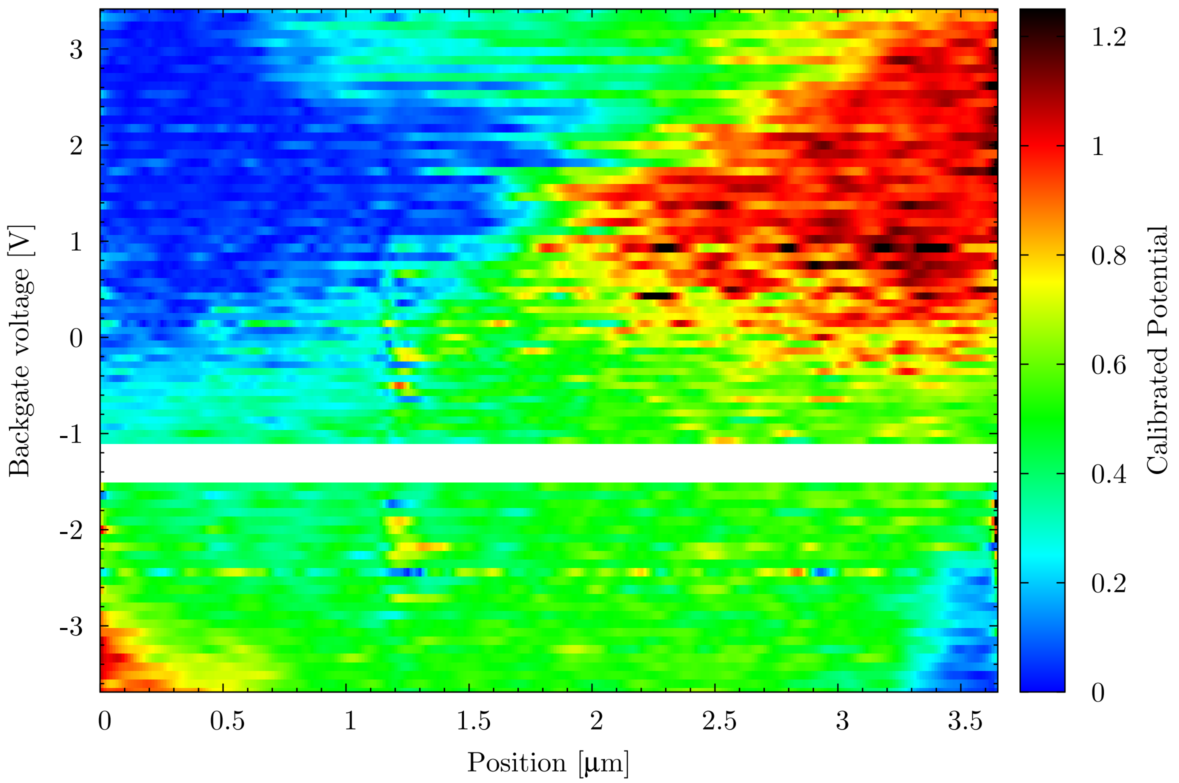

Figure G.9.: Measurement before the resistance maximum shift. All significant features that were discussed for this flake can be identified here too. The u-shaped structure for filling factor $\nu = -2$ is only partially visible. However the asymmetry across the resistance maximum is still observable.

regions we thus are positioned exactly on the parabola maximum giving zero measurement sensitivity. The zero sensitivity along the both edges below a back gate voltage of $-1.5\,\mathrm{V}$ is due to the back gate. The stray fields from the back gate at the edges of the flake do also affect the position of the parabola. Going with the SFM-tip closer to the flake edge shifts therefore the parabola maximum. In the blue regions we hit exactly the parabola maximum leading to zero sensitivity.

Low sensitivity is also found extending into the graphene flake from both edges for a back gate voltage of about $-7.5\,\mathrm{V}$. Artefacts as described in section G.4.1 are likely. Also in the back gate voltage range from $-1.0\,\mathrm{V}$ to $1.0\,\mathrm{V}$ the sensitivity is low. But due to the homogeneity of the sensitivity the interesting features are preserved.

G.6. Summary

In the theoretical discussion we have shown that the measurement signal for sinusoidal tip-sample voltage modulation is proportional to the resonance shift parabola curvature A, the modulation amplitude V_A, and the offset V_B between parabola maximum and the working point. For a rectangular modulation an additional quadratic term on the excitation amplitude enters the measurement output.

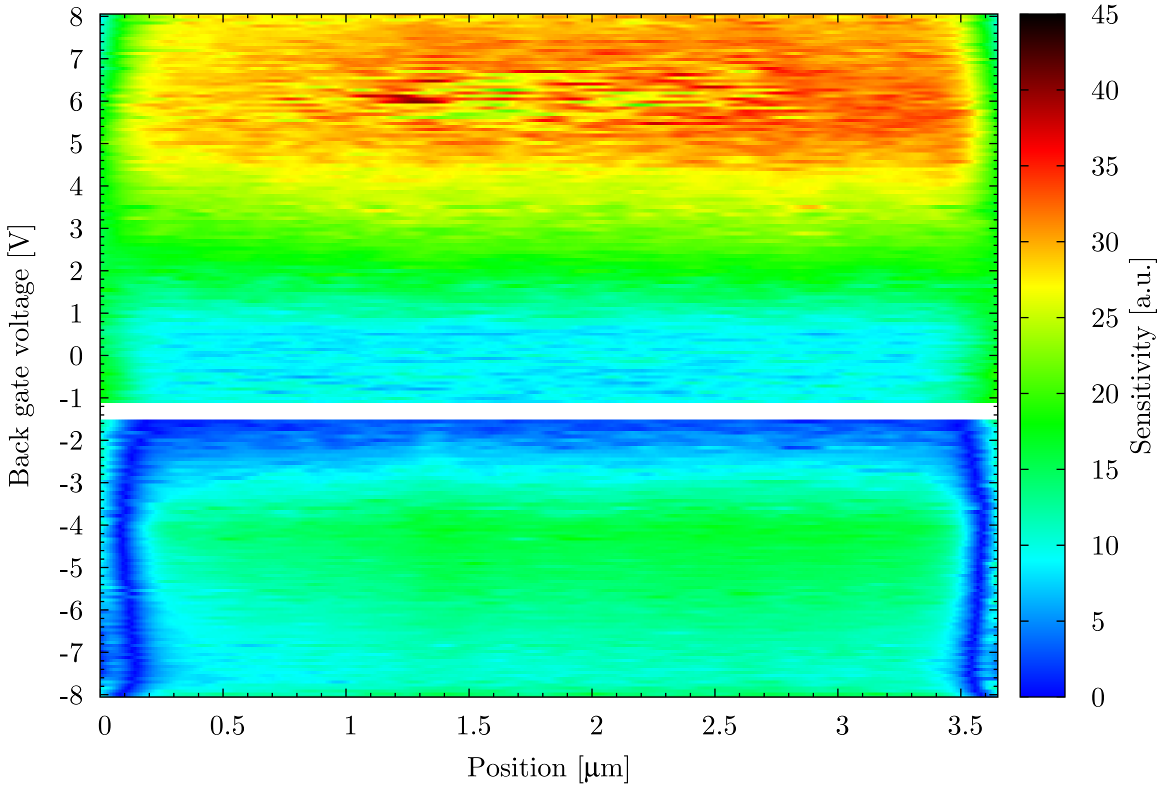

Figure G.10.: Sensitivity map over the measured back gate voltage and position range. Low sensitivity areas are shown in dark blue and artifacts can be expected. The light blue areas is not as critical but still lightly affected.

Based on this results we further explained the effect of setup noise onto our measurements, leading to a nonzero base line for the Hall potential profiles. Also sample related artefacts were discussed. So unintentional crashes of the tip on the sample surface create excess noise. Sensitivity can become besides the Hall bar higher than on the Hall bar.

Most dangerous artefacts from an interpretation point of view are current induced artefacts. They behave like a real signal coming from sudden electrostatic potential changes but are in reality only drivable charging events.

Finally we discussed the difficulties for the sample GB8113 and how they can be explained.

H. Sample parameter, geometry and processing

In the following chapter we want to discuss the details of the used samples. We want to focus on material parameters, processing and the chosen geometry.

Since graphene and GaAs/Al$_x$Ga$_{(1-x)}$As-heterostructures differ in processing we chose to describe them separately starting with graphene.

H.1. Graphene samples

H.1.1. Fabrication

The graphene samples used for this work where prepared in cooperation with Benjamin Krauss from Jurgen Smets group in our Institute. All the flakes were mechanically exfoliated with the so-called scotch tape method [6]. The flakes were attached thereby on a thermally grown silicon oxide on silicon substrate. The base material of the substrate was a 6 inch Arsenic doped silicon wafer (n-Si-wafer) and the thickness of the oxide was 300 nm. It turned out that standard passivation techniques to demobilize mobile ions were not applied on our substrate. In addition a marker system was written on the substrates before the flakes were deposited for finding the flakes.

An automated microscope system screened for single flakes after deposition while the final selection was done by us.

Finally the gold structure had to be written on the sample. For the design itself the following considerations had to be made:

- Bond pads had to be oriented only to one direction to reduce the tip crashing risk.
- To find the position of the flake, large gold patches were incorporated in the design. During the measurement we find and follow the borders of these patches towards the flake. For convenience we try to use borderlines with angel close to 45° with respect to the positioning system of the sample holder.
- Since there are many other flakes and graphite patches which can shortcut our contacts or gold patches care has to be taken to touch all other flakes only by one contact.

The lithographic process for getting the design onto the sample was as following:

(a) Cleaning of the substrate the flake was deposited with acetone followed by two times of isopropanol (IPA).

(b) Spin coating of e-beam resist:

   a) 200k polymethyl methacrylate (PMMA), in a solution of 3.5 % PMMA in IPA, was spin coated with with 3000 rpm for 5 s followed by 8000 rpm for 30 s. Resulting thickness 140 nm.
   b) Backing for 3 min on a hot-plate at 180 °C.
   c) 950k PMMA, in a solution of 1.5 % PMMA in IPA, was spin coated with with 3000 rpm for 5 s followed by 8000 rpm for 30 s. Resulting thickness 60 nm.
   d) Backing for 3 min on a hot-plate at 180 °C.

(c) E-line writing of the design.

(d) Development for 120 s with methyl isobutyl ketone (MIBK) in IPA and stopping of the development in IPA for 60 s. Drying with nitrogen.

(e) Evaporation of 5 nm Chromium and 100 nm Gold

(f) Lift off: 1 h in 55 °C in the organic solvent N-Ethylpyrrolidon (NEP) and cleaning three times in aceton and two times in IPA for 1 min each. Drying with nitrogen blow.

Further steps for the actual loading into the sample holder were the gluing on a sample chip and bonding.

H.1.2. Samples' characteristics

Two samples were fabricated as described above. Figure H.1 shows the sample with the flake named GB8113. And Fig. H.2 shows the sample with the flakes GB9438a and GB9438b. Features in the Hall potential measurements were easiest to interpret in flake GB8113. Our interpretation of the QHE in graphene as presented in chapter 9 was given only upon this sample. The flakes GB9438a and GB9438b show in principle the same features and lead to the same interpretation. But one has to include disorder to fully understand the results. This was done in chapter 10.

In table H.1 an overview of the three measured flakes is given. In addition some parameters are given for comparison.

ID	μ	ΔV_{FWHM}	$\Delta\eta$	Comment
GB8113	$2\,\mathrm{T}^{-1}$ at $2.0 \cdot 10^{15}\,\mathrm{m}^{-2}$	2.8 V	$2.0 \cdot 10^{15}\,\mathrm{m}^{-2}$	Nicest features
GB9438a	$1\,\mathrm{T}^{-1}$ at $3 \cdot 10^{15}\,\mathrm{m}^{-2}$	7.7 V	$5.5 \cdot 10^{15}\,\mathrm{m}^{-2}$	Bubbles
GB9438b	$0.7\,\mathrm{T}^{-1}$ at $3 \cdot 10^{15}\,\mathrm{m}^{-2}$	10.6 V	$7.6 \cdot 10^{15}\,\mathrm{m}^{-2}$	Fluctuations

Table H.1.: Overview of the three graphene flakes with the parameters mobility μ, the full width at half maximum of the resistance over back gate voltage trace ΔV_{FWHM}, and the charge carrier density variation $\Delta\eta$ within ΔV_{FWHM}.

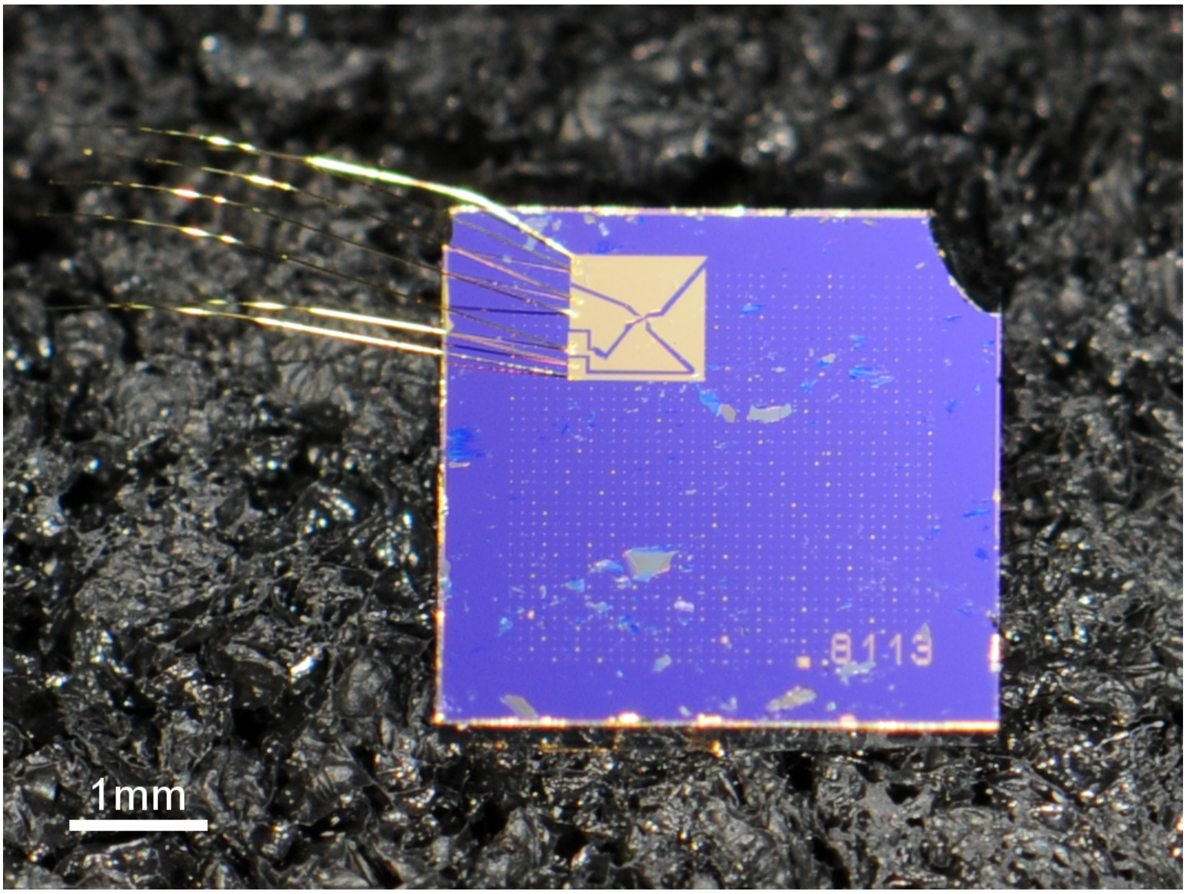

Figure H.1.: Macro picture of the sample with the graphene flake GB8113.

H.2. GaAs/Al$_x$Ga$_{(1-x)}$As-heterostructure samples

H.2.1. Fabrication

The GaAs/Al$_x$Ga$_{(1-x)}$As-heterostructure samples were fabricated with the help of Achim Güth and Marion Hagel while the heterostructure itself was grown by Mike Hauser from the group of Werner Dietsche, altogether people from our Institute.

The design was optimized during the course of this thesis and is shown in its final version on Fig. H.3. It includes the following features:

- Positioning areas to simplify finding the Hall bar to be scanned.
- A scanning tube calibration area.
- Hall bars for scanning and transport measurements.
- TLM (transmission line measurement) structures to determine the contact resistivity of the alloyed contacts to check for good electrical contact to the 2DES.
- A benchmark system to measure the exposure resolution and therewith identify problems with the exposure.

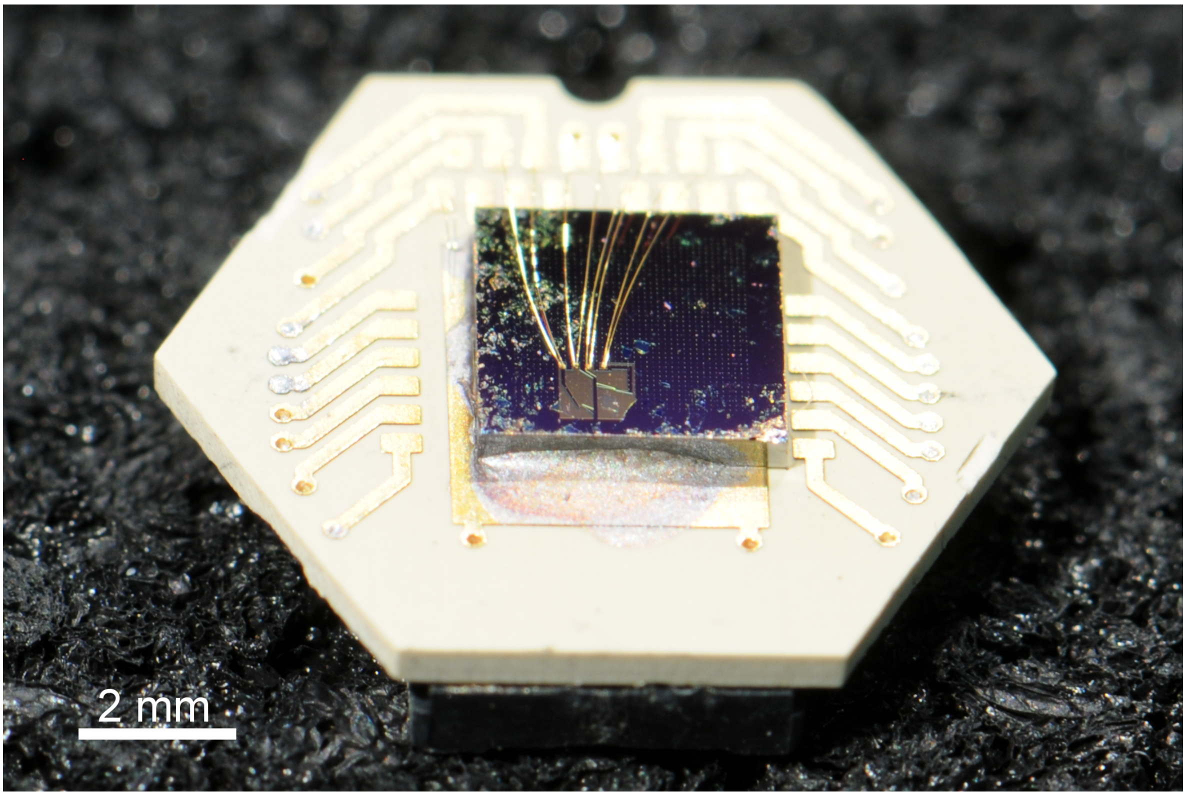

Figure H.2.: Macro picture of the sample with the graphene flakes GB9438a and GB9438b mounted on a chip carrier.

- Bond pads positioning only at a single side.

The optical lithography consisted of three patterning steps: defining the mesa, the alloyed contacts and the gold wire and bond pads.

The mesa was etched and the procedure is as following:

- Cleaning the sample two times with acetone and two time with IPA, one minute each.
- Spin-coat S1805 resist with 30 s at 4500 rpm.
- Baking two minutes at 90°.
- Mask exposure with UV-light.
- Development for 33 s in AZ726MIF and stopping the development in water.
- Etching in 1:8:1000 solution of $H_2SO_4 : H_2O_2 : H_2O$.
- Strip off with acetone.

Alloyed contacts are prepared next:

- Cleaning the sample two times with acetone and two time with IPA, one minute each.

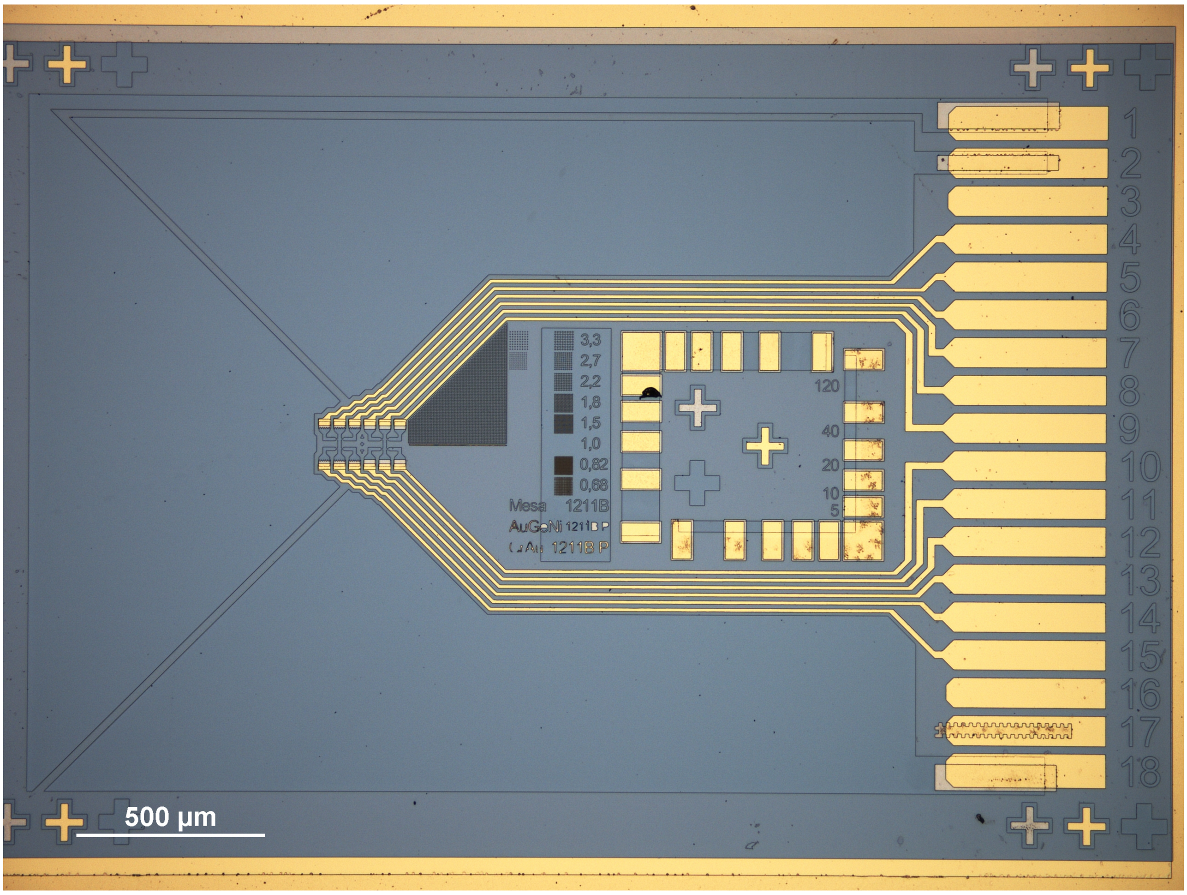
1
2
3
4
5
6
7
8
9
10
11
12
13
14
15
16
17
18
3,3
2,7
2,2
1,8
1,5
1,0
0,82
0,68
Mesa 1211B
AuGeNi 1211B P
1211B P
120
40
20
10
5
500 µm

Figure H.3.: Final design of our GaAs/Al$_x$Ga$_{(1-x)}$As-heterostructure samples.

- Spin-coat AZ5214E resist with 30 s at 6000 rpm.
- Baking four minutes at 90°.
- Removal of the resist at the edges to remove the resist bumps at the edges. This is done by the exposure of the edges for three minutes and development in AZ726MIF for 30 s.
- Mask exposure with UV-light.
- Inverse the exposure by baking for 60 s in 125°C followed by a flood exposure of 80 s.
- Development for 35 s in AZ726MIF and stopping the development in water.
- O_2 cleaning plasma for 30 s.
- Dip in semico-clean [241] for two minutes followed by 5 s water then 5 s Hydrochloric acid and finally one second water. The time between this dip and the evacuation before the evaporation should be caped as short as possible.

- Evaporation of 107.2 nm gold, 52.8 nm germanium and 40 nm nickel. (Thickness has to be adapted to the heterostructure see [107]).
- Lift off in acetone and cleaning with IPA.
- Alloying the contacts at 370°C for 120 s and letting them diffuse into the heterostructure for 30 s at 440°C.

Finally the gold wires and bond pads are structured.

- Cleaning the sample two times with acetone and two time with IPA, one minute each.
- Spin-coat AZ5214E resist with 30 s at 6000 rpm.
- Baking four minutes at 90°.
- Removal of the resist at the edges to increase resolution. Meaning exposure of the edges for three minutes and development in AZ726MIF for 30 s.
- Mask exposure with UV-light.
- Inverse the exposure by baking for 60 s in 125°C followed by a flood exposure of 80 s.
- Development for 33 s in AZ726MIF and stopping the development in water.
- O_2 cleaning plasma for 30 s.
- Evaporation of 20 nm chromium and 100 nm gold.
- Lift off in acetone and cleaning with IPA

H.2.2. Samples' characteristics

In this thesis we used two different GaAs/Al_xGa_{1-x}As heterostructures to fabricate samples. Details on the layer succession are given in chapter 2. Both used heterostructures had the 2DES 55 nm below the surface and a concentration of aluminum of 33%. The measurements on sample 8379_20100120_B, shown in Fig. H.4, were line scans close to the Hall bar center. We were able to distinguish two different types of breakdown on this sample. Measurements on sample 8957_201112_B, shown in Fig. H.5, were aiming on area scans to further understand the bulk dominated breakdown. In this type of breakdown it was important to understand what happens over the full area of the sample. Compare to the measurements on sample 8379_20100120_B, we measured at a lower number of magnetic field values but at higher number of locations.

To characterize our heterostructures we measured at a temperature of 1.5 K the QHE. The magnetic field $B|_{\nu=1}$ for filling factor $\nu = 1$ can be determined either by a linear fit of the Hall trace or by fitting the position of the longitudinal resistance minima. The second method is shown in Fig. H.6 (a) for sample 8379_20100120_B and delivers $B|_{\nu=1} = 11.7\,\mathrm{T}$. The two-terminal resistance of the scanned hall bar is shown in Fig. H.6

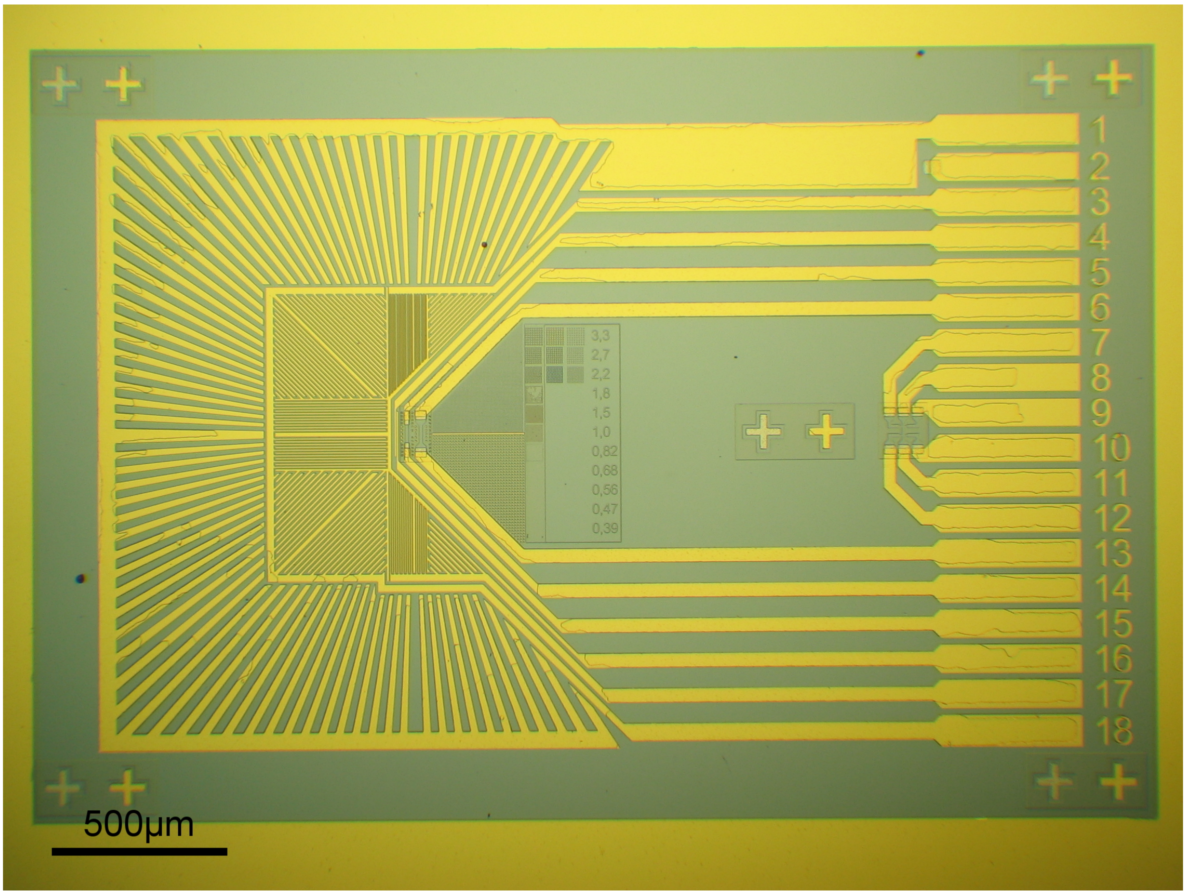

Figure H.4.: Optical microscope picture of sample 8379_20100120_B.

together with the longitudinal resistance we used for the analysis of the separate transport Hall bar positioned on the same chip. The charge carrier density n can then be calculated

$$n = \frac{B|_{\nu=1}}{eR_{\mathrm{K90}}} \approx 2.8 \cdot 10^{15}\,\frac{1}{\mathrm{m}^2}. \tag{H.1}$$

The zero magnetic field resistivity ρ of the 2DES was determined via the slope of a the TLM trace. It was found from Fig. H.6 (b) to be $\rho = 58.71\,\Omega$. The mobility can be calculated from the resistivity as following

$$\mu = \frac{R_{\mathrm{K90}}}{\rho B|_{\nu=1}} \approx 38\,\frac{1}{\mathrm{T}}. \tag{H.2}$$

The characterization of sample 8957_201112_B was done similar using the measurement shown in Fig. H.8. This time we used the linear fit on the Hall resistance trace to determine $B|_{\nu=1}$. They result into a $B|_{\nu=1} = 13.2\,\mathrm{T}$ and thus a charge carrier density of

$$n \approx 3.2 \cdot 10^{15}\,\frac{1}{\mathrm{m}^2}. \tag{H.3}$$

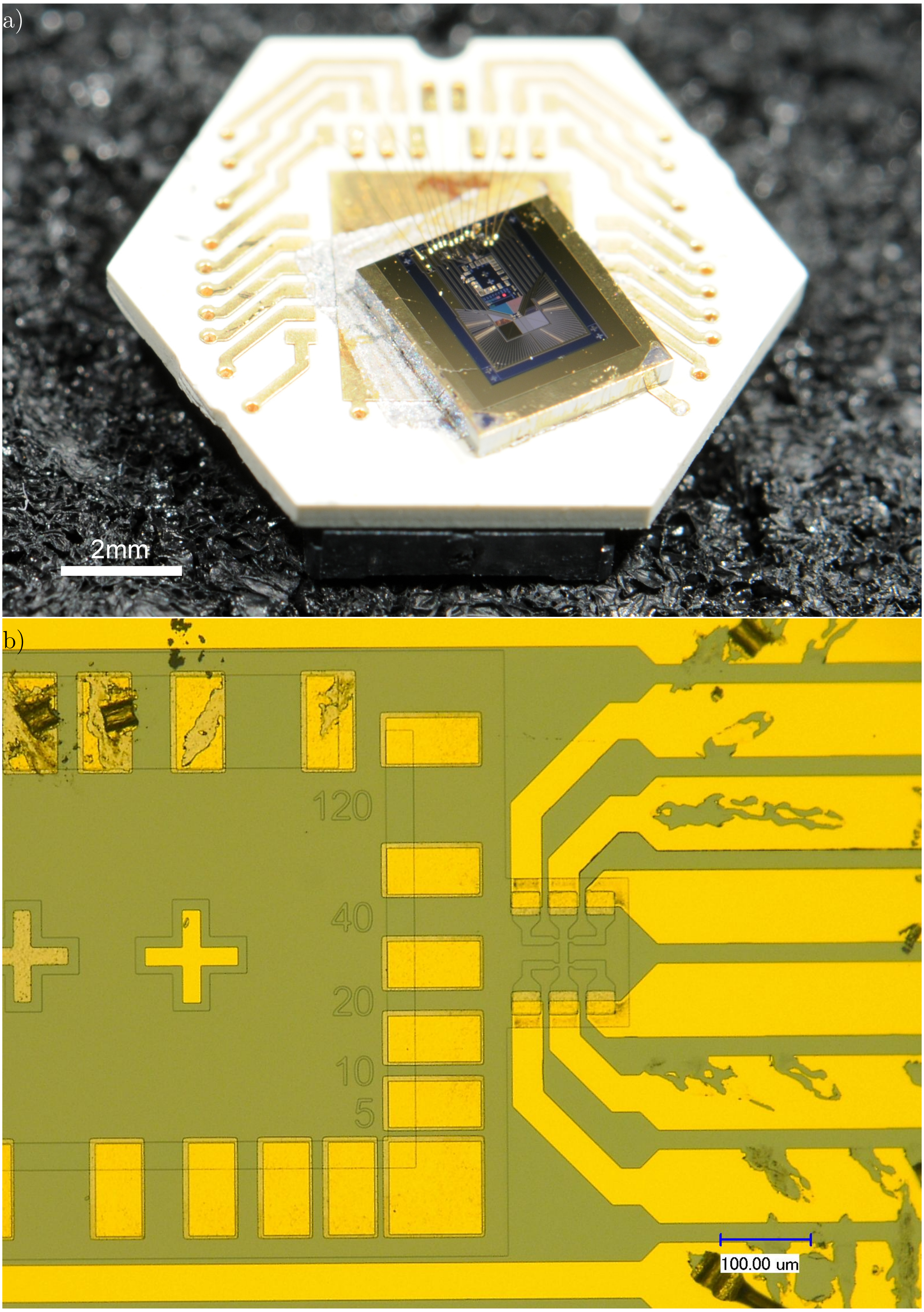
a)
2mm
b)
120
40
20
10
5
100.00 um

Figure H.5.: Macro picture of sample 8957_201112_B mounted on a chip carrier (a) and optical microscope picture of the scaned Hall bar and its surroundings (b).

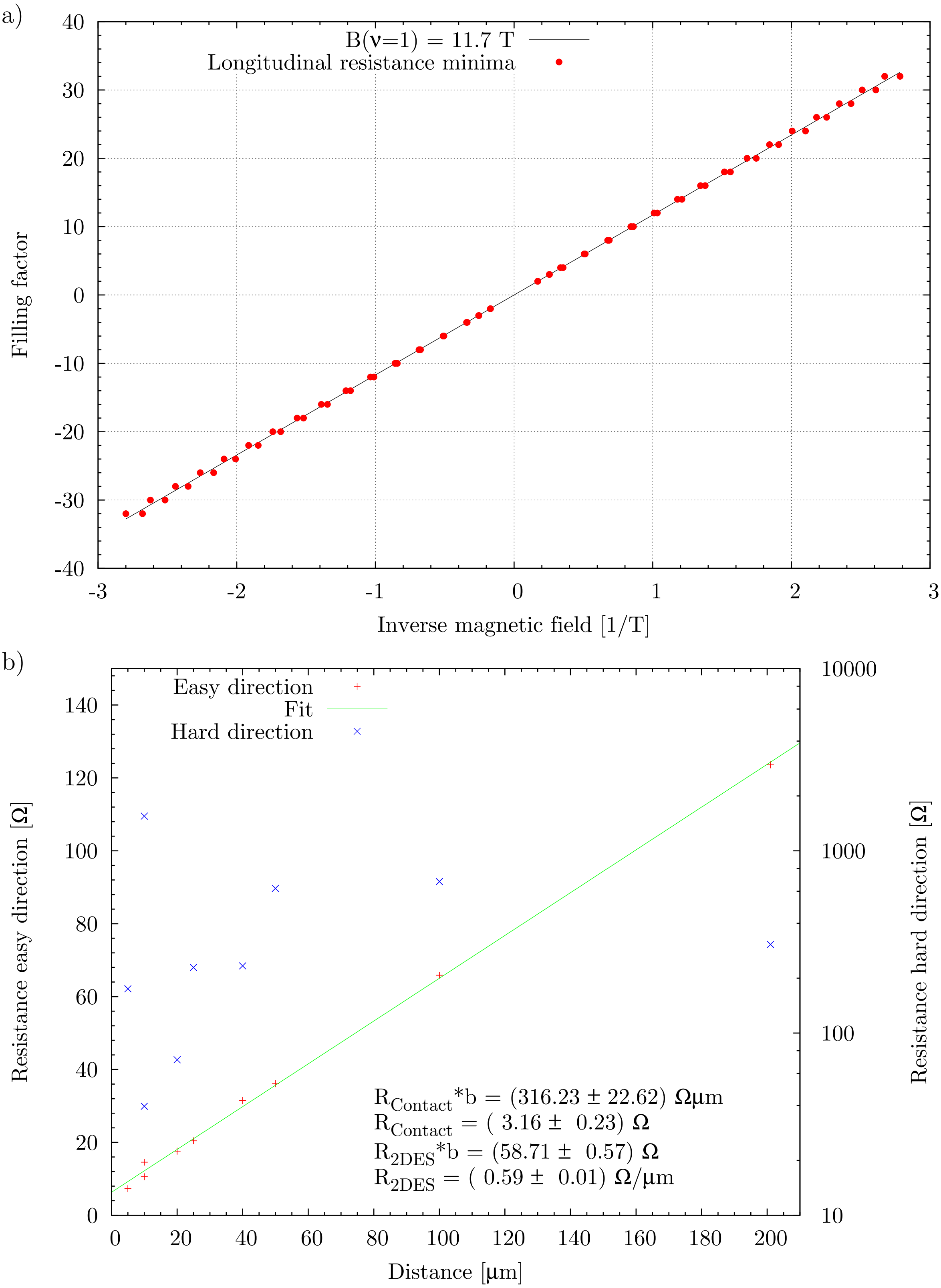

Figure H.6.: (a) Determination of the magnetic field $B|_{\nu=1}$ for filling factor $\nu = 1$ by fitting the longitudinal resistance minima of sample 8379_20100120_B shown in Fig. H.7. In (b) we show a TLM (transmision line measurement) trace by wich one can get the sheet resistance of the 2DES at zero field R_{2DES}.

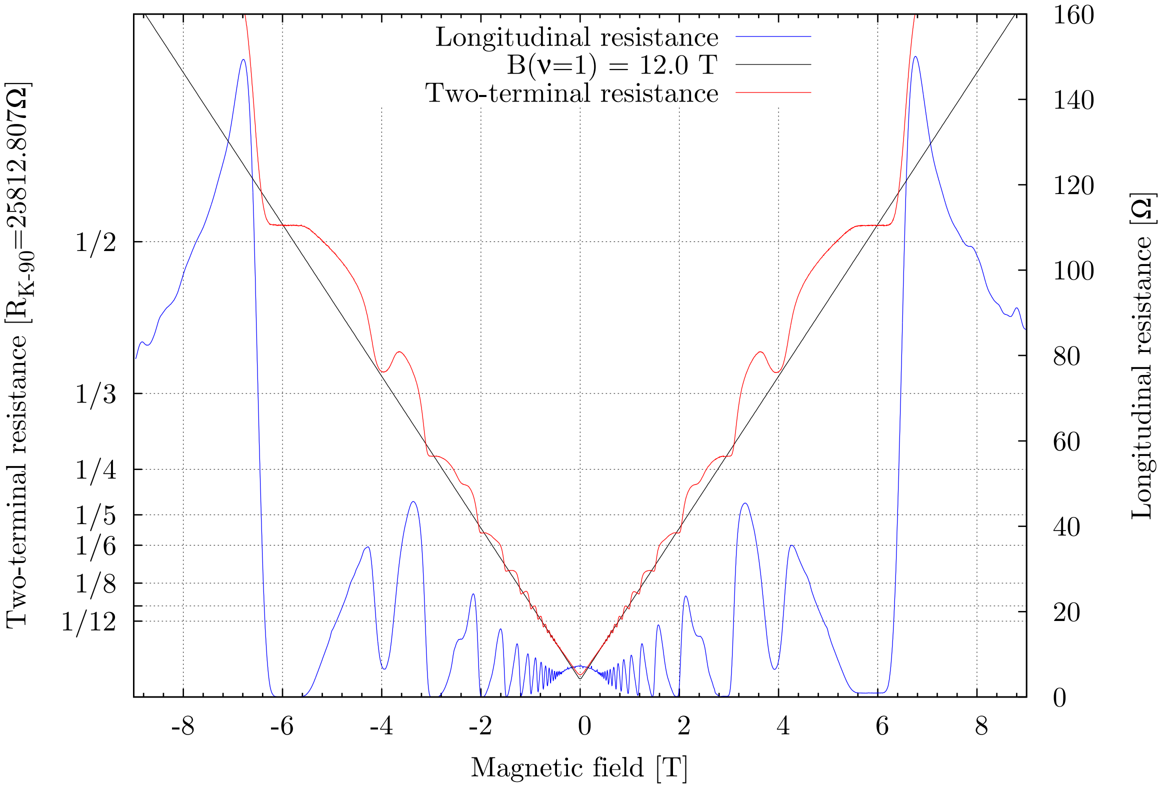

Figure H.7.: 2-point resistance of the scanned Hall bar in red and longitudinal resistance of the transport Hall bar in blue of sample 8379_20100120_B. The black line is a fit to determine the magnetic field $B|_{\nu=1}$ for filling factor $\nu = 1$. Nevertheless we prefer to take the value determined from the minima in the longitudinal resistance given in Fig. H.6.

The 2DES resistivity was $\rho = 38.12\,\Omega$ and results a mobility of

$$\mu \approx 51\,\frac{1}{\mathrm{T}}. \tag{H.4}$$

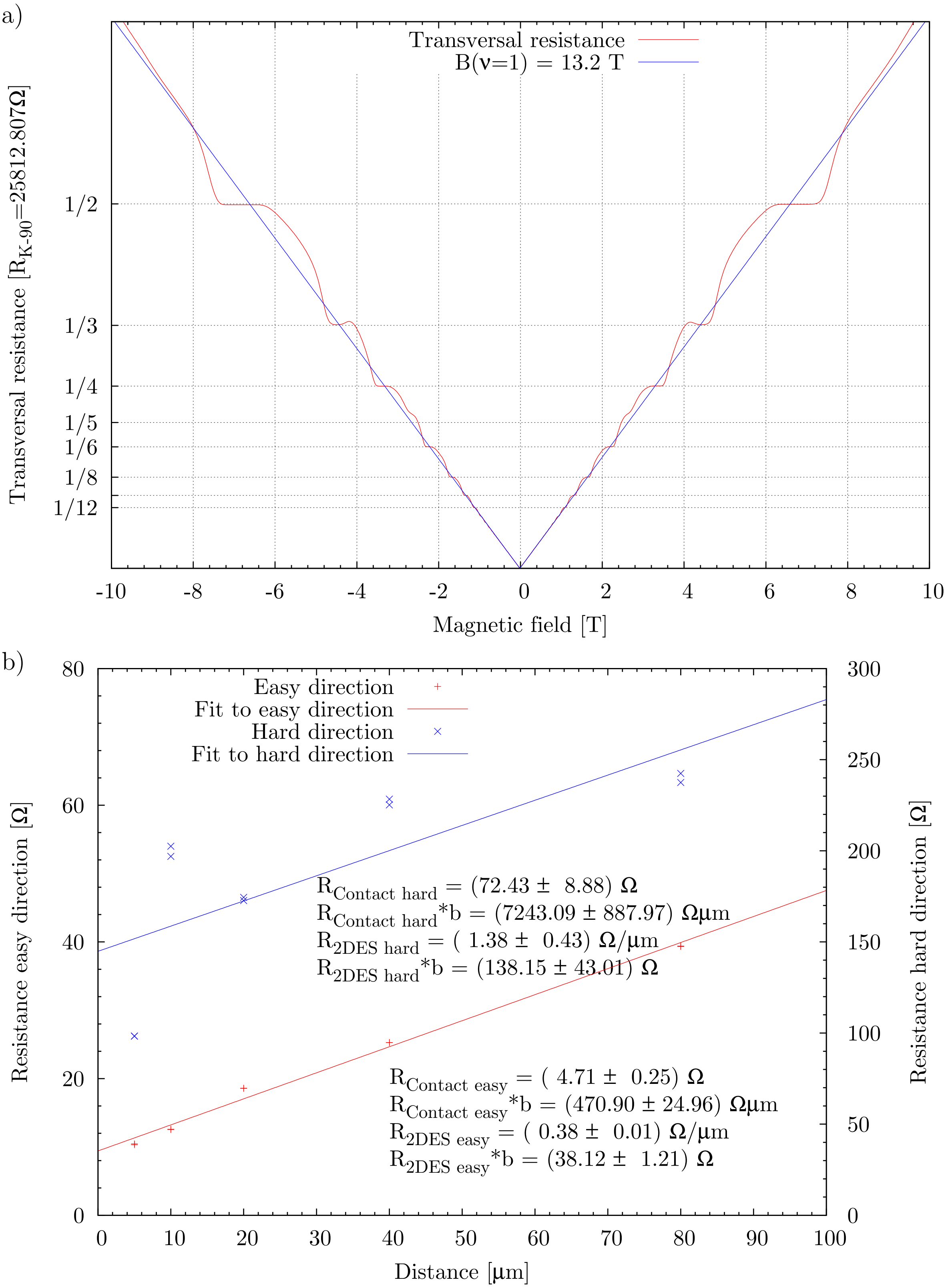

Figure H.8.: Determination of the charge carrier density (a) and mobility (b) of sample 8957_201112_B. In (b) only the easy direction was used for the mobility determination since the hard direction is affected strongly by the contact resistance.

I. Scanning tip properties and processing

The scanning tips "PRC400" used in the experiments are contact mode cantilevers made by the Japanese company SII NanoTechnology Inc. [242] and distributed by Epolead Service Inc. [243]. The parameters of the as bought piezoresistive silicon tips can be found table I.1.

For our scanning probe measurements which base on electrostatic interactions we require metal coated tips that can be contacted to be set on the desired potential. Unfortunately we were not able to find metal coated piezoresistive tips on the market and thus had to further handle the tips from SII to get usable tips. The presented processing method was developed together with Thomas Reindl from our Institute.

The tip processing consists of five steps:

- Backing the tips for 3 hours at 180°C to get rid of any out-gassing material and thus improve the quality of the next step.
- 200 steps of atom layer deposited of aluminum oxide at a temperature of 100°C resulting into a layer of about 20 nm. Short-circuits due to the following metal coating are prevented by the isolating aluminum oxide.
- Shadowmask evaporation of 10 nm titanium followed by 90 nm palladium. With the mask we cover the contact pads to avoid an electrical shortage.
- Manual coating with silverepoxy to contact the palladium plating and form a contact at the back side of the tip holding printed circuit board (pcb).
- Backing at 80° for three hours to harden the epoxy.

Resonance frequency	f	35 kHz to 40 kHz
Quality factor in atmosphere	Q_a	100 to 160
Spring constant	k	2 N/m to 4 N/m
Typical resistance	R	600 Ω to 800 Ω
Cantilever length	l	400 µm
Cantilever width	w	50 µm
Cantilever thickness	h	4 µm to 5 µm
Sensing constriction area		5 µm × 5 µm
Tip apex radius	a	$<$ 20 nm
Tip height	h_t	$>$ 5 µm

Table I.1.: Parameter summary of the used SII tips PRC400 according to the datasheet.

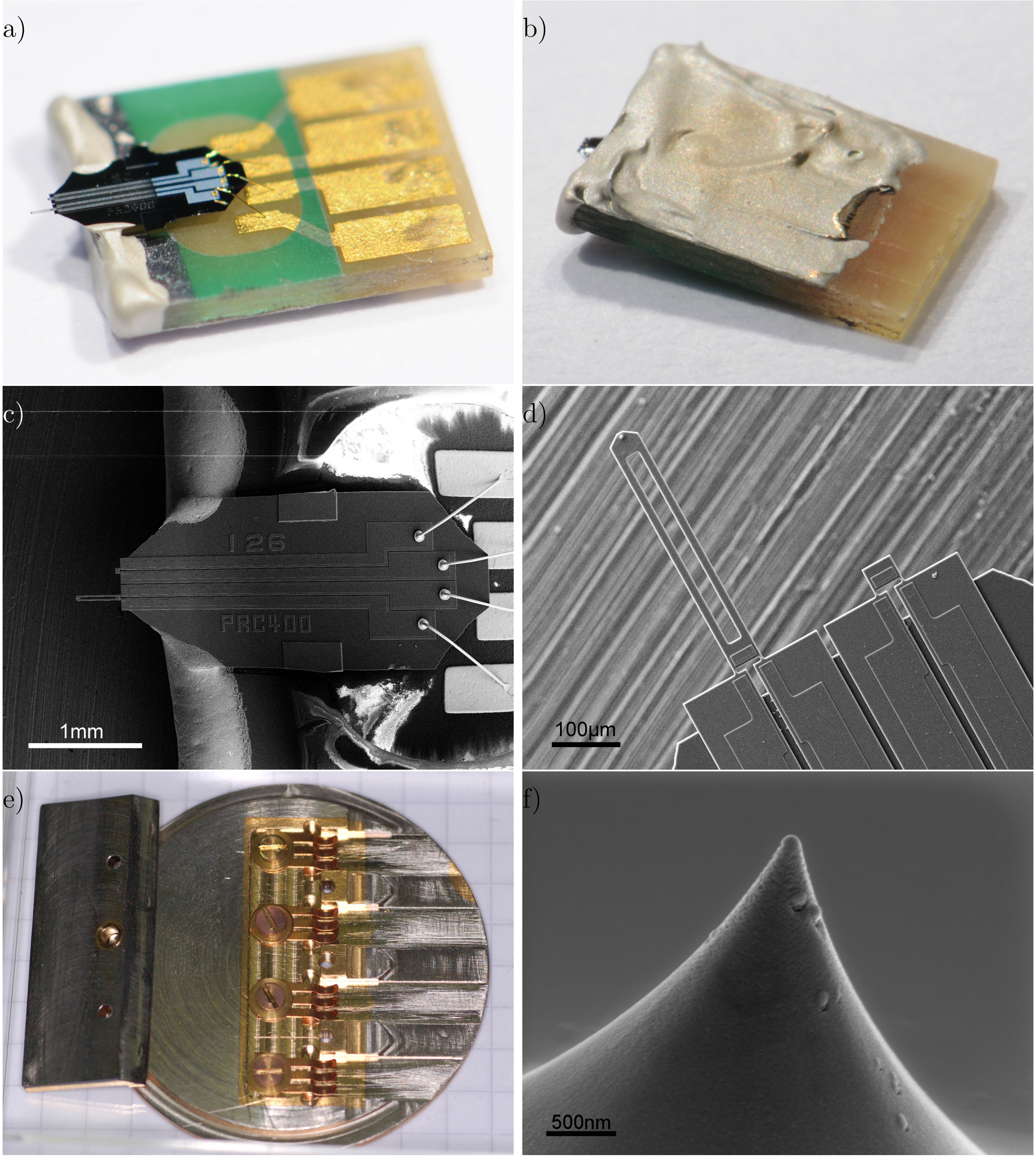

Figure I.1.: (a) Picture of the processed tip. (b) Picture of the back side of the processed tip. (c) SEM micrograph of the silicon die glued on a piece of PCB. (d) SEM picture of the cantilever and the dummy tip. (e) Shadow mask and holder for our scanning tips. (f) SEM close up micrograph of the scanning tip.

The finished tips get a quality check by measuring the resistance values of all possible pairs of contacts and the plating. In addition a final check is done within the sample holder by measuring the resonance frequency of the tips via an electrostatic excitation. Pictures of the tips and the shadow mask can be found in Fig. I.1.

J. Breakdown data

J.1. Sample 8379_20100120_B

In the following we will present all significant scans on sample 8379_20100120_B. Each row of graphs represents the data for one magnetic field value marked on the very left side. The two graphs on the left correspond to the current direction (i), see for details Fig. 13.4, while the two graphs on the right to the current direction (j). Selected line scans from the inner color-coded plots are plotted in the outer graphs.

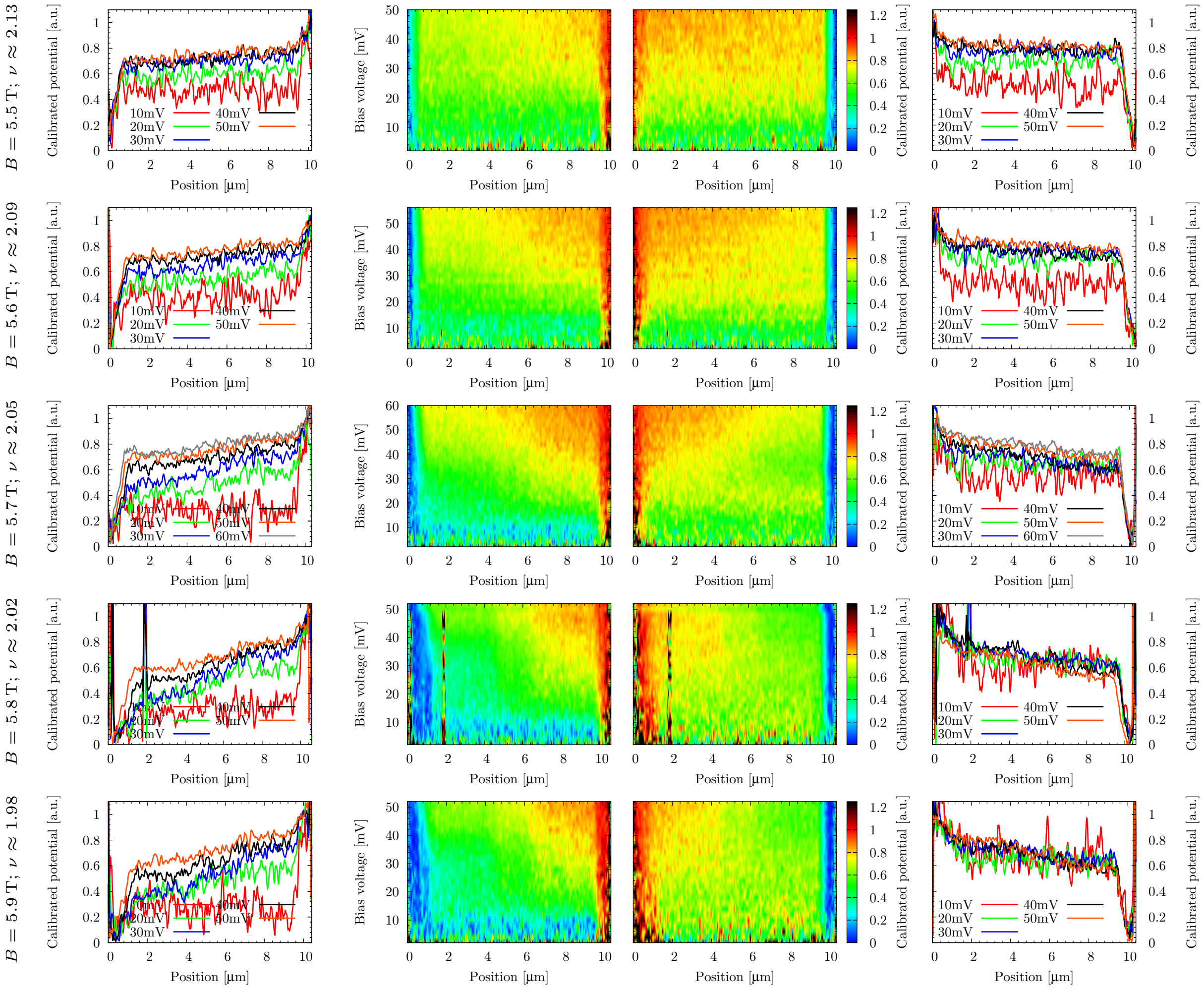

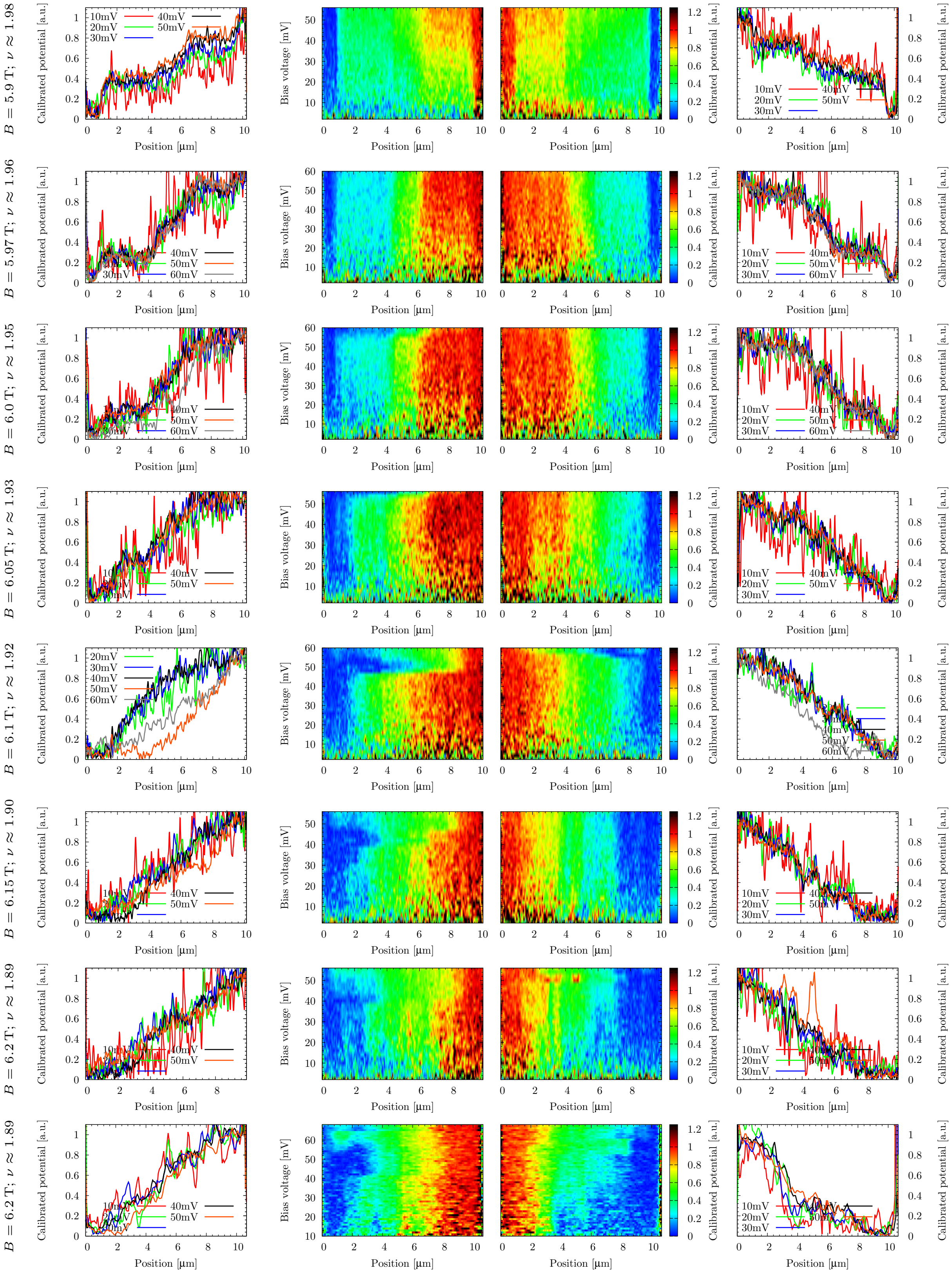
B = 5.9 T; ν ≈ 1.98
B = 5.97 T; ν ≈ 1.96
B = 6.0 T; ν ≈ 1.95
B = 6.05 T; ν ≈ 1.93
B = 6.1 T; ν ≈ 1.92
B = 6.15 T; ν ≈ 1.90
B = 6.2 T; ν ≈ 1.89
B = 6.2 T; ν ≈ 1.89
Calibrated potential [a.u.]
Bias voltage [mV]
Position [µm]
10mV
20mV
30mV
40mV
50mV
60mV
0
0.2
0.4
0.6
0.8
1
1.2
10
20
30
40
50
60
0
2
4
6
8
10

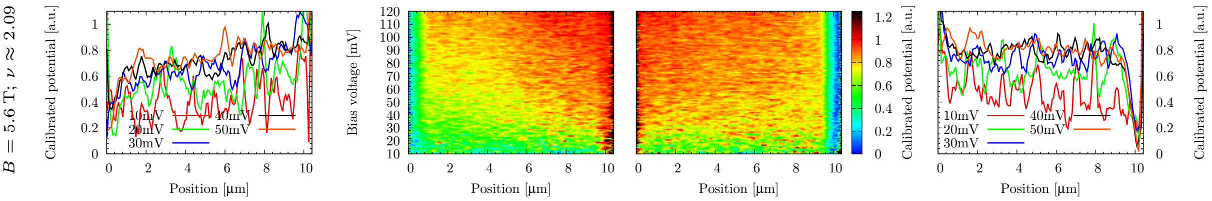

In the following we show the Hall potential drops at the left and right edge of the sample for the edge dominated breakdown within the above set of data. The error bars are not shown for clarity. A plot of a single trace and with error bars was shown in Fig. 13.12. The error bars for low bias are significantly bigger than for high bias.

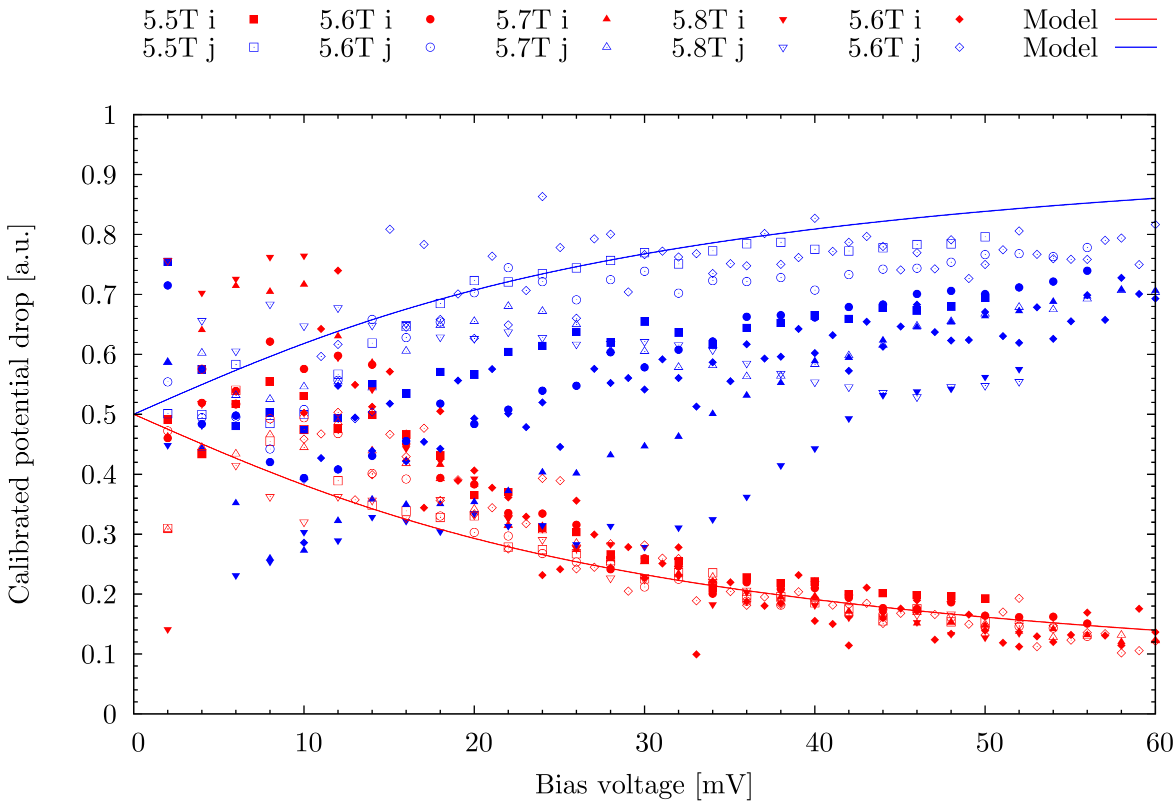

J.2. Sample 8957_201112_B

The measurements on sample 8957_201112_B were done with the focus on area scans. Following is shown the data set acquired to determine the magnetic field range for the edge- and and bulk-dominated regime. The graph on the left correspond to the current direction (i), see for details Fig. 13.4, and the graph on the right to the current direction (j). The magnetic field and the filling factor is mentioned for each row at the left side.

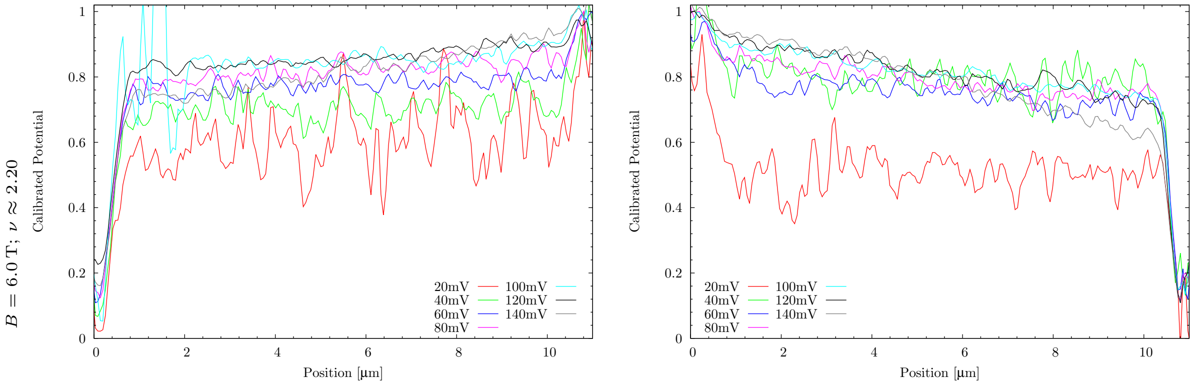

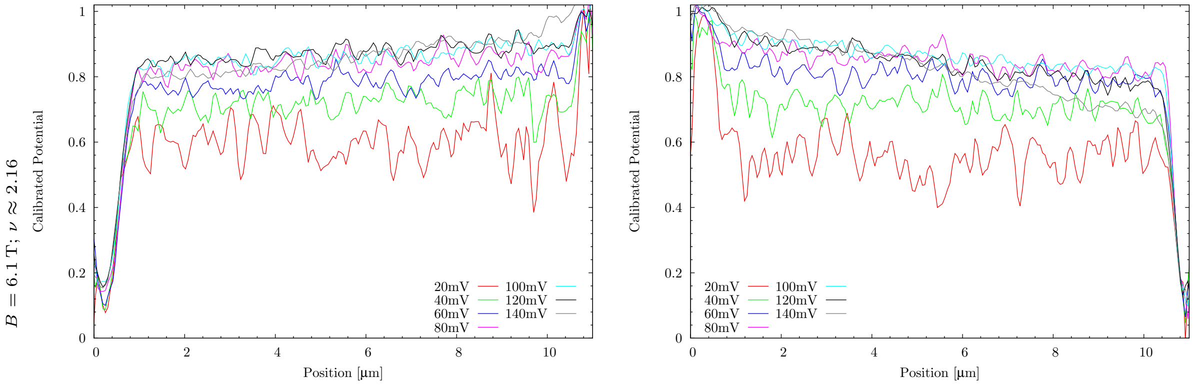

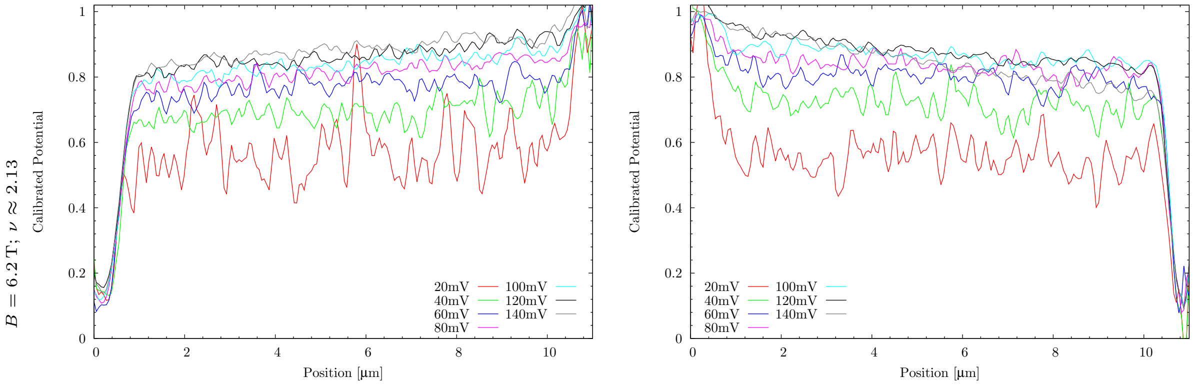

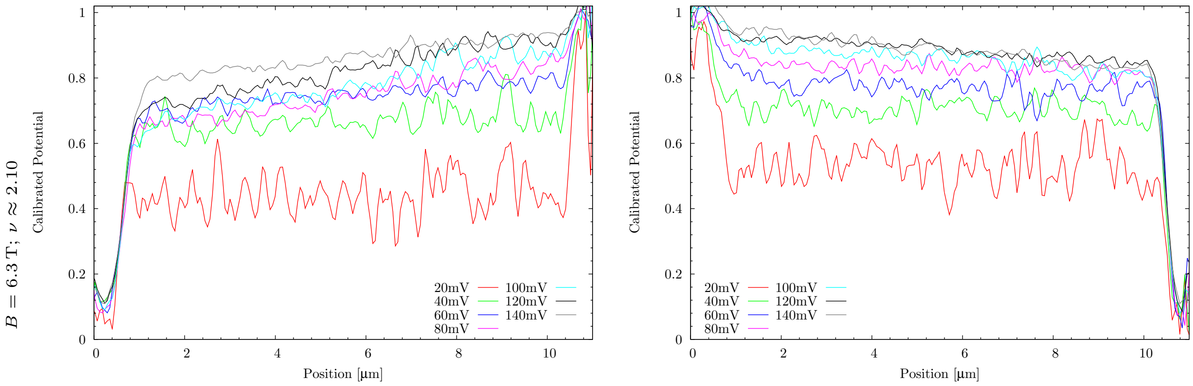
$B = 6.3$ T; $\nu \approx 2.10$
Calibrated Potential
Position [µm]
0
0.2
0.4
0.6
0.8
1
0
2
4
6
8
10
20mV
40mV
60mV
80mV
100mV
120mV
140mV

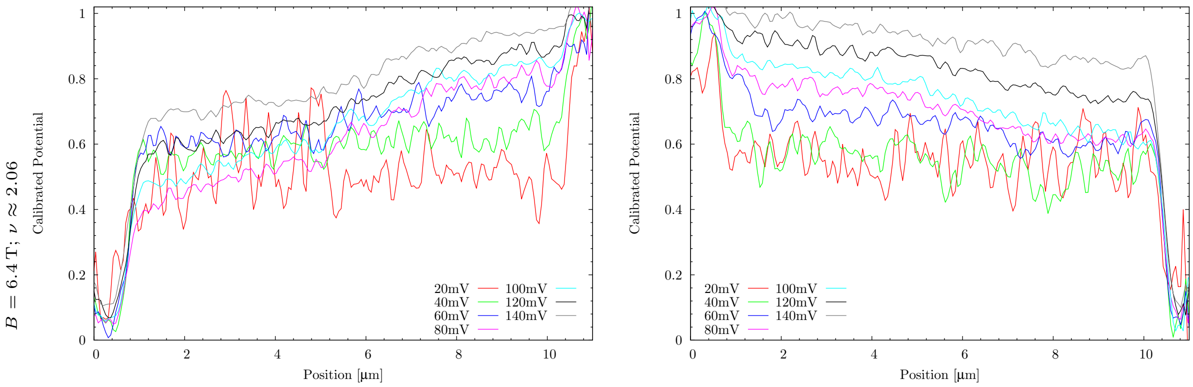
$B = 6.4$ T; $\nu \approx 2.06$
Calibrated Potential
Position [µm]
0
0.2
0.4
0.6
0.8
1
0
2
4
6
8
10
20mV
40mV
60mV
80mV
100mV
120mV
140mV

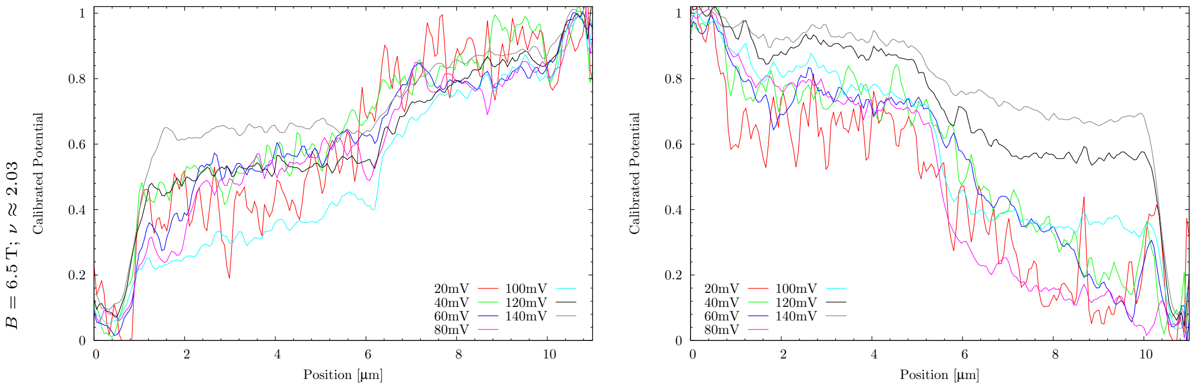
$B = 6.5$ T; $\nu \approx 2.03$
Calibrated Potential
Position [µm]
0
0.2
0.4
0.6
0.8
1
0
2
4
6
8
10
20mV
40mV
60mV
80mV
100mV
120mV
140mV

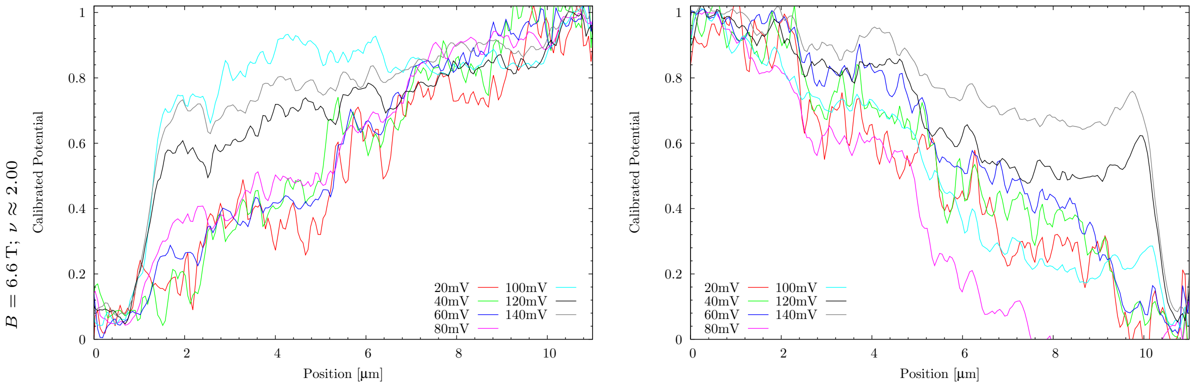
$B = 6.6$ T; $\nu \approx 2.00$
Calibrated Potential
Position [µm]
0
0.2
0.4
0.6
0.8
1
0
2
4
6
8
10
20mV
40mV
60mV
80mV
100mV
120mV
140mV

$B = 6.7\,\mathrm{T};\ \nu \approx 1.97$

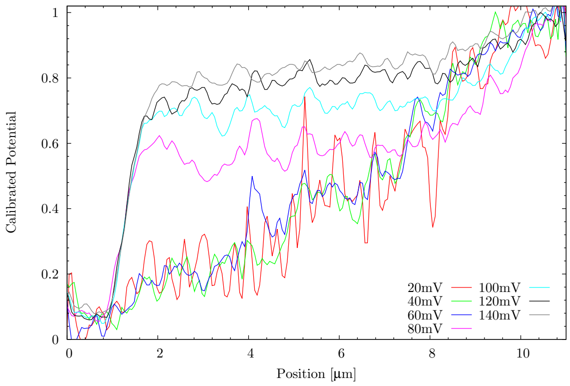

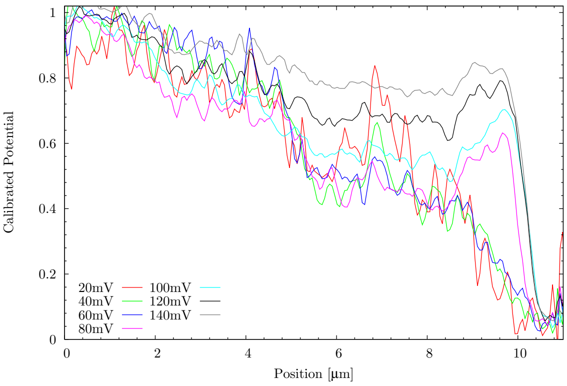

$B = 6.8\,\mathrm{T};\ \nu \approx 1.94$

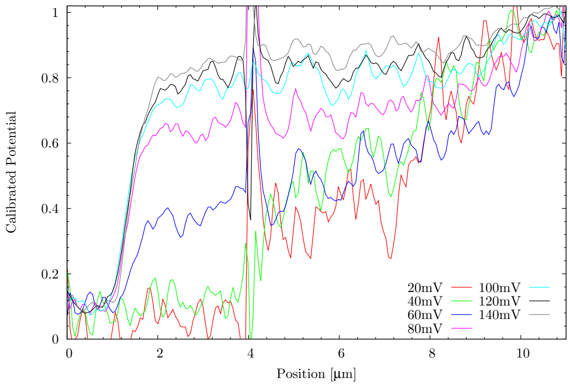

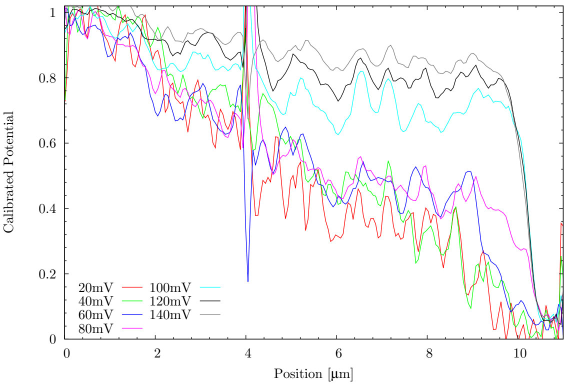

$B = 6.9\,\mathrm{T};\ \nu \approx 1.91$

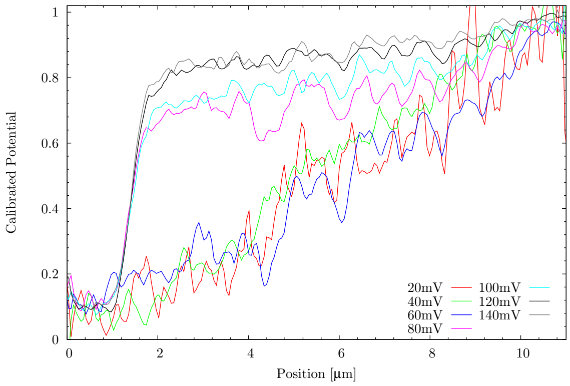

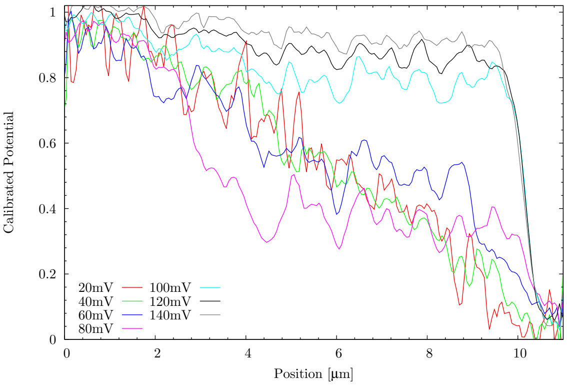

$B = 7.0\,\mathrm{T};\ \nu \approx 1.89$

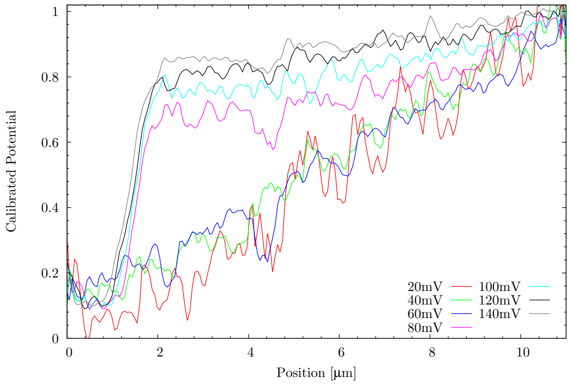

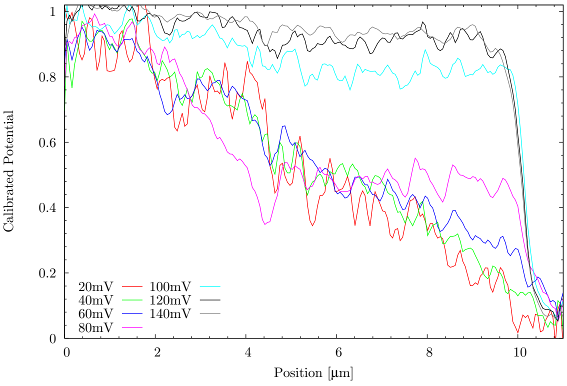

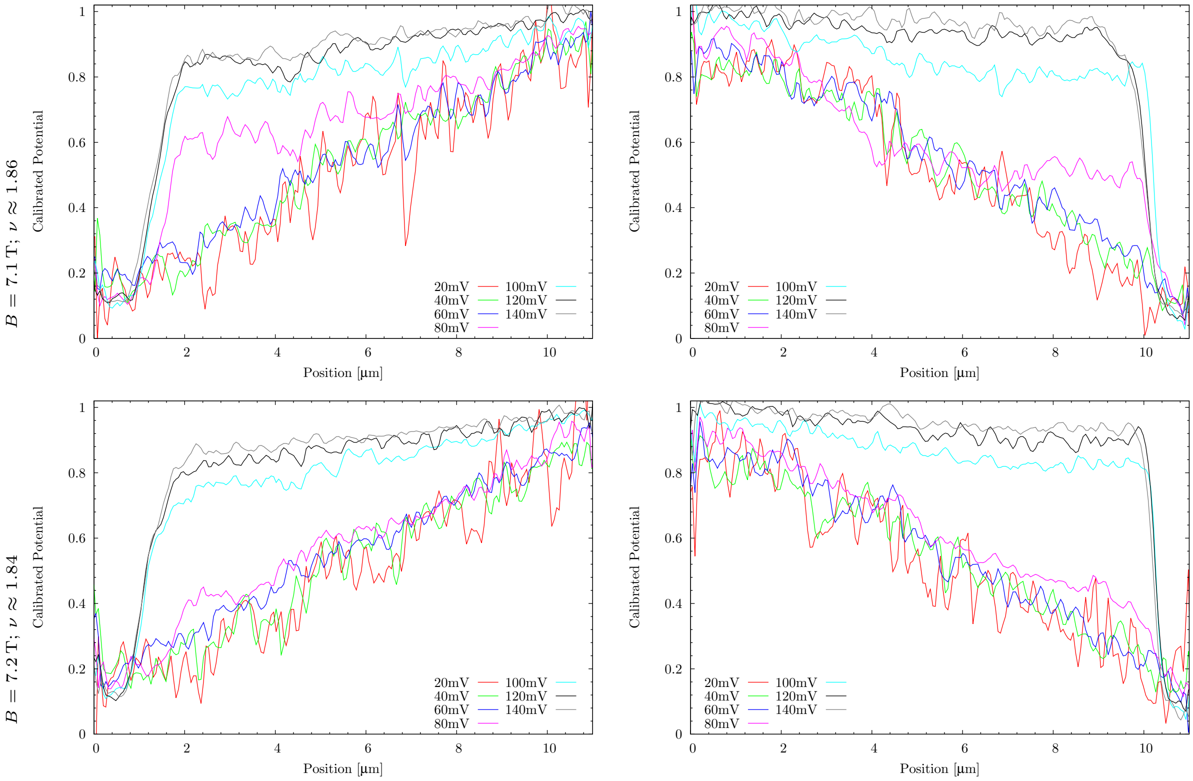
$B = 7.1\,\mathrm{T};\ \nu \approx 1.86$
$B = 7.2\,\mathrm{T};\ \nu \approx 1.84$
Calibrated Potential
Position [µm]
0
0.2
0.4
0.6
0.8
1
0
2
4
6
8
10
20mV
40mV
60mV
80mV
100mV
120mV
140mV

J.2.1. Area scans for $B = 6.8\,\mathrm{T}$, $\nu \approx 1.94$ for current direction (i)

Subsequently we show area scans from 20 mV to 135 mV measure in intervals of 5 mV and ordered in reading sequence. Current flow was from left to the right as depicted in Fig. 13.8 (b) and named (i)-direction.

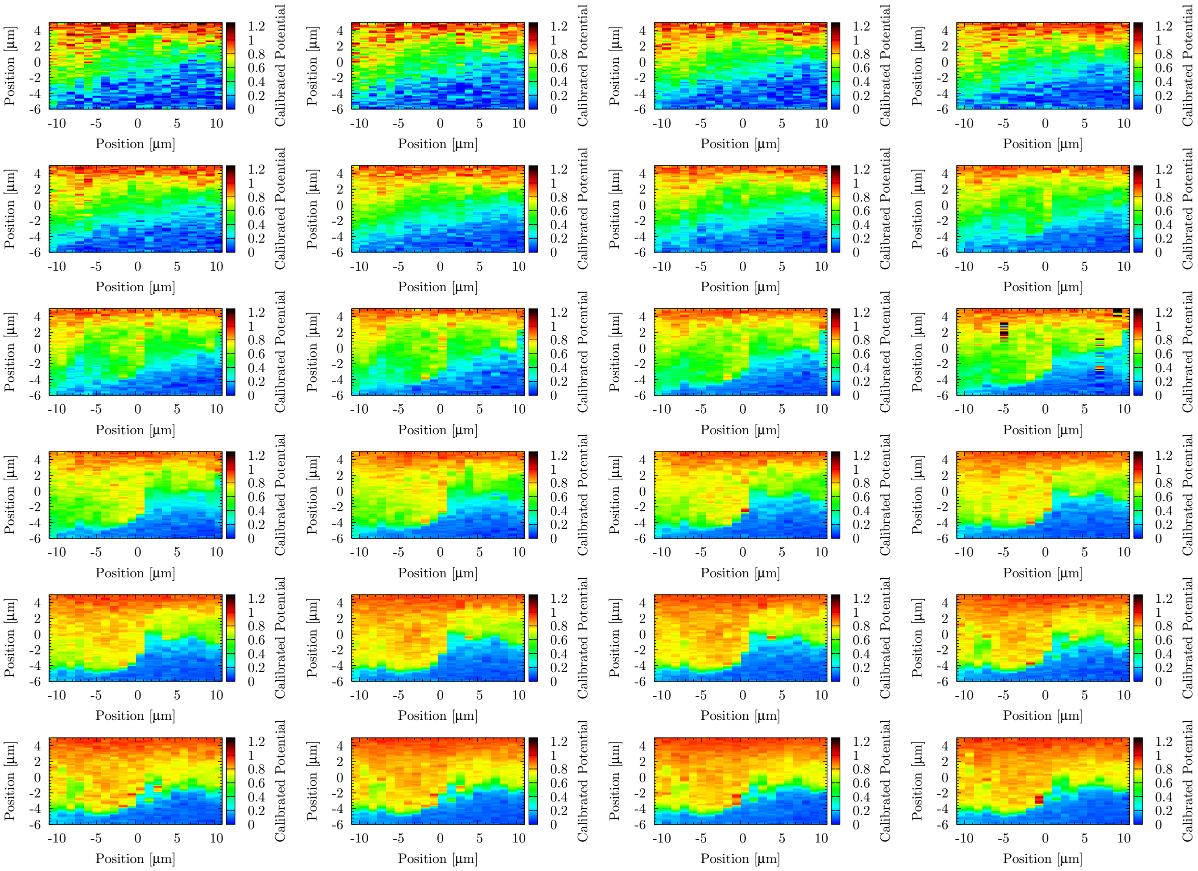

In the following are shown graph pairs where in the left graph the individual line scans of the above area scans are shown and in the left graph the longitudinal resistance measured simultaneously is plotted. Current flow was oriented from bottom to top. Simultaneously measured lines are plotted in the right and left graph in the same color. The Hall potentials and longitudinal voltage are offsetted by 0.2 relative to the adjacent lines. The area scans reach from 20 mV to 135 mV bias voltage, measured in intervals of 5 mV and ordered in reading sequence. Labels have been added every 10 mV.

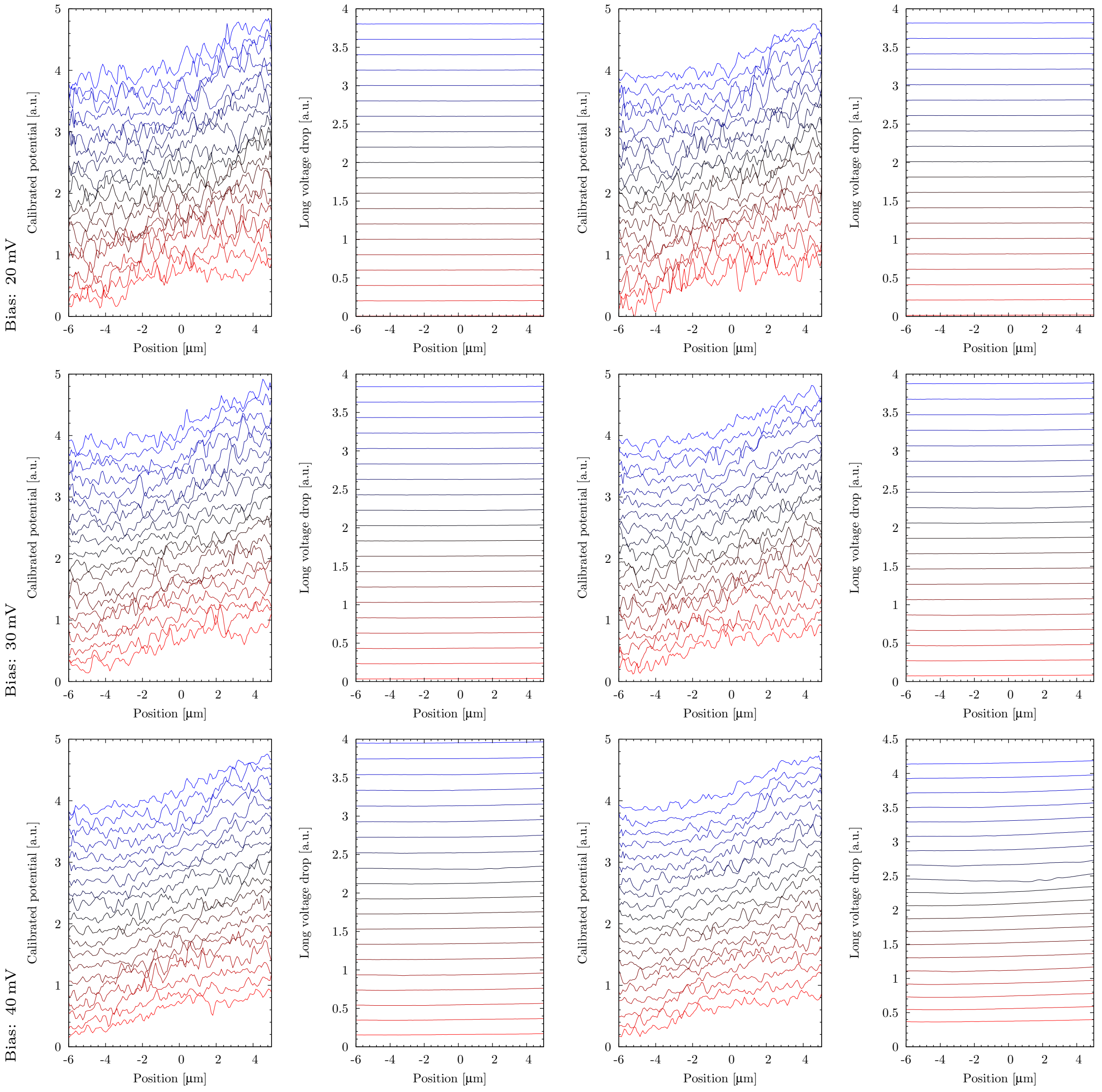

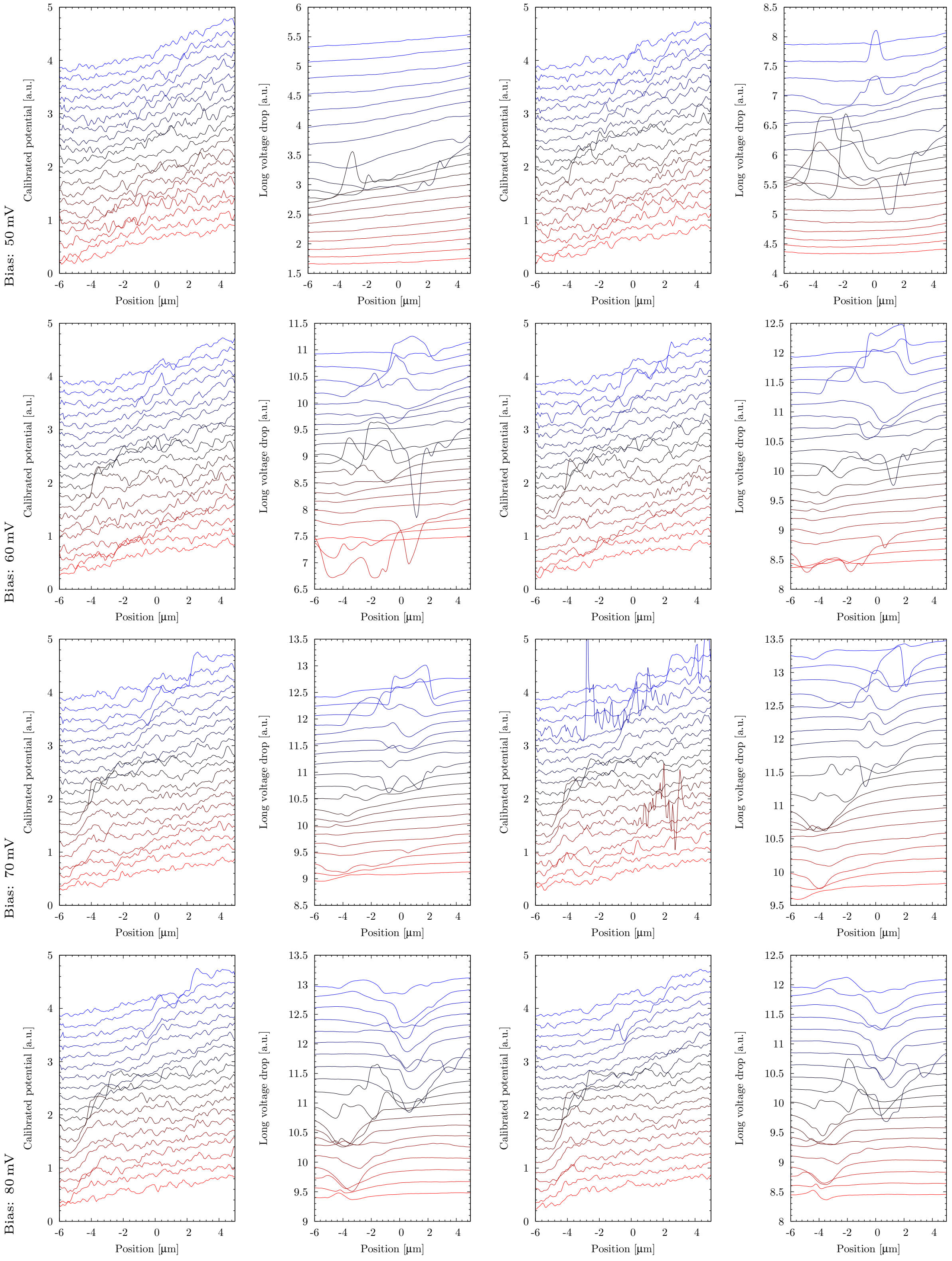
Bias: 50 mV
Bias: 60 mV
Bias: 70 mV
Bias: 80 mV
Calibrated potential [a.u.]
Long voltage drop [a.u.]
Position [µm]
-6
-4
-2
0
2
4

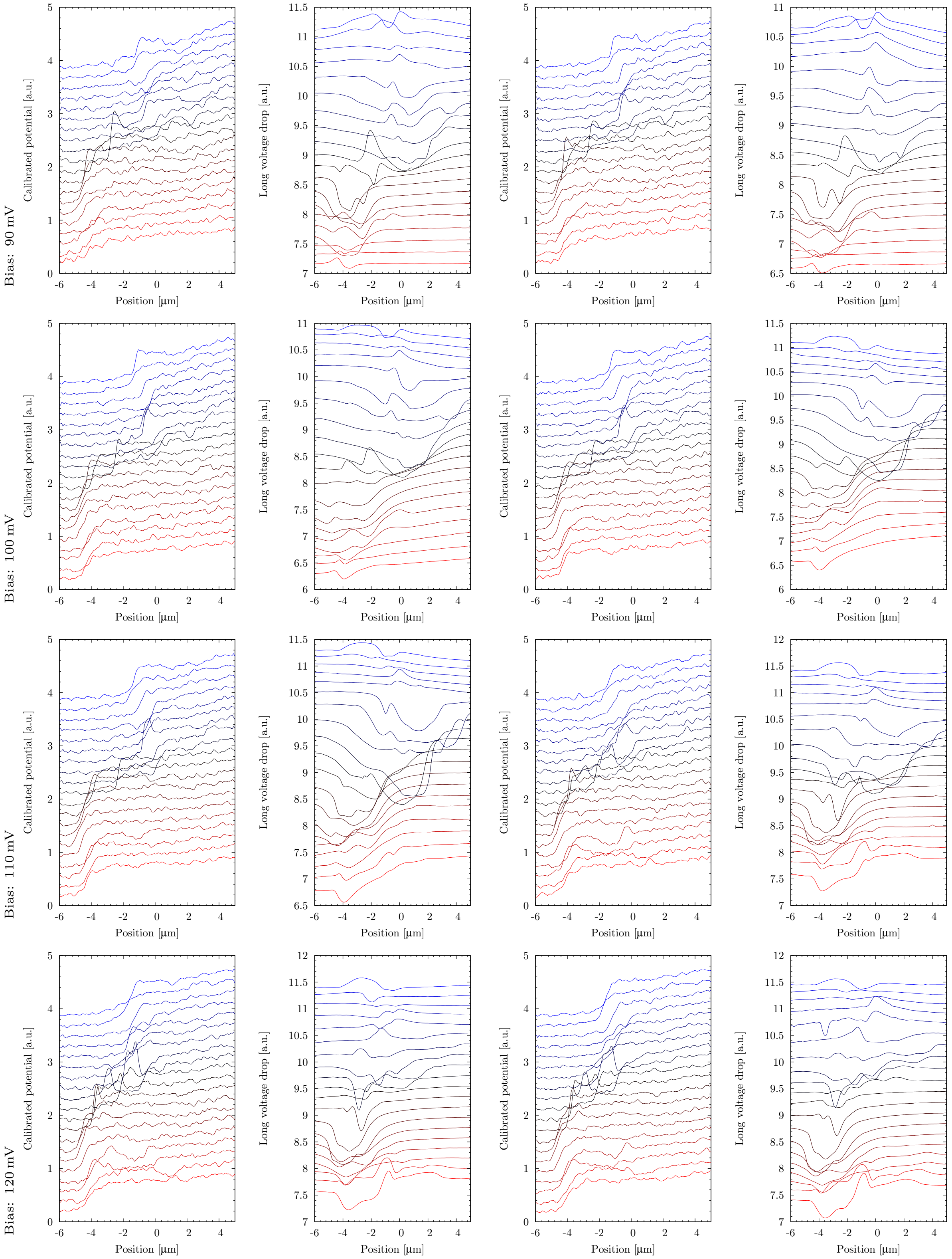
Bias: 90 mV
Bias: 100 mV
Bias: 110 mV
Bias: 120 mV
Calibrated potential [a.u.]
Long voltage drop [a.u.]
Position [µm]
-6
-4
-2
0
2
4
0
1
2
3
4
5
6.5
7
7.5
8
8.5
9
9.5
10
10.5
11
11.5
12

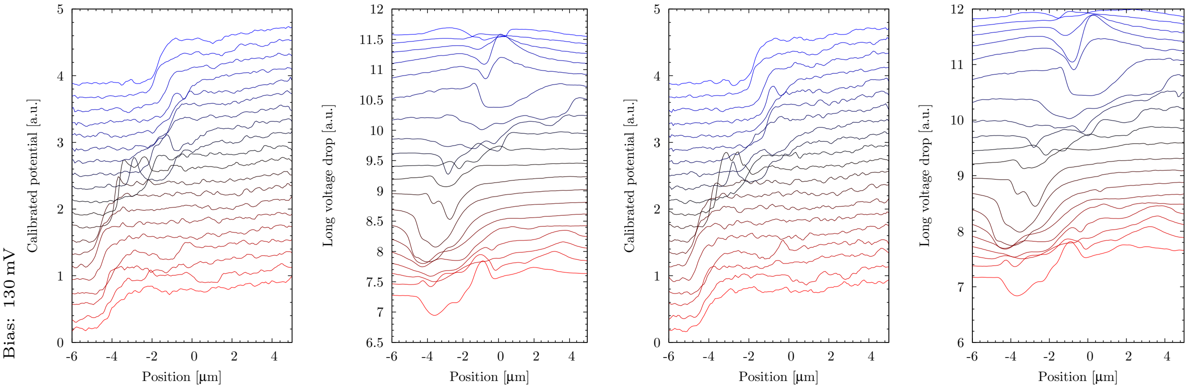
Bias: 130 mV
Calibrated potential [a.u.]
0
1
2
3
4
5
Position [µm]
-6
-4
-2
0
2
4
Long voltage drop [a.u.]
6.5
7
7.5
8
8.5
9
9.5
10
10.5
11
11.5
12
Position [µm]
-6
-4
-2
0
2
4
Calibrated potential [a.u.]
0
1
2
3
4
5
Position [µm]
-6
-4
-2
0
2
4
Long voltage drop [a.u.]
6
7
8
9
10
11
12
Position [µm]
-6
-4
-2
0
2
4

Subsequent is plotted the evolution of single scan lines from the above area scans. Again pairs of graphs are shown where on the left the Hall potential is plotted and with equal color the corresponding longitudinal voltage on the right. The Hall potential profiles are magnified by a factor of 20 mV and offsetted by the bias voltage they where measured. The longitudinal voltage lines are not offsetted. Plots follow the same sequence as above.

Line: 0 at $x = -10.5$ µm

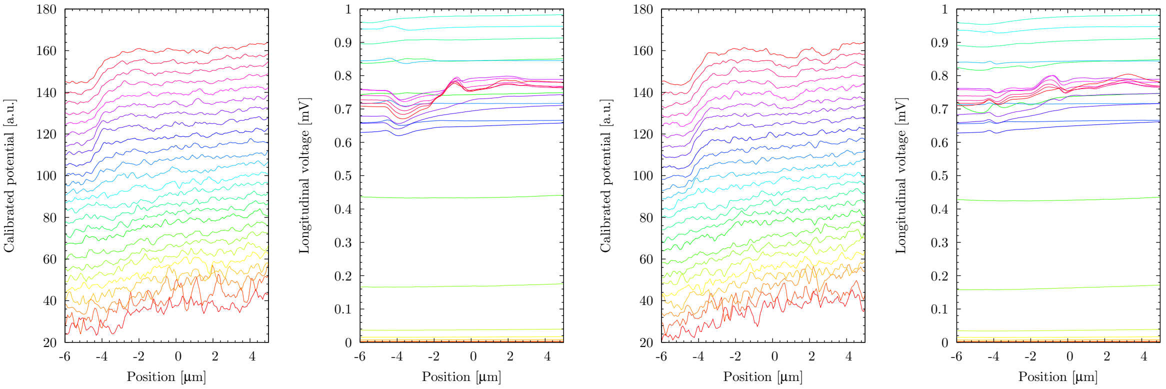

Line: 2 at $x = -8.3$ µm

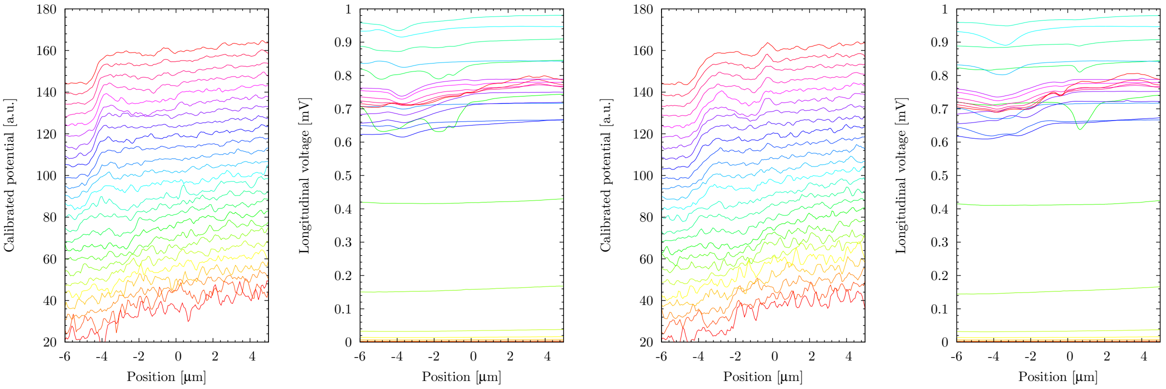

Line: 4 at $x = -6.0$ µm

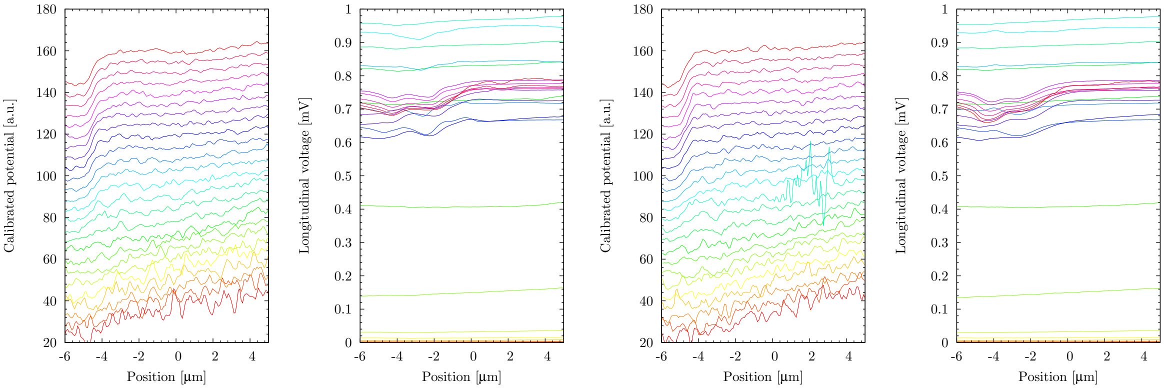

Line: 6 at $x = -3.8$ µm

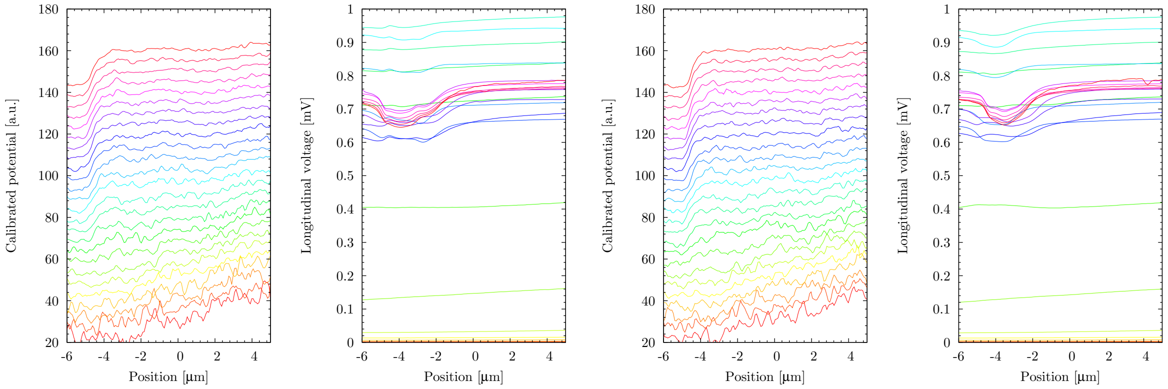

Line: 8 at $x = -1.6$ µm

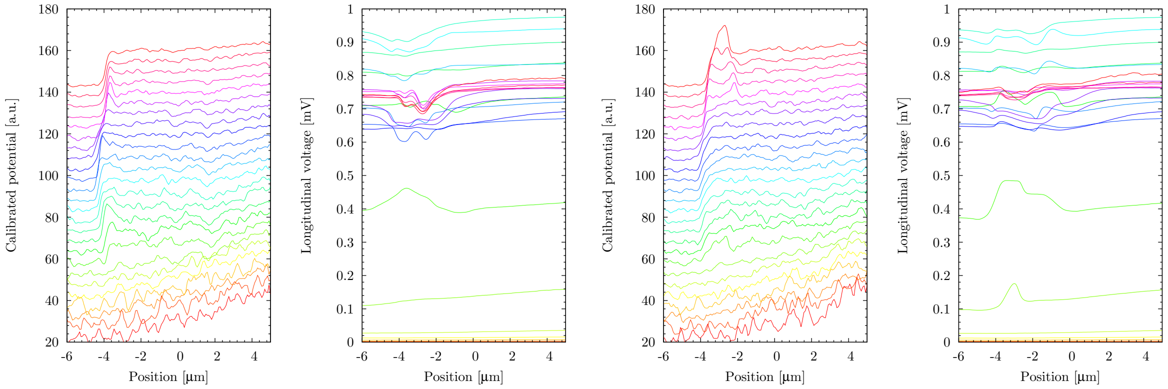

Line: 10 at $x = 0.6$ µm

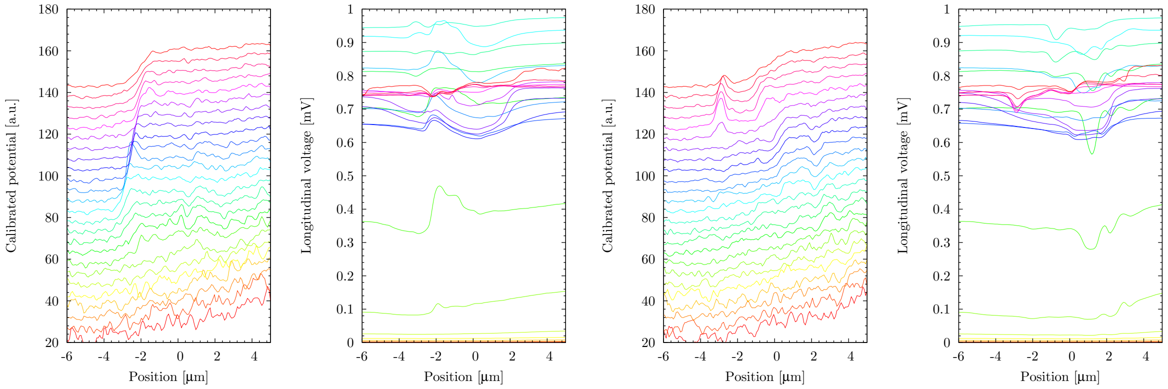

Line: 12 at $x = 2.7$ µm

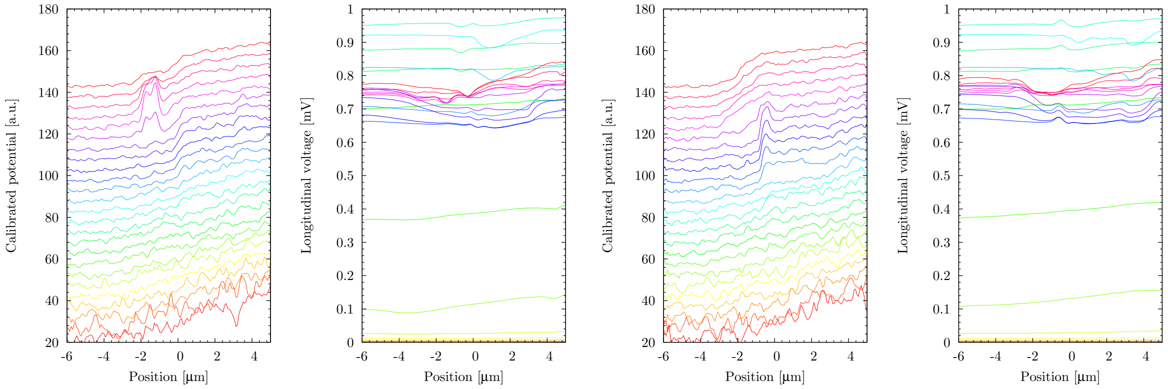

Line: 14 at $x = 5.0$ µm

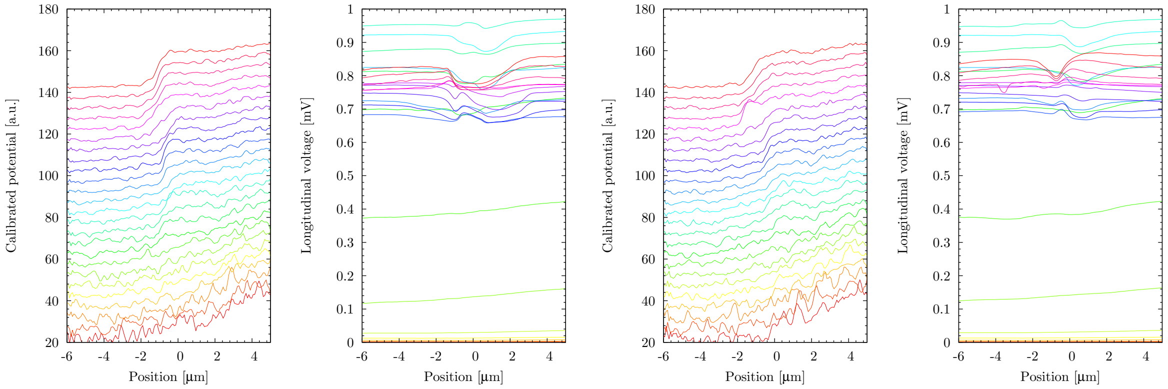

Line: 16 at $x = 7.2$ µm

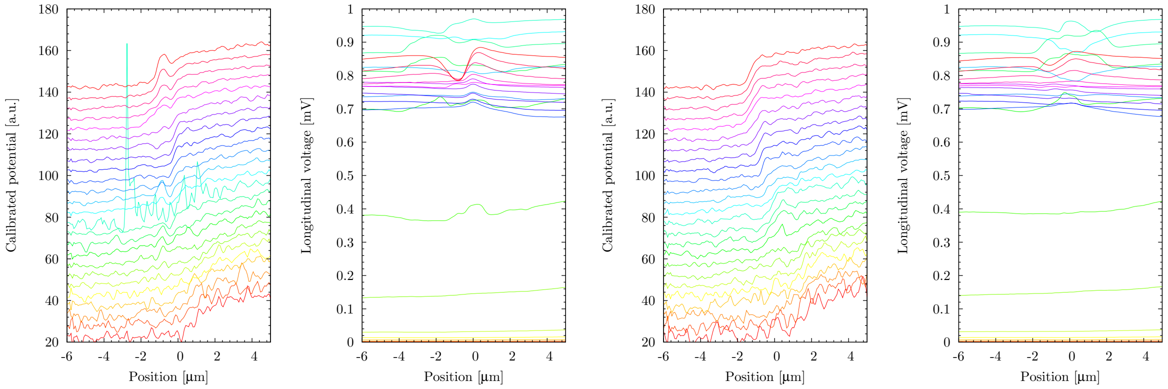

Line: 18 at $x = 9.4$ µm

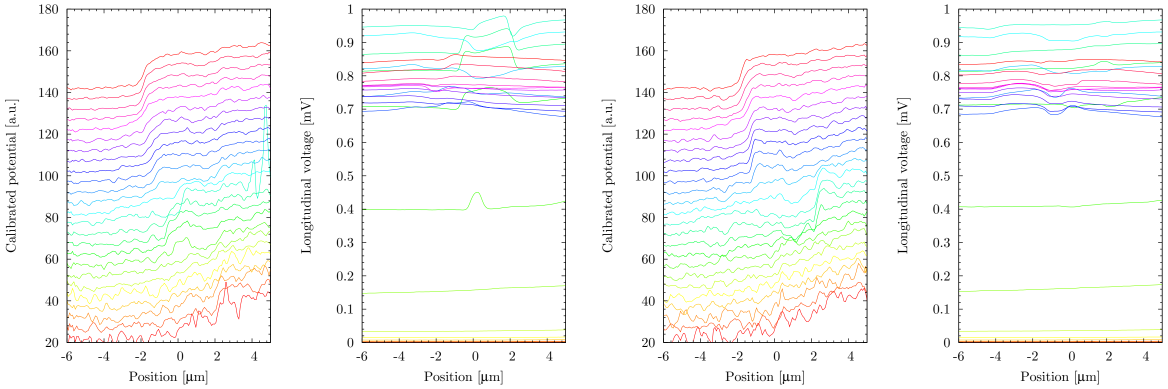

J.2.2. Area scans for $B = 6.8\,\mathrm{T}$, $\nu \approx 1.94$ for current direction (j)

Subsequently we show area scans from 20 mV to 135 mV measure in intervals of 5 mV and ordered in reading sequence. Current flow was from right to the left as depicted in Fig. 13.8 (c) and named (j)-direction.

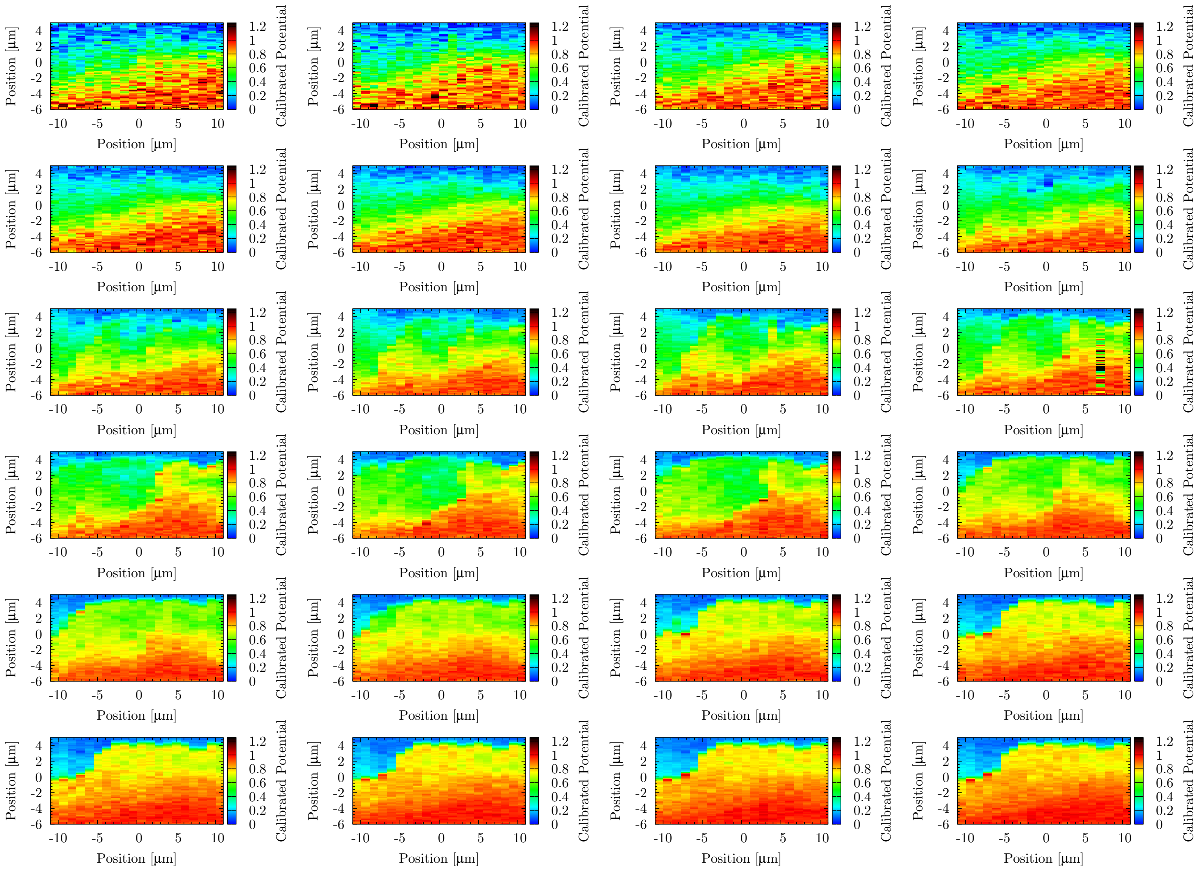

In the following are shown graph pairs where in the left graph the individual line scans of the above area scans are shown and in the left graph the longitudinal resistance measured simultaneously is plotted. Current flow was oriented from top to bottom. Simultaneously measured lines are plotted in the right and left graph in the same color. The Hall potentials and longitudinal voltage are offsetted by 0.2 relative to the adjacent lines. The area scans reach from 20 mV to 135 mV bias voltage, measured in intervals of 5 mV and ordered in reading sequence. Labels have been added every 10 mV.

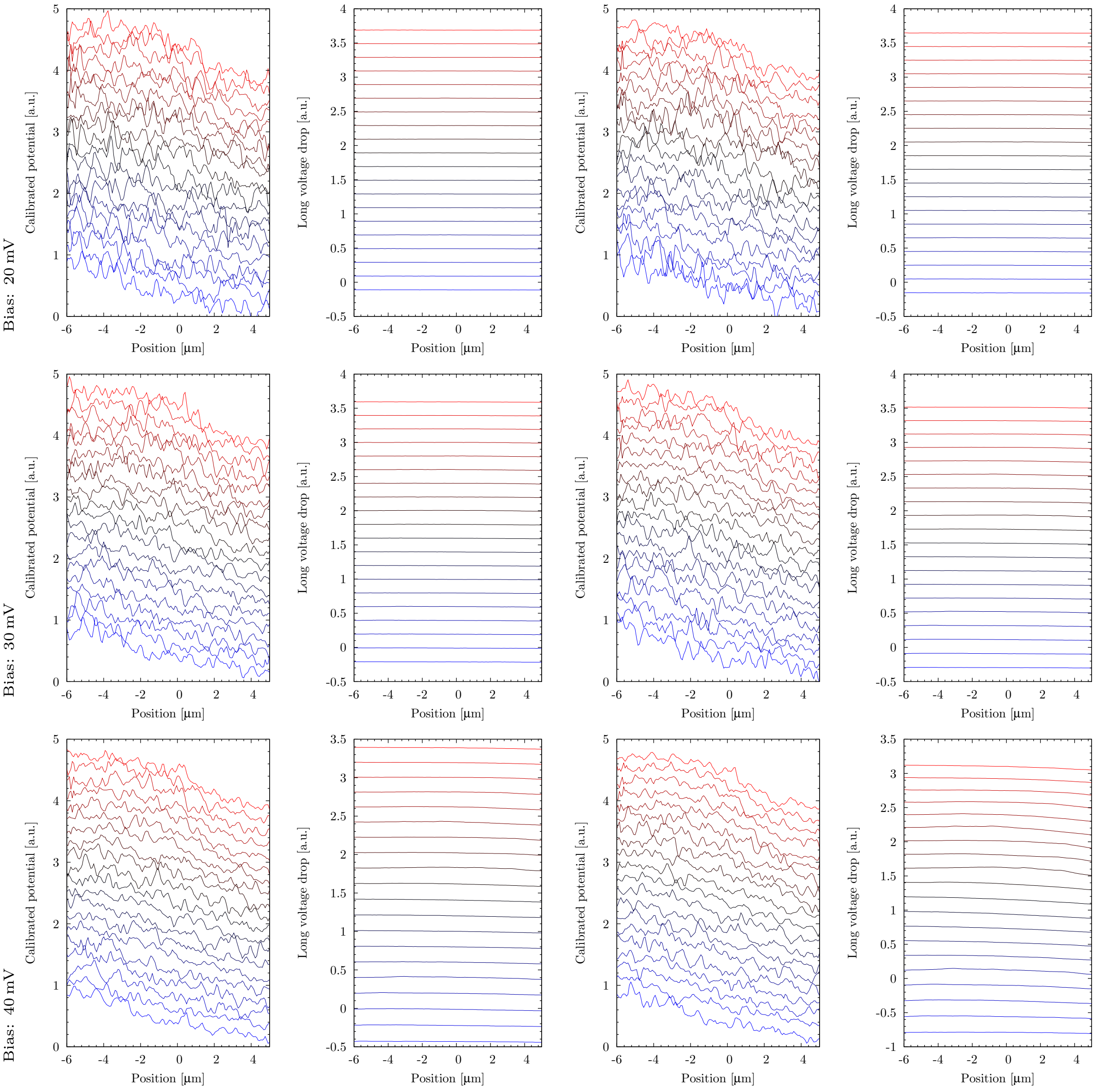

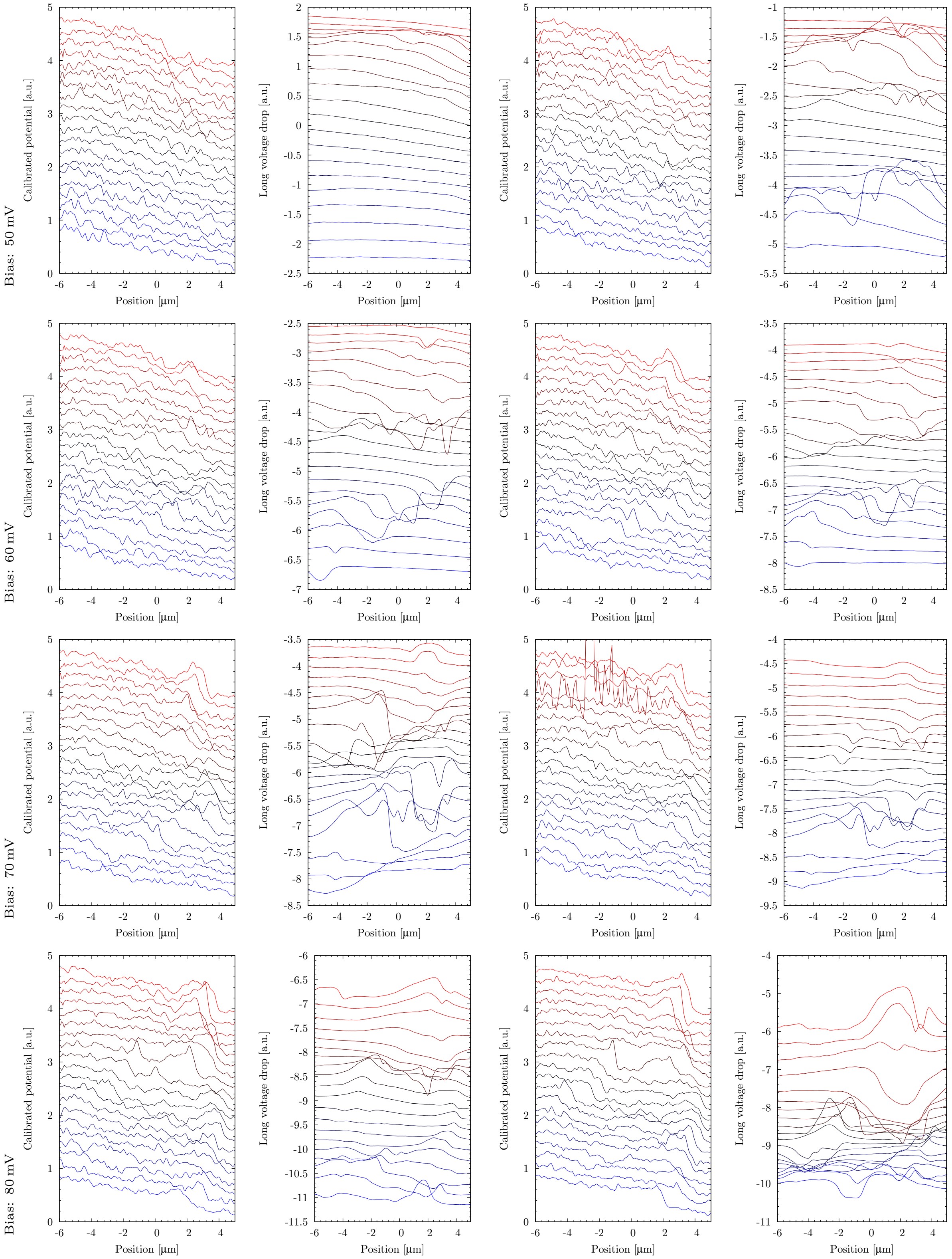
Bias: 50 mV
Bias: 60 mV
Bias: 70 mV
Bias: 80 mV
Calibrated potential [a.u.]
Long voltage drop [a.u.]
Position [µm]
-6
-4
-2
0
2
4
0
1
2
3
4
5
-2.5
-2
-1.5
-1
-0.5
0.5
1.5
-5.5
-5
-4.5
-4
-3.5
-3
-2.5
-2
-1.5
-1
-7
-6.5
-6
-5.5
-5
-4.5
-4
-3.5
-3
-2.5
-8.5
-8
-7.5
-7
-6.5
-6
-5.5
-5
-4.5
-4
-3.5
-9.5
-9
-8.5
-8
-7.5
-7
-6.5
-6
-5.5
-5
-4.5
-4
-11.5
-11
-10.5
-10
-9.5
-9
-8.5
-8
-7.5
-7
-6.5
-6
-11
-10
-9
-8
-7
-6
-5
-4

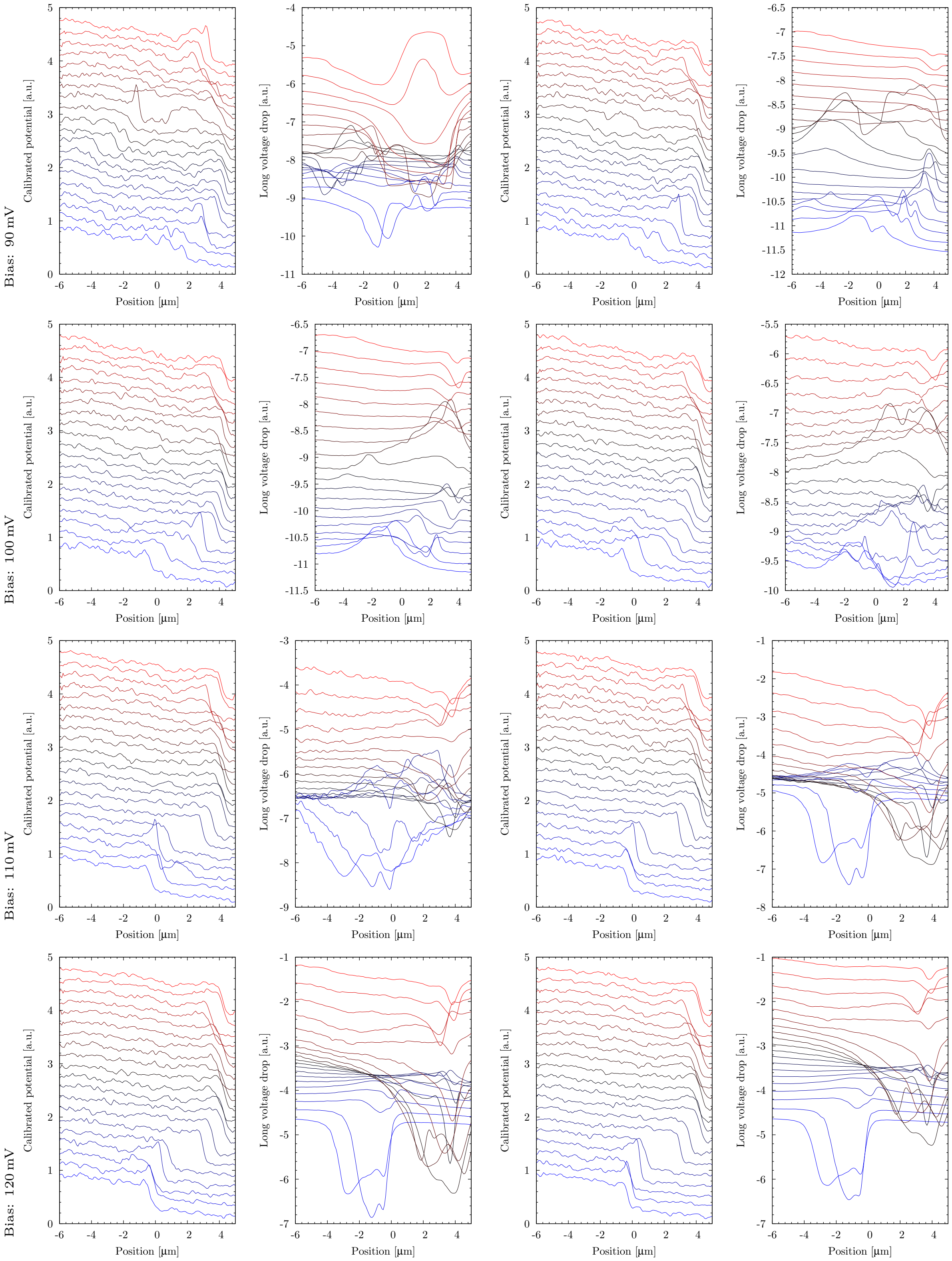
Bias: 90 mV
Bias: 100 mV
Bias: 110 mV
Bias: 120 mV
Calibrated potential [a.u.]
Long voltage drop [a.u.]
Position [µm]
-6
-4
-2
0
2
4
0
1
2
3
4
5

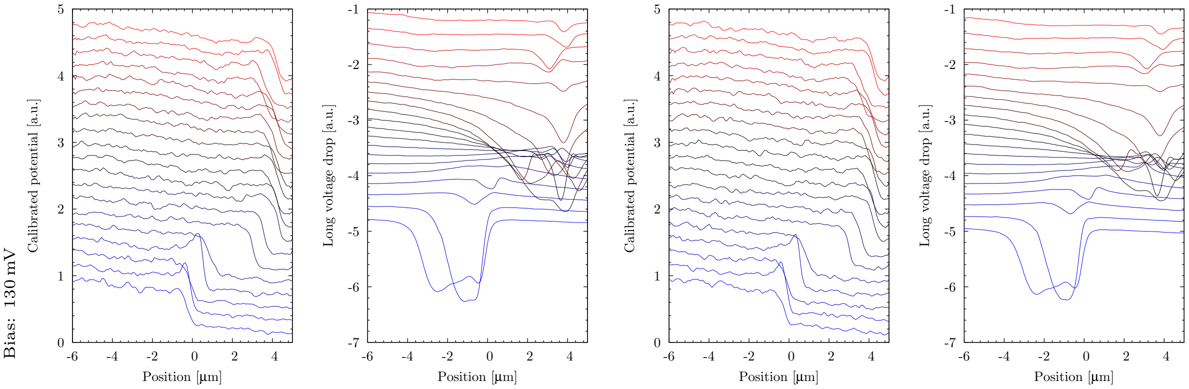
Bias: 130 mV
Calibrated potential [a.u.]
Position [µm]
Long voltage drop [a.u.]
Position [µm]
Calibrated potential [a.u.]
Position [µm]
Long voltage drop [a.u.]
Position [µm]
0
1
2
3
4
5
-7
-6
-5
-4
-3
-2
-1
-6
-4
-2
0
2
4

Subsequent is plotted the evolution of single scan lines from the above area scans. Again pairs of graphs are shown where on the left the Hall potential is plotted and in equal color the corresponding longitudinal voltage on the right. The Hall potential profiles are magnified by a factor of 20 mV and offsetted by the bias voltage they where measured. The longitudinal voltage lines are not offsetted. Plots flow the same sequence as above.

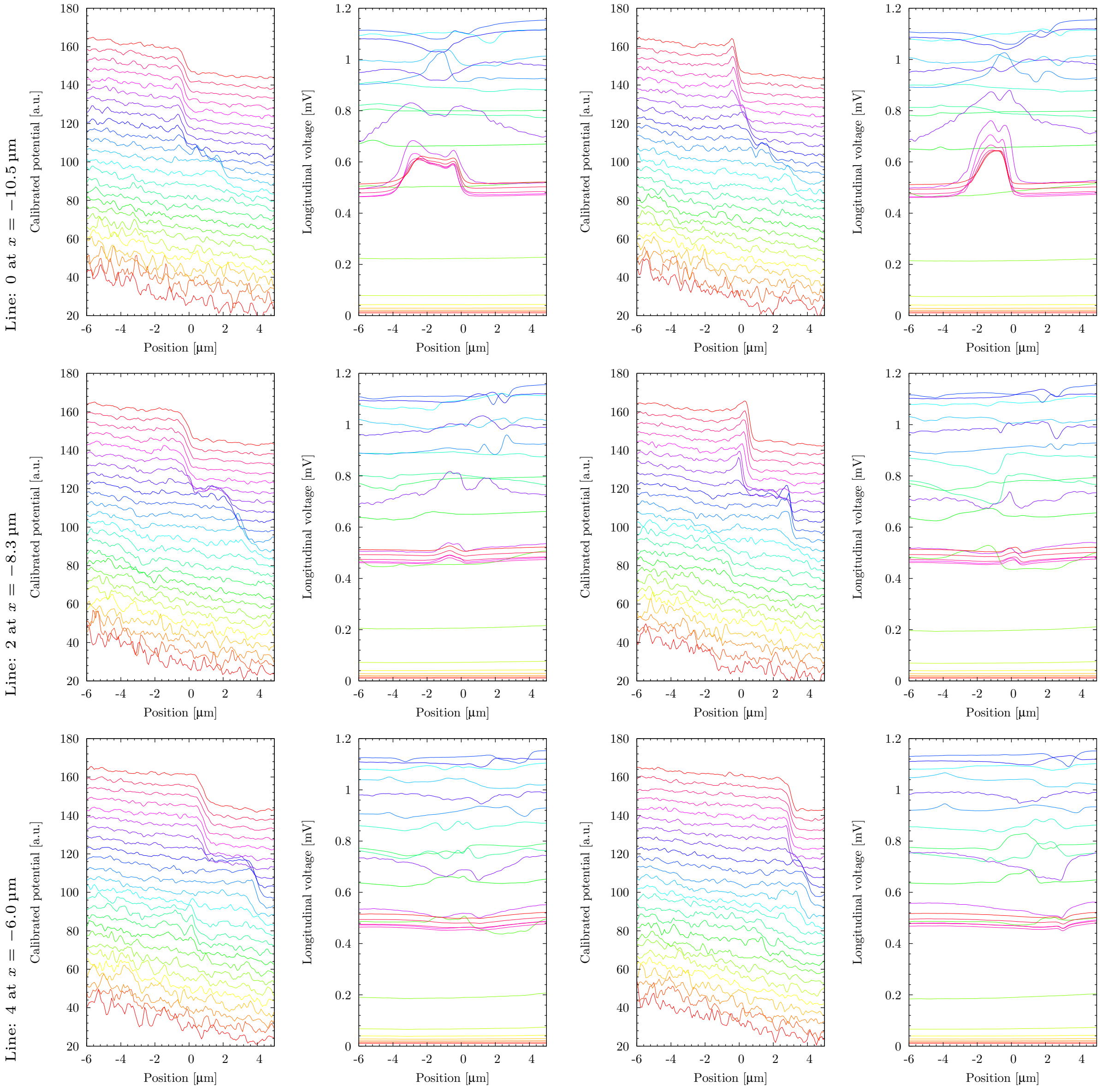

Line: 6 at $x = -3.8$ µm

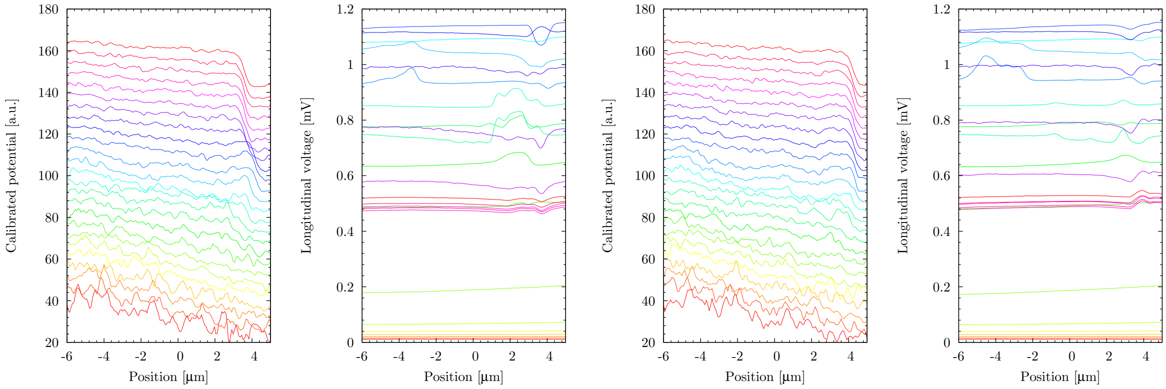

Line: 8 at $x = -1.6$ µm

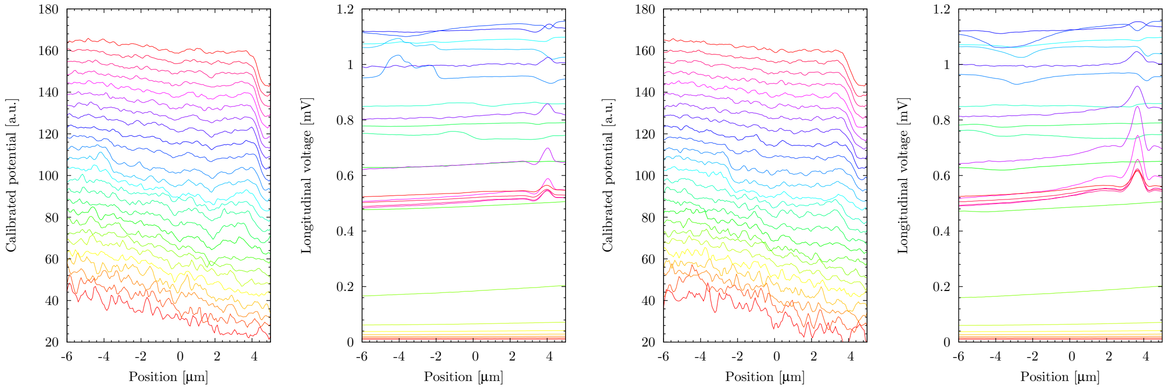

Line: 10 at $x = 0.6$ µm

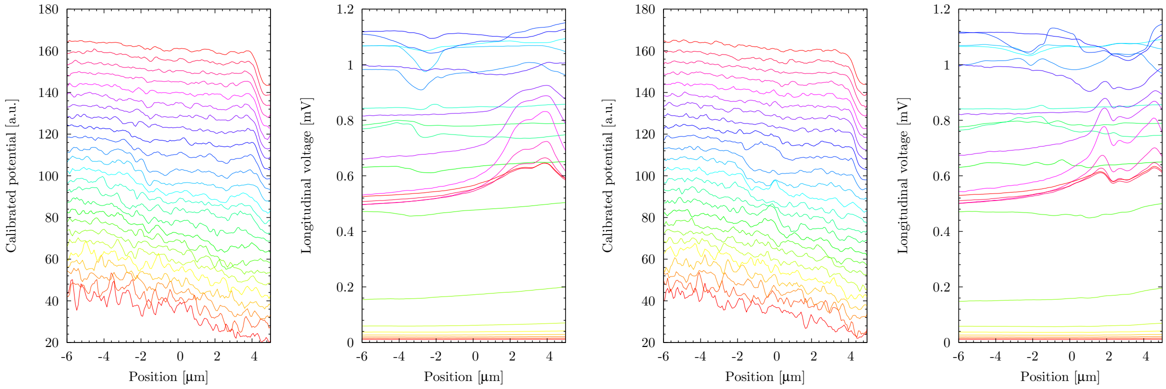

Line: 12 at $x = 2.7$ µm

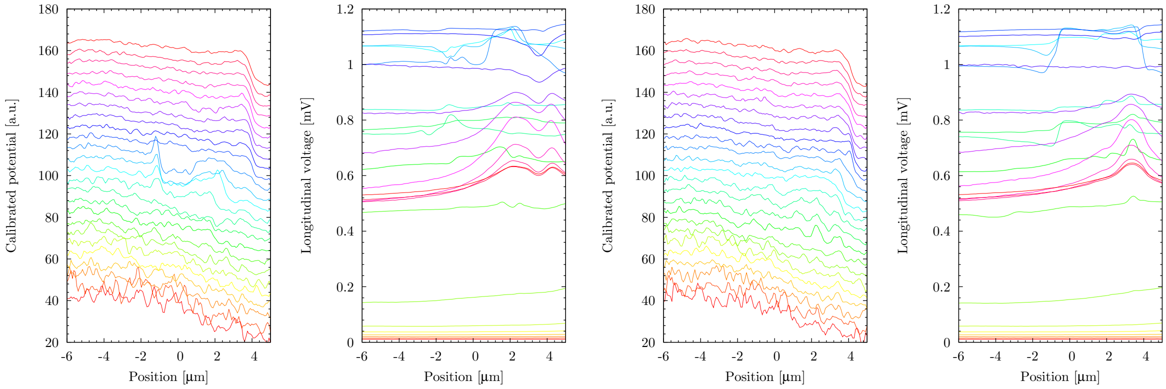

Line: 14 at $x = 5.0$ µm

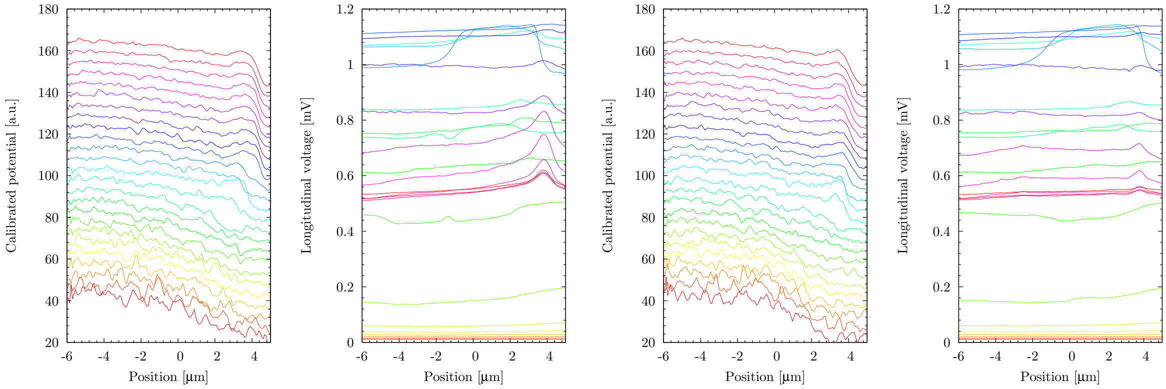

Line: 16 at $x = 7.2$ µm

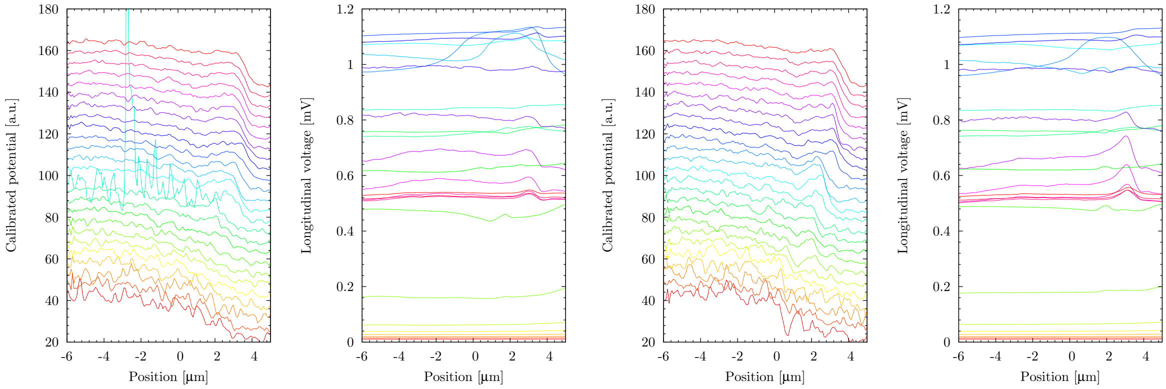

Line: 18 at $x = 9.4$ µm

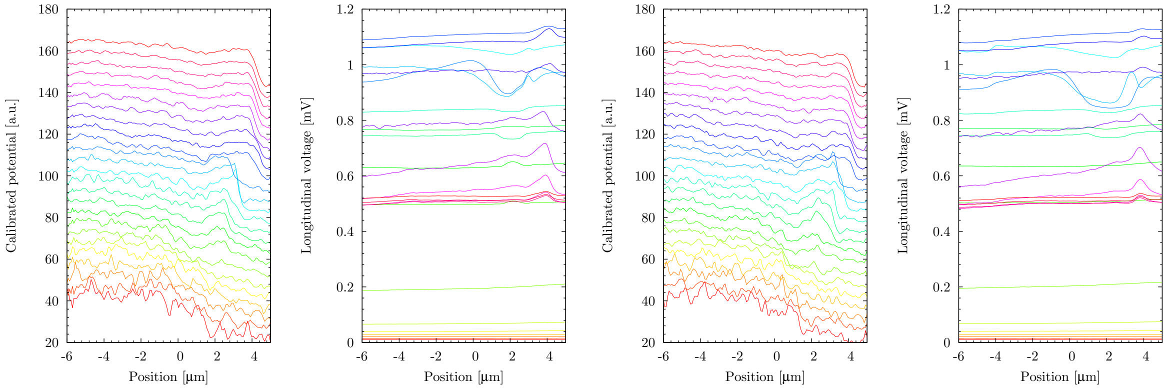

J.2.3. High resolution area scans for $B = 6.8\,\mathrm{T}$, $\nu \approx 1.94$

In the following area scans are shown from 20 mV to 120 mV measured in intervals of 20 mV. The bias voltage is marked at the very left. Also plotted on the right side of each row is the longitudinal voltage measured in parallel. Current flow was from left to the right as depicted in Fig. 13.8 (b) the here called (i)-direction.

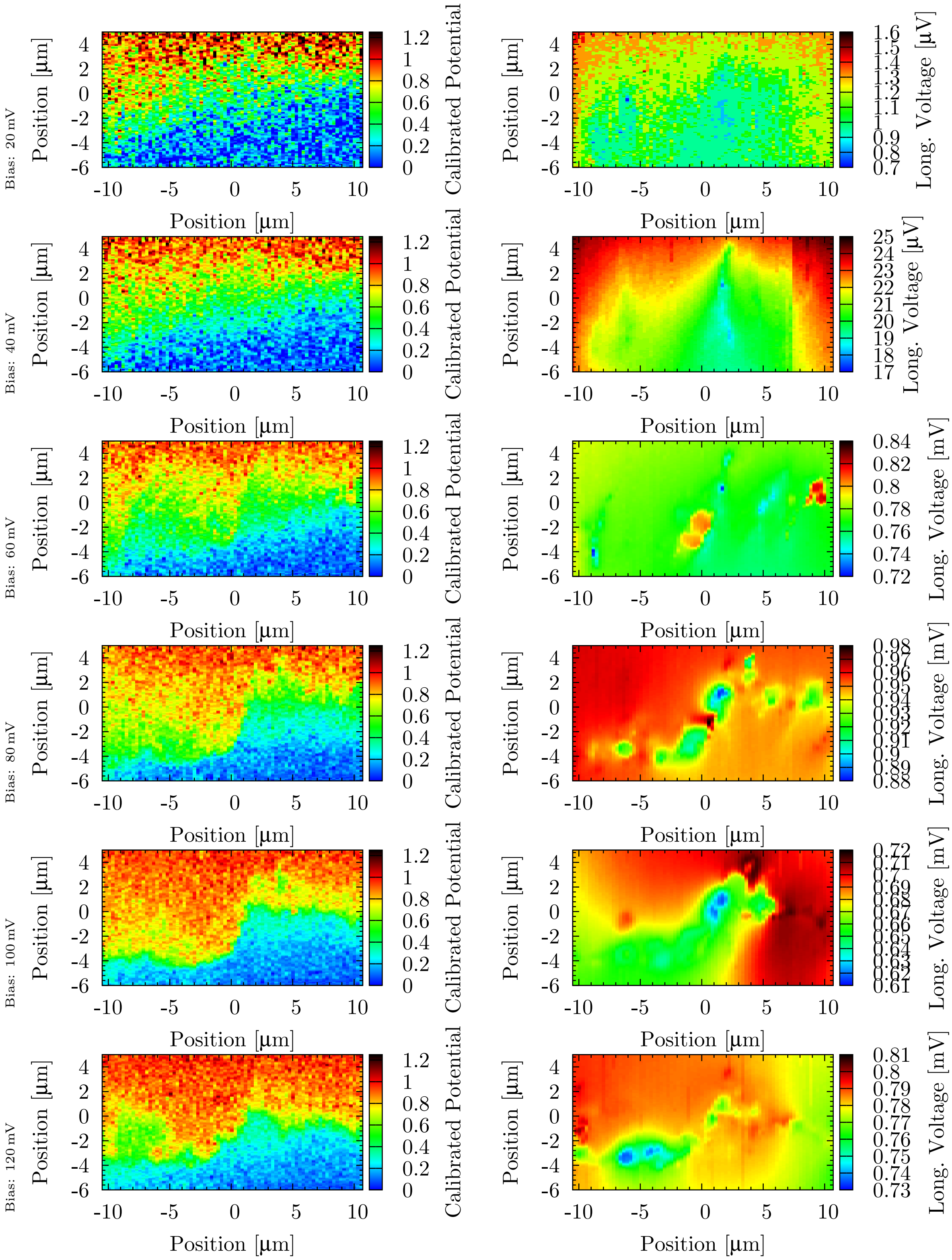

In the following area scans are shown from 20 mV to 120 mV measured in intervals of 20 mV. The bias voltage is marked at the very left. Also plotted on the right side of each row is the longitudinal voltage measured in parallel. Current flow was from right to the left as depicted in Fig. 13.8 (c) here called (j)-direction.

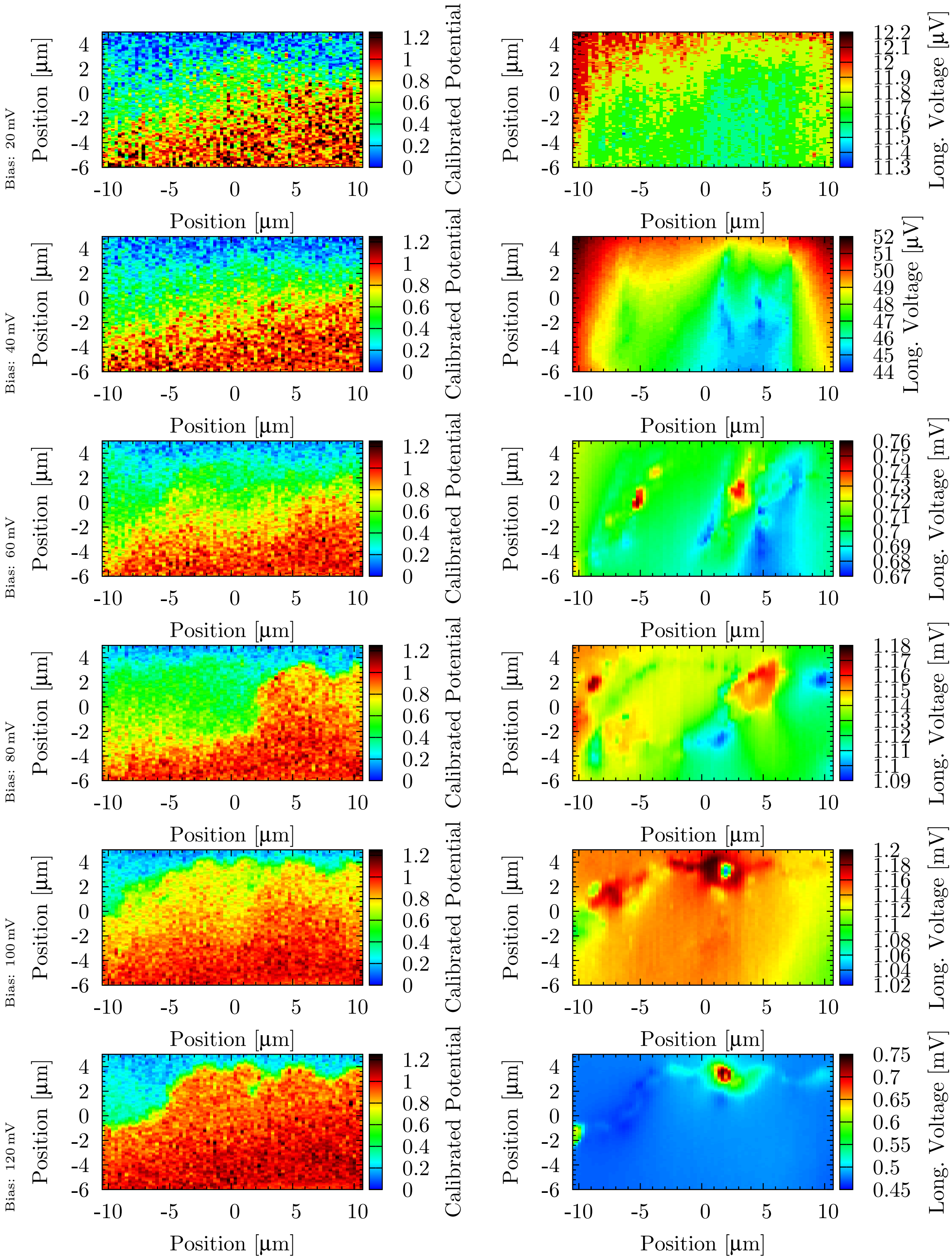

J.2.4. Area scans for $B = 6.1\,\mathrm{T}$, $\nu \approx 2.16$ for current direction (i)

In the following area scans are shown from 20 mV to 120 mV measured in intervals of 20 mV. The bias voltage is marked at the very left. Also plotted on the right side of each row is the longitudinal voltage measured in parallel. Current flow was from left to the right as depicted in Fig. 13.8 (b) and named (i)-direction.

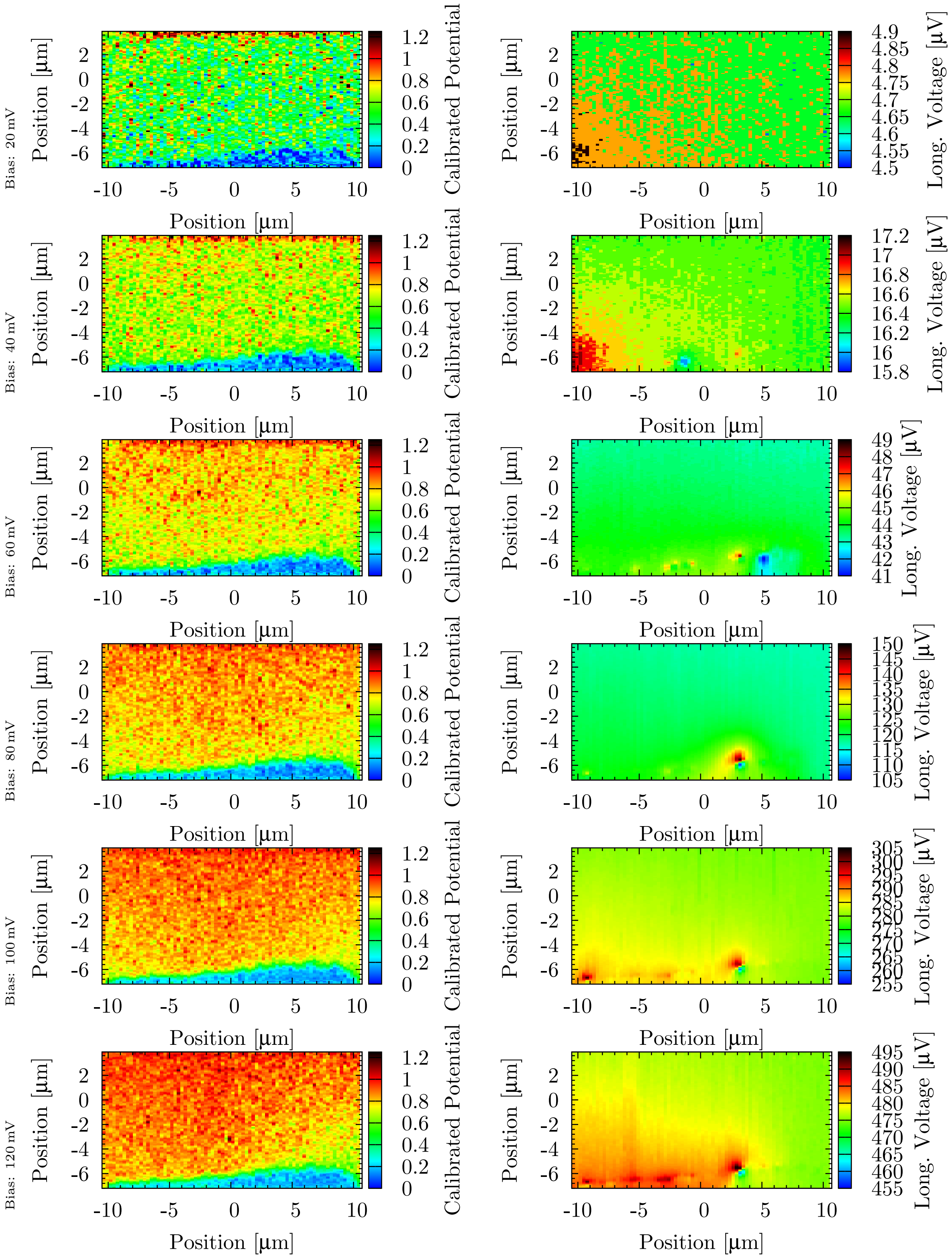

Subsequent are plotted area scans from 10 mV to 125 mV measure in intervals of 5 mV and ordered in reading sequence.

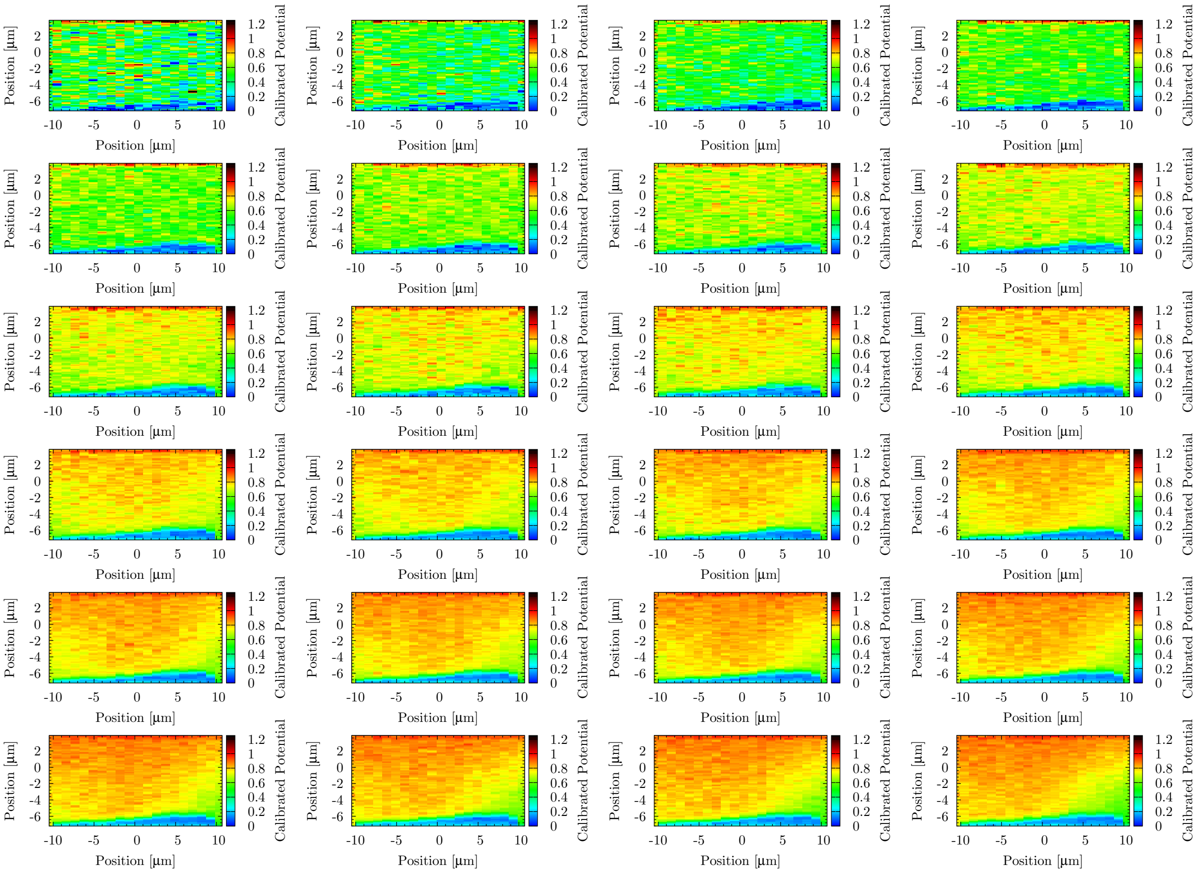

J.2.5. Area scans for $B = 6.1\,\mathrm{T}$, $\nu \approx 2.16$ for current direction (j)

In the following area scans are shown from 20 mV to 120 mV measured in intervals of 20 mV. The bias voltage is marked at the very left. Also plotted on the right side of each row is the longitudinal voltage measured in parallel. Current flow was from right to the left as depicted in Fig. 13.8 (c) and named (j)-direction.

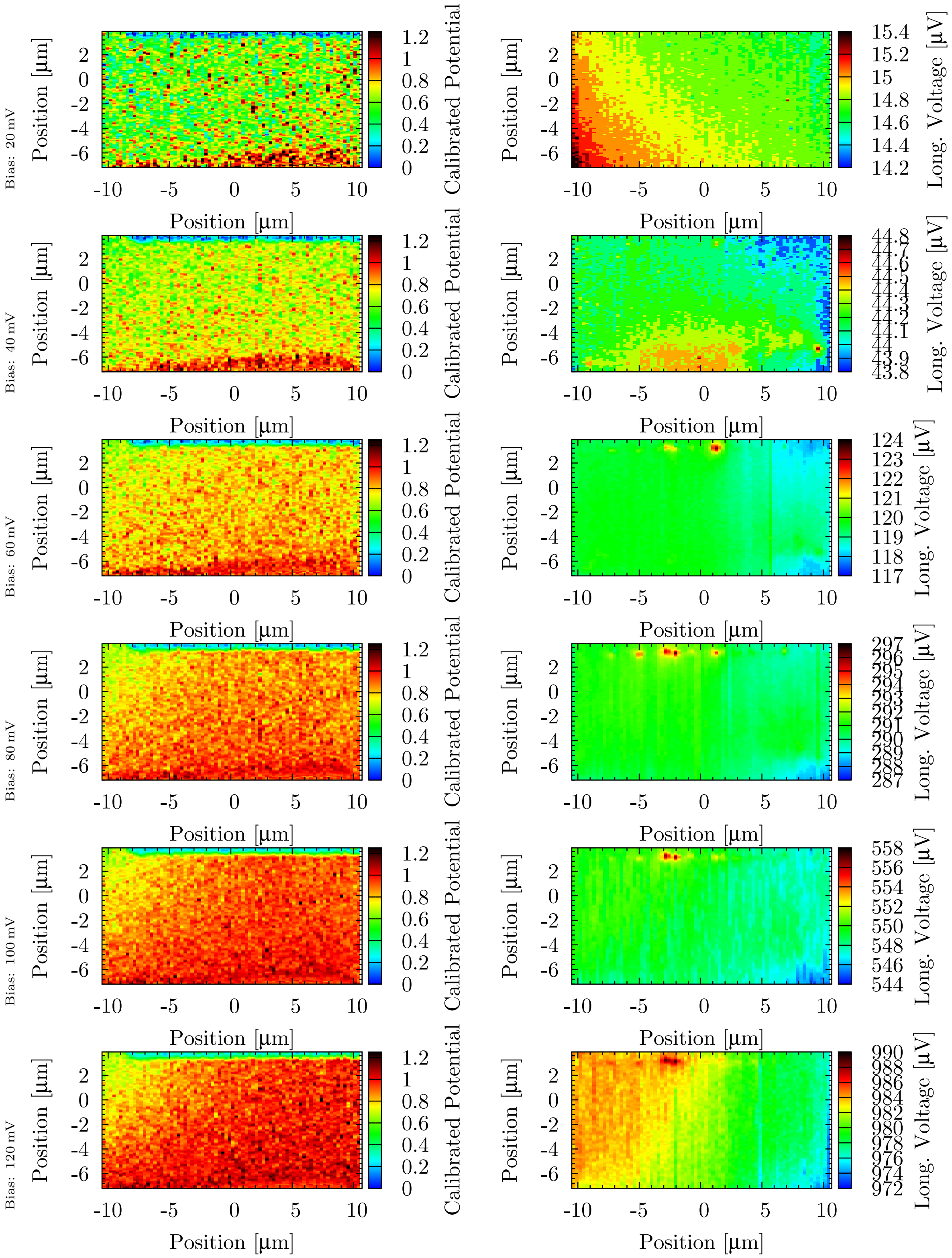

Subsequent are plotted area scans from 10 mV to 125 mV measured in intervals of 5 mV and ordered in reading sequence.

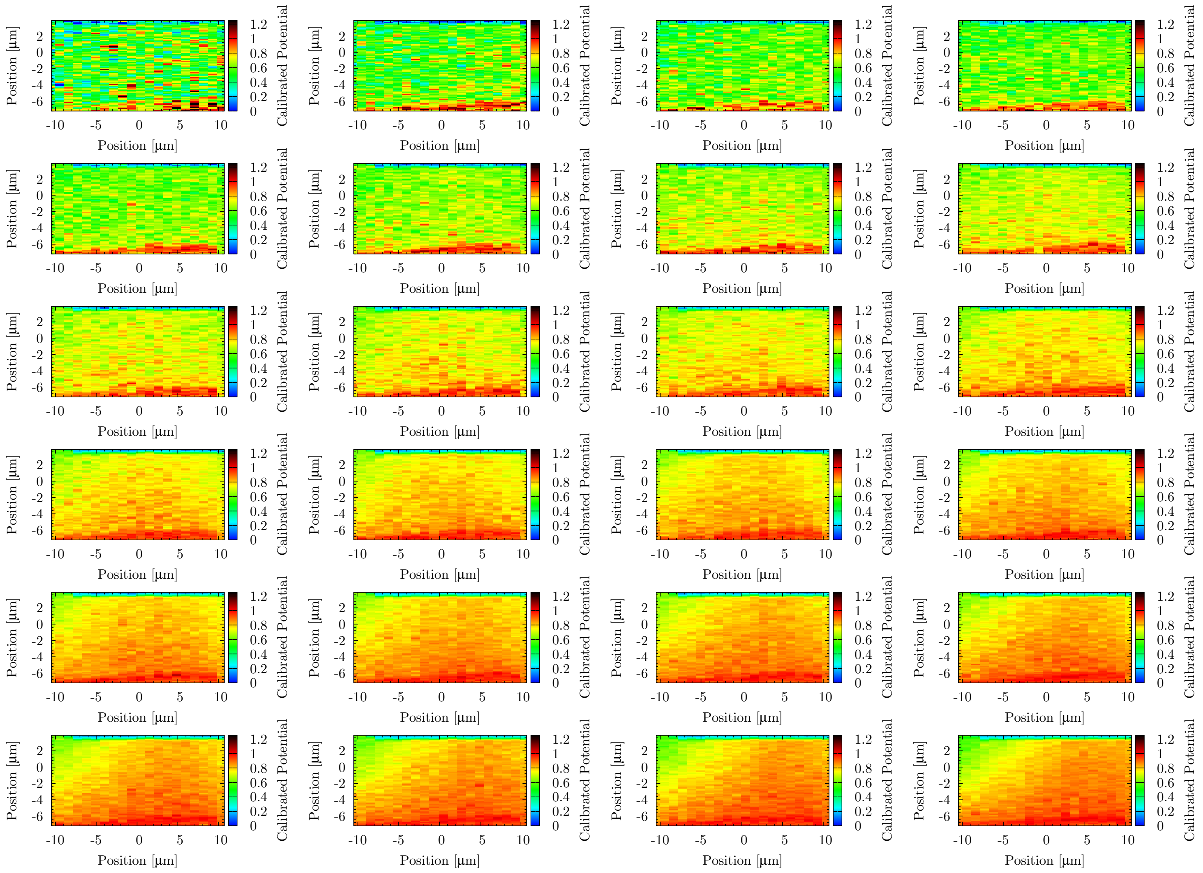

J.2.6. Area scans for $B = 6.55\,\mathrm{T}$, $\nu \approx 2.02$

The area scans from 40 mV to 155 mV have been measure in intervals of 5 mV and are shown subsequently. Ordering is the reading sequence. Current direction was for the following graphs from left to right which was shown in Fig. 13.8 (b) as (i)-direction.

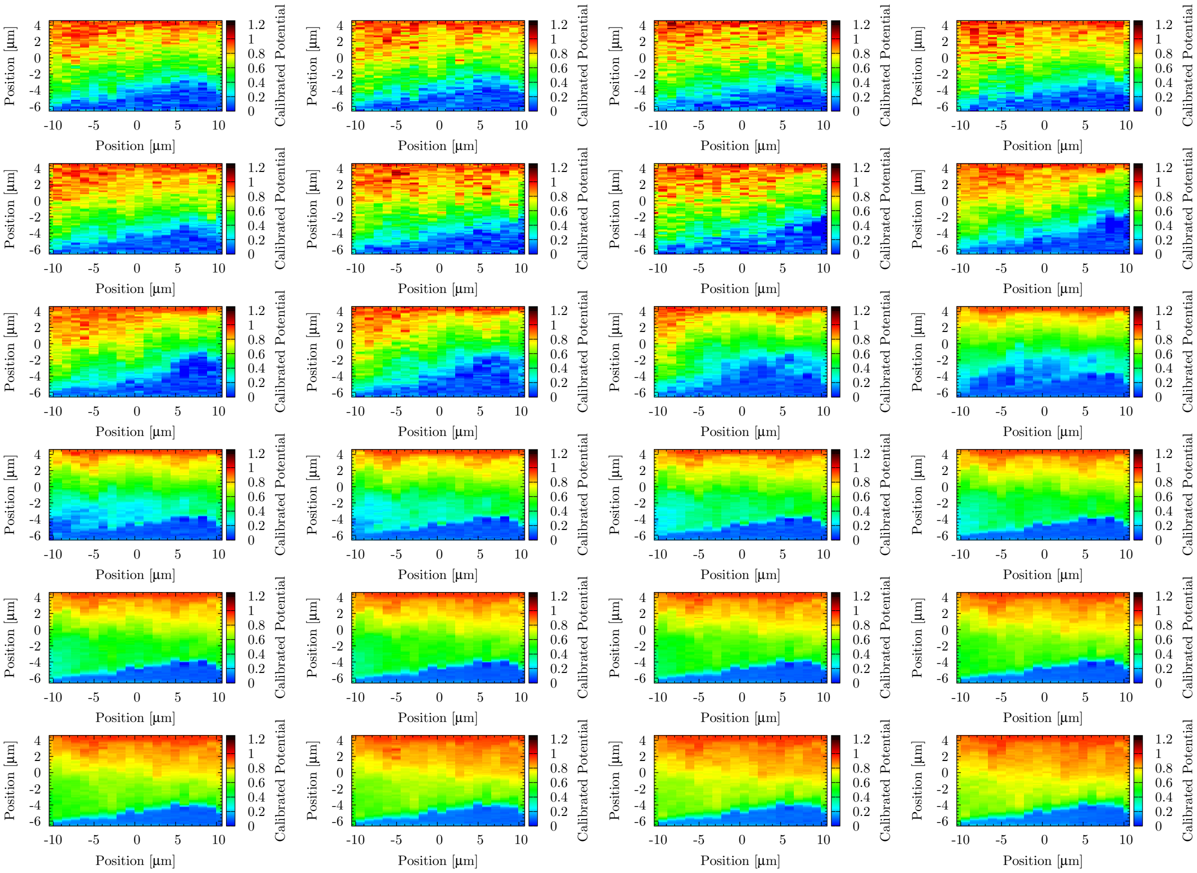

Parameters for the following graphs are the same as above but with reversed current direction, see Fig. 13.8 (c).

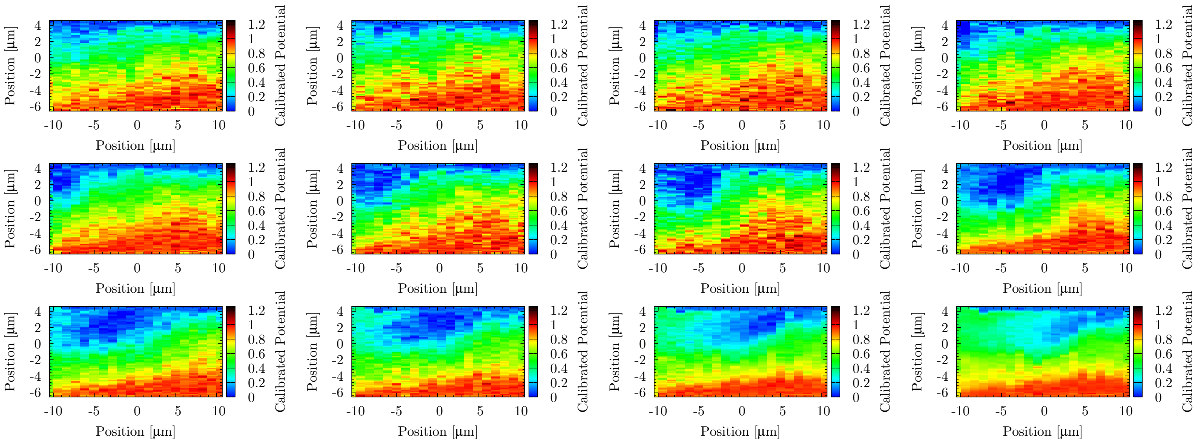

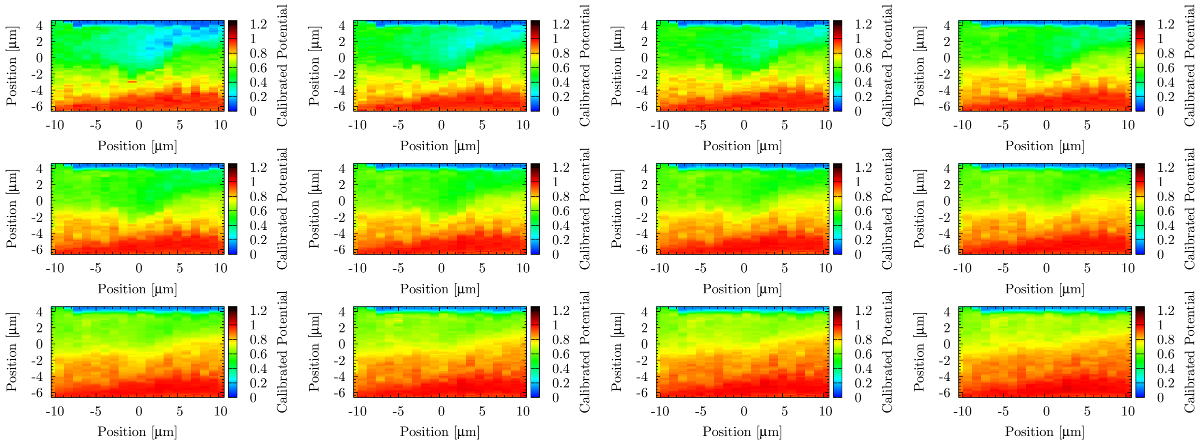

J.2.7. Area scans for $B = 6.5\,\mathrm{T}$, $\nu \approx 2.03$

The subsequent area scans were measured from 60 mV to 115 mV in intervals of 5 mV. Ordering is equal to the reading sequence. Current direction was for the following graphs from left to right which was shown in Fig. 13.8 (b) as (i)-direction.

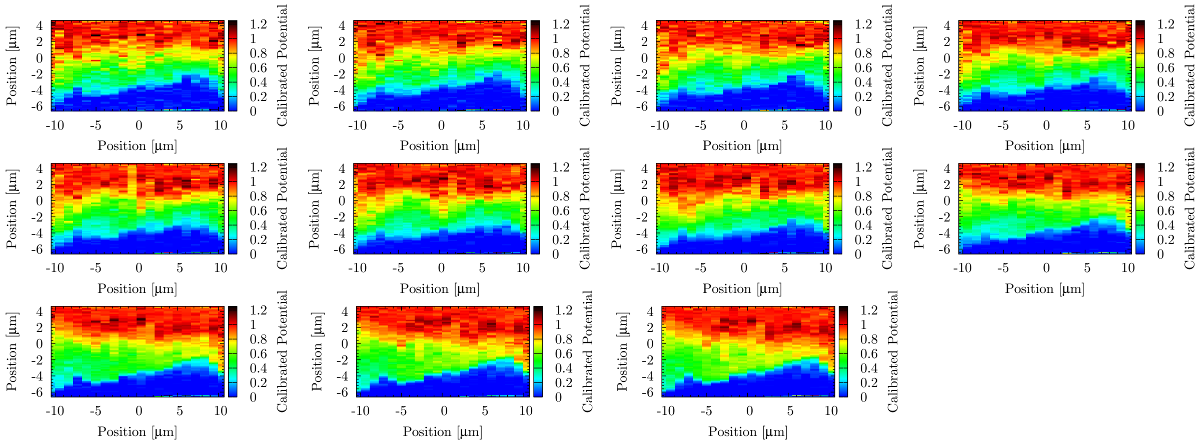

Parameters for the following graphs are the same as above but with reversed current direction, see Fig. 13.8 (c).

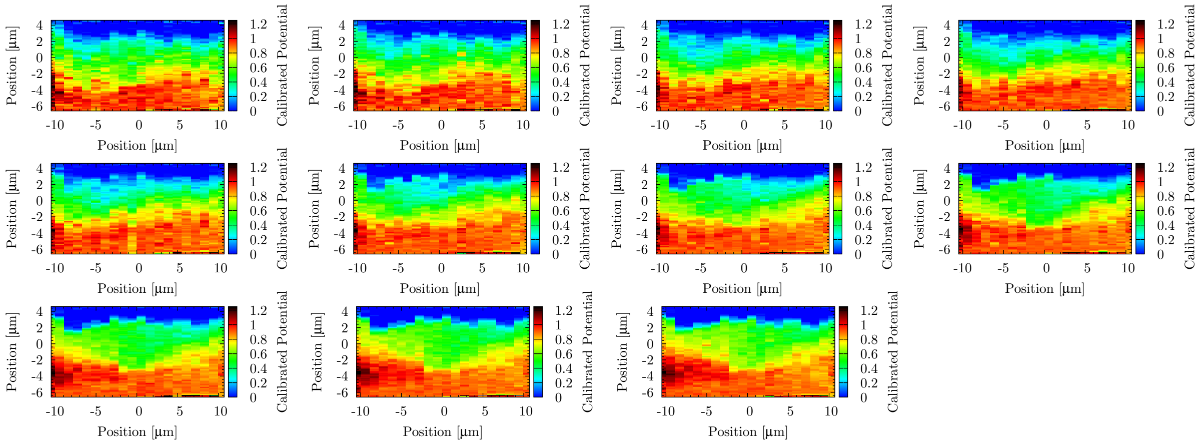

K. Bibliography

[1] P. J. Mohr, B. N. Taylor, and D. B. Newell. CODATA recommended values of the fundamental physical constants: 2006. *Rev. Mod. Phys.*, 80:633–730, Jun 2008.

[2] P. J. Mohr, B. N. Taylor, and D. B. Newell. CODATA recommended values of the fundamental physical constants: 2010. *Rev. Mod. Phys.*, 84:1527–1605, Nov 2012.

[3] Simon Sze. *Physics of Semiconductor Devices.* John Wiley and Sons, 1981.

[4] Peter Y. Yu and Manuel Cardona. *Fundamentals of Semiconductors.* Springer, 2010.

[5] K. von Klitzing, G. Dorda, and M. Pepper. New method for high-accuracy determination of the fine-structure constant based on quantized Hall resistance. *Phys. Rev. Lett.*, 45:494–497, Aug 1980.

[6] K. S. Novoselov, A. K. Geim, S. V. Morozov, D. Jiang, M. I. Katsnelson, I. V. Grigorieva, S. V. Dubonos, and A. A. Firsov. Two-dimensional gas of massless Dirac fermions in graphene. *Nature*, 438:197–200, 2005.

[7] M. König, S. Wiedmann, C. Brüne, A. Roth, H. Buhmann, L. W. Molenkamp, X.-L. Qi, and S.-C. Zhang. Quantum spin Hall insulator state in HgTe quantum wells. *Science*, 318(5851):766–770, 2007.

[8] C.-Z. Chang, J. Zhang, X. Feng, J. Shen, Z. Zhang, M. Guo, K. Li, Y. Ou, P. Wei, L.-L. Wang, Z.-Q. Ji, Y. Feng, S. Ji, X. Chen, J. Jia, X. Dai, Z. Fang, S.-C. Zhang, K. He, Y. Wang, L. Lu, X.-C. Ma, and Q.-K. Xue. Experimental observation of the quantum anomalous Hall effect in a magnetic topological insulator. *Science*, 340(6129):167–170, 2013.

[9] I. M. Mills, P. J. Mohr, T. J. Quinn, B. N. Taylor, and E. R. Williams. Adapting the international system of units to the twenty-first century. *Philosophical Transactions of the Royal Society A: Mathematical,Physical and Engineering Sciences*, 369(1953):3907–3924, 2011.

[10] I. M. Mills, P. J. Mohr, T. J. Quinn, B. N. Taylor, and E. R. Williams. Redefinition of the kilogram: a decision whose time has come. *Metrologia*, 42(2):71, 2005.

[11] R. Steiner. History and progress on accurate measurements of the Planck constant. *Reports on Progress in Physics*, 76(1):016101, 2013.

[12] K. L. McCormick, M. T. Woodside, M. Huang, M. Wu, P. L. McEuen, C. Duruoz, and J. S. Harris. Scanned potential microscopy of edge and bulk currents in the quantum Hall regime. *Phys. Rev. B*, 59:4654–4657, Feb 1999.

[13] Klaus Peter Weitz. *Untersuchungen zum Verlauf der Hall-Spannung in einem zweidimensionalen Elektronensystem unter den Bedingungen des Quanten-Hall-Effekts mittels eines Raster-Kraft-Mikroskops.* PhD thesis, Universität Hamburg, 1999.

[14] P. Weitz, E. Ahlswede, J. Weis, K. von Klitzing, and K. Eberl. Hall-potential investigations under quantum Hall conditions using scanning force microscopy. *Physica E: Low-dimensional Systems and Nanostructures*, 6(1–4):247 – 250, 2000.

[15] E. Ahlswede, P. Weitz, J. Weis, K. von Klitzing, and K. Eberl. Hall potential profiles in the quantum Hall regime measured by a scanning force microscope. *Physica B: Condensed Matter*, 298(1–4):562 – 566, 2001.

[16] E. Ahlswede, J. Weis, K. von Klitzing, and K. Eberl. Hall potential distribution in the quantum Hall regime in the vicinity of a potential probe contact. *Physica E: Low-dimensional Systems and Nanostructures*, 12(1–4):165 – 168, 2002.

[17] Erik Ahlswede. *Potential- und Stromverteilung beim Quanten-Hall-Effekt bestimmt mittels Rasterkraftmikroskopie.* PhD thesis, Universität Stuttgart, 2002.

[18] Franckh Dahlem. *Adiabatic transport in the quantum Hall regime: Comparison between trasport and scanning force microscopy investigations.* PhD thesis, Universität Stuttgart, 2008.

[19] F. Dahlem, E. Ahlswede, J. Weis, and K. von Klitzing. Cryogenic scanning force microscopy of quantum Hall samples: Adiabatic transport originating in anisotropic depletion at contact interfaces. *Phys. Rev. B*, 82:121305, Sep 2010.

[20] R. Dingle, H. L. Stormer, A. C. Gossard, and W. Wiegmann. Electron mobilities in modulation-doped semiconductor heterojunction superlattices. *Applied Physics Letters*, 33(7):665–667, 1978.

[21] D. C. Tsui, H. L. Stormer, and A. C. Gossard. Two-dimensional magnetotransport in the extreme quantum limit. *Phys. Rev. Lett.*, 48:1559–1562, May 1982.

[22] H. L. Stormer, A. Chang, D. C. Tsui, J. C. M. Hwang, A. C. Gossard, and W. Wiegmann. Fractional quantization of the Hall effect. *Phys. Rev. Lett.*, 50:1953–1956, Jun 1983.

[23] Robert Pierret. *Semiconductor device fundamentals.* Pearson Higher Education, 2003.

[24] V. Umansky, M. Heiblum, Y. Levinson, J. Smet, J. Nübler, and M. Dolev. MBE growth of ultra-low disorder 2DEG with mobility exceeding $35\cdot10^6$ cm^2/Vs. *Journal of Crystal Growth*, 311(7):1658 – 1661, 2009.

[25] E. Y. Andrei, G. Li, and X. Du. Electronic properties of graphene: a perspective from scanning tunneling microscopy and magnetotransport. *Reports on Progress in Physics*, 75(5):056501, 2012.

[26] L. Onsager. Interpretation of the de Haas-van Alphen effect. *Philosophical Magazine*, 43(344):1006–1008, 1952.

[27] S. Pancharatnam. Generalized theory of interference and its applications. I. Coherent pensils. *Proceedings of the Indian Academy of Sciences. Section A, Physical Sciences*, 44(5):247–262, 1956.

[28] M. V. Berry. Quantal phase-factors accompanying adiabatic changes. *Proceedings - Royal Society. Mathematical, physical and engineering sciences*, 392(1802):45–57, 1984.

[29] P. R. Wallace. The band theory of graphite. *Physical Review*, 71(9):622–634, 1947.

[30] A. Van Bommel, J. Crombeen, and A. Van Tooren. LEED and Auger electron observations of the SiC(0001) surface. *Surface Science*, 48(2):463 – 472, 1975.

[31] K. S. Novoselov, A. K. Geim, S. V. Morozov, D. Jiang, Y. Zhang, S. V. Dubonos, I. V. Grigorieva, and A. A. Firsov. Electric field effect in atomically thin carbon films. *Science*, 306(5696):666–669, 2004.

[32] E. V. Castro, H. Ochoa, M. I. Katsnelson, R. V. Gorbachev, D. C. Elias, K. S. Novoselov, A. K. Geim, and F. Guinea. Limits on charge carrier mobility in suspended graphene due to flexural phonons. *Phys. Rev. Lett.*, 105:266601, Dec 2010.

[33] F. Schwierz. Graphene transistors. *Nature Nanotechnology*, 5(7):487–96, 2010.

[34] X. Li, X. Wang, L. Zhang, S. Lee, and H. Dai. Chemically derived, ultrasmooth graphene nanoribbon semiconductors. *Science*, 319(5867):1229–1232, 2008.

[35] L. Jiao, L. Zhang, X. Wang, G. Diankov, and H. Dai. Narrow graphene nanoribbons from carbon nanotubes. *Nature*, 458(7240):877–80, 2009.

[36] F. Xia, D. B. Farmer, Y.-m. Lin, and P. Avouris. Graphene field-effect transistors with high on/off current ratio and large transport band gap at room temperature. *Nano Letters*, 10(2):715–718, 2010. PMID: 20092332.

[37] B. Radisavljevic, A. Radenovic, J. Brivio, V. Giacometti, and A. Kis. Single-layer MoS_2 transistors. *Nature Nanotechnology*, 6(3):147–50, 2011.

[38] L. Britnell, R. V. Gorbachev, R. Jalil, B. D. Belle, F. Schedin, A. Mishchenko, T. Georgiou, M. I. Katsnelson, L. Eaves, S. V. Morozov, J. Leist, A. K. Geim, K. S. Novoselov, and L. A. Ponomarenko. Field-effect tunneling transistor based on vertical graphene heterostructures. *Science*, 335(6071):947–50, 2012.

[39] W. Mehr, J. Dabrowski, J. C. Scheytt, G. Lippert, and Y.-H. Xie. Vertical graphene base transistor. *IEEE Electron Device Letters*, 33(5):691–693, 2012.

[40] H. Yang, J. Heo, S. Park, H. Song, D. Seo, K.-E. Byun, P. Kim, I. Yoo, H.-J. Chung, and K. Kim. Graphene barristor, a triode device with a gate-controlled Schottky barrier. *Science*, 336(6085):1140–3, 2012.

[41] S. Bae, H. Kim, Y. Lee, X. Xu, J.-S. Park, Y. Zheng, J. Balakrishnan, T. Lei, Y. Song, Y.-J. Kim, K. Kim, B. Ozyilmaz, J.-H. Ahn, B. Hong, and S. Iijima. Roll-to-roll production of 30-inch graphene films for transparent electrodes. *Nature Nanotechnology*, 5(8):574–8, 2010.

[42] K. S. Novoselov, Z. Jiang, Y. Zhang, S. V. Morozov, H. L. Stormer, U. Zeitler, J. C. Maan, G. S. Boebinger, P. Kim, and A. K. Geim. Room-temperature quantum Hall effect in graphene. *Science*, 315(5817):1379, 2007.

[43] A. J. M. Giesbers, G. Rietveld, E. Houtzager, U. Zeitler, R. Yang, K. S. Novoselov, A. K. Geim, and J. C. Maan. Quantum resistance metrology in graphene. *Applied Physics Letters*, 93(22):222109, 2008.

[44] A. Tzalenchuk, S. L. Avila, A. Kalaboukhov, S. Paolillo, M. Syväjärvi, R. Yakimova, O. Kazakova, and S. Kubatkin. Towards a quantum resistance standard based on epitaxial graphene. *Nature Nanotechnology*, 5(3):186–9, 2010.

[45] T.J.B.M. Janssen, A. Tzalenchuk, A.M.R. Baker, J.A. Alexander-Webber, R.J. Nicholas, R. Yakimova, S. Lara-Avila, S. Kubatkin, S. Kopylov, and V. I. Fal'ko. Breakdown of the quantum Hall effect in graphene. In *Precision Electromagnetic Measurements (CPEM), 2012 Conference on*, pages 510–511, 2012.

[46] A. M. R. Baker, J. A. Alexander-Webber, T. Altebaeumer, and R. J. Nicholas. Energy relaxation for hot Dirac fermions in graphene and breakdown of the quantum Hall effect. *Phys. Rev. B*, 85:115403, Mar 2012.

[47] N. O. Weiss, H. Zhou, L. Liao, Y. Liu, S. Jiang, Y. Huang, and X. Duan. Graphene: An emerging electronic material. *Advanced Materials*, 24(43):5782–5825, 2012.

[48] M. Batzill. The surface science of graphene: Metal interfaces, CVD synthesis, nanoribbons, chemical modifications, and defects. *Surface Science Reports*, 67(3):83 – 115, 2012.

[49] M. O. Goerbig. Electronic properties of graphene in a strong magnetic field. *Rev. Mod. Phys.*, 83:1193–1243, Nov 2011.

[50] F. Schwierz. Graphene transistors: Status, prospects, and problems. *Proceedings of the IEEE*, 101(7):1567–1584, 2013.

[51] A. K. Geim and K. S. Novoselov. The rise of graphene. *Nature Materials*, 6(3):183–91, 2007.

[52] P. Drude. Electron theory of metals. *Annalen der Physik*, 3(3):369–402, 1900.

[53] P. Drude. On the electron theory of metals. *Annalen der Physik*, 1(3):566–613, 1900.

[54] K. Nomura and A. H. MacDonald. Quantum transport of massless Dirac fermions. *Phys. Rev. Lett.*, 98:076602, Feb 2007.

[55] Y. Zhang, Y.-W. Tan, H. Stormer, and P. Kim. Experimental observation of the quantum Hall effect and Berry's phase in graphene. *Nature*, 438(7065):201–4, 2005.

[56] G. Li, A. Luican, and E. Y. Andrei. Scanning tunneling spectroscopy of graphene on graphite. *Phys. Rev. Lett.*, 102:176804, Apr 2009.

[57] G. Li and E. Andrei. Observation of Landau levels of Dirac fermions in graphite. *Nature Physics*, 3(9):623–627, 2007.

[58] A. Luican, G. Li, and E. Y. Andrei. Quantized Landau level spectrum and its density dependence in graphene. *Phys. Rev. B*, 83:041405, Jan 2011.

[59] K. S. Novoselov, D. Jiang, F. Schedin, T. J. Booth, V. V. Khotkevich, S. V. Morozov, and A. K. Geim. Two-dimensional atomic crystals. *Proceedings of the National Academy of Sciences of the United States of America*, 102(30):10451–3, 2005.

[60] P. Blake, E. W. Hill, A. H. C. Neto, K. S. Novoselov, D. Jiang, R. Yang, T. J. Booth, and A. K. Geim. Making graphene visible. *Applied Physics Letters*, 91(6):063124, 2007.

[61] Y. S. Dedkov, A. M. Shikin, V. K. Adamchuk, S. L. Molodtsov, C. Laubschat, A. Bauer, and G. Kaindl. Intercalation of copper underneath a monolayer of graphite on Ni(111). *Phys. Rev. B*, 64:035405, Jun 2001.

[62] P. Sutter, J.-I. Flege, and E. Sutter. Epitaxial graphene on Ruthenium. *Nature Materials*, 7(5):406–11, 2008.

[63] A. T. N'Diaye, J. Coraux, T. Plasa, C. Busse, and T. Michely. Structure of epitaxial graphene on Ir(111). *New Journal of Physics*, 10, 2008.

[64] T. A. Land, T. Michely, R. J. Behm, J. C. Hemminger, and G. Comsa. STM investigation of single layer graphite structures produced on Pt (111) by hydrocarbon decomposition. *Surface Science*, 264(3):261–270, 1992.

[65] Y. Pan, H. Zhang, D. Shi, J. Sun, S. Du, F. Liu, and H.-j. Gao. Highly ordered, millimeter-scale, continuous, single-crystalline graphene monolayer formed on Ru (0001). *Advanced Materials*, 21(27):2777–2780, 2009.

[66] L. Gao, W. Ren, H. Xu, L. Jin, Z. Wang, T. Ma, L.-P. Ma, Z. Zhang, Q. Fu, L.-M. Peng, X. Bao, and H.-M. Cheng. Repeated growth and bubbling transfer of graphene with millimetre-size single-crystal grains using platinum. *Nature Communications*, 3:699, 2012.

[67] C. Berger, Z. Song, T. Li, X. Li, A. Y. Ogbazghi, R. Feng, Z. Dai, A. N. Marchenkov, E. H. Conrad, P. N. First, and W. A. de Heer. Ultrathin epitaxial graphite: 2D electron gas properties and a route toward graphene-based nanoelectronics. *The Journal of Physical Chemistry B*, 108(52):19912–19916, 2004.

[68] E. Rollings, G.-H. Gweon, S. Zhou, B. Mun, J. McChesney, B. Hussain, A. Fedorov, P. First, W. de Heer, and A. Lanzara. Synthesis and characterization of atomically thin graphite films on a silicon carbide substrate. *Journal of Physics and Chemistry of Solids*, 67(9-10):2172 – 2177, 2006.

[69] J. Robinson, X. Weng, K. Trumbull, R. Cavalero, M. Wetherington, E. Frantz, M. LaBella, Z. Hughes, M. Fanton, and D. Snyder. Nucleation of epitaxial graphene on SiC(0001). *ACS Nano*, 4(1):153–158, 2010. PMID: 20000439.

[70] G. L. Creeth, A. J. Strudwick, J. T. Sadowski, and C. H. Marrows. Surface morphology and transport studies of epitaxial graphene on SiC($000\bar{1}$). *Phys. Rev. B*, 83:195440, May 2011.

[71] J. K. Hite, M. E. Twigg, J. L. Tedesco, A. L. Friedman, R. L. Myers-Ward, C. R. Eddy, and D. K. Gaskill. Epitaxial graphene nucleation on C-face silicon carbide. *Nano Letters*, 11(3):1190–1194, 2011.

[72] Y. Hernandez, V. Nicolosi, M. Lotya, F. Blighe, Z. Sun, S. De, I. T. McGovern, B. Holland, M. Byrne, R. Goodhue, J. Boland, P. Niraj, G. Duesberg, S. Krishnamurthy, J. Hutchison, V. Scardaci, A. Ferrari, and J. Coleman. High-yield production of graphene by liquid-phase exfoliation of graphite. *Nature Nanotechnology*, 3(9):563–8, 2008.

[73] U. Khan, A. O'Neill, M. Lotya, S. De, and J. N. Coleman. High-concentration solvent exfoliation of graphene. *Small*, 6(7):864–871, 2010.

[74] Y. Si and E. T. Samulski. Synthesis of water soluble graphene. *Nano Letters*, 8(6):1679–1682, 2008. PMID: 18498200.

[75] O. Compton and S. Nguyen. Graphene oxide, highly reduced graphene oxide, and graphene: versatile building blocks for carbon-based materials. *Small*, 6(6):711–23, 2010.

[76] J. Wu, W. Pisula, and K. Müllen. Graphenes as potential material for electronics. *Chemical Reviews*, 107(3):718–747, 2007.

[77] X. Yang, X. Dou, A. Rouhanipour, L. Zhi, H. J. Räder, and K. Müllen. Two-dimensional graphene nanoribbons. *Journal of the American Chemical Society*, 130(13):4216–4217, 2008.

[78] J. Cai, P. Ruffieux, R. Jaafar, M. Bieri, T. Braun, S. Blankenburg, M. Muoth, A. Seitsonen, M. Saleh, X. Feng, K. Müllen, and R. Fasel. Atomically precise bottom-up fabrication of graphene nanoribbons. *Nature*, 466(7305):470–3, 2010.

[79] J. Martin, N. Akerman, G. Ulbricht, T. Lohmann, J. H. Smet, K. von Klitzing, and A. Yacoby. Observation of electron-hole puddles in graphene using a scanning single-electron transistor. *Nature Physics*, 4(2):144–148, 2008.

[80] M. Ishigami, J. H. Chen, W. G. Cullen, M. S. Fuhrer, and E. D. Williams. Atomic structure of graphene on SiO_2. *Nano Letters*, 7(6):1643–1648, 2007.

[81] A. Deshpande, W. Bao, F. Miao, C. N. Lau, and B. J. LeRoy. Spatially resolved spectroscopy of monolayer graphene on SiO_2. *Phys. Rev. B*, 79:205411, May 2009.

[82] J.-H. Chen, C. Jang, S. Xiao, M. Ishigami, and M. Fuhrer. Intrinsic and extrinsic performance limits of graphene devices on SiO_2. *Nature Nanotechnology*, 3(4):206–9, 2008.

[83] C. R. Dean, A. F. Young, I. Meric, C. Lee, L. Wang, S. Sorgenfrei, K. Watanabe, T. Taniguchi, P. Kim, K. L. Shepard, and J. Hone. Boron nitride substrates for high-quality graphene electronics. *Nature Nanotechnology*, 5(10):722–6, 2010.

[84] L. Ponomarenko, R. Gorbachev, G. Yu, D. Elias, R. Jalil, A. Patel, A. Mishchenko, A. Mayorov, C. Woods, J. Wallbank, et al. Cloning of Dirac fermions in graphene superlattices. *Nature*, 497(7451):594–597, 2013.

[85] D. R. Hofstadter. Energy levels and wave functions of Bloch electrons in rational and irrational magnetic fields. *Physical review B*, 14(6):2239, 1976.

[86] E.-A. Kim and A. H. C. Neto. Graphene as an electronic membrane. *EPL (Europhysics Letters)*, 84(5):57007, 2008.

[87] A. Fasolino, J. H. Los, and M. I. Katsnelson. Intrinsic ripples in graphene. *Nature Materials*, 6(11):858–61, 2007.

[88] J. Meyer, A. K. Geim, M. I. Katsnelson, K. S. Novoselov, T. J. Booth, and S. Roth. The structure of suspended graphene sheets. *Nature*, 446(7131):60–3, 2007.

[89] J. Meyer, A. Geim, M. Katsnelson, K. Novoselov, D. Obergfell, S. Roth, C. Girit, and A. Zettl. On the roughness of single- and bi-layer graphene membranes. *Solid State Communications*, 143(1–2):101 – 109, 2007.

[90] W. Bao, F. Miao, Z. Chen, H. Zhang, W. Jang, C. Dames, and C. Lau. Controlled ripple texturing of suspended graphene and ultrathin graphite membranes. *Nature Nanotechnology*, 4(9):562–6, 2009.

[91] K. von Klitzing. The quantized Hall effect. *Rev. Mod. Phys.*, 58:519–531, Jul 1986.

[92] D. B. Chklovskii, B. I. Shklovskii, and L. I. Glazman. Electrostatics of edge channels. *Phys. Rev. B*, 46(7):4026–4034, Aug 1992.

[93] J. P. Eisenstein, L. N. Pfeiffer, and K. W. West. Compressibility of the two-dimensional electron gas: Measurements of the zero-field exchange energy and fractional quantum Hall gap. *Phys. Rev. B*, 50:1760–1778, Jul 1994.

[94] Alexander Fetter. *Quantum theory of many-particle systems.* Courier Dover Publications, 2003.

[95] K. Lier and R. R. Gerhardts. Self-consistent calculations of edge channels in laterally confined two-dimensional electron systems. *Phys. Rev. B*, 50:7757–7767, Sep 1994.

[96] J. H. Oh and R. R. Gerhardts. Self-consistent Thomas-Fermi calculation of potential and current distributions in a two-dimensional Hall bar geometry. *Phys. Rev. B*, 56:13519–13528, Nov 1997.

[97] K. Güven and R. R. Gerhardts. Self-consistent local equilibrium model for density profile and distribution of dissipative currents in a Hall bar under strong magnetic fields. *Phys. Rev. B*, 67:115327, Mar 2003.

[98] A. Siddiki and R. R. Gerhardts. Thomas-Fermi-Poisson theory of screening for laterally confined and unconfined two-dimensional electron systems in strong magnetic fields. *Phys. Rev. B*, 68:125315, Sep 2003.

[99] A. Siddiki and R. R. Gerhardts. Incompressible strips in dissipative Hall bars as origin of quantized Hall plateaus. *Phys. Rev. B*, 70:195335, Nov 2004.

[100] A. Siddiki and R. R. Gerhardts. Range-dependent disorder effects on the plateau-widths calculated within the screening theory of the IQHE. *International Journal of Modern Physics B*, 21(8/9):1362–1371, 2007.

[101] R. R. Gerhardts. The effect of screening on current distribution and conductance quantisation in narrow quantum Hall systems. *physica status solidi (b)*, 245(2):378–392, 2008.

[102] R. R. Gerhardts, K. Panos, and J. Weis. Current-induced asymmetries of incompressible strips in narrow quantum Hall systems. *New Journal of Physics*, 15(7):073034, 2013.

[103] A. Yacoby, H. Hess, T. Fulton, L. Pfeiffer, and K. West. Electrical imaging of the quantum Hall state. *Solid State Communications*, 111(1):1 – 13, 1999.

[104] K. Lai, W. Kundhikanjana, M. A. Kelly, Z.-X. Shen, J. Shabani, and M. Shayegan. Imaging of coulomb-driven quantum Hall edge states. *Phys. Rev. Lett.*, 107:176809, Oct 2011.

[105] H. Ito, K. Furuya, Y. Shibata, S. Kashiwaya, M. Yamaguchi, T. Akazaki, H. Tamura, Y. Ootuka, and S. Nomura. Near-field optical mapping of quantum Hall edge states. *Phys. Rev. Lett.*, 107:256803, Dec 2011.

[106] M. E. Suddards, A. Baumgartner, M. Henini, and C. J. Mellor. Scanning capacitance imaging of compressible and incompressible quantum Hall effect edge strips. *New Journal of Physics*, 14, 2012.

[107] O. Göktaş, J. Weber, J. Weis, and K. von Klitzing. Alloyed ohmic contacts to two-dimensional electron system in AlGaAs/GaAs heterostructures down to submicron length scale. *Physica E: Low-dimensional Systems and Nanostructures*, 40(5):1579 – 1581, 2008.

[108] Oktay Göktas. *Small alloyed ohmic contacts to 2DES and submicron scale corbino devices in strong magnetic fields : observation of a zero bias anomaly and single electron charging.* PhD thesis, Universität Stuttgart, 2009.

[109] U. Klass, W. Dietsche, K. von Klitzing, and K. Ploog. Imaging of the dissipation in quantum-Hall-effect experiments. *Zeitschrift für Physik. B, Condensed matter*, 82(3):351–354, 1991.

[110] S. Komiyama, H. Sakuma, K. Ikushima, and K. Hirakawa. Electron temperature of hot spots in quantum Hall conductors. *Phys. Rev. B*, 73:045333, Jan 2006.

[111] J. Weis and K. von Klitzing. Metrology and microscopic picture of the integer quantum Hall effect. *Philosophical transactions - Royal Society. Mathematical, Physical and engineering sciences*, 369(1953):3954–74, 2011.

[112] Seizo Morita, Roland Wiesendanger, and Ernst Meyer. *Noncontact atomic force microscopy*. Springer, Berlin ; Heidelberg [u.a.], 2002.

[113] Sergei N. Magonov and Myung-Hwan Whangbo. *Surface Analysis with STM and AFM - Experimental and Theoretical Aspects of Image Analysis*. VCH, 1996.

[114] Ernst Meyer, Hans Josef Hug, and Roland Bennewitz. *Scanning probe microscopy*. Springer, Berlin ; Heidelberg [u.a.], 2004.

[115] Adam Foster and Werner Hofer. *Scanning Probe Microscopy*. Springer, 2006.

[116] G. Binnig and H. Rohrer. Scanning tunneling microscopy. *Helvetica physica acta*, 55(6):726–735, 1982.

[117] G. Binnig, H. Rohrer, C. Gerber, and E. Weibel. 7×7 reconstruction on Si(111) resolved in real space. *Phys. Rev. Lett.*, 50(2):120–123, Jan 1983.

[118] G. Binnig, C. F. Quate, and C. Gerber. Atomic force microscope. *Phys. Rev. Lett.*, 56(9):930–933, Mar 1986.

[119] F. J. Giessibl. Atomic resolution of the Silicon (111)-(7×7) surface by atomic force microscopy. *Science*, 267(5194):68–71, 1995.

[120] S. Kitamura and M. Iwatsuki. Observation of 7×7 reconstructed structure on the silicon (111) surface using ultrahigh vacuum noncontact atomic force microscopy. *Japanese Journal of Applied Physics*, 34(Part 2, No. 1B):L145–L148, 1995.

[121] Konstantinos Panos. Aufbau eines Raster-Kraft-Mikroskopes zur Messung von Potentialverteilungen an Quanten-Hall-Proben. Master's thesis, Universität Stuttgart, 2009.

[122] E. M. Lifshitz. The theory of molecular attractive forces between solids. *Soviet physics, JETP*, 2(1):73–83, 1956.

[123] J. Chu, T. Itoh, C. Lee, T. Suga, and K. Watanabe. Frequency modulation detection high vacuum scanning force microscope with a self-oscillating piezoelectric cantilever. *Journal of Vacuum Science & Technology B: Microelectronics and Nanometer Structures*, 15(5):1647–1651, 1997.

[124] W. Clauss, J. Zhang, D. J. Bergeron, and A. T. Johnson. Application and calibration of a quartz needle sensor for high resolution scanning force microscopy. *Journal of Vacuum Science & Technology B: Microelectronics and Nanometer Structures*, 17(4):1309–1312, 1999.

[125] F. J. Giessibl. Atomic resolution on Si (111)-(7 x 7) by noncontact atomic force microscopy with a force sensor based on a quartz tuning fork. *Applied Physics Letters*, 76(11):1470–1472, 2000.

[126] M. Tortonese, R. C. Barrett, and C. F. Quate. Atomic resolution with an atomic force microscope using piezoresistive detection. *Applied Physics Letters*, 62(8):834–836, 1993.

[127] Gennadij L. Bir and Grigorij E. Pikus. *Symmetry and strain-induced effects in semiconductors*. Wiley, New York, 1974.

[128] S. Rast, C. Wattinger, U. Gysin, and E. Meyer. Dynamics of damped cantilevers. *Review of Scientific Instruments*, 71(7):2772–2775, 2000.

[129] M. Guggisberg, M. Bammerlin, C. Loppacher, O. Pfeiffer, A. Abdurixit, V. Barwich, R. Bennewitz, A. Baratoff, E. Meyer, and H.-J. Güntherodt. Separation of interactions by noncontact force microscopy. *Phys. Rev. B*, 61(16):11151–11155, Apr 2000.

[130] F. J. Giessibl. Forces and frequency shifts in atomic-resolution dynamic-force microscopy. *Phys. Rev. B*, 56(24):16010–16015, Dec 1997.

[131] P. J. de Pablo, J. Colchero, M. Luna, J. Gómez-Herrero, and A. M. Baró. Tip-sample interaction in tapping-mode scanning force microscopy. *Phys. Rev. B*, 61(20):14179–14183, May 2000.

[132] Y. Martin, D. W. Abraham, and H. K. Wickramasinghe. High-resolution capacitance measurement and potentiometry by force microscopy. *Applied Physics Letters*, 52(13):1103–1105, 1988.

[133] J. M. R. Weaver and D. W. Abraham. High resolution atomic force microscopy potentiometry. *Journal of Vacuum Science & Technology B: Microelectronics and Nanometer Structures*, 9(3):1559–1561, 1991.

[134] M. Nonnenmacher, M. P. O'Boyle, and H. K. Wickramasinghe. Kelvin probe force microscopy. *Applied Physics Letters*, 58(25):2921–2923, 1991.

[135] H. O. Jacobs, H. F. Knapp, S. Müller, and A. Stemmer. Surface potential mapping: A qualitative material contrast in SPM. *Ultramicroscopy*, 69(1):39 – 49, 1997.

[136] A. Chang. A unified transport theory for the integral and fractional quantum Hall effects: Phase boundaries, edge currents, and transmission/reflection probabilities. *Solid State Communications*, 74(9):871 – 876, 1990.

[137] B. Feldman, B. Krauss, J. Smet, and A. Yacoby. Unconventional sequence of fractional quantum Hall states in suspended graphene. *Science*, 337(6099):1196–9, 2012.

[138] G. Li, A. L. Mayer, D. Abanin, L. Levitov, and E. Andrei. Evolution of Landau levels into edge states in graphene. *Nature Communications*, 4:1744, 2013.

[139] E. J. H. Lee, K. Balasubramanian, R. T. Weitz, M. Burghard, and K. Kern. Contact and edge effects in graphene devices. *Nature Nanotechnology*, 3(8):486–490, 2008. Cited By (since 1996): 175.

[140] James Maxwell. *Treatise on electricity and magnetism.* Oxford University Press, 2002.

[141] S. Adam, E. H. Hwang, V. M. Galitski, and S. Das Sarma. A self-consistent theory for graphene transport. *Proceedings of the National Academy of Sciences*, 104(47):18392–18397, 2007.

[142] P. G. Silvestrov and K. B. Efetov. Charge accumulation at the boundaries of a graphene strip induced by a gate voltage: Electrostatic approach. *Phys. Rev. B*, 77:155436, Apr 2008.

[143] R. Ballard. The electron affinity of water and the structure of the hydrated electron. *Chemical Physics Letters*, 16(2):300 – 301, 1972.

[144] R. G. Pearson. Ionization potentials and electron affinities in aqueous solution. *Journal of the American Chemical Society*, 108(20):6109–6114, 1986.

[145] K. Nakada, M. Fujita, G. Dresselhaus, and M. S. Dresselhaus. Edge state in graphene ribbons: Nanometer size effect and edge shape dependence. *Phys. Rev. B*, 54:17954–17961, Dec 1996.

[146] N. Peres, F. Guinea, and A. C. Neto. Electronic properties of two-dimensional carbon. *Annals of Physics*, 321(7):1559 – 1567, 2006. July 2006 Special Issue.

[147] Y. Kobayashi, K.-i. Fukui, T. Enoki, K. Kusakabe, and Y. Kaburagi. Observation of zigzag and armchair edges of graphite using scanning tunneling microscopy and spectroscopy. *Phys. Rev. B*, 71:193406, May 2005.

[148] A. P. Seitsonen, A. M. Saitta, T. Wassmann, M. Lazzeri, and F. Mauri. Structure and stability of graphene nanoribbons in oxygen, carbon dioxide, water, and ammonia. *Phys. Rev. B*, 82:115425, Sep 2010.

[149] M. Luna, J. Colchero, and A. M. Baró. Study of water droplets and films on graphite by noncontact scanning force microscopy. *The Journal of Physical Chemistry B*, 103(44):9576–9581, 1999.

[150] W. Kim, A. Javey, O. Vermesh, Q. Wang, Y. Li, and H. Dai. Hysteresis caused by water molecules in carbon nanotube field-effect transistors. *Nano Letters*, 3(2):193–198, 2003.

[151] L. Zhuravlev. The surface chemistry of amorphous silica. Zhuravlev model. *Colloids and Surfaces A: Physicochemical and Engineering Aspects*, 173(1):1 – 38, 2000.

[152] Y. Yang, K. Brenner, and R. Murali. The influence of atmosphere on electrical transport in graphene. *Carbon*, 50(5):1727 – 1733, 2012.

[153] Z. H. Ni, H. M. Wang, Z. Q. Luo, Y. Y. Wang, T. Yu, Y. H. Wu, and Z. X. Shen. The effect of vacuum annealing on graphene. *Journal of Raman Spectroscopy*, 41(5):479–483, 2010.

[154] Y. Zhang, V. Brar, C. Girit, A. Zettl, and M. Crommie. Origin of spatial charge inhomogeneity in graphene. *Nature Physics*, 5(10):722–726, 2009.

[155] T. Lohmann, K. von Klitzing, and J. H. Smet. Four-terminal magneto-transport in graphene p-n junctions created by spatially selective doping. *Nano Letters*, 9(5):1973–1979, 2009.

[156] H. E. Romero, N. Shen, P. Joshi, H. R. Gutierrez, S. A. Tadigadapa, J. O. Sofo, and P. C. Eklund. n-type behavior of graphene supported on Si/SiO_2 substrates. *ACS Nano*, 2(10):2037–2044, 2008.

[157] Y.-W. Tan, Y. Zhang, K. Bolotin, Y. Zhao, S. Adam, E. H. Hwang, S. Das Sarma, H. L. Stormer, and P. Kim. Measurement of scattering rate and minimum conductivity in graphene. *Phys. Rev. Lett.*, 99:246803, Dec 2007.

[158] Y.-C. Lin, C.-C. Lu, C.-H. Yeh, C. Jin, K. Suenaga, and P.-W. Chiu. Graphene annealing: How clean can it be? *Nano Letters*, 12(1):414–419, 2012.

[159] N. Staley, H. Wang, C. Puls, J. Forster, T. N. Jackson, K. McCarthy, B. Clouser, and Y. Liu. Lithography-free fabrication of graphene devices. *Applied Physics Letters*, 90(14):143518, 2007.

[160] W. Bao, G. Liu, Z. Zhao, H. Zhang, and D. Yan. Lithography-free fabrication of high quality substrate-supported and freestanding graphene devices. *Nano research*, 3(2):98–102, 2010.

[161] J. Moser, A. Verdaguer, D. Jimenez, A. Barreiro, and A. Bachtold. The environment of graphene probed by electrostatic force microscopy. *Applied Physics Letters*, 92(12):123507, 2008.

[162] M. O. Andersson, K. R. Farmer, and O. Engstrom. Negative charging in ultrathin metal-oxide-silicon tunnel diodes. *Journal of Applied Physics*, 71(4):1846–1852, 1992.

[163] J. Zhang and B. Eccleston. Donor-like interface trap generation in pMOSFET's at room temperature. *Electron Devices, IEEE Transactions on*, 41(5):740–744, 1994.

[164] J. S. Chou and S. C. Lee. Application of liquid phase deposited silicon dioxide to metal-oxide-semiconductor capacitor and amorphous silicon thin-film transistor. *Electron Devices, IEEE Transactions on*, 43(4):599–604, 1996.

[165] T. Takahagi, S. Shingubara, H. Sakaue, K. Hoshino, and H. Yashima. Study on adsorption behavior of organic contaminations on silicon surface by gas chromatography mass spectrometry. *Japanese journal of applied physics*, 35(7A):L818–L821, 1996.

[166] D. Li, M. B. Mueller, S. Gilje, R. B. Kaner, and G. G. Wallace. Processable aqueous dispersions of graphene nanosheets. *Nature Nanotechnology*, 3(2):101–105, 2008.

[167] B. E. Deal. Standardized terminology for oxide charges associated with thermally oxidized silicon. *Electron Devices, IEEE Transactions on*, 27(3):606–608, 1980.

[168] Patrick Herlinger. Private communication.

[169] T. Aoyama, H. Tashiro, and K. Suzuki. Diffusion of boron, phosphorus, arsenic, and antimony in thermally grown silicon dioxide. *Journal of the Electrochemical Society*, 146(5):1879–1883, 1999.

[170] K. Güven and R. R. Gerhardts. Self-consistent local equilibrium model for density profile and distribution of dissipative currents in a Hall bar under strong magnetic fields. *Phys. Rev. B*, 67:115327, Mar 2003.

[171] X. Xie, L. Ju, X. Feng, Y. Sun, R. Zhou, K. Liu, S. Fan, Q. Li, and K. Jiang. Controlled fabrication of high-quality carbon nanoscrolls from monolayer graphene. *Nano Letters*, 9(7):2565–2570, 2009. PMID: 19499895.

[172] M. J. Allen, M. Wang, S. A. V. Jannuzzi, Y. Yang, K. L. Wang, and R. B. Kaner. Chemically induced folding of single and bilayer graphene. *Chem. Commun.*, pages 6285–6287, 2009.

[173] K. Kim, Z. Lee, B. D. Malone, K. T. Chan, B. Alemán, W. Regan, W. Gannett, M. F. Crommie, M. L. Cohen, and A. Zettl. Multiply folded graphene. *Phys. Rev. B*, 83:245433, Jun 2011.

[174] F. Guinea, M. I. Katsnelson, and A. K. Geim. Energy gaps and a zero-field quantum Hall effect in graphene by strain engineering. *Nature Physics*, 6(1):30–33, 2010.

[175] N. Levy, S. A. Burke, K. L. Meaker, M. Panlasigui, A. Zettl, F. Guinea, A. H. C. Neto, and M. F. Crommie. Strain-induced pseudo-magnetic fields greater than 300 tesla in graphene nanobubbles. *Science*, 329(5991):544–7, 2010.

[176] T. J. B. M. Janssen, N. E. Fletcher, R. Goebel, J. M. Williams, A. Tzalenchuk, R. Yakimova, S. Kubatkin, S. Lara-Avila, and V. I. Falko. Graphene, universality of the quantum Hall effect and redefinition of the SI system. *New Journal of Physics*, 13(9):093026, 2011.

[177] F. Schopfer and W. Poirier. Testing universality of the quantum Hall effect by means of the Wheatstone bridge. *Journal of Applied Physics*, 102(5):–, 2007.

[178] A. Hartland, K. Jones, J. M. Williams, B. L. Gallagher, and T. Galloway. Direct comparison of the quantized Hall resistance in gallium arsenide and silicon. *Phys. Rev. Lett.*, 66:969–973, Feb 1991.

[179] T. J. Witt. Electrical resistance standards and the quantum Hall effect. *Review of Scientific Instruments*, 69(8):2823–2843, 1998.

[180] F. Delahaye and B. Jeckelmann. Revised technical guidelines for reliable dc measurements of the quantized Hall resistance. *Metrologia*, 40(5):217, 2003.

[181] S. KawajiI and J. Wakabayashi. Quantum galvanomagnetic properties of n-type inversion layers on si(100) MOSFET. *Surface Science*, 58(1):238 – 245, 1976.

[182] K. Yoshihiro, J. Kinoshita, K. Inagaki, C. Yamanouchi, J. Moriyama, and S. Kawaji. High precision measurements of the Hall effect for silicon MOS inversion layers in strong magnetic fields. *Surface Science*, 113(1–3):16 – 21, 1982.

[183] G. Ebert, K. von Klitzing, K. Ploog, and G. Weimann. Two-dimensional magneto-quantum transport on GaAs-Al$_x$Ga$_{1-x}$As heterostructures under non-ohmic conditions. *Journal of Physics C: Solid State Physics*, 16(28):5441, 1983.

[184] M. E. Cage, R. F. Dziuba, B. F. Field, E. R. Williams, S. M. Girvin, A. C. Gossard, D. C. Tsui, and R. J. Wagner. Dissipation and dynamic nonlinear behavior in the quantum Hall regime. *Phys. Rev. Lett.*, 51:1374–1377, Oct 1983.

[185] A. A. Penin. Quantum Hall effect in quantum electrodynamics. *Phys. Rev. B*, 79:113303, Mar 2009.

[186] G. Nachtwei. Breakdown of the quantum Hall effect. *Physica E: Low-dimensional Systems and Nanostructures*, 4(2):79 – 101, 1999.

[187] S. Kawaji, K. Hirakawa, and M. Nagata. Device-width dependence of plateau width in quantum Hall states. *Physica B: Condensed Matter*, 184(1–4):17 – 20, 1993.

[188] N. Q. Balaban, U. Meirav, H. Shtrikman, and Y. Levinson. Scaling of the critical current in the quantum Hall effect: A probe of current distribution. *Phys. Rev. Lett.*, 71:1443–1446, Aug 1993.

[189] S. Kawaji, K. Hirakawa, M. Nagata, T. Okamoto, T. Fukase, and T. Gotoh. Breakdown of the quantum Hall effect in GaAs/AlGaAs heterostructures due to current. *Journal Of The Physical Society Of Japan*, 63(6):2303–2313, 1994.

[190] S. Kawaji, K. Hirakawa, M. Nagata, T. Okamoto, T. Fukase, and T. Goto. Magnetic field dependence of the device-width-dependent breakdown current in the quantum Hall effect. *Surface Science*, 305(1–3):161 – 165, 1994.

[191] T. Okuno, S. Kawaji, T. Ohrui, T. Okamoto, Y. Kurata, and J. Sakai. Electron concentration and mobility dependence of breakdown of the quantum Hall effect. *Journal Of The Physical Society Of Japan*, 64(6):1881–1884, 1995.

[192] F. Schopfer and W. Poirier. Quantum resistance standard accuracy close to the zero-dissipation state. *Journal of Applied Physics*, 114(6):–, 2013.

[193] A. Chang and D. Tsui. Experimental observation of a striking similarity between quantum Hall transport coefficients. *Solid State Communications*, 56(1):153 – 154, 1985.

[194] K. Yoshihiro, J. Kinoshita, K. Inagaki, C. Yamanouchi, J. Moriyama, and S. Kawaji. Quantized Hall and transverse resistivities in silicon MOS n-inversion layers. *Physica B+C*, 117–118, Part 2(0):706 – 708, 1983.

[195] M. E. Cage, B. F. Field, R. F. Dziuba, S. M. Girvin, A. C. Gossard, and D. C. Tsui. Temperature dependence of the quantum Hall resistance. *Phys. Rev. B*, 30:2286–2288, Aug 1984.

[196] A. Boisen, P. Bøggild, A. Kristensen, and P. E. Lindelof. Nonlinear current-voltage characteristics at quantum Hall resistance minima. *Phys. Rev. B*, 50:1957–1960, Jul 1994.

[197] R.J. Haug, K. von Klitzing, and K. Ploog. Hot electron magnetotransport in $Al_xGa_{1-x}As$-GaAs samples of different geometry. In Gottfried Landwehr, editor, *High Magnetic Fields in Semiconductor Physics II*, volume 87 of *Springer Series in Solid-State Sciences*, Pages 185–189. Springer Berlin Heidelberg, 1989.

[198] Y. Kawaguchi, F. Hayashi, S. Komiyama, T. Osada, Y. Shiraki, and R. Itoh. Disappearance of the breakdown of quantum Hall effects in short devices. *Japanese Journal of Applied Physics*, 34(8B):4309–4312, 1995.

[199] Y. Kawaguchi, S. Komiyama, T. Osada, and Y. Shiraki. Nonlocal nature of the breakdown of the integer quantum Hall effects. *Physica B: Condensed Matter*, 227(1–4):183 – 185, 1996.

[200] S. Komiyama, Y. Kawaguchi, T. Osada, and Y. Shiraki. Evidence of nonlocal breakdown of the integer quantum Hall effect. *Phys. Rev. Lett.*, 77:558–561, Jul 1996.

[201] I. I. Kaya, G. Nachtwei, K. von Klitzing, and K. Eberl. Spatially resolved monitoring of the evolution of the breakdown of the quantum Hall effect: Direct observation of inter-Landau-level tunneling. *EPL (Europhysics Letters)*, 46(1):62, 1999.

[202] I. I. Kaya, G. Nachtwei, K. von Klitzing, and K. Eberl. Spatial evolution of hot-electron relaxation in quantum Hall conductors. *Phys. Rev. B*, 58:R7536–R7539, Sep 1998.

[203] I. Kaya, G. Nachtwei, K. von Klitzing, and K. Eberl. Dynamics of nonequilibrium electrons at the breakdown of the quantum Hall effect. *Physica B: Condensed Matter*, 256–258(0):8 – 15, 1998.

[204] L. Bliek, E. Braun, G. Hein, V. Kose, J. Niemeyer, G. Weimann, and W. Schlapp. Critical current density for the dissipationless quantum Hall effect. *Semiconductor Science and Technology*, 1(2):110, 1986.

[205] P. C. van Son, G. H. Kruithof, and T. M. Klapwijk. Current contacts and the breakdown of the quantum Hall effect. *Phys. Rev. B*, 42:11267–11275, Dec 1990.

[206] P. van Son, G. Kruithof, and T. Klapwijk. Intrinsic sequence in the breakdown of the quantum Hall effect. *Surface Science*, 229(1–3):57 – 59, 1990.

[207] G. Ebert, K. von Klitzing, and G. Weimann. Hall potential distribution in quantum Hall experiments. *Journal of Physics C: Solid State Physics*, 18(10):L257, 1985.

[208] S. Dorozhkin and M. Dorokhova. Current filamentation in GaAs/AlGaAs heterojunctions preceding quantum-Hall-effect breakdown. *Journal of Experimental and Theoretical Physics Letters*, 68(9):732–737, 1998.

[209] Y. Kawano, Y. Hisanaga, and S. Komiyama. Cyclotron emission from quantized Hall devices: Injection of nonequilibrium electrons from contacts. *Phys. Rev. B*, 59:12537–12546, May 1999.

[210] Y. Kawano, Y. Hisanaga, H. Takenouchi, and S. Komiyama. Highly sensitive and tunable detection of far-infrared radiation by quantum Hall devices. *Journal of Applied Physics*, 89(7):4037–4048, 2001.

[211] Y. Kawano and T. Okamoto. Imaging of intra- and inter-Landau-level scattering in quantum Hall systems. *Physical Review. B, Condensed Matter and Materials Physics*, 70(8):081308, 2004.

[212] K. Ikushima, H. Sakuma, S. Komiyama, and K. Hirakawa. Imaging of cyclotron emission from edge channels in quantum Hall conductors. *Physical Review Letters*, 93(14):146804, 2004.

[213] K. Ikushima, H. Sakuma, S. Komiyama, and K. Hirakawa. Visualization of quantum Hall edge channels through imaging of terahertz emission. *Phys. Rev. B*, 76:165323, Oct 2007.

[214] M. Kawamura, K. Kono, Y. Hashimoto, S. Katsumoto, and T. Machida. Spatial gradient of dynamic nuclear spin polarization induced by breakdown of the quantum Hall effect. *Phys. Rev. B*, 83:041305, Jan 2011.

[215] M. E. Cage, G. M. Reedtz, D. Y. Yu, and C. T. V. Degrift. Quantised dissipative states at breakdown of the quantum Hall effect. *Semiconductor Science and Technology*, 5(4):351, 1990.

[216] M. E. Cage. Dependence of quantized Hall effect breakdown voltage on magnetic field and current. *Journal of research of the National Institute of Standards and Technology*, 98(3):361–373, 1993.

[217] L. Bliek, G. Hein, V. Kose, J. Niemeyer, and G. Weimann. A new quantum effect in the transverse magnetoresistance of two-dimensional conductors with a narrow constriction in the conducting channel. In *High Magnetic Fields in Semiconductor Physics*, Pages 113–117. Springer, 1987.

[218] D. C. Tsui, G. J. Dolan, and A. C. Gossard. Zener breakdown of the quantized Hall effect. *Bulletin of the American Physical Society*, 28:365, 1983.

[219] O. Heinonen, P. L. Taylor, and S. M. Girvin. Electron-phonon interactions and the breakdown of the dissipationless quantum Hall effect. *Phys. Rev. B*, 30:3016–3019, Sep 1984.

[220] L. Eaves and F. W. Sheard. Size-dependent quantised breakdown of the dissipationless quantum Hall effect in narrow channels. *Semiconductor Science and Technology*, 1(6):346, 1986.

[221] V. L. Pokrovsky, L. P. Pryadko, and A. L. Talapov. Resonance tunnelling and breakdown of the quantum Hall effect in strong electric fields. *Journal of Physics: Condensed Matter*, 2(6):1583, 1990.

[222] S. Komiyama and Y. Kawaguchi. Heat instability of quantum Hall conductors. *Phys. Rev. B*, 61:2014–2027, Jan 2000.

[223] P. Středa and K. von Klitzing. Critical non-dissipative current of quantum Hall regime. *Journal of Physics C: Solid State Physics*, 17(19):L483, 1984.

[224] H. J. McSkimin, A. Jayaraman, and J. P. Andreatch. Elastic moduli of GaAs at moderate pressures and the evaluation of compression to 250 kbar. *Journal of Applied Physics*, 38(5):2362–2364, 1967.

[225] S. Komiyama, T. Takamasu, S. Hiyamizu, and S. Sasa. Breakdown of the quantum Hall effect due to electron heating. *Solid State Communications*, 54(6):479 – 484, 1985.

[226] T. Takamasu, S. Komiyama, S. Hiyamizu, and S. Sasa. Effect of finite electric field on the quantum Hall effect. *Surface Science*, 170(1-2):202 – 208, 1986.

[227] K. Güven, R. R. Gerhardts, I. I. Kaya, B. E. Sağol, and G. Nachtwei. Two-level model for the generation and relaxation of hot electrons near the breakdown of the quantum Hall effect. *Phys. Rev. B*, 65:155316, Mar 2002.

[228] Konstantinos Panos, Rolf R Gerhardts, Jürgen Weis, and Klaus von Klitzing. Current distribution and Hall potential landscape at the breakdown of the quantum Hall effect in small samples. In preparation, 2014.

[229] A. Siddiki, J. Horas, D. Kupidura, W. Wegscheider, and S. Ludwig. Asymmetric nonlinear response of the quantized Hall effect. *New Journal of Physics*, 12(11):113011, 2010.

[230] B. E. Kane, D. C. Tsui, and G. Weimann. Evidence for edge currents in the integral quantum Hall effect. *Phys. Rev. Lett.*, 59:1353–1356, Sep 1987.

[231] A. Young, J. Sanchez-Yamagishi, B. Hunt, S. Choi, K. Watanabe, T. Taniguchi, R. Ashoori, and P. Jarillo-Herrero. Tunable symmetry breaking and helical edge transport in a graphene quantum spin Hall state. *Nature*, 2013.

[232] J. Gao, F. Liu, Y. Liu, N. Ma, Z. Wang, and X. Zhang. Environment-friendly method to produce graphene that employs vitamin C and amino acid. *Chemistry of Materials*, 22(7):2213–2218, 2010.

[233] M. I. Katsnelson. Nonlinear screening of charge impurities in graphene. *Phys. Rev. B*, 74:201401, Nov 2006.

[234] W. H. Press, B. P. Flannery, S. A. Teukolsky, and W. T. Vetterling. *Numerical Recipes in C: The Art of Scientific Computing, 2nd ed.* Cambridge University Press, 1992.

[235] Tao Pang. *An Introduction to Computational Physics.* Cambridge University Press, Cambridge, 2006.

[236] David Ferry. *Quantum Transport in Semiconductors*. Kluwer Academic/Plenum Publishers, 1992.

[237] Otfried Madelung. *Introduction to solid-state theory*. Springer, 1978.

[238] V. Lukose, R. Shankar, and G. Baskaran. Novel electric field effects on Landau levels in graphene. *Phys. Rev. Lett.*, 98:116802, Mar 2007.

[239] N. M. R. Peres and E. V. Castro. Algebraic solution of a graphene layer in transverse electric and perpendicular magnetic fields. *Journal of Physics: Condensed Matter*, 19(40):406231, 2007.

[240] Il'ja N. Bronštejn. *Taschenbuch der Mathematik*. Deutsch, Frankfurt am Main, 2006.

[241] Furuuchi Chemical Corporation. Semico clean. www.furuchi.co.jp.

[242] SII NanoTechnology Inc. www.siint.com.

[243] Epolead Service Inc. Self sensing cantilever PRC400(Mold less). K-A102003895.

List of Figures

2.1. Layer sequence of a GaAs/$\mathrm{Al}_x\mathrm{Ga}_{1-x}$As-heterostructures used in this work. 7

3.1. Lattice of graphene and its representation in reciprocal space. 12
3.2. Band structure of graphene. 13
3.3. Electrical characteristics of a graphene flake: (a) at zero magnetic field. Adapted by permission from Macmillan Publishers Ltd: Nature Materials [51], copyright (2014), (b) with magnetic field of 14 T. Reprinted by permission from Macmillan Publishers Ltd: Nature Materials [51], copyright (2014). 15
3.4. Landau levels measured by scanning tunneling spectroscopy for a flake weakly coupled on a graphite substrate [56]. 17
3.5. Landau levels measured by scanning tunneling spectroscopy for a flake on chlorinated silicon dioxide [58]. 18
3.6. Charge puddles measured with a scanning single-electron transistor by Martin et al. [79]. An area scan is shown to demonstrated the spatial extend of the puddles. Reprinted by permission from Macmillan Publishers Ltd: Nature Physics [79], copyright (2014). 19

4.1. Quantum Hall measurement consisting of the transverse resistance R_{xy} shown on the top and the longitudinal resistivity ρ_{xx} shown at the bottom. Adapted with permission from [91]. Copyrighted by the American Physical Society. 21
4.2. Hall potential profiles, measured over the width of a two-terminal sample (see inset on right side), across a quantum Hall plateau. The inset shows the plateau in the Hall resistance curve around filling factor $\nu = 2$. Adapted with permission from [14]. Copyrighted by Elsevier. . . 23
4.3. Hall potential measurements of Ahlswede et al. [17] and position of incompressible stripes according to Chklovskii et al. [92]. No free parameter was available to match data and calculations. The Hall potential is shown in color-scale versus position over the Hall bar width and the applied magnetic field. We thank Erik Ahslwede for the access to his data to create this plot. 24
4.4. Geometry used by Chklovskii, Shklovskii and Glazman [92] to calculate analytically the screening effects along a 2DES edge. 25
4.5. Landau level structure and charge carrier concentration at a 2DES edge (a) ,(d) neglecting electrostatic energy, (b),(e) neglecting the chemical potential and (c),(f) taking electrostatic energy as well as chemical potential into account. Adapted in parts from [92]. 26
4.6. Sketch of the Landau level bending from edge to edge of a 2DES. . . . 29

4.7. Hall potential landscape of an area in front of a potential probing ohmic alloyed contact. Adapted from [17]. 30
4.8. Evolution of the compressible/incompressible landscape inside the 2DES across a quantum Hall resistance plateau. Adapted with permission from [111]. Copyright © 2011, The Royal Society. 32

5.1. Arrangement of tip and sample. 36
5.2. Interaction potential between tip and sample over tip sample distance. . 37
5.3. Effect of chemical potential difference. 38
5.4. Sketch of some detection mechanisms adapted from [114]. 40
5.5. Resonance profile for an SPM cantilever with quality factor of $Q = 10000$. 41
5.6. Sketch of the tip behavior approaching the sample surface. 44
5.7. Operation principle of a Scanning Probe or Scanning Tunneling Microscope for measuring topography. 46
5.8. Sketch of a non-contact SPM setup. 47

6.1. Calibration technique to measure the current induced potential changes. 51
6.2. Example data showing trace α and β in arbitrary units and the resulting Hall potential profile. 52
6.3. Kelvin-probe measurement scheme used to determine the compensation voltage V_{DC}. 55
6.4. Determination of the compensation voltage between a gold covered tip and a 2DES within a GaAs/Al$_x$Ga$_{1-x}$AS-heterostructure. 56

7.1. Fully processed sample (GB8113) glued on a chip carrier and mounted on the coarse positioning stage. 61

8.1. (a) Schematics of the transport measurement setup and (b) the resulting resistance over back gate voltage. The applied bias voltage V was chosen at 10 mV to match the scanning bias situation. 63
8.2. A non contact topography scan of the graphene flake GB8113 and a SEM picture taken after the measurements. 64
8.3. (a) Mobility versus charge carrier concentration. (b) Color coded resistance versus back gate voltage and magnetic field. 64

9.1. Hall potential profiles across the middle of the flake on sample GB8113. 68
9.2. Fitting of the Hall potential drops measured at sample GB8113 with the CSG-formula (4.3). 69
9.3. Change of incompressible stripe position for n-type graphene. 71
9.4. Change of incompressible stripe position for p-type graphene. 72
9.5. Equipotential and force lines for a semi-infinite plane parallel to a infinite plane as calculated by Maxwell [140]. 73
9.6. Effect of the back gate simulated and compared to Maxwell's calculation [140]. 74
9.7. Simulated cross-section to study the influence of the back gate. Color coded is shown the potential in addition to equipotential lines. 75

9.8. Charge carrier density towards the graphene edge simulated for a fixed negative line charge at the edge. 76
9.9. Model for a homogeneous area charge arrangement. 77
9.10. Possible arrangements/positions for fixed charges. 79
9.11. Simulated cross-section to study fixed negative line charges at the graphene edges. Color coded is shown the potential in addition to equipotential lines. 80
9.12. Fit of the incompressible stripe position to our data with a line charge approach. 81
9.13. Fit of the incompressible stripe position to our data with a surface charge approach. 82
9.14. Simulated cross-section to study surface charges at the graphene edge. Color coded is shown the potential in addition to equipotential lines. . 83
9.15. Charges in thermally grown silicon dioxide on silicon, adapted from [167]. 86
9.16. Profile of the charge carrier distribution across a graphene flake as derived from the fits on the data. 88
9.17. Charge carrier concentration and resistivity found with our model. . . . 91
9.18. Back gate voltage value for the bulk charge neutrality point $V_{\mathrm{B-CNP}}$ (equation (9.19)) and the resistance maximum V_{Rmax} (minimum of equation (9.25)), both versus the flake width. Also the distance between V_{Rmax} and $V_{\mathrm{B-CNP}}$ is visible. 92
9.19. Effect of the threshold density n_t on $V_{\mathrm{Rmax}} - V_{\mathrm{B-CNP}}$. 93

10.1. (a) Topographic scan and (b) SEM image of the flake GB9438a. The SEM picture was taken after the measurements. The X,Y,Z coordinate system is the one of the scanning tube and is rotated around the Z axis to form the x, y, z-coordinate system of the flake. 96
10.2. SEM pictures taken at an angle of 45 °on the flake GB9438a to identify bumps and schematic of the flat flake regions. 96
10.3. Sensitivity and resonance frequency shift scans of the flake GB9438a. . 97
10.4. Hall potential profiles for the flake GB9438a. 98
10.5. Comparison of Hall potential profiles for flake GB9438a for magnetic field of (a) 5 T and (b) −5 T. 99
10.6. Incompressible stripe position when a surface charge density of $3 \cdot 10^{16}\,\mathrm{em}^{-1}$ is assumed. Data from Fig.. 10.4 (a). 100
10.7. Area scans on flake GB9438a demonstrating the presence of domains with QHE evolution as expected from usual unsegmented flakes. 101
10.8. SEM picture of the flake GB9438b. The picture was taken after the measurements. The scanned edge was the one on the left. 102
10.9. Scheme of flake edge and color coded Hall potential profiles for flake GB9438b which is fragmented in domains with different mean charge carrier concentration. 103
10.10. Lines of the Hall potential profiles around $\nu = 2$ for flake GB9438b. . . 104
10.11. Hall potential profiles for flake GB9438b and the position of incompressible stripes assuming a surface charge density of $1 \cdot 10^{17}\,\mathrm{em}^{-2}$. 105

12.1. Two biasing schemes for characterizing the breakdown of the QHE. (a) current biasing and (b) voltage biasing. 114
12.2. Landau level bending under high electric field along y-direction: Shown are the highest occupied and lowest unoccupied Landau level and possible inter Landau level transitions. 118

13.1. Sketch of the Hall bar geometries used for the sample characterization. 121
13.2. Longitudinal voltage drop over sample voltage for all potential scans on sample 8379_201001_B. 123
13.3. Color-coded absolute longitudinal voltage drop over magnetic field and bias voltage. 124
13.4. Biasing scheme for the two current directions (i) and (j) and the calibration measurement (n). 125
13.5. Color-coded Hall potential profiles over bias voltage and position for a magnetic filed of 5.5 T to 5.9 T in steps of 0.1 T. 126
13.6. Color-coded Hall potential profiles over bias voltage and position for a magnetic field of 5.97 T to 6.2 T in steps of 0.05 T except of the first step with amplitude of 0.03 T. 127
13.7. Hall potential profiles for a magnetic field of 5.6 T and filling factor $\nu = 2.09$. 129
13.8. Longitudinal voltage drop as a function of sample bias for sample 8957_201112_B and measurement arrangement for area scans. 130
13.9. Area scans on sample 8957_201112_B at a magnetic field of 6.1 T and filling factor $\nu = 2.17$. 131
13.10. Simulations by Gerhardts (similar data published in [102]) showing Hall potential profiles for increasing bias. 132
13.11. Bending of a Landau level during edge-dominated QHE: for zero bias in "light blue" and for finite bias in "black". Relevant voltages and widths are sketched. 132
13.12. Comparison of the asymmetry model with the measurement data. . . . 134
13.13. Landau level structure along the scan direction for the edge-dominated QHE region. 137
13.14. Hall potential profiles for a magnetic field of 6.1 T and filling factor $\nu = 1.92$. 139
13.15. Area scans on sample 8957_201112_B at a magnetic field of 6.8 T and filling factor $\nu = 1.94$. 140
13.16. Taking a small slice of a disorder dominated Hall potential landscape. In a first approximation the profile within this slice can be treated translation invariant. 141
13.17. Self-consistent calculated Hall potential profiles at a translation invariant sample with oscillating donor density, calculations by Gerhardts [228]. 141
13.18. Chosen line-scans out of the area scans that show weak spots. 142
13.19. Hall potential profiles for a magnetic field of 5.9 T and filling factor $\nu = 1.98$. 144

13.20. Data of calibrated Hall potential profiles by Ahlswede et al. [17] close to filling factor $\nu = 4$. 145
13.21. Charge carrier fluctuations near the edges. 146

14.1. Cyclotron emission of two samples at different filling factor by Ikushima et al. [213]. The samples were 3 mm in length and 0.5 mm in width. The magnetic field was in both cases 6.14 T. Reprinted with permission from [213]. Copyright (2014) by the American Physical Society. 148
14.2. Hall resistance over magnetic field for a gate-defined Hall bar with asymmetric edges taken from [229] and publisched under the creative commons BY-NC-SA licence. The inset shows in more detail the quantum Hall plateaus with filling factor $\nu = 6$ and $\nu = 4$, taken with different bias currents: 2 µA, 5 µA, 10 µA. 149
14.3. Data adapted from Kane et at. [230] demonstrating a collapse of the longitudinal resistance over length traces for the edge-dominated magnetic field regime independent of the sample width. Measurements were done at small currents before the breakdown. The inset shows the sample geometry. Adapted with permission from [213]. Copyrighted by the American Physical Society. 150

A.1. Sample geometries for experiments to shield edge effects. 171
A.2. Sample design to check for width dependence of the resistance maximum. 171
A.3. Landau level scheme for external currents within the incompressible stripe bigger than the persistent current. 173
A.4. (a) arrangement of the static SQUID measurement and (b) actual sample design. 174

B.1. Sketch of the self-consistent loop. 177
B.2. Schematic geometry of the calculated area. 178
B.3. Labeling of grid positions and physical quantities for the Poisson solver. 180
B.4. (a) Charge arrangement and simulated area. (b) Geometry for the calculations of the electric field $\vec{E}(r)$ of a line charge q. 181
B.5. Comparison between simulation and analytic solution of a single line charge. 183
B.6. Calculation scheme for finding the charge carrier concentration. 184
B.7. Labeling of points on the graphene flake. 185
B.8. Conformal mapping of the half-plane with positive real part in (a) by $f(x + iy) = (x + iy)^{1.5}$ resulting in (b). The equipotential and force lines keep their meaning after the transformation. 186
B.9. Geometry solved by Maxwell and definition of the local coordinate system. 187
B.10. Plot of the solution to a finite parallel plate capacitor described by equation (B.31) and (B.32). 188
B.11. (a) Real geometry with dielectric and (b) equivalent geometry without dielectric but scaled distance d/ϵ_r. 189

B.12. Comparison between Maxwell's charge carrier density from equation (B.40) and the simulation results. 190

C.1. Simulation of fixed line charge fitted with a y^{-2} function 194
C.2. Effect of line charge displacement from the graphene flake edge. 196
C.3. Definition of the Gauss volume (a) and position of the doping layer as well the directions of electric fields. Geometry used in the simulation (b). 197
C.4. Influence of doping on the graphene flake. 198
C.5. Simulation with fixed surface charges fitted with a y^{-1} function. 199
C.6. Testing with superposition of surface charges doping and back gate. . . 200

D.1. Data from Erik Ahlswerde [17] compared with the Chklovskii, Shklovskii and Glazman (CSG) model [92], black lines and no free parameters, and fitted with the line charge model, white lines. We thank Erik Ahslwede for the access to his data to create this plot. . . . 204

G.1. Transformation of a sine excitation via the resonance shift parabola. . . 214
G.2. Transformation of a rectangular excitation via the resonance shift parabola. 215
G.3. Effect on noise on measurements with a lock-in amplifier. 217
G.4. Topography related artefact measured on sample 8379_20100120_B . . 217
G.5. Sensitivity, curvature and position of maximum for the resonance frequency parabola. 219
G.6. Current induced artefacts. 221
G.7. Measurement of Hall potential profiles on a GaAs/Al$_x$Ga$_{1-x}$As-heterostructure sample as function of position and source-drain bias with several types of artefacts. 222
G.8. Determination of scaling factor and proof of linearity by adjusting three transport curves. 223
G.9. Measurement before the resistance maximum shift of sample GB8113. . 224
G.10. Sensitivity map over the measured back gate voltage and position range. Low sensitivity areas are shown in dark blue and artifacts can be expected. The light blue areas is not as critical but still lightly affected. 225

H.1. Macro picture of the sample with the graphene flake GB8113. 229
H.2. Macro picture of the sample with the graphene flakes GB9438a and GB9438b mounted on a chip carrier. 230
H.3. Final design of our GaAs/Al$_x$Ga$_{(1-x)}$As-heterostructure samples. 231
H.4. Optical microscope picture of sample 8379_20100120_B. 233
H.5. Macro picture of sample 8957_201112_B mounted on a chip carrier (a) and optical microscope picture of the scaned Hall bar and its surroundings (b). 234
H.6. (a) Determination of the magnetic field $B|_{\nu=1}$ for filling factor $\nu = 1$ by fitting the longitudinal resistance minima of sample 8379_20100120_B shown in Fig. H.7. In (b) we show a TLM (transmision line measurement) trace by wich one can get the sheet resistance of the 2DES at zero field R_{2DES}. 235

H.7. 2-point resistance of the scanned Hall bar in red and longitudinal resistance of the transport Hall bar in blue of sample 8379_20100120_B. The black line is a fit to determine the magnetic field $B|_{\nu=1}$ for filling factor $\nu = 1$. Nevertheless we prefer to take the value determined from the minima in the longitudinal resistance given in Fig. H.6. 236
H.8. Determination of the charge carrier density (a) and mobility (b) of sample 8957_201112_B. In (b) only the easy direction was used for the mobility determination since the hard direction is affected strongly by the contact resistance. 237

I.1. Used scanning tips in different stages of fabrication and different magnification. 240

List of Tables

C.1. Summary of fit functions for the free charge carrier profile η at the edge of the graphene flake caused by doping, applied back gate voltage, the presence of a line charge distribution at the edge or surface charges beside the graphene flake. 201

H.1. Overview of the three graphene flakes with the parameters mobility μ, the full width at half maximum of the resistance over back gate voltage trace ΔV_{FWHM}, and the charge carrier density variation $\Delta\eta$ within ΔV_{FWHM}. . 228

I.1. Parameter summary of the used SII tips PRC400 according to the datasheet. 239

Acknowledgment

Prof. Dr. Klaus von Klitzing gave me the great opportunity to join his group and allowed me to work under excellent working conditions. I acknowledge most that he enabled my study on fundamental physical questions even though it was clear that the scientific community is already looking far ahead of the questions here. In addition his questions pushed this thesis further. The model for the current partitioning during the edge-dominated breakdown has to be emphasized here. Even though Prof. Dr. Rolf Gerhardts together with me worked out all basic assumptions it was only him who managed to do the final step!

I also want to gratefully thank Prof. Dr. Peter Michler and Prof. Dr. Alejandro Muramatsu who both found time within their busy schedules to read and evaluate my thesis.

A major thanks goes to Prof. Dr. Jürgen Weis who was my supervisor throughout this thesis. With his safe and strong foundation for theoretical and experimental questions discussions became always an exciting challenge. The smooth course during my thesis was because of him. Also the quality of the present manuscript was increased dramatically due to his suggestions.

Stefan Falk introduced me to this topic and motivated me to extend my diploma to a PhD thesis. It was always a great pleasure to discuss about problems and topics beyond physics.

I want to thank also Dr. Peter Weitz, Dr. Erik Ahlswede and Dr. Franck Dahlem who finished their thesis on this measurement technique even before I had started. But they could help me a lot on detailed questions about the measurement technique.

Upon the breakdown results

The one who fixed the significance of my breakdown data was Dr. Franck Dahlem. He gave me with his experience the necessary certainty at a time where no clear interpretation and understanding of my breakdown results was present.

Prof. Dr. Rolf Gerhardts with his simulations was the key for the presented model. Discussions with him brought me further than the literature could do, especially because he could explain with his theoretical model features not even mentioned in the literature.

Of course I want to thank Prof. Dr. Werner Dietsche for giving me the wafer materials for this study. His support helped me a lot to overcome material related problems and his knowledge of the breakdown of the QHE was always inspiring. In this context I also want to thank Maik Hauser for doing the actual MBE growth.

There were also valuable discussions with Dr. Afif Siddiki and his group. I wish him especially a good start with his tavern.

Upon the graphene measurements

Special thanks goes here to Dr. Benjamin Krauß who took his time besides his thesis to prepare samples and discuss about the results.

Also Dr. Jurgen Smet and Patrick Herlinger helped me out a lot, especially for the presentation of the data and the interpretation in terms of the substrate.

Dr. Timm Lohmann was one of the first I discussed with about graphene and I want to thank him for his differentiated view.

Of course there were more valuable discussions about graphene especially with other members of the Smet group.

Samples fabrication

Achim Güth and Marion Hagel from the cleanroom facility helped out a lot by fabricating the heterostructure samples. The time boost was invested first in the measurement technique and later in the theoretical understanding. There was also lots of support on questions about sample design. And not to forget: nearly all of my samples were bonded by Marion Hagel.

Monika Riek introducing me to the cleanroom facility and helped me to create the first sample designs. I also want to thank Bernhard Fenk for letting me work on "his" FIB (focused ion beam).

Dr. Jochen Weber passed me his recipe for SET (single electron transistor) arrays. This gave me the opportunity to learn about electron beam lithography and FIB fabrication techniques. Even though far beyond the scope of my thesis it was a great experience to get involved in such a complex fabrication process with many different processing tools.

Scanning tip processing

Thomas Reindl was especially helpful for the final tip processing. His idea of using ALD (atomic layer deposition) improved the processing time dramatically. He also carried out the ALD and evaporation steps. Thomas Reindl was in addition a big help on any problem in the cleanroom.

Sample holder and other technical issues

Whenever there was a technical issue on my sample holder or my cryo system our technicians Gunther Euchner, Steffen Wahl, Ingo Hagel and Manfred Schmid had a helping hand. Special thanks also for helping out on problems not related to the cryo system and my sample holder! Dr. Sven Jamecsny, a former group member, had always inspiring ideas also beyond the technical level. Konrad Lazarus took the wonderful task of realizing a PLD control system in the department of Prof. Mannhart and prevented me that way from thinking seriously about applying for this job.

Beyond physics

The discussion and application of interactive decision theory within the institutes, especially with René Berktold, Stefan Falk, Andreas Gauß, Dr. Maximilian Köpke, Marcel Mauser, Leonhard Schulz, Claudia Stahl, Thomas Reindl, and Dr. Jochen Weber was an inspiring experience I enjoyed a lot.

Special thanks to Andreas Gauß for his suggestion of a logo for this thesis which made it on the spine of the printed version.

Thai Hien Tran, Sarah Parks, and Renate Zimmermann checked parts of my theses concerning spelling and grammar. Thank you for significant improvements!

Great thanks to all "Weis guys" as well as the members of the von Klitzing and Mannhart group for wonderful professional and private discussions and for the excellent working atmosphere. Beyond all freedom, expertise and modern facilities the institute can offer, its people made my time in the institute an extraordinary experience.

Curriculum Vitae

Personal data

Name:	Konstantinos Panos
Date of birth:	16.08.1983
Place of birth:	Reutlingen (Germany)

Education

1989-1998	Greek elementary and grammar school
1991-2003	German elementary, secondary modern and technical grammar school
2003	Abitur (general qualification for university entrance)
2003-2009	Study of Physics at Universität Stuttgart
2006-2007	Exchange to the Hong Kong University of Science and Technology for two semesters under a grant of the Baden-Württemberg Stiftung
2009-2014	PhD study at the Max Planck Institute for Solid State Research

Scientific contributions

2010	19th Int. Winterschool in Mauterndorf, Austria (Poster)
2011	NanoResonance2011 in Blaubeuren, Germany (Talk)
2011	EP2DS19 in Tallahassee, USA (Poster)
2012	HMF20 in Chamonix, France (Talk)
2012	ICPS2012 in Zürich, Switzerland (Poster)
2013	QHE2013 in Büsnau, Germany (Poster)

Working experience

2003-2006	Student assistant for the design and programming of embedded systems at VEGAS Universität Stuttgart.